HRVATSKO DRUŠTVO
ZA STROJARSKE TEHNOLOGIJE

CROATIAN SOCIETY
FOR MECHANICAL TECHNOLOGIES

In association with:

University of Split
Faculty of Electrical Engineering, Mechanical Engineering and Naval Architecture

Slovak Academy of Science
Institute of Materials and Machine Mechanics

University of Split
University Department of Professional Studies

Croatian Society for Materials and Tribology

Dublin Institute of Technology

Rogante Engineering Office

ISSN 1847-7917

12th International Conference

Mechanical Technologies and Structural Materials 2023

General sponsors:

University of Split - FESB
The City of Split,
EVN Croatia Plin d.o.o.
Tourist Board of Split

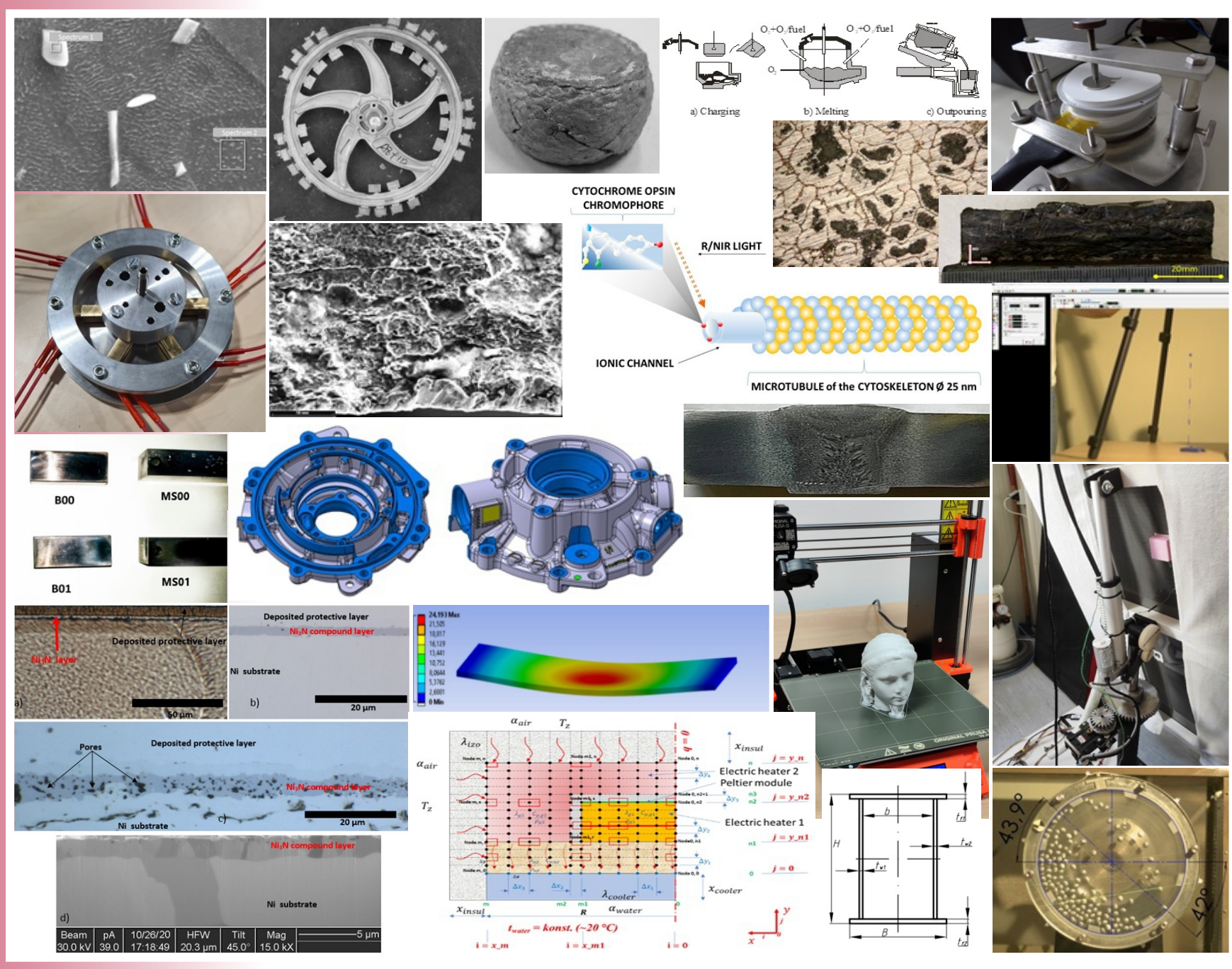

http://www.strojarska-tehnologija.hr

September, 21st - 22nd, 2023.
FESB, Ruđera Boškovića 32, Split

CONFERENCE PROCEEDINGS

MECHANICAL TECHNOLOGIES AND STRUCTURAL MATERIALS

Split

Croatia

21 - 22 September 2023

ORGANIZED BY:

CROATIAN SOCIETY FOR MECHANICAL TECHNOLOGIES, Croatia

CO-ORGANIZERS:

UNIVERSITY OF SPLIT
FACULTY OF ELECTRICAL ENGINEERING, MECHANICAL ENGINEERING AND NAVAL ARCHITECTURE

CROATIAN SOCIETY FOR MATERIALS AND TRIBOLOGY

DUBLIN INSTITUTE OF TECHNOLOGY

SLOVAK ACADEMY OF SCIENCE INSTITUTE OF MATERIALS AND MACHINE MECHANICS

ROGANTE ENGINEERING OFFICE

UNIVERSITY OF SPLIT
UNIVERSITY DEPARTMENT OF PROFESSIONAL STUDIES

SPONSORS:

University of Split - FESB

CITY OF SPLIT

EVN CROATIA PLIN d.o.o.

TOURIST BOARD OF SPLIT

PUBLISHER:

CROATIAN SOCIETY FOR MECHANICAL TECHNOLOGIES, Croatia

HRVATSKO DRUŠTVO ZA STROJARSKE TEHNOLOGIJE, Hrvatska

c/o FESB, Ruđera Boškovića 32, 21000 SPLIT

tel.: +385 21 305 910; fax.: +385 21 463 877

e-mail: info@strojarska-tehnologija.hr

http://www.strojarska-tehnologija.hr

EDITORS:

PhD Nikola Gjeldum, Associate Professor
PhD Nikša Čatipović, Assistant Professor
PhD Marko Mladineo, Assistant Professor

ISSN 1847-7917

ISSUE: 60

ORGANIZING COMMITTEE:

- Jure KROLO (Croatia) - Chairman
- Marina CRNJAC ŽIŽIĆ (Croatia) - Vice Chairman

- Igor BOŠNJAK (Bosnia and Herzegovina)
- Nikša ČATIPOVIĆ (Croatia)
- Domagoj KOJUNDŽIĆ (Croatia)
- Amanda ALJINOVIĆ (Croatia)
- Andrej BAŠIĆ (Croatia)
- Ivana DUMANIĆ (Croatia)
- Igor ĆULUM (Croatia)
- Nikola GJELDUM (Croatia)
- Karla GRGIĆ (Croatia)
- Jaroslav JERZ (Slovakia)
- Sonja JOZIĆ (Croatia)
- Branimir LELA (Croatia)
- Petar LJUMOVIĆ (Croatia)
- Ivan PEKO (Croatia)
- Massimo ROGANTE (Italy)

PROGRAMME AND SCIENTIFIC COMMITTEE:

- Dražen ŽIVKOVIĆ (Croatia) – President
- Dražen BAJIĆ (Croatia) – Vice President

- Boris ANZULOVIĆ (Croatia)
- Frane BARBIR (Croatia)
- Goran CUKOR (Croatia)
- Lidija ĆURKOVIĆ (Croatia)
- Natalia DOLIĆ (Croatia)
- Nikola GJELDUM (Croatia)
- Mirko GOJIĆ (Croatia)
- Krešimir GRILEC (Croatia)
- Senka GUDIĆ (Croatia)
- Fuad HADŽIKADUNIĆ (Bosnia and Herzegovina)
- Dario ILJKIĆ (Croatia)
- Vinko IVUŠIĆ (Croatia)
- Zlatko JANKOSKI (Croatia)
- Jaroslav JERZ (Slovakia)
- Sonja JOZIĆ (Croatia)
- Zoran JURKOVIĆ (Croatia)
- Erol KAM (Turkey)
- David KENNEDY (Ireland)
- Borut KOSEC (Slovenia)
- Darko LANDEK (Croatia)

- Juraj LAPIN (Slovakia)
- Branimir LELA (Croatia)
- Cândida MALÇA – Portugal
- João MALÇA - Portugal
- Dragan MARINKOVIĆ (Germany)
- Aleš NAGODE (Slovenia)
- Zoran PANDILOV (Macedonia)
- Mladen PERINIĆ (Croatia)
- Massimo ROGANTE (Italy)
- Liane ROLDO (Croatia)
- Zdravko SCHAUPERL (Croatia)
- Claudio SANTELLI (Italy)
- František SIMANČIK (Slovakia)
- Božo SMOLJAN (Croatia)
- Nikolay STOIMENOV (Bulgaria)
- Goran ŠIMUNOVIĆ (Croatia)
- Katica ŠIMUNOVIĆ (Croatia)
- Amra TALIĆ-ČIKMIŠ (Bosnia and Herzegovina)
- Matej VESENJAK (Slovenia)
- Ladislav VRSALOVIĆ (Croatia)
- Ivica VEŽA (Croatia)
- Anatoliy ZAVDOVEEV (Ukraine)
- Zdenka ZOVKO BRODARAC (Croatia)

Mechanical Technologies and Structural Materials MTSM2023

CONTENT

Biomanufacturing strategies towards bone and cartilage tissue regeneration

Carla Moura[1]

1) Polytechnic Institute of Coimbra, Applied Research Institute, Rua da Misericórdia, Lagar dos Cortiços – S. Martinho do Bispo, 3045-093 Coimbra, Portugal.

Corresponding author: carla.moura@ipc.pt

ABSTRACT

The human body presents some regenerative capacity upon trauma or diseases. However, its regenerative capacity is limited. This regeneration rate and capability also depend on the tissue type and patient health. Despite strategies developed, there is no complete solution to critical-size defects so far. This way appears a new field, Tissue Engineering (TE), which provides solutions by designing bioengineered implants. TE is important to bone and cartilage since it offers potential solutions for repairing or regenerating damaged or diseased tissues. It provides strategies to create biocompatible scaffolds that mimic the native tissue architecture and proper biochemical cues to guide cell behaviour. By creating engineered tissues that closely resemble native bone or cartilage, it becomes possible to restore mechanical strength and range of motion, leading to improved quality of life. Moreover, through the use of additive manufacturing techniques, also called biomanufacturing or biofabrication, it is possible to tailor the temporary implant to each individual patient's needs. TE also uses platforms or specialised systems (bioreactors) to enhance tissue growth through a controlled environment (temperature, oxygen levels, nutrient supply, and mechanical stimulation). By creating these devices, researchers can gain insights into the mechanisms underlying bone and cartilage disorders, test the efficacy and safety of new drugs or treatments, and develop more effective therapies.

BIOGRAPHY

Dr. Carla Moura is an assistant researcher at the Institute of Applied Research (I2A) of the Polytechnic Institute of Coimbra since November of 2022. She obtained her PhD from the MIT-Portugal Program in Bioengineering (2016). Moreover, she has a Master's Degree in Product Development (2011) and a degree in Biomechanics (2008), both from the Polytechnic Institute of Leiria. She works in the fields of medical biotechnology, bioengineering and biomaterials. Her research activity focuses on Tissue Engineering, especially on the manipulation of biomaterials using mainly Additive Manufacturing Techniques combined with cells, such as mesenchymal stem cells. Over the last years, she was part of several research projects, such as Biodiscus project [CENTRO-01-0247-FEDER-039969], Stimuli2Bioscaffolds [PTDC/EME-SIS/32554/2017], OptiBioScaffold [PTDC/EME-SIS/4446/2020] and InSilico4OCReg [PTDC/EME-SIS/0838/2021].

- LinkedIn: www.linkedin.com/in/carla-moura-aab56a25
- Research Interest: Tissue Engineering and Regenerative Medicine, bioengineering, biomaterials, bioreactors and additive manufacturing

Cognitive manufacturing – one model

Prof. Dr. Vidosav D. Majstorović[1]

1) University of Belgrade, Faculty of Mechanical Engineering, Belgrade, Serbia

Corresponding author: vidosav.majstorovic@gmail.com

ABSTRACT

Digital manufacturing technologies are already represented in production and industry and have become the basis for the application of the Industry 4.0 model in practice. The transformation marked by the Industry 4.0 model has applied a wide range of communication technologies, mechanisms for connecting machines and parts in the factory and the possibility of big data analysis with the use of artificial intelligence tools. These technologies provide powerful tools to create more flexible and profitable data-driven manufacturing processes using the Internet. As more and more factories and their equipment are equipped with IoT, the volume of data will only grow. Conventional computing is faced with demands to increase the amount of memory, the speed of data processing, as well as the accuracy of decision-making after processing that data. For these reasons, a cognitive model must be applied to process, analyze and optimize information. To truly pave the way forward to Industry 4.0 and beyond, manufacturing must evolve into cognitive manufacturing. Cognitive manufacturing fully uses data through systems, equipment and processes in order to have a practical insight into the entire value chain, from design, through manufacturing to operational support. Built on the foundations of IoT and using big data analytics combined with cognitive technologies, cognitive manufacturing achieves key improvements in productivity, quality, efficiency and reliability in the operation of the entire manufacturing environment. This paper presents the results of our research in the development of cognitive manufacturing models.

BIOGRAPHY

Publications / Projects: Published over 550 papers, of which more than 320 are in international journals, collections of international Conferences and books issued by foreign publishers; He has done over 250 projects (domestic, international). It has 55 references to the SCI / WoS list, with 1554 citations, h index - 21. The CIRP GA and CIRP Procedia have 15 references. Main topics: Quality Management, Manufacturing Metrology, Industry 4.0, AI.

Membership: CIRP (International Institution for Production Research), Paris, France (since 1995); IFIP (International Federation for Information Processing), Geneva, Switzerland (since 1998); IFAC (International Federation for Automation and Control), Vienna, Austria (since 1999); IMEKO (International Confederation for Measuring), Budapest, Hungary (since 1998); etc.

Utilizing 3D scanning, optimization, and 3D printing for cultural heritage conservation

***Andrej Bašić*[1], *Marko Mladineo*[1] *and Ivan Jerković*[2]**

1) University of Split, Faculty of Electrical Engineering, Mechanical Engineering and Naval Architecture, R. Boškovića 32, 21000 Split, Croatia

2) University Department of Forensic Sciences, University of Split, Ul. Ruđera Boškovića 33, 21000, Split, Croatia

Corresponding author: andrej@fesb.hr

Professional article

Abstract: The replication of cultural and historical heritage through accurate copies is a significant method for preservation and promotion, but it can often be a time-consuming and costly process. However, the technique of reversible engineering - consisting of 3D scanning, optimization of scanned models, and 3D printing - offers a more efficient and economical approach. This process is especially useful for replicating stone sculptures, which are an important part of cultural and historical monumental heritage.

In this study, one cultural-historical stone sculpture - a head sculpture of Plautilla, the wife of emperor Caracalla, from the first decade of the 3rd century, was scanned and then optimized with adequate CAD software to prepare the model for 3D printing. The 3D scanning resulted in a model with over one million points, which was too detailed and unsuitable for 3D printing, so the model was optimized and simplified to remove unnecessary details. Additional optimization was also done to remove any errors or deformations in the model. This process resulted in curved 3D models of the art sculpture from the cultural heritage of ancient Salona, obtained through the 3D scanning and optimization of the STL model.

Keywords: *3D scanning; model optimization; reversible engineering; FDM 3D printing; DLP printing; cultural heritage*

1. Introduction

Additive manufacturing, often referred to as 3D printing, is indeed considered a ground breaking technology of the 21st century. However, its conceptual roots can be traced back to the late 19th century, specifically in 1859. It is fascinating to note that the foundational ideas for additive manufacturing were laid out long before its practical implementation [1]. For many, the functional purpose of additive manufacturing might still be somewhat unclear, and some might view it as a futuristic concept. Yet, for those deeply involved in the industry, its revolutionary potential is evident. This revolutionary aspect lies in its ability to provide unparalleled design freedom, transform product development processes, and yield substantial cost savings, including raw material savings [1]. In light of these profound transformations that it brings to manufacturing and production processes, additive manufacturing can rightfully be regarded as the driving force behind what many consider the fourth industrial revolution. This "fourth industrial revolution" is characterized by the fusion of digital technologies, data analytics, and physical systems, fundamentally changing the way we manufacture goods and products. The potential of additive manufacturing is immense, and it continues to evolve, offering new possibilities and reshaping industries across the globe [1].

The commercial use of additive manufacturing (AM) began in 1987 with the introduction of stereolithography by 3D Systems. Stereolithography is a pioneering AM process that involves solidifying thin layers of ultraviolet (UV) light-sensitive liquid polymer using a laser. This innovative

technology marked the dawn of a new era in manufacturing and prototyping [2]. Stereolithography and the SLA-1 were instrumental in shaping the landscape of modern additive manufacturing, enabling rapid prototyping and the creation of intricate three-dimensional objects with precision and speed [2]. Today, besides stereolithography, there are various techniques and technologies available for 3D printing, each with its own unique advantages, applications, and limitations. Some of these techniques are: VAT Polymerisation which includes Stereolithography (SLA), Digital light processing (DLP), Continuous digital light processing (CDLP); Melt Extrusion (ME), which uses thermoplastic materials for 3D printing and the commonly used technique – Fused deposition modeling (FDM); Material jetting (MJ), that includes Nanoparticle jetting (NPJ), Drop on demand (DOD); Binder jetting (BJ); Powder bed fusion (PBF), that includes Multi jet fusion (MJF), Selective laser sintering (SLS), Selective laser melting (SLM), Electronic beam melting (EBM), Direct energy deposition (DED), that includes Lens engineering net shape (LENS), etc. [2, 3, 4 and 5].

In this article, the emphasis will be on two different 3D printing technologies, Fused deposition modeling – FDM and Digital light processing – DLP, which, apart from the technology itself, differ in terms of material and final product. FDM is a very widely used and very cost-effective technology. In this technology, a continuous wire-shaped thermoplastic filament is fed into the 3D printer. Inside the printer's extruder, the filament is heated to its melting point, turning it into a semi-liquid state. The extruder nozzle is responsible for precisely depositing this molten material onto the build platform [5, 6]. The advantage of FDM 3D printing is that the process is relatively fast and straightforward, and it can produce very precise and high-quality parts. It does not use a laser beam, there are no special requirements for cooling and ventilation, so the energy consumption is also lower. This 3D printing process allows a wide variety of materials to be printed and can be used to produce different parts and products. However, one of the disadvantages of FDM 3D printing is that layers of material can be visible in the finished product, which can limit some applications. Also, some materials can be challenging to process in FDM 3D printing, which requires greater accuracy and control of printing parameters [5, 6, 7 and 8]. FDM 3D printing uses thermoplastic materials, such as PLA (Polylactic Acid), ABS (Acrylonitrile Butadiene Styrene), PETG (Polyethylene Terephthalate Glycol), Nylon, ASA (Acrylonitrile Styrene Acrylate), Polycarbonate (PC), TPU (Thermoplastic Polyurethane), PVA (Polyvinyl Alcohol) and many others. Each material has unique properties and use cases, allowing for a wide range of applications in FDM 3D printing [7, 8, 9 and 10].

Digital light processing – DLP, as part of VAT Polymerisation 3D printing, has become a very widely and popular technique. DLP printer uses a digital light processing chipset that contains thousands or even millions of micromirrors (DMD) to project patterned UV light layer images onto the photocurable material, curing each individual layer to achieve a precise shape [11, 12]. In the realm of DLP printing, every individual layer takes shape through a single, all-encompassing exposure. The unique arrangement within a single layer can be resized to an extremely diminutive scale, typically ranging from 20 to 50 µm, contingent upon the capabilities of the optical system. The entire digital model is constructed in a stepwise fashion, one layer at a time [11, 12]. As a result, the layer-curing approach employed in DLP printing yields superior efficiency and precision compared to alternative 3D printing methodologies. Furthermore, DLP technology is characterized by its free-form capability, eliminating the necessity for support structures when producing hollow or porous components [11]. Due to its ability for free-form fabrication, exceptional fidelity to desired shapes, and accelerated printing speeds, DLP printing has found extensive applications in areas such as tissue engineering, drug delivery systems, implantation, and the reconstruction of cultural heritage, owing to its remarkable attributes [11, 13]. However, it is worth noting that this technology does come with certain limitations, particularly in terms of material selection. Presently, the predominant materials of choice are photopolymers, which can be relatively costly and susceptible to degradation from light and heat if not stored according to recommended guidelines [14].

2. Materials and methods

The utilization of 3D technologies has been an enduring trend in the realm of cultural heritage preservation and presentation. These technologies encompass digitization, augmented reality, virtual reality, and 3D printing. Their growing prevalence exerts a profound influence on the cultural heritage domain. While a substantial body of research concentrates on the technical dimensions of 3D technologies, a comparatively smaller subset delves into critical areas like restoration and conservation.

The aim of this work is to apply the technology of 3D scanning and printing on a sculpture given by the Museum "Dom kulture Zvonimir" in Solin, Croatia. The sculpture represents one of two heads believed to depict the tragic princess and Caracalla's betrothed, the later empress Fulvia Plautilla (Figure 1.), dating from the first decade of the 3rd century [15]. A portrait of exceptional artistic quality comes from Salona, but without further information about the circumstances of the find [15]. This portrait has so far not been associated with Plautilla, but due to the uncanny similarity of the hairstyle found on the coins with Plautilla's image, whose mintage begins in the year 202, as well as the similarity in facial appearance between that portrait and the coin, it can almost be said with certainty that the marble portrait it really represents that tragic princess. A similar hairstyle can be found on a portrait from the Vatican (Sala dei Busti, 300), and based on a comparison with the images on the money, this portrait is associated with Plautilla [15].

Figure 1. *Head of Plautilla, the wife of Emperor Caracalla, the first decade of the 3rd century*

The sculpture was scanned using the DAVID SLS-3 3D scanner (Figures 1, 2, 3, and 4), which was purchased in 2016 by the HP company and then offered for sale under the new name HP 3D Structured Light Scanner PRO S3, for some time before its withdrawal from the market. It is a scanner that uses structured light to capture the contours, dimensions, and structure of the scanned object [16].

The scanning process begins with the scan head's light source projecting a sequence of parallel black-and-white patterns onto the designated scan target. As these patterns encounter the object's surface, they undergo distortion. Subsequently, specialized cameras capture these distorted patterns and transmit them to the 3D scanning software for further processing and analysis [16].

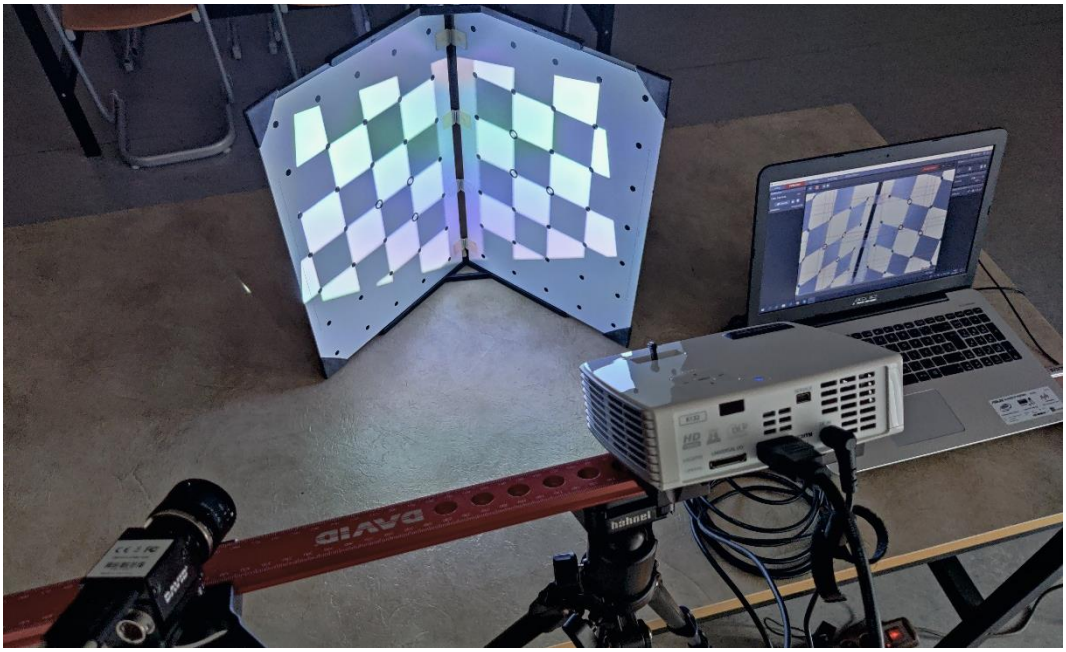

Figure 2. *The image shows DAVID SLS-3 3D Scanner*

Figure 3. *The image shows a scanned head of Empress Plautilla, where each colour represents a different scanned view*

Figure 4. *The image shows texture captured in the 3D scanning process that has been added to the virtual model*

Figure 5. *The image shows a fused virtual model ready for 3D printing*

Following the completion of the fusion process, the resulting model was exported as an STL file. However, before it could be suitable for 3D printing, it required optimization. This was due to the 3D model's complexity, with over 300000 vertices and 600000 triangles, resulting in a file size exceeding 100 megabytes. To prepare the model for 3D printing and address various issues, CAD optimization techniques were applied. These optimizations aimed to simplify the model by removing unnecessary detail that would not be visible on the printed replica. Additionally, the process involved rectifying irregularities introduced both by the 3D scanning process and generic irregularities inherent to the model, which arise because scans cannot perfectly align.

Post-processing of the model was carried out using Autodesk® MeshmixerTM software [17], which offers a number of tools and options for this purpose, such as the "Reduce" tool to significantly reduce the number of points, which achieved a 60% reduction, "Smoother" to remove irregularities from certain surfaces and "Draw" to fill the residual space gaps leftovers after fusing scans into a complete virtual model. The above tools were used as necessary to achieve the necessary refinement of the model.

In summary, this comprehensive post-processing workflow using Autodesk® MeshmixerTM was instrumental in optimizing the 3D model for 3D printing, making it more suitable for the printing process, and addressing various technical challenges associated with complex 3D scans.

After the preparation was completed, the model was ready for 3D printing. The printing process was executed using two distinct technologies, FDM - Fused Deposition Modeling and DLP - Digital Light Processing (Figure 6), with the same resolution so that a detailed analysis of the influence of the set parameters on the final appearance of the model could be carried out. A Prusa Mk3 i3 3D [18] printer was used for the FDM printing process, and an Anycubic Photon M3 [19] resin 3D printer was used for the DLP 3D printing process.

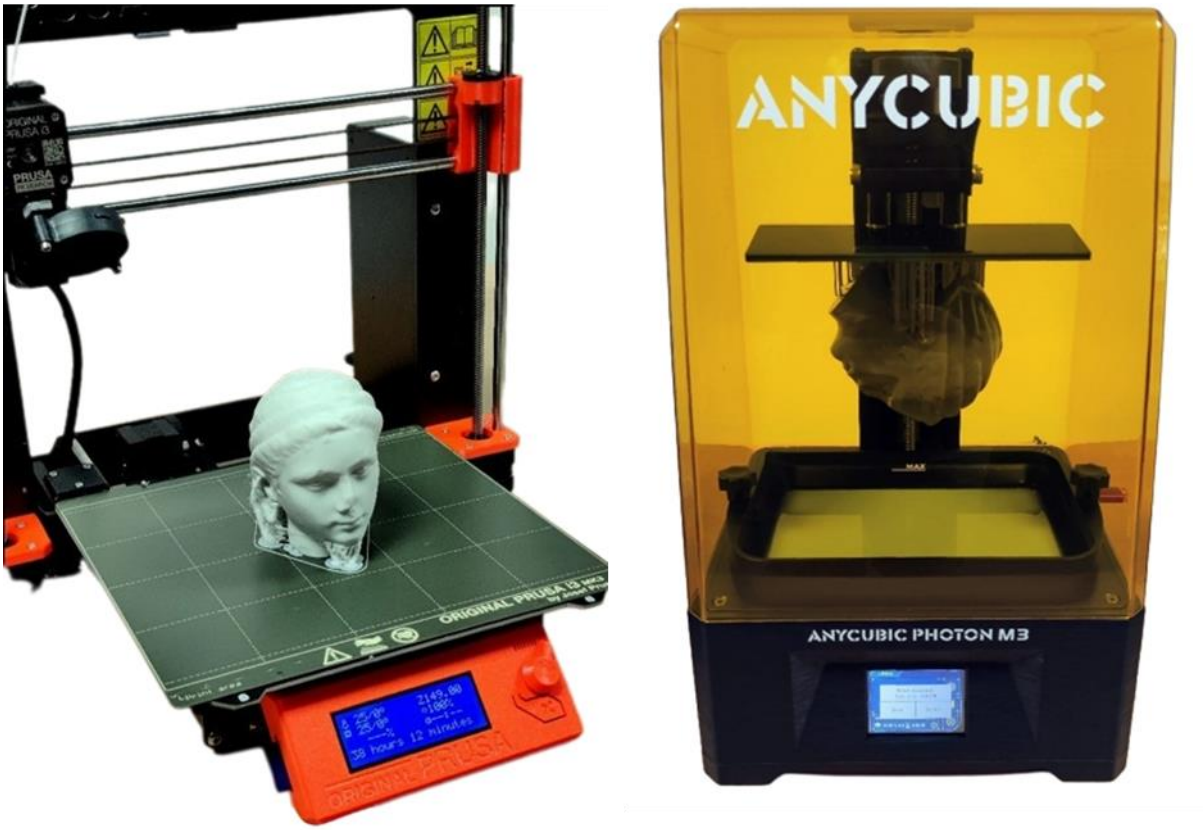

Figure 6. *The image shows a 3D model printed with different types of technologies, left is FDM - Fused deposition modelling 3D printer, and on the right is DLP - Digital light processing 3D printer*

The material used for 3D printing using FDM technology is Facilan™ C8 produced by 3D4Makers [20]. Facilan™ C8 filament is a new biodegradable material, designed to be the optimal material for 3D printing in industrial production. It has a wide range of applications due to its very easy printability, high strength and toughness, easy processing, and fine detail that you can achieve. With higher impact strength compared to PLA, it is the ideal choice for producing robust and durable 3D printed objects. Its ability to 3D print without visible layers ensures that printed creations have a smooth and polished appearance [20]. Its combination of high-impact strength, smooth printing, and exceptional layer adhesion make it a top choice for a wide range of 3D printing applications. The aforementioned properties make it a top choice for a wide range of 3D printing applications, including 3D printing of cultural heritage.

On the other hand, Sensitive UV resin produced by Anycubic was used to print 3D models using DLP technology [21]. Anycubic Sensitive UV resin is a well-engineered resin solution designed to meet the demands of LCD 3D printing. This resin strikes a harmonious balance between various critical factors, such as printing precision, hardness, and fluidity. It ensures that 3D prints not only look great but also possess the necessary strength, all while minimizing excessive shrinkage. One standout feature of this resin is its ability to optimize the 3D printing process. It achieves this by improving print speed and reducing curing times, thereby enhancing overall printing efficiency on LCD machines. This means that one can finish projects faster while maintaining the quality you expect. Anycubic Standard Coloured UV Resin is also highly sensitive to UV wavelengths, particularly in the 365-410 nm range [21]. This makes it an ideal choice for use with Anycubic 3D resin printers, as it is tailored to deliver outstanding results with these machines, as in this case.

Between these two 3D printing technologies, there is also a difference in the approach to the post-processing of the printed 3D model. When it comes to FDM, postprocessing often involves several key steps:

- Support Removal: Since FDM relies on support structures to print overhangs and complex geometries, one of the primary post-processing tasks is the removal of these supports. This can be done manually or with specialized tools (Figure 7).
- Sanding and Smoothing: FDM prints can exhibit visible layer lines due to the layer-by-layer deposition of material. Post-processing may include sanding the printed object and, optionally, applying filler or primer to achieve a smoother surface finish.
- Painting and Finishing: Depending on the desired appearance and functionality of the printed object, additional post-processing steps such as painting, assembly, or adding other finishing touches may be required.

Figure 7. *The image shows support on the figure printed by the FDM 3D printing process from different views*

In contrast, DLP 3D printing often requires less post-processing due to its ability to produce smoother and more detailed surfaces. Key aspects of post-processing for DLP printing include:

- Cleaning: After printing, DLP parts may need to be cleaned to remove any residual uncured resin. This can involve rinsing the object in a solvent or isopropyl alcohol (Figure 8).

- Support Removal (if applicable): Depending on the complexity of the printed object, DLP typically requires fewer supports compared to FDM, they would need to be removed, similar to FDM (Figure 9).
- UV Curing: DLP-printed objects require post-curing under UV light to ensure complete hardening of the resin and to enhance the final mechanical properties. After curing, the surface of the figure is no longer soft and susceptible to mechanical damage (Figure 10).

Figure 8. *The image shows a figure printed using the DLP 3D printing process before treatment with isopropyl alcohol to remove excess resin material from the surface*

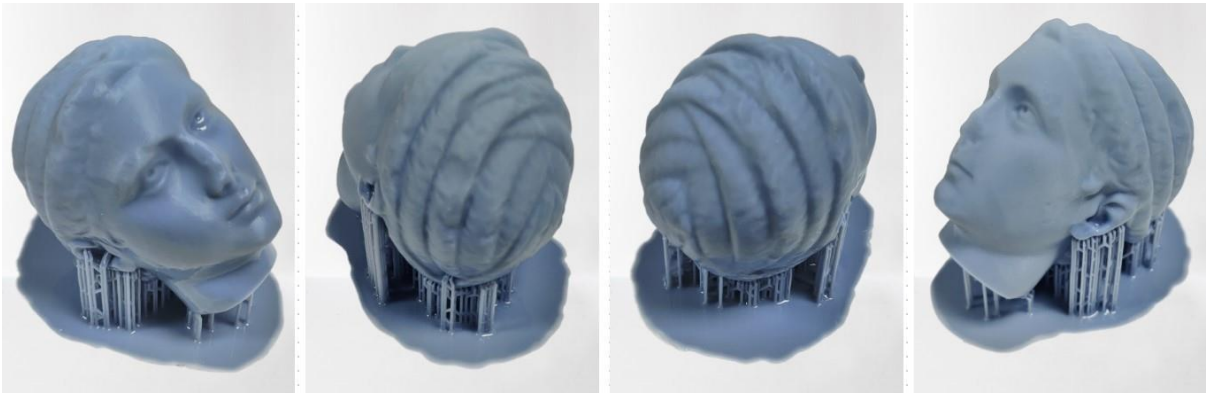

Figure 9. *The image shows the figure after treatment with isopropyl alcohol and a clean surface with supports ready for removal*

Figure 10. *The image shows curing process of the printed 3D model with DLP 3D resin printer*

3. Results

The results of 3D printed models using FDM and DLP 3D technologies are shown in the Figures 11 – 15. On the left is a model printed with DLP technology (grey), and on the right of the photo is a model printed with FDM 3D printing technology (white).

Figure 11. *Front view*

Figure 12*. Side view*

Figure 13. *Top view*

Figure 14. *Back view*

***Figure 15**. Isometric view*

In the comparison photos shown above, both models printed with different 3D printing technologies at the same print resolution appear very similar in terms of the quality of retained detail. However, a closer inspection shows that the model obtained with the DLP 3D printing process has more prominent details than the model printed with FDM technology (Figure 16, 17).

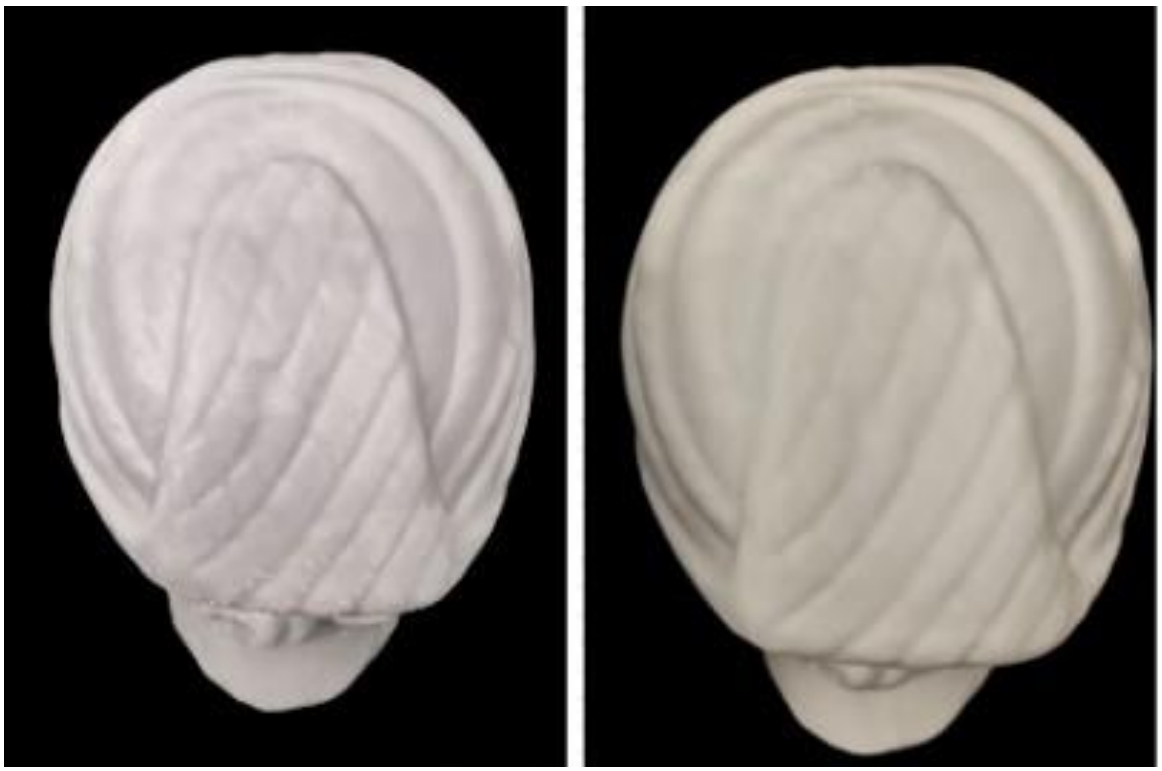

***Figure 16**. A detailed view of the braid on the printed figure, on the left obtained by the DLP process, and on the right by the FDM process of 3D printing*

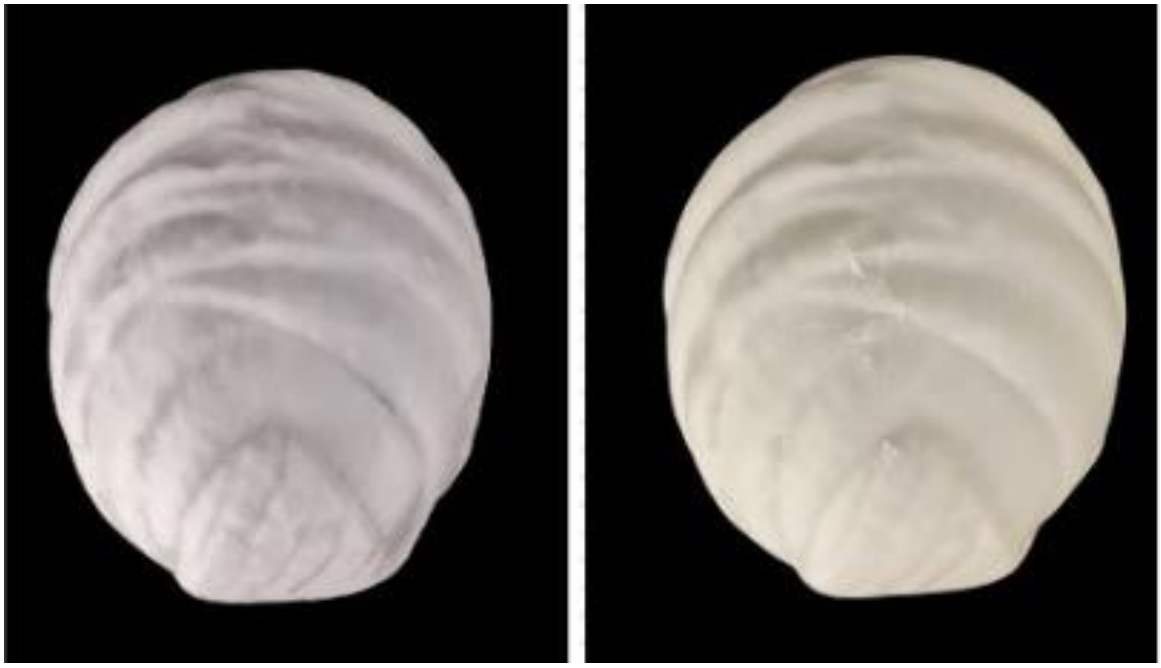

Figure 17. *View of braid details from above, on the left obtained by the DLP process, and on the right by the FDM 3D printing process*

The retention of details is obvious on more complex transitions as well as depressions, which are much more pronounced in models printed with resin using DLP technology. It is also important to mention that the model printed with DLP technology does not require additional mechanical processing, and for this reason, there is no risk that details will be lost during processing, as is the case with the model obtained with FDM technology. The amount of retained details, considering the identical print size of 100x92.20x75.08 mm and a resolution of 50 µm, as well as the quality of the surface, is most noticeable on the resin model, DLP technology (Figures 18 – 20).

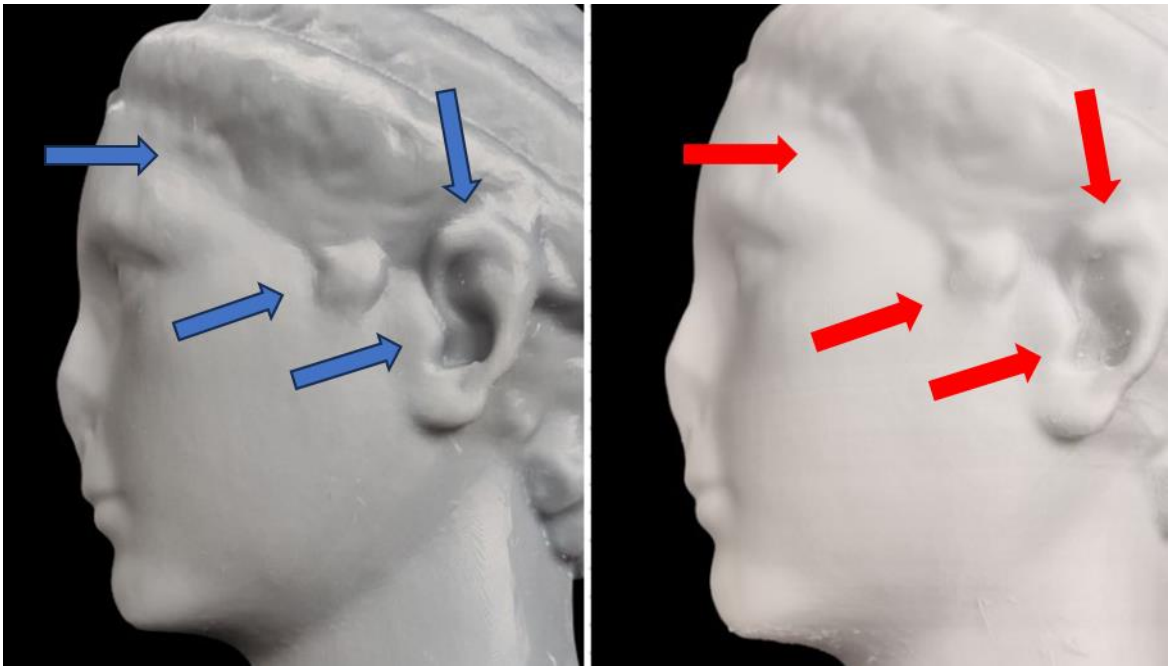

Figure 18. *Left side view with highlighted details, on the left obtained by the DLP process, and on the right by the FDM 3D printing process*

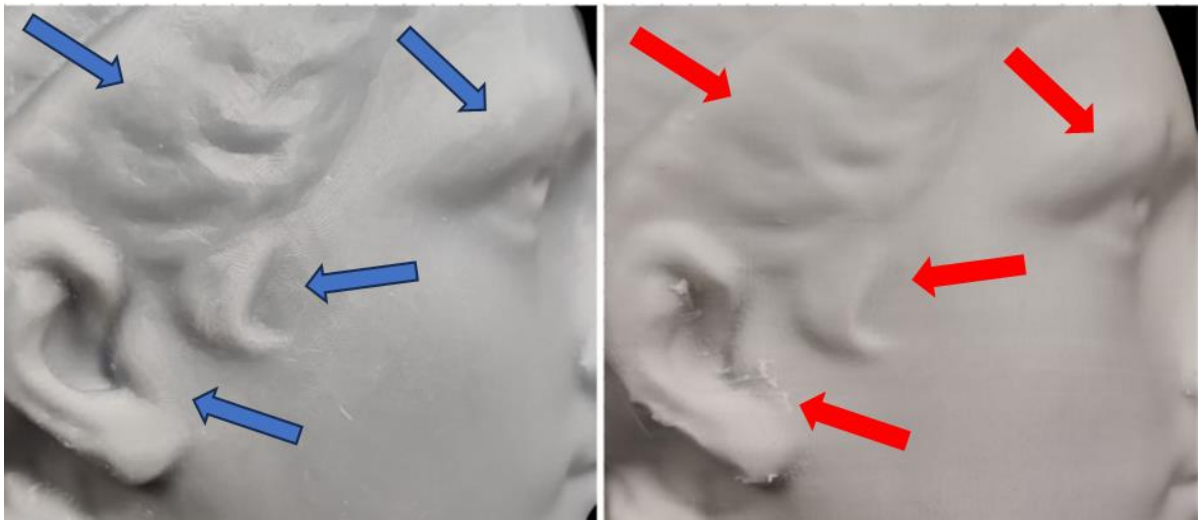

Figure 19. *Right side view with highlighted details, on the left obtained by the DLP process, and on the right by the FDM 3D printing process*

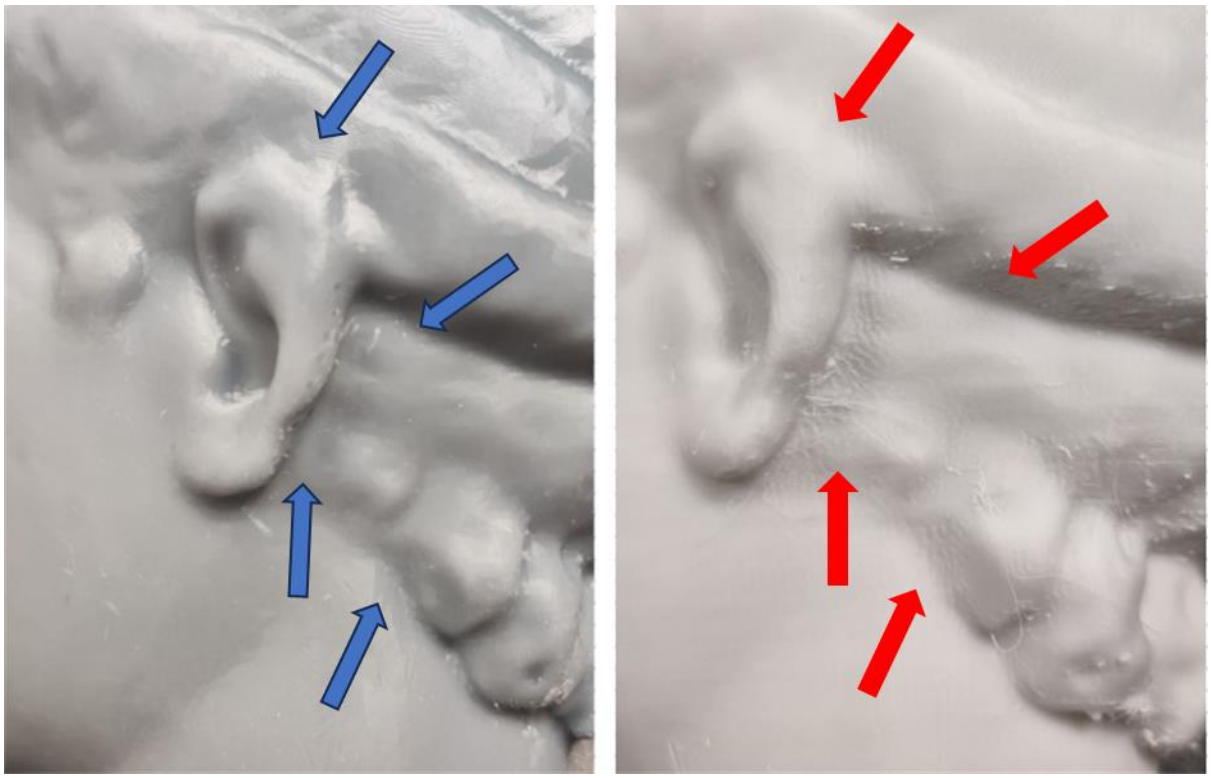

Figure 20. *Highlighted details, on the left obtained by the DLP process, and on the right by the FDM 3D printing process*

It is important to note that given the same print settings as the size of the printed model, the DLP 3D process is remarkably faster than the FDM process. While the DLP process took 7 hours and 33 minutes, the FDM 3D printing process took more than 38 hours. The speed and quality of the printed model are unconditionally in favour of stereolithographic technology, or DLP 3D technology when it comes to printing cultural heritage.

4. Discussion and conclusion

This study presented and critically evaluated two different commonly used technical approaches for 3D scanning and printing processes using the real example of a high-value cultural heritage specimen. Although the number of specimens and sample size generally hampers us for strong conclusions and generalization, it must be considered that the study assessed delicate and time-consuming processes that, with preparation, optimization, and finalization, can last (like in our case) up to 48 hours per specimen to construct the final product. As our study considered the comparison of technologies, features, and quality of the product, as well as process effectiveness and complete workflow, the results could provide new findings to the field and contribute to the process optimization in applying 3D technologies to cultural heritage. The study findings could also open space for further studies that will have an opportunity to include a greater number of cultural heritage artifacts of different properties, as well as various techniques and methodologies. The use of 3D technology has played a crucial role in the preservation and presentation of our cultural heritage. These technologies include not only digitization but also immersive experiences that provide augmented reality, virtual reality, and tangible creations made possible by 3D printing. These innovations significantly reshaped the landscape of cultural heritage, leaving an indelible mark.

It is important to recognize that even before the advent of modern 3D technologies, there were replicas of cultural artifacts. However, modern 3D technologies offer many unprecedented possibilities, including the creation of scaled-down replicas of entire archaeological sites, the establishment of virtual museums, and the provision of downloadable files for 3D printing from the museum's website. The real power of these 3D technologies lies in their inherent digital nature, which facilitates easy sharing, storage, exchange, and transmission. These technologies bridge geographic divides, offering individuals virtual proximity to artifacts located in far-flung corners of the world. While most of the research so far has focused on experts from different backgrounds who are involved in cultural heritage or those who collaborate externally for its improvement [22], it is imperative that we shift the focus to the end users, the general public, and museum visitors. In light of the myriad possibilities these technologies bring, it is our duty to explore how these end users perceive virtual and physical recreations of cultural heritage. Understanding the perspectives and expectations of the general population and museum visitors is essential to effectively communicate information about our rich cultural heritage. Moreover, nuanced research is warranted to understand how end users make connections with the physicality of virtual and tangible replicas. Only in this way can we hope to satisfactorily present cultural heritage to our end users, ensuring that it resonates with them on a deep level.

References

[1] The History of Additive Manufacturing -Timeline, Ireland, 2018. The Irish Examiner https://www.linkedin.com/pulse/history-additive-manufacturing-timeline-clare-moore/ (accessed 05 September 2023).

[2] Wohlers, T., Gornet, T., Mostow, N., Campbell, I., Diegel, O., Kowen, J., Huff, R., Stucker, B., Fidan, I., Doukas, A. and Drab, B., 2016. History of additive manufacturing.

[3] Grimm, T., 2004. User's guide to rapid prototyping. Society of Manufacturing Engineers.

[4] Jacobs, P.F., 1992. Rapid prototyping & manufacturing: fundamentals of stereolithography. Society of Manufacturing Engineers.

[5] Wong, K.V. and Hernandez, A., 2012. A review of additive manufacturing. International scholarly research notices, 2012.

[6] Bašić, A., Mladineo, M., Peko, I. and Aljinović, A., 2018. 3D Scanning, CAD Optimization and 3D Print Application in Cultural Heritage: An Example on Statue from the Ancient Salona. In Mechanical Technologies and Structural Materials; MTSM Conference Proceedings: Split, Croatia.

[7] Peko, I., Krolo, J., Bagavac, P., Đurić, S., Kostić, N. and Bašić, A., 2017. Modeling and optimization of tensile strength of ABS parts manufactured by the fused deposition modeling process. In Mechanical Technologies and Structural Materials; MTSM Conference Proceedings: Split, Croatia.

[8] Basic, A., Peko, I., Krolo, J. and Bagavac, P., 2021. Fuzzy logic modeling of ultimate tensile strength and cost in fused deposition modeling process of additive manufacturing. In International Conference Mechanical Technologies and Structural Materials (pp. 1-10).
[9] Mazurchevici, A.D., Nedelcu, D. and Popa, R., 2020. Additive manufacturing of composite materials by FDM technology: A review.
[10] Swetham, T., Reddy, K.M.M., Huggi, A. and Kumar, M.N., 2017. A Critical Review on of 3D Printing Materials and Details of Materials used in FDM. Int. J. Sci. Res. Sci. Eng. Technol, 3, pp.353-361.
[11] Li, Y., Mao, Q., Yin, J., Wang, Y., Fu, J. and Huang, Y., 2021. Theoretical prediction and experimental validation of the digital light processing (DLP) working curve for photocurable materials. Additive Manufacturing, 37, p.101716.
[12] Wang, Y., Wang, Y. and Mei, D., 2020. Scalable printing of bionic multiscale channel networks through digital light processing-based three-dimensional printing process. 3D Printing and Additive Manufacturing, 7(3), pp.115-125.
[13] Zhou, Y., Aura-Castro, E. and Nebot Díaz, E., 2023. 3D PRINTING TECHNOLOGY AND ITS APPLICATION IN THE CONSERVATION AND RESTORATION OF PORCELAIN. ISPRS Annals of the Photogrammetry, Remote Sensing and Spatial Information Sciences, pp.301-307.
[14] Zhu, G., Hou, Y., Xu, J. and Zhao, N., 2021. Reprintable polymers for digital light processing 3D printing. Advanced Functional Materials, 31(9), p.2007173.
[15] Buzov, M., 2008. Plautilla, sudbina jedne princeze. Archaeologia Adriatica, 2(2), pp.473-488.
[16] https://www.cnc-step.com/3d-scanner-david-sls/ (accessed 05 September 2023).
[17] https://meshmixer.com/ (accessed 05 September 2023).
[18]https://www.prusa3d.com/product/original-prusa-i3-mk3s-3d-printer-kit/(accessed 05 September 2023).
[19] https://www.anycubic.com/products/photon-m3 (accessed 05 September 2023).
[20] https://www.3d4makers.com/ (accessed 05 September 2023).
[21] https://www.anycubic.com/ (accessed 05 September 2023).
[22] Duranti, D., 2017. Tangible interaction in museums and cultural heritage sites: towards a conceptual and design framework.

Application of modal analysis on machine tool for stability lobe diagram generation

***Igor Ćulum*[1], *Sonja Jozić*[1], *Dražen Bajić*[1] *and Luka Celent*[2]**

1) Faculty of Electrical Engineering, Mechanical Engineering and Naval Architecture, Ruđera Boškovića 32, 21000 Split, Croatia
2) Faculty of Technology, School of Mechanical and Design Engineering, University of Portsmouth, Portsmouth PO1 3DJ, UK
Corresponding author: iculum00@fesb.hr

Professional article

Abstract: Machining chatter is a major limiting factor affecting productivity. Machining chatter leads to increased tool wear, surface dimension errors, high surface roughness, increased noise levels etc. Machining chatter has been a topic of research since the 1950s and multiple chatter avoidance methods have been documented. One chatter avoidance technique involves choosing stable cutting parameters such as spindle speed and axial depth of cut. Stability lobe diagrams play a vital role in parameter selection as they graphically show the boundary between stable and unstable cutting parameters. To generate a stability lobe diagram, modal parameters of the machining system must be determined. In this paper, modal analysis is conducted on a machining system consisted of a vertical machining centre, end mill and workpiece to acquire modal parameters of the machining system. Using modal parameters, a stability lobe diagram was generated for an up-milling operation with a 5,77 mm (28.85 % of the tool diameter) radial depth of cut. Nine milling experiments were conducted to test the stability lobe diagram. The tests showed that the diagram was accurate in the stable and unstable regions while inaccuracies in form of chatter were observed at low spindle speeds near the stability limit.

Keywords: *chatter; vibrations; milling; modal analysis; stability lobe diagram*

1. Introduction

There are three basic types of vibrations that occur during metal machining: free vibrations, forced vibrations and self-excited vibrations. If an external excitation source acts upon a body and is then removed, the excited body will continue vibrating freely until the body's natural damping stops the vibrations. Forced vibrations occur when there is a continuous external excitation source acting upon the observed body. If the excitation frequency is close to the system's natural frequency it can lead to resonance which causes additional stress in the machining system. Self-excited vibrations are a type of vibration in which the excitation source lies within the vibrating system itself. Self-excited vibrations are a common occurrence in machining and are often referred to as chatter. This form of vibrations occurs when cutting forces excite a single or multiple modes of the machining system. Machining chatter leads to poor surface quality, workpiece dimension errors, loud noise, reduced productivity, increased production costs both in terms of wasted energy and the amount of scrapped product, short tool life and machine tool damage [1]. There are multiple ways to reduce machining chatter such as: increasing the stiffness of the machining system, using vibration isolators, using cooling and lubrication etc. The most common way to reduce chatter, however, involves choosing stable machining parameters. Stability lobe diagrams (SLDs) allow quick identification of stable and unstable cutting parameters. As shown in Figure 1 the diagram plots spindle speed, n [min^{-1}] and axial depth of cut, a_p [mm]. The diagram consists of multiple lobes that act as a boundary between stable and unstable cutting conditions. Cutting conditions within the lobes present unstable conditions while the area outside the lobes presents stable cutting conditions. The horizontal line that is a tangent to every lobe is called a stability limit, b_{lim} [mm]. This value presents the axial depth of cut where chatter will

never occur no matter the spindle speed. The intersecting points of the lobes presents the highest material removal rate that can be achieved without the occurrence of chatter.

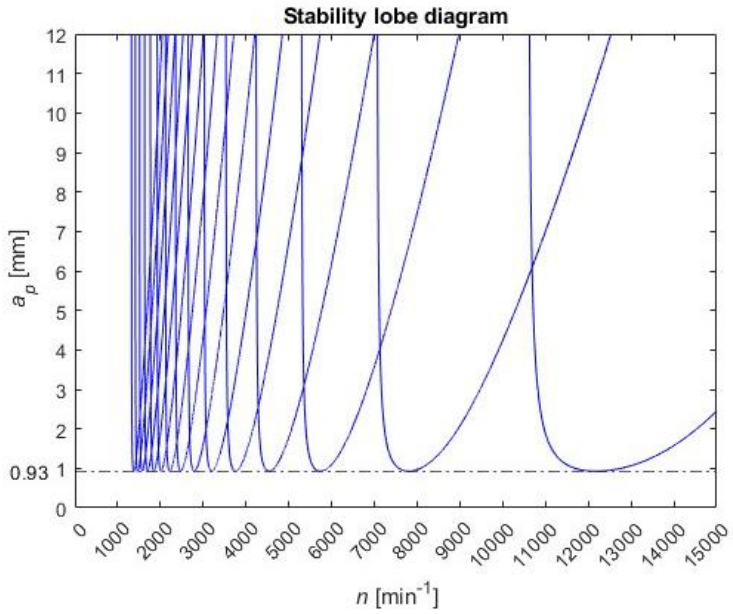

Figure 1. *Stability lobe diagram*

Stability lobe diagrams can be generated analytically, experimentally or by a combination of the two methods. Experimental analysis involves measuring the vibration amplitude of tool during machining at a specified spindle speed with varied cutting depth. A sharp increase in tool oscillations indicates the presence of self-excited chatter in the machining system. The main issue with this method is that it requires a high number of measurements that would facilitate the generation of a stability lobe diagram. Analytical generation of stability lobe diagrams is based on Tlusty’s [2] and Tobias’ [3] theory of regenerative machine tool chatter. Regenerative tool chatter theory states that, as the tool cuts through the workpiece material under the influence of chatter, a wavy surface is imprinted on the workpiece. The surface waviness of the workpiece causes variations in the thickness of the chip. Variable chip thickness causes great variations in the cutting forces and leads to increased tool vibrations. Regenerative tool chatter theory can be used to calculate the stability limit and generate stability lobe diagrams.

A combination of analytical and experimental analysis can be used to generate a stability lobe diagram. This method consists of modal analysis of the machining system to obtain modal parameters such as natural frequency, ω_n [Hz], damping ratio, ζ [/] and machining system stiffness, k [N/m]. Modal testing involves exciting the machining system with a modal hammer and measuring the response with an accelerometer. Once the response of the machining system is identified, an oriented frequency response function (FRF) can be obtained and a stability lobe diagram can be generated [4]–[6].

In this paper, modal analysis will be conducted on a vertical machining centre to obtain the modal parameters necessary to calculate the stability limit of the machining system and to generate a stability lobe diagram. A series of nine milling experiments will be conducted to test the accuracy of the generated diagram.

2. Modal analysis

To obtain the modal parameters necessary for stability lobe generation, modal analysis was conducted. The measuring equipment, shown in Figure 2, used for modal analysis consisted of a three axis accelerometer Dytran 3023 A, an impact hammer Dytran 5800 B4 equipped with a hard plastic tip and a Dewesoft Dewe 43 A data acquisition card.

Figure 2. *Modal testing equipment*

The tests were conducted on a vertical machining centre Spinner VC 560 which was equipped with an R390-020A20-11M, 20 mm end mill produced by Sandvik Coromant. Before the measurements could be conducted, measuring sensitivities had to be input into the Dewesoft X software. The accelerometer sensitivity was set to 10.84 mV/g and the modal hammer sensitivity was set to 2.19 mV/N. Similar to the work of Graham et al. [7] and Lacerda et al. [8] the accelerometer was placed on the edge of the end mill first in line with the x-axis and then the y-axis of the machine tool table as is shown in Figure 3. This way, modal parameters in both cutting directions could be obtained. Tests were conducted by means of five tap tests on the end mill which were averaged by the software. Figure 4 shows the response of the machining system as a fast Fourier transform (FFT) for both x and y-axis of the machine. A spike was noted on both diagrams corresponding to the dominant natural frequency of the machining system. For this system, the dominant natural frequencies of this system are 1277 Hz and 1234.7 Hz for x and y-axis respectively. Using a modal circle implemented into the software, damping ratios of the machining system can be obtained. The modal circle plots the real and imaginary FFT values for the observed frequency and calculates the damping ratio. For this machining system, the damping ratios were calculated as 0.032445 and 0.030554 for x and y-axis respectively.

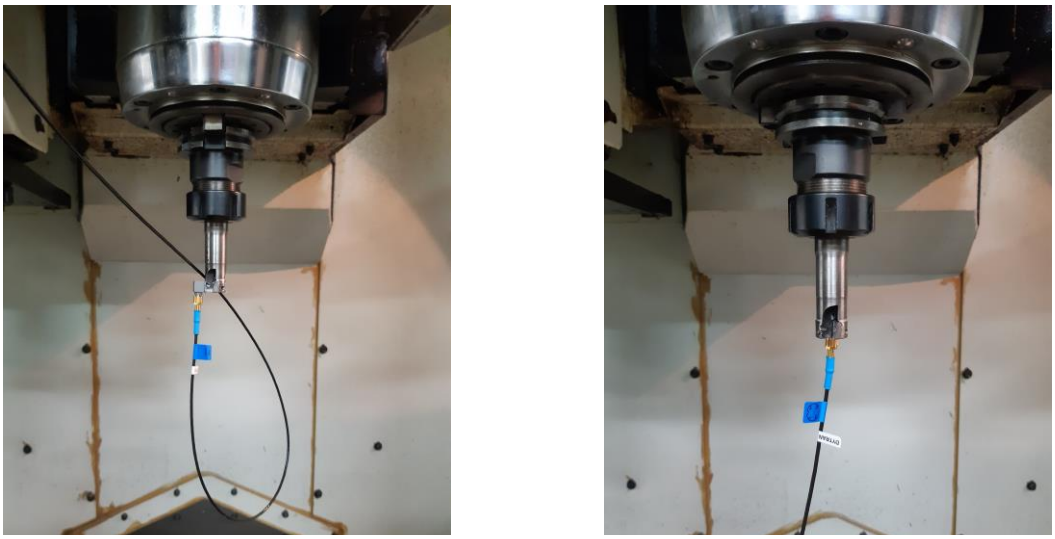

a) b)

Figure 3. *Accelerometer setup for modal testing: a) x-axis, b) y-axis*

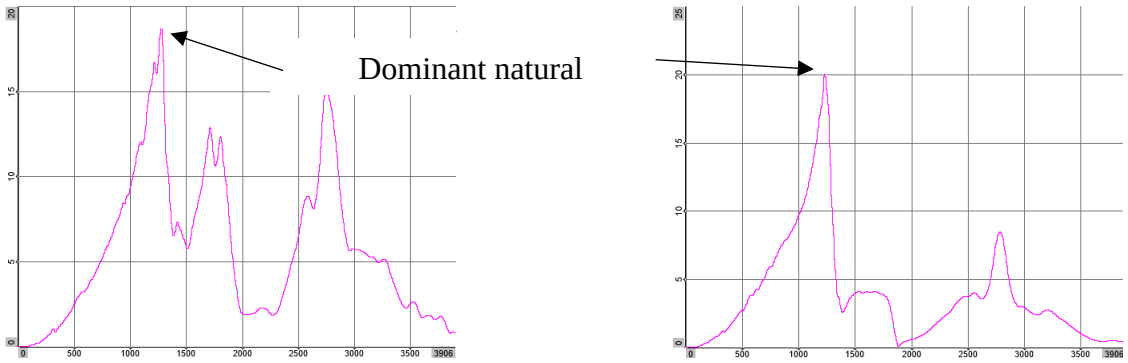

a) ω_{nx} = 1277 Hz
ζ_x = 0.032445

b) ω_{ny} = 1234.7 Hz
ζ_y = 0.030554

Figure 4. *Fast Fourier transform and modal parameters for: a) x-axis, b) y-axis*

Similar to the work of Shephard [9], stiffness of the machining system was identified by applying a known displacement on the tip of the tool and measuring the resulting force. To achieve this, a square aluminium EN AW 7075 T6 workpiece was placed on a Kistler 9257 A dynamometer which was attached to the table of the machining centre. Five displacements were applied to the end mill by the machine tool table in both x and y-axis and the resulting forces were measured. Displacements, test results and G-codes used to achieve the necessary tool movements are presented in Table 1. Displacements and forces were input into MATLAB's curve fitting tool to generate a linear function, shown in Figure 5, through the measurement points.

Table 1. *Resulting force and G-codes used to calculate the machine system stiffness*

X-axis:			Y-axis:		
G-code:	Displacement [mm]	Resulting force [N]	G-code:	Displacement [mm]	Resulting force [N]
G54 G00 X-35 Y5 Z10 G01 Z-10 F400 X-9.65 F1250 X-20 F500 Z10 M02 ==eof==	0.3	838	G54 G00 Y-35 X5 Z10 G01 Z-10 F400 Y-9.65 F1250 Y-20 F500 Z10 M02 ==eof==	0.3	863
	0.35	981		0.35	1060
	0.4	1118		0.4	1246
	0.45	946		0.45	1383
	0.5	1366		0.5	1308

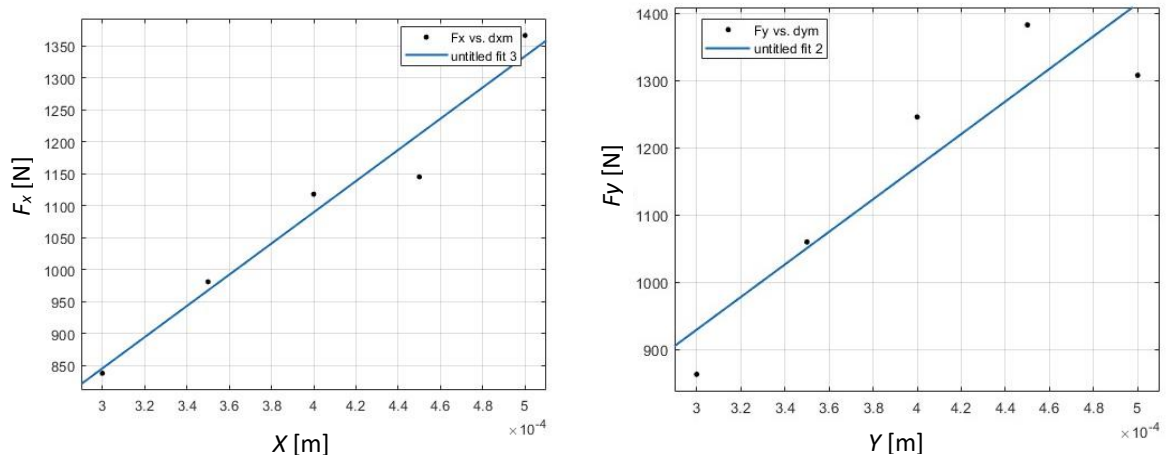

a) k_x = 4.9064 10^6 N/m

b) k_y = 4.4179 10^6 N/m

Figure 5. *Linear fits of the force response for: a) x-axis, b) y-axis*

The slopes of the generated lines represent the machining system stiffness. The machining system stiffness in the x-axis was calculated to be 4.9064 10^6 N/m and 4.4179 10^6 N/m in y-axis.

3. Generating a stability lobe diagram

After the modal parameters of the machining system were identified, a stability lobe diagram can be generated. For this purpose, a MATLAB code based on Schmitz's [5] work was developed. The code starts by initializing the input modal parameters for both x and y-axis. In the next step, real and imaginary frequency response functions for both axes are calculated using the following formulas:

$$Re(FRF) = \frac{1}{k}\left(\frac{1-r^2}{(1-r^2)^2+(2\zeta r)^2}\right) \quad (1)$$

$$Im(FRF) = \frac{1}{k}\left(\frac{-2\zeta r}{(1-r^2)^2+(2\zeta r)^2}\right) \quad (2)$$

Where:

$$r = \frac{\omega}{\omega_n} \quad (3)$$

r – ratio between vibration frequency and natural frequency of the system [/],
ω – vibration frequency [Hz],
ω_n – natural frequency of the system [Hz].
To calculate the oriented FRF functions, orientational factors, μ_x, μ_y must be calculated. For this purpose, an up-milling operation with 5.77 mm radial tool immersion (28.85 % of the tool diameter) was selected. Considering tool diameter and milling type, start angle, ρ_s [°], exit angle, ρ_e [°] and average angle of tooth in cut, ρ_{avg} [°] can be calculated. As shown in the Figure 6 below, the start angle during up-milling is 0° and the exit angle is 65°. Averaging start and exit angles produces an average angle of tooth in the cut of 32.5°.

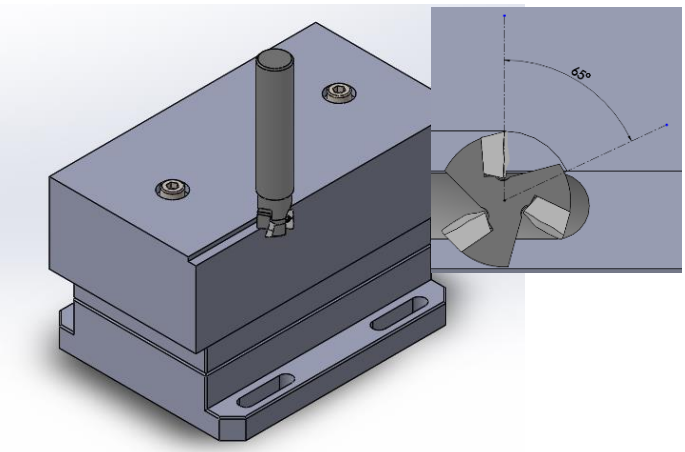

Figure 6. *Entry and exit angles for up-milling with a 20 mm end mill and 28.85 % radial immersion*

Considering a force angle of 60° and the average angle of tooth in the cut, the orientational factors were calculated. Finally, oriented FRF vectors can be calculated:

$$Re(FRF_{oriented}) = \mu_x Re(FRF_x) + \mu_y\, Re(FRF_y) \quad (4)$$

$$Im(FRF_{oriented}) = \mu_x Im(FRF_x) + \mu_y\, Im(FRF_y) \quad (5)$$

Plots for real and imaginary oriented FRF functions are shown in Figure 7.

Having calculated the oriented FRF functions, the vibration phase, ε [/] can be calculated:

$$\varepsilon = 2\pi - 2\tan^{-1}\frac{Re(FRF_{oriented})}{Im(FRF_{oriented})} \tag{6}$$

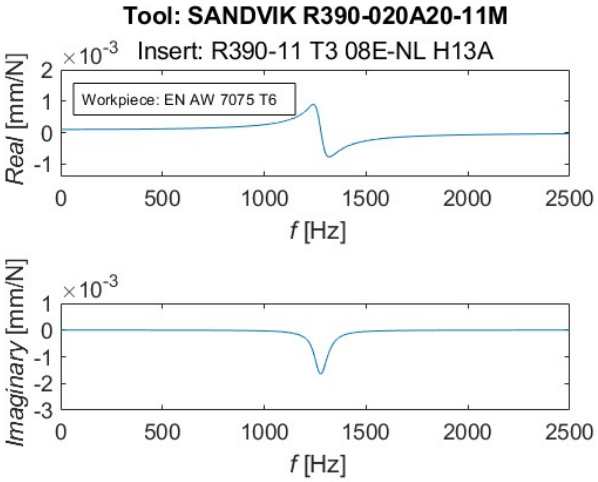

Figure 7. *Calculated real and imaginary oriented FRF functions*

Finally, the spindle speeds for a desired number of lobes can be calculated and plotted against the stability limit:

$$n = \frac{\omega}{N_t\left(N + \frac{\varepsilon}{2\pi}\right)} \tag{7}$$

$$b_{lim} = \frac{-1}{2\,k_c\,Re(FRF_{oriented})\,N_t} \tag{8}$$

Where:
N_t – average number of teeth in the cut [/],
N – number of lobes [/],
k_c – specific cutting force [N/mm^2] [5].
The specific cutting force for EN AW 7075 T6 is 850 N/mm^2 and the selected number of lobes was set to three. Figure 8 shows the generated stability lobe diagram. The axis limits were set to 12 000 min^{-1} and 10 mm as it is the maximum spindle speed the machining centre can achieve and the maximum cutting depth of the tested tool. The stability limit for this machining system was calculated at 1.41 mm.

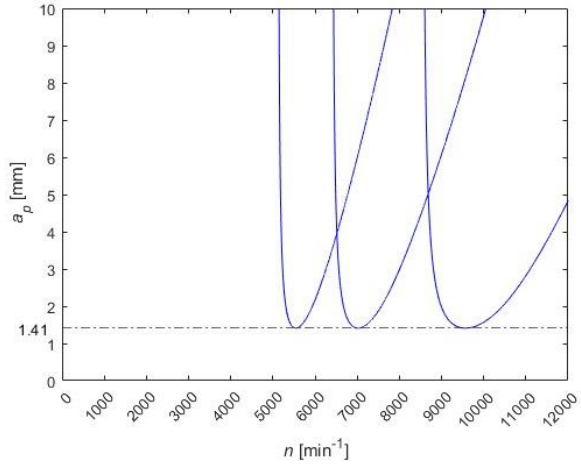

Figure 8. *Generated stability lobe diagram*

4. Testing a stability lobe diagram

To test the validity of the generated stability lobe diagram, a series of nine milling experiments was conducted. As shown in Table 2, the parameters were selected to test the stable and unstable areas of the graph as well as the stability limit. Axial depth of cut and spindle speeds were varied while the feed per tooth value was kept at a constant 0.05 mm/tooth. To measure the response of the machining system, a Dytran 3023 A accelerometer was placed on the workpiece [10]. The test results showed a high amount of accuracy when predicting stable and unstable cutting conditions. When testing the stability limit line, significant chatter was noted at lower spindle speeds such as in test number 7, shown in Figure 9a. Tests numbered 8 and 9 showed a stable cutting condition and no chatter was noted. Similar findings were noted by Paliwal et al. [11]. The cause of this discrepancy could be due to the difference between the modal parameters obtained when the tool is stationary and when the tool is in motion. This causes the stability lobe to be accurate only within a short range of spindle speeds.

Table 2. *Parameter sets used for SLD validation*

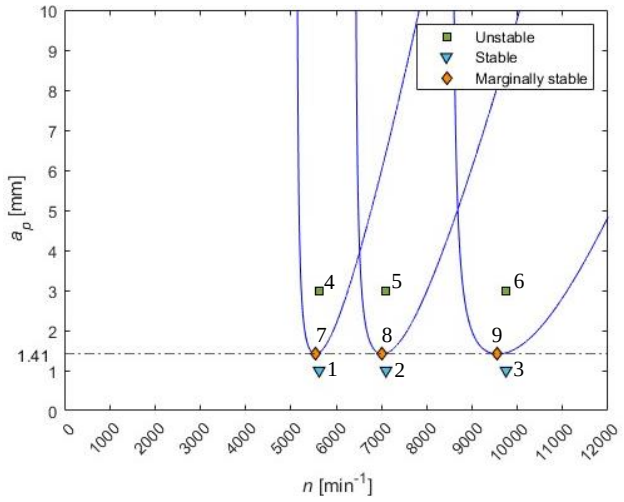

Test no.	n [min^{-1}]	a_p [mm]	Cutting condition
1	5675	1	Stable
2	7100		
3	9750		
4	5675	3	Unstable
5	7100		
6	9750		
7	5543	1.41	Marginally stable
8	7019		
9	9555		

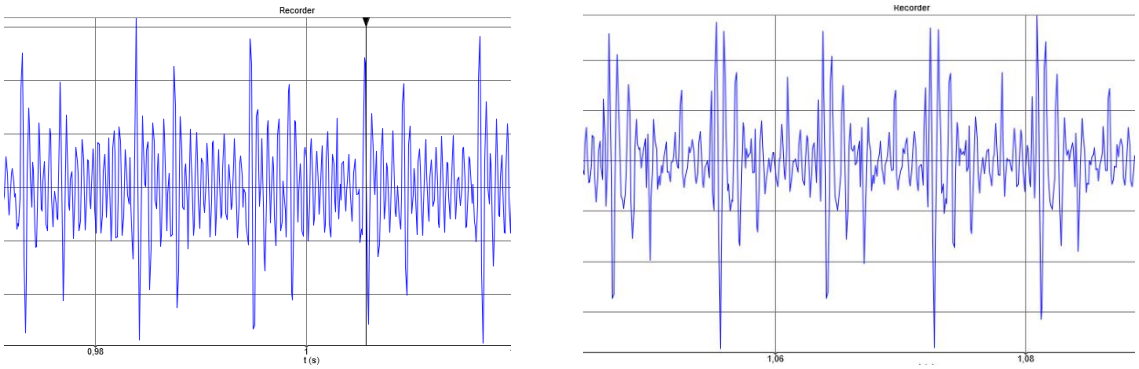

a) b)

Figure 9. *Vibration signals on the stability limit: a) a_p = 1.41 mm, n = 5543 min^{-1}, b) a_p = 1.41 mm, n = 7016 min^{-1}*

5. Conclusion

Machining chatter is a source of many issues such as low productivity and increased tool wear. Choosing stable cutting parameters can drastically reduce the influence of chatter. Stability lobe diagrams are a useful tool for determining stable and unstable cutting parameters. In this paper a stability lobe diagram is generated for a machining system consisting of a vertical machining centre, end mill and workpiece. Modal analysis was conducted on the observed machining system to obtain the natural frequencies, damping ratios and system stiffness. Using the modal parameters, a stability lobe diagram was generated using MATLAB and a stability limit was calculated for an up-milling

operation with a radial depth of cut of 5.77 mm. The stability lobe diagram was then validated by means of nine milling experiments within the stable and unstable regions. The test results showed that the diagrams produce reliable results within the stable and unstable regions. Chatter was noted at lower spindle speeds on the stability limit while no chatter was observed while machining at higher spindle speeds. The cause for this discrepancy could be the variation between stationary modal parameters in comparison to dynamic modal parameters.

Acknowledgement

This reasarch has been supported and funded by The Croatian Science Foundation through the project ALURECSS(IP-2020-02-8284).

References

[1] Quitana, G., Ciurana, J., 2011. Chatter in machining processes: A review. International Journal of Machine Tools and Manufacture. 51, 363-376.
[2] Tulsty, J., Polacek, M., 1963. The Stability of Machine Tools against Self Excited Vibrations in Machining. International research in production engineering. 465-474.
[3] Tobias, S.A., Fishwick, W., 1958. Theory of Regenerative Machine Tool Chatter. The engineer. 205, 199-203.
[4] Košarac, A., Mlađenović, C., Živković, A., 2014. Eksperimentalno-analitički metod za definisanje karte stabilnosti pri obradi struganjem, INFOTEH-JAHORINA 2014, Jahorina
[5] Schmitz, T. L., Scott Smith, K., 2009. Machining Dynamics Frequency Response to Improved Productivity, Springer, Heidelberg
[6] Yue, C., Gao, H., Liu, X., Liang, S.Y., Wang L., 2019. A review of chatter vibration research in milling. Chinese Journal of Aeronautics. 32, 215-242.
[7] Graham, E., 2013. Investigation of Robust Chatter Stability in Milling, University of Calgary, Calgary
[8] Lacerda, H.B., Lima, V.T., 2004. Evaluation of Cutting Forces and Prediction of Chatter Vibrations in Milling. Journal of Brazilian Society of Mechanical Sciences and Engineering. 26, 74-81.
[9] Shepard, J.S., 2017. Chatter Simulation and Detection in CNC milling, University of New Hampshire, Durham
[10] Yuan, N., Rahman, M., Wong Y.S., 2000. Monitoring of Chatter in High Speed End Milling Using Audio Signals Method. MATADOR 2000, Manchester
[11] Paliwal, V., Ramesh Babu, N., 2020. Prediction of Stability Lobe Diagrams in High-Speed Milling by Operational Modal Analysis, NAMRC 48, Knoxville

The corrosion behaviour of alumina ceramics in nitric acid

***Lidija Ćurković*[1], *Ivana Ropuš*[2] *and Ivana Gabelica*[1]**

1) Department of Materials, Faculty of Mechanical Engineering and Naval Architecture, University of Zagreb, Ivana Lučića 5, 10000 Zagreb, Croatia

2) Energoatest zaštita Ltd., Potočnjakova 4, 10000 Zagreb, Croatia

Corresponding author: lidija.curkovic@fsb.hr

Original scientific article

Abstract: In this work, the corrosion behaviour of cold isostatically pressed (CIP) high purity alumina ceramics was invesigated in three different concentrations of nitric acid (0.5, 1.25 and 2 mol dm^{-3}) at 25, 40 and 55 °C through 10 days. Purity of used alumina ceramics was 99.8345 wt. % with 0.1655 wt. % of both sintering aid (MgO) and impurities (SiO_2, CaO, Na_2O and Fe_2O_3). The obtained results indicated that Al_2O_3 ceramics exhibit good corrosion resistance in nitric acid. Al_2O_3 corrosion behaviour varies depending on the temperature, time and HNO_3 concentration. In view of the reaction kinetics, it proceeds in the near-parabolic law in HNO_3 aqueous solution and decreases with an increase of the HNO_3 concentration.

Keywords: *alumina; corrosion activation energy; corrosion rate*

1. Introduction

The capacity of inorganic materials to withstand chemical alterations is impacted by several factors. These include their chemical composition, mineral makeup, porosity, structure, and the conditions of the surrounding environment, such as temperature, pressure, and the dynamic nature of the environment itself [1,2]. Conventional ceramic materials like oxides, fluorides, silicates, borates, and phosphates are known for being excellent electrical insulators. The deterioration of their surfaces primarily arises from acid-base reactions and various dissolution mechanisms, as opposed to the electrochemical corrosion observed in metals [3].

The corrosion of ceramic materials can be categorized based on the type of the corrosive medium: (i) corrosion caused by exposure to liquid phases (including solutions of acids, bases, salts; molten salts; seawater and freshwater, etc.), (ii) corrosion of ceramics due to contact with molten metals and non-metals, (iii) corrosion arising from exposure to high-temperature gases [4].

When studying the corrosion of ceramics, it is essential to tailor the investigative techniques according to the specific corrosive media to which the ceramics are exposed.

The dissolution mechanisms and dissolution speed of ceramics and glass are heavily contingent upon the initial surface properties. The ability of ceramics to withstand chemical corrosion is shaped by multiple factors: the nature of the corrosive surroundings, the chemical composition and microstructure of the ceramics, and the specific conditions under which corrosion takes place. The assessment of ceramic corrosion resistance across diverse corrosive settings facilitates the prediction of their performance attributes.

In their research, Huang et al. [5] investigated the corrosion tendencies of alumina when exposed to HCl and NaOH solutions. They observed that as the exposure time increased, there was an increase in mass loss, while the corrosion rate actually decreased.

Schacht et al. [6] explored the corrosion behavior of alumina and zirconia-toughened alumina in aqueous acidic environments, particularly HCl solutions. Their findings indicated that alumina with high purity exhibited the greatest resistance to corrosion. This superiority can be attributed to the

limited solubility of impurities and sintering aids in Al_2O_3, causing them to segregate to the grain boundaries. The researchers also established a hierarchy of corrosive impact among acids on alumina ceramics, ranking as follows: H_3PO_4 > HCl > H_2SO_4. This order was explained by the higher solubility of alumina in H_2SO_4, attributed to the formation of complexes like $Al(SO_4)^+$ and $Al(SO_4)^{2-}$.

Nickel and Seipel [7] conducted an investigation of the corrosion of advanced ceramics in elevated-temperature aqueous fluids. They employed a range of techniques, including mass change measurements, eluate chemistry analysis, optical microscopy for cross-section analysis, chemical profiling, and Raman spectroscopy. Their findings indicated that all these methods effectively facilitated corrosion monitoring.

In a separate study, Herrmann et al. [8] investigated the corrosion behavior of diverse technical ceramics in acidic and basic environments under hydrothermal conditions. Their research emphasized the substantial influence of the grain boundary phase composition on the ceramics' corrosion tendencies. Notably, high-purity alumina exhibited a comparatively lower reduction in strength due to corrosion, compared to other technical ceramics.

Mikeska et al. [9] undertook an exploration into the resistance of ceramics to aqueous hydrofluoric acid corrosion. Their study revealed that in the case of polycrystalline alumina ceramics with a purity of 99.9%, corrosion primarily transpired along the grain boundaries rather than through the dissolution of the bulk material.

Alumina ceramics possess a diverse array of applications in industries, serving as filters, insulators, catalyst carriers, structural components in chemical reactors, bearings, ball valves, armatures, and more [10,6]. These applications often involve exposure to highly corrosive environments due to the presence of various chemical compounds inherent to industrial settings. Consequently, the evaluation of alumina's stability in acidic conditions holds immense significance. Such assessments aid in predicting the behavior of ceramics across diverse environments, contributing to the reduction of maintenance expenses and the enhancement of the lifespan of ceramic materials—particularly alumina [5].

This study examined the impact of varying nitric acid concentrations and temperatures during 240 hours on the corrosion characteristics of alumina ceramics. The investigation involved the quantification of eluted ions from the ceramics by means of inductively coupled plasma atomic emission spectrometry (ICP-AES). Beyond the corrosion assessments, the research also encompassed the calculation of corrosion kinetics. These calculations establish a theoretical framework for the potential utilization of Al_2O_3 ceramics in environments susceptible to acid-induced corrosion.

2. Experimental part

2.1. Preparation of Al2O3 ceramics

The composition of the raw alumina powder with the average particle size of 0.3-0.4 μm used in this research was provided from Alteo, France (Table 1). Alumina used in this research contains MgO as sintering aid and the usual impurities, i.e. SiO_2, CaO, Na_2O and Fe_2O_3.

Table 1. *Chemical composition of alumina used in this research*

Component	Fe_2O_3	CaO	SiO_2	MgO	Na_2O	Al_2O_3
wt. %	0.018	0.02	0.0325	0.045	0.05	balance

Green compacts of alumina samples (cylindrical pellets with diameter of 10 mm and height of 20 mm) were formed by cold isostatic pressing (CIP) of alumina granules obtained by spray drying at Applied Ceramics Inc, Sisak, Croatia.

2.2. Investigation of alumina ceramics corrosion in aqueous HNO3 solution

Prior to corrosion test, sintered alumina samples were cleaned with alcohol and dried in a sterilizer at 150 ± 5 °C for 4 h. Polypropylene (PP) tubes were marked and filled with 10 cm^3 of the adequate concentration of HNO_3. Following this, the samples were immersed into the nitric acid solutions with

varying concentrations and the PP tubes were sealed. Concentrations of HNO_3 used in this experiment were 0.50, 1.25 and 2.00 mol dm^{-3}. Static corrosion test was carried out at 25, 40 and 55 °C up to 10 days.

Finally, alumina samples were removed from the tubes, rinsed with distilled water, and dried in an oven for 3 h at 150 °C.

To monitor the mechanisms responsible for the corrosion phenomena, the concentration of ions (Al^{3+}, Ca^{2+}, Fe^{3+}, Mg^{2+} and Na^{+} ions) eluted from alumina surface samples into the corrosive aqueous HNO_3 solution were determined by ICP – AES, Teledyne Leeman Labs. (Hudson, NH, SAD).

3. Results and discussion

Mass loss of alumina ceramics during corrosion monitoring in different concentrations of nitric acid was below detection limit of analytical balance (10^{-5} g). Therefore, the corrosion mechanisms were monitored and described by determining the amount of eluted ions from alumina ceramic samples in the corrosive solution and corrosion rate of the corrosion process.

ICP-AES was used to determine concentration of Al^{3+}, Ca^{2+}, Fe^{3+}, Mg^{2+}, Na^{+} and Si^{4+} ions. Concentration of Si^{4+} in all samples was under the quantification limit [LOQ (Si^{4+}) < 0.45 µg g^{-1}] [11].

Figure 1 provides the intercorrelations among the amount of eluted ions Al^{3+}, Ca^{2+}, Fe^{3+}, Mg^{2+}, Na^{+} from Al_2O_3 ceramics and time of the exposure of alumina samples to the different concentrations of nitric acid at 25 °C. It was found that the elution of ions increased daily throughout the observed period (10 days) for all concentrations of corrosive media. Furthermore, the increase of the HNO_3 concentration led to the decrease of eluted ions amount during the period of investigation.

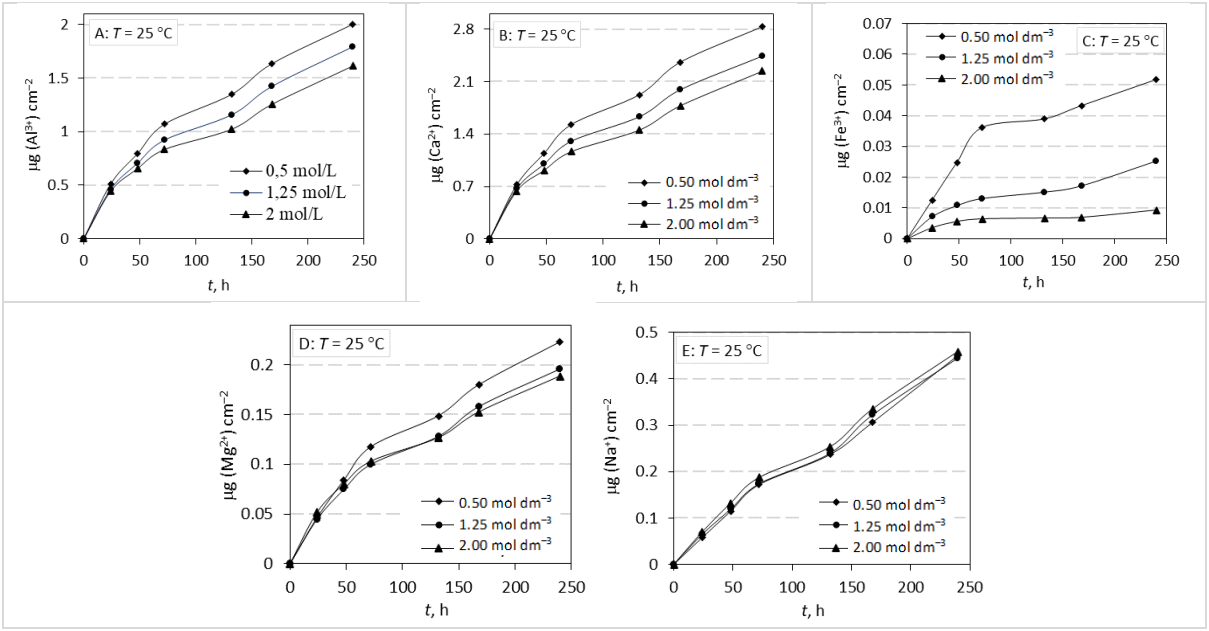

Figure 1. *The amount of eluted ions (A) Al^{3+}, (B) Ca^{2+}, (C) Fe^{3+}, (D) Mg^{2+} and (E) Na^{+} of Al_2O_3 ceramics at HNO_3 concentrations of 0.50 mol dm^{-3}, 1.25 mol dm^{-3} and 2.00 mol dm^{-3} at constant temperature 25 °C*

Figure 2 presents the results obtained from the measurement of elution of ions (Al^{3+}, Ca^{2+}, Fe^{3+}, Mg^{2+}, Na^{+}) from Al_2O_3 ceramics and exposure time to the different temperatures in 0.50 mol dm^{-3} HNO_3. It can be seen that the increase of nitric acid solution temperature led to the increase of the elution of ions from alumina ceramics, especially at the highest temperature (55 °C). The distribution of impurities is specified by the solubility of cations in the alumina lattice. The solubility depends on the differences in the charge and the ionic radius of impurities (Mg^{2+}, Ca^{2+}, Fe^{3+} and Na^{+}) and Al^{3+} from alumina lattice.

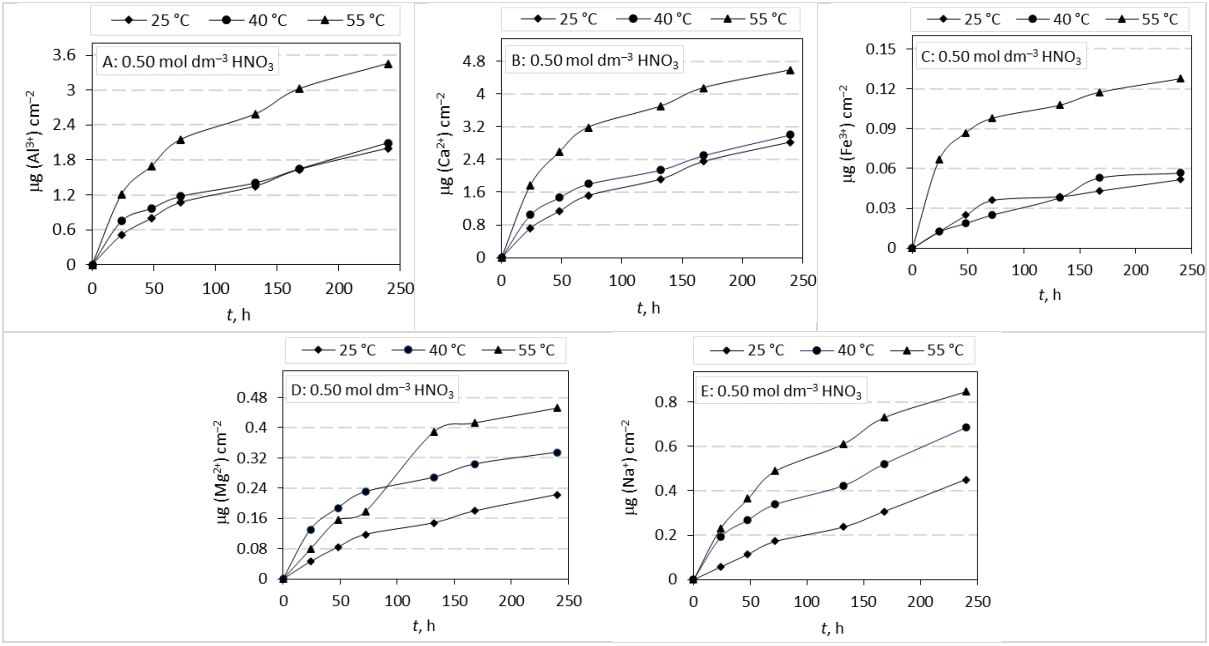

Figure 2. *The amount of eluted ions (A) Al^{3+}, (B) Ca^{2+}, (C) Fe^{3+}, (D) Mg^{2+} and (E) Na^{+} of Al_2O_3 ceramics at temperature of 25 °C, 40 °C and 55 °C at constant HNO_3 concentration 0.50 mol dm^{-3}*

In the present study, measuring the amount of eluted ions was used to study corrosion kinetics. Variation of corrosion rate with time can be linear, parabolic, logarithmic, etc. Following equation was used to determine which rate law the curves obey:

$$\left(\sum \frac{m(M^{n+})}{A}\right)^{n} = K_p \cdot t \qquad (1)$$

Where Σm (M^{n+}) stands for mass of overall amount of eluted ions (Al^{3+}, Ca^{2+}, Fe^{3+}, Mg^{2+}, Na^{+}), μg; *A* for specific surface, cm^2; *n* for the power exponent, K_p for corrosion rate constant, μg^n cm^{-2n} h^{-1} and *t* for time of the ceramic exposure to the corrosive media, h [12].

The overall amount of eluted ions is the sum of the amounts of each ion eluted from alumina ceramics in monitored HNO_3 solutions during an experiment. The overall amount of eluted ions monitored during 10 days may be seen at Figure 3, as well as the increase of ions elution due to the HNO_3 solution temperature increase. In contrary, an increase of HNO_3 solution concentration led to the decrease of the ceramic's ions elution.

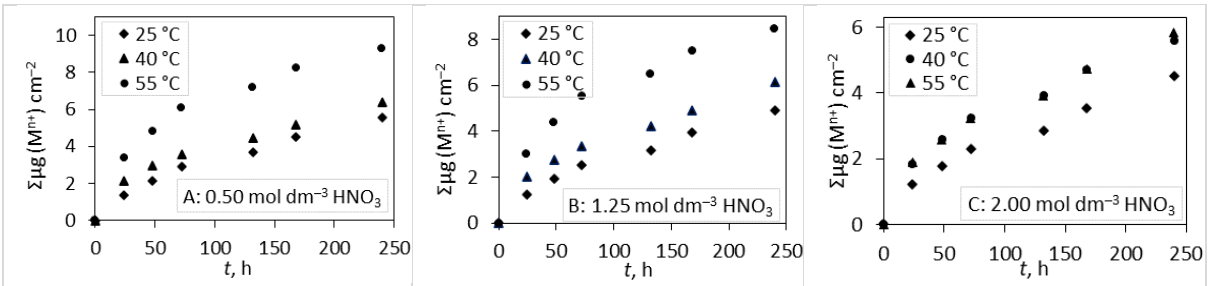

Figure 3. The amount of all eluted ions from Al_2O_3 ceramics at 25 °C, 40 °C and 55 °C and concentration of HNO_3 solution (A) 0.50, (B) 1.25 and (C) 2.00 mol dm^{-3}

The power exponent *n* was estimated from a graphic of ln (Σμg (M^{n+}) cm^{-2}) versus ln *t* (not shown here). Therefore, *n* values were calculated from the slope. The values of the corrosion rate constants, were obtained from the slope of the graphic of (Σμg (M^{n+}) cm^{-2})^n versus *t* (not shown here). Obtained values of the power exponent (*n*), the corrosion rate constants (K_p, μg^n cm^{-2n} h^{-1}) as well as the corresponding correlation coefficients (R^2), are listed in Table 2.

Table 2. *The power exponent (n), corrosion rate constants values (K_p) of Al_2O_3 ceramics at different HNO_3 concentrations (0.50 mol dm^{-3}, 1.25 mol dm^{-3} and 2.00 mol dm^{-3}) at three temperatures (25 °C, 40 °C and 55 °C)*

T, °C	*c* (HNO_3), mol dm^{-3}	*n*	R^2	K_p, µg^n cm^{-2n} h^{-1}	R^2
25	0.50	1.67	0.9926	0.0719	0.9935
	1.25	1.73	0.9943	0.0645	0.9914
	2.00	1.81	0.9916	0.0620	0.9836
40	0.50	2.17	0.9957	0.2266	0.9899
	1.25	2.14	0.9939	0.1972	0.9856
	2.00	2.121	0.9941	0.1595	0.9908
55	0.50	2.31	0.9874	0.7107	0.9897
	1.25	2.28	0.9864	0.5353	0.9898
	2.00	2.1	0.9910	0.1665	0.9827

4. Conclusion

The present study was designed to determine the effect of time, temperature and concentration of acid media (nitric acid) on the corrosion resistance of the alumina ceramics.

The most obvious finding to have emerged from this study is that an increase in the temperature of corrosive media leads to the increase of the elution of impurities segregated in grain boundaries of the alumina. In contrary, higher nitric acid concentration led to the decrease of the elution of cations from Al_2O_3. It was found that the elution of ions increased daily throughout the observed period so it can be concluded that time is a parameter that inevitably contributed to the corrosion of ceramics.

The amount of eluted ions from alumina ceramics was obtained at corrosion experiments in the following order: $Fe^{3+} < Mg^{2+} < Na^{+} < Al^{3+} < Ca^{2+}$, thus purity of the ceramics has an important role in the corrosion process.

The corrosion rate of Al_2O_3 was found to be in the range 0.0620 - 0.7107 µg^n cm^{-2n} h^{-1} where the highest rate was achieved at lower HNO_3 concentration and highest temperature.

Acknowledgments

This work was financed by the Croatian Science Foundation within the project Monolithic and composite advanced ceramics for wear and corrosion protection (WECOR) (IP-2016-06-6000).

References

[1] McCauley, R.A., 2005. Corrosion of Ceramic and Composite Materials, 2nd ed., Marcel Dekker, Inc., USA

[2] Medvedovski E., 2013. Influence of corrosion and mechanical loads on advanced ceramic components. Ceram. Int. 39, 2723–2741.

[3] White, W.B., 1992. Theory of Corrosion of Glass and Ceramics. Corros. Glas. Ceram. Ceram. Supercond. 2–28.

[4] Breviary Technical Ceramics, Germany, 2004. https://www.nonmet.mat.ethz.ch/education/courses/Materialwissenschaft_2/brevier.pdf (accessed on 4 December 2022).

[5] Huang L., Luo S.S., Li W., 2012. Corrosion Behavior of Al_2O_3 Ceramics in the Acid and Alkaline Solutions. Key Eng. Mater. 512-515, 509–512.

[6] Schacht M., Boukis N., Dinjus E., Corrosion of alumina ceramics in acidic aqueous solutions at high temperatures and pressures. 2000. J. Mater. Sci. 35, 6251–6258.

[7] Nickel K.G., Seipel B., Corrosion Penetration Monitoring of Advanced Ceramics in Hot Aqueous Fluids. 2004. Mater. Res. 7, 125–133.

[8] Herrmann M., Schlim J., Michael G., Corrosion Behaviour of Different Technical Ceramics in Acids, Basic Solutions and under Hydrothermal Conditions. 2004. Key Eng. Mater. 264-268, 877–880.

[9] Mikeska K.R., Bennison S.J., Grise S.L., Corrosion of Ceramics in Aqueous Hydrofluoric Acid. 2000. J. Am. Ceram. Soc. 83, 1160–64.
[10] Citak B., Kirsever D., Ayday A., Boussebha H., Demirkiran A. S., The corrosion kinetics of cordierite based ZrO_2 composites obtained from natural zeolite in dilute HCl acid solution. 2021. J. Compos. Mater. 55, 1–13.
[11] Souza A.L., Lemos S.G., Oliveira P.V., A method for Ca, Fe, Ga, Na, Si and Zn determination in alumina by inductively coupled plasma optical emission spectrometry after aluminum precipitation. 2011. Spectrochim. Acta - Part B At. Spectrosc. 66, 383–388.
[12] Kurajica S., Mandić V., Ćurković L., Mullite ceramics acid corrosion kinetics as a function of gel homogeneity. 2017. Biointerface Res. Appl. Chem. 7, 2295–2299.

Synergetic approach to planning a scalable manufacturing system

***Sandro Dobovičeka*[1], *Elvis Krulčić*[1], *Duško Pavletić*[1] *and Sandi Tominić*[1]**

1) University of Rijeka – Faculty of Engineering, Vukovarska 58, 51000 Rijeka, Croatia

Corresponding author: sdobovicek@riteh.hr

Original scientific article

Abstract: Manufacturing systems design and planning often focus on current or short-term capacity and space requirements and neglect long-term future needs. However, due to changing market conditions, the importance of reconfiguring and adapting manufacturing systems to changes is becoming increasingly apparent. This paper presents a synergetic approach to the design of scalable manufacturing systems that brings together the two main design forces - the process view and the spatial view. The design considerations include three different classes of configurations. The paper presents an example of the design of a scalable system for processing a product from the automotive industry for which market demand is expected to increase in the long term.

Keywords: *reconfigurable manufacturing system; dynamic cellular manufacturing system; system scalability; system configuration; operation clusters setup*

1. Introduction

Ever-evolving products and market conditions require a manufacturing company to constantly change its processes and reorganise the available space within a factory in order to keep operating costs down and remain competitive. The space available for manufacturing is usually limited and costly, so it needs to be managed appropriately.

The main purpose of spatial planning in factories is to create a rational use of space that balances current and future needs, considering factory facilities from a functional and technological point of view [1]. Because of this close connection between production planning and spatial planning, the term "synergetic factory planning" is often used. Neglecting any aspect of synergetic planning (transport, energy, maintenance, media, ventilation, redesign options, etc.), possibly due to tight deadlines, can lead to unsatisfactory planning results [2]. For example, a planning approach that prioritises process considerations may ignore the physical spaces in which these processes take place, reducing the controllability of material movement through the process or making the manufacturing process less reliable than it is at its highest potential. Spatial planning, and thus synergetic planning can also influence the potential scalability of manufacturing system [3]. In terms of manufacturing systems, scalability is a key principle to achieve the required flexibility, agility, and adaptability. Scalability can be achieved according to two main principles: a) by increasing or decreasing number of multiple, mutually linked elements (e.g. workstations) that provide a scaled manufacturing system architecture and b) by scaling up or downsizing single system element [4], Figure 1.

Several concepts for dynamically changing manufacturing systems that enable scalability through synergetic planning have been developed, such as Dynamic Cellular Manufacturing Systems (DCMS) [5] or Reconfigurable Manufacturing Systems (RMS) [6]. The term manufacturing system can be used to refer to different levels of manufacturing, from a single workstation to an entire supply network. In this paper, the manufacturing system is considered at the level of a manufacturing cell. Cell configuration is one of the most important considerations when designing manufacturing system. In addition to the obvious spatial requirements, the configuration chosen has a major impact on process performance in terms of product quality, productivity, capacity, reliability and scalability [7]. Dynamic cell configurations allow for the necessary changeability in turbulent manufacturing environments,

such as decreasing product life cycles and high varying product demand and production lot sizes [8]. These types of cells are called dynamic because their configuration is dynamic and corresponds to manufacture requirements for a given planning horizon before it's workstations can be physically allocated within a zone or a physical department division. The initial system configuration, i.e. the spatial arrangement, is crucial for achieving cost-effective scalability in the long run [9]. Therefore, scalability planning must be done at the same time as the initial design of a new manufacturing system [10].

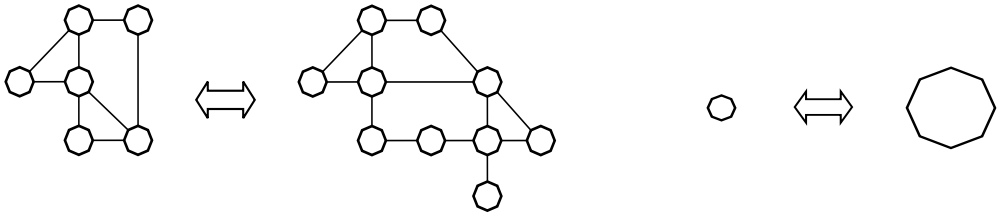

Figure 1. *Main principles of scalability, adopted from [4]*

2. Problem description

When designing the manufacturing system from a process point of view (processing tasks, interdependence of tasks and the machine functionality required to perform them) and from spatial point of view (transportation, spatial distribution of energy), the manufacturing system designer should consider the following information about: product demand scenario consisting of several periods with expected product demand, processing operations, machines/workstations, system configurations, space constraints, capacity constraints, and conformity of the configuration performance with the design objectives.

2.1. The product demand scenario

The necessary reconfiguration of the system and future spatial requirements are determined by predictions about the future state of the market and the manufacturing system, such as the predicted level of product demand and the predicted reliability of the elements of the manufacturing process. Forecasts are an important aspect of planning because they determine the minimum number of machines needed in the future, as well as the possible configurations of the system and its spatial requirements. The forecast demand for product p in period h is represented as q_{ph}. This type of information is provided by top management according to the company's market requirements and objectives [11].

2.2. Processing operations

The processing information for each product p are defined by a set of operations OP_s where s is a indexing set of processing stages s={1,2,...,NS} with information about processing time t_p and the corresponding required machine configuration MC, accompanied by the operations precedence diagram. An operation cluster is a set of operations that must be processed together due to various constraints such as logical or datum tolerance constraints. An operation cluster setup OS_p is a set of one or more operation clusters of product p that can be executed together on a particular machine with a particular machine configuration [11].

2.3. Machines/workstations

A typical configuration of a dynamically changing manufacturing system consists of several stages s with n_s identical parallel machines of type m_s and corresponding machine configurations c_s. Each stage processes a particular operation cluster setup OS_p of product p. Figure 2 shows such configuration of manufacturing system for processing two different parts from part family. Processing and machine-related variables are [11]:

- number of stages $NS \in \{1, 2, \ldots, \mathrm{NSL}\}$ where NSL is the maximum number of processing stages
- machine types $M = \{1, 2, \ldots, m_s, \ldots, m_{NS}\}$, where m_s represents machine type associated to a processing stage s
- machine configurations $MC = \{1, 2, \ldots, c_s, \ldots, c_{NS}\}$ where c_s represents the configuration selected for machine type m_s in stage s
- number of machines within a stage $NMS = \{1, 2, \ldots, n_s, \ldots, n_{NS}\}$ where n_s represents the number of identical parallel machines in stage s
- operation clusters setup $OS_p = \{o_{p,1}, o_{p,2}, \ldots, o_{p,s}, \ldots, o_{p,NS}\}$ $\forall$ $p = 1, 2, \ldots, \mathrm{NP}$ is a set of one or more operation clusters that can be executed in a sequence on a particular machine with a particular machine configuration, where $o_{p,s}$ represents the operation clusters setup assignment of machine m_s used in stage s to produce product p and NP is the number of products to be processed.

Figure 2 shows two parallel machines of type M6 and configuration MC67 in the first processing stage of the system, processing a setup of 17 operation clusters of product P1 and a setup of 1 operation cluster of product P2 etc. The minimum number of parallel machines of machine type m_s in processing stage s with the corresponding machine configuration c_s is equal to:

$$n_s = \sum_{p=1}^{\mathrm{NP}} \frac{t(o_{p,s}) \cdot q_p}{A_s \cdot R_s} \tag{1}$$

where $t(o_{p,s})$ is a time required to perform operation clusters setup $o_{p,s}$, q_p is a demand for product p, A_s is time in which machine m_s is available for processing and R_s is a reliability of machine m_s. The resulting number of machines n_s required in segment s for processing a set of NP products must be rounded to the first larger integer. The reliability data of machines can be assessed using manufacturer's data and/or historical operating data based on machine failure and repair rates.

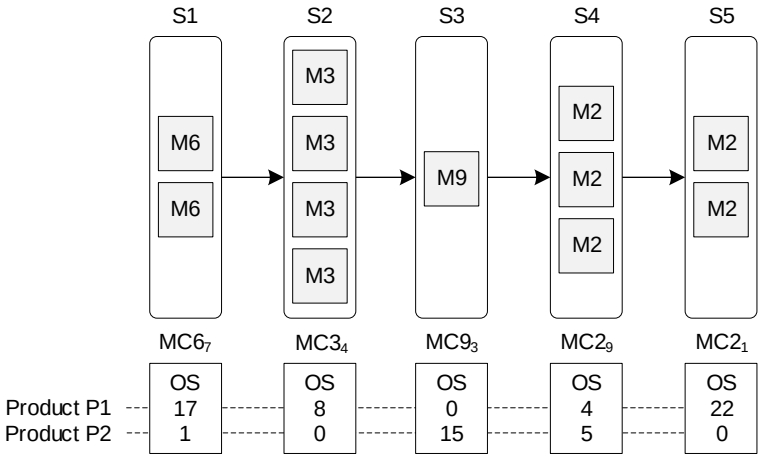

Figure 2. *Configuration of dynamically changing manufacturing system for processing two parts, adopted from [11] (S-stages, M-machine types, MC-machine configurations, OS-operation clusters setup)*

2.4. System configurations

The system configuration shown in Figure 2 allows for 48 different processing paths (2×4×1×3×2=48), as material processed in any machine in the previous phase can be passed to any machine in the subsequent phase. This is what is known as a symmetrical configuration. Symmetrical configurations are those where each path contains the same number of machines. Non-symmetrical configurations are characterised by a non-identical flow path for the product and therefore require multiple process plans. Symmetric configurations can be divided into three different classes, Figure 3 [12]:

I. cell configurations consisting of multiple serial lines (cells) arranged in parallel, with no crossovers
II. reconfigurable manufacturing system (RMS) configurations with crossover connections between stages
III. combined configurations where they are crossovers only between some stages. These are a combination of the previous two classes of configurations.

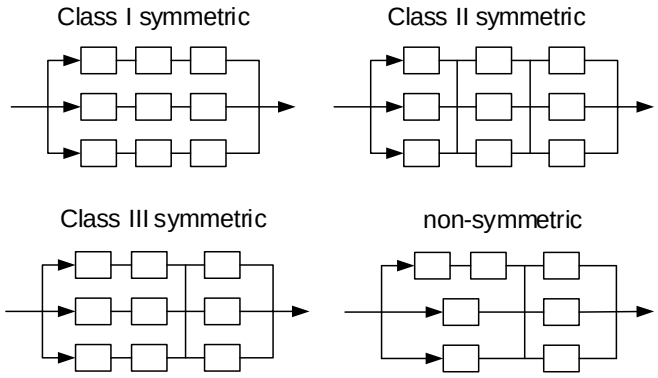

Figure 3. *Symmetrical and non-symmetrical configurations*

In general, the number of possible system configurations increases logarithmically with the number of machines in the system. The number of possible configurations of the class II (RMS) with m machines arranged up to s stages is equal to [12]:

$$K = \sum_{s=1}^{m} \binom{m-1}{s-1} = 2^{m-1} \tag{2}$$

The number of possible configurations of the class II (RMS) with m machines arranged in exactly s stages is equal to

$$K = \left(\frac{(m-1)!}{(m-s)!\,(s-1)!} \right) \tag{3}$$

2.5. Spatial constraints

In practise, there are often constraints on the space allocated to the system configuration in terms of the maximum number of stages NSL where

$$NS \leq \mathrm{NSL} \tag{4}$$

Constraints also exists for the maximum number of parallel machines MMS within a stage where

$$n_s \leq \mathrm{MMS} \quad \forall\, s = 1,2,\dots,NS \tag{5}$$

2.6. Capacity constraints

Acceptable system configurations should have sufficient capacity to process an entire set of NP products in such way that

$$\sum_{p=1}^{\mathrm{NP}} \frac{DS(p)}{n_s \cdot PROS_{p,m_s}} \leq 1 \quad \forall\, s = 1,2,\dots,NS \tag{6}$$

where $DS(p)$ is the product demand rate scenario for the product p and $PROS_{p,ms}$ is a processing rate of the operation cluster of the product p processed at stage s with the machine type m_s.

2.7. Conformity of the system performance with the design objectives

In the decision-making process, the system designer should analyse the system performance for all possible configurations and choose a system development path for a particular product demand scenario. Design decisions about system configuration can have a major impact on system performance, such as:

- initial cost,
- quality (ability to process products with little variation),
- expected productivity which accounts reliability and productivity,
- scalability (cost of expanding capacity to meet changing market demand).

The material flow system of Class I symmetric configurations is simpler than that of Class II symmetric configurations and should therefore require lower investment costs. However, if product demand increases the capacity of a single Class I symmetric configuration, investment in another parallel cell is required to satisfy product demand. Configurations with multiple parallel machines in a stage and crossovers between stages can produce products with greater variation resulting from differences in the process means of the parallel machines. Class I symmetric configurations typically have a smaller total number of material flow paths and therefore less variation in product characteristics. If one machine of the Class I symmetric configuration in Figure 3 fails, the total line throughput is zero. Therefore, configurations with several parallel machines in one stage can cover machines with lower reliability. In general, the scalability of Class II symmetric configurations is better than that of Class I configurations. A system that can adapt to different product demands with less reconfiguration (and cost) is strongly preferred when product demand conditions change.

3. Example of system design

To convey the process of the synergetic approach to manufacturing system design, a real-life example of a manufacturing system for machining a single machine part ($\mathrm{NP}=1$) is used. Electric motor cover shown in Figure 4. is an integral element of a product whose market demand has increased in recent years - an electric car. The initial product demand is 260 parts/day. The demand scenario forecasts an increase in demand of up to 90%.

3.1. Machine processing operations

The starting material for the machining process is a casting made of the aluminium alloy AlSi7Mg, which is produced using the low-pressure casting process. The castings are machined on a 4-axis CNC horizontal milling centre. In the manufacturer's nomenclature, this machine type is referred to as M7. The geometry of the product and the chosen 4-axis CNC machining centre require machining with two different fixtures, i.e., two machine configurations: $\mathrm{MC7}_1$ and $\mathrm{MC7}_2$. Both fixtures are designed for clamping two products in one machining cycle. Total machining time for two parts are 25.87 minutes. The sequence of machining operations with the corresponding required machining times (for two parts) can be found in Tables 1 and 2. The time available for machining on both machine configurations is 1290 min/day.

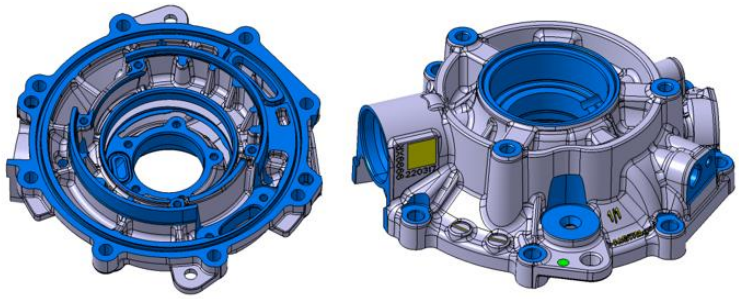

Figure 4. Electric motor cover

Table 1. *Processing times of machine configuration $M7_1$*

Machine	Machine configuration	Operation	Processing time (min)
M7	$MC7_1$	1-1	1.62
		1-2	1.18
		1-3	0.30
		1-4	0.25
		1-5	0.75
		1-6	1.30
		1-7	0.20
		1-8	0.73
		1-9	1.20
		1-10	0.35
		1-11	0.40
		1-12	1.29
		1-13	1.10
		1-14	0.96
		1-15	0.50
		1-16	0.42
		1-17	0.32
		1-18	0.25
		1-19	0.17
		1-20	1.26
		1-21	0.66
		1-22	0.64
		1-23	0.55
		1-24	0.33
		1-25	0.26
		1-26	0.45
		1-27	0.70

Table 2. *Processing times of machine configuration $M7_2$*

Machine	Machine configuration	Operation	Processing time (min)
M7	$MC7_2$	2-1	0.98
		2-2	0.43
		2-3	0.20
		2-4	0.31
		2-5	0.32
		2-6	0.20
		2-7	0.53
		2-8	0.81
		2-9	0.28
		2-10	0.23
		2-11	0.48
		2-12	0.55
		2-13	0.96
		2-14	1.45

3.2. Spatial and demand requirements

The product demand scenario includes four intervals, Table 3. The available floor space is asymmetrical. In a single manufacturing line configuration, it can accommodate up to 6 serially connected stages in a U-shape, with one machine per stage and the associated material handling system, Figure 5. In a Class I configuration, two parallel lines with up to three machines are possible, Figure 6. In a class II configuration, four segments of the reconfigurable manufacturing system are possible, with up to two parallel machines per stage for all stages except the first (or fourth), where only one machine is possible, Figure 7.

3.3. Assumptions and rules

For the purposes of this article, the following assumptions are made:

- it is assumed that the processing and transport equipment is 100% reliable,
- set-up and transport times are negligible,
- as a rule, for setting up an operations cluster, those configurations that achieve the best balancing efficiency are selected where the system configuration balancing efficiency is calculated as

$$\eta_h = \frac{\sum_{s=1}^{NS} T_{C,s,h}}{NS_h \cdot \max\limits_{s} T_{C,s,h}} \cdot 100\% \quad (7)$$

where $T_{C,s,h}$ is the cycle time of stage s and NS_h is the number of processing stages in period h.

Table 3. Product demand scenario and required process cycle time

h	1	2	3	4
$q_{1,h}$ (parts/day)	260	320	360	500
$T_{C\,max,h}$ (min)	9.92	8.06	7.17	5.16

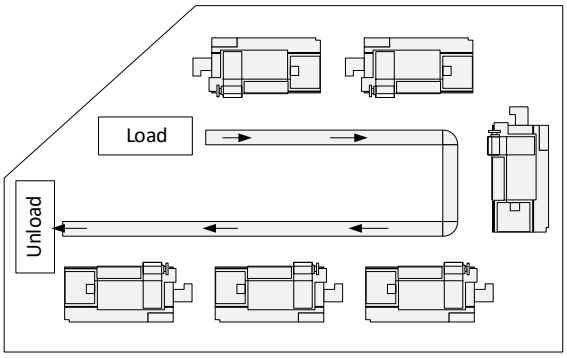

Figure 5. Single cell configuration

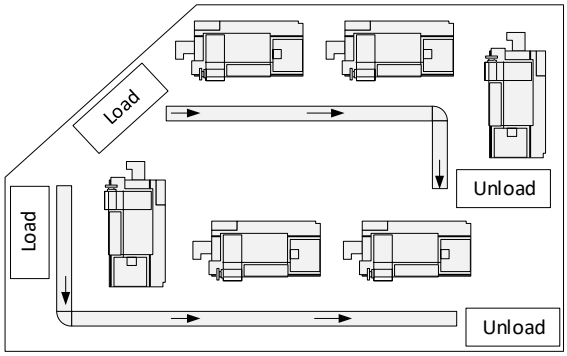

Figure 6. *Class I symmetric configuration*

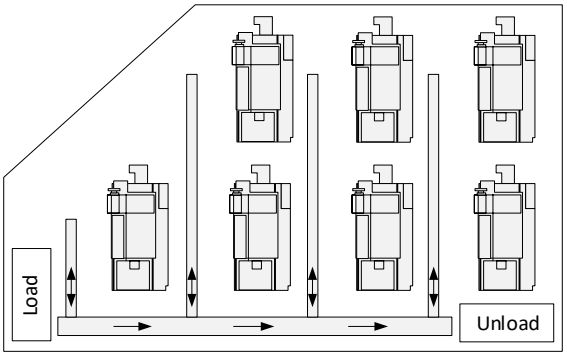

Figure 7. *Class II symmetric configuration*

4. Results

According to Equation 1 required number of machines in the system for specific interval is shown in Figure 8. The required process cycle time for a batch size of 2 is calculated as follows

$$T_{C\,max,h} = 2 \cdot \frac{A_h}{q_h} \quad (8)$$

where A_h is the time available for processing in interval h, and q_h is the demand for the product in period h. System designer should consider all possible symmetric configurations. Single cell configuration can be gradually adjusted as product demand increases. In period h=2, three machines are needed in configuration $MC7_1$, one more than in previous period, Table 4. Since this configuration only allows serial connections between the machines, there is only one possible configuration. A new machine must be assigned to the system. Rebalancing the system requires changes in the setup of the operations cluster for two existing machines and one new machine in configuration $MC7_1$, so that the first machine in configuration $MC7_1$ processes the operations cluster from 1-1 to 1-8 (instead of from 1-1 to 1-12 in the previous period), the second machine in configuration $MC7_1$ processes the operations cluster from 1-9 to 1-16, and so on.

Table 4. *System performance characteristics in a product demand scenario*

		Spatial constraints	h			
			1	2	3	4
Configuration	Single cell	NSL=6 MMS=1	$NS=3$ $NMS=\{1,1,1,0,0,0\}$ $MC=\{7_1,7_1,7_2,0,0,0\}$ $OS_1=\{\frac{1}{12}, \frac{13}{27}, \frac{1}{14}, -, -, -\}$ $\eta = 90.1\%$ $NPP=1$ $T_C=9.57$ min	$NS=4$ $NMS=\{1,1,1,1,0,0\}$ $MC=\{7_1,7_1,7_1,7_2,0,0\}$ $OS_1=\{\frac{1}{8}, \frac{9}{16}, \frac{17}{27}, \frac{1}{14}, -, -\}$ $\eta = 83.7\%$ $NPP=1$ $T_C=7.73$ min	$NS=5$ $NMS=\{1,1,1,1,1,0\}$ $MC=\{7_1,7_1,7_1,7_2,7_2,0\}$ $OS_1=\{\frac{1}{8}, \frac{9}{16}, \frac{17}{27}, \frac{1}{8}, \frac{9}{14}, -\}$ $\eta = 81.7\%$ $NPP=1$ $T_C=6.33$ min	$NS=6$ $NMS=\{1,1,1,1,1,1\}$ $MC=\{7_1,7_1,7_1,7_1,7_2,7_2\}$ $OS_1=\{\frac{1}{5}, \frac{6}{11}, \frac{12}{19}, \frac{20}{27}, \frac{1}{8}, \frac{9}{14}\}$ $\eta = 86.1\%$ $NPP=1$ $T_C=5.01$ min
	Class I	NSL=3 MMS=1	$NS=3$ $NMS=\{1,1,1\}$ $MC=\{7_1,7_1,7_2\}$ $OS_1=\{\frac{1}{12}, \frac{13}{27}, \frac{1}{14}\}$ $\eta = 90.1\%$ $NPP=1$ $T_C=9.57$ min	$NS=3$ $NMS=\{1,1,1\}$ $MC=\{7_1,7_1,7_2\}$ $OS_1=\{\frac{1}{12}, \frac{13}{27}, \frac{1}{14}\}$ $\eta = 90.1\%$ $NPP=2$ $T_C=4.79$ min	$NS=3$ $NMS=\{1,1,1\}$ $MC=\{7_1,7_1,7_2\}$ $OS_1=\{\frac{1}{12}, \frac{13}{27}, \frac{1}{14}\}$ $\eta = 90.1\%$ $NPP=2$ $T_C=4.79$ min	$NS=3$ $NMS=\{1,1,1\}$ $MC=\{7_1,7_1,7_2\}$ $OS_1=\{\frac{1}{12}, \frac{13}{27}, \frac{1}{14}\}$ $\eta = 90.1\%$ $NPP=2$ $T_C=4.79$ min
	Class II	NSL=4 MMS=2 $\forall s \backslash \{1\}$ MMS=1	$NS=2$ $NMS=\{0,0,2,1\}$ $MC=\{0,0,7_1,7_2\}$ $OS_1=\{-, -, \frac{1}{27}, \frac{1}{14}\}$ $\eta = 92.6\%$ $NPP=2$ $T_C=9.07$ min	$NS=3$ $NMS=\{0,1,2,1\}$ $MC=\{0,7_1,7_1,7_2\}$ $OS_1=\{-, \frac{1}{8}, \frac{9}{27}, \frac{1}{14}\}$ $\eta = 86.1\%$ $NPP=2$ $T_C=7.73$ min	$NS=4$ $NMS=\{1,1,1,2\}$ $MC=\{7_1,7_1,7_1,7_2\}$ $OS_1=\{\frac{1}{8}, \frac{9}{16}, \frac{17}{27}, \frac{1}{14}\}$ $\eta = 86.9\%$ $NPP=2$ $T_C=6.33$ min	$NS=4$ $NMS=\{1,2,1,2\}$ $MC=\{7_1,7_1,7_1,7_2\}$ $OS_1=\{\frac{1}{5}, \frac{6}{19}, \frac{20}{27}, \frac{1}{14}\}$ $\eta = 89.7\%$ $NPP=4$ $T_C=4.85$ min

In period h=3, an additional machine in configuration $MC7_2$ is needed, and both that machine and the existing machine in this configuration must be adapted for the operations cluster setup to maximise balancing efficiency, etc. This serial configuration has only one path and should therefore have the least variation in product characteristics. However, if a single element of the system fails, productivity drops to zero.

Class I configuration requires the installation of a completely new parallel path with three machines in period h=2, resulting in a doubling of installation and reconfiguration costs, Figure 9. However, the existing processing path does not require reconfiguration or additional configuration balancing.

The configuration of the Class II allows crossovers between stages and thus number of configurations increases as the number of machines increases. For example, in period h=4, four machines are required in configuration $MC7_1$ and two in configuration $MC7_2$, resulting in eight configurations of machines $MC7_1$ and two configurations of machines $MC7_2$ according to Equation 2. Some configurations are not possible due to spatial limitations, e.g. those where more than one machine is needed in stage 1. Of all possible configurations, the one with the best balancing efficiency is again selected. Overall, this configuration allows the largest number of processing paths, which can be unfavourable if product quality has higher priority than, for example, the productivity of the system in case of a machine failure.

5. Conclusion

In recent years, the paradigm of designing larger production operations has been replaced by the paradigm of designing smaller and shorter production operations, which offer more opportunities to reconfigure the system under changing market conditions. The system designer has the opportunity to choose between different configurations of the manufacturing system and his choice depends on

the investment constraints set, the space constraints and the primary objectives of the design process. Single manufacturing cells that provide only one processing path can have the least variation within a process and the highest expected quality. However, they can suffer from productivity losses if a single machine fails. Due to the small number of material handling devices, this system also requires the lowest initial investment compared to the other system configurations, Table 5. Although single cell configurations are scalable, the Class II configuration may offer better balancing efficiency.

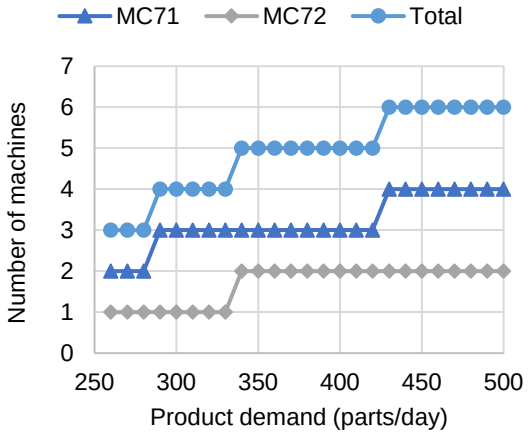

Figure 8. Required number of machines

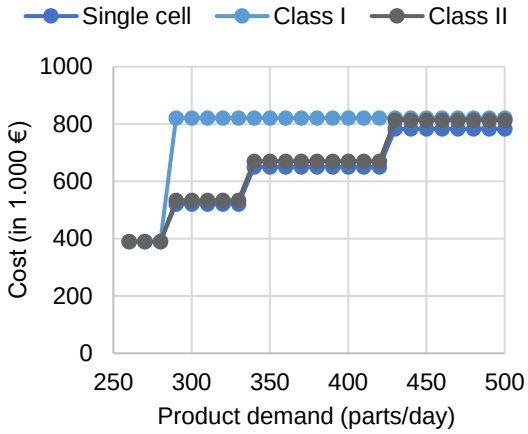

Figure 9. System installation and reconfiguration cost

The Class II configuration is preferred when the main design goals are scalability and productivity (with unreliable system equipment). However, the high initial investment due to the complex material handling system and most variation streams (processing paths) can be an issue if product quality is a system design priority. Class I symmetric configurations may suffer from scalability options, but overall, they provide a good balance between the system performances of the two previously mentioned configurations.

Table 5. *System performance characteristics*

System performance	Configuration		
	Single cell	Class I	Class II
Initial cost	low	medium	high
Quality	high	medium	low
Productivity	low	medium	high
Scalability	medium	low	high

Regardless of which system configuration the system designer has chosen, it is extremely important to think about this aspect in the early design phase and to consider the spatial requirements of the configuration, which in the long term will be able to provide the space needed to transport materials and energy and the necessary scalability of the system during its life cycle.

Acknowledgments

This work has been fully supported by the University of Rijeka (contract no. uniri-tehnic-18-33).

References

[1] Wiendahl, HP., Reichardt, J., Nyhuis, P., 2015. Functional Design of Workplaces. In: Handbook Factory Planning and Design. Springer, Berlin, Heidelberg.

[2] Wiendahl, HP., Reichardt, J., Nyhuis, P., 2015. The Synergetic Factory Planning Process. In: Handbook Factory Planning and Design. Springer, Berlin, Heidelberg.
[3] Putnik G., Sluga A., ElMaraghy H., Teti R., Koren Y., Tolio T., Hon B., 2013. Scalability in manufacturing systems design and operation: State-of-the-art and future developments roadmap. CIRP Annals. 62(2), 751-774.
[4] Fricke E., Schulz AP., 2005. Design for Changeability (DfC): Principles To Enable Changes in Systems Throughout Their Entire Lifecycle. Systems Engineering. 8(4), 342-359.
[5] Rheault M., Drolet JC., Abdulnour G., 1995. Physically reconfigurable virtual cells: A dynamic model for a highly dynamic environment. Computers & Industrial Engineering. 29(1-4), 221-225.
[6] Koren Y., Heisel U., Jovane F., Moriwaki T., Pritschow G., Ulsoy G., Van Brussel H., 1999. Reconfigurable Manufacturing Systems. CIRP Annals. 48(2), 527-540.
[7] Koren Y., Hu SJ., Weber TW., 1998. Impact of Manufacturing System Configuration on Performance. CIRP Annals. 47(1), 369-372.
[8] Rheault M., Drolet JR., Abdulnour G., 1996. Dynamic cellular manufacturing system (DCMS). Computers & Industrial Engineering. 31(1-2), 143-146.
[9] Ariafar S., Ismail N., 2009. An improved algorithm for layout design in cellular manufacturing systems. Journal of Manufacturing Systems. 28(4), 132-139.
[10] Wang W., Koren Y. 2012. Scalability Planning for Reconfigurable Manufacturing Systems. Journal of Manufacturing Systems. 31(2), 83-91.
[11] Youssef AMA., ElMaraghy HA., 2008. Availability consideration in the optimal selection of multiple-aspect RMS configurations. International Journal of Production Research. 46(21), 5849-5882.
[12] Koren, Y., Shiptalni, M., 2010. Design of reconfigurable manufacturing systems. Journal of Manufacturing Systems. 29, 130-141.

Review of materials used to manufacture magnesium wheels for light vehicles

***Anna Dziubińska*[1], *Krzysztof Majerski*[2], *Ewa Siemionek*[2], *Monika Kulisz*[2] *and Julia Longwic*[1]**

1) Warsaw University of Technology, Pl. Politechniki 1, 00-661 Warsaw, Poland

2) Lublin University of Technology, Nadbystrzycka 38 D, 20-618 Lublin, Poland

Corresponding author: anna.dziubinska@pw.edu.pl

Review article

Abstract: This article presents an overview of materials used to manufacture magnesium wheels for light vehicles. The analysis was carried out for the ForMag project, which aims to develop a new, efficient technology for the forming of magnesium alloy wheels for light vehicles from a preform cast into metal molds[1]. Knowledge compiled to date concerning the materials as well as their properties for the production of magnesium wheels will enable the design of a new technology for the forming of wheels from materials of the highest quality and durability. At present, magnesium wheels are mostly produced from cast magnesium alloys and magnesium alloys for metal forming. The cast magnesium alloys used to manufacture magnesium wheels include AZ91, AM50, AM60, AE44, ZK61, ZE41, EZ33, EQ21, WE43, and the newly developed Mg-2.96Nd-0.21Zn-0.39Zr alloy. The magnesium alloys for metal forming used to produce magnesium wheels include AZ31, AZ61, AZ80, and ZK30, ZK60. The study contains an analysis of their properties and examples of application.

Keywords: *magnesium wheels; light vehicles; magnesium alloys; casting alloys; metal forming alloys*

1. Introduction

The development of magnesium-based light metal alloys, which are increasingly used as a construction material for modern means of transport, is of fundamental importance for the development of the economy. The use of these alloys in the industry makes it possible to significantly reduce the weight of the means of transport while improving a number of technical parameters of vehicles (Figure 1).

It is predicted that magnesium consumption in a modern car may soon exceed 100 kg [2]. As far as the means of transport are concerned, magnesium alloys are used in all kinds of wheels of vehicles such as cars, motorbikes, bicycles, wheelchairs, etc. Figure 2).

Due to their unique properties, such as lightness, high vibration damping capacity, and high specific strength, they are an attractive material for the production of wheels. Magnesium is the lightest construction metal available. It is 1,5 times less dense than aluminum. Consequently, magnesium wheels can be designed to be much lighter than aluminum wheels and to have comparable strength properties at the same time. Currently, magnesium wheels are manufactured using cast magnesium alloys and magnesium alloys for metal forming. Magnesium wheels are produced using the following technologies: machining (high material losses generated); shaped casting - products are almost ready to be molded with little machining [3-8]; metal forming [9-11], including die forging [12], [13-14], extrusion [15-17] and rolling [18].

[1] The research leading to these results received funding from the Norway Grants 2014-2021 via the National Centre for Research and Development.

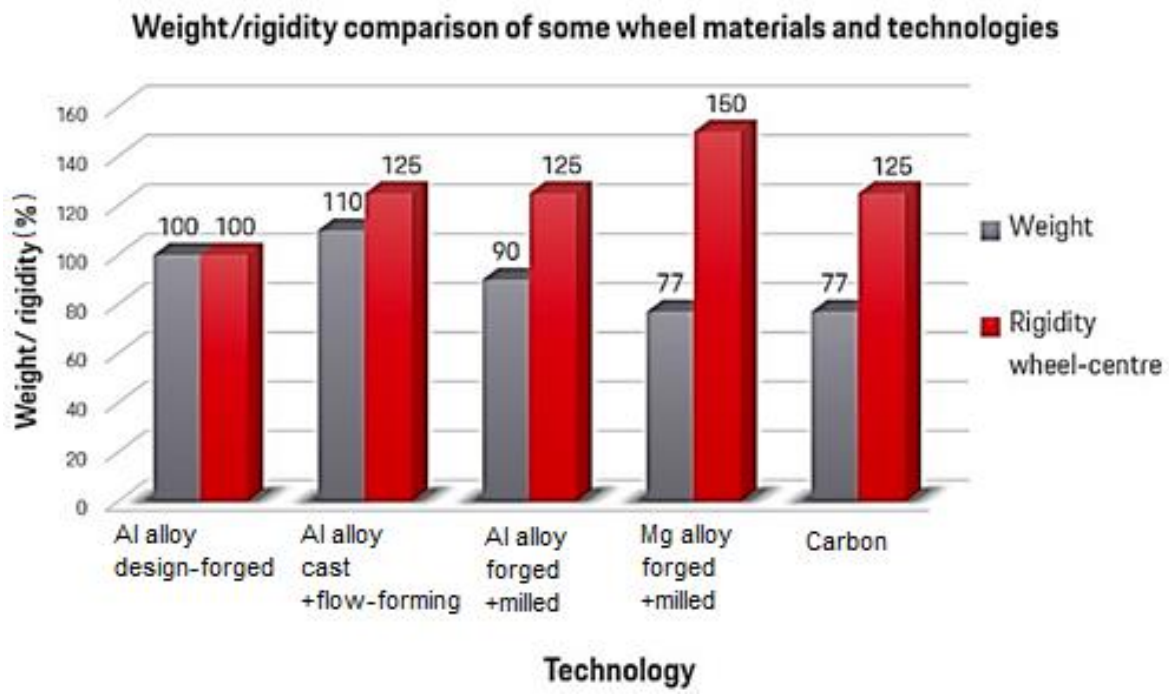

Figure 1. *Weight/rigidity comparison of certain wheel materials and technologies [1]*

Figure 2. *Magnesium alloy wheels: (a) car, (b) motorbike, (c) bicycle, (d) wheelchair*

At present, cast magnesium wheels are most frequently used in industrial applications. This is due to their greater availability on the market owing to well-developed casting technology and their lower

price. Foundries specializing in non-ferrous metals have the equipment and technological experience to produce cast magnesium wheels on a large scale. Cast magnesium wheels are characterized by high dimensional accuracy. Although cast wheels are cheaper than those produced by plastic metal processing methods, they are heavier than forged wheels for a given required load. Cast wheels are of inferior quality compared to forged wheels. The production disadvantages of cast wheels include cavities or porosity and other metallurgical microstructures such as larger grain sizes. Cast magnesium wheels have a higher tendency to crack during a strong impact at a high speed. On the other hand, forged wheels have a higher tendency to bend.

Metal forming of magnesium alloy wheels is a difficult task due to their narrow range of forming temperature parameters and sensitivity to deformation speed. Therefore, the forming process of magnesium wheels is carried out hot on forging machines with low working speeds while maintaining isothermal temperature conditions during deformation. Magnesium wheels are usually deformed in several stages from a billet in the form of a rod. The process is carried out in several forging operations, with repeated heating, on many tool sets, with heat treatment between operations. The resulting forgings are then machined (turned on a lathe and milled) to the final wheel shape by removing excess metal from the forged semi-finished product. Forged wheels have a fine-grained structure and better mechanical properties than cast wheels. The process of metal forming of wheels allows a favorable fiber flow to be obtained and the alignment of the directional pattern along the wheel spokes to be optimized. Although forged magnesium wheels are 25 percent lighter than cast wheels, they are less frequently used due to their high production cost.

The following article presents an overview of materials used in the manufacturing of magnesium wheels. The analysis of properties pertains to casting grades and those intended for metal forming processes.

2. Analysis of materials used in the manufacture of magnesium wheels

Magnesium wheels are manufactured from magnesium alloys due to several reasons:

- Low density- magnesium alloys are approx. 30-40% lighter than steel and aluminum. This means that magnesium wheels are much lighter than wheels manufactured from other metals. This lower mass translates into the enhancement of the vehicle’s performance, reduced fuel consumption, and improved handling of the vehicle.
- High durability- magnesium alloys are characterized by high mechanical strength, which allows them to be applied in the production of magnesium wheels. The tensile strength of AZ91, AM50, and AM60 magnesium alloys ranges from 180 to 300 MPa, while that of the WE43 alloy may reach up to 400 MPa.
- Ease of processing- magnesium alloys are relatively easy to process. This means that magnesium wheels may be designed in a variety of shapes and styles in order to meet aesthetic and functional requirements.
- Low heat sensitivity- magnesium alloys are characterized by strong resistance to high temperatures. Consequently, magnesium wheels made from such alloys retain their properties in extreme conditions.
- Good vibration-damping properties.

For designating magnesium alloys, the industry applies an American system approved by the ASTM (the American Society for Testing and Materials) specified in the ASTM B951-10 standard. In general, as far as the technological application is concerned, magnesium alloys may be divided into cast alloys and alloys for metal forming.

The cast magnesium alloys used to manufacture magnesium wheels include AZ91, AM50, AM60, AE44, ZK61, ZE41, EZ33, EQ21, WE43, and the newly developed Mg-2.96Nd-0.21Zn-0.39Zr alloy. The magnesium alloys for metal forming used in the production of magnesium wheels include AZ31, AZ61, AZ80, and ZK30, ZK60.

The review of the literature concerning cast magnesium alloys employed in the manufacture of magnesium wheels revealed the application of the following alloy grades:

• AZ91 (Mg-9Al-1Zn-0,1Mn) [12], [19–25]
The MgAl9Zn1 constitutes the most popular magnesium alloy for casting. It is characterized by good tensile properties and fluidity. Considerable aluminum content (approx. 9% of the mass) gives the alloy low ductility in room temperature. The alloy undergoes precipitation hardening. In order to enhance ductility, the alloy is homogenized within the 420-435 °C range for a minimum of 16 h. Supersaturation is conducted typically within the 415-430°C range, while aging, depending on the sought after properties may be carried out in the 170-200 °C range.

• AM50 (Mg-5Al-0,5Mn) [26]
The AM50 alloy is intended for cast production, especially for pressure die casting. It is used in the production of structural elements in the automotive industry, electronics, and telecoms. Its chief advantages include very good fluidity, high durability-mass ratio, and very high corrosion resistance. The alloy undergoes homogenization and precipitation hardening.

• AM60 (Mg-6Al-0,25Mn) [12], [27], [28]
The AlMg6 alloy belongs to the casting alloys group. It is predominantly used in pressure die casting processes. Its properties are similar to those discussed for the AM50 alloy. Manganese must be present in order to for the alloy to undergo precipitation hardening. The element is present in the AM60B grade.

• AE44 (Mg-4Al-4RE) [29]
The Mg-4Al-4RE alloy is used in pressure die casting. Its composition includes rare earth elements: a mixture of cerium and lanthanum. The application of this mixture allows hardening with the use of T5 heat treatment. The employment of such a process enables improved tensile strength to be obtained without losing any ductility.

• ZK61 (Mg-6Zn-0,8Zr) [30]
The Mg6Zn0,8Zr alloy is a high-strength cast alloy grade. The ZK61 alloy was developed to be used in sand casting. The content of zirconium facilitates grain fragmentation. On the other hand, Zn enables precipitation hardening. Supersaturation temperature is high and may reach up to 510 °C for 3 h. Aging may be performed in 120 °C for 24 h. Even though it is characterized by high strength, the alloy is not broadly used due to the tendency to form microporous structures when cast. It is also unweldable due to high Zn content.

• ZE41 (Mg-4,5Zn-1,5RE, EZ33 (Mg-2RE-2,5Zn-0,6Zr), EQ21 (Mg-RE-2Ag-1,5Zr) and WE43 (Mg-4Y-3,4RE-0,6Zr) [19]
Cast alloys group. The ZE41 alloy is characterized by high tensile strength up to 200 °C. The EZ33 alloy manifests a higher creep resistance and may operate in temperatures up to 250 °C. The alloy is characterized by good fluidity. It is employed in the manufacture of tight castings. A high degree of precipitation hardening was determined in alloys containing Zn and rare earth elements. Maximum hardening while aging is obtained for those alloys where secretions are coherent with the metallic base. Such alloys are applied in the manufacture of engines and gearboxes operating at 120-205 °C. The EQ21 magnesium alloy contains silver and manifests considerable tensile strength at room temperature. It also exhibits good creep resistance up to 200 °C. It also welds well. The good mechanical properties of the Mg-RE-Ag-Zr group, to which EQ21 belongs, make it ideal for the manufacture of critical parts of machines. Owing to the high content of yttrium, the WE43 alloy manifests high flashpoint (750 °C) and strong hardening properties. Its broad application is limited due to its high price.

• Mg-2,96Nd-0,21Zn-0,39Zr [6]
This cast alloy has been recently developed. According to the authors of the study [6], the alloy manifests high strength properties and corrosion resistance as well as high fatigue limit. The alloy may be used for sand casting and metal casting. When using the alloy, it is beneficial to apply T6 heat treatment.
Cast magnesium alloys may be shaped by means of casting processes such as continuous casting and shape casting. As far as shape casting is concerned, the following methods can be distinguished: sand casting (Mg-Al-Zn, Mg-RE-Zr, Mg-Zn-Zr magnesium alloys); die casting (due to high temperature brittleness Mg-Zn-Zr group is not applied); pressure casting (application of Mg-Al-Zn, Mg-Al-Mn, Mg-Al-Si, Mg-Al-Ca, Mg-Al-Sr groups); pressure casting with compression, and casting from semi-solid state [31].

The review of literature in terms of magnesium alloys for metal forming used in the manufacture of magnesium wheels revealed the application of the following grades:

• AZ31 (Mg-3Al-1Zn) and AZ61 (Mg-6Al-1Zn) [14]
The AZ31 and AZ61 alloys are intended for plastic metal forming processes. They deform in high temperatures especially when fine grains are present (<3 μm). They manifest good tensile strength and ductility. Alloy additives - aluminum and zinc - enable precipitation hardening of AZ31 and AZ61, and enhance the granularity of the microstructure. Additionally, the alloys can be reinforced by plastic deformation. The AZ91 alloy is intended for operation in room temperature or elevated temperatures up to 100 °C. The alloy is weldable. Once welded, elements made from this alloy should undergo stress-relief annealing in order to reduce the probability of stress corrosion cracking. The homogenization of the AZ31 alloy is conducted in 390 °C for 22 h, while for AZ61 in 415 °C for 24 h. As far as supersaturation is concerned, the temperature range for the AZ91 alloy reaches 415 °C and for AZ31 it amounts to 450 °C. The maximum aging temperature for AZ61 amounts to 175 °C and for AZ31 it is 300 °C.

• AZ80 (Mg-8Al-0,5Zn)[15–19]
The AZ80 alloy is characterized by high strength and can be heat treated. It can also undergo plastic metal forming and forging. Semi-finished products are manufactured by means of extrusion. Elements made from this alloy may be operated at room temperature. The high maximum solubility of aluminum in magnesium (12,7% by weight) enhances the precipitation capability of the alloy, favorably with fine Mg17Al12 precipitates. The typical homogenization temperature range reaches 400-430 °C, and time reaches up to 10 h. Supersaturation temperatures are analogous. On the other hand, aging is conducted in the 170-200 °C range for 15-30 h.

• ZK30 (Mg-3Zn-0.8Zr-0,3S) and ZK60 (Mg-5,5Zn-0,45Zr) [19]
The ZK30 and ZK60 alloys are intended for plastic metal forming. Semi-finished products are obtained by extrusion and aging or precipitation hardening. They are also intended for the production of forgings to be operated at room temperature, the same as the AZ80 alloy. If fine grains are obtained, the ZK60 alloy may undergo superplasticity. The ZK30 and ZK60 alloys manifest a slightly better forging capacity than other alloys. Typical homogenization conditions for ZK60 are as follows: temperature of 420 °C, time of 8-12 h. For aging they are 180 °C and 18 h.

3. Examples of magnesium alloy applications for magnesium wheels

Example applications of cast magnesium alloys for the production of magnesium wheels are discussed below.

AZ91D alloy motorcycle wheels are formed by die casting and double control forming [20]
The study presents a comparison of microstructures and mechanical properties of samples derived from motorcycle wheels manufactured by means of pressure die casting as well as by a novel method

of double control forming from the AZ91D alloy (Figure 3). The novel method consists of the compression of the ingot. Functional properties exceed those obtained by means of pressure die casting.

(a) (b)

Figure 3. *Motorcycle wheel parts are formed by: (a) die casting, (b) double control forming [20]*

Optimization of Magnesium Alloy Wheel Dynamic Impact Performance [21]
The study analyzed wheels made from AZ91 as regards vibration modeling in relation to 6061-T6 aluminum and SPFH540 steel. The magnesium alloy manifested the best vibration-damping characteristics.

AZ91 automobile wheel based on bending and radial loads [22]
The authors conducted a FEM analysis for wheels made from, inter alia, AZ91. The analysis revealed that despite inconclusive results, for light structures, the magnesium alloy is preferred.

Numerical simulation of low-pressure die casting of AZ91 magnesium wheel [23]
The study outlined the results of numerical simulations of low-pressure die casting of wheels from the AZ91D alloy. Critical areas were indicated in relation to structural defects (e.g. pores in spokes). Additionally, the adjustment of filling parameters was proposed in order to solve the problem.

Low-pressure die casting of AZ91D magnesium alloy wheel castings [24]
The authors analyzed the parameters of low-pressure die casting in metal forms. Optimal parameters were determined in order to obtain structural homogeneity, reduce shrinkage porosity, and lower dendritic segregation. The most suitable parameters for a wheel made from AZ91D are as follows: filling temperature of 689 °C and filling pressure of 6,5 kPa.

Passenger Car Tires and Wheels Development - Manufacturing – Application [12]
The study discussed examples of actual wheels made from AZ91 and AM60 by means of sand casting and metal casting as well as pressure die casting (Figure 4). Both advantages and drawbacks of each method were determined.

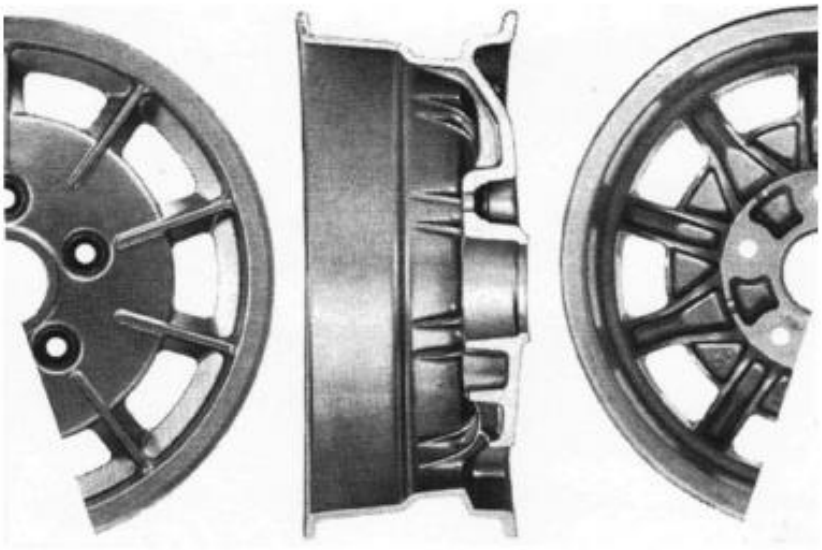

Figure 4. *Magnesium pressure-cast wheel made for the Porsche 914/6 [12]*

Selection of the Magnesium Alloy by MADM Methods for Automobile Wheels [25]
The authors compared a variety of magnesium alloys in terms of their applicability for the manufacture of wheels. The study analyzed alloys such as: AZ91, AM50, AM60, AZ31, ZE41, EZ33, ZE63, and ZC63. The Multi-Attribute Decision Making (MADM) method was applied. For all cases, the AZ91 alloy proved the most suitable.

AM50A Magnesium Alloy Components Prepared by Die Casting (DC) and Double Control Forming (DCF) [26]
The authors of the work compared the results of strength tests for samples derived from motorcycle wheels made in the DC and DCF technologies. It was established that the DCF enables much better properties to be obtained for the AM50A alloy.

Die Casting Process of the AM60B Magnesium Alloy Motorcycle Wheel [28]
The study analyzed the AM60B alloy and pressure die casting for the manufacture of motorcycle wheels. The work revealed that the material and technology meet the requirements for motorcycle wheels.

Bicycle magnesium wheels made from the AM60B magnesium alloy [32]
Apart from motorcycle wheels, magnesium alloys may be used to manufacture bicycle wheels. For example, the Shuangye electric bicycle introduced integrated magnesium wheels with six or three spokes (Figure 5). These wheels are lighter than those made from aluminum alloys [33]. The bicycle industry employs the AM60B alloy [32]. The study modified the width of the spoke and the radius of the wheel. Optimized radius parameters were established for the redesigned wheel. The optimal values are as follows: R1=24.45 mm, R2=13 mm, R3=13 mm, R4=307.5 mm, and R5 value is constant. The maximum stress was lowered to 65.612 MPa.

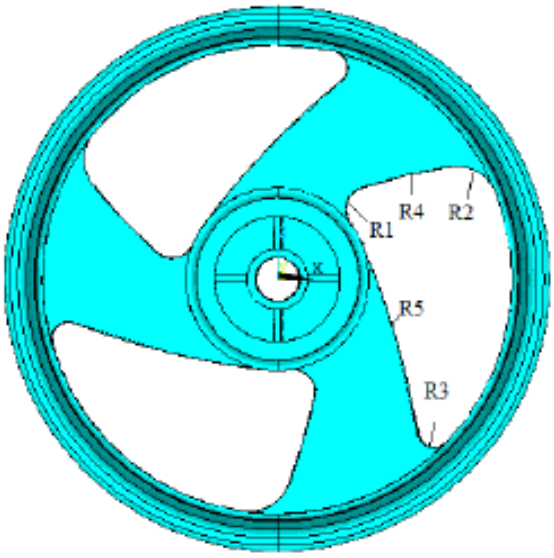

Figure 5. *AM60B magnesium alloy electric bicycle wheel*

AE44 magnesium casting technology for structural applications [29]
The study discussed examples of the application of magnesium alloys in the production of, inter alia, automotive wheels. High costs and insufficient corrosion resistance were indicated as chief barriers to the mass production of magnesium wheels. The AE44 (Mg-4Al-4RE) alloy was indicated as the one possessing high strength and ductility both in a room and at elevated temperatures. The authors argued that the introduction of anticorrosion coatings and the development of various casting technologies may broaden the application range of magnesium alloy wheels.

ZK61-Y Magnesium Alloy Wheel Hub via Liquid Forging—Isothermal Forging Process [30]
The work outlined the results of studies concerning the impact of yttrium additive upon the microstructure and properties of the ZK61 alloy used for the manufacture of the wheel's hub by means of liquid forging. The study revealed that the best mechanical properties and correct microstructure were obtained for 1% of yttrium additive by weight. The analysis of thermal conditions showed that the best results were obtained for the forging temperature of 380 °C.

Materials used for the manufacturing of alloy wheels [27]
The review type paper (conference materials) compares selected properties of magnesium alloys, aluminum, and titanium as regards the manufacture of wheels. Additionally, the authors analyzed individual manufacturing technologies for the surveyed materials. Magnesium wheels are characterized by low mass, high specific strength, and resistance to dynamic deformations. One of the chief problems is corrosion resistance. The authors indicated that casting and forging constitute predominant technologies. Pressure casting has also become a developing technology in recent years. The AM60 alloy, the A356 aluminum alloy, and unspecified titanium alloy were selected for the comparative analysis. The analysis revealed that the aluminum alloy manifests the greatest effectiveness (cost-effect ratio).

Properties of Cast Mg-2.96Nd-0.21Zn-0.39Zr Magnesium Wheels [6]
The work discusses the results of fatigue tests of samples derived from cast magnesium wheels. The wheels were manufactured from Mg-2,96Nd-0,21Zn-0,39Zr by means of low-pressure die casting into a steel form. The wheels were tested at the post-casting stage and T6. A fatigue test with controlled deformation was conducted. The results proved conclusively that samples that were heat treated are characterized by considerably higher fatigue limits. The authors of the work highlighted the effect of hardening and the decline of structural defects (shrinkage porosity) due to heat treatment. The test was conducted with a frequency of 2 Hz with push-roll loading.

Examples of the application of magnesium alloys for plastic metal forming in the manufacture of magnesium wheels are discussed below.

New extrusion process of AZ80 magnesium alloy automobile wheels [15]
The study reviewed methods employed in the manufacture of magnesium wheels, especially AZ80. Forging and flow-forming, forging and rotary compression, and extrusion of the perforated charge were discussed. This last method was of particular interest. It was stressed that the application of the method along with T6 heat treatment enables properties that meet automotive industry requirements to be obtained.

Extruded AZ80 automotive wheel [17]
The work discusses the results of fatigue tests of samples derived from magnesium wheels manufactured from the AZ80 alloy by means of extrusion. The wheels were manufactured by extruding perforated charge from cast rods homogenized at 385 °C for 12 h. The results of fatigue tests were compared to the results obtained for rolled samples.

Effects of aging treatments on low-cycle fatigue behavior of extruded AZ80 for automobile wheel disks [16]
The authors of the work analyzed wheel discs made from extruded AZ80 alloy and the impact of T5 and T6 heat treatment upon low-cycle fatigue. The results clearly suggest that T5 heat treatment offers the greatest applicability as far as low-cycle fatigue is concerned.

AZ80 magnesium wheels for vehicles
AZ80 constitutes another alloy used in the production of vehicle wheels. Rivers et al. studied controlled fatigue of samples derived from the spokes of a vehicle’s cast wheel made from AZ80. It was proven that the fatigue limit amounted to approx. 98 MPa [34].
The application of magnesium in a vehicle's wheel leads to the improvement of handling owing to the reduction of unsprung mass. The authors of the studies [35], [36] developed a new magnesium alloy based upon AZ80. It manifests excellent mechanical properties. As a result, a magnesium wheel was obtained which is 30% lighter than aluminum wheels. Excellent granularity for continuous casting in the manufacture of wheels was obtained by means of Sr or CaNCN additive [35], [36].

Precision forging technologies for magnesium alloy brackets and wheels [14]
The study proposes the application of homogenized AZ31 and AZ80 alloys in the manufacture of wheels by means of extruding the perforated charge. The application of homogenization and perforated charge considerably reduces processing forces.

Application of AZ31 magnesium alloy to produce aircraft magnesium wheels [37], [38]
Magnesium wheels are employed, inter alia, in the aviation industry, e.g. in the hubs of aircraft wheels. Śliwa et al. discuss the application of AZ31 for that purpose [37]. This alloy was also studied by Kuc et al. [38]. They conducted studies concerning the production of aircraft wheel hubs by means of hot forging from magnesium alloys with a diverse aluminum content ranging from 3% to 8% (AZ31, AZ61, AZ80). Their research shows that the selected element possessing specific properties can only be made from the AZ31 alloy.

Vehicle wheels made from the ZK30 alloy [39]
Otto Fuch produced a prototype of a wheel forged from ZK30 by means of the same tools used to manufacture an aluminum wheel of the same setup present on the market today (Figure 6) [39]. It weighs 6,8 kg (35%) less than the aluminum wheel. The strength is isotropous because deformation stages are uniaxial and stress in all parts of the wheel amounts to 12-14%.

Figure 6. *Prototype of magnesium wheel forged from ZK60*

4. Conclusion

The article presents the current state of knowledge in the field of materials used in the manufacture of magnesium wheels. It also presents their properties and examples of their use in previously applied methods of wheel manufacturing. The analysis of the problem was carried out on the basis of the literature and available standards as well as commercial offers from magnesium wheel manufacturers. This study systematizes knowledge available in this area. The collected information will be used for the international project entitled "New technology of forming magnesium alloy wheels for light vehicles" delivered in the framework of the Applied Research Programme of the Norwegian Financial Mechanism 2014-2021, which involves developing a new, efficient technology for forming magnesium alloy wheels for light vehicles from a preform cast into metal molds. The selection of materials with good forming properties for the project will ensure that the final product (wheels) possesses the assumed shape and dimensions and will be of the highest usable quality.

Acknowledgments

Project “New technology of forming magnesium alloy wheels for light vehicles”; No. NOR/SGS/ForMag/0083/2020-00. The research leading to these results has received funding from the Norway Grants 2014-2021 via the National Centre for Research and Development.

References

[1] Burk, G., 2018. Porsche 911 Turbo carbon wheel, 9th International Munich Chassis Symposium 2018, Proceedings Springer, Vieweg, Wiesbaden

[2] Blawert, N. C., Hort, N., Kainer, K.U., 2004. Automotive applications of magnesium and its alloys, Trans. Indian Inst. Met. 57, 397-408.

[3] Zhang, Z., Zhang, Y., Zhang, H., Pan, A., Liu, J., 2019. Research on Die Casting Process of Magnesium Alloy Motorcycle Wheel Based on New Engineering Construction, Journal of Physics: Conference Series 1302, 1-7.

[4] Ying, F., Tang, H., Peng, T., 2008. Numerical simulation of low pressure die-cast of magnesium alloy wheel, Asia Simulation Conference - 7th International Conference on System Simulation and Scientific Computing, IEEE.

[5] Luo, A.A., 2013. Magnesium casting technology for structural applications, J. Mag. Al. 1(1), 2-22.

[6] Li, Z., Luo, A.A., Qigui, W., Liming, P., Peng, Z., 2016. Fatigue Properties of Cast Magnesium Wheels, Met. Mat. Trans. A 47(8), 4239-4257.

[7] Wang, Y., Li, D., Peng, Y., Zeng, X., 2007. Numerical simulation of low pressure die casting of magnesium wheel. Int. J. Adv. Manuf. Technol. 32, 257-264.
[8] Zhang, C., Fu, Y., Wang, H., Hao, H., 2018. Multi-objective optimization of process parameters during low-pressure die casting of AZ91D magnesium alloy wheel castings. Ch. Foun. 15, 327-332.
[9] Fujita, M., Yamamoto, Y. Sakate, N., Hirabara, S., 1995. Method of Manufacturing a Forged Magnesium Alloy. US Patent no. 5409555.
[10] Zhao, M.J., Wu, Z.L., Chen, Z.R., Huang, X.B, 2017. Analysis on flow control forming of magnesium alloy wheel, IOP Conf. Ser.: Mater. Sci. Eng. 170, 1-6.
[11] Fujita, M., Yamamoto, Y. Sakate, N., Hirabara, S., 1999. Method of Making an Article of Manufacture Made of a Magnesium. US Patent no. 5902424.
[12] Leister, G., 2018. Wheels. In: Passenger Car Tires and Wheels, Springer Publisher, 283, Cham
[13] Fujita, M., Sakate, N. Hirahara, S., Yamamoto, Y., 1995. Development of Magnesium Forged Wheel, Section 5: J. Mat.&Man. SAE Transactions. 104, 327-331.
[14] Wang, Q., Zhang, Z., Zhang, X., Yu, J., 2008. Precision forging technologies for magnesium alloy bracket and wheel. Tran. Non. Met. Soc. Ch. 18, 205-208.
[15] Wang, Q., Zhang, Z., Zhang, X., Li, G., 2010. New extrusion process of Mg alloy automobile wheels. Tran. Non. Met. Soc. Ch. 20, 599-603.
[16] Zhao, X., Gao, P., Chen, G., Wei, J., Zhu, Z. Yan, F., Zhang, Z., Wang, Q., 2021. Effects of aging treatments on low-cycle fatigue behavior of extruded AZ80 for automobile wheel disks. Materials Science & Engineering A. 799, 1-13.
[17] Zhao, X., Gao, P., Zhang, Z., Wang, Q., Yana, F., 2020. Fatigue characteristics of the extruded AZ80 automotive wheel. Int. J. Fat. 132, 1-29.
[18] Yang, H., Huang, L., Zhan, M., 2010. Coupled thermo-mechanical FE simulation of the hot splitting spinning process of magnesium alloy AZ31. Comp. Mat. Scien. 47, 857-866.
[19] Friedrich, H.E., Mordike, B.L., 2006. Magnesium Technology: Metallurgy, Design Data, Applications, Springer Berlin, Heidelberg.
[20] Jiang, J., Wang, Y., Chen, G., Liu, J., Li, Y., Luo, S., 2012. Comparison of Mechanical Properties and Microstructure of AZ91D Alloy Motorcycle Wheels Formed by Die Casting and Double Control Forming. Mater. Des. 40, 541-549.
[21] Jiang, X., Liu, H., Lyu, R., Fukushima, Y., Kawada, N., Zhang, Z., Ju, D., 2019. Optimization of Magnesium Alloy Wheel Dynamic Impact Performance. Adv. Mater. Sci. Eng. 1-12.
[22] Jiang, X., Lyu, R., Fukushima, Y., Otake, M., Ju, D.Y., 2018. Lightweight Design and Analysis of Automobile Wheel Based on Bending and Radial Loads, IOP Conf. Series: Materials Science and Engineering. 372, 1-7.
[23] Wang, Y.C., Li, D.Y., Peng, Y.H., Zeng, X.Q., 2007. Numerical Simulation of Low Pressure Die Casting of Magnesium Wheel. Int. J. Adv. Manuf. Technol. 32, 1-4.
[24] Zhang, C., Fu, Y., Wang, H., Hao, H., 2018. Multi-Objective Optimization of Process Parameters during Low-Pressure Die Casting of AZ91D Magnesium Alloy Wheel Castings, China Foundry. 15, 327–332.
[25] Kumar Sameer, D., Suman, K.N.S., 2014. Selection of Magnesium Alloy by MADM Methods for Automobile Wheels, I.J. Eng. Manuf. 2, 31–41.
[26] Jiang, J., Nie, X., Wang, Y., Yang, J., 2014. Microstructure and Mechanical Properties of AM50A Magnesium Alloy Components Prepared by Die Casting and Double Control Forming. Adv. Mech. Eng. 6, 1-11.
[27] Naim, A., Kumar, R., Bhatia, S., 2021. A Review Paper on Materials Used for Manufacturing of Alloy Wheels, IOP Conf. Ser. Mater. Sci. Eng. 1136, 1-10.
[28] Zhang, Z., Zhang, Y., Zhang, H., Pan, A., Liu, J., 2019. Research on Die Casting Process of Magnesium Alloy Motorcycle Wheel Based on New Engineering Construction. Journal of Physics: Conference Series. 1302(4), 1-8.
[29] Luo, A.A., 2013. Magnesium Casting Technology for Structural Applications. J. Magnes. Alloy. 1(1), 2-22.

[30] Qi, Y., Wang, H., Chen, L., Zhang, H., Chen, G., Chen, L., Du, Z., Preparation and Mechanical Properties of ZK61-Y Magnesium Alloy Wheel Hub via Liquid Forging—Isothermal Forging Process, Metals. 10, 1-19.
[31] Kawalec, A., Oczos, K.E., 2012. Light Metal Forming, PWN Publisher. 573, Warsaw
[32] Pan, B.S., Gong, H.L., Peng, T.H., Zhang, M., 2009. Magnesium Alloy Material Substitution Redesign Method for Wheels of Electric Bicycle. Adv. Mat. Res. 69–70, 631–635.
[33] Magnesium Alloy Integrated Wheel Mountain Batteries Bicycle, Ebike Shuangye, available online: https://www.zhsydz.com/magnesium-alloy-integrated-wheel-mountain-batteries-bicycle (accessed 26 October 2022).
[34] Rivers, G., 2011. Cyclic Fatigue Behaviour of Wrought AZ80 Magnesium Alloy from Forged Automotive Wheel, Master Thesis - McMaster University - Materials Science and Engineering.
[35] Wang, J., Yang, F., Ma, J., Zhang, T., Cao, H., Che, X., Geng, L., Zhang, Z., Wang, Q., Yang, Y., 2020. Effects of Ageing on Low-Cycle Fatigue (LCF) Properties of AZ80 Magnesium Alloy Wheel Hub, Mater. Res. Express. 7(9), 1-9.
[36] Fujita, M., Sakate, N., Hirahara, S., Yamamoto, Y., 1995. Development of Magnesium Forged Wheel, SAE Transactions. 104, 327-331.
[37] Śliwa, R.E., Balawender, T., Hadasik, E., Kuc, D., Gontarz, A., Korbel, A., Bochniak, W., 2017. Metal Forming of Lightweight Magnesium Alloys for Aviation Applications, Archives of Metallurgy and Materials. 62, 1559–1566.
[38] Kuc, D., Hadasik, E., Gontarz, A., 2012. Forging Technology of Magnesium Alloys, Metallurgist – Metallurgical News. 8, 610–613.
[39] Kainer, K.U., 2003. Magnesium Alloys and Technology, WILEY -VCH Publisher. 284, Weinheim

The influence of thermo-plastic processing parameters on the structure of the AZ91 cast magnesium alloy

***Anna Dziubinska*[1], *Krzysztof Majerski*[2], *Ewa Siemionek*[2], *Piotr Surdacki*[2] *and Wojciech Presz*[1]**

1) Warsaw University of Technology, Pl. Politechniki 1, 00-661 Warsaw, Poland

2) Lublin University of Technology, 38D Nadbystrzycka, 20-618 Lublin, Poland

Corresponding author: anna.dziubinska@pw.edu.pl

Professional article

Abstract: The article discusses the impact of thermo-plastic processing parameters on the structure of the AZ91 cast magnesium alloy. The study examined the sand-cast AZ91 Mg alloy. The alloy was homogenized and subsequently underwent upsetting tests and further heat treatment in the form of supersaturation and aging. The homogenization of the AZ91 alloy was conducted at 415 °C for 24 h with argon as the shielding gas. The upsetting tests were conducted at 380 °C; 400 °C; 420 °C for two deformation values: ε=0.7 and 1.1. After upsetting, the samples were water- and air-cooled. Subsequently, samples without cracks underwent supersaturation at 415 °C for 6 h, and artificial aging at 175 °C for 24 h. After that, laboratory testing was conducted to evaluate microstructures and Vickers microhardness. Based on the results obtained from the swelling, structure and hardness tests, the most favorable heat treatment conditions were determined for AZ91 alloy. It is recommended that before deformation, heat treatment of the alloy should be carried out in the form of homogenization at 415 °C for 24 h with argon as a shielding gas. Among the tested temperature parameters for conducting plastic processing in the range of 380-420 °C, forging of sand-cast AZ91 magnesium alloy at 420 °C with water cooling and deformation of 0.7 seems to be the most favorable. After plastic processing of the alloy, further heat treatment in the form of supersaturation at 415 °C for 6 hours with argon as a shielding gas, as well as artificial aging at 175 °C for 24 hours is recommended.

Keywords: *cast magnesium alloys; AZ91 alloy; homogenization; upsetting test; heat treatment; structure; microhardness*

1. Introduction

Magnesium alloys have enjoyed considerable interest in aviation, automotive, and machine industries [1–4]. Characteristics enabling such a wide application of the alloys include low density, dimensional stability, vibration-damping capacity, good machining properties, and resistanceto indentation [5], [6]. The limitations of the alloys' application encompass low corrosion resistance, high price, low ductility, and tendency to self-ignite [7–9]. Due to problems with the plastic metal forming of magnesium alloys, their full potential as a construction material has not been completely exploited. The alloys manifest a high tendency for cracking. Therefore, they require slow hydraulic pressing and multi-stage and time-consuming heat treatment. The treatment is not easy due to the fact that Mg alloys are very sensitive to temperature changes and other processing parameters. As a consequence, it is worthwhile to devote particular attention to the parameters of individual thermo-plastic processing stages, beginning with homogenization, then plastic metal forming, and final heat treatment. The objective of the present study was to determine the impact of thermo-plastic processing parameters on the structure of sand-cast AZ91 magnesium alloy.

2. Research methodology

The present study surveyed the magnesium alloy whose chemical composition was outlined in Table 1.

Table 1. *Chemical composition of the AZ91C magnesium alloy*

Al	Zn	Mn	Si	Cu	Ni	Mg
8.1-9.3	0.40-1.0	0.13-0.35	0.3	0.1	0.01	balance

Cylindrical samples (Ø20×30 mm) derived from the sand-cast AZ91 magnesium alloy were used in the tests. After casting, the samples were homogenized at 415 °C for 24 h with argon as the shielding gas [10], [11] (Figure 1).

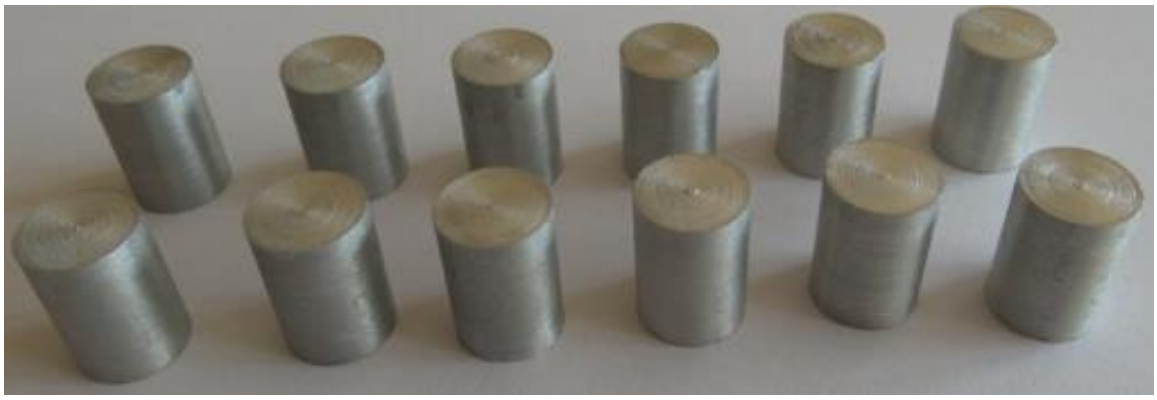

Figure 1. *Example cylindrical samples used in the study*

After homogenization, the cylindrical samples underwent upsetting tests (Figure 2). The following sample temperature conditions were adopted for the study: 380 °C, 400 °C, and 420 °C [12–14]. Upsetting dies were heated to 200 °C. The samples were upset to two final heights for each temperature, i.e. 15 and 10 mm. As a consequence, two logarithmic deformation values were obtained: ε = 0.7 and 1.1. After upsetting, the samples were water- and air-cooled. Samples without cracks were heat treated (Figure 4).

Subsequently, samples without cracks underwent supersaturation at 415 °C for 6 h with argon as the shielding gas, and artificial aging at 175 °C for 24 h [10], [11], [15], [16]. After these thermo-plastic processing steps were completed, crack-free samples were cut and underwent inclusion in epoxy resin. Such metallographic specimens were ground and polished (Figure 3). Table 2 outlines the material's grinding parameters.

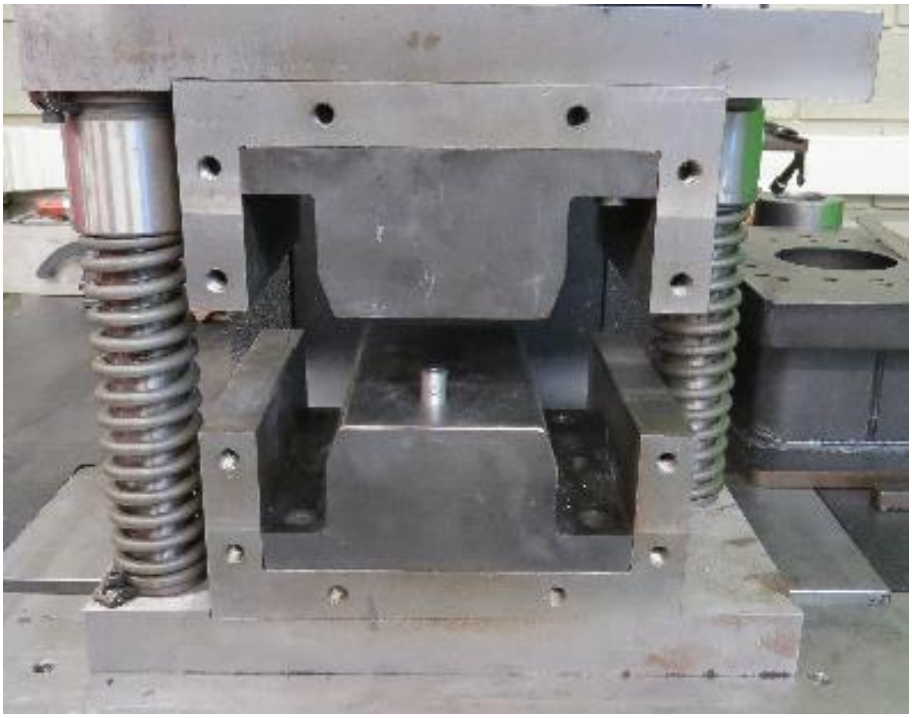

Figure 2. *Device for upsetting samples made from the cast AZ91 alloy*

(a) (b)

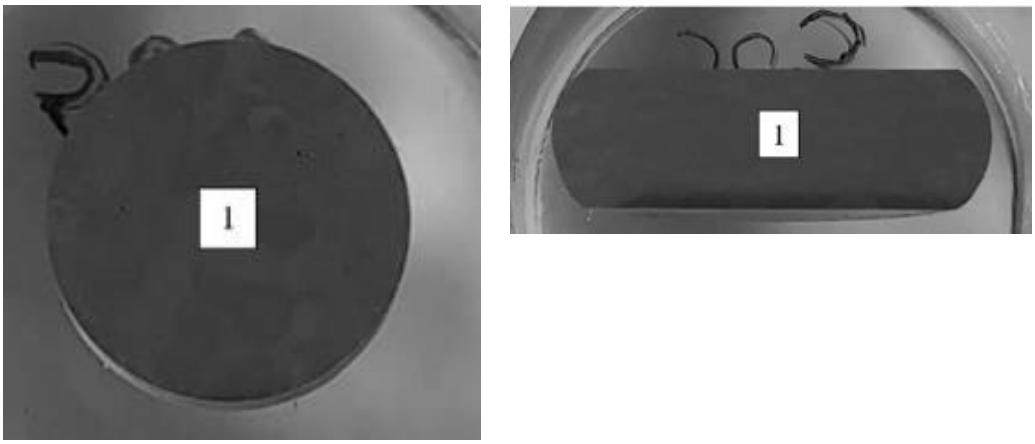

Figure 3. *An example of the metallographic specimen from the cylindrical AZ91 magnesium alloy samples before upsetting (a) and after upsetting (b) with the area marked for structural examination*

Table 2. *Grinding parameters of AZ91 alloy samples*

No.	The granularity of the disc	Oscillations (rev./min)	Time (min)	Force (N)	Grinding direction
1.	P80	240	4	25	Up-grinding
2.	P220	240	4	25	Up-grinding
3.	P500	240	4	25	Up-grinding

Grinding discs used for grinding the samples were diamond-coated. When grinding, the disc was sprayed with water. Table 3 outlines the polishing parameters of the samples.

Table 3. *Polishing parameters of the AZ91 alloy samples*

No.	Abradant size	Oscillations (rev./min)	Time (min)	Force (N)	Grinding direction
1.	9	220	5	25	Up-grinding
2.	3	220	4	25	Up-grinding
3.	0.05	150	4	20	Down-grinding

Initially, the samples were polished with a diamond suspension (9 µm and 3 µm), and then with an OPS silica suspension (0.05 µm). In between the individual steps of the procedure, the samples were washed with distilled water and alcohol and then dried. After the above steps, the samples were etched by immersion and gentle stirring for 5-15 seconds in a solution of the following composition: 100 ml ethanol, 10 ml distilled water, 10 ml acetic acid, and 5 g picric acid etchant. Then, the samples' microstructure was examined by means of Nikon MA200 microscope. The samples' Vickers microhardness was also tested with the Future-tech FM800 hardness tester. The measurements were made on the HV 0.5 scale in accordance with the PN-EN ISO 6507-1:2006 standard.

3. Analysis of the results

The analysis of the capacity for deformation of the cast AZ91 magnesium alloy was conducted based on the visual inspection of the upset samples developed under varying process parameters such as forging temperature and deformation. The emergence of defects in the form of cracks disqualified samples. Figure 4 outlines the results of upsetting tests.

CRACKING			
Cooling medium after forging	Forging temperature (°C)		
	380	400	420
deformation value: ε=0.7			
air	no	yes	no
water	no	yes	no
deformation value: ε=1.1			
air	yes	yes	yes
water	yes	yes	yes

Figure 4. *Results of upsetting tests of cast AZ91 magnesium alloy*

Based upon Figure 4, crack-free samples were obtained for a deformation value equal to 0.7 for the upsetting test conducted at 380 °C and 420 °C. An example crack-free sample was obtained for the forging temperature of 420 °C. The sample with cracks was obtained for the temperature of 400 °C (Figure 5). For the deformation value of 1.1, cracks in samples emerged in each of the surveyed temperatures.

(a) (b)

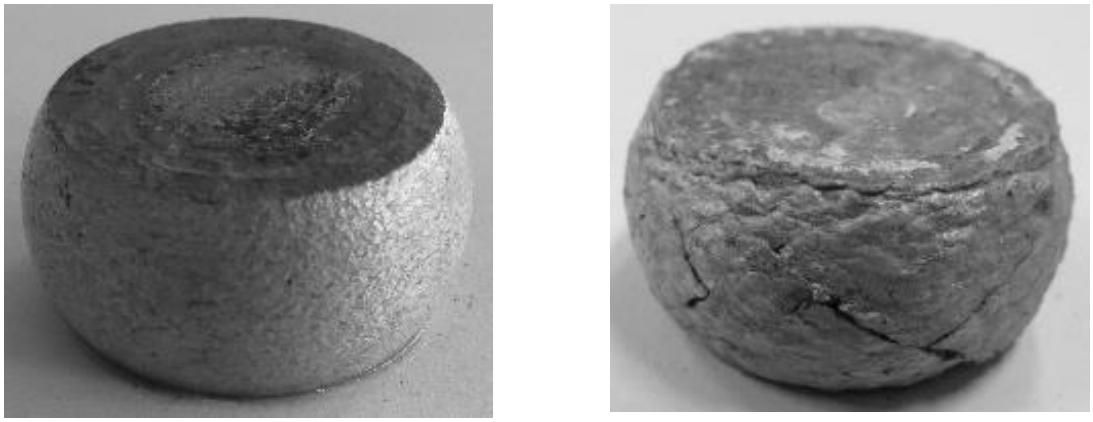

Figure 5. *Photographs of selected samples from the AZ91 magnesium alloy after upsetting in temperature: (a) 420 ℃, (b) 400 ℃*

Figures 6 to 12 detail selected structures of the AZ91 magnesium alloy after casting, after homogenization, after upsetting, and after upsetting and heat treatment.

The microstructure of the cylindrical sample from AZ91 after casting (Figure 6) revealed the emergence of a base (a-Mg) and numerous secretions of networks of intermetallics, probably γ (Mg17Al12). Non-equilibrium eutectics are also present around the secretions.

(a) (b)

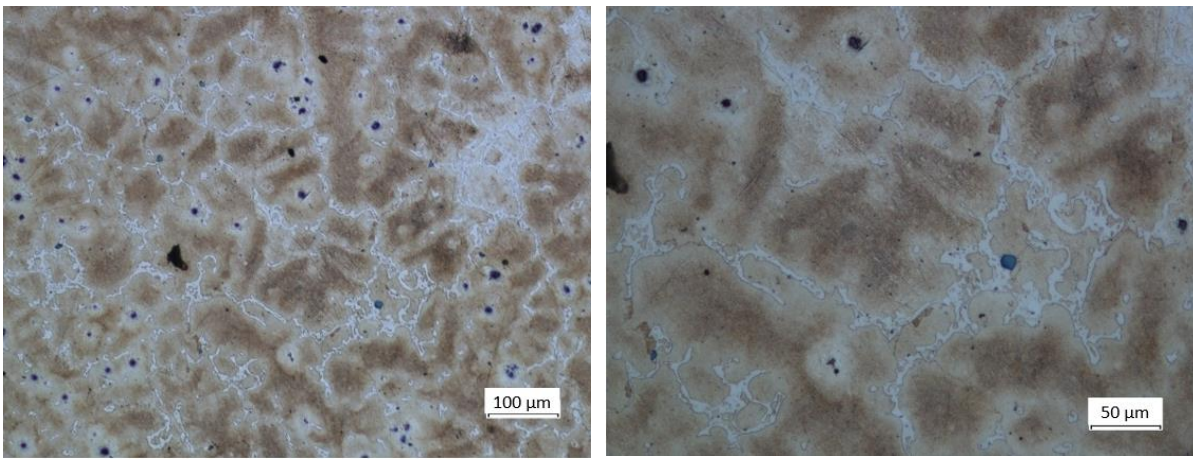

Figure 6. *Microstructure of the cylindrical sample from AZ91 after casting: (a) and (b)*

After homogenization of the cylindrical samples of AZ91 at 415 °C, the majority of secretions dissolved in the base (Figure 7). Equiaxial grains have considerable but acceptable size. Merely individual undissolved secretions remained.

(a) (b)

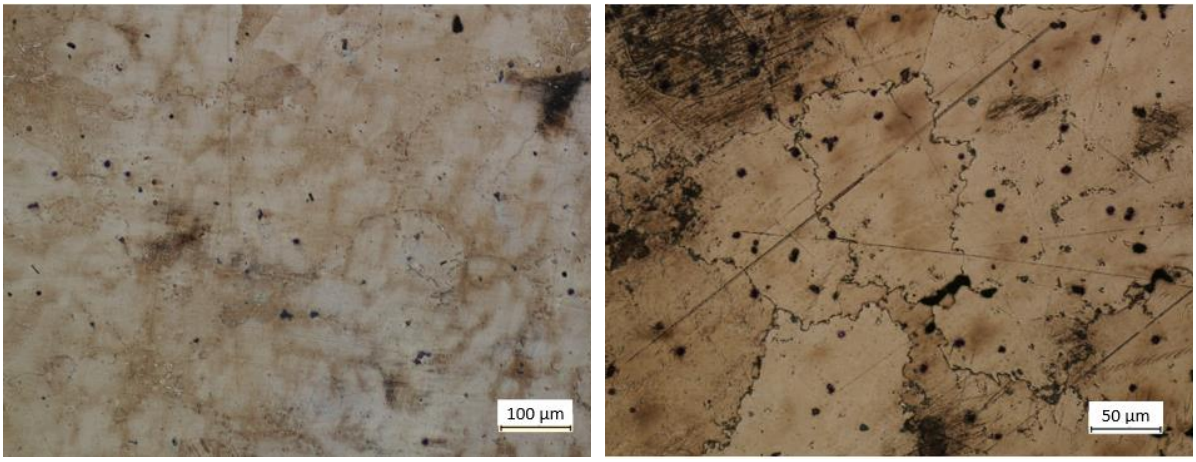

Figure 7. *Microstructure of the cylindrical sample from AZ91 after casting and homogenization: (a) and (b)*

(a) (b)

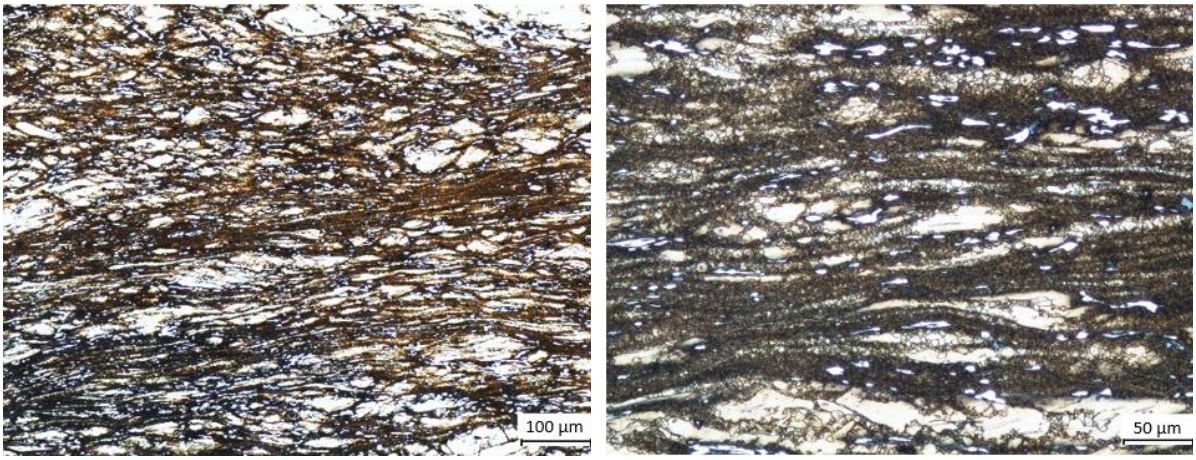

Figure 8. *Microstructure of the cylindrical sample from AZ91 after homogenization and upsetting in 380 °C and water-cooling: (a) and (b)*

The microstructure of the AZ91 alloy after homogenization and upsetting at 380 °C and after water-cooling was presented in Figure 8. Fine dynamically recrystallized grains arranged in strands are visible in the central area of the sample. In between the strands, individual grains which were not fragmented are visible. The structure is considerably heterogeneous due to significant zonal deformation and irregular flow.

The microstructure of the AZ91 alloy after homogenization and upsetting in 380 °C and after air-cooling was presented in Figure 9. Fine dynamically recrystallized grains arranged in strands are visible in the central area of the sample. In between the strands, individual grains which were not fragmented are visible. The microstructure is considerably heterogeneous due to significant zonal deformation and irregular flow. The size of the finest recrystallized grains is larger in relation the those visible in the water-cooled sample.

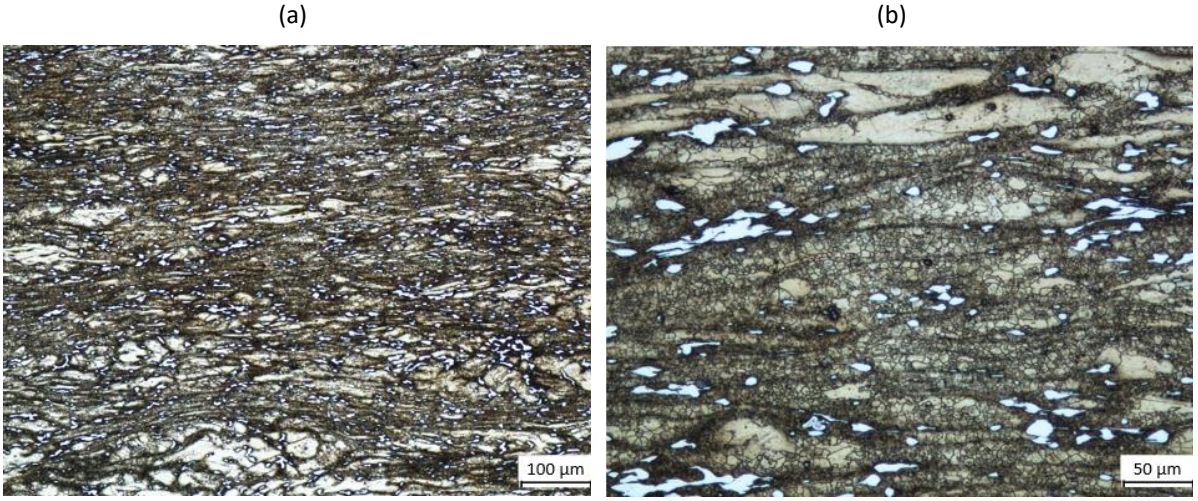

Figure 9. *Microstructure of the AZ91 alloy after homogenization and upsetting in 380 °C and air-cooling: (a) and (b)*

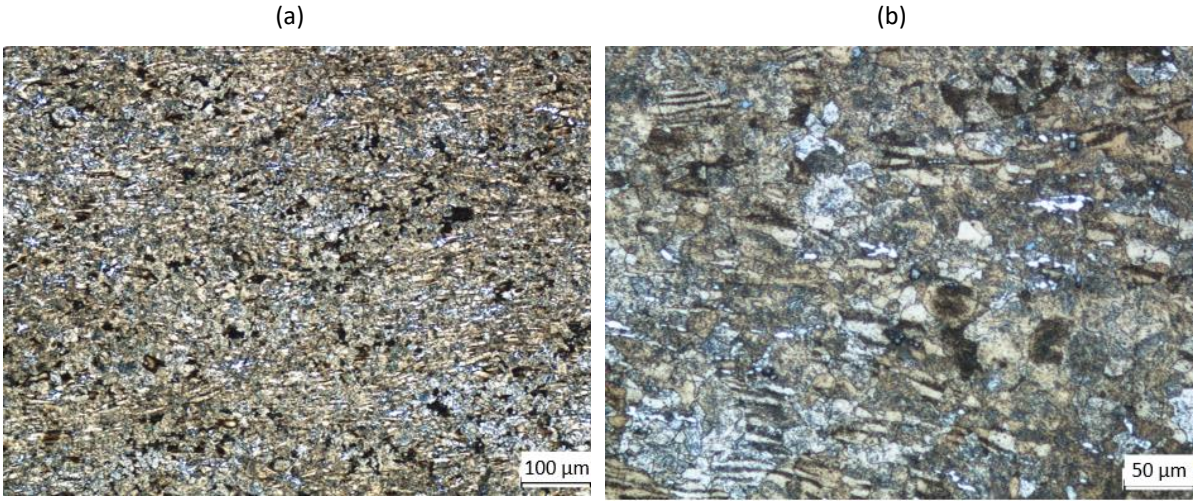

Figure 10. *Microstructure of the AZ91 alloy after homogenization and upsetting in 380 °C, after air-cooling, supersaturation, and artificial aging: (a) and (b)*

The microstructure of the AZ91 alloy after homogenization and upsetting at 380 °C, after air-cooling, supersaturation, and artificial aging is detailed in Figure 10. The microstructure completely recrystallized across the cross-section. The size of grains differs to a lesser extent in relation to the post-forging state. A strong etching effect is linked with aging.

The microstructure of the AZ91 alloy after homogenization and upsetting at 420 °C and after water-cooling was presented in Figure 11. The microstructure completely recrystallized across the cross-section. It manifests no strands. Grains characteristic for the particular alloy are regular and of various sizes.

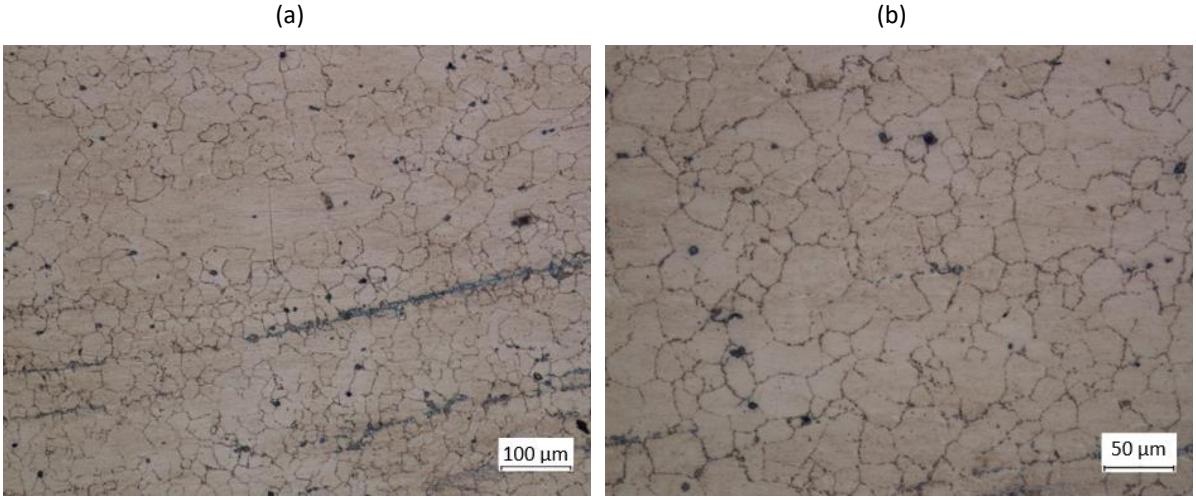

Figure 11. *Microstructure of the AZ91 alloy after homogenization and upsetting in 420 ℃ and water-cooling: (a) and (b)*

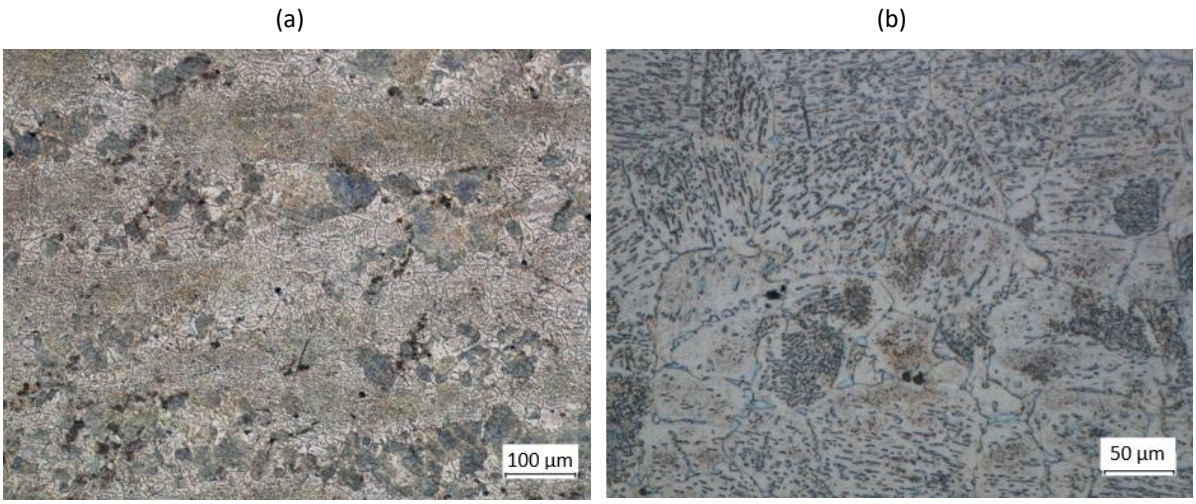

Figure 12. *Microstructure of the AZ91 alloy after homogenization and upsetting in 420 ℃, after water-cooling, supersaturation, and artificial aging*

The microstructure of the AZ91 alloy after homogenization and upsetting at 420 °C, after air-cooling, supersaturation, and artificial aging is presented in Figure 12. The photos detail secretions of the reinforcing phase around grains. It forms a needlelike microstructure with an overall regular distribution except in certain areas where the secretions are densely packed. As a result of heat treatment, proper distribution of reinforcing particles was obtained.

The results of microhardness tests are outlined in Table 4. It can be observed that the hardness of the homogenized material declined in relation to the raw state. It stems from the dissolution of secretions of the reinforcing phase. After forging, a significant growth of hardness was observed in relation to the material after homogenization. It is a consequence of compression. After precipitation hardening, hardness increased in relation to that of the alloy after forging. The study revealed that it arises from fine secretions of the reinforcing intermetallics. The analysis of the results suggests that the thermo-plastic processing is valid. The precipitation-hardened alloy (after homogenization at 415 °C) improved its hardness by 15% in relation to the cast material. The highest hardness was obtained for samples homogenized at 415 °C, forged at 420 °C, water-cooled, supersaturated, and artificially aged.

Table 4. *Microhardness of samples from cast AZ91 magnesium alloy at different stages of thermo-plastic processing*

No.	State of the alloy	Average from microhardness tests (HV05)	Standard deviation
1.	Cast	78.5	4.0
2.	Cast after homogenization	73.3	3.7
3.	Cast after homogenization and forging at 380 °C and after water-cooling	83.5	1.9
4.	Cast after homogenization and forging at 380 °C and after air-cooling	74.2	3.2
5.	Cast after homogenization and forging tt 380 °C and after water-cooling, supersaturation, and artificial aging	88.3	1.4
6.	Cast after homogenization and forging at 380 °C and after air-cooling, supersaturation, and artificial aging	87.2	2.9
7.	Cast after homogenization and forging at 420 °C and after water-cooling	77.9	1.6
8.	Cast after homogenization and forging at 420 °C and after air-cooling	78.9	2.3
9.	Cast after homogenization and forging at 420 °C and after water-cooling, supersaturation, and artificial aging	93.1	2.8
10.	Cast after homogenization and forging at 420 °C and after air-cooling, supersaturation, and artificial aging	91.4	4.5

4. Conclusion

The article outlines the results of experimental studies concerning the impact of thermo-plastic processing on the structure of sand-cast AZ91 magnesium alloy. The study aimed to determine the most favorable processing conditions for the cast alloy. Based upon upsetting tests, the deformation capacity of the sand-cast AZ91 magnesium alloy was determined in view of variable processing parameters such as temperature, degree of deformation, and means of cooling immediately after forging. On the basis of the results of upsetting tests and the examination of the structure and hardness, the most favorable thermo-plastic conditions for the AZ91 alloy were established. Preferably, before deformation, heat treatment of the alloy should be conducted in the form of homogenization at 415 °C for 24 h with argon as the shielding gas. As far as the structure and hardness are concerned, among the studied thermo-plastic processing parameters in the 380-420 °C range, the forging of the sand-cast AZ91 magnesium alloy at 420 °C with water-cooling and 0.7 deformation seems the most favorable. After thermo-plastic processing of the alloy, further heat treatment in the form of supersaturation at 415 °C for 6 h with argon as the shielding gas as well as artificial aging at 175 °C for 24 h are recommended. When analyzing the structure of the AZ91 alloy after forging and cooling, flow strands with considerable fragmentation of grains due to dynamic recrystallization are visible. In between the flow strands, dynamically recrystallized grains of larger size are visible. Due to the heat treatment after deformation, full recrystallization occurs. Additionally, the size of grains across the cross-section becomes homogeneous. Hardness analysis of the cast and deformed AZ91 magnesium alloy suggests that the material becomes strengthened due to the heat

treatment. The highest hardness emerges after forging at 420 °C and water-cooling and in the course of further heat treatment (supersaturation and artificial aging).

Acknowledgments

Project “New technology of forming magnesium alloy wheels for light vehicles”; No. NOR/SGS/ForMag/0083/2020-00. The research leading to these results has received funding from the Norway Grants 2014-2021 via the National Centre for Research and Development.

References

[1] Papenberg, N. P., Gneiger, S., Weißensteiner, I., Uggowitzer, P. J., Pogatscher, S., 2020. Mg-alloys for forging applications-A review. Materials (Basel). 13 (4), 1–61.
[2] Powell, B. R., Luo, A. A., Krajewski, P. E. 2021. Magnesium alloys for lightweight powertrains and automotive bodies. Woodhead Publishing Limited, 125-186.
[3] Dziubińska, A., Surdacki, P., Majerski, K. 2021. The analysis of deformability, structure, and properties of AZ61 cast magnesium alloy in a new hammer forging process for aircraft mounts. Materials (Basel) 14 (10), 1-11.
[4] Dziubinska, A., Gontarz, A., Zagórski, I. 2018. Qualitative research on AZ31 magnesium alloy aircraft brackets with a triangular rib produced by a new forging method. Aircr. Eng. Aerosp. Technol. 90(3), 482–488.
[5] Banaszek, G., Bajor, T., Kawałek, A., Garstka, T. 2020. Magnesium Alloy Plate. Materials (Basel) 13, 1–20.
[6] Chelliah, N.M., Kumar, R., Singh, H., Surappa, M.K. 2017. Microstructural evolution of die-cast and homogenized AZ91 Mg-alloys during dry sliding condition. J. Magnes. Alloy. 5(1), 35–40.
[7] Yan, H., Wang, Z. 2016. Effect of heat treatment on wear properties of extruded AZ91 alloy treated with yttrium. J. Rare Earths 34 (3), 308–314.
[8] Cizek, L., Rusz, S., Hilser, O., Sliwa, R., Kuc, D., Tanski, T., Tkocz, M. 2017. Microstructure and properties of selected magnesium-aluminum alloys prepared for spd processing technology. Arch. Metall. Mater. 62(4), 2365–2370.
[9] Kunz, L., Fintová, S. 2014. Fatigue behaviour of AZ91 magnesium alloy in as-cast and severe plastic deformed conditions. Adv. Mater. Res. 891–892, 397–402.
[10] Reguła, T., Bronicki, M., Lech-Grega, M., Czekaj, E. 2008. An Assessment of the Possibilities to Shape the Mechanical Properties of Cast AZ91 Magnesium Alloy Through Application of Proper Heat Treatment. Foundry Inst. Work. XLVIII (1), 39–45.
[11] Liu, C., Liang, J., Zhou, J., Li, Q., Peng, Z., Wang, L. 2016. Characterization and corrosion behavior of plasma electrolytic oxidation coated AZ91-T6 magnesium alloy. Surf. Coatings Technol. 304, 179–187.
[12] Ebrahimi G.R., Maldar, A.R., Monajati, H., Haghshenas, M. 2012. Hot deformation behavior of AZ91 magnesium alloy in temperature ranging from 350°C to 425°C. Trans. Nonferrous Met. Soc. China 22 (9), 2066–2071.
[13] Nie, K. B. , Deng, K. K. , Wang, X. J. , Xu, F. J. , Wu, K., Zheng, M. Y. 2015. Multidirectional forging of AZ91 magnesium alloy and its effects on microstructures and mechanical properties. Mater. Sci. Eng. A 624, 157–168.
[14] Tan, M., Liu, Z., Quan, G. 2012. Effects of Hot Extrusion and Heat Treatment on Mechanical Properties and Microstructures of AZ91 Magnesium Alloy. Energy Procedia 16, 457–460.
[15] Friedrich, H., Mordike, B. 2016. Magnesium Technology. Springer, Berlin.
[16] Pilehva, F., Zarei-Hanzaki, A., Fatemi-Varzaneh, S. M. 2012. The influence of initial microstructure and temperature on the deformation behavior of AZ91 magnesium alloy. Mater. Des. 42, 411–417.

Gaseous nitriding of pure nickel - observation and interpretation of microstructural features

***Matej Fonović*[1], *Dario Kvrgić*[1], *Dario Iljkić*[1] *and Lovro Liverić*[1]**

1) Faculty of Engineering, University of Rijeka, Vukovarska 58, 51000 Rijeka, Croatia

Corresponding author: mfonovic@riteh.hr

Original scientific article

Abstract: Nitriding is a surface heat treatment technique, where nitrogen diffuses into the surface-*adjacent* layers of various metals and alloys. This can for some metals be a desired process leading to improved properties of the treated material, e.g. in iron or iron-based alloys. However, in other cases, like in nickel-base superalloys, nitriding can even be regarded as a corrosion process, degenerating favourable properties. Various nitriding experiments on pure nickel plates were performed. Specimens were nitrided in pure ammonia (100 % NH_3), as function of temperature and time. Upon nitriding treatment, a closed Ni_3N layer is developed between 300 °C and 550 °C, which can be clearly observed after etching with Fe^{3+} solution. A nitriding temperature of 500 °C causes a high amount of porosity within the surface layer, which is connected with formation of N_2 (gas) inside the solid. All nitrided specimens show compressive residual macrostresses for the Ni_3N layer.

Keywords: *gaseous nitriding; nickel; Ni_3N; microstructure; residual stress*

1. Introduction

Nitriding is one of the most common thermochemical surface process employed to introduce nitrogen into the surface-adjacent regions of various metallic materials, leading to significant improvement in surface hardness, toughness, corrosion resistance, fatigue life and many other properties [1, 2, 3]. Consequently, this process effectively increases the lifespan of various engineering components. This demand stems from the wide array of engineering components that must endure external loads and meet specific criteria set forth by engineers or designers. One very common practical objective, for instance, involves a very hard case surrounding a soft core, effectively prolonging the lifespan of the engineering components by formation of different microstructural features within the hard case. The nitriding treatment can be carried out through few methods such as plasma nitriding, gaseous nitriding in ammonia/hydrogen gas atmospheres, or even by immersion in various salt baths. The processes involved in the nitriding treatment include the absorption of nitrogen, beginning from nitrogen-delivering species such as NH_3 or N_2, the diffusion of nitrogen into the surface areas of metal, and finally the formation of nitrides either as a surface (compound) layer or as precipitates within the nitrided zone. While nitriding is predominantly utilized for iron-based alloys [4, 5], specifically ferritic steels, it is also a viable treatment for other metals such as nickel or nickel-based alloys [3, 6, 7]. In the case of nitriding nickel-base alloys the nitriding treatment can even be regarded as a corrosion process, degenerating beneficial properties. Even though some literature exists on nickel nitriding there is still limited information regarding the formation of Ni_3N and microstructure development upon nitriding of pure nickel. Hence, the objective of this investigation was to analyze the behavior and evaluate the development of Ni_3N compound layer upon nitriding of pure nickel plates. The investigations revealed existence of compressive residual macrostresses of the Ni_3N layer developed upon nitriding of pure nickel. Furthermore, various microstructural characterization techniques such as, x-ray diffraction (XRD), optical microscopy and scanning electron microscopy, are employed in order to identify and gain insights into the formation of microstructural features developed upon nitriding treatment.

2. Experimental procedure

Most of the nitriding studies on nickel-based alloys or iron-based alloys were conducted by plasma nitriding [5]. Although the outcome of plasma nitriding can be influenced by modification of the treatment parameters, no easy thermodynamic equilibrium considerations are possible as in the case of gaseous nitriding in ammonia/hydrogen gas atmospheres [8, 9]. Under the local equilibrium condition at the specimen's surface, the solid can be equilibrated with an NH_3+H_2 gas atmosphere by the following reaction:

$$NH_3 \rightleftarrows [N] + \frac{3}{2}H_2 \tag{1}$$

where [N] denotes N in some form in the solid solution or a solid nitride. However, it should be mentioned that a portion of ammonia in the gas phase will undergo decomposition in accordance with:

$$NH_3 \rightleftarrows \frac{1}{2}N_2 + \frac{3}{2}H_2 \tag{2}$$

The nitrogen activity a_N at the specimen's surface present in the solid in case of equilibrium of reaction (1) is, at a specific temperature, proportional to the nitriding potential r_N [9]:

$$r_N = \frac{p_{NH_3}}{p_{H_2}^{3/2}} \propto a_N \tag{3}$$

where p_{NH_3} and p_{H_2} indicate the partial pressures of the gas *constituents (i.e.,* ammonia and hydrogen). Furthermore, it can be said that the nitriding potential (r_N), at any specific temperature, typically quantifies the thermodynamic ability of an ammonia and hydrogen gas containing atmosphere to provide nitrogen to a solid. In the Table 1 examples of nitriding potentials and corresponding partial pressures of ammonia and hydrogen are presented.

Table 1. *Example of nitriding potential and corresponding gas composition of ammonia and hydrogen. Note that max. overall gas flow flowing through the furnace corresponds to 300 ml/min.*

r_N, $atm^{-1/2}$	p_{NH_3}, vol. %	p_{H_2}, vol. %	NH_3 flow, ml/min	H_2 flow, ml/min
0	0	100	0	300
10	81,25	18,75	243,8	56,3
100	95,50	4,50	286,5	13,5
1000	99,00	0,99	297,0	3,0
10000	99,79	0,21	299,37	0,63
∞	100,00	0	300	0

In order to study the formation of Ni_3N compound layer a previously described tube furnace was used [2]. Pure, recrystallized nickel specimens (99.99% annealed, *Sigma-Aldrich*) of dimensions 20x20x2 mm were nitrided at the temperatures between 300 °C and 550 °C for 1 h, 5 h and 20 h respectively in an atmosphere mixed from ammonia and hydrogen with the fluxes been controlled by the mass-flow controllers. At room temperature, the overall gas flow rate of 300 ml/min was employed at 1 atm, resulting in a linear gas velocity of 8.12 mm/s. It's important to maintain a high linear gas velocity in order to minimize the potential change of the gas atmosphere resulting from the dissociation of

ammonia in the furnace [2]. Before the nitriding treatment, the specimens underwent grinding, polishing, and thorough cleaning with methyl alcohol to eliminate any potential surface contaminants. After the nitriding process, the specimens were rapidly immersed in a liquid water for quenching purposes. The nitriding potential values (as defined in Eq. (3)) were carefully chosen to ensure the exclusive formation of Ni_3N at the specimen’s surface. Following the nitriding treatment, the specimens underwent initial cutting into smaller pieces (20 mm x 20 mm) using a circular saw. Subsequently, a nickel protective layer with varying thicknesses of up to 15 microns was electroplated onto the specimens to prevent any surface deformation and contamination during the metallographic preparations. For the optical microscopy analysis, the specimens were embedded in an epoxy resin to create cylindrical shape block, which were then subjected to grinding using SiC abrasive paper and polished with 1-micron particle-sized diamond paste to achieve the desired surface finish. For the metallographic analysis, the specimens were subjected to chemical etching at the room temperature for 30 seconds using Fe^{3+} solution (Solution containing 5g $FeCl_3$, 50 ml HCl and 200 ml H_2O). Subsequently, the specimens were examined using a Keyence VHX-900S digital microscope equipped with an advanced auto-focusing imaging system. To conduct further microstructural investigations on the nitrided cross-sections, a Zeiss EVO® MA10 scanning electron microscope equipped with an EDS detector was applied in order to obtain information regarding the chemical composition. The identification of phases and stress measurements of the nitrided specimens was established by using the X-ray diffraction (XRD) method conducted on a Philips diffractometer equipped with Cu-tube.

3. Results and discussion

3.1. Morphology of the nitrided layer

The formation of Ni_3N, as indicated by XRD at the surface of the specimen has been observed after the nitriding treatment between 300 °C and 550 °C in pure ammonia for 5 hours. In the Figure 1, the typical cross-sectional microstructures of the nitrided pure nickel at different temperatures are presented.

As observed in Figure 1. a) and b) light microscopy investigations of the cross-sections of the nitrided nickel specimen clearly discloses the presence of a closed Ni_3N compound layer at the surface of the specimen. Furthermore, the SEM analysis conducted on the nitrided cross section reveals a characteristic columnar grain microstructure of the Ni_3N compound layer located on top of the Ni substrate (Figure 4 (d)). A visual comparison of the layers formed at 450 °C and 550 °C after the nitriding treatment for 5h shows a significant level of porosity observed in the Ni_3N layer for the specimen treated at 550 °C (cf. Figs, 1(b) and 1(c)). Similar observation of the nitrided morphology are also reported in the literature [10]. It is believed that the primary source of this porosity is likely due to formation of nitrogen gas (N_2) inside the solid, which is caused by the metastable nitride decomposition. This *process of nitride decomposition* is known for occurring in iron nitrides, especially for longer periods of time, as reported in Ref. [11]

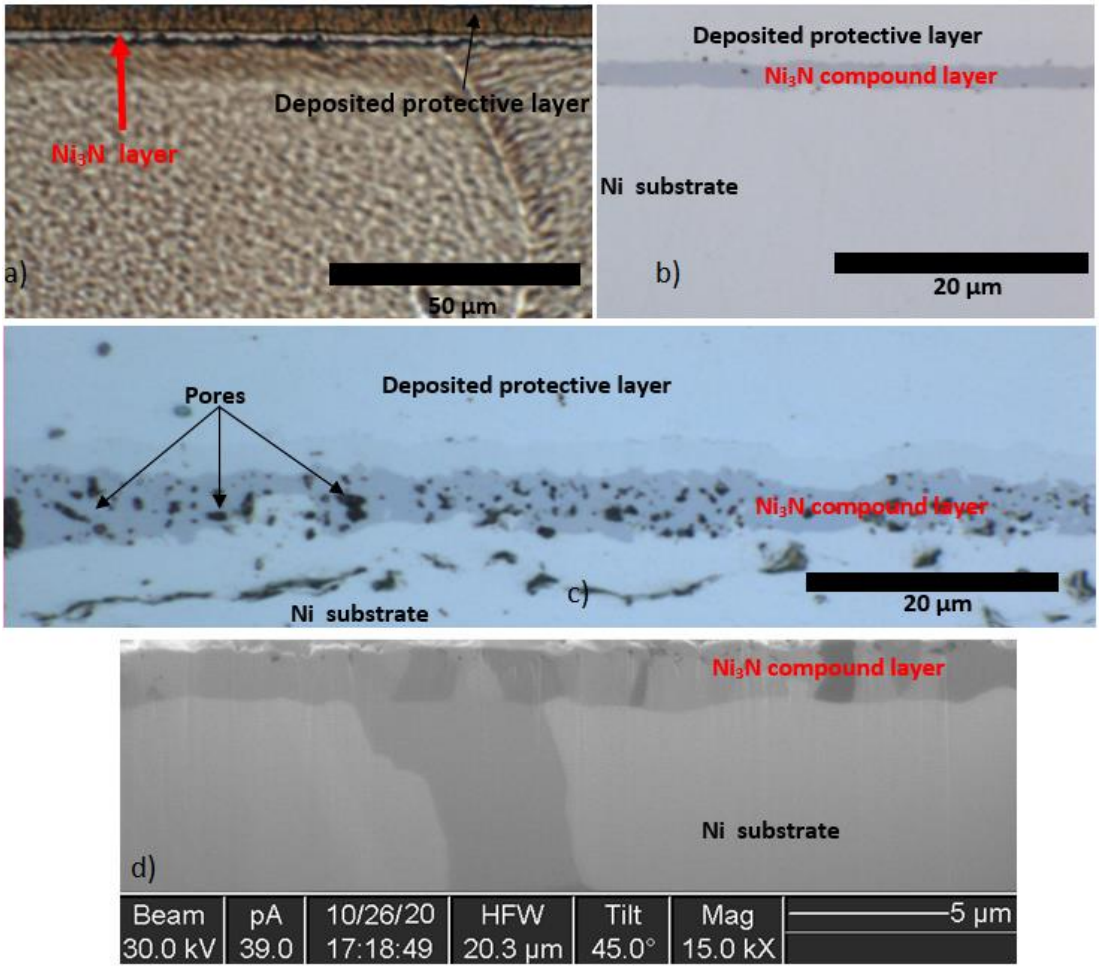

Figure 1. Optical micrographs showing a cross-section of the Ni_3N compound layer formed on pure nickel upon gaseous nitriding treatment for 5 hours in 100 % ammonia at various temperatures: a) 450 °C; etched with Fe^{3+} containing solution, b) 400 °C; as polished, c) 550 °C; as polished and d) 400 °C; as polished, however, obtained by scanning electron microscope

3.2. Residual macrostresses

The XRD stress analysis was conducted on the surface of the Ni_3N compound layer obtained after the nitriding process at 400 °C, 450 °C and 500 °C for 1 h, 5 h and 20 h. The analysis involved an X-ray diffractometer equipped with a Eulerian cradle, where diffraction patterns were measured and $\sin^2\psi$ method was applied for various *hkl* reflections. The experimentally obtained data were utilized to derive stress values based on determined slopes (not shown here) and by employing X-ray elastic constants (XECs) by the following equation:

$$S_{1,2}^{hkl} = (1-x)S_{1,2}^{\mathrm{R},hkl} + xS_{1,2}^{V} \quad (4)$$

where $S_{1,2}^{\mathrm{R},hkl}$ and $S_{1,2}^{V}$ represents Reuss and Voigt factors of extreme cases of the XECs and *x* serves as a fitted weighting parameter, which plays a crucial role in determining the grain-interaction model (isostrain or isostress) within the Ni_3N compound layer. The Reuss factor was determined by utilizing the elastic constants of the hexagonal Ni_3N with space group $P6_322$, which were calculated based on single-crystal elastic constants derived from the first-principles calculations [10]. In this evaluation the experimentally determined Bragg reflection positions of Ni_3N as a function of tilting angle ψ were directly compared with the calculated Bragg reflection positions. The Bragg reflection positions parameters were obtained by fitting pseudo-Voight functions to the respective measured diffraction

patterns using the ProFit software. In a symmetric biaxial state of stress within the Ni_3N layer the general stress-strain relation can be expressed as:

$$\varepsilon_{\psi}^{hkl} = \left(2S_1^{hkl} + \frac{1}{2}S_2^{hkl}\sin^2\psi\right)\left(\sigma_{II}^{S}\right) \tag{5}$$

where σ_{II}^{S} is the tensile or compressive macrostress developed within the Ni_3N layer, S_1^{hkl} and $\frac{1}{2}S_2^{hkl}$ are the X-ray elastic constants. The ε_{ψ}^{hkl} represents the elastic strain of the *hkl* planes at different tilt angle ψ and it can be defined as:

$$\varepsilon_{\psi}^{hkl} = \frac{\left(d_{\psi}^{hkl} - d_0^{hkl}\right)}{d_0^{hkl}} \tag{6}$$

where the d_0^{hkl} is the strain-free interplanar *hkl* lattice spacing and d_{ψ}^{hkl} is the experimentally determined interplanar lattice spacing at different tilt angle ψ. Furthermore, the strain ε_{ψ}^{hkl} is measured at several tilt angles ψ and when ε_{ψ}^{hkl} is plotted against $\sin^2\psi$, a line is obtained from where the σ_{II}^{S} can be obtained from the slope of the curve. The determination of the residual stresses and *complete calculation procedure for* stress analysis of surface regions and polycrystalline thin films based on X-ray diffraction is *described elsewhere [12, 13]*. Based on above method of stress analysis the residual stresses in the Ni_3N compound layer are calculated. Table 2 presents results of macrostress evaluation for nine Ni_3N layers, produced through the gaseous nitriding treatment of nickel plates followed by rapid quenching in water.

Table 2. *Results of the residual stress evaluation of the surface Ni_3N layer of nine specimens produced by gaseous nitriding treatment of pure nickel at 400 °C, 450 °C, 500 °C for 1 h, 5 h, and 20 h respectively*

duration / temperature	1 h	5 h	20 h
400 °C	**-229 MPa**	**-210 MPa**	**-170 MPa**
450 °C	**-244 MPa**	**-237 MPa**	**-186MPa**
500 °C	**-136 MPa**	**-104 MPa**	**-73 MPa**

The evaluation shows that all specimens exhibit residual compressive macrostress which is parallel to the specimen's surface. This residual macrostresses most likely develop upon fast cooling from nitriding temperature (where stress-free state exists) up to the room temperature. Furthermore, due to different thermal expansion coefficient of nickel substrate and Ni_3N compound layer compressive stress is induced by quenching. Additionally, the specimens nitrided at the higher temperatures (>500 °C) show significant amount of porosity which can be attributed to the nitride decomposition during gaseous nitriding treatment.

4. Conclusions

Gaseous nitriding treatment in ammonia/hydrogen gas mixture of pure nickel at temperature range between 300 °C and 550 °C causes development of a featureless thin Ni_3N compound layer at the specimen's surface. Depending on the nitriding parameters/conditions (time, temperature and nitriding potential) a thicker or thinner Ni_3N compound layers develop. All nitrided specimens show presence of compressive residual macrostresses parallel to the specimen's surface, however of different magnitude. Upon quenching, the variation in thermal expansion coefficient of Ni_3N and Ni lead to macrostresses and macrostrains. In order to compensate the misfit of the Ni_3N layer and the nickel substrate the Ni_3N compound layer must experience a strain leading to compressive

macrostresses. The degree of compressive stresses is reduced by longer nitriding treatments due to development of porosity as a result of the nitride decomposition.

Acknowledgments

This research has been supported by University of Rijeka through the project uniri-mladi-tehnic-22-35.

References

[1] Mittemeijer, E.J., 2013., ASM Handbook, (Editors: J.I. Dosset and G.E. Totten)
[2] Fonović, M., 2015. Nitriding behaviour of Ni and Ni-based binary alloys, PH. D dissertation, University of Stuttgart
[3] Makishi, T., Nakata, K., 2004. Surface hardening of nickel alloys by means of plasma nitriding. Metall. Mater. Trans. A. 35, 227–238.
[4] Diaz, N.V., Hosmani, S.S., Schacherl, R.E., Mittemeijer, E.J., 2008. Nitride precipitation and coarsening in Fe–2.23 at.% V alloys: XRD and (HR)TEM study of coherent and incoherent diffraction effects caused by misfitting nitride precipitates in a ferrite matrix. Acta mater. 56, 4137– 4149.
[5] Dong, H., 2010. S-phase surface engineering of Fe-Cr, Co-Cr and Ni-Cr alloys. Int. Mater. Rev. 55, 65–98.
[6] Fonović, M., Leineweber, A., Robach, O., Jägle, E.A., Mittemeijer, E.J., 2015. The Nature and Origin of “Double Expanded Austenite” in Ni-Based Ni-Ti Alloys Developing Upon Low Temperature Gaseous Nitriding. Metall. Mater. Trans. A. 46, 4115–4131.
[7] Sudha, C., Anand, R., Thomas Paul, V., Saroja, S., Vijayalakshmi, M., 2013. Nitriding Kinetics of Inconel 600. Surf. Coat. Technol. 226, 92–99.
[8] Eliasen, K.M., Chrisiansen, T.L., Somers, M.A.J., 2010. Low temperature gaseous nitriding of Ni based superalloys. Surf. Eng. 26, 248–255.
[9] Mittemeijer, E.J., Somers, M.A.J., 1997. Thermodynamics, kinetics, and process control of nitriding. Surf. Eng, 13. 483–497.
[10] Leineweber, A., Lienert, F., Shang, S., Liu, Z., Mittemeijer, E.J., 2012. Ni_3N compound layers produced by gaseous nitriding of nickel substrates; layer growth, macrostresses and intrinsic elastic anisotropy. J. Mater. Res. 27, 1531–1541.
[11] Grabke, H.J., Strauss, S., Vogel, D., 2003. Nitridation in NH_3-H_2Omixtures. Mater. Corros. 54, 895–902.
[12] Welzel, U., Ligot, J., Lamparter, P., Vermeulen, A.C., Mittemeijer, E.J., 2005. Stress analysis of polycrystalline thin films and surface regions by x-ray diffraction. J. Appl. Crystallogr. 38, 1–29.
[13] Welzel, U., and Mittemeijer, E.J., 2003. Diffraction stress analysis of macroscopically elastically anisotropic specimens: On the concepts of diffraction elastic constants and stress factors. J. Appl. Phys. 93, 9001–9011.

Analysis of experimental device for measuring the thermal conductivity of thermal insulation materials using FDM method

***Igor Gabrić*[1], *Zlatko Jankoski*[1], *Stjepan Marković*[2] *and Josip Martinić*[1]**

1) University Department of Professional Studies, University of Split, Kopilica 5, 21000 Split, Croatia

2) EKSERGIJA Ltd., Put Krunika 7/B, 21210 Kučine, Croatia

Corresponding author: igor.gabric@oss.unist.hr

Original scientific article

Abstract: In order to build an experimental device for measuring the thermal conductivity of thermal insulation materials, a numerical analysis was performed using the finite difference method (FDM) and the Python programming language. A conceptual solution of an experimental device is proposed, which is based on the guarded hot plate method. The device is equipped with two heaters, internal and external. The observed heat flow is the heat generated by the internal heater. The external heater maintains a uniform heat flow over the entire surface of the test sample, so that the thermal conductivity can be determined based on the power of the internal heater and the temperature difference of the top and bottom surface of the test sample when stationary heat flow is achieved. The purpose of the numerical analysis was to determine the basic dimensions and operating parameters of the experimental model, such as the power of both electric heaters, the thickness of the thermal insulation layer of the device, dimensions of the test sample and others. The criterion parameters used in the numerical analysis were the measurement precision and the time required to achieve a stationary heat flow. Several numerical analyses were performed using different operating parameters. The plan for conducting the experiments was generated using a central composite plan, while the results were analysed and presented in the paper.

Keywords: *thermal conductivity; finite element method; design of experimental device; measurement; thermal insulation material*

1. Introduction

As part of the continuous development of laboratory activities, special attention is given to the development and construction of laboratory equipment. Regarding the measurement of thermal conductivity, the first experiences were gained by developing and constructing an experimental device for measuring thermal conductivity of metals ([1], [2]). A similar approach is used to propose a conceptual solution and design of experimental device for measuring the thermal conductivity of thermal insulation materials. As a first step the numerical analysis is performed. Several approaches and methods ([3], [4]) can be applied to measure the thermal conductivity of thermal insulation materials, which are generally divided into stationary and non-stationary methods. In this analysis a stationary method is selected over a non-stationary, as it involves considerably simplified construction of the measuring device, however, at cost of relatively longer time to reach a stationary heat flow.
For the purposes of designing the experimental device, the stationary method of the guarded hot plate is selected (Figure 1). The method determines thermal conductivity based on the Fourier law for stationary thermal conduction:

$$q = -\lambda \cdot \nabla T \tag{1}$$

where q is the local heat flux density (W/m^2), λ is the thermal conductivity (W/mK) and ∇T is the temperature gradient (K/m).

The problem is reduced to one-dimensional infinite plate, which greatly simplifies the determination of the thermal conductivity by applying the following expression:

$$q_x = -\lambda \cdot \frac{dT}{dx} \tag{2}$$

The problem is further simplified by introducing the assumption that there is no significant change in the thermal properties of the materials used within the operating temperature range of the device. Thus, some of the operating parameters are assumed as constants, while some of them are selected for the optimisation of the experimental model. Analysis and optimisation of their values is the subject of this numerical analysis. Detailed design of the experimental device is out of the scope of this paper. Numerical analysis is performed using the finite difference method [5] and employing Python programming code [6]. The objectives of numerical experiments are optimal values of the most important structural dimensions and operating parameters of the experimental model (design parameters), and their influence on the time period required to achieve stationary heat flow model. Finally, the precision of the obtained numerical results is analysed and clarified.

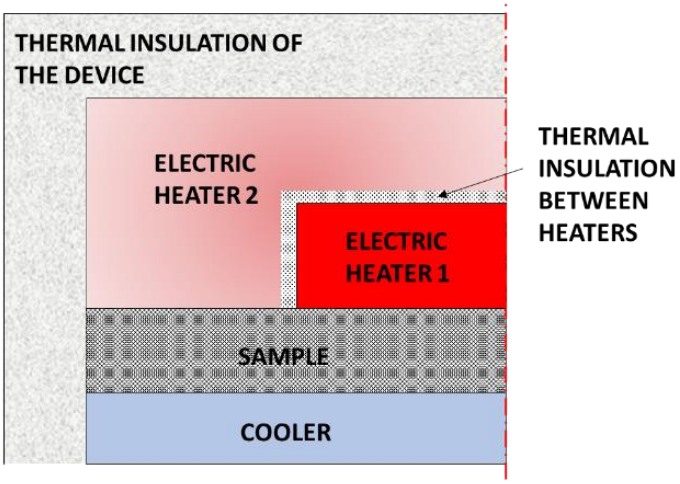

Figure 1. *Schematic of guarded hot plate method*

2. Physical model

The basic layout at the cross-section and the major parts of the experimental device are shown in Figure 2. Electric heaters placed inside the aluminium plate are used as heat sources. Aluminium plates are selected primarily due to easy machining and high thermal conductivity. The power of electric heater 1 is variable, from 1 to 10 W, while the power of electric heater 2 is constant (20 W). The electric heater 2 is automatically regulated (on/off) using an electronic relay in such way that the temperature difference between heaters 1 and 2 is maintained nearly zero. This can be achieved by installing a Peltier module between heaters 1 and 2, which generates a measurable voltage signal if there is a temperature difference between the upper and lower surfaces of the Peltier module. The sign of the measurable voltage signal depends on which side of the module has higher temperature and it is a direct indicator for the regulation of temperature difference by switching on and off the electric heater 2.

For the simulation purposes Peltier module is not considered. However, the simulation of switching on and off of the electric heater 2 is implemented in the programming code. This regulation should ensure an approximately uniform flow of heat through the test sample. The water cooler is also made of aluminium. The water flow through the water cooler and the temperature of inflowing water are assumed constant as the water cooler will be connected to the grid source of tap water.

The values of temperatures on both sides of the test sample and along the symmetry line of the device will be read after a stationary heat flow has been reached. It is important to note that the measuring surface only corresponds to the surface defined by the diameter of electric heater 1.
The time required for reaching a steady state solution is limited to 20 hours. After reaching the steady state solution the temperature difference at the measuring points has to be large enough, at least 50°C. This is important as the precision of the temperature measurements directly affects the precision of value of determined thermal conductivity. It is also important that the maximum temperatures, reached within the volume of experimental model, are not too high in order to minimise the influence of the temperature change on the thermal properties of test sample.

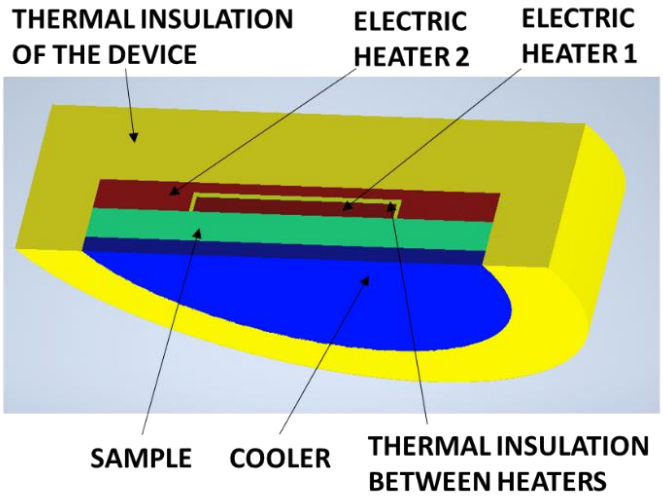

Figure 2. *The basic layout and major parts*

The temperature difference between two surfaces (top and bottom surface) of the test sample, temperatures t_2 and t_1 respectively, will be measured at the distance Δl, which is nearly the thickness of the test sample (Figure 3). Given that the temperatures of heaters 1 and 2 are approximately the same, and that the test sample and heaters are thermally isolated from the surrounding air, a uniform one-dimensional heat flow through the test sample should be developed. Part of the heat that will be transferred through the thermal insulation of the device to the surrounding air is assumed to be compensated by the electric heater 2. The heat generated by the electric heater 1 ($\dot{Q}_1$) is assumed to be entirely conducted through the test sample. Since the heat is continuously removed from the cold surface of the test sample (bottom surface) to the water cooler, after some time a stationary heat flow will be established. At that point, when the temperature difference between top and bottom surfaces of the test sample ($t_2 - t_1$) are constant, the value of thermal conductivity (k_{sample}) could be finally quantified. Radiative heat transfer is neglected due to the specific design of experimental device, and the temperature levels achieved at the surfaces of the test sample.
Finally, the physical model is defined by the main design parameters, where some of them are constants, while some of them are variable and require further optimisation. As constant parameters the following are selected:

- electric power of heater 2 ($P_{heater\_2} = 20$ W),
- properties of thermal insulation material (calcium silicate, $\lambda = 0.07 \frac{W}{m \cdot K}, C_p = 1030 \frac{W}{kg \cdot K}, \rho = 245 \frac{kg}{m^3}$),
- thickness of thermal insulation between electric heaters 1 and 2 ($x_{heater\_ins} = 3$ mm),
- properties of electric heaters 1 and 2, and water cooler (aluminium, $\lambda = 220 \frac{\mathrm{W}}{\mathrm{m \cdot K}}$, $C_p = 900 \frac{\mathrm{W}}{\mathrm{kg \cdot K}}$, $\rho = 2700 \frac{\mathrm{kg}}{\mathrm{m^3}}$),
- temperature of cooling water and surrounding air ($T_{cooler} = T_{air} = 293$ K),

- coefficient of thermal convection from cooling water to cooler ($\alpha_{cooler} = 1000 \frac{\mathrm{W}}{\mathrm{m^2 \cdot K}}$), and
- coefficient of thermal convection from surrounding air to device ($\alpha_{air} = 5 \frac{\mathrm{W}}{\mathrm{m^2 \cdot K}}$).

Variable design parameters include:
- thermal insulation thickness of the device ($x_{device\_ins} = 10 \div 50$ mm),
- diameter of the test sample ($d_{sample} = 100 \div 300$ mm),
- thickness of the test sample ($h_{sample} = 10 \div 30$ mm),
- diameter of the electric heater 1 ($d_{heater\_1} = 33 \div 250$ mm), and
- electric power of heater 1 ($P_{heater\_1} = 1 \div 10$ W)

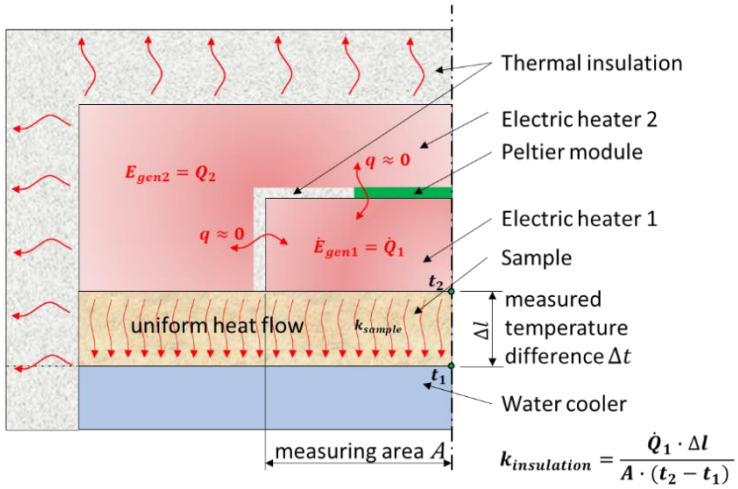

Figure 3. *Experimental device – concept*

3. Numerical model

The numerical model is developed based on the geometry and design of the physical model. The numerical grid is defined within the 2D numerical domain, which is represented by one half of the longitudinal section of the experimental device (Figure 3). The numerical grid is non-uniform in order to adjust the size of numerical cells to the specific construction details of the experimental device (Figure 4).

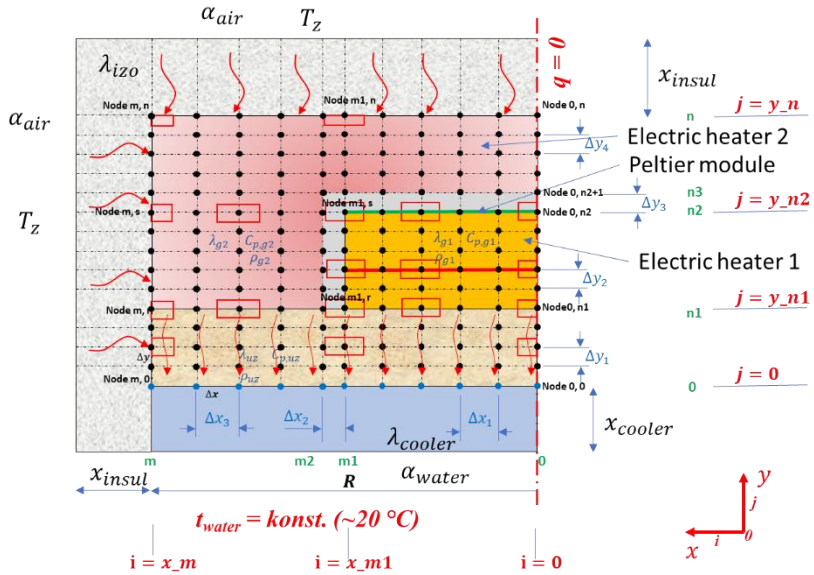

Figure 4. *Finite elements grid with nodes*

The numerical simulations are carried out using the numerical grid comprised of 9 × 10 cells (x and y axis respectively). Dimensions of numerical cells are additionally adjusted to the values of variable design parameters. Although the numerical grid is two-dimensional, the numerical simulations are performed for the physical domain in the form of a volume. This is achieved by calculating the heat fluxes while rotating the numerical grid around the axis of symmetry.
The numerical model is simplified by specifying some of the physical values as constant, as specified in chapter 2. Since the experimental device will be used only for educational purposes, this simplification could be considered as acceptable, while the estimated inaccuracies of the measured values to be insignificant. The heat balance for each numerical element (i, j) is based on conductive and convective heat transfers from/to the neighbouring numerical element (Figure 5). The internally generated heat is also taken into account within the e_{gen} element (Equation 3). Since the physical problem is axisymmetric, it is considered that the heat flux perpendicular to the symmetry line of the experimental device is equal to zero.
The equation for Fourier's law of two-dimensional heat conduction with heat generation could be written as [5]:

$$\frac{\partial}{\partial x}\cdot\left(k\cdot\frac{\partial T}{\partial x}\right)+\frac{\partial}{\partial y}\cdot\left(k\cdot\frac{\partial T}{\partial y}\right)+\dot{e}_{gen}=\rho\cdot c\cdot\frac{\partial T}{\partial t} \tag{3}$$

where k is the thermal conductivity of the material, $\frac{\partial T}{\partial x}$ i $\frac{\partial T}{\partial y}$ are the temperature gradients, $\dot{e}_{gen}$ is the rate of heat generation, ρ is the density of the material, c is the specific heat capacity of the material, while $\frac{\partial T}{\partial t}$ is the rate of change of the temperature.
The general relation for Newton's law of heat convection could be written as [5]:

$$\dot{Q}_{conv}=h\cdot A_s\cdot(T_s-T_\infty) \tag{4}$$

where h is the convection heat transfer coefficient, A_s is the heat transfer surface area, T_s is the temperature of the surface, while T_∞ is the temperature of the fluid sufficiently far from the surface.

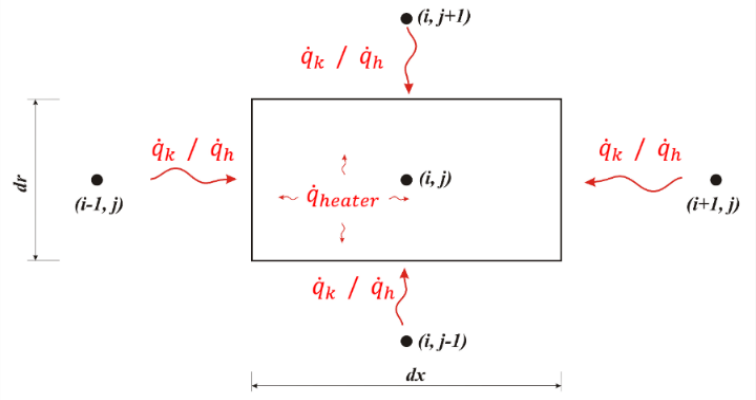

Figure 5. *Numerical cell – heat balance*

The governing equations include the heat balance (Eq. 5, 6 and 7) of each cell where the sum of conductive and convective heat transfer, together with the internally generated heat, give the rate of total energy change. The calculations are time dependent, where each iteration considers the calculations of physical values at the specific time step.

$$\sum\dot{Q}_k+\sum\dot{Q}_h+\sum\dot{E}_{gen}=\frac{\Delta E_{el}}{\Delta t} \tag{5}$$

$$\sum\left(k_{el}\cdot\frac{T_{i\pm1,j}-T_{i,j}}{dx}\cdot A_i\right)+\sum\left(k_{el}\cdot\frac{T_{i,j\pm1}-T_{i,j}}{dr}\cdot A_i\right)+\sum\left(h\cdot(T_{fluid}-T_{i,j})\cdot A_i\right)+\sum\dot{e}_{gen}\cdot V_{el}=\rho_{el}\cdot C_{p,el}\cdot V_{el}\cdot\frac{T_{i,j}^{\,t+\Delta t}-T_{i,j}^{\,t}}{\Delta t} \quad (6)$$

$$T_{i,j}^{\,t+\Delta t}=T_{i,j}^{\,t}+\frac{\sum\left(k_{el}\cdot\frac{T_{i\pm1,j}-T_{i,j}}{dx}\cdot A_i\right)+\sum\left(k_{el}\cdot\frac{T_{i,j\pm1}-T_{i,j}}{dr}\cdot A_i\right)+\sum\left(h\cdot(T_{fluid}-T_{i,j})\cdot A_i\right)+\sum\dot{e}_{gen}\cdot V_{el}}{\rho_{el}\cdot C_{p,el}\cdot V_{el}}\cdot\Delta t \quad (7)$$

Due to the convergence issues, each time step is selected as 1/100 seconds, while the duration of simulation is limited to 20 hours. Additionally, the accuracy of the calculated thermal conductivity and temperature difference between two surfaces of test sample (top and bottom surface) is analysed as a function of the following parameters:

- the power of electric heater 1 (from 1 to 10 W),
- diameter of the test sample (from 100 to 300 mm),
- thickness of the test sample (from 10 to 30 mm),
- thickness of the thermal insulation of the device (from 10 to 50 mm), and
- the diameter of the electric heater 1 (from 33 to 250 mm).

In order to find a general solution for satisfying the equilibrium conditions of all numerical elements, each numerical element is divided into 4 parts in such a way that the node is located in the centre of the element (Figure 6). This has solved the problem of varying the dimensions of finite elements and differences in the generation of internal heat at the boundaries of different materials. In other words, a unique function is created in the numerical programme that corresponds to each finite element with the associated transferred parameters.

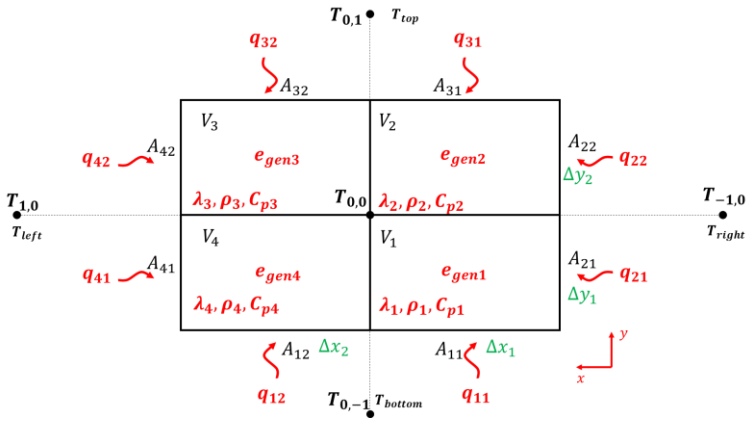

Figure 6. *Expanded numerical cell – heat balance*

4. The plan of experimental trials and numerical results

Numerical experimental planning is carried out with the Design Expert programme [7] and by applying a central composite plan for variable design parameters. The generated test plan and the results obtained by the numerical analysis are shown in Table 1. The calculated values of thermal conductivity and the temperature at the measuring points are observed as a response variable, i.e. the temperature difference of the cold and warm side of the test sample along the symmetry line of the experimental device and after 20 hours of numerical calculations.

Table 1. *Design of experiment and results*

Factors:						Response:				
Sample no.	A:Heater 1 power: P_g1, W	B: Sample diameter: d_uz, mm	C: Sample thickness: h_uz, mm	D: Insulation thickness: x_izo	E: Heater 1 diameter: d_g1, mm	Calculated heat conductivity, W/mK	Cold side temperature, °C	Warm side temperature, °C	Temperature difference, °C	Calculation error,%
24	5.5	200	20	30	167	0.0704	293.3	364.6	71.3	0.57%
33	1	300	10	50	250	0.0712	293.0	295.9	2.9	1.75%
15	10	300	10	50	250	0.0712	293.2	321.8	28.6	1.77%
3	1	300	10	10	250	0.0713	293.0	295.9	2.9	1.85%
5	10	300	10	10	250	0.0713	293.2	321.8	28.6	1.87%
12	1	100	10	50	83	0.0715	293.2	319.0	25.9	2.09%
31	10	100	10	50	83	0.0715	294.8	553.4	258.6	2.12%
29	10	100	10	10	83	0.0716	294.8	553.1	258.3	2.22%
41	1	300	30	50	250	0.0718	293.0	301.5	8.5	2.54%
43	10	300	30	50	250	0.0718	293.2	378.3	85.1	2.56%
36	1	300	30	10	250	0.0723	293.0	301.5	8.5	3.29%
6	1	300	10	50	100	0.0741	293.1	310.3	17.2	5.83%
27	10	300	10	50	100	0.0741	293.1	310.3	17.2	5.83%
1	1	300	10	10	100	0.0741	293.1	310.3	17.2	5.92%
38	1	300	30	50	100	0.0743	293.1	344.6	51.4	6.10%
11	1	200	20	30	95	0.0744	293.1	331.1	37.9	6.25%
10	1	100	10	10	83	0.0753	293.2	317.7	24.6	7.55%
28	1	100	30	50	83	0.0787	293.2	363.6	70.5	12.39%
32	1	300	30	10	100	0.0828	293.1	339.2	46.1	18.32%
25	1	100	10	50	33	0.0832	294.0	434.5	140.5	18.86%
22	1	100	10	10	33	0.0832	294.0	434.5	140.5	18.89%
35	1	100	30	50	33	0.0852	294.0	705.5	411.5	21.77%
17	1	100	30	10	83	0.0868	293.1	357.1	63.9	23.95%
42	10	100	30	50	83	0.0872	294.5	930.3	635.8	24.58%
2	5.5	200	10	30	95	0.0891	293.6	380.7	87.1	27.23%
40	10	300	30	10	250	0.0919	293.2	359.6	66.5	31.33%
20	5.5	200	20	50	95	0.1039	293.5	442.9	149.4	48.39%
26	5.5	300	20	30	143	0.1056	293.2	358.1	64.9	50.82%
14	5.5	200	20	30	95	0.1140	293.5	429.6	136.1	62.91%
30	1	100	30	10	33	0.1203	293.7	585.2	291.6	71.85%
39	10	100	30	10	83	0.1314	294.0	716.0	422.0	87.70%
4	5.5	200	20	10	95	0.1441	293.4	401.1	107.7	105.79%
21	5.5	100	20	30	48	0.1441	294.5	716.4	421.9	105.85%
23	5.5	200	30	30	95	0.1454	293.4	453.5	160.1	107.71%
8	10	200	20	30	95	0.1659	293.6	463.7	170.1	137.00%
13	5.5	200	20	30	67	0.2084	293.5	443.3	149.7	197.66%
9	10	300	10	10	100	0.2158	293.4	352.4	59.0	208.34%
16	10	100	10	50	33	0.2473	296.3	769.2	472.9	253.21%
7	10	100	10	10	33	0.2948	295.8	692.4	396.6	321.10%
37	10	300	30	50	100	0.2993	293.3	420.9	127.6	327.62%
34	10	300	30	10	100	0.4210	293.2	383.9	90.7	501.47%
19	10	100	30	50	33	0.4646	294.6	1049.6	754.9	563.72%
18	10	100	30	10	33	0.6485	294.1	835.0	540.9	826.38%

The most accurate results of all performed analyses (presented in the first row, Table 1) are obtained using the following combination of design parameters:

- the power of electric heater 1: 5.5 W
- diameter of the test sample: 200 mm
- diameter of the electric heater 1: 167 mm
- thickness of the test sample: 20 mm
- thickness of the thermal insulation of the device: 30 mm

After 20 hours of numerical experiment, the calculated value of thermal conductivity of test sample was 0.0704 W/mK, which is a deviation from the actual value by approximately 0.57 %. Figure 7 shows a diagram how value of calculated thermal conductivity changed over time during the numerical test. For the above defined combination of operating parameters and after 20 hours of numerical simulation, the temperatures at the measuring points were obtained as follows (Figure 8):

- cold side: 20.05°C
- hot side: 91.45°C

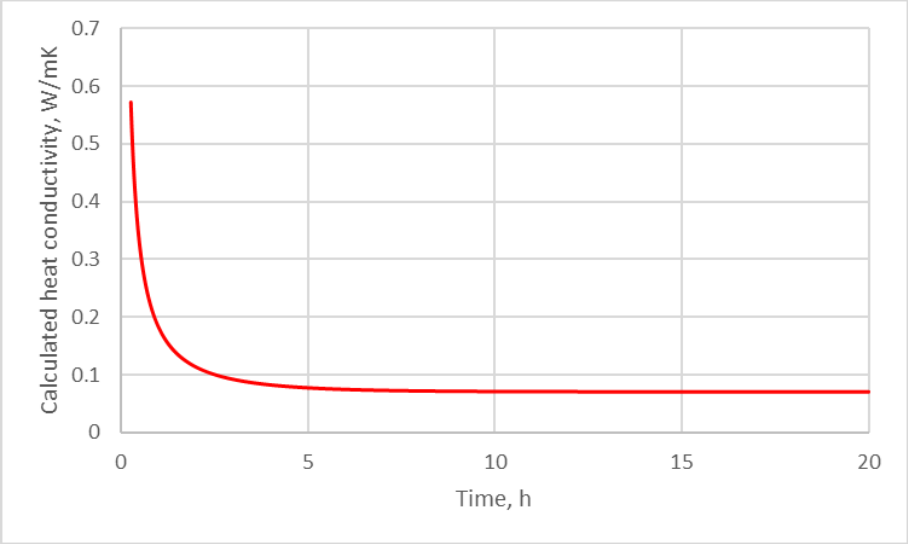

Figure 7. *Calculated thermal conductivity vs time*

After constructing the experimental device, the resulting relatively large temperature difference will enable precise measurement using standard thermocouples whose accuracy is +/-1°C. In case the differential temperature would be measured, then the measurement error will be within 1.5% for test samples with thermal conductivity less than or equal to 0.07 W/mK. With test samples of higher thermal conductivity, the temperature difference will be smaller, affecting the measurement precision by increasing the error. The upper limit of obtained temperature of 91.45°C is still not too high to significantly affect the results of measurement, considering the assumption that some thermal properties are taken as constants.

Table 1 shows all of the testing conditions of the numerical experiments as well as the results obtained by numerical analyses. From the results shown in Table 1, it is evident that in case of other testing conditions the calculated thermal conductivity has resulted in fairly accurate value, however with either too small or too large temperature difference (see the test results in the red frame, Table 1), or with more deviated value of calculated thermal conductivity when compared with the reference value.

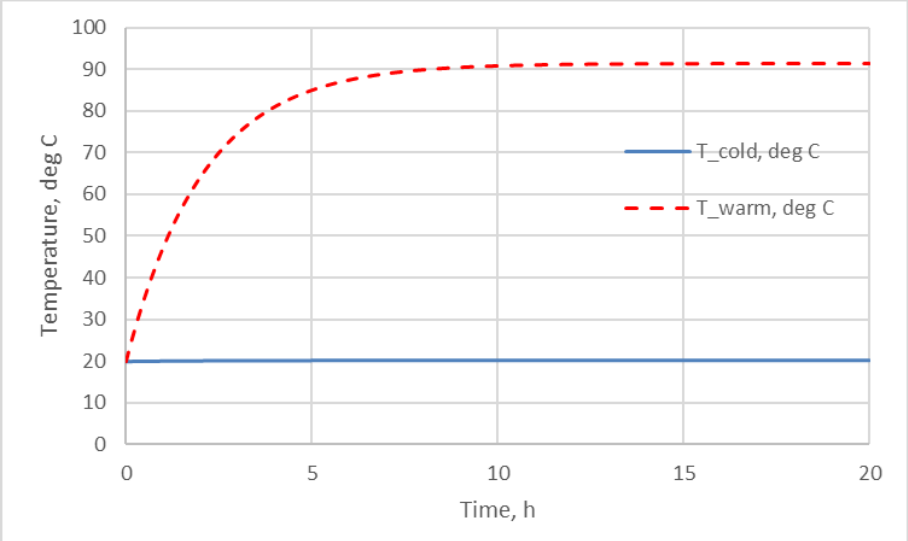

Figure 8. *Temperature changes of hot and cold side of test sample*

5. Conclusion

The application of numerical simulations to evaluate the optimal combination of operating parameters proved to be very useful tool for analysing the performance of future experimental device for measuring the thermal conductivity of thermal insulation materials. The analysis has determined the values of the most important design parameters, and it has produced other important data for defining the final design of the experimental device.

For the numerical analysis a 9×10 finite element mesh was used, with 9 elements per device radius and 10 elements per device height. The applied time step in the analysis was 1/100 seconds. Given that in the previous work [1] an analysis of the impact of grid density and the time step was carried out, and it was determined of insignificant influence, no such analysis is presented in this paper.

The analysis has determined the main dimensions of the experimental device, such as the diameter of 260 mm and height above the cooler of 100 mm (including thermal insulation of the device). The recommended size of the test sample is defined by the diameter of 200 mm and height of 20 mm, the power of internal electrical heater (heater 1) of 5.5 W, and the thickness of the thermal insulation of the device of 30 mm. Since the variation of the power of external electrical heater (heater 2) was out of the scope, it was selected as constant value of 20 W. The external heater was considered as a heat source which periodically turns on and off, thus maintaining the surface temperature of both electric heaters approximately the same.

After constructing the experimental device according to the obtained design parameters, representative values of measured thermal conductivity could be expected already after 10 hours of system operation. In that case the approximate error will be around 1.2 %.

Based on the obtained numerical results and the values of main design parameters, the following step is to construct the experimental device for measuring the thermal conductivity of thermal insulation materials. After the construction and optimisation of the device, a series of measurements will be performed in order to generate a variety of experimental data. This data will be used to verify the results of numerical analysis, and to further develop the numerical tool presented in this paper.

References

[1] Gabrić, I. and Jankoski, Z. 2020. The Numerical Modelling of Experimental Device for Measuring Thermal Conductivity of Metals, Contemporary issues in economy and technology – CIET 2020, Split, Croatia

[2] Jankoski, Z. and Gabrić, I. 2022. Experimental Device for Measuring the Thermal Conductivity of Metals, International conference “Mechanical Technologies and Structural Materials” – MTSM 2022, Split, Croatia

[3] Numan Yüksel, “The Review of Some Commonly Used Methods and Techniques to Measure the Thermal Conductivity of Insulation Materials”, August, 2016, ISBN 978-953-51-2625-6
[4] Boulaoued I., Amara I., and Mhimid A., Experimental Determination of Thermal Conductivity and Diffusivity of New Building Insulating Materials, International Journal of Heat and Technology, Vol. 34, No. 2, June 2016, pp. 325-331
[5] Yunus A. Cengel and Afshin J. Ghajar, Heat and Mass Transfer: Fundamentals and Applications, Fifth Edition in SI Units, McGraw-Hill Education, New York, 2015
[6] Python Software Foundation, https://www.python.org/
[7] Stat Ease, Inc.: DESIGN – EXPERT version 11.0.3.0; 2021 East Hennepin Ave., Suite 480 Minneapolis. MN 55413

Steel production in electric arc furnaces in the world and in Croatia

***Mirko Gojić*[1,2], *Stjepan Kožuh*[1], *Ivana Ivanić*[1], *Daniela Dumenčić*[1] *and Borut Kosec*[3]**

1) University of Zagreb, Faculty of Metallurgy, Aleja narodnih heroja 3, 44000, Sisak, Croatia

2) University North, Trg dr. Žarka Dolinara 1, 48000, Koprivnica, Croatia

3) University of Ljubljana, Faculty of Natural Sciences and Engineering, Aškerčeva 12, 1000 Ljubljana, Slovenia

Corresponding author: gojic@simet.unizg.hr

Review article

Abstract: It is known that steel is the most important metallic material. Steel production in the world today is carried out by means of oxygen converters and electric arc furnaces. The main raw material for steel production in electric arc furnace is steel scrap. The first production of steel in electric arc furnace in the Republic of Croatia was started in 1966. Steel production in electric arc furnaces in Croatia was in iron and steel works in Sisak and Split. Currently, steel is produced only in steel mill in Sisak. The article gives an overview of steel production in electric arc furnaces in the world and in Croatia in the period from 1966 to 2022. In the last 30 years, the total production of steel in electric arc furnaces in the Republic of Croatia was about 2.5 Mt.

Keywords: *steelmaking; iron and steel works*; *electric-arc furnace; steel scrap*

1. Introduction

As the most important metallic material, steel is of enormous importance to any national economy. Global steel production is more than 20 times higher than the production of aluminium and copper combined. The economic power of any country is determined by steel production as progress in the main industries (metal processing, transport, shipbuilding, civil engineering, mining, agriculture, etc.) is not possible without steel. One of the indicators of a country's industrial development is the production and consumption of steel per capita. For centuries, the production of iron and steel was synonymous not only with economic power, but also with political power. Today, the situation is not much different. From historical times until today, the use of steel has not lost its importance, but continues to grow. Steel is a material of the past, present, and future [1-3].

In 1870, the world steel production was about 500 kt. At that time, more than 90 % of the total British and 50 % of the European steel production was made in Sheffield. In 1900, 28.3 Mt of steel was produced worldwide, most of it in the United States of America (36 %) and the United Kingdom (17 %) [4]. Steel production over the last 120 years is shown in Table 1.

Table 1. *The world steel production from 1900 to 2020 [5]*

Year	1900	1920	1940	1960	1980	2000	2020
10^6 t	28.3	72.5	140.6	346.4	716.2	848.9	1878

In the 20th century, steel production showed a constant increase. In the first 60 years of the 20th century, world steel production increased by almost 12.2 times. The fact that after the World War II (1951) the Western European countries joined together to form the European Coal and Steel Community, the forerunner of the European Economic Community (1957) and today's European Union (1993), speaks volumes about the role and importance of steel as a material. In 2020, 1.878 Gt of steel was produced, which is 2.2 times increase by comparison with 2000 (Table 1).

The most significant increase in steel production was in the period from 1950 to 1975, by 3.4 times. In the 1950s and 1960s, world steel production increased at an annual growth rate of about 5 %. In

the middle 1970s, the global oil crisis led to a decline in steel production in almost all parts of the world. From 1980 to the end of the 20th century, steel production was between 716.2 and 848.9 Mt, as a result of restructuring in technological, quality and regional aspects.
At the end of 1980, i.e. at the end of the "Cold War", there was an increase in steel production in Asia, especially in China, which compensated for the lower steel production in the Eastern European countries. Developed countries concentrated on steels with higher quality, while the "new" producers produce mainly "massive" steels.
Steel is a universal material for which there is no satisfactory substitute, and it is mainly used in construction (52 %), mechanical engineering (16 %) and the automotive industry (12 %) [6,7]. Steel has a wide range of applications due to its exceptional properties, which can be combined in various ways. It is characterised by the possibility of shaping by deformation and can be processed by heat treatment and/or surface engineering (surface modification and coating processes), joining possibilities with the same and/or different metallic materials (welding, soldering, etc.), etc.
Steel is the most recycled of all materials (98 %). The situation with steel scrap changed significantly in the 1960s thanks to the rapid development of steel production in electric arc furnaces (including in the Republic of Croatia), but also thanks to the development of steel production technology in oxygen converters. Every year, more steel is recycled than all other materials combined (such as paper, plastic, aluminium, glass, etc.) [8,9].

2. Today´s steel production processes

Modern steelmaking in the world today is predominantly carried out by so-called “coke metallurgy”. The main raw materials for steel production are white pig iron, steel scrap and products of direct reduction and reduction smelting. However, the production of steel by remelting steel scrap as the most important secondary raw material is becoming very important. It is by far the cheapest raw material for steel production. Direct reduction iron is obtained by reduction with natural gas (in shaft furnaces) or coal (in rotary furnaces) [10].
Today, steel is produced in oxygen converters and electric arc furnaces as well as in primary aggregates. It should be noted that converter and electric steel do not compete but complement each other in terms of primary raw materials. While in the oxygen converter the main raw material is white pig iron, in the electric arc process the main raw material is steel scrap. The steel produced in the electric arc furnace is cheaper and more environmentally friendly (lower CO_2 emissions). In 2022, 1.885 Gt of crude steel was produced. With respect to steelmaking processes, 71.5 % of steel in 2022 was produced in basic oxygen converters (BOC), 28.2 % in electric arc furnaces (EAF), and 0.4 % in other processes.

2.1. Steel production in electric arc furnaces

Electro-steel has been produced in electric arc furnaces (mainly) and induction furnaces since the beginning of the 20th century [1]. The heat required for electro-steel production comes primarily from electrical energy, i.e., from the electric arc generated between the graphite electrodes and the charge, which causes the melting of steel scrap. The development of electro-steel production depends on the availability and price of electrical energy, raw materials for steelmaking, and the availability and quality of coal for coke production, needed for the so-called "coke metallurgy" (steelmaking by means of coking plant, blast furnace and basic oxygen converter). The first industrial electric arc furnace was put into operation in Germany in 1906. For the first 70 years, mainly higher quality precious steels were produced there. Initially, electro-steel was used mainly for production of long products (wire, girders, tubes, etc.). The advantages of electro-steel production are lower price, greater flexibility, more environmentally friendly process, etc. The production program has been expanded to include some flat products (sheet, strips, etc.) and the production of melts for further processing of stainless steels.
A few innovations have been introduced at EAF. One of the most significant innovations is the introduction of water-cooled panels that can simultaneously withstand high thermal and mechanical

loads (e.g., impact of steel scrap on panels). As a result, the consumption of refractory material was reduced by 50-70 %, the durability of the furnace dome was increased by 50 %, the operation with a longer electric arc was ensured, and the melting time was reduced by 5-10 minutes. Additionally, the use of foaming slag has been introduced. Intensive carbon combustion and the release of gases from the bath through the slag, create a foamy slag that „closes" the electric arc and protects the lining and furnace panels from radiation. The foamy slag allows working with a more stable and longer arc. Working with a longer arc at a higher voltage in the secondary circuit of the transformer requires a lower current intensity, resulting in lower electrode consumption.

Formerly, all stages of steel production (preheating, melting, refining, and alloying) were carried out in a single furnace, but this concept has long been outdated. The development of secondary metallurgy (since 1970) has meant that the EAF is now mainly an aggregate for remelting of steel scrap. However, the technological process consists of charging the furnace, melting, and casting the molten metal (Figure 1). The central phase of EAF operation is the melting period. Melting involves the use of electrical energy (via graphite electrodes) and chemical energy (oxidation of impurities with O2/fuel burners and oxygen lance). Heat transfer to the steel scrap is by radiation and convection, and within the steel scrap by conduction. Additional blowing with oxygen or another fuel gas mixture accelerates melting. When the oxygen lance is aimed directly at the molten steel, oxidation of elements such as Al, Si, Mn, P, C, and Fe occurs, generating heat for further melting (these reactions are exothermic, as shown in Table 2). The resulting metal oxides pass into the slag, while the gaseous CO output from the molten steel into the empty space of the furnace, where it can continue to burn (with additional oxygen supply). The EAF operating cycle refers to the time from charging to pouring of the molten metal, i.e tape to tape time. The aim is to obtain molten steel of sufficient quality in the shortest possible time (less than 60 minutes).

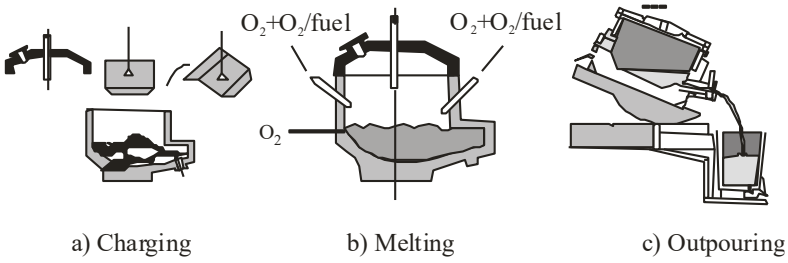

Figure 1. *Schematic illustration of the individual phase of steelmaking in EAF [1]*

Electric arc furnaces can operate on alternating current (AC furnace) with three electrodes (they are primary), and since the late 1980s there have also been direct current arc furnaces (DC furnaces), with one electrode. The purpose of the graphite electrodes during EAF operation is to ensure continuous and uniform transfer of electrical energy to the molten metal. Due to the three-phase electricity system, three graphite electrodes are used in AC furnaces. To obtain the appropriate low voltage for the electric arc, transformers (power up to 100 MVA) are used to convert the high network voltage to an acceptable level of arc voltage. Direct current EAF is characterized by the central position of a graphite electrode acting as a cathode, but with built-in counter electrodes (of different constructions) in the furnace bottom.

Additional energy for EAF operation is provided by using an O2/fuel burner (gas mixture) and oxidising admixtures by injecting oxygen. The main raw material is prepared steel scrap (more than 90 %), increasingly using direct reduced iron (DRI) and/or hot briquetted iron (HBI). The electric arc furnaces can produce melts for all steel grades, from unalloyed to high-alloy steel.

Table 2. *Values of the heat released during individual oxidation reactions of the admixture [1]*

Oxidation reaction		Released heat, kWh/kg of the oxidized element
Carbon oxidation	$C + ½ O_2 = CO$	2.85
	$C + O_2 = CO_2$	9.40
Silicon oxidation	$Si + O_2 = SiO_2$	8.90
Oxidation of manganese	$Mn + ½ O_2 = MnO$	1.95
Iron oxidation	$Fe + ½ O_2 = FeO$	1.32

When the desired composition and temperature of the molten metal is achieved, the electric arc furnace (EAF) is tilted, and the steel is poured through an open and/or groove in the furnace into a ladle for further processing (usually a ladle-furnace or stationary ladle). The steel is poured from the bottom of the furnace or with the help of various-shaped groove (especially for casting stainless steel melts). In most modern furnaces, the steel is poured through an opening on the bottom into a ladle (slag-free outpouring, lower temperature drop, working with a liquid residue), which is previously placed under the opening of the EAF. Placement of the slide gate at the outlet of the EAF reduced slag penetration into the ladle, ensuring lower sulfur and phosphorus content in the steel and a shorter time for secondary metallurgy. During casting, the steel is deoxidized (with aluminum or silicon with the addition of Fe-Si, Si-Mn, etc.), and alloying elements can also be added. After the casting is finished, the furnace is quickly set up again so that the hot residue remains in the furnace. Steelmaking in the electric arc furnace produces a smaller content of slag, which also has a lower basicity than steelmaking in the basic oxygen converter.

The process of electro-steel production is highly automated and computer-controlled, using online systems and dynamic models for continuous monitoring and control of almost all process parameters with a display of the current state [11,12]. The basic indicators of the success of EAF operations that affect the price of steel are furnace productivity (time from pouring to pouring of molten steel, called "tape to tape"), consumption of electrical energy, electrodes, and refractory materials. Productivity depends not only on the power of the transformer and the operation of the furnace, but also on the preparation of the charge and the organization of work (degree of automation, coordination of work with other sections). Steel scrap preheating, which began in the 1960s, is increasingly being used to improve energy efficiency and reduce operating costs. Numerous modifications of the electric arc furnace have been introduced (K-ES process, Danarc process, Fuchs and tandem furnaces, as well as processes with continuous furnace charging [1: Consteel process, IHI process, Comelt process, Conarc process, Contiarc process, etc.). Based solely on EAF steel production, a large number of so-called mini-iron steel works have been built around the world. During the production of steel in EAF, primary emissions (e.g. during melting) and secondary emissions (e.g. during charging, casting of steel, etc.) occur. Special importance is also attached to environmental protection. Special attention is taken to install a filter to collect electric furnace dust, as it is classified as hazardous waste. Electro-steel production is also increasing in the first two decades of the 21st century (Figure 2). The share of electric arc furnaces in global steel production in 2020 is 26.3 %, and in the EU [13] it is higher (42.4 %). Electric arc furnaces will continue to be one of the most important procedures of steel production in the future. It is expected that the steel content produced in electric arc furnaces will increase. Efforts are being made to ensure the flexibility of the process, increase productivity, and improve steel quality, while taking into consideration environmental criteria.

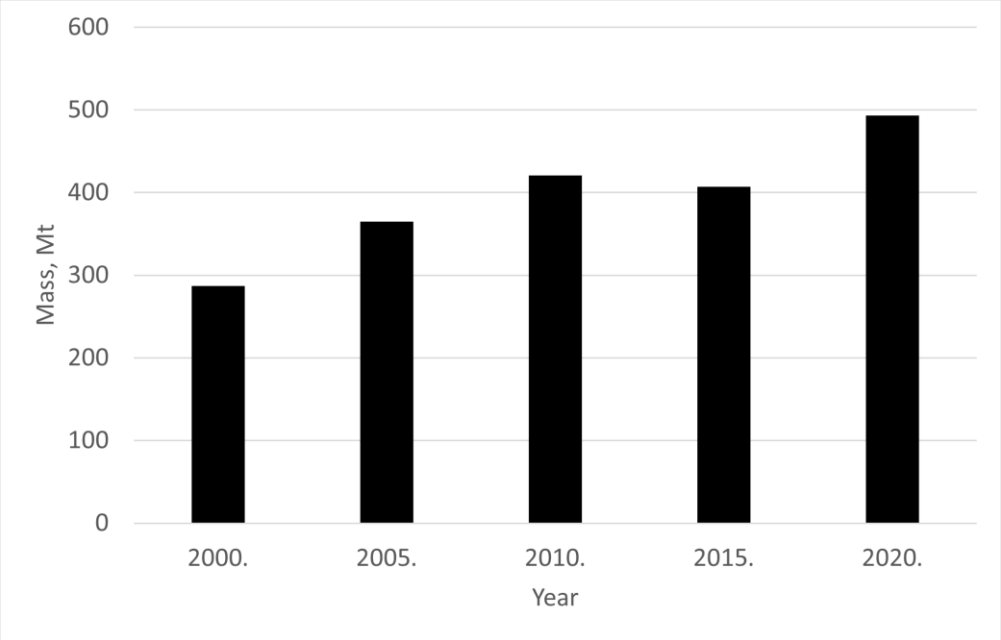

Figure 2. *The world steelmaking by the electric-arc process (2000 – 2020) [8]*

3. Steel production in electric-arc furnaces in the Republic of Croatia (1966 – 2022)

The Republic of Croatia did not and still does not have the capacity, raw material and energy base to produce steel using the basic oxygen converter process, which has dominated the world since 1970 [14-16].

The production of crude steel took place in two iron steel works: Iron and steel works Sisak and Adriatic Iron and steel works (later Iron and steel works Split). Due to its structure, the Iron and steel works Sisak belonged to the integral type, as it contained facilities to produce coke, pig iron (including the preparation of iron ore), crude steel and facilities for hot and cold processing of steel, but also with a considerable metalworking production of finished products [15]. The Iron steel works Split has always been a small iron steel works, because here steel scrap was remelted into steel, which was processed in hot and cold processing facilities. However, according to the production volume, both iron steel works belonged to the small iron steel works [16]. Today, crude steel is produced only in the company ABS Sisak Ltd. in a new electric arc furnace by remelting steel scrap using secondary metallurgy (ladle-furnaces and vacuum degassing). Figures 3 and 4 show steel production in electric-arc furnaces in the Republic of Croatia in the period from 1996 to 2022. Figure 3 shows the continuous increase of steel production, especially including steel production in Adriatic Iron steel works (1971). Table 3 shows the trend of increasing electric steel production, especially after the starting the second electric arc furnace (EAF) in Split during 1980. In the early 1990s, the work of the metallurgical industry, including steel production has changed or interrupted due to war circumstances, difficulties in importing raw materials, market losses, and so on. Steel production continued in the electric arc furnaces in Sisak and Split, but on a significantly reduced level. Both iron steel works were privatized three times without success. The Iron and steel works Sisak was successfully privatized in 2012 and produces steel in modernized facilities; the Iron and steel works Split was closed in 2018. Figure 4 shows large oscillations in the steel production, with the gap in steelmaking for some years (2016 and 2017). In 2020, a large decrease in steel production (45 kt) was recorded due to the pandemic caused by the virus COVID-19. The total production of electro-steel from 1992 to 2022 was about 2.5 Mt.

Table 3. *Steelmaking in the Republic of Croatia in the period from 1976 to 1982, t [17]*

Iron steel works/year	1976	1978	1980	1982
Sisak	69169	77191	75343	66843
Split	40505	43126	35382	58824
Total	109674	120317	110725	125667

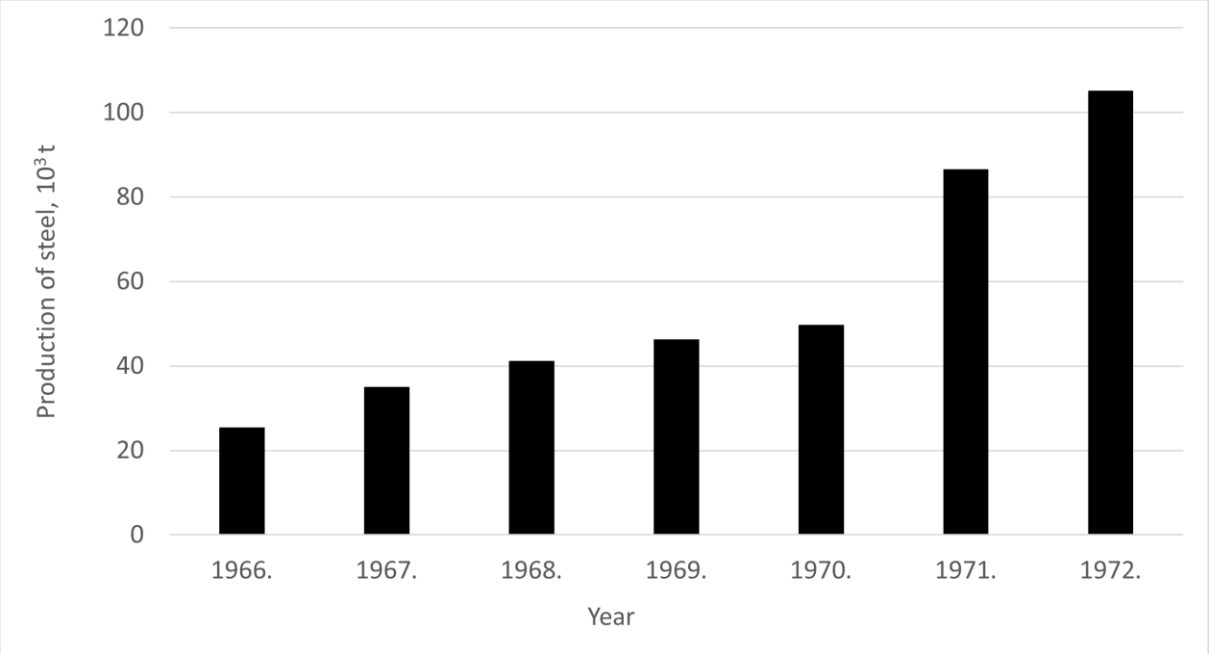

Figure 3*. Electro-steel production in the Republic of Croatia in the period from 1966 to 1972*

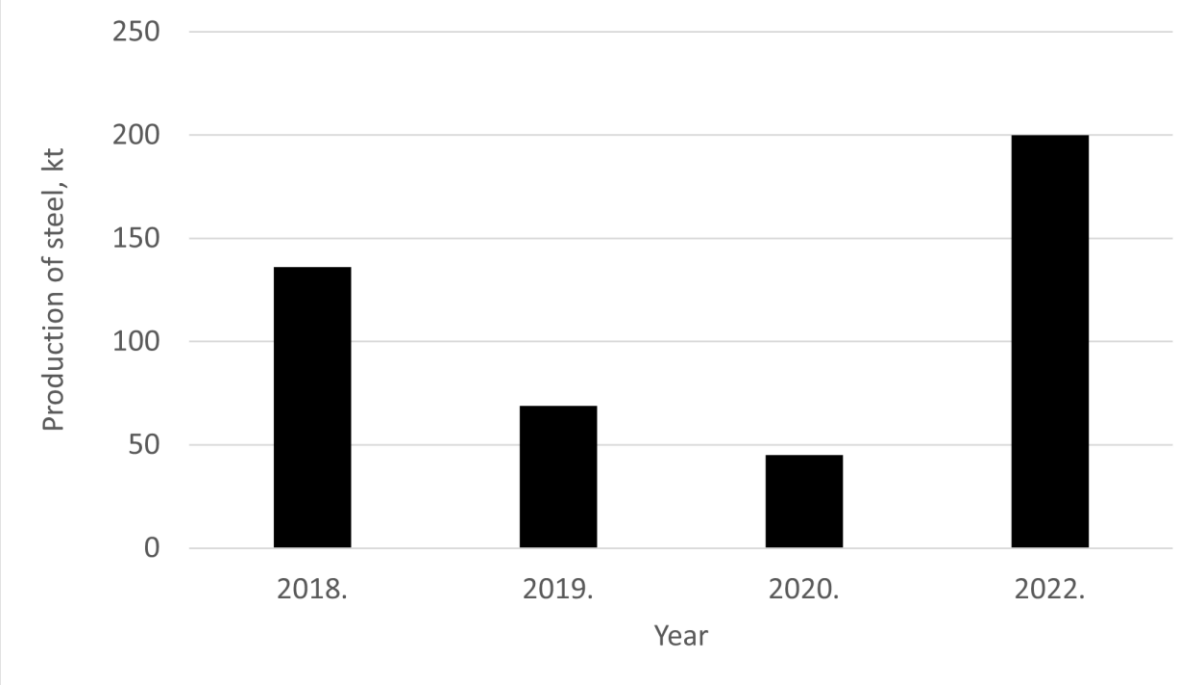

Figure 4*. Steelmaking in the Republic of Croatia in the period from 2018 to 2022*

3.1. Electro-steel production in Iron steel works Sisak

Steel production at the Iron and steel works Sisak using an electric arc furnace began with trial operation on February 21, 1966 [18]. The initial capacity of the Tagliaferri furnace was 25 t with an installed transformer power of 15 MVA (Figure 5).

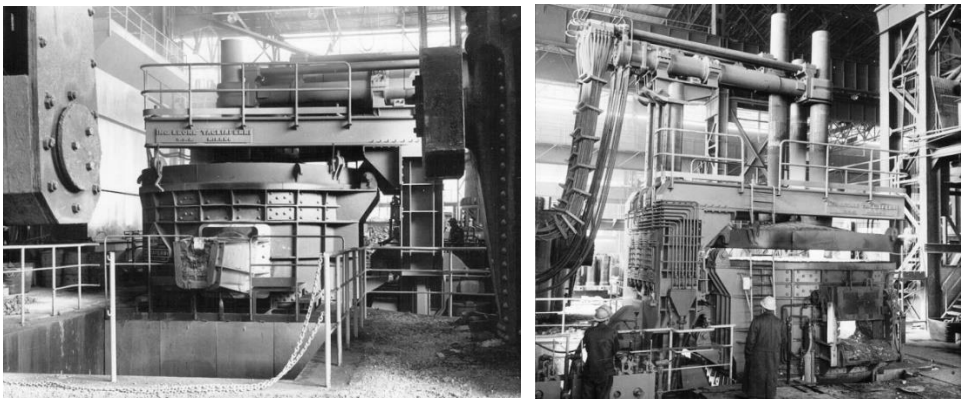

Figure 5. *Electric arc furnace in the Sisak Ironworks from 1966*

The initial technical capacity of the electric arc furnace was 42 kt of steel per year. The main raw material for the steel production in EAF was prepared steel scrap. The EAF was used to produce higher-quality steels, specifically steels to produce tubes for the oil industry. In the first year of operation, 25.4 kt of EAF steel was produced. By intensifying the process, production increased to 65.6 kt of electro-steel in 1977 (Table 4). Later, the capacity of electric arc furnace was increased to 30 t with a monthly production of 4 - 6 kt. The steelmaking process lasted for approximately three hours.

Table 4. *Electro-steel production in the Iron and steel works Sisak in the period from1966 to 1995, kt [18]*

Year	1966	1970	1974	1977	1980	1982.	1990	1991	1995
Electro-steel	25.4	49.8	60.1	65.6	69.3	66.8	52.4	50.1	21.9

From the 1970s onwards, blowing the molten steel with inert gas (argon) in the ladle was carried out as part of the secondary metallurgical processes. The aim of this process was to homogenize the temperature and chemical composition of the steel while reducing the amount of non-metallic inclusions, thus increasing the purity of the steel [19,20]. The steel was poured into a ladle and then cast exclusively in metal moulds (Figure 6a) of various formats (until 1973). With the introduction of continuous steel casting facilities in 1973 (Figure 6b), the extraction was increased (6-7 %). Continuous casting was carried out on two lines, each with three "strands" with a radius of curvature of 11 m.

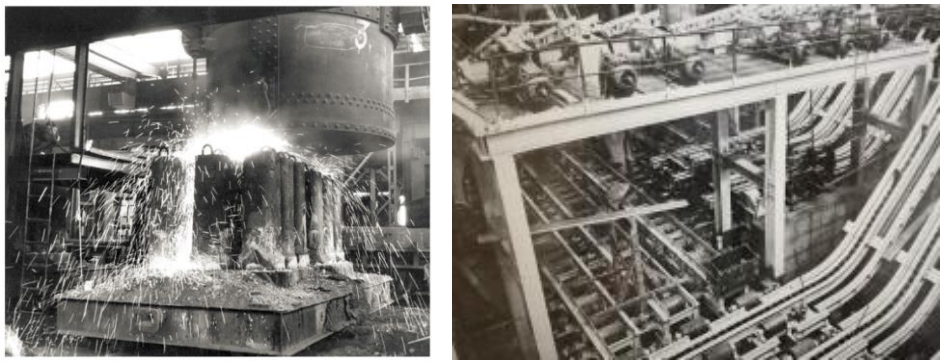

a) b)

Figure 6. *Classic (a) and continuous casting of steel in Iron and steel works Sisak (b)*

Slabs (rectangular section 350 x 190 mm and 430 x 190 mm), blooms (square 300 x 300 mm, octagonal with diameters of 245, 276 and 320 mm, etc.) were produced by continuous casting. At the end of 1980s, most of the continuous cast products were slabs (more than 60 %) [21]. In the period from 1970 to 1990, the Iron and steel works Sisak produced an average of 4-6 kt of electro-steel per month. The steel produced (classically cast in ingots and/or as continuously cast semi-finished products) was further processed in the rolling mills of the Iron and steel works Sisak: rolling mills of seamless tubes, rolling mills of strip and billet, rolling mills welded tubes and rolling mills of precision welded tubes, as well as in the cold processing plants (cold drawing and pilgering of tubes).

3.2. Steelmaking in Iron and steel works Split

Despite resistance from the Association of Yugoslav Iron steel works, the Municipal Assembly of Split established the construction company "Adriasider" on March 6, 1968, and the construction of the Iron and steel works in Split began in April 1969 [22]. The sudden increase in the consumption of so-called concrete steel in the construction sector led to the building of the iron steel works in Kaštel Sućurac, near to Split (Figure 7). In addition to market conditions, Split also had a particularly important advantage as a source of raw materials for steel production, namely the steel scrap from the existing cutting mill of ships.

Figure 7. *Iron and steel works in Kaštel Sućurac [23]*

The assembly of the equipment for the electric arc furnace began on June 15, 1970. The furnaces and equipment came from the Swiss company "Brown Boweri und C". The inner diameter of the electric arc furnace was 3.9 m, and the diameter of the graphite electrodes used was 350 mm. The electric arc furnace was supplied with electricity via a 35/6 kV transformer at the main transformer station and a 6/4 kV transformer near the furnace itself. The electric arc furnace, with a capacity of 25 t and a transformer power of 7.5 MVA, was started up on a trial operation at 10:14 p.m. on January 8, 1971. Mass from 25 t of prepared steel scrap was charged (Figure 8). The storage for the steel scrap was in the open air (outdoor). The first melt was poured at dawn on January 9, 1971. The trial operation period was 2-3 months.

Figure 8. *Preparation of steel scrap in Iron and steel works Split [23]*

The technological process of steel production was similar to that of the EAF in Iron and steel works Sisak (Figure 9). However, in Split, amortized steel scrap was primarily used as the charge, and steel casting was 100 % continuous process (Figure 10). The facilities for continuous casting of billets (100 x 100 mm) with two strands with a radius of curvature of 4 m putted into operation on January 28, 1971. It was the first installed facilities for continuous steel casting in Yugoslavia. The manufacturer of the facilities was the Swiss-Italian company "Concast-Innocenti". The annual capacity of the EAF was 60 kt of crude steel and the capacity of cast steel billets was 57 kt. The resulting semi-finished steel products were billets cut to length by automatic shears for the wire rolling mill installed in September 1971. The rolling mill was from the Italian company "Pomini-Farrell" and was the first in Yugoslavia with rolling plates for rolling prestressed wire. This supplied a deficit wire for the so-called bi-steel, screws, taks, construction nets, ribbed concrete steel, etc. at that time.

Figure 9. *Pouring steel into a casting ladle from an electric-arc furnace at the Iron and steel works Split [24]*

Figure 10. *Countinuous casting of billets in Iron and steel works Split [24]*

At the end of 1971, 34 kt of steel billets were produced in Split, and later production increased to about 48 kt per year. With the building of a second EAF (1980) with a capacity of 25 t and transformer power 12.5 MVA [13] and a new facility for continuous casting, steel production increased to 55-67 kt of steel between 1981 and 1984. In the late 1980s, the technical capacity of electrosteel production in Split was increased to 120 kt for continuous casting of billets 100 x 100 x 2000 - 6000 mm. The average monthly production of electrosteel in Iron steel works Split was about 9 kt.

After the reconstruction of the Iron steel works Split in 2002/2003, financed by credit funds, a new 26 t electric arc furnace (EAF) was built (melting time of about 60 minutes). Steel refining in the ladle-furnace was introduced (capacity of 26 t, transformer power 15/12.5 MVA). The production program of cast semi-finished products was expanded, and the annual production capacity of the facilities was increased to 185 kt of continuous cast billets [25,26]. In addition to the billet with dimensions of 100 x 100 x 6000 mm, billets with dimensions of 125 x 125 x 6000 mm were also produced by continuous

casting. These billets were made of low-carbon, medium-carbon and low-alloy steels for hot and cold processing, with a product range similar to the pre-war period.

3.3. Today´s steelmaking in the Republic of Croatia

Today, steel production in the Republic of Croatia is limited to the production of electro-steel in the former Iron and steel works Sisak, but in new and modernized facilities of the Italian company Danieli (since May 31, 2012). The steelworks existed under the name ABS Sisak Ltd., which has invested significant funds in the modernization of steel production, including secondary metallurgy (installing of ladle-furnace and vacuum-degasser) and continuous casting (casting on three strand). Steel scrap is prepared from small collectors, but also purchased in domestic and foreign markets. The investment of steel scrap into the electric arc furnace is commonly done using with 2-3 charging baskets. The mass of steel scrap is determined based on the so-called "hot residue" from the production of the previous melt. The charge consists of processed steel scrap, hot reduced iron briquettes (product of direct reduction), carbons blooms (reject, technological scrap), steel shavings, own waste (e.g., so-called "steel bears"), coke, lime for slag formation, etc. [27]. Melting takes place in the new electric arc furnace using alternating current and electric arc energy between the electrodes and the steel scrap, which melts the charge. To intensify the process, a "chemical package" is also used, consisting of burners that provide additional heat through exothermic reactions of impurity oxidation. Oxygen, carbon, natural gas and powdered MgO are injected into the furnace.

The burners contribute to the melting of the charge, but also assist to the formation of slag in the furnace. After melting, a sample is taken for chemical composition analysis using an automated robotic arm, and a rapid analysis of oxygen and carbon content and temperature measurement of the molten metal is performed. Remelting the charge in EAF takes between 60 and 70 minutes, depending on the type of steel. The molten steel is then tapped into the ladle with a tapping time of 2-4 minutes. During this process, deoxidation with aluminium and ferrosilicon (FeSi), pre-alloying of the steel with manganese (by adding silicomanganese - FeSiMn) and addition of synthetic slag is carried out. If necessary, a carburizing agent based on petroleum coke (known commercially as "carburite") is also added. During outpouring of melt, argon is continuously blown into the molten steel through a porous stone attached to the bottom of the ladle. The ladle is then transported to the secondary metallurgy (ladle-furnace), where (in addition to electrode heating) the necessary secondary metallurgical processes are carried out. These operations include argon blowing, desulfurization, alloying, carbonization, deoxidation, and so on. Processing of the melt in the ladle-furnace takes about 60 minutes. After achieving the desired chemical composition and temperature, the molten metal is transfer to vacuum-degasser to reduce the hydrogen content (below 2 ppm). Vacuum degassing usually takes 50-60 minutes, followed by continuous casting, which takes about 50 minutes. It is possible to perform the so-called sequential casting (the next melt is poured immediately after the previous one, without interrupting the casting). After primary and secondary water cooling, tertiary cooling of the continuously cast products takes place in the air.

The semi-finished steel products obtained are round sections with a diameter of 210-410 mm and billets with a diameter of 160 x 160 and 170 x 170 mm. After continuous casting, the semi-finished products cuts by gas cutting, usually with a length of 12 meters, followed by visual inspection. In addition, the geometry, length, flatness, hardness, and radioactivity of the cast semi-finished products are monitored. Samples are also taken for macroscopic analysis, including detection of cracks, porosity, central segregation, etc. Unlike in the past, very little is done manually today. Control and monitoring of the steel production process is done online through computer systems, ensuring that the required variables are always visible. The semi-finished steel products (90 %) produced by ABS Sisak Ltd. are delivered to a wire rolling mill in Udine for wire production.

In the period July - September 2022, ABS Sisak Ltd. was modernized, i.e., a new EAF capacity (75 t) was installed with a completely new digital transformer for the lowest possible power consumption. In addition, the arch of the ladle-furnace was replaced and the facilities for continuous casting in the secondary cooling zone was modernized. According to media reports, ABS Sisak Ltd. will further

modernize, increase production, but also invest in rolling mill capacity for steel processing in Sisak [28].

4. Conclusion

Since 1970, steel has been produced worldwide mainly in oxygen converters. The main raw material for steel production in oxygen converters is white pig iron. The most important steelmaking processes worldwide today are oxygen converters (71.5 %) and electric arc furnaces (28.2 %), combined with secondary metallurgical processes and continuous casting (96.8 %). The main raw material for steel production in electric arc furnaces is steel scrap. In the Republic of Croatia, the production of EAF steel has taken place in Iron and steel works Sisak (1966 - present) and in Split (1971 - 2018). In Sisak, steel was primarily produced for the tube industry, including both welded and seamless tubes. In Split, the production focused on so-called “concrete steel” used in construction. Both iron and steel works produced low-carbon, medium-carbon, and low-alloy steels. Today, steel production in the Republic of Croatia is limited to the production of electro-steel in the former Iron and steel works Sisak, but in new and modernized facilities owned by the Italian company Danieli (since May 31, 2012). The steelworks existed under the name ABS Sisak Ltd., which has invested significant funds in the modernization of steel production, including secondary metallurgy (ladle-furnace and vacuum-degasser) and continuous casting (casting in three strand). The total production of electro-steel in the Republic of Croatia in the last 30 years was about 2.5 Mt.

References

[1] Gojić, M., 2006. Metalurgija čelika, Sveučilište u Zagrebu, Metalurški fakultet, Sisak.
[2] Pavlović, P., 1990. Materijal čelik, SKTH/Kemija u industriji, Zagreb.
[3] Gojić, M., 2022. Enciklopedijska natuknica: čelik, Hrvatska tehnička enciklopedija, sv. 2, Leksikografski zavod Miroslav Krleža, https://tehnika.lzmk.hr/?s=%C4%8Delik (accessed February 28, 2023)
[4] Fenton, M. D., 2000. Steel in the 20th Century, U.S. Geological Survay Minerals Yearbook.
[5] https://worldsteel.org/steel-by-topic/statistics/steel-statistical-yearbook/ (accessed January 31, 2021)
[6] Knežević, D., 2021. Pregled svjetske proizvodnje čelika u razdoblju od 2000. do 2019. godine, Završni rad, Sveučilište u Zagrebu, Metalurški fakultet, Sisak.
[7] Gojić, M., Ivanić, I., Knežević, D., 2022. Svjetska proizvodnja čelika u razdoblju od 2000. do 2020. godine, Kemija u industriji 71, 497-506.
[8] Gojić, M., 2022. Proizvodnja čelika u prva dva desetljeća 21. stoljeća, Zavarivanje 65, 103-108.
[9] Gojić, M., Črnko, J., Kožuh, S., 2002. Proizvodnja čelika u dvadesetom stoljeću, Kemija u industriji 51, 317-328.
[10] Gojić, M., Kožuh, S., 2006. Development of Direct Reduction Processes and Smelting Reduction Processes for the Steel Production, Kemija u industriji 55, 1-10.
[11] Holappa, L., 2017. Recent achievements in iron and steel technology, Journal of Chemical Technology and Metallurgy 52, 159-167.
[12] Tomasović Teklić, A., Filipović-Grčić, B., Pavić, I., 2017. Modelling of three-phase electric arc furnace for estimation of voltageflicker in power transmission network, Electric Power Systems Research 146, 218–227.
[13] Gojić, M., 2002. Stanje i trend proizvodnje čelika u svijetu i Republici Hrvatskoj u: Materijali i tehnologijski razvoj (ur. T. Filetin), ATZH, Zagreb.
[14] Gojić, M., Kožuh, S., Ivanić, I., Bakić, M., 2023. Značajke masovne proizvodnje sirovog čelika u Republici Hrvatskoj od 1954 do 2020. godine, Kemija u industriji 72, 87-93.
[15] Gojić, M., 2022. Metalurgija čelika u Republici Hrvatskoj, Studia lexicographica 16, 79-110.
[16] Gojić, M., 2022. Proizvodnja i potrošnja čelika u Republici Hrvatskoj, Zavarivanje 65, 177-181.
[17] Izvještaj o poslovanju TEF-a za 1983. godinu, (1984). tef 22, 10.
[18] Čepo, Z., Željezara Sisak 1938-1978, 1978., SOUR Metalurški kombinat „Željezara Sisak “, Sisak.

[19] Krajcar, J., Ferketić, V., Krajcar, B., 1972. Prvi pokusi ispiranja čelika inertnim plinovima u Željezari Sisak, Metalurgija 11, 15-20.
[20] Ferketić, V., Krajcar, J., 1973. Obrada SM čelika argonom i dušikom u loncu, Metalurgija 12, 3-13.
[21] Krajcar, J., Ferketić, V., Vuković, D., 1991. Problemi kontinuiranog lijevanja čelika nakon prestrukturiranja i modernizacije pogona u „Željezari Sisak“, Metalurgija 30, 149-153.
[22] Bonačić-Mandinić, A., Jerković, A., 1972. Poduzeće “Jadranska željezara”, Institut za pomorsku, turističku i obalnu privredu, Split.
[23] Katalog proizvoda Željezara Split d.d., 2006. Split.
[24] Šimunović, V., 1976. Jadranska željezara-novi član Udruženja jugoslavenskih željezara, Čelik 60, 25-29.
[25] Živković, V., 2004. Reconstructure of Reinforcing Steel Bars Mill in Željezara Split, Metalurgija 43, 227-238.
[26] Živković, V., 2006. Results of Reconstruction of Steel Works in Željezara Split, Metalurgija, 45, 227-239.
[27] Dundjer, M., 2022. Industrijska proizvodnja čelika u ABS Sisak, d.o.o., Diplomski rad, Sveučilište u Zagrebu, Metalurški fakultet, Sisak.
[28] Pušić, M., 2022. Mega investicija u Hrvatskoj: Talijani pokrenuli projekt koji bi trebao oživjeti sisački kraj! https://novac.jutarnji.hr/novac/aktualno/mega-investicija-u-hrvatskoj-talijani-pokrenuli-projekt-koji-bi-trebao-ozivjeti-sisacki-kraj-15191851 (accessed August 8, 2022)

SEM analysis of hydrated titanium alloy TiAl6Nb7 produced using HDH technology

***Aida Imamović*[1], *Borut Kosec*[2], *Aleš Nagode*[2], *Mirsada Oruč*[1], *Šaban Žuna*[3], *Zijad Alibašić*[3], *and Ensar Mulaosmanović*[3]**

1) Faculty of Metallurgy and Technology, University of Zenica, Travnička cesta 1, 72000 Zenica, Bosnia and Herzegovina

2) Faculty of Natural Sciences and Engineering, University of Ljubljana, Aškerčeva cesta 12, 1000 Ljubljana, Slovenia

3) JU "Center for advanced technologies" , Vilsonovo šetalište 9, 71000 Sarajevo, Bosnia and Herzegovina

Corresponding author: aida.imamovic@unze.ba

Original scientific article

Abstract: Due to its resistance to corrosion and chemical action, the TiAl6Nb7 alloy is one of the most suitable materials for medical use such as implants, instruments, etc. The microstructure properties of this alloy enable the application of HDH technology as an economical process for the production of "low-cost" high-value powder based on titanium alloys.
This paper presents the properties of hydrated titanium alloy after the application of HDH technology. The TiAl6Nb7 alloy was subjected to thermochemical treatment in a furnace in a hydrogen atmosphere, which made it possible to achieve appropriate brittleness. The hydrated sample, i.e. its specific phases, was examined by SEM analysis. They identified individual elements on the phases using energy dispersive spectroscopy (EDS-analysis). The results showed that a particular increase in the concentration of certain elements, especially niobium, contributes to the formation of secondary phase, Ti hydride, leading to an increase in the brittleness of the TiAl6Nb7 alloy at the room temperature. This brittleness is favorable from the aspect of crushing the alloy, i.e. grinding it to a certain granulation of particles.

Keywords: *TiAl6Nb7 alloy; titan hydride; HDH technology; SEM/EDS analysis*

1. Introduction

TiAl6Nb7 alloy is an (α + β) titanium alloy with high specific strength, corrosion resistance and exceptional biocompatibility. This titanium alloy with the designation Ti6Al7Nb (TiAl6Nb7) became of particular interest when the cytotoxic vanadium was replaced by niobium [1] in the TiAl6V4 alloy and it is of great importance for powder production technology. The production of powder based on titanium alloys is very expensive, so the research on the technology of recycling titanium alloys while obtaining powder is interesting.
One such process is the HDH (hydride-dehydride) process, which is used for the production of titanium powder from waste material, that is, for the recycling of titanium alloys that no longer have a useful value.
The HDH process is an economical process for the production of "low-cost" high-value powder based on titanium alloy, which is used to obtain titanium alloy powder with unchanged chemical composition [2].
The hydration process is carried out by exposing the waste to hydrogen gas at an elevated temperature. If it is done in such a way, the titanium waste is exposed to the influence of the hydrogen atmosphere at a temperature between 550 °C and 800 °C for one to ten hours or longer, depending on the size and character of the waste [3].

The essence of the HDH procedure consists in initiating the formation of intermetallic compounds of metal and hydrogen in the titanium alloy, the so-called hydride by absorbing a considerable amount of hydrogen. If the hydrogen pressure is above the equilibrium pressure, a metal hydride is formed, otherwise if the hydrogen pressure is below that level, the hydrogen atoms diffuse from the metal into the gas atmosphere [4]. The formed compounds cause brittleness of the alloy, which can then be mechanically crushed to the desired particle size. The hydrated powder is then reheated in a vacuum or protective atmosphere, where hydrogen is removed. In this process, titanium alloy powder with unchanged chemical composition, with irregular particle shape, is obtained.
The solubility of hydrogen varies depending on the amount and type of phases present. In general, in alloys where the alpha phase is predominant (in the TiAl6Nb7 alloy, there is about 90% of the alpha phase at room temperature), solubility is lower compared to alloys in which the beta phase is more present.
Alpha and beta phases can coexist at the temperatures at which most titanium alloys are used (up to 600 °C), which depends on the total amount of beta stabilizing elements. So, for example, the increased content of niobium in the titanium alloy causes at room temperature the appearance of, in addition to the alpha phase, the presence of the beta phase, which has a significantly higher hydrogen solubility. Alloying Ti with V, Zr, Nb, Mo and others in sufficient quantity, it enables the existence of the beta phase even at room temperature, which leads to the precipitating of complex Ti-hydrides and an increase in brittleness [4]. The following elements Al, Zr and Sn are the Alpha stabilizers.
In the case of microstructures in which mixed alpha and beta phases are present, hydrogen solubility increases as the proportion of beta phase increases. Alloying elements such as Mo, Nb, Cr, V, Mn and Fe stabilize the beta phase (ordered by the strength of influence) at lower temperatures, so the total solubility of hydrogen increases compared to unalloyed titanium. The solubility of hydrogen in the beta phase is approximately 20x higher than in the alpha phase, so in the mixed crystal hydrogen is concentrated in the beta phase and at the boundaries of the alpha and beta phases.
The solubility of hydrogen varies depending on the amount and type of phases present. In general, in alloys where the alpha phase predominates (in the TiAl6Nb7 alloy, there is about 90% of the alpha phase at room temperature), solubility is lower compared to alloys in which the beta phase is more present [5].

2. Hydration procedure of alloy TiAl6Nb7

In the practical part of the research, a simulation of hydrogenation using the HDH process was carried out at the "Center for Advanced Materials“ in Sarajevo [6]. Using laboratory equipment for chemical and thermal treatment of materials, the HDH procedure for obtaining powder from recycled titanium alloy TiAl6Nb7 with a defined thermochemical treatment is experimentally investigated.
To obtain the hydrated powder, a rod with a diameter of 16 mm of titanium alloy for medical use TiAl6Nb7 according to ASTM F1295 and ISO5832-11 was used. The chemical composition of the TiAl6Nb7 alloy, which was used in the thermochemical treatment to obtain the hydrated powder, is shown in Table 1, [7].

Table 1. *Chemical composition of TiAl6Nb7 alloy in mass percentage, wt.% [7]*

C	Al	Nb	Fe	Ta	O	N	H	Ti
0.01	6.23	6.7	0.22	0.01	0.17	0.01	0.001	rest

Alloying with hydrogen in a hydrogen and nitrogen atmosphere according to a predetermined program of heating, holding at a temperature lower than the α-β transformation temperature, controlled cooling, as well as switching on and off protective gases was carried out in the TPS 21 furnace of the "Center for Advanced Technologies“ in Sarajevo [6, 7]. The hydration treatment carried out according to the defined parameters, with the aim of increasing brittleness, proved to be

successful because the hydrated sample could be relatively easily mechanically crushed to the desired powder size.
The hydration treatment carried out according to the defined parameters, with the aim of increasing brittleness, proved to be successful because the hydrated sample could be relatively easily mechanically crushed to the desired powder size. In the process of grinding in a planetary mill, a hydrated powder based on the titanium alloy TiAl6Nb7 was obtained, with an irregular shape of particles, but extremely favorable granulation, where a significant portion has the particle sizes below 60 μm.
Also, the chemical analysis of the sample after the thermochemical hydration procedure indicates that there were no significant changes in the content of the most important elements compared to their content before hydration [7].

3. SEM/EDS analysis of hydrated sample of alloy TiAl6Nb7

For a detailed analysis of the microstructure phases of the hydrated sample of the TiAl6Nb7 alloy, SEM and EDS tests were performed, where it was possible to determine the existence of two phases with different chemical compositions. For microstructural characterization, the specimen was metallographically prepared by grinding, polishing and etched prior to examination. Microstructural characterization of the hydrated sample was researched using the scanning electron microscope (SEM) type JEOL JSM 5610 at the Faculty of Natural Sciences and Engineering - Department of Metallurgy and Materials, University of Ljubljana. The JSM-5610 is equipped with secondary and backscattered electron detectors and an EDS system, capable of qualitative, pseudo-quantitative analyses, and x-ray mapping. This SEM microscope works with excitation energy up to 30 keV and with theoretical increase up to 300000x.
The microstructure of the TiAl6Nb7 alloy sample after hydration at different magnifications of 250 and 1000 times is shown in Figures 1 and 2, [7]. Two phases can be observed in these images, a darker phase as the primary phase of the matrix, and a lighter phase as the secondary phase.

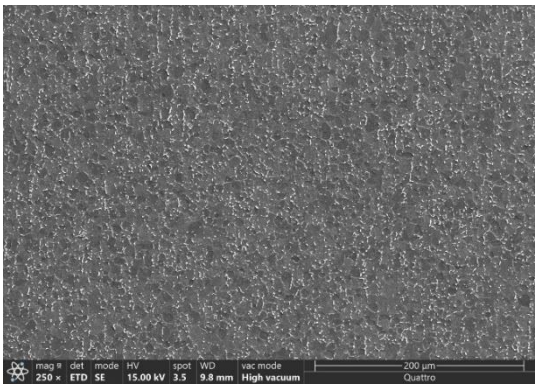

Figure 1. *Microstructure of a hydrated sample of Ti6Al7Nb alloy, observed on SEM*

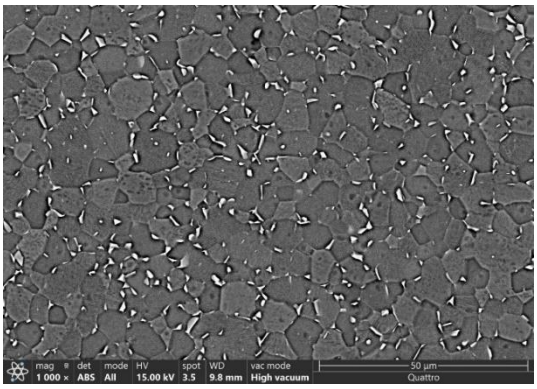

Figure 2*. Microstructure of a hydrated sample of Ti6Al7Nb alloy, observed on SEM*

It can be seen from Figure 1 that the primary phase of the matrix is quite uniform with the separated secondary phase along the grain boundaries. In Figure 2, at a higher magnification of 1000x, the grain boundaries of the matrix phase with the separated secondary phase of different thickness and size, mostly along the grain boundaries, are clearly visible. The characteristic of this secondary phase is that it causes brittleness of the titanium material at the room temperature and it is assumed that it is titanium hydride.

3.1. Phase mapping analysis of the hydrated TiAl6Nb7 alloy sample

During the process of hydration of the sample based on titanium alloy, phases are formed, which can be additionally identified by metallographic research, and of particular interest are changes in the concentration of the chemical elements Fe, Nb, Ti and Al.

Figure 3 shows the EDS representation of the characteristic phases of the hydrated titanium alloy TiAl6Nb7, from which the presence of two phases can be clearly observed, namely the primary phase of the matrix and the precipitate of secondary phase. For the mentioned phases, mapping analyzes were done for chemical elements: Fe, Nb, Ti and Al, [7]. Using EDS analysis, the chemical composition of individual phases was investigated, especially from the aspect of the concentration of the mentioned elements in the primary and in the secondary phases.

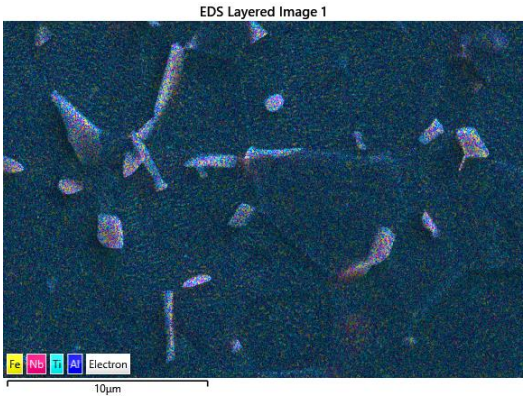

Figure 3. *EDS representation of the primary phase of the matrix and the secondary phase of hydrated sample of titanium alloy TiAl6Nb7*

Map distribution analysis of chemical elements: Ti, Al, Nb and Fe (from left to right) for the hydrated TiAl6Nb7 alloy sample are shown in Figure 4.

Analysis of the mapping for chemical elements: Ti, Al, Nb and Fe, from Figure 4 for the hydrated TiAl6Nb7 alloy indicates a change in concentration distribution. Thus, areas on the map of darker color indicate the depletion of the phase on the observed chemical element, and conversely, the area of lighter color represents the enrichment of the phase on the observed chemical element. Mapping analysis of the secondary phase of the hydrated sample indicates a depletion of this phase in titanium and aluminum and a strong enrichment in niobium and slightly in iron.

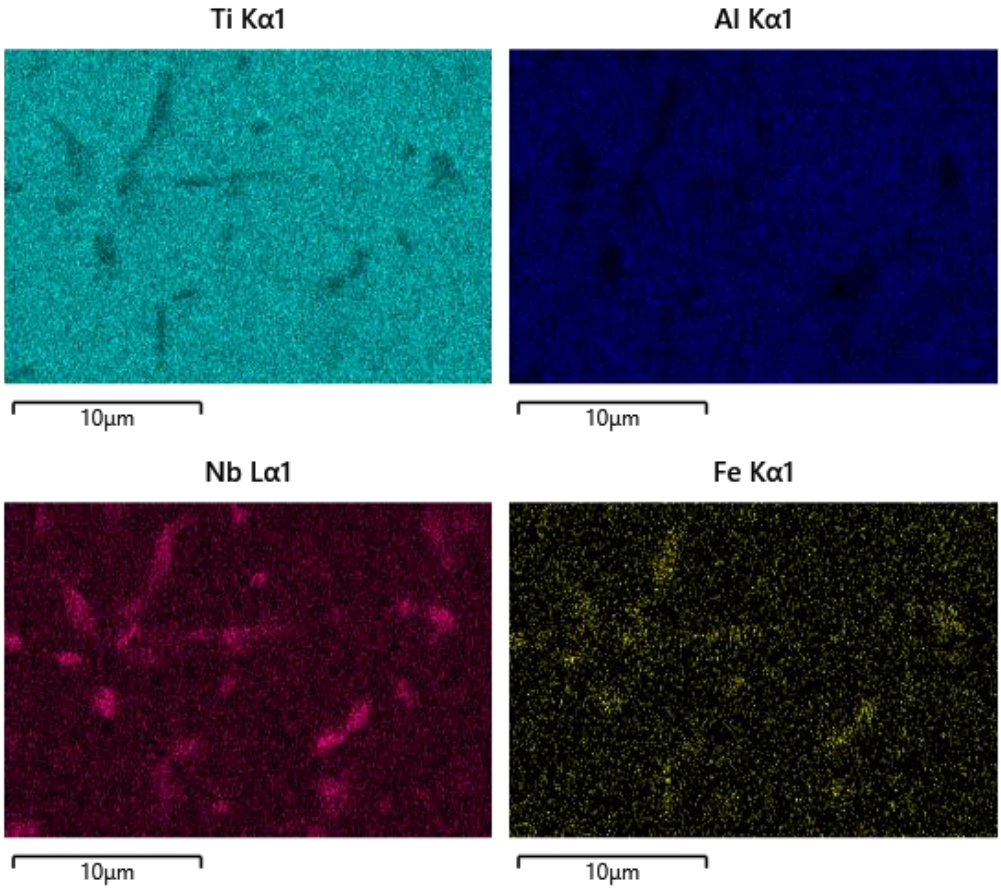

Figure 4. *EDS elemental mapping of Ti, Al, Nb and Fe (from left to right) for the hydrated alloy TiAl6Nb7*

3.2. EDS phase analysis of the hydrated alloy sample TiAl6Nb7

Using energy dispersive spectroscopy (EDS), the chemical analysis of the characteristic phases of the hydrated TiAl6Nb7 alloy sample was determined. The chemical analysis of specific elements was performed by spectrum regions 1 and 2, for the microstructure of the sample shown in Figure 5.

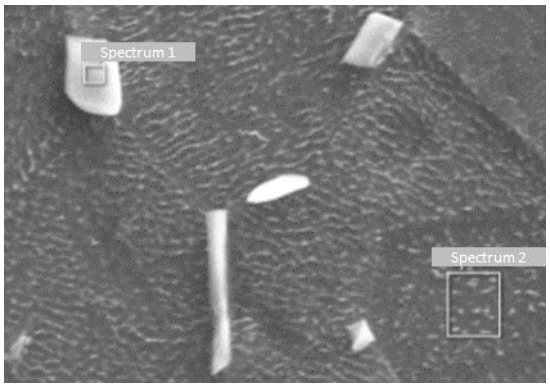

Figure 5. *SEM image with marked regions of the primary and secondary phases*

Figures 6 and 7 show the EDS analysis of regions 1 and 2 presented in figure 5. Region 1 represents the secondary phase of the hydrated TiAl6Nb7 alloy, while region 2 represents the primary matrix phase of the hydrated TiAl6Nb7 alloy.

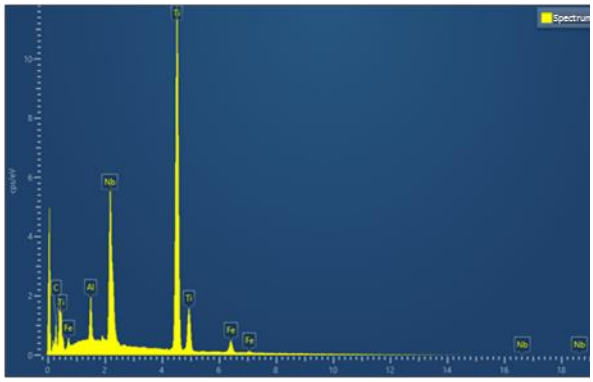

Figure 6. *EDS spectrum of region 1 (from figure 5) secondary phase of hydrated alloy TiAl6Nb7*

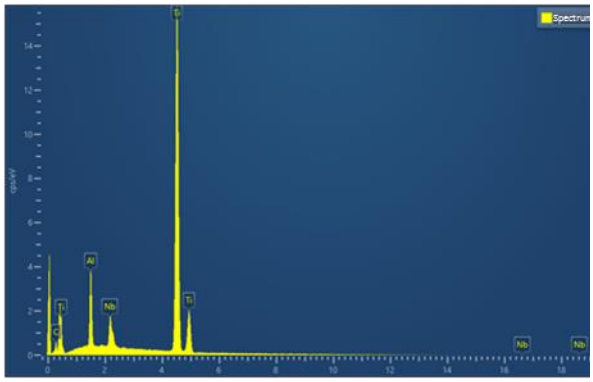

Figure 7. *EDS spectrum of region 2 (from figure 5) primary phase of hydrated alloy TiAl6Nb7*

The EDS analysis of region 1 from Figure 6, i.e. the secondary phase of the hydrated alloy TiAl6Nb7 shows a significantly lower content of the basic elements titanium and aluminum compared to the primary phase from Figure 7. Also, the secondary phase is richer in Nb and Fe.
For the mentioned regions, which are shown in Figure 5, chemical analyzes of region 1 and region 2 were performed for the hydrated Ti6Al7Nb alloy sample. The average chemical analysis for Al, Ti, Fe and Nb for regions 1 and 2 of figure 5 is given in Table 2.

Table 2. *Average chemical analysis of Al, Ti, Fe and Nb for regions 1 and 2 (from figure 5) for Ti6Al7Nb alloy, wt. %*

Chemical analysis, wt. %	Region 1 (from figure 5)	Region 2 (from figure 5)
Al	2.60	5.93
Ti	67.92	87.85
Fe	5.36	
Nb	24.11	6.23
Total	100.00	100.00

The chemical analysis of region 1 of the secondary phase indicates a depletion of this phase in titanium and aluminum and a strong enrichment in niobium and iron, as shown by the map image in Figure 4.
According to the chemical composition, the primary and secondary phases differ due to diffusion processes during the phase transformation. Thermochemical treatment in a hydrogen atmosphere caused the hydration of titanium and the appearance of a secondary phase at the boundaries of the primary matrix phase. For the secondary phase, which is characterized by a smaller proportion of alphagenic (HGP) elements Ti and Al, and a larger proportion of betagenic (VCK) Nb and Fe, it indicates the assumption that it is a complex intermetallic compound, i.e. a complex titanium-niobium hydride, which causes the brittleness of the hydrated alloy TiAl6Nb7. Also in this sense, it can be assumed that the alpha titanium phase represents the primary matrix phase.
The implemented thermochemical treatment with defined parameters was successful and caused an increase in the brittleness of the titanium alloy sample and enabled mechanical crushing, i.e. grinding the hydrated sample into powder using a planetary mill, Figure 8.

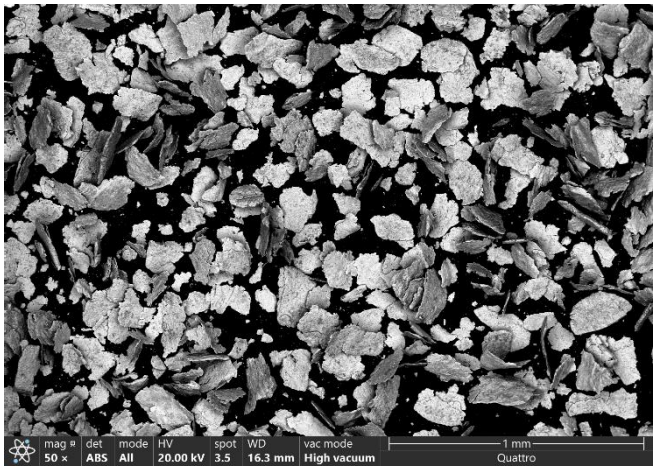

***Figure 8**. TiAl6Nb7 titanium powder after grinding the hydrated sample*

In the grinding process, a powder based on titanium alloy was obtained, with an irregular shape of particles, but favorable granulation, with a significant share of particle sizes below 60 μm, which means that a "low-cost" high-value powder based on titanium alloy can be obtained.

4. Conclusion

Titanium alloy TiAl6Nb7 has high strength, corrosion resistance, excellent biocompatibility and is of particular importance for medical use when cytotoxic vanadium is replaced by niobium. By simulating the HDH procedure, a sample of titanium alloy, which is intended for recycling, was hydrated. The enrichment of this material with hydrogen by the hydration process led to an increase in the brittleness of the titanium alloy, which could then be mechanically crushed to a favorable powder granulation.

This paper presents the properties of the hydrated titanium alloy Ti6Al7Nb, after a sample of this material was exposed to thermochemical treatment in a hydrogen atmosphere, making it possible to achieve appropriate brittleness.

The phases of the hydrated sample, i.e. its primary and secondary phases, were investigated in more detail by means of SEM and EDS analysis. On the phases, they identified the presence and contents of chemical elements for specific phases of the hydrated sample. The results showed that a particular increase in the concentration of niobium leads to the formation of a secondary phase of a complex intermetallic compound at the boundaries of the matrix phase, which at the room temperature leads to an increase in the brittleness of the Ti6Al7Nb alloy. The hydrated sample could be mechanically pulverized at the room temperature and thus obtaining titanium alloy powder of unchanged chemical composition, with irregular particle shape and powder granulations below 60 μm.

The research conducted in this work represents a good assumption for obtaining the starting material, i.e. the powder that will be the basis for the production of the finished product from (α + β) titanium alloy by powder metallurgy procedures.

Acknowledgments

Many thanks to the Ministry of Education and Science of Federation BiH for its support in the publication of this scientific research work.

References

[1] Hein M., Kokalj D., Lopes Dias N. F., Stangier D., Oltmanns H., Pramanik S., Kietzmann M., K.-P. Hoyer, Meißner J., Tillmann W., Schaper M., 2022., Low Cycle Fatigue Performance of Additively Processed and Heat-Treated Ti-6Al-7Nb Alloy for Biomedical Applications, Metals 2022, 12, 122. https://doi.org/10.3390/met12010122 (accessed 20. Jul 2023).

[2] An Overview of Highly Porous Titanium Processed via Metal Injection Molding in Combination with the Space Holder Method Metals 2022, 12(5), 783; https://doi.org/10.3390/met12050783 (accessed 27. Jul 2023).
[3] Powell R. L., Tao L.C., 1961. Reclaiming Scrap Titanium, Official Gazette of the United States Patent Office, Volume 768, By United States. Patent Office.
[4] Phillips J., Janssen A., Y. Ansell T, C. Luhrs C., 2020. Creating Strong Titanium/Titanium Hydride Brown Bodies at Ambient Pressure and Moderate Temperatures, Materials 13(21): 5008, Basel.
[5] Zak Fang Z., Paramore J. D., Sun P, Ravi Chandran K. S., Zhang Y., Xia Y., Cao F, Koopman M., Free M., 2018. Powder metallurgy of titanium – past, present, and future, International Materials Reviews, Vol 63, no 7, 407–459.
[6] Imamović A., Žuna Š., Oruč M., Hadžibulić E., 2023. Zbornik radova XIV naučno/stručnog simpozija Metalni i nemetalni materijali, Hydration Process of Titanium Alloy for Biomedical Purposes, ISBN 978-9958-785-38-2, Zenica.
[7] Žuna Š., 2022. Projekat-Osvajanje tehnologije dobijanja praha legura titana za medicinske i druge svrhe, Javna ustanova “Centar za napredne tehnologije“ Sarajevo.

Fixed tilt vs. tracking system – an experimental analysis of photovoltaic system

Zlatko Jankoski[1], Igor Gabrić[1], Stjepan Marković[2], Ivan Vrljičak[1] and Luka Vuković[1]

1) University Department of Professional Studies, University of Split, Kopilica 5, 21000 Split, Croatia

2) EKSERGIJA Ltd., Put Krunika 7/B, 21210 Kučine, Croatia

Corresponding author: zlatko.jankoski@oss.unist.hr

Original scientific article

Abstract: In order to analyse the operating parameters of the photovoltaic module at different values of azimuth and inclination angle, an experimental photovoltaic system is constructed. The photovoltaic system with a thin film cadmium telluride (CdTe) photovoltaic module is built as a two-axis solar tracker that can also operate at a fixed tilt. The system is equipped with a solar charge controller, a battery monitoring system and a rechargeable battery. During operation, solar radiation was measured with a pyranometer, while the production and storage of electrical energy was monitored by appropriate software connected to the battery monitor and charge controller. The first measurement was carried out for a fixed position, where the photovoltaic module was facing south (azimuth) at an angle of inclination of 32°. The second measurement was made using a tracking system, where the photovoltaic module continuously followed the path of the sun. Measurements included the amount of available solar radiation during system operation, the amount of stored electrical energy and other relevant operating parameters. The results for both modes of operation were compared and analysed.

Keywords: *photovoltaic module; fixed system; tracking system; production of electrical energy*

1. Introduction

In general, the world's energy needs are in constant rise. The requirements for production of energy from renewable energy sources are in constant rise as well. According to the International Energy Agency (IEA), during the last 47 years the world's total energy supply has increased for around 2.4 times, while the electrical energy generation for some 4.4 times [1]. Although fossil fuels still hold the biggest share of electrical energy production of more than 70%, the utilisation of renewable energy sources is in rise due to their lower impact on the environment and climate. For example, from 2005 to 2019 the world's solar photovoltaic electrical energy production has increased from 4 TWh to 681 TWh [1]. According to EurObserv'ER publication [2], there were installed some 32.8 GW of photovoltaic capacity in the European Union during the year 2022, giving the total installed power of 195.4 GW. The gross electrical energy production from solar photovoltaic in the European Union was around 158.3 TWh during the year 2021, while some 205.2 TWh are estimated for the year 2022 [2]. The existing solar photovoltaic technologies are continuously improving, increasing the efficiency of energy transformation and the viability of photovoltaic power plants. In addition to other parameters, such as materials used, temperature levels, etc., an additional increase in the energy yield from photovoltaics can be achieved by using solar tracking systems.

In general, the increase of electric energy production of a solar tracking system ranges between 22% and 56% compared to a fixed photovoltaic solar system [3]. There are many papers available in literature that analyse the advantages of dual-axis tracking photovoltaic systems over fixed-tilt systems. For example, the research in [4] reports the electrical output and solar conversion efficiency of five types of photovoltaic modules installed on a fixed and on a dual-axis tracked photovoltaic platform. A one-year analysis showed that the amount of received solar energy increased by 28%, and

the production of electrical energy by 29.6% when using the dual-axis tracked photovoltaic system. The efficiency of solar conversion remained almost the same, around 14.17% and 14.34% for fixed and tracked photovoltaic system, respectively. However, these results were obtained for the entire photovoltaic platform, which contained five types of modules such as monocrystalline silicon, polycrystalline silicon, and three types of thin-film modules (CIS, CIGS and CdTe). Apart from reporting the performance of different types of photovoltaic modules, the analysis in [4] showed the seasonal variability of operating parameters, where, for example, in June the production of electrical energy of the tracked system was 52% higher than the production of the fixed system. The smallest difference in production of electrical energy was reported in January, and is 9.4% in favour of the tracked system. Another annual analysis, which includes 39 photovoltaic plants equipped with dual-axis systems and 35 photovoltaic plants with fix-mounting systems, presented in [5], showed that the average performance of dual axis systems is on average 34.5% higher than fix-mounted systems. The measured average annual energy yield per installed 1 kW_P of power was 1,522 kWh/kW_P and 2,047 kWh/kW_P for fix-mounted and dual-axis photovoltaic systems respectively. More details on the development and operation of different tracking photovoltaic systems, their advantages and disadvantages compared to fixed photovoltaic systems can be found in the literature ([6], [7], [8], [9]). However, higher investment costs should be taken into account when planning the construction of a single-axis or dual-axis tracking photovoltaic power plant, which must be justified by a profitable increase in energy yield. This paper focuses only on the production of electrical energy from in-house built photovoltaic system, operating in fixed and dual-axis tracking mode.

2. Experimental Photovoltaic System

An in-house experimental photovoltaic system (Figure 1) was designed and constructed as part of the laboratory activities and student's final theses ([10], [11]). Similar approach could be found in [12]. The system is designed to operate at a fixed tilt angle (inclination or elevation angle), or as a dual-axis tracker. When working at a fixed angle, any tilt angle can be selected, while an angle of 32° (considering the horizontal plane as reference) is defined as the default value. The angle of azimuth is defined by the spatial orientation of the entire system.

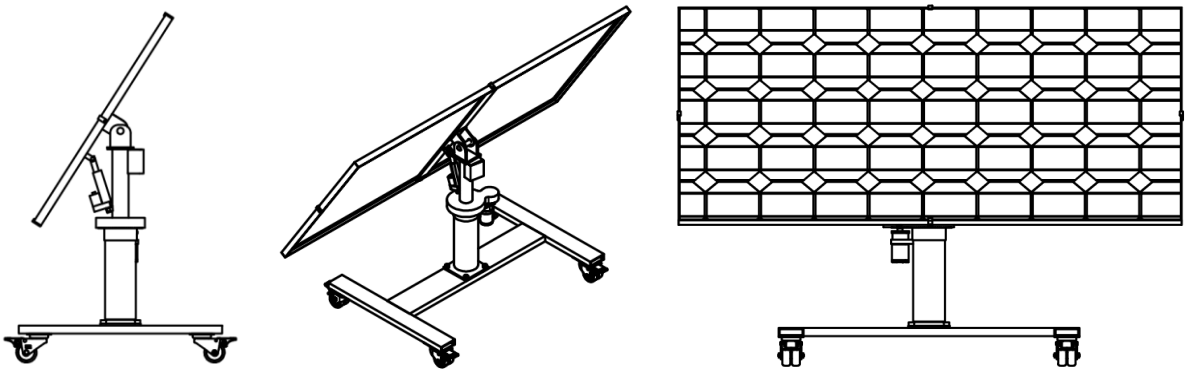

Figure 1. *Experimental photovoltaic system - conceptual solution*

When operating as a dual-axis tracker, the system continuously tracks the position of the sun throughout the day, orienting the photovoltaic module so that the solar irradiation is perpendicular to the normal of the module surface. The experimental system uses a 10-years-old thin film CdTe photovoltaic module CX3 72 (Table 1) [13], placed on the aluminium frame (Figure 2). The nominal power of the photovoltaic module is 72.5 W_P, while the current and voltage at maximal power are 1.62 A and 45.8 V respectively. Since the active area of the photovoltaic module is not defined in the product data sheet [13], for the purpose of this study a total area of 0.72 m^2 (length $\times$ width = 1.2 m $\times$ 0.6 m) will be used in the analysis.

The production of energy of the photovoltaic module is maximised by the MPPT solar charge controller BlueSolar MPPT 75/10 (Table 2) [14], while the energy is stored in the rechargeable battery AGM 12V 60 Ah [14].

Figure 2. *Experimental photovoltaic system in operation*

Table 1. *Photovoltaic module CX3 72 – technical characteristics under standard test conditions* [13]*

Nominal power (+10% / -5%)	P_{MPP}	W	72.5
Current at maximal power	I_{MPP}	A	1.62
Voltage at maximal power	V_{MPP}	V	45.8
Short circuit current	I_{SC}	A	1.87
Open circuit voltage	V_{OC}	V	61.5

* Standard test conditions (1000 W/m^2, 25°C, AM = 1.5)

Table 2. *Solar charge controller BlueSolar MPPT 75/10 – technical characteristics [14]*

Battery voltage (auto select)	V	12/24
Rated charge current	A	10
Nominal PV power, 12V	W	145
Max. PV short circuit current	A	13
Max. PV open circuit voltage	V	75
Peak efficiency	%	98

The system is based on dual-axis tracking, where a rotary actuator with a servo motor and a pair of gears is used for horizontal tracking (azimuth, Figure 3), while a linear actuator is used for vertical tracking (inclination, Figure 4).

The tracking system is equipped with 12 V DC electric motors, which are operated by a microprocessor control system (Figure 3). The control system used to actuate the drive assemblies is based on an

“open-loop” control tracking system, which uses an algorithm loaded into the microprocessor of the control unit.

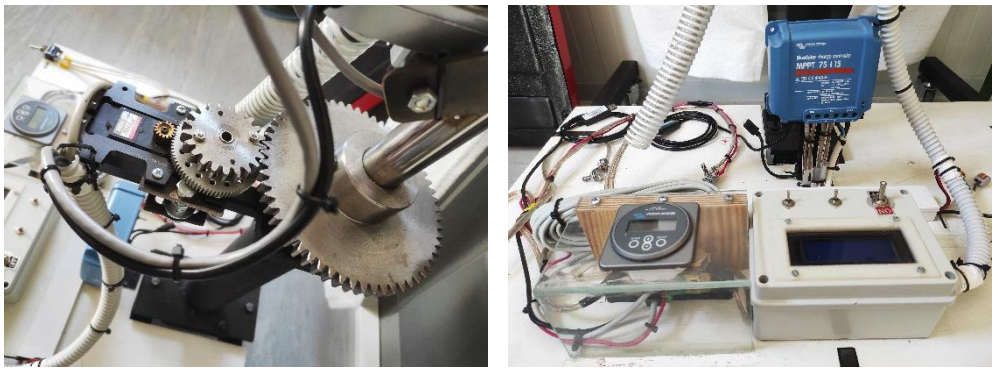

Figure 3. *Drive for horizontal tracking (left); Control and measurement system (right)*

The position of the photovoltaic module is periodically adjusted to direct sunlight, based on an in-house written programming code that changes the position of the photovoltaic module for every 0.5-degree deviation from the optimal inclination angle and azimuth. The calculations are based on known geographic location of the system, the date and time of day, and the initial position of the photovoltaic module. The electrical energy required for the operation of the DC electric motors and the control system is supplied from the same battery that is used to store the produced energy (AGM 12 V 60 Ah).

Figure 4. *Drive for vertical tracking*

Solar irradiance is measured with a calibrated pyranometer (LP02) and a handheld read-out unit/data logger (LI-19) [15]. LP02 is a solar radiation sensor that complies with the second class specifications of the corresponding ISO standard. A pyranometer is attached to the aluminium frame holding the photovoltaic module to measure solar irradiance at the same angles as of the photovoltaic module. During system operation, energy production and its storage in the rechargeable battery are logged using a battery monitoring device (BMV-700) [14]. The operating parameters of the photovoltaic module and the amount of energy consumed by the tracking and control systems are monitored using the VictronConnect application [14]. Finally, in order to measure and monitor the surface temperature of the photovoltaic module, the temperature sensor (standard thermocouple) is attached and

thermally insulated on the back side of the photovoltaic module. The measurement of temperature was periodically performed using the standard digital thermometer.
To evaluate the advantages of a dual-axis tracked vs. a fixed photovoltaic system, the following relevant indicators are defined and assessed.
The available global solar energy (E_A) at the angles defined by the position of the photovoltaic module is calculated using:

$$E_A = \sum_{t_1}^{t_2} \frac{E}{60} \ \left[\frac{Wh}{m^2}\right] \tag{1}$$

where:
- E is the available global solar irradiance measured by the pyranometer each minute [W/m^2],
- t_1 and t_2 are the starting and ending times of the measurement.

The global solar energy (E_D) delivered on the active surface of the photovoltaic module is calculated using:

$$E_D = E_A \cdot A_{PV} \ [Wh] \tag{2}$$

where:
- E_A is the available global solar energy [Wh/m^2],
- A_{PV} is the active area (in this case the total area) of photovoltaic module [m^2].

The electrical power output of the photovoltaic system (P_{PV}) is calculated using:

$$P_{PV} = U_C \cdot I_C \ [W] \tag{3}$$

where:
- U_C is the voltage of charging the battery measured each minute [V],
- I_C is the current of charging the battery measured each minute [A].

The energy produced and stored in the rechargeable battery (E_S) is calculated using:

$$E_S = \sum_{t_1}^{t_2} \frac{P_{PV}}{60} \ [Wh] \tag{4}$$

where:
- P_{PV} is the electrical power output of photovoltaic module measured/calculated each minute [W],
- t_1 and t_2 are the starting and ending times of the measurement.

Finally, the overall efficiency of the conversion of solar energy into electrical energy (η_S), showing how much of the solar energy is transformed and stored in the rechargeable battery, is calculated using:

$$\eta_S = \frac{E_S}{E_D} \cdot 100 \ [\%] \tag{5}$$

where:
- E_S is the energy produced and stored in the rechargeable battery [Wh],
- E_D is the global solar energy delivered on the active surface of photovoltaic module [Wh].

3. Experimental Analysis of Photovoltaic Systems

3.1. Experimental Analysis of Fixed Tilt Photovoltaic System

The analysis of the operation of the experimental photovoltaic system in the fixed tilt mode was held on 3rd July 2023. The system operated from 08:06 am to 01:07 pm (5 working hours), at the location of the University Department of Professional Studies, University of Split, Croatia (43°31'21" N and

16°27’01” E). Since the sun is at its highest position on the sky at around 01:00 pm, it was assumed that the selected time frame of measurement is representative for the purpose of this analysis due to the mirroring of the amount of solar irradiation after the symmetry line at 01:00 pm.
Figure 5 shows the available solar irradiance during the period of measurement, and the available solar power delivered to the photovoltaic module considering the total area of the module of 0.72 m^2. Since in the fixed tilt mode the angle of azimuth of the photovoltaic module was 0° (south-oriented), while the angle of inclination was 32°, the amount of solar irradiance varied from a minimum value of 320 W/m^2 at 08:07 am to a maximum value of about 1000 W/m^2 which was reached at 01:00 pm. The resulting solar power delivered to the photovoltaic module varied from 230 W to some 720 W.

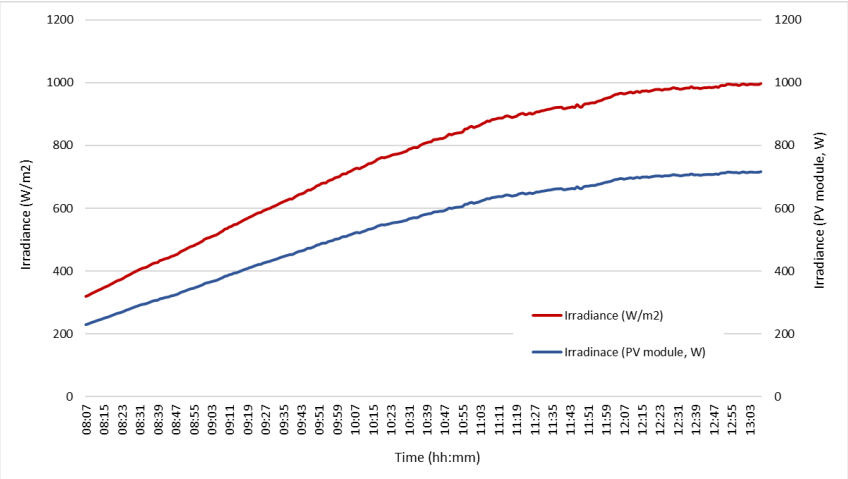

Figure 5. *Solar irradiance and available power on PV module - Fixed tilt photovoltaic system*

Figure 6 shows the variation of battery charging voltage and current during the system operation. The values of voltage slightly increased, from starting 12.35 V to the final value of 13 V. In relation to the voltage, the values of charging current changed significantly during system operation, from 1 A to 3.5 A. Sudden and periodic changes in the charging current can be observed on the graph, which are believed to be due to the operating algorithm of the MPPT solar charge controller. This could be the result of the MPPT solar charger periodic checking the output of the PV module, comparing it to the battery voltage and then determining the best power to charge the battery and converting it to the best voltage to get maximum current into the battery. Perhaps some of the peaks of changing current are not recorded on the graph (Figure 6) due to the time frame of data logging (1 minute), which probably did not match at specific time the time frame of MPPT solar charger operating algorithm.

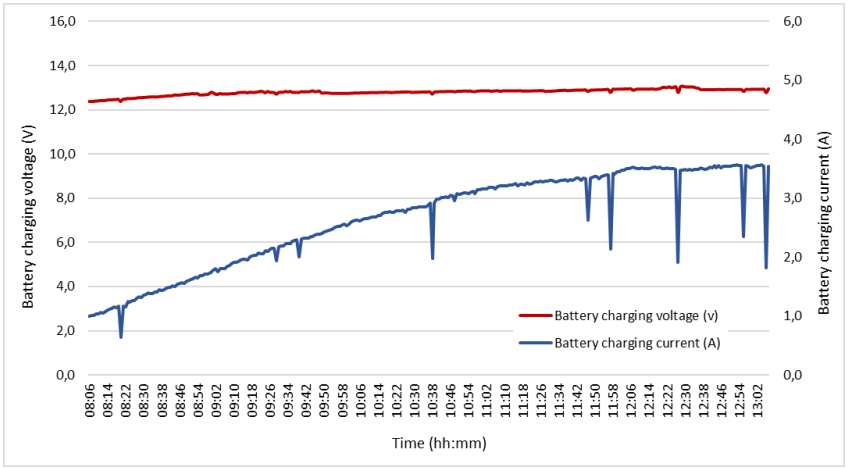

Figure 6. *Battery charging voltage and current - Fixed tilt photovoltaic system*

The rate of battery charging power is shown in Figure 7. At the beginning of the measurement, the power of battery charging was about 12.3 W. Over time, as the amount of solar irradiance increased (Figure 5), the power of battery charging continuously increased reaching some 46 W by the end of the measurement. Periodic changes in charging power are the result of periodic changes in charging current, as already mentioned.

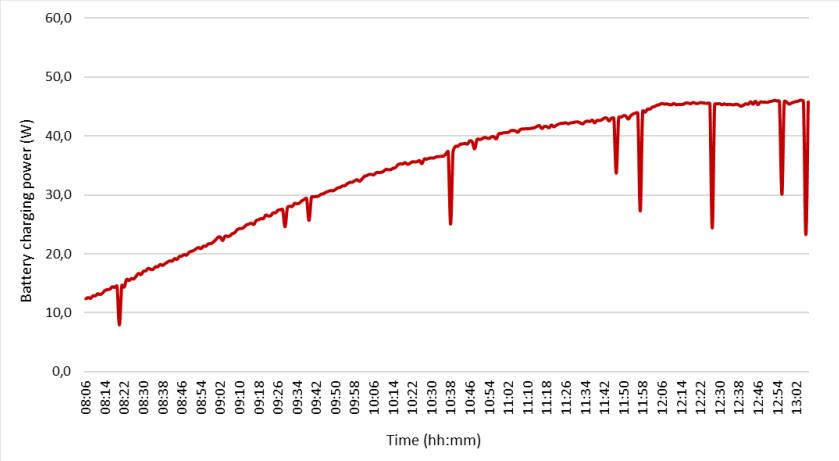

Figure 7. *Battery charging power - Fixed tilt photovoltaic system*

The monitoring of the system operation included the operation parameters of the photovoltaic module (VictronConnect), the parameters of battery charging (BMV Reader), and measurement of solar irradiance (LI-19). Based on the data monitoring, it is possible to read the main operating parameters of the system at a certain time. For example, at 10:33 am the power of the photovoltaic module was 37 W, while the voltage and current of the module were 36.65 V and 1.0 A, respectively. The operating power of the system was 1 W, resulting in a total system energy consumption of 5 Wh (5 working hours). Solar irradiance varied between 791 and 794 W/m^2 during the data logging time frame (1 minute).

Based on the measured vales, the total stored electrical energy of the photovoltaic system operating in the fixed tilt mode was about 171.3 Wh, while, considering the total area of the module of 0.72 m^2, the total solar irradiance delivered to the photovoltaic module was 2,721.6 Wh. The energy consumption of the system of 5 Wh represents about 2.9% of the energy produced. Since the active area of the photovoltaic module is not specified in the product data sheet (Table 1), the overall efficiency of energy transformation was estimated based on the total module area of 0.72 m^2. The overall solar efficiency, from the delivered solar irradiance to the energy stored in the rechargeable battery, was about 6.3%. Since the total area of the module was used in calculations, this value does not represent the actual value of the overall solar efficiency, and will only be used to compare the efficiency of both modes of operation (fixed vs. tracking).

The surface temperature of the photovoltaic module varied from 28°C at the begging of the measurement to some 56.4°C. The surface temperature did not show an overall increasing trend. It increased in the early phase of system operation, and later it oscillated between 52°C and 56.4°C. The reason for this is the free-standing mounting of the photovoltaic module and variable wind speed during the measurement.

3.2. Experimental Analysis of Tracking Photovoltaic System

The analysis of the experimental photovoltaic system in tracking mode was performed on 30th June 2023, at the same location and in the same time period as in the case of operation in fixed tilt mode. Figure 8 shows the available solar irradiance during the measurement period, and the available solar power delivered to the photovoltaic module of 0.72 m^2 of total area.

During the tracking mode, the amount of solar irradiance in the measurement period varied from 874 W/m^2 at the beginning of the measurement at 08:07 am, to some 1040 W/m^2 which was available for

almost half of the measurement time. The resulting solar power delivered to the photovoltaic module varied from 630 W to some 750 W.

Figure 9 shows the variation of battery charging voltage and current during system operation. The values of voltage changed slightly, from 12.62 V to 12.93 V. The same applies to the charging current, which varied from 3.4 A to 3.7 A. Periodic changes in the charging current can also be observed in this case, due to for the same reason as was mentioned before.

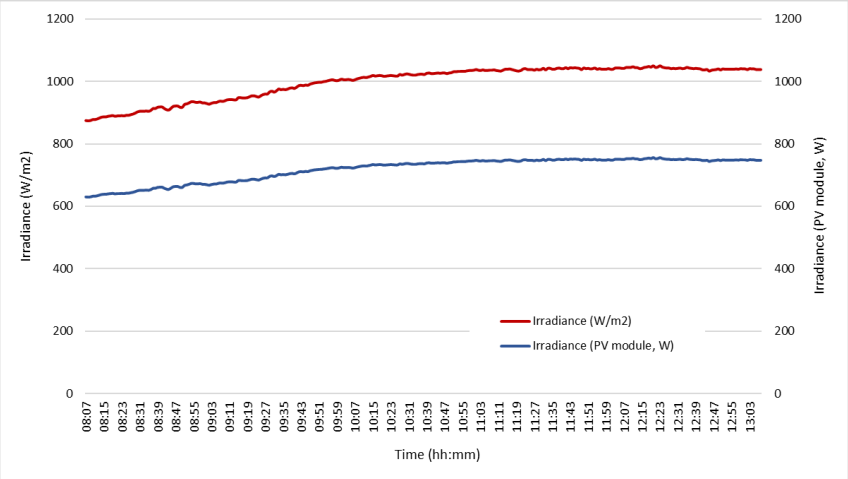

Figure 8. *Solar irradiance and available power on PV module - Tracking photovoltaic system*

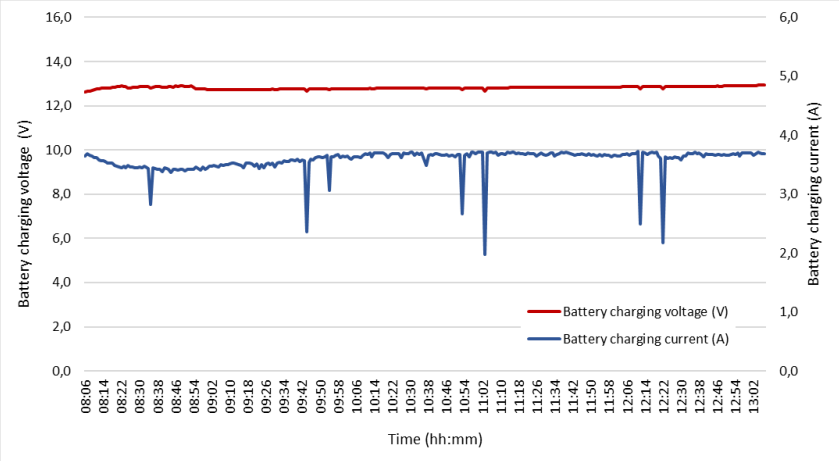

Figure 9. *Battery charging voltage and current - Tracking photovoltaic system*

The rate of battery charging power is shown in Figure 10. At the beginning of the measurement, the power of battery charging was about 46 W, which after about 90 minutes decreased slightly to 43.5 W. After that, the power of battery charging continuously increased to some 47.7 W and remained almost constant. Periodic changes in charging power are again the result of periodic changes in charging current.

An example of system monitoring is shown in Figure 11. The monitoring included the same operating parameters as in the case of a photovoltaic system working in a fixed tilt mode. For example, at 11:50 am the power of the photovoltaic module was 49 W, while the voltage and current of the module were 35.54 V and 1.4 A, respectively. The working power of the system was 3 W, which resulted in a total energy consumption of the system of 15 Wh. Solar irradiance varied between 1041 and 1044 W/m^2 during the data logging time frame (1 minute).

Based on the measured vales, the stored electrical energy of the photovoltaic system operating in tracking mode was about 231.2 Wh, while, considering the total area of the module of 0.72 m^2, the total solar irradiance delivered to the photovoltaic module was 3,617.6 Wh. The energy consumption

of the system of 15 Wh represents about 6.4% of the produced energy. The overall solar efficiency was about 6.4%, based on the module area discussed earlier. The surface temperature of the photovoltaic module varied from 30°C at the begging of the measurement to some 56.6°C. Again, the surface temperature of the photovoltaic module did not show an overall increasing trend. It increased in the early phase of system operation, while afterwards it oscillated at around 54°C.

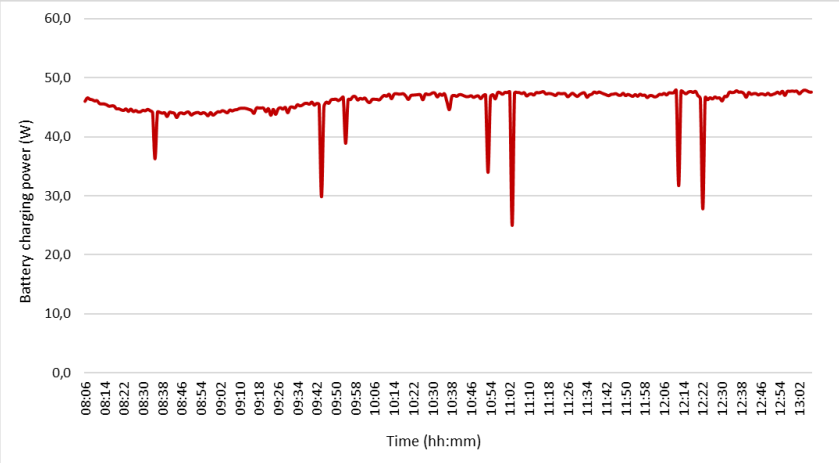

Figure 10. *Battery charging power - Tracking photovoltaic system*

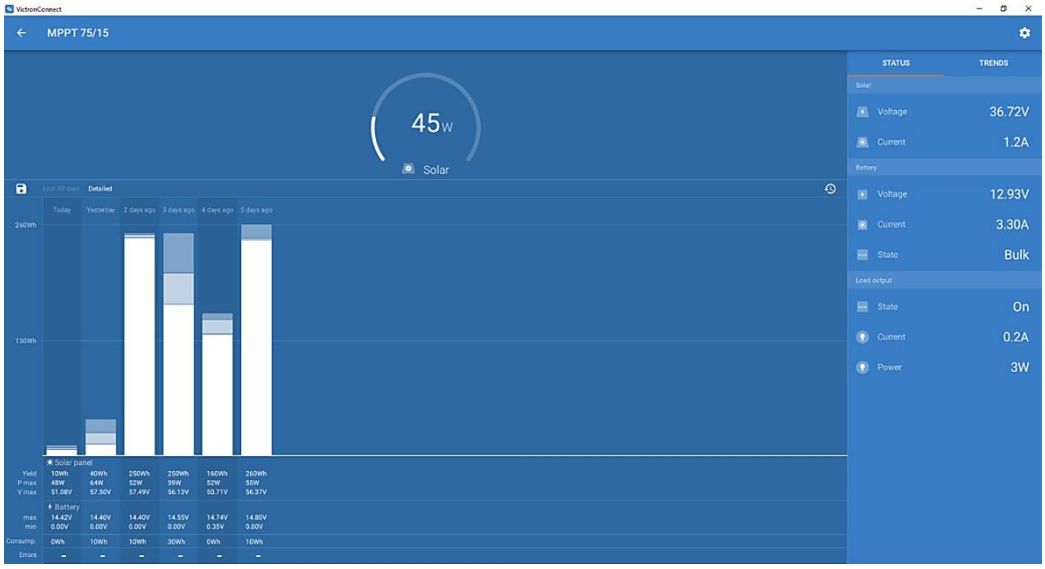

Figure 11. *Monitoring of photovoltaic system – VictronConnect [14]*

4. Conclusions

Measurement of electrical energy production from an experimental photovoltaic system operating in fixed tilt and dual-axis tracking mode has shown the advantage of using solar tracking systems. In order for the measurement results to be comparable, the measurements were performed three days apart, and both measurements were performed during the day with a clear sky in order to reduce the influence of clouds or haze on the measured values.

During the measurement period, the total solar irradiance delivered to the total area of the photovoltaic module was 2,721.6 Wh and 3,617.6 Wh for the fixed tilt and dual-axis tracking modes respectively. The increase in total solar irradiance was shown to be about 32.9%.

The fixed tilt operation mode resulted in production of electrical energy of 171.3 Wh, while the dual-axis tracking mode produced some 231.2 Wh. A comparison of the operating modes gave a higher electrical energy production in the case of dual-axis tracking by about 35%.

A more detailed analysis, which is not presented in this paper, showed that the ratio of produced electrical energy can be even higher if the operation of both solar systems included the earlier morning period (from sun rise), as that is the period when tracking system has an advantage over the fixed tilt system. This advantage is shown in Figure 12, where a significant difference in solar irradiance can be observed in the early morning hours. This results in significantly higher power values of the photovoltaic system in the early morning hours (Figure 13), which finally results in significantly higher electrical energy production in that period.

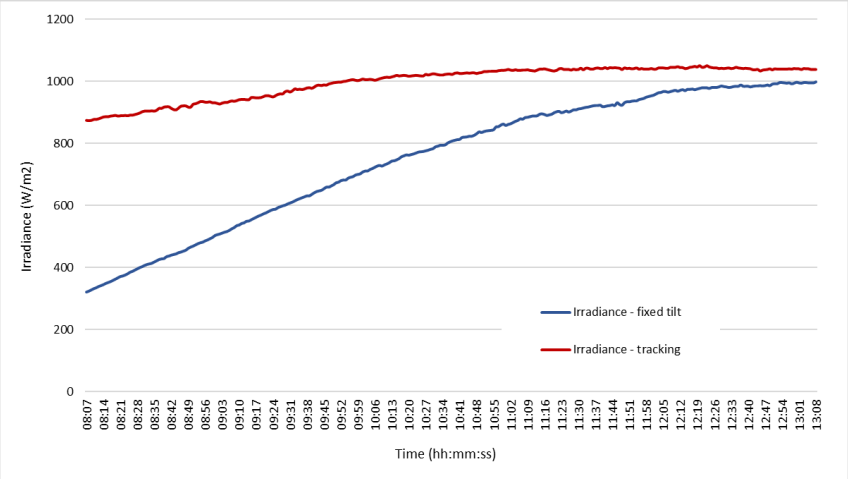

Figure 12. *Solar irradiance - Fixed tilt vs. tracking photovoltaic system*

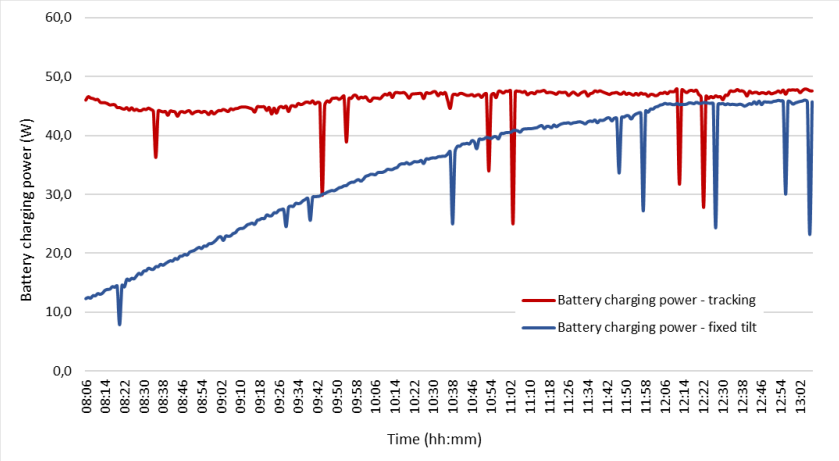

Figure 13. *Battery charging power - Fixed tilt vs. tracking photovoltaic system*

For the purposes of this analysis, the performance ratio of the photovoltaic solar power plant can also be presented. Although the optimal analysis period for calculating the performance ratio is one year, in this case it will be calculated based on the one-day measured values shown above.
The performance ratio (*PR*) is expressed as a percentage and describes the relationship between the actual and nominal (theoretical) energy outputs of the photovoltaic plant [16], and is calculated using:

$$PR = \frac{actual\ energy\ output}{nominal\ energy\ output} \cdot 100 \tag{6}$$

The actual energy output represents the total electric energy produced by the photovoltaic system, or in this case, the total electrical energy stored in the battery. The nominal energy output (*NEO*) is calculated based on the amount of solar energy received by the photovoltaic module multiplied by

the active area of the photovoltaic module and the relative efficiency of the conversion to electrical energy [16]:

$$NEO = TSI \cdot AE \cdot Eff \tag{7}$$

TSI – total solar irradiation [Wh/m^2]
AE – active area of photovoltaic module [m^2]
Eff – relative efficiency of photovoltaic module

The reliability of the calculated nominal energy output could be further discussed knowing that the conversion efficiency of a photovoltaic module changes with temperature as well as with other parameters such as module ageing. Since this is beyond the scope of this paper, the calculation of nominal energy output is simplified and defined as above. A further topic for discussion is the conversion efficiency of the thin film CdTe photovoltaic module used in this analysis. Since the efficiency is not defined in the product data sheet [13], a value of 11.89% was used in this study based on the data available in the literature [4], although the value of efficiency of some commercially used CdTe modules is reported as 8.51% [17]. Finally, the total area of 0.72 m^2 was considered as the active area of the photovoltaic module. Taking into account the above assumptions, the calculated value of the performance ratio will only be used to compare the fixed and tracking modes and does not represent the actual value.
In the case of fixed tilt mode, the actual energy output was 171.3 Wh, while the nominal energy output is calculated as follows:

$$NEO = 3780 \cdot 0.72 \cdot 0.1189 = 323.6 \text{ Wh} \tag{8}$$

Thus, the performance ratio for fixed tilt mode is:

$$PR = \frac{171.3}{323.6} \cdot 100 = 52.9\% \tag{9}$$

In the case of dual-axis tracking mode, the actual energy output was 231.2 Wh, while the nominal energy output is calculated as follows:

$$NEO = 5024.5 \cdot 0.72 \cdot 0.1189 = 430.1 \text{ Wh} \tag{10}$$

Thus, the performance ratio for dual-axis tracking mode is:

$$PR = \frac{231.2}{430.1} \cdot 100 = 53.7\% \tag{11}$$

The performance ratio shown to be almost the same for both modes, and is slightly increased in the case of the dual-axis tracking mode. A slight change in the value of the performance ratio can be explained by the interrelationship between the values of the total solar irradiation and the actual energy output.
The overall solar efficiency in both operating modes was found to be almost the same. The efficiency in the case of tracking mode is slightly increased (6.4%) compared to fixed mode (6.3%). It follows that the application of the solar tracking system does not significantly affect the overall solar efficiency of the photovoltaic system, due to the same interrelationship between the values of the total solar irradiation and the energy output. The same was reported in the literature ([3], [4], [11]). The surface temperatures of the photovoltaic module where almost the same in both modes, however, in the tracking mode, the photovoltaic module warmed up slightly faster in the early stages of operation. The temperature values varied during the measurement due to the variable wind speed.

It can be concluded that the experimental analysis proved the advantage of dual-axis tracking over a fixed tilt photovoltaic system considering the production of electrical energy, as already reported in literature ([3], [4], [5], [6], [7], [8], [9], [12]). However, in this case, a more representative analysis should include the operation of both systems during the whole day, from sunrise to sunset. An even more representative analysis should be based on the annual measurement of the operation of photovoltaic systems. However, since the experimental photovoltaic system is built as an off-grid system, continuous year-round operation of the system is difficult to implement. Finally, the following experimental analysis will include the application of different types of photovoltaic modules, such as monocrystalline or polycrystalline silicon.

References

[1] Key World Energy Statistics 2021 – Statistical report, International Energy Agency (IEA), Website: www.iea.org

[2] Photovoltaic Barometer 2023, EurObserv’ER, April 2023, Website: www.eurobserv-er.org

[3] Seme, S., Štumberger, B., Hadžiselimović, M., Sredenšek, K., 2020. Solar Photovoltaic Tracking Systems for Electricity Generation: A Review. Energies 2020, 13, 4224.

[4] Moldovan, M., Burduhos, B. G., Visa, I., 2023. Efficiency Assessment of Five Types of Photovoltaic Modules Installed on a Fixed and on a Dual-Axis Solar-Tracked Platform. Energies 2023, 16, 1229. https://doi.org/10.3390/en16031229

[5] Vokas, G. A., Zoridis, G. C., Lagogiannis, K. V., 2015. Single and dual axis PV energy production over Greece: Comparison between measured and predicted data. Energy Procedia 2015, 74, 1490 – 1498

[6] Awasthi, A., Shukla, A. K., Manohar, M. S. R., Dondariya, C., Shukla, K. N., Porwal, D., Richhariya, G., 2020. Review on sun tracking technology in solar PV system. Energy Reports 2020, 6, 392 – 405

[7] Racharla, S., Rajan, K., 2017. Solar Tracking System – A Review. International Journal of Sustainable Engineering. Vol. 10. No. 2. 72-81

[8] Kumar, N., Stalin, J., 2020. A Review on Solar Tracking Methods. IOP Conf. Ser.: Mater. Sci. Eng. 912 042045

[9] Kumar, K., Varshney, L., Ambikapathy, A., Saket, R. K., Mekhilef, S. 2021. Solar tracker transcript - A review. Int. Trans. Electr. Energ. Syst. 31. 13250.

[10] Najev, I., 2017. Solar Photovoltaic Tracking System, Final Thesis, University Department of Professional Studies, University of Split, Split, Croatia

[11] Čavka, F., 2021. The Efficiency of Fixed and Solar-Tracker Photovoltaic System, Final Thesis, University Department of Professional Studies, University of Split, Split, Croatia

[12] Mohanapriya, V., Manimegalai, V., Praveenkumar, V., Sakthivel, P. 2021. Implementation of Dual Axis Solar Tracking System. IOP Conf. Ser.: Mater. Sci. Eng. 1084 012073

[13] Calyxo CdTe thin film solar module CX3, Germany, 2013, https://www.secondsol.com/en/index.php?page=ad_showup&ID_AD_UPLOAD=10163 (accessed 20th August 2023).

[14] Victron Energy, The Netherlands, 2023, Products, https://www.victronenergy.com/products (accessed 12th July 2023).

[15] Hukseflux Thermal Sensors, The Netherlands, 2023, Pyranometers, https://www.hukseflux.com/products/pyranometers-solar-radiation-sensors/pyranometers (accessed 14th July 2023).

[16] SMA Solar Technology AG, Performance ratio – Quality factor for the PV plant, https://files.sma.de/downloads/Perfratio-TI-en-11.pdf, (accessed 24th July 2023).

[17] Boddula, I. R., Asiri, A. M., Rahman, M. M., 2021. Green Sustainable Process for Chemical and Environmental Engineering and Science: Solid State Synthetic Methods, Elsevier, 2021.

Industrial perspectives of Atomic Layer Deposition technique used for metal oxides coating of magnesium alloy powders

***Jaroslav Jerz*[1] *and Ľubomír Orovčík*[1]**

1) Institute of Materials & Machine Mechanics, Slovak Academy of Sciences, Dúbravská cesta 9/6319, 845 13 Bratislava, Slovakia

Corresponding author: ummsjerz@savba.sk

Professional paper

Abstract: **A**tomic **L**ayer **D**eposition (ALD) is a technique that currently enjoys the greatest research interest between all nanometric deposition technologies. It offers the possibility to obtain conformal coatings even on very complex 3-dimensional substrates with a strict thickness tolerance. Only one molecular layer is deposited on the substrate surface during the whole ALD cycle. This enables the theoretical possibility to taylor the composition of the deposit up to molecular resolution.
A brief history of ALD techniqiue in recent years to better understathe current state-of-the-art is presented in this contribution. A more detailed description of ALD technique used for metal oxides coating of magnesium alloy powders is given, considering their main advantages and drawbacks. The paper further describes the importance of ALD technnique not only for today's industry but also for solving the global problems of our world.

Keywords: *atomic layer deposition; corrosion protection; magnesium alloys; powder metallurgy*

1. Introduction

ALD is a layer-by-layer deposition technique which allows to obtain even a complete substrate coverage including narrow porosities and hollows. The compositional, mechanical, tribological as well as chemical protective properties of ALD coatings can easily be precisely tailored on the requirements of particular industrial application, varying four parameters:

- ✓ the type and composition of precursor gases
- ✓ the number of applied ALD layers
- ✓ the thickness of each different layer controlled by number of deposition cycles
- ✓ the chamber temperature, which may be varied to obtain crystalline as well as amorphous phases.

The highest attention was paid during the development of ALD technique primarily to optical (reflective and transmitting coatings, lens protection, light filters, etc.) and electronic (corrosion and wear protection of parts, components and connections, layers of memory devices, parts of screens, nanocomponents, etc.) applications. However, the investigations on ALD technique were in the past decades focused on various new possible applications such as thermite materials [2], $La_{0.8}Sr_{0.2}MnO_3$ (LSM) cathodes for solid oxide fuell cells [3], encapsulation of organic solar cells [4], etc.

2. ALD technique

ALD processing involves a sequence of self-limiting surface reactions differing from any other **C**hemical **V**apour **D**epositions (CVD) technologies. ALD process is clearly divided into four steps (Figure 1):

A) A precursor chosen so that its molecules do not reacts with each other at the deposition temperature, is injected in the deposition chamber (a single monolayer is thus formed as a result of the reaction with the substrate,

B) The chamber is purged with nitrogen or argon gas to remove the excess of reactant and prevent "parasitic" CVD on the substrate, which will eventually occur if two different precursors are present in the deposition chamber at the same time,
C) The second precursor is injected in the chamber (in the case of metal oxide layers, this is an oxidant agent, usually simple H_2O),
D) During the last step of the deposition cycle is a second purge to remove the excess of reactant with purging gas.

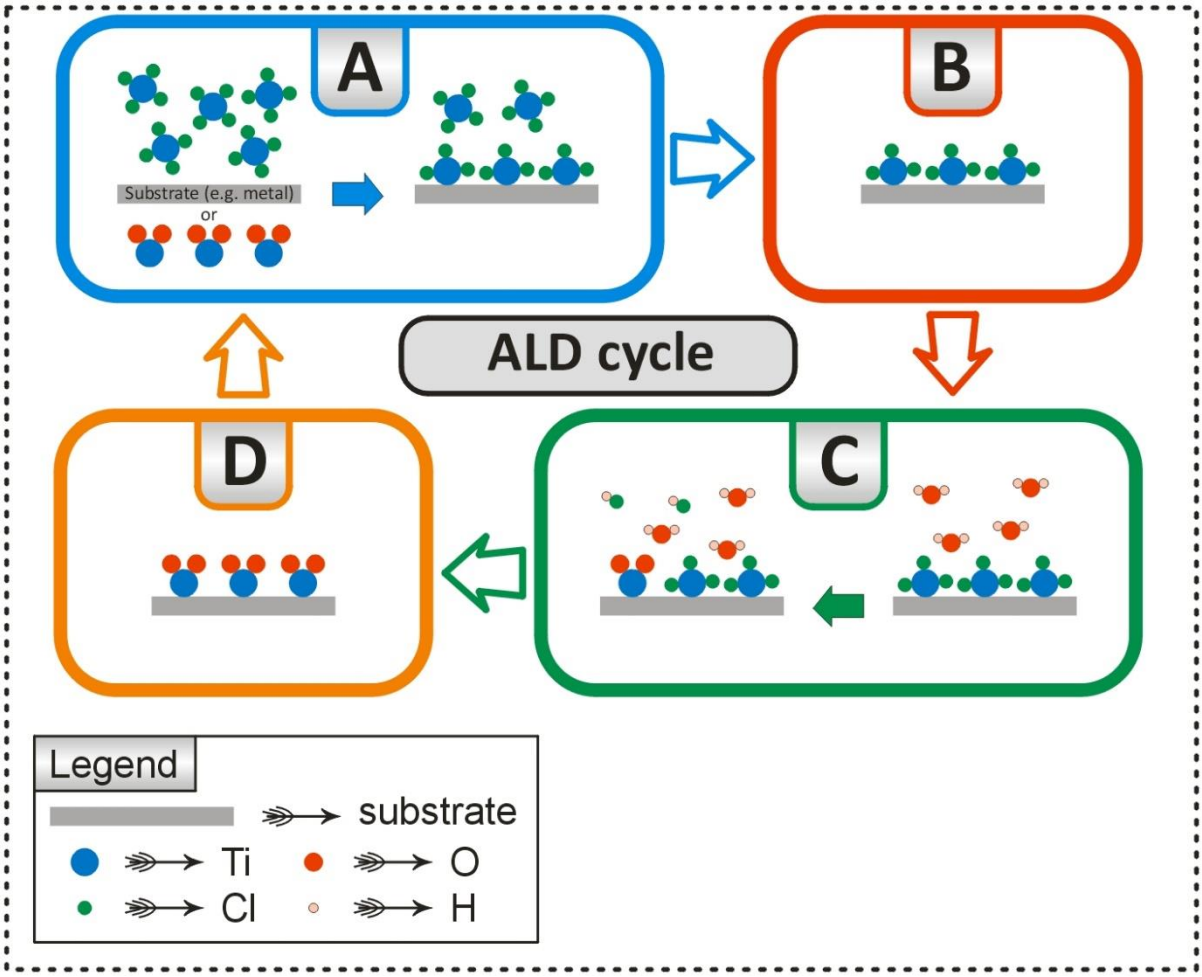

Figure 1. *Scheme of 4 steps that comprise an ALD cycle: (A) after 1st precursor (e.g.: $TiCl_4$) pulse it reacts with metallic substrate, the substrate becomes the last deposite layer, (B) 1st purge to remove exceeding precursor and volatile reaction products, (C) after 2nd precursor (e.g.: H_2O) pulse it reacts with 1st precursor (e.g.: HCl is by-product) and (D) 2nd purge to remove exceeding precursor and volatile reaction products [1].*

ALD coatings seem to have promising barrier effects against gas as well as liquid diffusion. The barrier effect resulted in being dependent on the specific deposition parameters, the chosen precursors, the exercise temperature, and the chemical composition of the final layer. For these reasons, ALD diffusion barriers must be selected based on the specific application. However, not all effective ALD diffusion barriers can be applied conformally to any substrate due to chemical compatibility.
ALD oxide coatings may be considered an artificial imitation of spontaneously formed oxide layers that can be found on the surface of different metals and metallic alloys and in particular titanium and tantalum. They are both well known for their excellent corrosion protection in most aggressive media, owing to their conformity, the absence of defects and the wide ranges of chemical and thermal stability in most common environments.
Several properties offered by ALD coatings are very important and they give to ALD technique many advantages when compared with other technologies. The substrate coated by ALD is excellently

resistant against corrosion in aggressive medium. The ALD coatings are usually very compact leading to low porosity even applying a nanometric film and they chemical reactivity and conformability is significantly low. However, the low adhesion to the substrate (poor mechanical and chemical interaction between ALD coating and substrate) and defects generated during the coating deposition are the main reason for the low long-term corrosion performance of the coatings prepared using ALD technique. The growth process of the two layers is completely different if compared to the protection given by the naturally formed oxide superficial layers even in the case that it has a similar effect to corrosion resistance. However, the other properties of natural oxides are not offered by ALD, such as:

- ✓ adhesion between coating and substrate, which in highly corrosion resistant alloys is given by the chemical affinity and the high stability of the metallic oxide in aqueous media,
- ✓ ability to "repassivate" in the presence of even low oxygen concentrations.

3. Metal oxides coating of magnesium alloy powders using ALD.

Magnesium alloys have attracted great scientific and industrial interest for their low density and high strength to weight ratio. They provide promising alternatives to aluminum alloys for light-weight structural components in different applications, from automotive to aerospace and biomedical industries.

The main limitations for wider industrial application of magnesium alloys are their low melting points (around 650°C) and their strong sensitivity to corrosion in different environments. Those that have been investigated include various concentrations of NaCl; biological fluids; aqueous sulfate solutions; ethylene glycol based engine coolants; urban, marine and even rural environments; and even simple humid air. Magnesium alloys may undergo galvanic corrosion, stress corrosion cracking, hydrogen embrittlement as well as pitting corrosion. A wide array of techniques can be used to protect magnesium alloys: anodic oxidations, solgel depositions (plasma enhanced), **C**hemical **V**apor **D**epositions (CVD), electrodepositions, conversion coatings, etc.

ALD is a deposition technique patented by Suntola in the late 1970s [5]. ALD technology has successfully been used to deposit several types of nanometric films, including in particular various metal oxides (e.g., Al_2O_3, CaO, CuO, Er_2O_3, Ga_2O_3, HfO_2, La_2O_3, MgO, Nb_2O_5, Sc_2O_3, SiO_2, Ta_2O_5, TiO_2, Y_2O_3, Yb_2O_3, ZnO and ZrO_2), nitrides (e.g., TiN, TaN, AlN, GaN, WN and NbN), sulfides (e.g., SrS and ZnS), carbides (e.g., TaC and TiC), fluorides (e.g., CaF_2, LaF_3 and MgF_2), pure metals (e.g., Ru, Ir and Pt), biomaterials (e.g., hydroxyapatite ($Ca_{10}(PO_4)_6(OH)_2$)) and even polymers (e.g., PMDA-DAH and PMDA-ODA) [6].

Marin et al. in 2012 investigated possibilities to apply ALD technique for coating of innovative TiO_2/Al_2O_3 mono/multilayers on ASTM-AZ-31 magnesium/aluminum alloy to enhance its well-known scarce corrosion resistance. Single TiO_2, single Al_2O_3 layer, Al_2O_3/TiO_2 bilayer as well as $Al_2O_3/TiO_2/Al_2O_3/TiO_2$ multilayer were deposited using $Al[(CH_3)]_3$ (trimethylaluminum, TMA), $TiCl_4$ and H_2O precursors. All depositions were performed at 120°C to obtain an amorphous-like structure of both oxide layers. The results of experiments obtained from this study clearly show that ALD may be an interesting technology to be used for the corrosion protection of magnesium alloys despite of the fact that ALD process requires an intrinsically long time to be performed.

However, ALD coatings on magnesium alloy powders seem to have three advantages over the actual and consolidate commercial techniques: (i) The reactive gases are not expensive, (ii) the deposited layers are nanometric and well controlled and (iii) the coating itself has a low residual porosity.

4. Conclusions

The technology of ALD for deposition of various nanometric multilayers prepared by alternating deposition of various metal oxides (e.g. $Al_2O_3/TiO_2/Al_2O_3/TiO_2$) to surface of magnesium alloy powders is currently only in the initial stage of its development. However, it can be assumed due to the technological possibilities to increase significantly the resistance to chemical corrosion of these powders that in the near future may ALD technique find application not only in the production of magnesium based structural components. The opportunity to prepare functional materials based on

magnesium alloys by powder metallurgy for the purpose of repeatable hydrogen storage is also currently a huge challenge for the scientific community.

Acknowledgments

The financial support by the Slovak Grant Agency for Science under the contract VEGA 2/0124/23 (project: Development of a new type of metal matrix composites strengthened by the oxide network prepared from ALD-coated metalpowders) and by the Structural funds of EU for R&D/Innovation (project: Research on possibilities of using waste heat from industry for heating in the public and commercial sector in Slovakia, ITMS: 313011BWF3) is gratefully acknowledged.

References

[1] Marin, E., Lanzutti, A., Andreatta, F., Lekka, M., Guzman, L., Fedrizzi, L., 2011. Atomic layer deposition: state-of-the-art and research/industrial perspectives. Corros Rev. 29, 191–208.
[2] Ferguson, J. D., Buechler, K. J., Weimer, A. W., George, S. M., 2005. Atomic layer deposition of ultrathin and conformal Al_2O_3 films on BN particles. Powder Technol. 156, 154–163.
[3] Holme, T. P., Lee, C., Prinz, F. B, 2008. Atomic layer deposition of LSM cathodes for solid oxide fuel cells. Solid State Ionics 179, 1540–1544.
[4] Sarkar, S., Culp, J. H., Whyland, J. T., Garvan, M., Misra, V., 2010. Encapsulation of organic solar cells with ultrathin barrier layers deposited by ozone-based atomic layer deposition. Organic Electr. 11, 1896–1900.
[5] Suntola, T., Antson, J., 1977. US Patent 4,058,430.
[6] Marin, E., Lanzutti, A., Guzman, L., Fedrizzi, L., 2012. Chemical and electrochemical characterization of TiO_2/Al_2O_3 atomic layer depositions on AZ-31 magnesium alloy. J. Coat. Technol. Res. 9 (3), 347–355.

Structural and thermal analysis of poly(ethylene oxide)/magnesium alginate blends for use in Mg-ion batteries

***Sanja Perinović Jozić*[1], *Mirna Duktaj*[1], *Dražan Jozić*[1] *and Miće Jakić*[1]**

1) University of Split, Faculty of chemistry and technology, Ruđera Boškovića 35, 21 000 Split, Croatia

Corresponding author: sanja@ktf-split.hr

Original scientific article

Abstract: Modification of poly(ethylene oxide) (PEO) properties was carried out by addition of magnesium alginate (MgAlg), as a natural polymer, to prepare new polymer blend that can be potentially used as solid polymer electrolyte (SPE) in magnesium batteries. PEO/MgAlg blends were successfully prepared using twin-screw extruder with counter-rotating screws. Fourier transform infrared spectroscopy (FTIR) confirmed interactions between PEO and MgAlg at some blend compositions. According to X-ray diffraction analysis (XRD) and differential scanning calorimetry (DSC) MgAlg has no significant influence on the PEO crystallinity, but partial miscibility of PEO and MgAlg was observed. Non-isothermal thermogravimetry (TG) point out that addition of MgAlg to PEO led to deterioration of blend thermal stability. According to all data only blend with 20 wt.% of MgAlg has the potential for the preparation of SPE with magnesium salts.

Keywords: *poly(ethylene oxide); magnesium alginate; extrusion; structure; thermal properties*

1. Introduction

The main problems of modern society relate to exploitation of non-renewable fossil resources with constant negative influence on the environment, which led to intensive research of alternative energy sources for the electrical vehicles or the portable electronic devices. Magnesium-ion batteries (MBs) made a great progress over the past few years as a green alternative to lithium-ion batteries (LIBs) [1-3]. Solid-state batteries using solid electrolytes are considered as the best option for the energy storage systems due to their high level of safety, reliability, long life and low cost [2,3]. Solid polymer electrolytes (SPEs) are materials that basically consist from a polymer matrix and an alkali metal salt whit biggest advantage as unleakage electrolyte material that has low flammability, low mass, good flexibility and processability, it is safe and stabile in contact with electrodes etc. [4-6]. They have dual functionality as an electrolyte and an electrode separator [5]. To be able to use SPEs in MBs their properties has to meet the requirements of good thermal stability, high ionic conductivity at room temperature and a wide range of electrochemical stability [4,5]. The years of intensive research led to the fact that biodegradable and water-soluble poly(ethylene oxide) (PEO) became a distinctive polymer choice for the preparation of SPEs because of their great ability to dissolve ionic salts, but they also shows a high tendency to form a crystalline phase [4-6]. The cation transfers or high ionic conductivity is associated with the motion of the polymer chain segments that are more flexible in the amorphous phase of the polymer electrolyte [4,5]. It is crucial to prevent the formation of the crystalline phase of PEO in order to enable the unhindered movement of the polymer chain [4]. Improvement of SPEs conductivity can be done in several ways and some of them are synthesis of a new amorphous polymers or copolymers and preparation of amorphous polymer blends [4]. Preparation of polymer blends implies on preparation of miscible or partially miscible blends because of their better mechanical properties, such as flexibility [4]. Bostan M.S. et al. determined the miscibility of chitosan/PEO/levan blend, which led to a decrease of the crystalline phase and improvement of its thermal and the mechanical properties [7]. Partial miscibility was determined by Dhatarwal P. et al. in the PEO/poly(methyl methacrylate) blend with lithium salt, where an amorphous

blend with good ionic conductivity and electrochemical stability was obtained [8]. Alginates are ammonium and metal salts of alginic acid, which belongs to the group of natural biodegradable polysaccharides that can be found in various brown seaweeds [9-11]. They are water-soluble polyelectrolytes, if they constitute from a monovalent metal cation, commonly used in pharmaceutical and food industry [9,10,12]. Because they are polyelectrolytes it is interesting to test them as a SPE modifiers. Their main purpose in the battery system is as aqueous binders, an alternative to the conventional binders [13]. Investigation of them as the polymer matrix in solid state Li-ion and Na-ion batteries proofed that alginates are excellent candidates for use in electrochemical devices whit necessity of further investigations [13]. Alginate are used in green electronic devices in a form of gel and solid electrolytes, but the gels dominates [12]. Algal polysaccharides, among them alginates, display favourable property of low crystallinity for the preparation of SPEs, but exhibit negligible ionic conductivities that only can be improved with addition of some salt [12]. The aim of magnesium alginate (MgAlg) addition to PEO is to prevent its crystallization in order to improve the electrical conductivity of the SPE. So, the influence of different MgAlg content on the crystalline phase of PEO in extruded PEO/MgAlg blends was investigated. The novelty of this research lies in this new never investigated material. Processing of the blends were done using optimized conditions on the twin-screw extruder with counter-rotating screws. The polymer blends structural and morphological features have been investigated using Fourier transform infrared spectroscopy (FTIR) and X-ray diffraction (XRD). Thermal properties and thermal stability were investigated by using differential scanning calorimetry (DSC) and thermogravimetry (TG).

2. Experimental

2.1. Materials

Poly(ethylene oxide) (PEO) molecular weight $\bar{M}_V$=300 000 g mol^{-1}, Sigma-Aldrich, Inc. (USA). Magnesium alginate (MgAlg) with $\bar{M}_V$ in the range from 10 000 to 600 000 g mol^{-1}, Qingdao Hyzlin Biology Development Co., Ltd. (China). MgAlg was additionally dried in vented oven at 100 °C for 3h, prior to the processing, to remove moisture.

2.2. Preparation of PEO/MgAlg blends

PEO/MgAlg blends were extruded on HAAKE MiniLab 3 twin-screw extruder with counter-rotating screws and circulation channel (Thermo Scientific, USA) at 160 °C for 1.5 min after the whole amount of material was added, Figure 1. The concentration of MgAlg in PEO was 0, 5, 10, 15, 20, 25 and 30 wt%.

Figure 1. *HAAKE MiniLab 3 twin-screw extruder with counter-rotating screws and circulation channel*

2.3. FTIR analysis

Fourier transform infrared (FTIR) spectra of PEO/MgAlg blends were recorded using spectrometer Spectrum Two (Perkin-Elmer, USA) by the Universal Attenuated Total Reflectance (UATR) technique in the range from 4000 to 650 cm^{-1}, at a resolution of 4 cm^{-1} in 10 scans at 25 °C. The reflection crystal was diamond. The aim was to investigate the possible interaction between the polymers.

2.4. X-ray diffraction analysis

Structural characterization was performed using a 3rd generation Malvern Panalytical Empyrean X-ray diffractometer. The X-ray source was a tube with a Cu anode and the generator was set at 45 kV and 40 mA. The detector used was a PIXcel^{3D} detector with Medipix3. The diffraction patterns were recorded in the range (^{o}2Theta) from 4 to 70^o, with a step size of 0.026^o and with a constant size of the incident beam (0.3x0.2 mm). The size of the incident beam was optimized using iCore on the primary side of the goniometer. The collected patterns were corrected for systematic errors (external Si standard). Qualitative interpretation of the XRD patterns was performed in comparison to standard patterns from the PDF2 database (ICDD, PDF2 Released 2020).

2.5. DSC analysis

Thermal characteristics of the blends were determined by DSC 823^e (Mettler-Toledo, Switzerland) equipped with an intracooler. The measurements were performed in the closed aluminum pans under nitrogen atmosphere (30 cm^3 min^{-1}). Approx. 10 mg samples were cooled from 25 °C to -90 °C at 20 °C min^{-1} (first cooling scan) and kept at -90 °C for 10 min, then heated from -90 °C to 110 °C at 20 °C min^{-1} (first heating scan) and kept at 110 °C for 5 min. After isothermal step, the samples were cooled to -90 °C (second cooling scan) and again kept at that temperature for 10 min. Finally, heated from -

90 °C to 110 °C at 20 °C min^{-1} (second heating scan). The melt crystallization temperature (T_{mc}) and the melting temperature (T_m) were taken as the extrapolated onset temperature ($T_{ei,mc}$, $T_{ei,m}$) and the peak temperature ($T_{p,mc}$, $T_{p,m}$). The glass transition temperature (T_g) was taken as the extrapolated onset temperature ($T_{ei,g}$) and the midpoint temperature ($T_{m,g}$). Degree of crystallinity (X_c) of PEO was calculated according to Eq. (1) [14]:

$$X_c(\%) = \frac{\Delta H_m}{\Delta H_m^0 \times w_{PEO}} \times 100 \quad (1)$$

where ΔH_m^0 is the enthalpy of melting of 100% crystalline PEO (188.1 J g^{-1}) and w is the mass fraction of PEO in the sample.

2.6. TG analysis

Thermal degradation of the blends was investigated thermogravimetrically by Pyris 8000 TGA (Perkin-Elmer, USA). Sample mass was 5.0 ± 0.5 mg. TG analysis was carried out in the temperature range from 30 to 600 °C under nitrogen atmosphere (flow rate was 40 cm^3 min^{-1}) at the heating rate of 10 °C min^{-1}.

3. Results and discussion

3.1. FTIR analysis

Investigation of possible interactions between PEO and MgAlg was performed by Fourier transform infrared spectroscopy. This interaction can be manifested by the shift of the characteristic vibrational bands or peaks towards higher or lower wavenumbers and the change of size, shape and intensity of the absorption bands. Among the possible interactions is the hydrogen bond that can occur between the O-H group of MgAlg and the O atom of the ether group of PEO and it is good indicator of the miscibility between two polymers. Figure 2 shows the FTIR spectra of PEO/MgAlg blends and MgAlg powder, while the corresponding wavenumbers of the minimum of the vibrational bands are shown in Table 1. Only the most significant vibrational bands were taken into consideration. The characteristic vibrational bands of the pure PEO (PEO0) at 2945/2878/2806 cm^{-1} belong to the symmetric and asymmetric C-H stretching, 1144/1099/1059 cm^{-1} to the *triplet* of the symmetric stretching of the C-O-C group, while the band at 841 cm^{-1} belongs to the rocking of the CH_2 group and the scissoring of the C-O-C group [15]. MgAlg powder shows the characteristic vibration bands of O-H stretching at 3215 cm^{-1}, asymmetric and symmetric stretching of the COO^- group at 1590 and 1413 cm^{-1}. This absorption bands of MaAlg are in a good agreement with the data found in the literature [16,17].

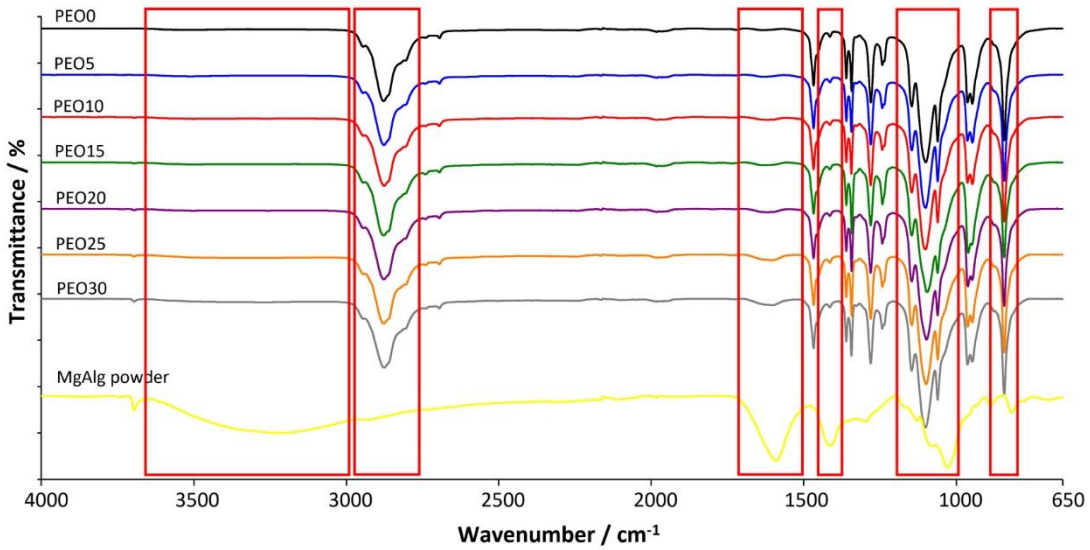

Figure 2. *FTIR spectra of PEO/MgAlg blends and MgAlg powder*

The FTIR spectra of PEO/MgAlg blends, Figure 2, shows the characteristic vibrational bands of both polymers, and their intensity is proportional to the content of the polymers in the blend. The stretching of the O-H group of MgAlg in the PEO/MgAlg blends appears as a weak, broad vibrational band whit the shift of the band towards lower wavenumbers (from 3432 to 3269 cm^{-1}) as the content of MgAlg increases, Table 1. This may indicate the presence of interactions in the form of hydrogen bonds established between MgAlg and PEO. Çaykara T. et al. observed the same changes and confirmed the hydrogen bonds, but in the blends of PEO and sodium alginate [17]. There is no literature data that deals with MgAlg in polymer blends, so it isn’t possible to make more comparison with presented research. In the case of the symmetric and asymmetric C-H stretching of PEO, there is no change in the wavenumbers and the intensity of the vibration bands, Table 1. The asymmetric stretching of the COO^- group shifts towards lower wavenumbers (from 1623 to 1598 cm^{-1}) with the increase of the MgAlg content and simultaneously the band intensity increases too, Figure 2 and Table 1. Unlike the asymmetric stretching, the symmetric stretching of the COO^- group of MgAlg doesn’t appear, that is, it is not visible in the FTIR spectra of PEO/MgAlg blends. It looks like that this vibrational band is obstructed by the presence of PEO in the blends or that the band is too weak to be detected by FTIR spectroscopy. The symmetric stretching of C-O-C (*triplet*) shifts towards lower wavenumbers with only one wavenumber of the *triplet*, 1099 cm^{-1}, as the MgAlg content increases. Patel G. et al. also observed this change in the blend PEO/poly(acrylamide) and according to that confirmed the miscibility between the polymers, i.e. the establishment of hydrogen bond [18]. The same conclusion was made by Çaykar T. et al. too [17]. The *triplet* is also a reflection of the existence of a crystalline phase in PEO [15]. According to this peak intensity it seems like that crystalline content didn’t change significantly with the presence of MgAlg. The change is irregular and it is in the range from 1100 to 1094 cm^{-1}, Table 1. Only for the blends with 15 and 20 wt.% of MgAlg this shift can be considered as the significant, the wavenumber is changed by 3 and 5 cm^{-1}, respectively. This change and the change noticed at O-H group of MgAlg points to the formation of the hydrogen bond. The rocking of the CH_2 group and the scissoring of the C-O-C group that belongs to PEO occurs at 841 cm^{-1} and didn’t change with the increase of MgAlg content in the blend. It looks like that different content of MgAlg didn’t hinder the strong ability of PEO to crystallize in the blends. The changes in the FTIR spectra of the investigated blends show indications of the hydrogen bonds as the basic bonding mechanism between PEO and MgAlg, but just in some blend compositions. Additional confirmation of this claim will have to be proven by DSC in the form of change related to the glass transition and/or the melting of PEO.

Table 1. *Wavenumbers of characteristic vibrations of PEO/MgAlg blends and MgAlg power*

Sample	O-H stretching / cm^{-1}	C-H stretching (sym./asym.) / cm^{-1}	Asymmetric stretching of COO^- / cm^{-1}	Symmetric stretching of COO^- / cm^{-1}	Symmetric stretching of C-O-C (*triplet*) / cm^{-1}	Rocking of CH_2, scissoring of C-O-C / cm^{-1}
PEO0	-	2945/2878/2806	-	-	1144/1099/1059	841
PEO5	3432	2945/2877/2809	1623	-	1144/1099/1060	841
PEO10	3423	2944/2876/2808	1620	-	1144/1100/1060/	841
PEO15	3419	2945/2878/2806	1612	-	1144/1094/1060	841
PEO20	3417	2945/2877/2808	1603	-	1145/1096/1060	841
PEO25	3335	2945/2877/2808	1599	-	1144/1098/1060	841
PEO30	3269	2942/2876/2807	1598		1145/1099/1060	841
MgAlg powder	3215	-	1590	1413	-	-

3.2. XRD analysis

The diffraction patterns of the PEO/MgAlg blends are shown in Figure 3. From the diffraction pattern of MgAlg, which was taken as powder, the presence of two diffuse diffraction maxima in the range of 2Theta from 10 to 25° indicate that it is an amorphous material. The diffraction pattern of PEO shows a structurally ordered form of PEO, which, when compared with the ICDD database, has a similar structural arrangement to that of poly(ethylene glycol) 7500 PDF#00-067-1538. According to these data, the PEO used crystallizes in the monoclinic crystal system of space group P21/a, with unit cell parameters a=0.8069 nm, b=1.3094 nm and c=1.9513 nm, while angles $\alpha=\gamma=90$ and $\beta=125.5°$. From the diffraction patterns of the PEO/MgAlg blends compared with the diffraction patterns of PEO, it is evident from the position of strongest diffraction maxima of PEO that the addition of MgAlg has no effect on the crystallinity of PEO.

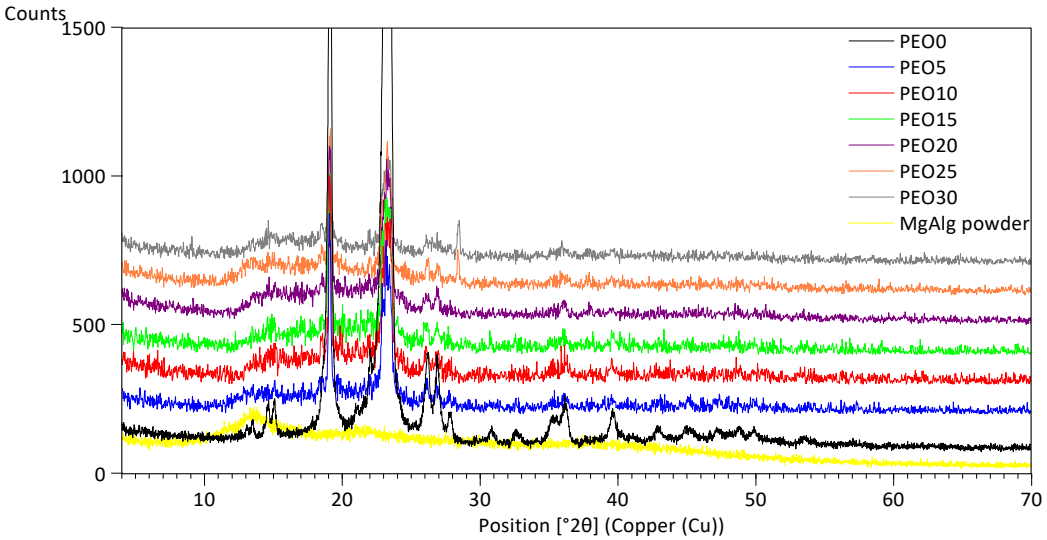

Figure 3. *Diffraction patterns of PEO/MgAlg blends and MgAlg powder*

3.3. DSC analysis

Influence of the natural polymer on the thermal properties and crystallinity of the synthetic water-soluble polymer was investigated by differential scanning calorimetry (DSC). Normalized DSC curves of extruded PEO/MgAlg blends and MgAlg powder are shown in Figure 4 (the cooling scan) and Figure 5 (the second heating scan). The characteristic temperatures of the phase transitions are shown in Tables 2. The first heating scan was performed just to remove the influence of the variable thermomechanical

history of the extruded samples and to obtain data that will give the better insight of MaAlg influence on the thermal properties and crystallinity of PEO. The MgAlg powder in the investigated temperature region doesn't show phase transitions, Figure 4 and 5.

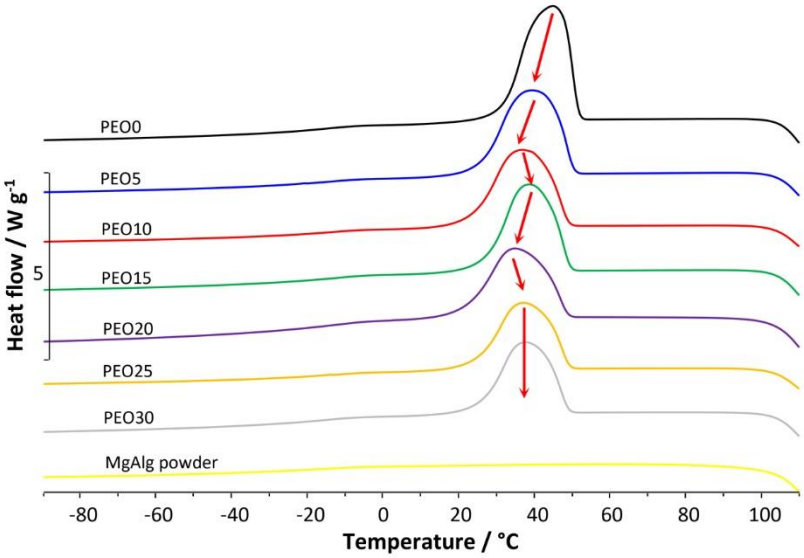

Figure 4. *DSC curves of the cooling scan for PEO/MgAlg blends and MgAlg powder*

The melt crystallization occurs at all extruded samples, Figure 4 and Table 2. The extrapolated onset melt crystallization temperature ($T_{ei,mc}$) of PEO in the samples is in the range from 49 to 52 °C. It doesn't change significantly with the increase of MgAlg content up to 30 wt.%. The peak melt crystallization temperature ($T_{p,mc}$) of PEO is reduced by 6 °C with the addition of 5 wt.% of MgAlg, but the further increase of MgAlg content in the blend doesn't change it significantly and it is in the range from 35 to 40 °C, Table 2. The biggest change of the mentioned thermal characteristics occurs in the blend with 20 wt.% of MgAlg. The enthalpy of melt crystallization (ΔH_{mc}) of PEO decreases from 131.9 to 91.0 J g^{-1} by increase of MgAlg content, Table 2. The lower T_{mc} values of PEO in the blends compared to the pure extruded PEO (PEO0) indicates that MgAlg postpones the crystallization of PEO during the controlled cooling. The biggest change is noticed in the blend with 20 wt.% of MgAlg.

After the cooling, the controlled heating was applied on the samples, Figure 5. The extrapolated onset glass transition temperature ($T_{e,ig}$) and the midpoint glass transition temperature ($T_{m,g}$) was obtained. They are in the range from -54 to -50 °C and -48 to -45 °C, respectively (Table 2). Only the blend with 20 wt.% of MgAlg shows a slightly larger shift of the mentioned thermal characteristics compared to pure PEO, max. 4 °C to the higher temperature. The aforementioned mild change in the glass transition of PEO in the blends can indicate the existence of the interactions between PEO and MgAlg. The same behaviour was observed in two different blends, poly(vinyl alcohol)/sodium alginate and poly(N-vinyl-2-pyrrolidone)/sodium alginate blends. It is attributed to the hydrogen bond formation between the polymers. Hydrogen bonds decrease the mobility of the polymers chains because they act as cross-links [11]. It is well known that an increase of T_g can be the result of hydrogen bonds if there is a structural predisposition for it [19]. Taking into account the changes in the FTIR spectra of PEO20 blend compared to the pure extruded PEO, the partial miscibility of the polymers can be confirmed. The specific heat capacity of glass transition (Δc_p) of PEO in the extruded blends goes through the irregular change with the increase of MgAlg content and it is in the range from 0.10 to 0.19 J g^{-1} K^{-1}, Table 2. PEO25 blend will heat up somewhat faster than the other samples, while PEO30 blend will heat up slowest.

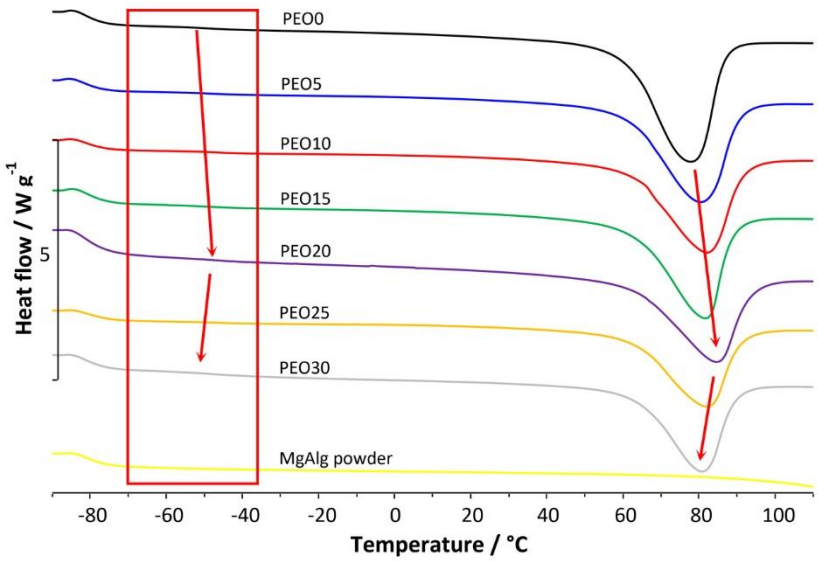

Figure 5. *DSC curves of the second heating scan for PEO/MgAlg blends and MgAlg powder*

Table 2. *Thermal characteristics of PEO/MgAlg blends and MgAlg powder from the cooling scan and the second heating scan*

Sample	$T_{ei,mc}$ /°C	$T_{p,mc}$ /°C	$-\Delta H_{mc}$ /J g^{-1}	$T_{ei,g}$ /°C	$T_{m,g}$ /°C	Δc_p /J g^{-1} °C^{-1}	$T_{ei,m}$ /°C	$T_{p,m}$ /°C	$-\Delta H_m$ /J g^{-1}	X_c /%
PEO0	52	46	131,9	-54	-48	0,13	60	77	136,5	73
PEO5	51	40	119,1	-53	-48	0,11	60	80	124,2	70
PEO10	49	37	109,6	-53	-47	0,12	61	81	117,0	69
PEO15	50	39	108,7	-52	-47	0,11	62	81	114,1	71
PEO20	49	35	102,2	-50	-45	0,13	62	83	105,3	70
PEO25	50	38	91,0	-52	-47	0,10	62	81	95,4	68
PEO30	49	38	91,8	-54	-48	0,19	63	80	95,5	73
MgAlg powder	-	-	-	-	-	-	-	-	-	-

The extrapolated onset melting temperature ($T_{ei,m}$) and the melting peak temperature ($T_{p,m}$) of PEO in the PEO/MgAlg blends have the higher values compared to the sample of pure PEO. These thermal characteristics are in the range from 60 to 63 °C and 77 to 83 °C, respectively (Table 2). There is no regular change with the increase of MgAlg content. Only in the case of the blend with 20 wt.% of MgAlg a slightly larger shift in the values of the mentioned thermal characteristics is observed. The max. 6 °C towards higher temperatures compared to the pure PEO was measured. This is unexpected because the miscible polymers tend to show melting point depression. This depression in hydrogen-bonded blends can be more than 15 °C like in poly(3-hydroxybutyrate)/poly(vinylphosphonic acid) blend with poly(vinylphosphonic acid) content of 30 wt% or just 1 to 2 °C like in poly(3-hydroxybutyrate)/poly(vinyl acetate) blend with 30 wt% of poly(vinyl acetate), while an immiscible blend will not show depression of the melting point [20]. It is usually the same as in pure polymers but there is no information about what does it means when it increases in combination with T_g increment. The PEO/MgAlg blend with 20 wt.% of MgAlg is definitely interesting blend for the further investigation. The presence of Mg ion in the alginate brought different and complex behaviour from the previous investigation of PEO/NaAlg [21]. The melt enthalpy of melting($-\Delta H_m$) of PEO decreases from 136.5 to 95.4 J g^{-1} with the increase of MgAlg content up to 30 wt.% in the blend, Table 2. As the content of PEO in the blend decreases it is expected that $-\Delta H_m$ will anyway decrease and the real influence of MgAlg is not noticeable until degree of crystallinity (X_c) is calculated. Addition of MgAlg to PEO didn't suppress or prevent crystallization ability of PEO because X_c of PEO didn't change

significantly no matter the content of MgAlg in the blend. It is in the range from 68 to 73%, Table 2. The lowest value of X_c of PEO occurs in the blend with 25 wt.% of MgAlg and is 68%. The melt crystallization, glass transition and melting point of PEO are under the influence of MgAlg and its content in the blend, but the amount of the crystalline phase remained almost unchanged in all blends compared to PEO. Although the aim of this research was to significantly reduce the amount of PEO crystalline phase due to the achievement of its better conductivity when magnesium salt is added to it, this didn’t happen but the thermal properties of the extruded PEO20 blend showed the potential for the preparation of SPE. Also, it should be noted that the extruded samples containing up to 20 wt.% of MgAlg show better processing properties and do not have a rough surface after extrusion as the blends with a higher content of MgAlg.

3.4. TG analysis

If some material wants to be used as SPEs it must have a minimum thermal stability up to 150 °C [22]. Thermal stability of extruded PEO/MgAlg blends and MgAlg powder was analysed by nonisothermal thermogravimetry (TG). The obtained TG and derived TG curves (DTG) of the samples are shown in Figure 6 and 7, while the characteristic thermal features are presented in Tables 3. Degradation stages of pure PEO (PEO0) and MgAlg are marked with numbers from 1 to 5, whereby numbers 1, 2 ,3 and 5 indicate degradation of MgAlg while the number 4 refers to the degradation of PEO. The numbers are given by the chronological order of the degradation stage in the investigated temperature range.

MgAlg degrades in four degradation stages, Figure 6 and 7. The first degradation stage (mark 1) represents the removal of absorbed water (the mass loss in the degradation stage (Δm) is 20.2%), Table 3. The blends were prepared with dried MgAlg, but as MgAlg tends to absorb moisture easily, the undried MgAlg was used in the analysis. The goal was to point out the high hygroscopicity of the alginate and the necessity of storing samples under the vacuum, especially important for the intended purpose. The second degradation stage (mark 2) is the largest one (Δm=31.3%), while in the third and fourth degradation stage (mark 3 and 5) only 6.6% and 9.9% mass is lost, respectively. The final mass at the end of degradation (m_f) is 31.9% and points to the inorganic part of the alginate molecule, that during degradation forms the molecules which will not degrade in the investigated temperature range. This statement agrees well with the data found in the literature that refers to sodium alginate, but they are comparable with MgAlg [23]. The main degradation stage of MgAlg is the second one and occurs in the temperature range from 200 to 300 °C, while third and fourth stages occur in the temperature range from 330 to 380 °C and from 400 to 580 °C, respectively (Figure 6 and 7). MgAlg tends to degrade slowly with the biggest maximum degradation rate (R_{max}) at second degradation stage, 4.2 % °C^{-1}, Table 3. The sample of pure PEO (PEO0) decomposes in one degradation stage in the temperature range from 330 to 450 °C (mark 4), Figures 6 and 7. It is much thermally stable, degrades much faster (28.2 % °C^{-1}) and almost complete (m_f=4.5%), in contrast to MgAlg.

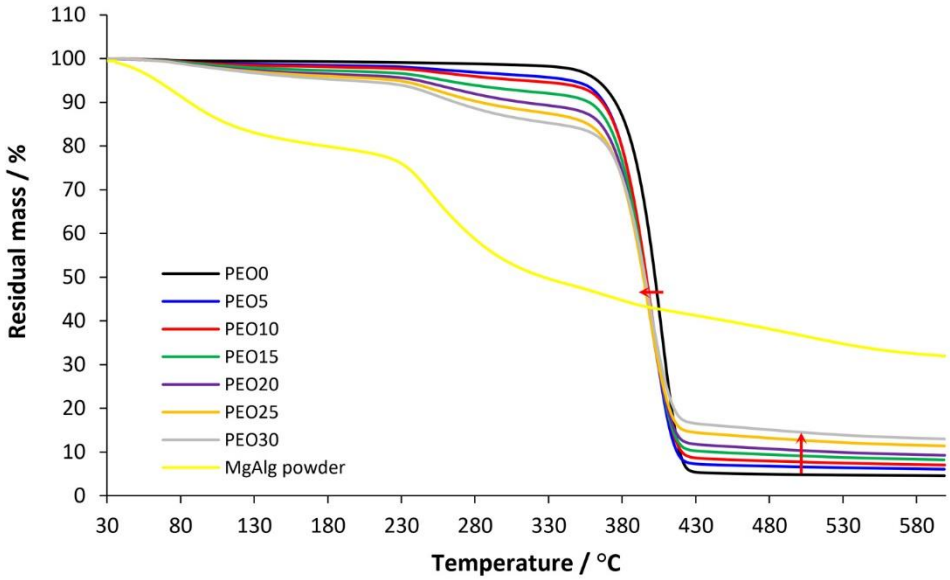

Figure 6. *TG curves of nonisothermal degradation of PEO/MgAlg blends and MgAlg powder*

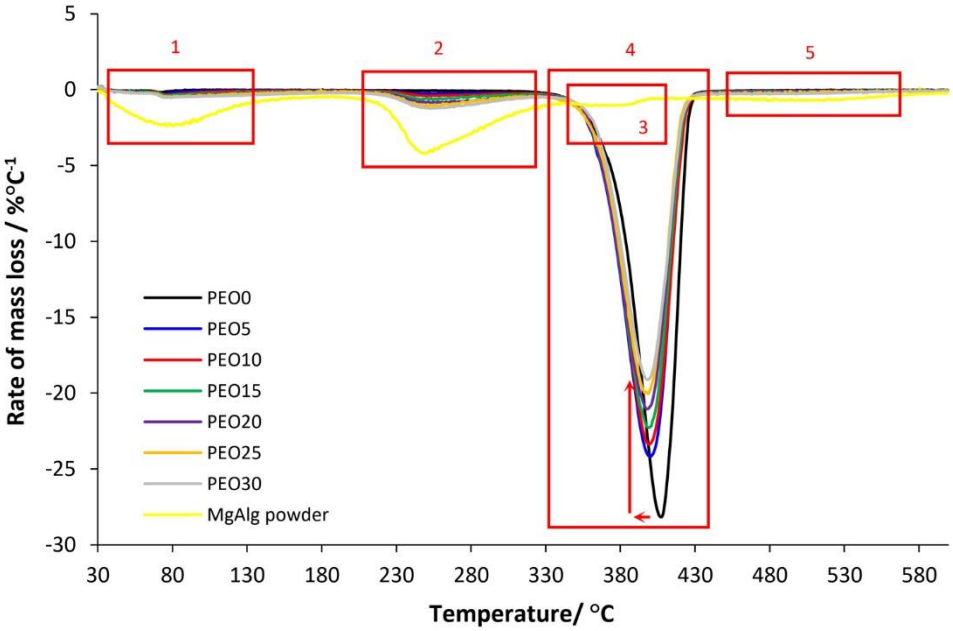

Figure 7. *DTG curves of nonisothermal degradation of PEO/MgAlg blends and MgAlg powder*

The PEO/MgAlg blends degrade in three degradation stages, as marked on the DTG curves (1-removal of absorbed water, 2-degradation of MgAlg and 4-degradation of PEO), Figure 7. The presence of moisture in the extruded samples stored under the vacuum confirms the high hygroscopicity of the alginate, although the rapid preparation for all analysis was done. Due to their structural predispositions, alginates show a tendency to absorb water from the environment [11]. As the MgAlg content increases in the blend, the ability of the material to absorb moisture from the environment increases, Δm ranges from 1.4 to 5.0% (Tables 3). Considering the above, the first degradation stage will not be considered as degradation of PEO/MgAlg blends but as drying. Although the moisture in the blends affects the temperature at 5% mass loss ($T_{5\%}$), its reduction is clearly observed with the addition and increase of MgAlg content in the blend (from 363 to 194 °C). In PEO/MgAlg blends, MgAlg (mark 2 in Figures 6 and 7) has about 160 °C worse thermal stability than PEO (mark 4 in Figures 6 and 7), Table 3. The onset temperature (T_{onset}) of MgAlg in the blends gradually increases from 214 to about 228 °C and moves toward value of MgAlg powder, but the temperature at maximum degradation rate

(T_{max}) is for maximum 6 °C higher from the value of MgAl powder, Tables 3. This shift can be indication of the hydrogen bond formation. The similar shift of T_{max} was found in the chitosan/PEO/levan blend for one of the three components and attributed to the hydrogen bonds [7]. The residual mass at the onset (m_{onset}) and the residual mass at the maximum degradation rate (m_{max}) of MgAlg in the blends decreases from 98.7 to 94.9% and from 97.5 to 91.5% with an increase of MgAlg content, respectively. R_{max} of MgAlg in the blends are small and by the increase of MgAlg content in the PEO/MgAlg blend, R_{max} of MgAlg increases from 0.3 to 1.2% °C^{-1}. As the MgAlg content increases in the blend, Δm increases from 2.1 to 9.8%. All the thermal characteristics of MgAlg in PEO/MgAlg blends gradually approaches the values of MgAlg powder as the MgAlg content increases.

Table 3. *TG and DTG data of PEO/MgAlg blends and MgAlg powder*

Sample	Temp. region	$T_{5\%}$ / °C	T_{onset} / °C	m_{onset} / %	T_{max} / °C	m_{max} / %	$(dm/dt)_{max}$ / % °C^{-1}	Δm / %	m_f / %
PEO0	4	363	385	98.4	407	36.3	28.2	95.4	4.5
PEO5	1	345	51	100.0	73	99,4	0.3	1.4	6.1
	2		214	98.7	255	97,5	0.3	2.1	
	4		377	9.5	400	41.3	24.2	90.4	
PEO10	1	312	80	99.3	77	99.4	0.4	1.9	7.0
	2		221	98.2	253	96.9	0.4	3.2	
	4		378	9.0	399	44.1	23.4	87.9	
PEO15	1	260	57	100.1	76	99.3	0.4	2.7	8.2
	2		225	97.1	248	95.7	0.6	4.9	
	4		376	92.2	399	42.2	22.2	84.1	
PEO20	1	241	66	99.6	76	99.1	0.5	3.6	9.3
	2		226	96.2	255	93.9	0.8	7.0	
	4		376	89.2	399	41.8	21.0	80.1	
PEO25	1	227	53	100.0	76	99.0	0.5	4.3	11.5
	2		226	95.7	252	93.0	1.1	8.0	
	4		375	87.7	398	43.2	20.0	76.3	
PEO30	1	194	58	100.1	76	99.0	0.5	5.0	13.1
	2		228	94.9	254	91.5	1.2	9.8	
	4		378	85.2	398	45.3	19.1	72.1	
MgAlg powder	1	64	46	99.9	80	91.5	2.4	20.2	31.9
	2		226	79.6	249	69.8	4.2	31.3	
	3		346	48.3	371	45.6	1.0	6.6	
	5		427	41.8	515	35.8	0.7	9.9	

Analysis of the thermal characteristics of PEO in the blends indicates a lowering of T_{onset} (mark 4 in the figures and Table 3) from 385 to 377 °C with the addition of 5 wt.% of MgAlg, but as the MgAlg content increases up to 30 wt. % it remains in the temperature range from 375 to 378 °C. The similar change is observed with T_{max} of PEO, i.e. with the addition of 5 wt.% of MgAlg to PEO it decreased from 407 to 400 °C, but with the further increase of MgAlg content, it doesn't change significantly, Tables 3. Addition of MgAlg to PEO results in a worse thermal stability of PEO in the blend, regardless to the MgAlg content. The value of m_{onset} gradually decreases from 98.4 to 85.2% with the increase of MgAlg content, while m_{max} initially increased from 36.3 to 41.3% with the addition of 5 wt.% of MgAlg, but with the further increase of MgAlg content is in the range from 41.3 to 45.3%, Tables 3. Degradation of PEO in the blends slows down with an increase in the MgAlg content, i.e. R_{max} decreases from 28.2 to 19.1 % °C^{-1}. By increasing the MgAlg content and decreasing the PEO content in the blend, Δm of the PEO degradation stage (mark 4) decreases from 95.4 to 72.1%, Table 3. In the PEO/MgAlg blends

m_f increase from 4.5 to 13.1% as the content of MgAlg increases. It is obvious that magnesium in the structure of the alginate molecule contributes to the creation of degradation products stable up to 600 °C. In the literature, the TG data of alginates were found just for the sodium alginate and in the temperature range up to 500 °C. Its m_f is about 40% due to the formation of sodium carbonate [23]. Degradation of the extruded PEO/MgAlg blends takes place at the lower temperatures than pure extruded PEO. This deterioration of the thermal stability is due to the more thermally unstable MgAlg. Regardless of that the established thermal stability of the blends is sufficient for this material to be used as a solid polymer electrolyte, with the mandatory removal of residual water.

4. Conclusion

PEO/MgAlg blends were successfully prepared by extrusion on the twin-screw extruder with counter-rotating screws. Extruded blends containing up to 20 wt.% of MgAlg showd the better processing properties and better appearance of the material. Observed changes in the FTIR spectra of PEO/MgAlg blends showed indications of the hydrogen bonds as the basic bonding mechanism between PEO and MgAlg, but just in some blend compositions. XRD analysis confirmed the amorphous nature of MgAlg and that it doesn’t have influence on the crystallinity of PEO. DSC analysis indicated that MgAlg has insignificant effect on the crystallinity content in the blends, regardell of its content. The blend with 20 wt.% of MgAlg showd the significant change of the thermal characteristics compared to the other blends that led to the miscibility of the polymers in the blend. According to the TG analysis the extruded PEO/MgAlg blends decompose in three degradtion stages. PEO/MgAlg blends are more thermally unstable than pure PEO, but their thermal stability is still above the minimum required thermal stability of SPE. All analysis indicated that the PEO/MgAlg blend with 20 wt.% of MgAlg has the greatest potential for the preparation of SPE with some magnesium salts.

References

[1] Huiea, M.M., Bock, D.C., Takeuchi, E.S., Marschilok, A.C., Takeuchi, K.J., 2015. Cathode Materials for Magnesium and Magnesium-ion based Batteries. Coord. Chem. Rev. 287, 15–27.
[2] Sarangika, H.N.M., Dissanayake, M.A.K.L., Senadeera, G.K.R., Rathnayake, R.R.D.V., Pitawala, H.M.J.C., 2017. Polyethylene oxide and ionic liquid-based solid polymer electrolyte for rechargeable magnesium batteries. Ionics. 23, 2829–2835.
[3] Anilkumar, K.M., Jinisha, B., Manoj, M., Jayalekshmi, S., 2017. Poly(ethylene oxide) (PEO) – Poly(vinyl pyrrolidone) (PVP) blend polymer based solid electrolyte membranes for developing solid state magnesium ion cells. Eur. Polym. J. 89, 249–262.
[4] Yue, L., Ma, J., Zhang, J., Zhao, J., Dong, S., Liu, Z., Cui, G., Chen, L., 2016. All solid-state polymer electrolytes for high-performance lithium ion batteries. Energy Storage Mater. 5, 139–164.
[5] Arya, A., Sharma, A.L., 2017. Polymer electrolytes for lithium ion batteries: a critical study. Ionics. 23, 497–540.
[6] Gurusiddappa, J., Madhuri, W., Padma Suvarna, R., Priya Dasan, K., 2015. Electrical Properties of PEO-Based Electrolytes. Inter. J. Innov. Sci. Eng. Tech. 4, 11447–11454.
[7] Bostan, M.S., Mutlu, E.C., Kazak, H., Keskin, S.S., Oner, E.T., Eroglu, M.S., 2014. Comprehensive characterization of chitosan/PEO/levan ternary blend films. Carbohydr. Polym. 102, 993–1000.
[8] P. Dhatarwal, R. J. Sengwa, Influence of solid polymer electrolyte preparation methods on the performance of (PEO–PMMA)–LiBF4 films for lithium-ion battery applications. Polym. Bull. 75 (2018) 5645–5666.
[9] Ren, L., 2008. Production of Alginate Beads, Massey University, Auckland, 2–23.
[10] Soares, J.P., Santos, J.E., Chierice, G.O., Cavalheiro, E.T.G., 2004. Thermal behavior of alginic acid and its sodium salt. Ecl. Quím. 29, 53–56.
[11] Eds. by Zia, K.M., Zuber, M., Ali, M., 2017. Algae Based Polymers, Blends, and Composites, Elsevier Inc.

[12] Torres, F.G., De-la-Torre, G.E., 2021. Algal-based polysaccharides as polymer electrolytes in modern electrochemical energy conversion and storage systems: A review. Carbohydrate Polymer Technologies and Applications. 2, 100023.
[13] Vijay, A., 2019. Improving Solid State Batteries Using Bio-derived Alginates, Delft University of Technology, Netherlands
[14] Rocco, A.M., Pereira, R.P., Felisberti, M.I., 2001. Miscibility, crystallinity and morphological behavior of binary blends of poly(ethylene oxide) and poly(methyl vinyl ether-maleic acid). Polymer 42, 5199-5205.
[15] Sim, L.H., Gan, S.N., Chan, C.H., Yahya, R., 2010. ATR-FTIR studies on ion interaction of lithium perchlorate in polyacrylate/poly(ethylene oxide) blends. Spectrochim. Acta - A: Mol. Biomol. Spectrosc. 76, 287–292.
[16] Sanchez-Ballester, N.M., Soulairol, I., Bataille, B., Sharkawi, T., 2019. Flexible heteroionic calcium-magnesium alginate beads for controlled drug release. Carbohydr. Polym. 207, 224-229.
[17] Çaykara, T., Demirci, S., Eroğlu, M.S., Güven, O., 2005. Poly(ethylene oxide) and its blends with sodium alginate. Polymer 46, 10750–10757.
[18] Patel, G., Sureshkumar, M.B., Patel, P., 2015. Spectroscopic Investigation and Characterizations of PAM/PEO Blends Films. Soft 4, 9–24.
[19] Liu, Q., Wang, C., Guo, Y., Peng, C., Narayanan, A. Kaur, S., Xu, Y., Weiss, R.A., Joy, A., 2018. Opposing Effects of Side-Chain Flexibility and Hydrogen Bonding on the Thermal, Mechanical, and Rheological Properties of Supramolecularly Cross-Linked Polyesters. Macromol. 51, 9294−9305.
[20] He, Y., Zhu, B., Inoue, Y., 2004. Hydrogen bonds in polymer blends. Prog. Polym. Sci. 29, 1021–1051.
[21] Perinović Jozić, S., Sesar, A., Grubač, Z., Andričić, B., 2020. Utjecaj natrijeva alginata na svojstva poli(etilen-oksida) kao matrice za pripravu čvrstih polimernih elektrolita. Kem. Ind. 69, 503–514.
[22] Yue, L., Ma, J., Zhang, J., Zhao, J., Dong, S., Liu, Z., Cui, G., Chen, L., 2016. All-solid state polymer electrolytes for high-performance lithium ion batteries, Energy Storage Mater. 5,139-164.
[23] Soares, J.P., Santos, J.E., Chierice, G.O., Cavalheiro, E.T.G., 2004. Thermal behaviour of alginic acid and its sodium salt, Ecl. Quím 29, 53-56.

Thermal properties of selected metal dental materials

***Borut Kosec*[1,2], *Mateja Vodlan*[3], *Aleš Nagode*[1], *Alenka Pavlič*[4], *Igor Kopač*[4], *Hennry Taubmann*[5], *Mirko Gojić*[6,7], *Igor Budak*[8], *Ladislav Vrsalović*[9], *Matija Zorc*[1], *Tatjana Puškar*[10], *Milan Bizjak*[1] *and Blaž Karpe*[1]**

1) *University of Ljubljana, Faculty of Natural Sciences and Engineering, Aškerčeva 12, 1000 Ljubljana, Slovenia*

2) *University of Ljubljana, Faculty of Mechanical Engineering, Aškerčeva 6, 1000 Ljubljana, Slovenia*

3) LEK d.d., Verovskova 57, 1526 Ljubljana, Slovenia

4) University of Ljubljana, Faculty of Medicine, Korytkova 2, 1000 Ljubljana, Slovenia,

5) C3 Prozess und Analysentechnik Gmbh, Peter Henlein Str. 20, Munich, Germany

6) University of Zagreb, Faculty Metallurgy, Aleja narodnih heroja 3, 43000 Sisak, Croatia

7) University North, Trg dr. Žarka Dolinara 1, 48 000, Koprivnica, Croatia

8) University of Novi Sad, Faculty Technical Sciences, Trg D. Obradovića 6, 21000 Novi Sad, Serbia

9) University of Split, Faculty of Chemistry and Technology, R. Boškovića 35, 21000 Split, Croatia

10) University of Novi Sad, Faculty of Medicine, Hajduk Veljkova 6, 21000 Novi Sad, Serbia

Corresponding author: borut.kosec@ntf.uni-lj.si

Professional article

Abstract: The thermal properties of dentine and tooth enamel affect the rate of response of the tooth nervous system to the temperature changes to which the tooth is exposed on a daily basis.
Today almost all manufacturers of dental materials in their certificates of material quality describe material chemical composition, mechanical properties, process ability and aesthetic characteristics, while information about thermal properties (thermal conductivity, heat capacity, and temperature diffusivity) are not available.
Within the interdisciplinary international teamwork, thermal properties of three typical metal dental materials: commercially pure titanium (99% Ti), titanium alloy TiAl6V4 and CoCr alloy were measured, and analyzed by modern transient plane source (TPS) method in accordance with the standard ISO 22007-2 at ambient and elevated temperatures.

Keywords: *dental materials; thermal properties; thermal conductivity; TPS method*

1. Introduction

The thermal properties of dentine and tooth enamel affects the rate of response of the tooth nervous system to the temperature changes to which the tooth is exposed on a daily basis. In addition to strength and aesthetic requirements, artificial dental materials must also provide a similar thermal protection for the tooth pulp. Likewise, implants and artificial tooth crowns must transfer similar heat flow to the bone as is transferred by a natural tooth, which has a strong influence on the patient's general acceptance of the foreign body [1].
Manufacturers of dental materials in their certificates of material quality describe chemical composition, mechanical properties, aesthetic characteristics and machinability, while thermal properties of the material are rarely given [2].
The reported values of human teeth thermal properties show significant discrepancies, with data for thermal conductivity of dentine between 0.11 to 0.98 W/(m·K), and 0.7 to 0.8 W/(m·K)for tooth enamel, while temperature diffusivity varies between 0.058 to 0.269 mm^2/s and 0.092 to 0.42 mm^2/s for dentin and enamel respectively. The significant discrepancy between the reported results may be attributed to several challenges associated with the measurements, like tooth heterogeneous

microstructure and associative anisotropic thermal properties, difficulties at establishing perfect thermal contact or lack of precise emissivity data when axial heat flow or laser flash measuring methods are applied [3].

2. Thermal properties measurement

Thermal conductivity, specific heat and thermal diffusivity are basic thermal properties of material that determine the heat transfer in the system under consideration. Despite the remarkable progress of measuring methods and techniques, it is still difficult to determine them with an error of less than ±2 %, even for bulk materials.

In our research, we used one of the most advanced instruments for determining the thermal properties, Hot Disk TPS 2200, a product of Hot Disk AB company, Gothenburg, Sweden [4]. The instrument can be used for determining thermal properties of various materials including pure metals, alloys, minerals, ceramics, plastics, glasses, powders and viscous liquids with thermal conductivity in the range from 0.01 to 500 W/(m·K), thermal diffusivity from 0.01 to 300 mm^2/s and heat capacity up to 5 MJ/K. Measurements can be performed in a temperature interval between 0 up to 750 °C [5].

Hot disk measuring method is a transient plane source (TPS) technique. Based on the theory of TPS, instrument utilizes a sensor element in the shape of 10 μm thick double spiral, made by etching from pure nickel foil. Spiral is mechanically strengthen and electrically insulated on both sides by thin polyimide foil (Kapton ®Du Pont) for measurements up to 300 °C or mica foil for measurements up to 750 °C. Sensor acts both as a precise heat source and resistance thermometer for recording the time dependent temperature increase (Figure 1).

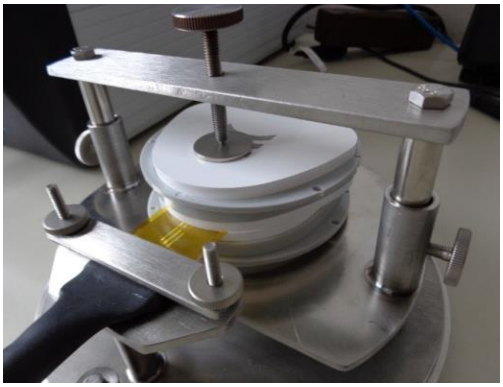

Figure 1. *Sensor element sandwiched between two halves of a testing sample during measurement.*

During measurement of solids, encapsulated Ni-sensor is sandwiched between two halves of the sample and constant precise pre-set heating power is released by the sensor, followed by 200 resistance recording in a pre-set measuring time, from which the relation between time and temperature change is established. Based on time dependent temperature increase of the sensor, thermal properties of the tested material are calculated.

3. Experimental

In our study, we measured thermal properties of important dental materials, used in dental praxis at the Medical Faculty, University of Ljubljana, and Medical Faculty, University of Novi Sad. Tested materials were:

- 99 % (commercially) pure titanium [6] (Figure 2),
- titanium alloy TiAl6V4 [7], and
- CoCr alloy [8].

Figure 2. *Standard disks from 99 % (commercially)pure titanium [6].*

Measurements and analysis of thermal properties of selected dental materials were performed in accordance with ISO 22007-2 standard in the Laboratory for measurements, Chair of Thermal Engineering, Faculty of Natural Sciences and Engineering, University of Ljubljana. Thermal properties were measured in the temperature interval that teeth are most frequently exposed, 0 °C to 50 °C.
Titanium and its alloys are used in dentistry because of their resistance to electrochemical decomposition, excellent compatibility with live tissues, easily combine with bone (osseointegration), are relatively light (4,61 g/cm^3) and have high tensile (450 MPa) and yield (275 MPa) strength. Titanium forms a very persistent oxide layer on the surface, formed in a few nanoseconds. Because of this oxide layer, it is corrosion-resistant and biocompatible. It is used for manufacturing of dental implants, crowns, braces, bridges, partial prostheses and orthodontic wires. Commercially pure titanium (impurities < 1%) disks were measured in the temperature interval between 0 °C and 50 °C, and as expected, changes of thermal properties were negligible (Table 1).

Table 1. *Thermal properties of pure Ti disks (impurities < 1%)*

Thermal conductivity [W/(m·K)]	Thermal diffusivity [mm^2/s]	Heat capacity [MJ/K]
22.546	6.720	3.362

TiAl6V4 (Grade 5: 6% Al, 4% V, 0.25% > Fe and 0,2% > O (balance Titanium)) is the most commonly used titanium alloy in dentistry. It is significantly stronger (R_m > 895 MPa, $R_{p0,2}$ > 828 MPa) than commercially pure titanium while having the same stiffness. This grade is an excellent combination of strength, corrosion resistance, weldability and machinability, and has good osseointegration properties. Alloying elements reduce thermal conductivity and diffusivity considerably compared to commercially pure titanium. In the temperature interval between 0 and 50 °C thermal properties can be considered as constant (Table 2).

Table 2. *Thermal properties of TiAl6V4 disks*

Thermal conductivity [W/(m·K)]	Thermal diffusivity [mm^2/s]	Heat capacity [MJ/K]
6.668	2.809	2.376

Co-Cr alloys exhibit material properties considered suitable for dental reconstructions, such as high tensile (900 - 1000 MPa) and yield (640 – 700 MPa) strength, high modulus of elasticity (> 200 GPa), and high corrosion resistance, and are the most common base-metal alternative for patients known to be allergic to nickel. They are relatively inexpensive compared to noble alloys and somewhat easier to manipulate than titanium alloys.
In dentistry, Co-Cr alloys are commonly used for the fabrication of metallic frameworks of removable partial dentures, as metallic substructures for the fabrication of porcelain-fused-to-metal restorations and implant frameworks. The increased worldwide interest in utilizing Co-Cr alloys for dental

applications is related to their low cost, excellent biocompatibility and adequate mechanical properties. Chemical composition of tested sample is complex including 63% Co, 24% Cr, 8% W, 3% Mo, 1% Si, ≈1% Nb and trace elements < 0.1%. As with other samples, thermal properties can be considered as constant in measuring temperature interval (Table 3).

Table 3. *Thermal properties of CoCr dental alloy*

Thermal conductivity [W/(m·K)]	Thermal diffusivity [mm^2/s]	Heat capacity [MJ/K]
10.735	2.828	3.798

4. Conclusions

Measurements and analysis of the thermal properties of selected characteristic dental materials were performed using the Hot Disk method on the Hot Disk TPS 2200 in accordance with the standard ISO 22007-2 in the Laboratory for measurement of the Chair of Thermal Engineering, Department of Materials and Metallurgy, Faculty of Natural Sciences and Engineering, University of Ljubljana.

The teeth and dental supplements are most often exposed to temperatures at an interval between 0 °C and 50 °C, which was the reason why we selected this temperature interval to perform our measurements. We found that for all dental materials there is no significant difference in thermal properties in this temperature interval and can be considered as constant.

As expected, metallic materials transmit heat much faster than tooth structure. With the performed measurements, we have completed the existing material quality certificates of dental materials with their thermal properties.

References

[1] J.F. McCabe, A.W.G. Walls, Applied Dental Materials, Blackwell Publishing Ltd, Oxford, 2008.

[2] I. Budak, B. Kosec, M. Sokovic, Application of contemporary engineering techniques and technologies in the field of dental prosthetics, Journal of Achievements in Materials and Manufacturing Engineering, 54 (2012) 2, 233-241.

[3] C. Scheller-Sheridan, Basic Guide to Dental Materials, Wiley-Blackwell, Dublin, 2010.

[4] Internal script Hot Disk AB; Hot Disk Thermal Constants Analyser, Instruction Manual, Gothenburg, 2019.

[5] B. Kosec, B. Karpe, Instrument for thermal properties analysis Hot Disk TPS 2200, IRT3000, 70 (2017), 67.

[6] Certificate CC DISK Ti2, Interdent d.o.o., Celje, 2014.

[7] Certificate CC DISK Ti5, Interdent d.o.o., Celje, 2014.

[8] Certificate CC DISK NF Co-Cr, Interdent d.o.o., Celje, 2014.

Tribological processes in the material for 3D printing filament HIPS

***Gabriela Kotseva*[1], *Mara Kandeva*[1] *and Nikolay Stoimenov*[1]**

1) Institute of Information and Communication Technologies – Bulgarian Academy of Sciences, Acad. G. Bonchev str., bl. 2, 1113 Sofia, Bulgaria

Corresponding author: nikistoimenow@gmail.com

Professional article

Abstract: This article focuses on investigating the tribological processes of EasyFil™ HIPS (Dark Blue), a material used for 3D printing. To print this filament successfully, according to the manufacturer's instructions, it is necessary to heat the print head to 220-260°C and heat the printing bed to 90-110° C with cooling of 0-30%. The study establishes the optimal parameters required for printing the material and produce printed samples such as a 120x60x10 mm tile, a 60x60x10 mm tile, and a 9 mm sphere. A comparative analysis was made in the direction of other conducted experiments on filaments by the collective.

Keywords: *EasyFil™ HIPS; filament; tribological processes; sliding friction; friction coefficient; 3D printing materials; 3D printing*

1. Introduction

The use of engineering plastics is becoming more and more vital due to contemporary needs in the fields of industry, science, art, etc. One of the methods for producing plastic parts, which can be included in everyday life is the 3D printing method. With the introduction and development of additive manufacturing techniques, the production of plastic parts through 3D printing is gradually becoming more popular. The characteristics of the 3D printed materials are extremely important for production, therefore an analysis of the tribological processes occurring in 3D printed samples is required [1]. Depending on the printing settings different tribological parameters can be achieved [2]. The 3D printed materials can contribute to the analysis of different scientific and industrial processes such as the mining industry. Their accessible way of production can contribute to examining and understanding the processes in ball mills, namely the movement and interaction of grinding bodies with their grinding environment (liners, lifters, and mill shells).
The goal of the study is to determine the coefficients of friction, rolling friction, and restitution, aiming at their subsequent use for monitoring different shapes of lifters and using the determined coefficients in simulations.

2. Material

High Impact Polystyrene (HIPS) is a thermoplastic polymer composed of a mixture of polystyrene and polybutadiene rubber. Many popular materials used in 3D printing are characterized by their resistance to chemical solvents. However, in the case of HIPS, solubility is a great advantage because the material is mainly used in the filament form as a support material in 3D printing [3], [4].
High Impact Polystyrene, is widely recognized as a light and versatile material which serves the primary purpose of being a dissolvable support structure for models built from ABS material.
HIPS is a highly popular material in the field of 3D printing due to its versatile nature and unique properties. The material is made from polystyrene, a synthetic polymer involved in many household items. HIPS is produced through extrusion where the filament is heated and melted extruded through a nozzle to create the desired shape layer by layer. HIPS possesses properties that are similar to ABS

but is harder, more durable, and impact-resistant [3]. The used EasyFil™ HIPS filament is resistant to impact, acids, and more flexible and softer than the basic HIPS materials [4].

3. Printing method

3.1. Sample preparation

The production of the samples was executed through the use of a 3D printing device. This present-day printing method is financially feasible and offers a variety of options for the manufacturing of convoluted configurations. Its usage facilitates designers to actualize tangible entities based on a computer-aided design (CAD) model. It has been embraced across different sectors including agriculture, industry, medicine, and more. Among the most popular additive production methods is the fused deposition modeling (FDM) which involves the extrusion of thermoplastic filaments, in increments, to create layers [5].

According to the manufacturer's instructions, to print this HIPS filament successfully, it is necessary to heat the print head to 220-260 °C and heat the printing bed to 90-110 °C with cooling of 0-30%. For this study, tiles with dimensions of 120x60x10 mm, and 60x60x10 mm are prepared for the experiments. The samples are with the following parameters required for 3D printing the material [4]: Nozzle Temperature – 245 °C; Bed Temperature – 70 °C; Layer height – 0.2 mm; Wall Line Count – 2; Infill – 20%; Infill Pattern – Triangles; Printing Speed –60 mm/s; Cooling of 0%; Used Build plate – Raft with air gap 0.1 mm; Manufacturer – FormFutura.

For determining the coefficient of restitution a 3D printed 9 mm diameter sphere is prepared, with the same characteristics except for the infill, which is set to 100%.

4. Results

4.1. Sliding friction coefficient

In tribology, friction is distinguished into three kinetic states of the "body-antibody" tribosystem: friction at rest (static friction), friction in the transition from rest to motion, and friction in motion.

Numerous studies in the 1930s showed that in the transitional state of the system from rest to movement, a frictional force occurs, accompanied by microdisplacements in the contact spots. It can be definitely said that static friction is a complex boundary condition of the tribosystem, which is characterized by static friction force, static friction coefficient, incomplete friction angle, and contact microdisplacements. The phenomenon of preliminary displacement of the contact body was first established in 1926 simultaneously and independently by two scientists A. Verkhovsky (USSR) and Rankin (England). Predisplacement is of great importance not only for revealing the essence of the phenomenon of friction but also in the technique in cases where external friction is used to transmit motion, for example, the mode in which the driven wheels of vehicles work. Pre-movement is essential for the accurate positioning of tools, gauges, and items. For metal surfaces, it varies from 0.1 to 40 μm depending on their roughness, their physical properties, and the duration of the stationary contact. 0 a surface inclined at an angle θ (guide), which is in a state of apparent rest (Figure 1). The forces acting on the tribosystem form a static zero and the equilibrium conditions are represented by the equations: [5], [6], [7], [8], [9], [10], [11], [12], [13], [14], [15].

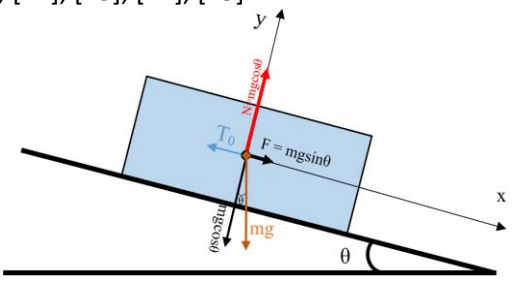

***Figure 1**. Free body diagram for a block subject to friction as it slides on an inclined surface*

The force of kinetic friction is given by:

$$\sum X_i = 0 \ \rightarrow -T_0 + mgsin\theta = 0 \quad (1)$$
$$\sum Y_i = 0 \ \rightarrow N - mgcos\theta = 0 \quad (2)$$

where T_0 is the static frictional force, which is determined by Amonton's law by neglecting the adhesion component of the frictional force, i.e.

$$T_o = \mu_0 N \quad (3)$$

In equation (3), the dimensionless parameter μ_0 is the static coefficient of friction (COF), and *N* is the normal reaction. From equation (2) for *N* is obtained

$$FN = mgcos\theta \quad (4)$$

From equations (1), (3) and (4) it follows:

$$-\mu_o mgcos\theta + mgsin\theta = 0 \quad (5)$$

and for the static COF the expression is obtained:

$$\mu_o = \frac{mgsin\theta}{mgcos\theta} = tg\theta \quad (6)$$

It can be summarized that the static COF in sliding is equal to the tangent of the angle (θ) at which the body goes from rest to apparent motion (sliding). This moment is accompanied by a jump in the force/coefficient of friction to a smaller value, known as a stick slip.
Figure 2 shows the measurements from the experiments to determine the slip angle. For each determined coefficient six measurements are made. The 3D printed samples (120x60x10 and 60x60x10) are used for obtaining the results. The obtained results from the experimental determination of the coefficient of sliding friction are shown in Table 1. In the table the measured angles in degrees and radians are given, as well as the coefficient of sliding friction is calculated for the EasyFil™ HIPS material according to the formulas mentioned above.
Compared to previous experiments [5] where the PLA+PLA average coefficient of sliding friction is experimentally determined to be 0,351, and the PETG+PETG average coefficient of sliding friction is 0,408. The material PLA and PETG materials have lower coefficient of friction, compared to the HIPS.

***Figure 2**. Photos from the experiments*

Table 1. *Coefficient of sliding friction HIPS+HIPS*

Material	Angle of friction, [θ°]	Angle of friction, [θ rad]	Coefficient of sliding friction
Hips+Hips (1)	25,01	0,436507	0,46652
Hips+Hips (2)	22,06	0,38502	0,405245
Hips+Hips (3)	23,68	0,413294	0,438553
Hips+Hips (4)	19,98	0,348717	0,363575
Hips+Hips (5)	23,64	0,412596	0,437721
Hips+Hips (6)	24,23	0,422893	0,450047
Hips+Hips avg	23,1	0,403171	0,426536

4.2. Static coefficient of rolling friction

From a mechanical point of view, friction is a type of resistance that arises when one body rolls over the surface of another body. This phenomenon cannot be explained by the absolute solid model, which considers the contact between a sphere and a surface as a point, i.e. excludes deformations in the contact. Tribology considers the contact not at one point (A), but the presence of a contact area with a distribution of normal stresses in the direction of movement (Figure 3). A "sphere-inclined plane" tribosystem is in a state of equilibrium before passing into a state of rolling. The contact area is the result of the presence of plastic, elastic or elastoplastic deformations in the direction of movement of the sphere. The normal reaction, by which the distributed normal stresses are reduced, is displaced from point A by a distance f in the direction of travel [5], [6], [7], [8], [9], [10], [11], [12], [13], [14], [15].

The conditions for equilibrium of the planar force system are obtained

$$\sum X_i = 0 \rightarrow T_o = F \tag{7}$$

$$\sum Y_i = 0 \rightarrow N = mgcos\theta \tag{8}$$

$$\sum M_{i,A} = 0 \rightarrow f_o N = Fr, \tag{9}$$

where f_0 is the lever of the force couple ($mgcos\theta$, N), and r is the radius of the sphere.

The moment of the couple ($mgcos\theta$, N) is a measure of rolling resistance and is called the static moment of rolling friction:

$$M_{f_o} = f_o N. \tag{10}$$

From equation (9) for the static coefficient of rolling friction, the expression is obtained:

$$f_o = \frac{Fr}{N} = \frac{r.mgsin\theta}{mgcos\theta} = r.tg\theta \tag{11}$$

From equation (10) it follows that the static rolling friction coefficient is defined as the product of the radius of the sphere and the tangent of the angle (θ) at which the apparent rolling of the sphere begins.

Experiments for determining the rolling friction are shown in Figure 4. For determining the angle 3 experiments are made with the same used 3D printed materials (plate with dimensions 120x60x10 mm, and 9 mm sphere) from Hips filament. The average results are taken into account. The obtained experiments are shown in Table 2.

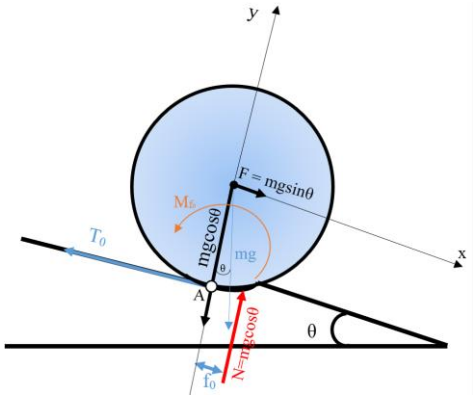

***Figure 3**. Rolling friction*

***Figure 4.** Photos from the experiments*

***Table 2.** Coefficient of rolling friction HIPS+HIPS*

Material	Angle of friction, [θ°]	Angle of friction, [θ rad]	Coefficient of rolling friction
Hips+Hips (1)	6,33	0,110479	0,110255
Hips+Hips (2)	7,94	0,138579	0,138136
Hips+Hips (3)	17,21	0,300371	0,295875
Hips+Hips avg	10,49333	0,183143	0,182121

Compared to previous experiments [8] where the PLA+PLA average coefficient of rolling friction is experimentally determined to be 0,06, and the PETG+PETG average coefficient of rolling friction is 0,07. From the table, it can be seen that EasyFil HIPS has a significantly higher value coefficient of rolling friction than the other two compared materials.

4.3. Coefficient of restitution

The coefficient of recovery (restitution) is used to demonstrate the rate of energy dissipation involving collisions of surfaces, most often a sphere. The recovery rate depends on many elements, such as the geometry of the bodies in contact, the speed of approach, the properties of the material, the duration of the contact, and any friction. The coefficient is determined by taking into account the heights before and after impact. A free-falling sphere is released from a height of 650 mm (Figure 5).

The HIPS sphere, which is 9 mm, falls on a HIPS plate with dimensions of 60x60x10 mm, after which the rebound is recorded using a high-speed camera NAC MEMRECAM HX-6 [16], [17].

For the coefficient of rolling friction 3 experiments are made, and the average value was taken. The obtained results from the experiments are shown in Table 3. To determine the recovery factor, the formula [18], [19], [20] was used:

$$e = \frac{v_2}{v_1} = \left(\frac{h_2}{h_1}\right)^{\frac{1}{2}} \tag{12}$$

where:
e - coefficient of recovery;
v_2 - velocity after bounce;
v_1 - speed before rebound;
h_1 - height before bounce;
h_2 - velocity before the rebound.

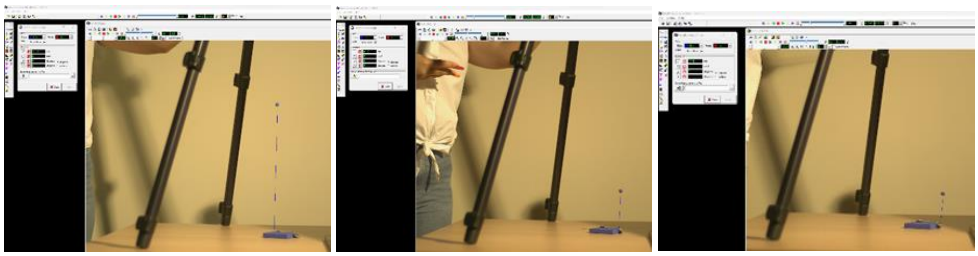

Figure 5. *Restitution experiments HIPS+HIPS*

Table 3. *HIPS+HIPS restitution coefficient*

Material+sphere	starting height [mm]	bounce height [mm]	Bounce height/starting height	Coefficient of restitution
Hips+Hips (1)	650	320,41	0,492938	0,702096
Hips+Hips (2)	650	94,47	0,145338	0,381233
Hips+Hips (3)	650	67,65	0,104077	0,32261
Hips+Hips avg	650	160,8433	0,247451	0,497445

Compared to previous experiments [17] where the PLA+PLA average coefficient of restitution is experimentally determined to 0,549, From table 3 it can be seen that EasyFil HIPS has a lower value of the coefficient of rolling friction than the other two compared materials.

5. References Future work

The experimentally determined sliding friction, rolling friction, and restitution coefficients will be used for 3D simulation modeling of mining processes. The coefficients are required for proper simulation results. The aim of using the coefficients in simulations is to experiment with different shapes of milling bodies and milling environments.

6. Conclusion

In conclusion, the coefficient of sliding friction, rolling friction, and restitution were experimentally determined for HIPS 3D printed material by the gravitation-based device method. The coefficient of sliding friction is experimentally determined to be 0,426, the coefficient of rolling friction is experimentally determined to be 0,182, and the coefficient of restitution is 0,497. There is not a significant difference between the compared PLA and PETG materials, except for the rolling friction. The proper use of the coefficients can contribute to better results in simulations for experiments aiming at interactions and movements of different materials.

Acknowledgments

This research was carried out as part of project No КП-06-N47/5 "Research and optimization of the interaction between grinding bodies and media with an innovative shape", financed by the Bulgarian National Science Fund.

References

[1] Kotseva G., Stoimenov N., Klochkov L., Tribological studies of 3D printed filaments. An overview, XXXII International Scientific and Technical Conference, ADP - 2023., Sozopol, Bulgaria., Publishing house of TU-Sofia ISSN – 2682-9584, pp. 150-154, Publisher Department “Automation of Discrete Production Engineering“ Mechanical Engineering Faculty, Technical University – Sofia, 2023
[2] Hanon, M.M., Alshammas, Y. & Zsidai, L. Effect of print orientation and bronze existence on tribological and mechanical properties of 3D-printed bronze/PLA composite. Int J Adv Manuf Technol 108, (2020). pp. 553–570 https://doi.org/10.1007/s00170-020-05391-x
[3] All You Need to Know About HIPS for 3D Printing, Published on June 19, 2023 by Aysha M., https://www.3dnatives.com/en/hips-support-240820205/#! (last accessed July 2023)
[4] 3D Jake - https://www.3djake.com/3d-printer-filaments/hips-filament (last accessed July 2023)
[5] Gyoshev S., Stoimenov N, Paneva M., Determination of the friction coefficient of 3D printed materials - Part II - Sliding friction, 10th International Conference on Mechanical Technologies and Structural Materials (MTSM 2021), ISSN: 1847-7917, pp. 43-46, Split, Croatia, September 23-24, 2021, Croatian Society for Mechanical Technologies, Croatia
[6] J O Bird BSc, CEng, MIEE, CMath, FIMA, FCollP, MIEIE, P J Chivers BSc, PhD, 1993 Newnes Engineering and Physical Science Pocket Book
[7] Malyshev V.N., (1871), Advances in Friction-Stir Welding and Processing, 201Benjamin Silliman, Principles of Physics, Or Natural Philosophy, Ivison, Blakeman, Taylor & company publishers.
[8] Stoimenov N., Gyoshev S., Paneva M. Panev P., Determination of the friction coefficient of 3D printed materials - Part I - Rolling friction, 10th International Conference on Mechanical Technologies and Structural Materials (MTSM 2021), Split, Croatia, September 23-24, 2021, Croatian Society for Mechanical Technologies, Croatia, ISSN: 1847-7917, pp. 149-152,
[9] Kragelsky I., Friction and wear, Mashinostroyeniye, M., 1968.Bowden F. P., D. Tabor, The friction and lubrication of solids, Oxford at the clarendon Press, 1964.
[10] Moore D. F., Principles and application of Tribology, Pergamon Press, Oxford, 1975.
[11] Moore D., The friction and lubrication of elastomers, Pergamon Press, 1977.
[12] Gras R., Tribologie, Principes et Solutions Industrielles, L'usinenouvelle, Dunod, 2008.
[13] R. Bassani, Tribology, Pisa University Press, 2013.
[14] Kandeva M., The contact approach in engineering tribology, TU-Sofia publishing house, 2012.
[15] Kandeva M., Dynamics and tribology of machines, Part II: Tribology, TU-Sofia Publishing House, 2020 (in Bulgarian).
[16] NAC MEMRECAM HX-6 Specification Sheet
[17] NAC Memrecam https://www.nacinc.com/ (last accessed July 2023)
[18] N. Ayrilmis, M. Kariz, J.H. Kwon, M. Kitek Kuzman, Effect of printing layer thickness on water absorption and mechanical properties of 3D-printed wood/PLA composite materials, Int. J. Adv. Manuf. Technol., 102 (5-8) (2019), pp. 2195-2200, 10.1007/s00170-019-03299-9
[19] Stoimenov N., Paneva M., Kotseva G., Sokolov B., Simulation Modelling of Coefficient of Restitution, International Scientific Congress Machines, Technologies, Materials, 09-12 March 2022, Borovets, Bulgaria, Vol. 2, Scientific Technical Union of Mechanical Engineering Industry – 4.0, pp. 30-34, 2021, ISSN:2535-0021
[20] Adli Haron and K A Ismail 2012 IOP Conf. Ser.: Mater. Sci. Eng. 36 012038

Methodical concept development for a leakproof diameter-variable nozzle for the FLM process in additive manufacturing

Michael Krampe[1] ***and Bernd Kuhlenkötter***[1]

1) Chair of Production Systems, Ruhr-Universität Bochum, Universitätsstraße 150, 44801, Germany

Corresponding author: krampe@lps.rub.de

Original scientific article

Abstract: The aim of this paper is to develop a concept for a variable-diameter nozzle which enables a continuously adjustable volume flow in the FLM process. The intention is to reduce the known conflict between fast printing with a large nozzle diameter and detailed printing with a small diameter. For this development, existing ideas and patents were investigated and analysed. The consensus of previous approaches was worked out and it was found that most approaches are based on very fine mechanics through which the liquid plastic is to be carried out. This raises the problem of the leaking of such fine mechanics, which no previous concept addresses. As a new approach, the nozzle was equipped with a hose, which means that the liquid plastic has no direct contact with the mechanism and the nozzle is leakproof. Initial tests show that the design works and that variable strand deposition is possible.

Keywords: *additive manufacturing; fused layer modeling; variable-diamter nozzle; 3D-printing; leakproof nozzle*

1. Introduction

The importance of additive manufacturing processes in today's fast-paced industry continues to grow rapidly. Through its utility in producing functional samples and prototypes quickly and easily, it can reduce development time and new product development costs in many industries. But the number of additively manufactured end products also continues to become more relevant as the processes improve in quality [1, 2] Fused Layer Modeling (FLM), arguably the most common additive manufacturing technique, is often preferred for creating prototypes and small batches due to its low cost of entry. The FLM procedure involves guiding a filament of thermoplastic into a heating system via an extruder, which then melts the material into a semi-solid state. This semi-molten material is then forced through a nozzle, laying it out in predetermined paths onto either a construction base or an existing layer. Upon contact, the newly extruded material fuses with the existing strands, solidifying to form a stable bond once it cools [3].

In the operation of Fused Layer Modeling (FLM) systems, the nozzles typically have a standard circular exit aperture of a fixed size. However, depending on the degree of precision required for a component, operators can choose to use a smaller nozzle, ranging from 0.1 mm to 0.4 mm in diameter, although at the cost of a slower production speed. Conversely, for quicker manufacturing times, larger nozzles up to 2 mm or more in diameter can be used, but this sacrifices the level of detail that can be achieved. Therefore, it's up to the FLM system operator to decide whether speed or detail is a priority, which is determined by the chosen nozzle size. An innovative solution comes in the form of contemporary multi-nozzle systems that accommodate various nozzle sizes within a single FLM setup [4, 5]. This is useful for alternating between different materials during the construction process, such as support and building materials. However, the advantage of varying nozzle sizes in this context is yet to be proven. Another possibility is a nozzle with an adjustable diameter, which can be modified by increasing or decreasing its size. This would allow high-precision manufacturing with a smaller diameter nozzle in detailed sections of a component, and quicker production with a larger diameter

nozzle in less detailed areas. There are already various concepts in existence for this kind of system, some of which have been derived from academic research while others are outlined in patent specifications. The approaches are very different. There are attempts to make the adjustment possible through a fine mechanism, but some also try it with the help of special materials. In most nozzles, a small opening at the end of the nozzle is adjusted, while some solutions also change more complex outlet openings. In addition, the approaches can be classified according to whether the adjustment should be discrete or continuous. In other words, whether there are two or more predefined states of the nozzle that can be switched between, or whether the opening is continuously adjustable. So far, only a few of the approaches have been implemented in a prototype or even a product. Most of them, especially the fine-mechanical approaches, seem highly complex and might be difficult to produce due to the small size they aim for. One implemented approach, which can at least demonstrate the principle of mechanical adjustment in reality, uses a larger variable nozzle for depositing strands of liquid concrete [6]. In the following chapters, some approaches are presented and then methodically analysed. In doing so, we will look at how the approaches taken so far are similar, both in terms of their approach and the problems that can still arise. Based on this, an own concept for a continuously variable nozzle will be presented. This will also be manufactured and the first test runs will be presented.

2. Related work

The development of an FLM nozzle with a variable nozzle diameter is not a new idea. The oldest approach researched dates back to 2011 and shows a two-stage nozzle in which it is possible to switch between two different diameters with the help of an additional casing inside the nozzle [7]. The nozzle is shown in Figure 10. This approach for discrete adjustment was subsequently taken up and pursued by several developers in a similar way [8, 9, 10, 11, 12].

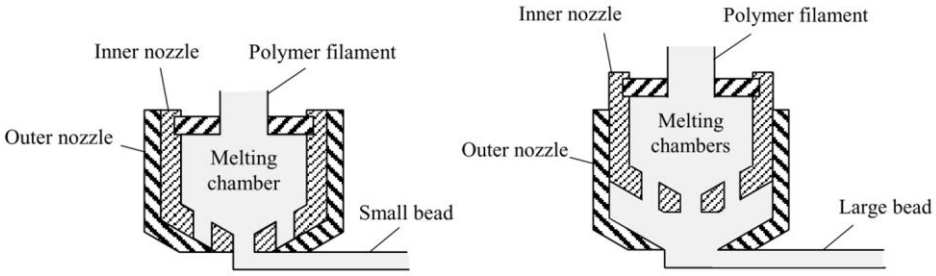

Figure 10. *Two stage nozzle with a small diameter (left) or a large diameter (right) [7]*

The more recent approaches show in more detail how the mechanics are designed to be movable. An advantage of this design is the possibility to maintain a round nozzle outlet despite the adjustment, which is common in the FLM process. The effects of non-round nozzle outlet geometries have already been investigated in previous tests by the authors [13]. Furthermore, there is an approach to make the nozzle opening discretely variable with the help of an additional plate in front of the nozzle opening [14]. This approach is very similar to the concept of a multi-nozzle system, which will not be discussed further in this paper. Finally, in the case of discretely variable nozzles, there is also the idea of changing the deposition behaviour of the strand by means of a special shape of the outlet geometry. Through a slit as an opening, it is possible to change between a narrow and a wider deposited strand with the help of a 90° rotation [15]. However, since the cross-sectional area of the opening is not varied, the influence on the printing speed is limited. For the continuously adjustable variable nozzles, there are more different implementation approaches. The research shows two approaches in which the adjustment should be carried out through special material properties. In the first, a soft ring is pressed through a mechanism, which compresses the inside of the ring and thus reduces its size [16]. However, it is questionable which material can be compressed in such a targeted manner and also withstand the conditions inside the nozzle. In the second variant, the material Terfenol-D is to be used, whereby the opening is to be magnetically adjustable [17]. Unfortunately, it is not clear from the

publication how exactly the system is to be implemented and controlled in detail. The other approaches use different mechanical solutions to enable the adjustment. For example, there are approaches that are constructed similar to a camera lens from many overlapping lamellae [18, 19]. Some approaches use individual sliding elements to create a movable opening of different shapes, such as a square [6] or a hexagonal [20]. One approach is based on continuously closing an opening with a pointed cone from the inside, resulting in an increasingly fine ring as a cross-sectional area [21]. A further one is based on closing an opening continuously from the inside with a pointed cone, resulting in an increasingly fine ring as the cross-sectional area. Another would like to overlay two triangular nozzle openings and make them rotatable so that they overlap and form a triangle or, when twisted, produce a hexagon with a smaller cross-sectional area [22]. Furthermore, a triangular nozzle could also be used, in front of whose opening a plate is gradually moved from one edge of the triangle. In this way, the shape of the opening remains triangular throughout, but the triangle becomes smaller. In order to ensure that the tip of the triangle is always in the direction of the printing, an additional axis has been considered for this nozzle in order to be able to rotate the nozzle [23]. In another approach, the nozzle opening consists of a slit that can be shortened from both sides by sliding elements. This allows the width of the strand to be adjusted variably. As long as no spiky paths with many directional changes are to be deposited, this nozzle can be well suited for producing hollow bodies, for example [24]. A similar approach dispenses with the rotation and instead lengthens the slit and adds an chamber of liquid melt. In this way, it is intended that an entire layer of the component can be printed as a whole [25]. In the following chapter, a strategy for a new construction is methodically applied on the basis of the researched previous ideas and approaches, which analyses them and tries to learn from them.

3. Methodical approach

After the presentation of the state of the art in research and technology, the research results are now to be analysed. The aim should be to form a consensus from the previous ideas and to incorporate this into a new development of a possible variable nozzle. To achieve this, comparative categories will first be presented to analyse the previous approaches. The first point of comparison is the number of moving parts. Here, only the components that provide adjustment directly at the nozzle tip are considered. The number of components that trigger the mechanism, for example a motor with gear parts, is not counted. This can give an overview of the complexity of the nozzle mechanism. Especially due to the often very small form factor, many moving parts can also create or amplify potential problems. For example, more moving parts create more sliding surfaces, which can cause leaks in the system. On the other hand, the number of moving parts often influences the possible shape of the nozzle exit. To create a moving hexagon shape, more parts are needed than for a square. Previous investigations by the authors have shown that as many corners as possible, and thus as round a nozzle exit shape as possible, enables a cleaner strand deposit [13]. Most of the moving parts have the approaches, which are shaped like a camera lens. Here, due to the lamellar structure, another point of discussion comes into view. the smaller the nozzle is set, the stronger the relationship between the nozzle opening and the thickness of the lamellae becomes. Viewed in detail, it is as if the plastic does not have to glide through a smooth hole but has to complete a kind of spiral staircase. Since the laminar effect is very fragile when it comes out of an FLM nozzle, there is reason to suspect that the strand will come out of the nozzle slightly uneven. Furthermore, the lamellae, and thus directly the gliding surfaces of the adjustment mechanism, come into contact with the plastic. Together with the pressure, the hot temperatures and the efforts to make the fins as thin as possible in order to weaken this spiral staircase effect, some problems can arise here. Thus, a high number of moving parts can also bring advantages. Next, the nozzles are classified as to whether their adjustment is discrete or continuous. The new nozzle to be designed should be continuous, but the experience of the discrete nozzles should also be included. The tightness of the nozzle is then assessed. Since most of the nozzles presented were not implemented and therefore could not be tested in real life, the authors were only able to look at the design images and use their experience to rate whether the leaktightness could

cause problems. Thus, the assumption is that many sliding surfaces between the moving components have a rather negative effect on the leaktightness. Furthermore, the operating principle that generates the adjustment of the nozzle is outlined. With most nozzles, simple mechanical movements are intended to make the opening variable. Due to the small form factor, this requires complex fine mechanics and could therefore be seen negatively. On the other hand, some of the alternatives are very questionable in their function or have other limitations. Finally, the shape of the nozzle opening is described. As already mentioned, preliminary tests by the authors show that by increasing the number of corners of the geometry, the quality of the strand deposition can be very well matched even with non-circular nozzles. The print result of a hexagonal orifice can nearly not be differentiated from a round nozzle, whereas a triangular nozzle produces visible differences. The summary of the comparisons can be viewed in Table 3 and Table 4.

Table 3. *Comparison of the research findings (part 1)*

	Bachmaier et al. 2015	Feiyue et al. 2011	H. Brooks et al. 2011	Heel et al. 2018	Hetschel et al. 2012	Lind et al. 2015	Löffler et al. 2019	Ramia 2020	Rode et al. 2021
Moving parts	1	1	1	1	12	1	0	6	1
Discreet/Continuous	C	C	D	C	C	D	D	C	D
leakproofness	high	medium	high	high	medium	high	high	low	medium
Operating principle	material compression	shape rotation	mechanical	mechanical	mechanical	mechanical	shape rotation	mechanical	mechanical
exit geometry	round	triangle, hexagon	round	round	polygon	round	slit	hexagon	round

Table 4. *Comparison of the research findings (part 2)*

	Schuh et al. 2017	Sertoglu 2021	Sharma et al 2021	Shin 2015	Tseng et al. 2001	Vanacker 2017	Wan	Xu et al. 2016	Xu et al. 2018
Moving parts	1	2	2	4	1	2	18	1	4
Discreet/Continuous	C	C	C	D	C	C	C	C	C
leakproofness	medium	medium	medium	medium	high	medium	medium	high	low
Operating principle	mechanical	mechanical	mechanical	mechanical	mechanical	mechanical	mechanical	magnetic	mechanical
exit geometry	triangle	slit	slit	round	ring	slit	polygon	round	square

If you analyse the comparisons between the approaches, you will notice some commonalities from which you can draw a kind of scientific consensus on this topic. A continuously adjustable nozzle, for example, appears to be significantly more complex, since it usually requires more moving parts, which then also results in complex nozzle exit geometries. Discretely adjustable nozzles, on the other hand, can usually retain the round exit geometry common to the process and require fewer moving parts. Since the number of moving parts is also suspected to be related to leakages, the more complex continuously adjustable nozzles have a further disadvantage here.

Thus, it can be summarized that if a continuous adjustment is desired, a non-round geometry as well as a higher number of moving parts seems more appropriate. This in turn will probably increase the chance of leakage problems. Since none of the approaches investigated so far addresses the problem of leaktightness, the authors suspect that this could often be a reason for not pursuing the idea further. Therefore, the leakage problem will be addressed in the design as well. Finally, the results of their own preliminary investigations are to be included, from which it has emerged that a hexagonal shape should be chosen if possible, since this enables a continuous adjustment mechanism and at the same time produces very similar qualities in strand deposition as the usual round opening geometry. The implementation of these analysis results in a design that will be presented in the next chapter.

4. Results

With the help of the results obtained from the analysis of the previous approaches, an initial concept is now being created as shown in Figure 11. The filament is to be fed using standard components and only the tip of the nozzle is to be redesigned and continuously adjustable. The variability is to be created by sliding elements that generate a hexagonal opening. The adjustment is not to take place in one point, but a kind of tunnel is to be variably designed so that the sliding elements do not bend despite pressure and temperature, as could happen with thin lamellae. To deal with the issue of leaktightness, a plastic hose was found that can withstand the temperatures of additive manufacturing with the plastic polylactides and yet is very soft and flexible and also shows no signs of abrasion. This hose is installed via a hose fitting which serves as the first nozzle and melts the filament and guides it into the hose. This hose lies inside the slider elements and is squeezed by them, thus reducing the opening. Since the sliding elements increase the mass of the system to be heated and the plastic filament must be kept at temperature while passing through the hose, the sliding elements are hollow and contain additional heating cartridges and temperature sensors. The hose itself is held to the fitting by a hose clamp to prevent slippage due to pressure and friction within the hose.

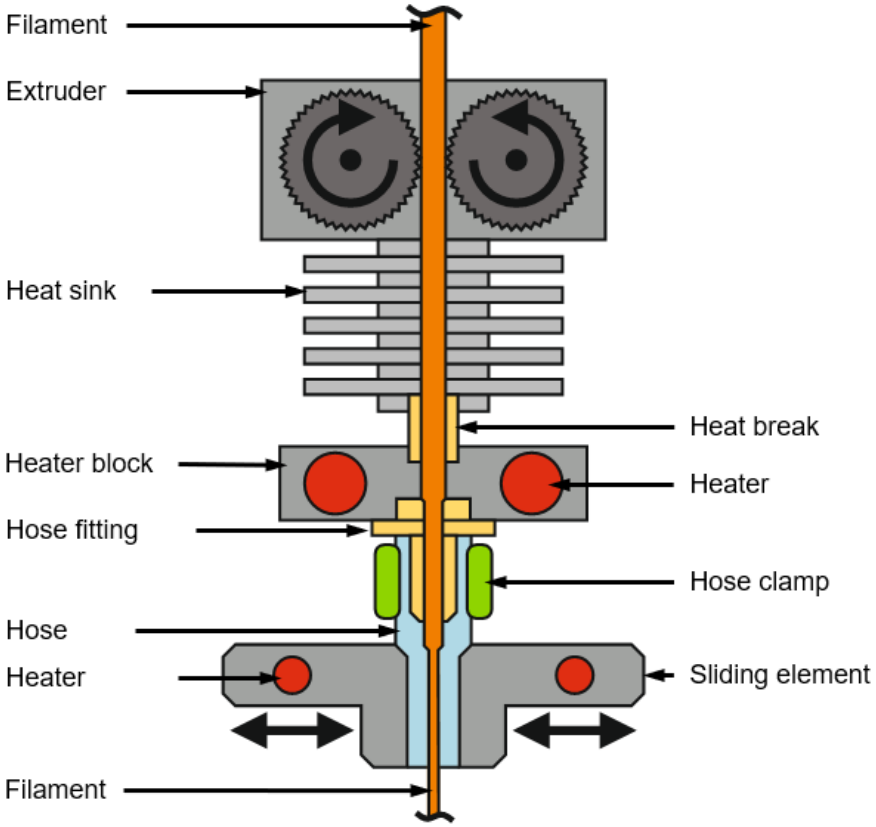

Figure 11. *Concept of the continuously variable nozzle*

On the basis of the concept presented, the design and manufacture of a prototype is started. The goal is first to test the hose as an element for leak tightness as well as the continuously variable adjustment mechanism itself. The nozzle consists of a base plate on which everything is built. The six sliding elements form a kind of tunnel which emerges from the nozzle as the lowest point and ends evenly with the hose. In addition, the sliding elements are hollow, as previously explained, and contain heating cartridges and temperature sensors. As a counterpart to the base plate, there is a cylinder in which the hose fitting and further heating elements are attached. This cylinder is then attached to the usual extruder via a heatbrake. Due to the heavy weight of the entire system, everything is currently attached to a six-axis industrial robot. Furthermore, there is a ring on the sliding elements, which is used for adjustment. If this ring is turned, all the slide elements move uniformly and the nozzle

opening is continuously expanded or reduced. In the future, this ring will also be driven electrically so that the variable adjustment can be included in the programming of the system. Figure 12 to Figure 15 show the prototype and some described details. Figure 12 shows the sliding elements and the ring for adjustment. Figure 13 shows the nozzle outlet with the tips of the slide elements and the hose. As can be seen in Figure 14 and Figure 15, printing through the nozzle works. The hose withstands the conditions and the heated plastic leaves the nozzle clean. It was also possible to test the adjustment mechanism in initial trials by moving the ring with a pair of pliers. The nozzle outlet adjusts accordingly and a narrower strand leaves the nozzle. As was to be expected, however, the motor speed of the extruder must also be adjusted depending on the adjustment of the nozzle. This connection of variables also exists with the usual use of different nozzle diameters and should be taken into account in future programming.

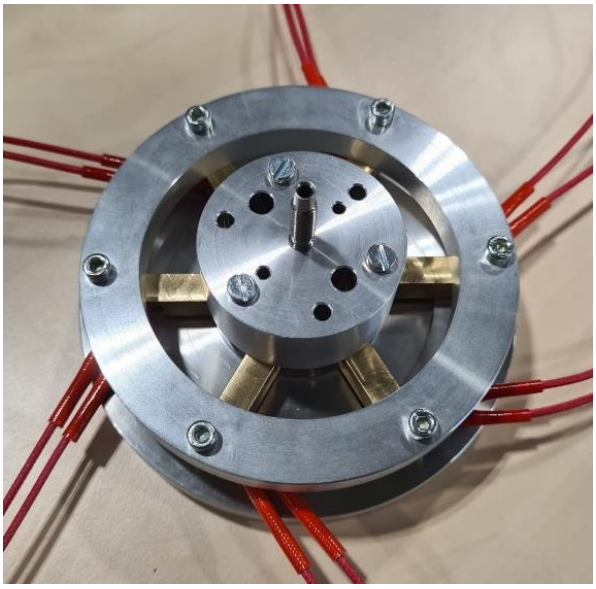

Figure 12. *The view from above of the nozzle element with the brass sliding elements*

Figure 13. *The nozzle exit geometry with the inserted hose in detail*

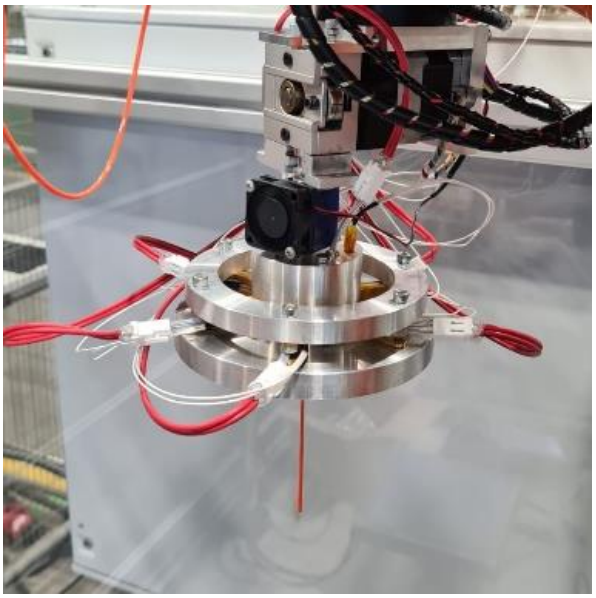

Figure 14. *The nozzle from above when printing into the air*

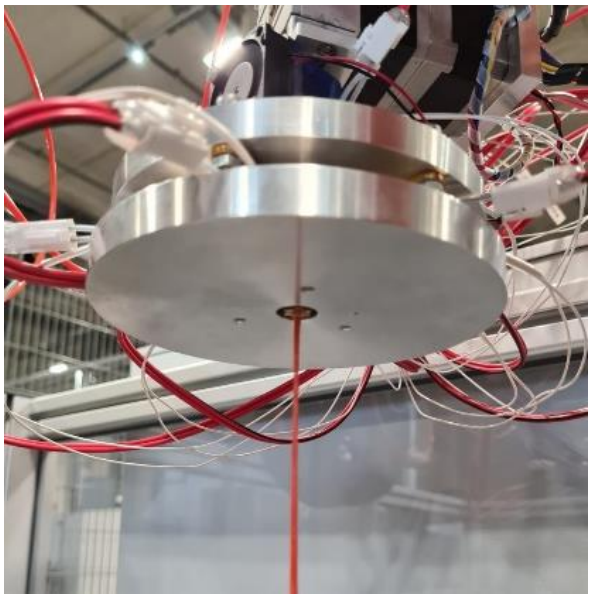

Figure 15. *The nozzle from below when printing into the air*

5. Conclusion

In conclusion, the detailed research on previous approaches of variable adjustable nozzles in additive manufacturing shows a good overview, with the help of which some kind of consensus of the previous ideas can be created. The consensus from the previous design trials of a variable size nozzle shows that a mechanical solution is the most desired, as only this allows a clean continuous variability of the exit geometry. Furthermore, the analysis shows that this requires several moving parts, resulting in an atypical non-round exit geometry. From the authors' own previous experiments, it is already known that a hexagonal shape can be generated well with a moving mechanism and, moreover, that the deposited strands are very similar to those of a round nozzle. Furthermore, the problem of leakage can be suspected by the analysis over almost all approaches. From this information and experience, a new concept for a nozzle with an approximately round, continuously variable outlet geometry is formed. A hose serves to separate the liquid plastic from the fine moving mechanics and seems to keep the nozzle completely leakproof. This sets the new concept apart from all previous approaches. The prototype produced shows that the hose can withstand the conditions of pressure and temperature and that the adjustment mechanism works in the application. Even though printing has so far only been done into the air and no strands have yet been deposited on a build platform, the material flow can be altered by the variability of the nozzle.

The next step is to make the adjustment electrically controllable and to include it as a variable in a program sequence. This should make it possible to deposit strands whose dimensions can be changed significantly more variably during deposition than it is possible with present additive manufacturing systems. The overall goal of developing a nozzle to resolve the conflict between fast printing with a high volume flow and the fine printing of details can thus be continued.

References

[1] Javaid M, Haleem A, Singh RP et al. (2021) Role of additive manufacturing applications towards environmental sustainability. Advanced Industrial and Engineering Polymer Research 4:312–322. doi: 10.1016/j.aiepr.2021.07.005

[2] Shaqour B, Abuabiah M, Abdel-Fattah S et al. (2021) Gaining a better understanding of the extrusion process in fused filament fabrication 3D printing: a review. Int J Adv Manuf Technol 114:1279–1291. doi: 10.1007/s00170-021-06918-6

[3] Gebhardt A, Hötter J-S (2016) Additive manufacturing. 3D printing for prototyping and manufacturing. Hanser Publications; Hanser Publishers, Cincinnati, OH, Munich, Cincinnati

[4] Abilgaziyev A, Kulzhan T, Raissov N et al. (2015 - 2015) Design and development of multi-nozzle extrusion system for 3D printer. In: 2015 International Conference on Informatics, Electronics & Vision (ICIEV). IEEE, pp 1–5

[5] Ali MH, Mir-Nasiri N, Ko WL (2016) Multi-nozzle extrusion system for 3D printer and its control mechanism. Int J Adv Manuf Technol 86:999–1010. doi: 10.1007/s00170-015-8205-9

[6] Xu J, Ding L (2018) Volume - forming 3D concrete printing using a variable - diameter square nozzle. In: Creative Construction Conference 2018 - Proceedings. Budapest University of Technology and Economics, pp 104–113

[7] H. Brooks, A. Rennie, T. Abram et al. Variable fused deposition modelling - concept design and tool path generation. doi: 10.13140/2.1.2280.2887

[8] Heel M, Hermann D, Schlichting K (2018) DE 10 2018 114 008 A1. Offenlegungsschrift(DE 10 2018 114 008 A1)

[9] Iee C (2017) Koreanisches Patent. Eingetragene Patentveröffentlichung(10-1967699)

[10] Lind RF, Post BK, Cini CL (2015) US 9 , 821 , 502 B2. United States Patent(US 9 , 821 , 502 B2)

[11] Meshorer Y, Vasilevski A (2016) Extruder System for Additive Manufacturing. EUROPEAN PATENT(EP 3 081 364 B1)

[12] Shin B (2015) Düse mit variablem Durchmesser eines 3D-Druckers und ihre Steuerungsmethode. Eingetragende Patentveröffentlichung(10-1725302)

[13] Krampe M, Walter F (2022) Experimental investigation of the influence of different nozzle exit geometries in fused layer modelling
[14] Rode S, Sarraf S, Hamine S et al. (2021) Design and Simulation of a System fpr Variable Bead Size Deposition in FDM. Virtual International Conference on Product Design, Development, and Deployment 2021
[15] Löffler R, Koch M (2019) Innovative Extruder Concept for Fast and Efficient Additive Manufacturing. IFAC-PapersOnLine 52:242–247. doi: 10.1016/j.ifacol.2019.10.071
[16] Bachmaier G, Morra C, Vittorias J et al. (2015) DE 10 2015 217 143 A1. Offenlegungsschrift(DE 10 2015 217 143 A1). https://patents.google.com/patent/DE102015217143A1/en
[17] Xu P, Hu M, Li N et al. (2016) Magnetic Controlled Variable Diameter Nozzle for Wood Powder 3D Printer. Rev Téc Ing Univ Zulia. doi: 10.21311/001.39.8.11
[18] Hentschel M, Pape S (2012) DE 10 2012 013 381 A1. Offenlegungsschrift(DE 10 2012 013 381 A1)
[19] Wan Q, Xu Y, Lu C (2018) A fundamental study of parameter adjustable additive manufacturing process based on FDM process. MATEC Web Conf 189:5001. doi: 10.1051/matecconf/201818905001
[20] Ramia M (2020) US 2021/0031436 A1. US Patent(US 2021/0031436 A1)
[21] Tseng AA, Tanaka M (2001) Advanced deposition techniques for freeform fabrication of metal and ceramic parts. Rapid Prototyping Journal 7:6–17. doi: 10.1108/13552540110365117
[22] Feiyue W, Zhen S, Xue L (2011) Eine 3D-Druckerdüse. Gebrauchsmusterpatent(CN 204020008 U)
[23] Schuh CA, Myerberg JS, Fulop R (2017) WO 2017/106787. International Application(WO 2017/106787)
[24] Vanacker G (2017) EP 3 117 982 A1. European Patent Application(15177165.6)
[25] Sharma V, Roozbahani H, Alizadeh M et al. (2021) 3D Printing of Plant-Derived Compounds and a Proposed Nozzle Design for the More Effective 3D FDM Printing. IEEE Access 9:57107–57119. doi: 10.1109/ACCESS.2021.3071459

Selection of the gating system for gravity casting using numerical simulation

***Ivana Dumanić Labetić*[1], *Sonja Jozić*[1], *Dražen Bajić*[1] *and David Stipić*[1]**

1) Faculty of Electrical Engineering, Mechanical Engineering and Naval Arhitecture, University of Split

Ruđera Boškovića 32, 21000 Split, Croatia

Corresponding author: sjozic@fesb.hr

Professional paper

Abstract: The primary object of this study was to simulate the gravity casting of lead through the utilization of casting process simulation tool. The analysis of the casting procedure relied on the simulation software known as NovaFlow&Solid. A software suite designed for computer-aided design/computer-aided manufacturing (CAD/CAM) was employed to aid in the design process. Furthermore, this paper presents an examination of the impact of the gating system on both shrinkage and air entrapment, ultimately identifying the optimal configuration.

Keywords: *gravity casting; simulation; NovaFlow&Solid; gating system*

1. Introduction

Casting, one of the oldest manufacturing processes, remains a fundamental technique for producing complex metal shapes economically and with minimal machining requirements. The process involves pouring a liquid material into a mould, allowing it to solidify and take the desired shape. Casting production comprises of two main stages: the filling process and the solidification process [1].

Ensuring quality casting remains a challenge, particularly in the design of gating and riser systems, which largely relies on the experience of technicians. A particular concern in casting are shrinkage defects, which lead to voids and porosity as the casting material cools and solidifies. To address this, there is need for a computer-aided casting process design tool, integrating CAD, simulation, and optimization functionalities to ensure casting quality [2].

Casting simulation software plays an important role in optimizing production processes, predicting defects, and reducing the need for costly trial-and-error methods. Casting simulation programs employ a variety of methodologies to predict casting outcomes, taking into account factors such as thermo-physical properties of alloys and boundary conditions. These simulations can achieve a relatively high degree of accuracy in predicting the casting and solidification processes [3]. By virtually simulating casting procedures, potential defects like shrinkage and porosity can be anticipated, enabling the identification of flaws before actual casting takes place and thereby preventing costly trial and error processes [4]. Adjustments to gating and feeder systems, as well as technological modifications to casting parameters, can be made using computer simulations to mitigate such defects and challenges [5–7].

For instance, Kwon et al. utilized the AnyCasting software to optimize the gate and runner design for an automotive component in high-pressure die casting. They also employed ProCAST simulation software to simulate the high-pressure die casting of tensile test samples [8] and automotive parts [9]. Radiša et al. [10] employed numerical simulation to validate their design methodology and optimize the feeding system in the casting process of Pelton turbine buckets. Dučić et al. [11] used MAGMA5 software to verify the optimized gating system geometry in gravitational sand casting for cutting tooth holders. Vossel et al. [12] utilized Magmasoft software to simulate casting and solidification processes in gravity casting. Additionally, Duan et al. [13] found that FLOW-3D software provided more accurate results for high-pressure die casting of automotive parts compared to ProCAST software.

In this paper, numerical simulations are used to optimize the gating system. The goal is to assess the effectiveness of the selected simulation program in identifying and resolving casting defects for gravity casting of lead component.

2. Theory and material

During the cooling of molten metal from the liquid state to room temperature, there are three different phases of the contraction volume, commonly known as shrinkage, Figure 1.
Shrinkage in liquid metal typically undergoes several stages. Initially, there is the first contraction, followed by solidification contraction while the material is in a semi-solid state, and finally, additional contraction upon solidification at the freezing point. Generally, materials with face-centred-cubic and hexagonal close-packed structures tend to exhibit the highest levels of contraction upon solidification. Lead, Pb, has a face-centred cubic lattice and shows a contraction of approximately 3.2 %. This dense material has great value for contraction on solidification which is why the goal of this work is to make an appropriate gating system without the usage of a feeding system.

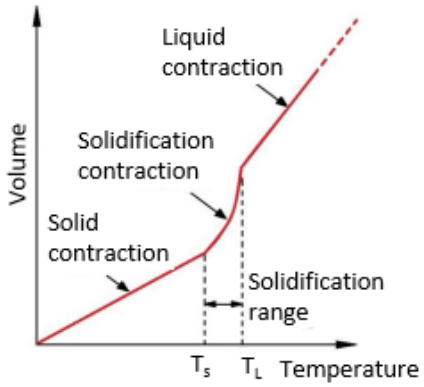

Figure 1. *Schematic illustration of shrinkage regimes* [14]

NovaFlow&Solid software employs the finite volume method to solve the equation of state, and is founded on control volume mesh technology, enabling the 3D model's surface to influence the shape of the mesh elements along the casting's boundary [16]. In the theory of quasi-equilibrium two-phase zones, which is implemented in the NovaFlow&Solid software, it is assumed that the sum of the volumetric fractions of the solid phase, denoted as *s(t),* the volumetric fraction of the liquid phase, denoted as *l(t),* and the volumetric fraction of the void or empty space, denoted as *e(t),* equals 1 [16]:

$$s(t) + l(t) + e(t) = 1 \tag{1}$$

where *t* is a time.
The time derivation of the two-phase balance equation takes the following form:

$$\frac{\partial s(t)}{\partial t} + \frac{\partial l(t)}{\partial t} + \frac{\partial t(t)}{\partial t} = 0 \tag{2}$$

Reduced law of mass conservation is expressed as a function of the density of the liquid phase of the metal, $\rho_s(T)$, which varies with temperature, and the density of the solid phase of the metal, $\rho_l(T)$:

$$\rho_s(T)\frac{\partial s}{\partial t} + \frac{\partial}{\partial t}(\rho_l(T)l) = 0 \tag{3}$$

The heat conduction equation, accounting for sources and convective heat transfer, is as follows:

$$S\rho_S(T)C_S(T)\frac{\partial T}{\partial t} + l\rho_l(T)C_l(T)\left(\frac{\partial T}{\partial t} + V\nabla T\right) - q\rho_S(T)\frac{\partial s}{\partial t} = \mathrm{div}(\lambda(T)\nabla T) \tag{4}$$

where C_S is specific heat of the solid phase, C_l is the specific heat of the liquid phase, λ is heat conduction coefficient of alloy which is temperature-dependent and q is crystallization heat of alloy. The heat conduction equation for die is given by the equation:

$$\rho_k(T)X_k(T)\frac{\partial T}{\partial t} = \mathrm{div}(\lambda_k(T)\nabla \mathrm{T}) \tag{5}$$

where *k* indicates die material.

In this paper, Pb is used for producing fishing sinkers. Lead is one of the first metals that appeared in production. It has good properties such as high flexibility and ductility, and corrosion resistance. Today, due to its proven recyclability, lead is widely used in the production of battery grids, ammunition, anti-radiation, etc. Fishing sinkers serve as crucial weights to accompany baited hooks, aiding in adjusting the lure or bait to reach the desired depth. These sinkers play a vital role in enhancing casting distance and anchoring ability, which is why they are typically crafted using poured lead due to their ease of casting. Diverse fishing methods call for different styles of sinkers, each tailored to optimize effectiveness. The various shapes of sinkers cater to a wide range of fishing applications, and the selection depends on factors like bottom conditions and the current in the fishing area. For instance, sandy, muddy, or rocky bottoms necessitate specific sinker designs for optimal performance. Therefore, it is essential to choose the right type of fishing sinker according to the specific circumstances.

3. Gating system setup

In the experimental part of the work, the construction of the mould and the simulation of casting were processed. Casting is under the action of gravity while the mould is permanent (Al-alloy). The casting component is a lead sinker used in fishing. The purpose of such lead is to ensure quick sinking and easier throwing of the lure. The 3D model of the fishing sinkers is conducted by means of Solidworks, as shown in Figure 2, with the largest dimension of 110 mm.

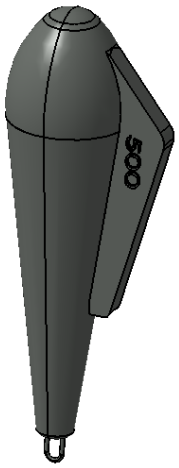

Figure 2. *3D model of sinker*

The 3D model serves as a critical input for both design and analysis purposes. The dimensioning of the gating system is a crucial consideration, as it needs to facilitate the efficiency and enable the filling of the mould with molten metal. Gating systems can be classified based on their orientation in relation to the dividing plane, resulting in two main categories: vertical and horizontal. Additionally, gating systems can further be classified based on their positioning as top, parting line, and/or bottom configurations. By trial and error procedure, the vertical gating system was chosen for gravitational casting. The gating system is placed on top of the casting and includes the pouring basin and sprue.

The purpose of the casting simulation was to find out which gating system gives the best quality castings. Four simulations were carried out, each of which contains different dimensions of the gating system, Figure 3.

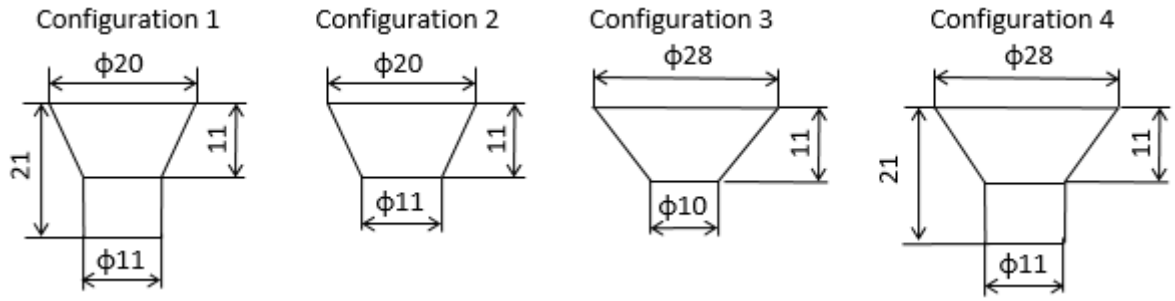

Figure 3. *The different configurations*

The 3D casting model with gating system is imported into the software as *.stp* file, Figure 4.

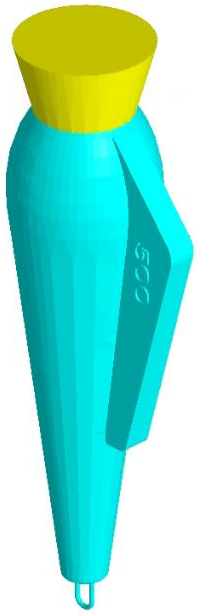

Figure 4. *3D model of casting used for simulation – Configuration type 3*

The total number of cells depended on gating system and for all simulation are presented in Table 1. The initial temperature of al-alloy mould was set to room temperature. Dimensions of the mould are also presented in Table 1.

Table 1. *Parameters of mesh*

	Dimension of cell, mm	Total number of cells	Mould dimension (*x, y, z*), mm
Configuration 1	0.991	430 050	50, 60, 140
Configuration 2	0.973	423 708	50, 60, 130
Configuration 3	0.957	445 536	50, 60, 130
Configuration 4	0.979	444 873	50, 60, 140

The simulation results are also subject to the effects of heat transfer, specifically the thermal boundary conditions existing between the hot casting material (alloy) and the cooler mould. Substantial variations in temperature between these two entities can impede the flow of heat. To address this, the heat transfer coefficient is frequently employed to manage interfacial heat transfer. This study

relies on the temperature-dependent heat transfer coefficients extracted from the software's pre-existing database.

4. Results and discussion

Mould filling process and solidification of the casting are presented in Figure 5.

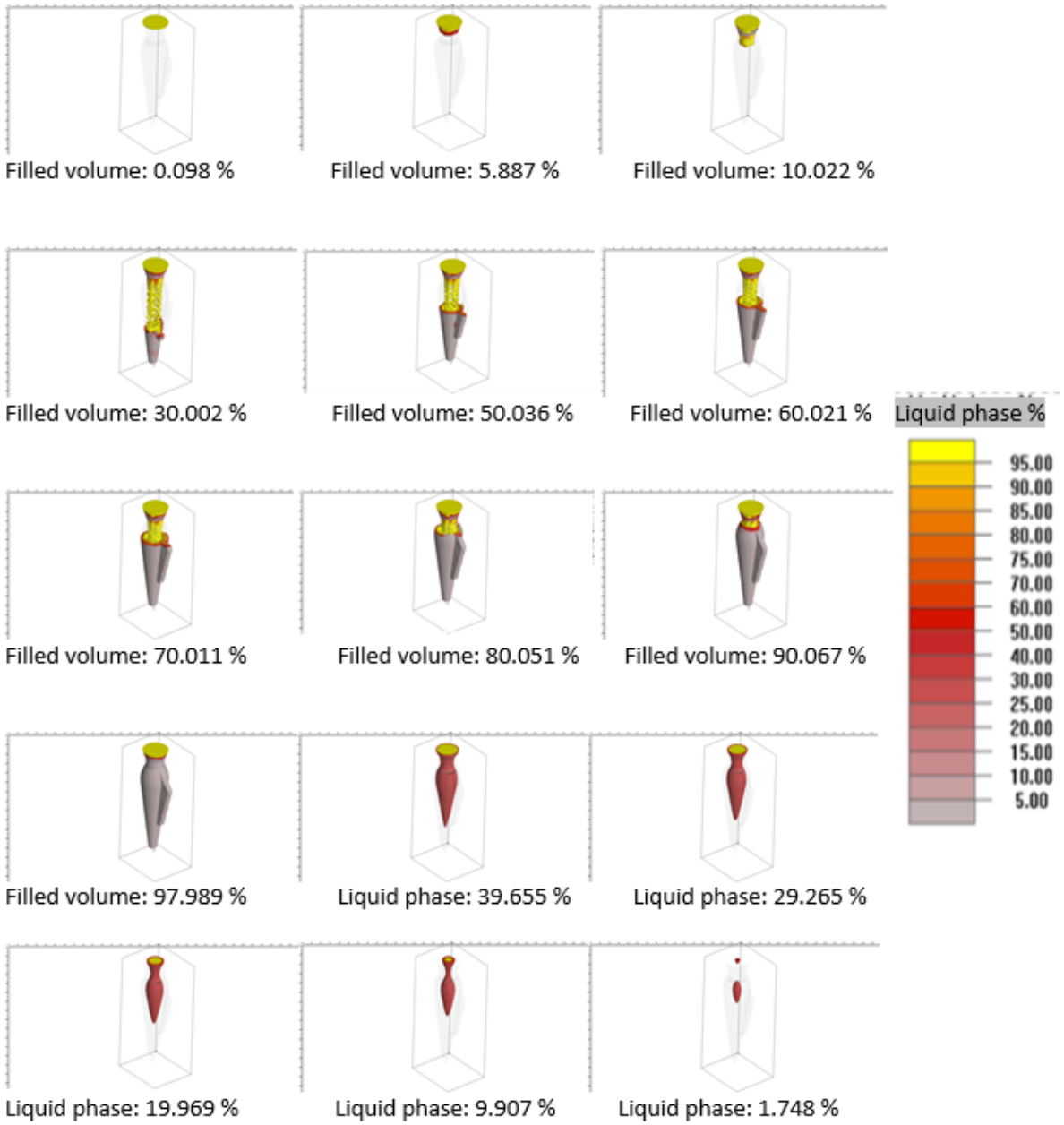

Figure 5. *Simulation results for configuration 2*

After each process simulation run, values of the shrinkage of material (total shrinkage of casting without gating system) and values of the total casting times (until casting solidifies) are obtained from the report and presented in Table 2. Both considered results are similar for all configurations.

Table 2. *Postprocessing records*

	Configuration 1	Configuration 2	Configuration 3	Configuration 4
Total time, s	6.822	6.908	7.192	7.197
Shrinkage, %	4.835	4.769	4.581	4.650

Predictions of the shape and location of porosities and air entrapment are presented in Figure 6. For configurations 1 and 2 the accumulation of air inclusions causes the formation of cavities in the middle of the casting, Figure 7.

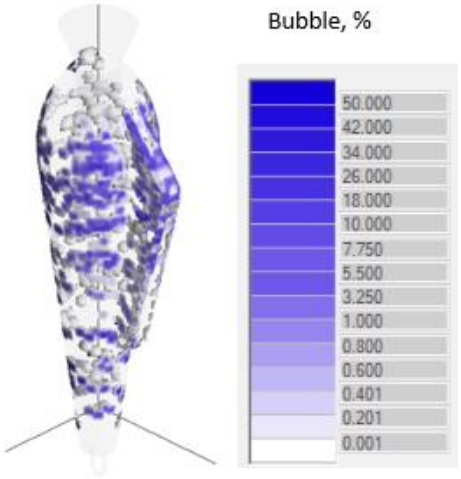

Figure 6. *Bubble formation*

The simulation provides a lot of information about the casting process, of which shrinkage and porosity are the most important for this case, Figure 7. In casting processes, it is generally desirable to achieve small values for both the total casting time and the material's shrinkage. Although the shrinkage on the outer surface is about the same for all configurations, the shrinkage inside the casting is different. Therefore, the gating system used in configuration 3 is considered as most suitable.

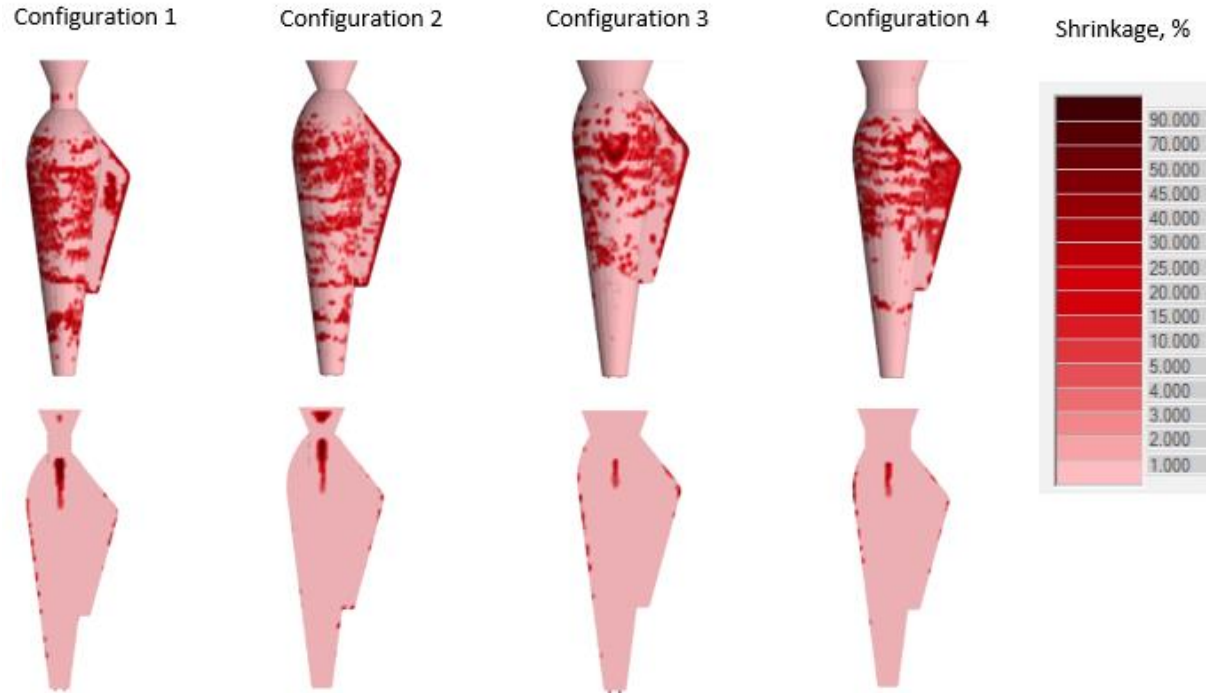

Figure 7. *Shrinkage of material*

5. Conclusion

The aim of this study was to simulate the gravity casting process of lead. The simulation provides useful information about the course of the casting process and makes it possible to monitor the movement of the melt and check the correctness of the mould construction. Therefore, the number of rejected products can be significantly reduced. In addition, by application of simulation software predictions of porosities and air entrapment can be observed. According to the simulation results, the most suitable gating system was chosen. In future research, experimental casting will be carried out and will be compared with the results obtained by simulations.

References

[1] Desu M. V., Yadav Y.C.S., Krupa C.H.S., Battula S., 2017, Casting simulation method along with changes in the gating design. In: National Conference on Rapid Casting Techniques. Hyderabad, India.
[2] Swapnil Ambekar A., Jaju S.B., 2014, A Review on Optimization of Gating System for Reducing Defect. Int J Eng Res Gen Sci. 2(1), 93–8.
[3] Šabík V., Futáš P., Pribulová A., Delimanová P., 2021, Optimization of a gating system by means of simulation software to eliminate cold shut defects in casting. J Cast Mater Eng. 5(1), 1–4.
[4] Piyapong M., 2007, Solidification Modeling of Iron Casting Using SOLIDCast. West Virginia University.
[5] Olofsson J., Salomonsson K., Svensson I.L., 2015, Modelling and simulations of ductile iron solidification- induced variations in mechanical behaviour on component and microstructural level. IOP Conf Ser Mater Sci Eng. 84(1).
[6] Bhatt H., Barot R., Bhatt K., Beravala H., Shah J., 2014, Design Optimization of Feeding System and Solidification Simulation for Cast Iron. Procedia Technol, 14, 357–64.
[7] Futáš P., Pribulová A., Fedorko G., Molnár V., Junáková A., Laskovský V., 2019, Failure analysis of a railway brake disc with the use of casting process simulation. Eng Fail Anal. 95(2018), 226–38.
[8] Dou K., Lordan E., Zhang Y.J., Jacot A., Fan Z.Y., 2019, Numerical simulation of fluid flow, solidification and defects in high pressure die casting (HPDC) process. IOP Conf Ser Mater Sci Eng. 529(1).
[9] Borlepwar P., Biradar S., 2019, Study on Reduction in Shrinkage Defects in HPDC Component by Optimization of Localized Squeezing Process. Int J Met.13(4), 915–22.
[10] Radiša R., Dučić N., Manasijević S., Marković N., Ćojbašić Ž., 2017, Casting improvement based on metaheuristic optimization and numerical simulation. Facta Univ Ser Mech Eng. 15(3), 397–411.
[11] Dučić N., Slavković R., Milićević I., Ćojbašić Ž., Manasijević S., Radiša R., 2017, Optimization of the gating system for sand casting using genetic algorithm. Int J Met. 11(2), 255–65.
[12] Vossel T., Wolff N., Pustal B., Bührig-Polaczek A., Ahmadein M., 2022, Heat Transfer Coefficient Determination in a Gravity Die Casting Process with Local Air Gap Formation and Contact Pressure Using Experimental Evaluation and Numerical Simulation. Int J Met. 16(2), 595–612.
[13] Duan H., Shen J., Li Y., 2012, Comparative analysis of HPDC process of an auto part with ProCAST and FLOW-3D. Appl Mech Mater. 184–185, 90–4.
[14] Campbell J., 2015, Complete casting handbook: metal casting processes, metallurgy, techniques and design. Elsevier.
[15] Ferhathullah Hussainy S., Viquar Mohiuddin M., Laxminarayana P., Krishnaiah A., Sundarrajan S., 2015, A Practical Approach To Eliminate Defects in Gravity Die Cast Al-Alloy Casting Using Simulation Software. Int J Res Eng Technol. 4(1), 114–24.
[16] NOVAFLOW&SOLID 6.4; Manual—2018-08-29; NovaCastSystems AB.

Relationship between hardness distribution and residual stresses on the weld cross-section of a thick-walled plate made of S235JR steel

***Darko Landek*[1], *Ivica Garašić*[1] *and Mislav Štefok*[1]**

1) University of Zagreb, Faculty of Mechanical Engineering and Naval Architecture, Ivana Lučića 5,

10002 Zagreb, Croatia

Corresponding author: dlandek@fsb.hr

Original scientific article

Abstract: After welding, a change in microstructure, hardness and residual stress occurs in the weld and in the heat-affected zone. In the work, two 120 mm thick plates made of structural steel S235JR were welded into a butt joint using the process of electric arc welding under powder protection (EPP). By choosing the annealing temperature and time for the reduction of residual stresses, according to the ISO 14745:2007 standard, three different states of hardness distribution and residual stresses on the weld section were obtained. Using statistical modeling, the correlation coefficient between the hardness tested by the Vickers method and the residual stresses determined by the X-ray diffraction (XRD) method was determined.

Keywords: *S;, S235JR steel; residual stresses; XRD analysis*

1. Introduction

Submerged arc welding (SAW) belongs to the group of electric arc highly productive processes for joining thicker and longer sheets of unalloyed and low-alloy structural steels. Economic application of this procedure is for welds longer than 0.5 m and sheets thicker than 10 mm. Due to the strong welding currents, a large amount of melt is created, which penetrates deep into the welded joint. The welding place is covered with a layer of powder and slag during the entire process. The powder protects the melt in the weld from oxidation, prevents rapid cooling of the weld and shapes the weld. The shape of the weld most significantly depends on the shape of the joint (I-joint, Y-joint), welding parameters, inclination of the weld to the horizontal plane, type of powder, place of connection of the mass to the workpiece and the chemical composition of the welded steel. The most influential welding parameters are current density, voltage and welding speed. A layer of powder on the weld prevents heat loss by radiation and directs the passage of heat towards the interior of the workpiece. This reduces the consumption of electricity power compared to electric arc welding for the same amount of melt and results in less pollution of the surrounding atmosphere [1],[2].

When welding thick sheets, due to the high input heat and slower cooling, a larger grain is formed in the weld, which can cause a weaker weld toughness [1]. Also, the input of a large amount of thermal energy and the deep penetration of the melt at the joint of thicker welded sheets cause the appearance of longitudinal and transverse tensile thermal stresses in the weld and compressive stresses in the heat-affected zone. Due to the greater thickness of the section of the welded sheets, it is difficult to collect the material around the weld and the residual stresses cannot be decomposed independently after the SAW process. Therefore, annealing is usually applied to reduce residual stresses. By holding the welded structure at the annealing temperature, plastic deformation is initiated in the areas of elevated residual stresses, which partially or completely remove them, without microstructural changes in the weld. The implementation of this annealing is prescribed by the standard ISO/NP 14745:2007. For unalloyed and low-alloyed steel constructions, annealing to a temperature between 550 °C and 600 °C is prescribed. Holding time at annealing temperatures depending on the thickness of the welded sheet (between 2 h and 6 h), where the highest value of the

Hollomon-Jaffe parameter P_{crit}=17.5 should be achieved. Its value is determined according to the expression:

$$P = T \cdot (20 + logt) \cdot 10^{-3} \quad (1)$$

where *T* [K] is the annealing temperature and t [h] is the holding time. The rate of heating and cooling of welded constructions of sheets thicker than 90 mm must be less than 55 K/h, in the interval between 300 °C and the annealing temperature, i.e. it is necessary to achieve the so-called programmed welding heating and coolingDuring the heating and holding cycle, the protective atmosphere in the furnace must be controlled to avoid excessive oxidation of the workpiece surface.
The condition and residual stress values in the weld before and after annealing can be determined using non-destructive methods, of which the magnetic Barkhausen noise (MBN) method, X-ray diffraction, neutron diffraction and ultrasound methods are the most used [4], [5]. The application of destructive methods such as the hole-drilling method and the measurement of stress on the weld cross-section are mainly used for research purposes, and less often in welding quality control. By examining the hardness on the surface and weld cross-section, it is also possible to qualitatively determine the presence of residual stresses, although it is not possible to determine their sign [6], [7].
The paper investigates the relaxation of residual stresses on welds made of structural steel S235JR produced by welding under powder protection by measuring residual stresses by X-ray diffraction, testing hardness and statistical analysis of the relationship between residual stresses and the tested hardness of the weld cross-section.

2. Materials and methods

Two panels of 150 mm x 120 mm x 150 mm made of structural steel S235JR with mechanical properties according to EN-10025-2:2004 were prepared for the test. An X-joint for welding is prepared on the plates by milling. The panels were welded using the EPP process in two passes with direct current with the following parameters: current strength 600 A, voltage 28 V, welding speed 45 cm/min, wire diameter 4 mm. Protective powder S A FB 1 55 AC H5 intended for welding carbon and low-alloy steels was used for welding. The properties of the powder are prescribed by EN ISO 14174:2012. In the first pass, the upper segment of the X-joint was welded in a horizontal position, and then the plates were turned to the other side in order to weld the second segment of the X-joint in the second pass. Between the first and second pass, the weld is cooled to room temperature. Three test samples measuring 290 mm x 120 mm x 18 m were cut from the welded plate on a metal band saw, with emulsion cooling. The surface of the samples was additionally processed by planing and tool grinding to remove cutting marks and achieve a flat surface for residual stress and hardness testing. Figure 1 shows a test sample with a drawn grid for testing hardness. Hardness was tested on 48 network nodes before and after annealing heat treatment. The residual stresses were measured at 6 points marked with green marks in Figure 1. The distance between the nodes of the rectangular grid was 20 mm. The weld border to the base metal is also drawn in the grid.
The heat treatment of the welded samples was carried out in a laboratory electric chamber furnace without a protective atmosphere with internal chamber dimensions of 190 mm x 190 mm x 300 mm. The heating of the samples to the annealing temperature and the cooling to 300 °C were automatically regulated to achieve a constant rate of temperature change of 55 K/s. Marks of welded samples and annealing parameters are listed in Table 1.

Table 1. *Annealing parameters of EPP welded samples made of steel S235JR*

Sample mark	Annealing parameters	Hollomon-Jaffe parametar
A1	550 °C / 2 h /air	16.71
B1	600 °C / 3 h /air	17.88
C1	650 °C / 4 h / air	18.26

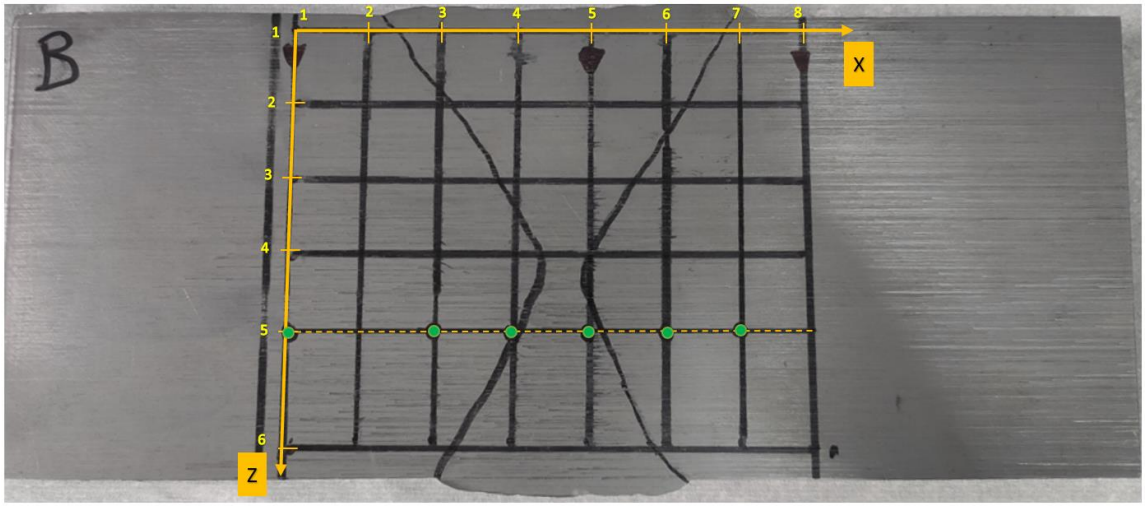

Figure 1. *A example of a test specimen of S235JR steel cut from plates welded by the SAW process with a marked grid of measuring points for testing hardness (intersections of the grid lines) and residual stresses (green marked points)*

The hardness test on the nodes of the rectangular network shown in Figure 1 was carried out with a United Precision Instruments AHT200 Leeb portable device with a type D measuring probe. The tested hardness is expressed in Vickers (HV) units. The hardness test in each node was repeated three times. The error of testing the hardness by the Leeb method and converting the results into hardness according to the Vickers scale was $\pm$ 6 HV.

Residual stresses were tested with a Sentenso Pulstec μ-X360s portable X-ray diffractometer, which was mounted on the robot arm. Residual stresses were measured at 6 points, shown in Figure 1 in the longitudinal (*x*) and transverse (*z*) directions on the welded X-joint. The principle of measurement with this diffractometer is described in reference [8] and is shown schematically in Figure 2a. The measuring part of the device consists of a source of low-intensity X-rays obtained from the ionization of the Chromium (Cr) K-alpha electrode (Kα), a filter for passing X-rays of a certain frequency, a plate with a diameter of 30 mm with sensors for detecting the reflected beam of X-rays from the surface of the sample. A plate with 2-D sensors for measuring the intensity of reflected X-radiation is placed perpendicular to the incident beam. The incident beam of X-rays is directed at an angle ψ0 in relation to the normal to the surface of the sample, penetrates the surface layer at a depth of up to 10 μm and is reflected from the crystal planes at the angles characteristic of the examined material. The reflected beam excites 2D on-board sensors that record the Debye-Scherrer (D-S) ring of backscattering X-rays. The surface of the sample without residual stresses shows the characteristic diameter of the D-S ring for a certain material. The presence of residual stresses changes the spacing between crystallographic planes in the microstructure, which patterns X-ray reflection at different angles compared to material without residual stresses. Therefore, the appearance of the D-S ring and the intensity distribution of the registered radiation recorded on a material with residual stresses are different from that recorded on a material without stress. The essential advantage of applying this cosα two-dimensional method compared to other methods for measuring residual stresses is that the determination of the amount of residual stresses on the surface of the sample needs to be determined only by the relative difference in diameter between individual points on the D-S ring for different angles α and by applying a mathematical model for elastic deformations ε_x , ε_y calculates the residual stress σx in the x direction and the shear stress τ_{xy}. In conducted test the samples were irradiated using a beam current of 1.5 mA and voltage of 30 kV. The X-ray beam was directed to be incident on each sample at an angle of 35.0 degrees. The distance from the specimen and detector to capture the D-S ring image was set to *D* = 50 mm. The X-ray Cr Kα wavelength (λ) used for X-ray diffraction was 2.29Å.

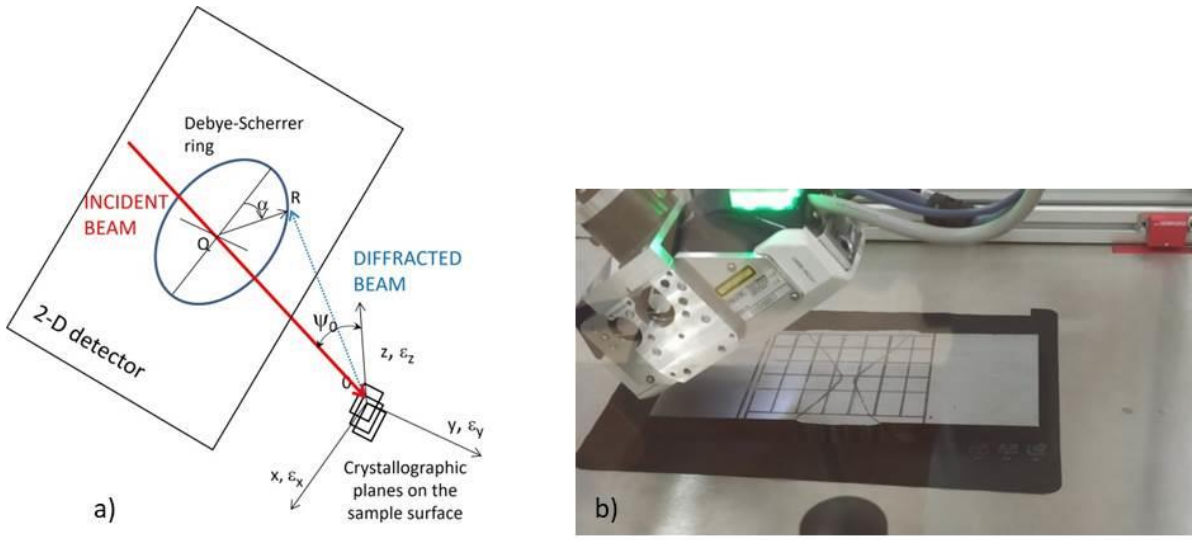

Figure 2. *Measurement of residual stresses on the weld test sample with a portable XRD device Sentenso μ-X360s: a) Debye-Scherrer ring recorded on a two-dimensional detector by a single-exposure of X-rays, b) position of the sample according to the measuring device*

3. Results and discussion

3.1. Hardness testing

Figure 3 shows the results of the hardness test of the weld cross-section before annealing in the furnace. On the display of the hardness distribution, the ordinal numbers of the nodes are marked according to the row and column marks of the grid shown in Figure 1. The highest hardness values, between 171 HV and 231 HV, are found in the root of the weld located at the intersections of rows 4th and 5th , with columns 4th and 5th.

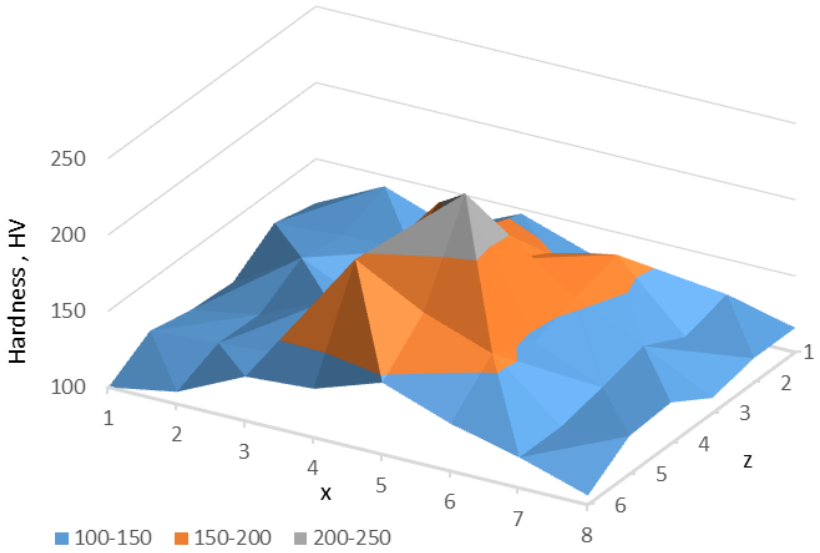

Figure 3. *Hardness distribution across the section of sample A0 before annealing [9]*

Figure 4 shows the results of the hardness test after annealing the weld according to the parameters listed in Table 1. In all tested samples, the highest hardness value was measured at the root of the weld, at the intersection of rows 4th and 5th, with columns 4th and 5th. On sample A1, annealed at 550°C/2 h, the hardness decreased from 197 HV to 185 HV. On sample B1 annealed at 575 °C/3 h, the hardness decreased from 201 HV to 146 HV. On sample C1 annealed at 650°C/4 h, the hardness

decreased from 205 HV to 150 HV. The spatial distribution of hardness in the weld and in the heat-affected zone is similar for all three annealed samples. Table 2 shows the change in hardness after annealing in line 5th of the grid marked in Figure 1. By comparing the results of hardness measurements before and after annealing, a trend of decreasing hardness per weld cross-section can be observed. However, the reduction in hardness was not enough and uniform hardness was not achieved across the weld cross-section.

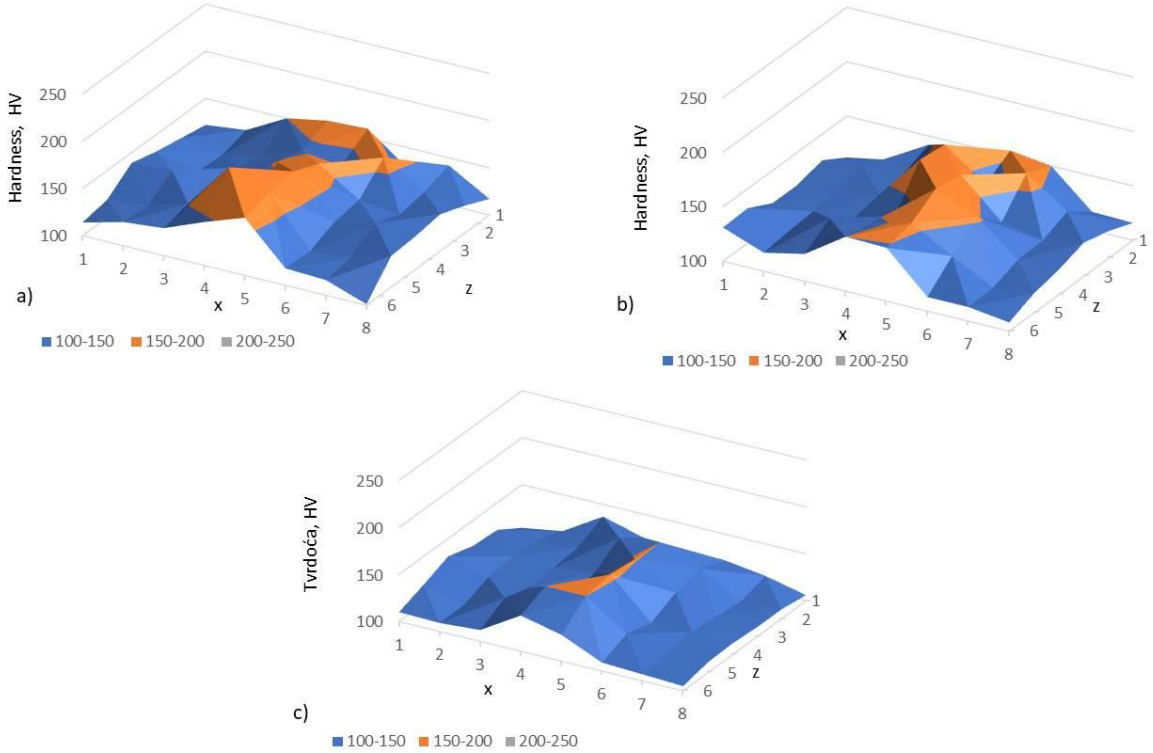

Figure 4. *Weld hardness after annealing in the furnace according to the parameters listed in table 1: a) sample A1, b) sample B1, c) sample C1[9]*

Table 2. *Weld hardness and heat-affected zone before and after annealing along the axis of the x-axis in the 5th row of the grid marked in Figure 1*

Sample mark		Hardness of the welded sample, HV							
		Column number on the x-axis							
		1	2	3	4	5	6	7	8
A	Before annealing (A0)	117	120	124	197	173	157	120	125
	After annealing (A1)	119	123	136	185	169	117	121	133
B	Before annealing (B0)	115	125	130	201	170	160	122	118
	After annealing (B1)	132	120	141	146	155	134	114	118
C	Before annealing (C0)	119	115	128	205	183	147	115	105
	After annealing (C1)	120	109	127	150	150	120	112	111

3.2. Residual stresses

Due to the small penetration depth of the X-ray beam, the measurement of residual stresses gives results for the biaxial state of stress on the surface of the samples. Table 3 lists the test results of residual stresses in the direction of the x and z axes (σ_x, σ_z, τ_{xz}), before and after annealing, measured at the 6 points marked in Figure 1. From the distribution and sign of the stress σ_x along the x axis, the presence of compressive stresses in the root of the weld and tensile stresses in the base material

outside the heat-affected zone (HAZ) can be observed. This stress distribution is a consequence of the SAW welding process in two passes, where the heat removed from the weld in the second pass partially relaxes the residual stresses in the weld from the first pass.

Table 3. *Residual stresses in the weld and heat-affected zone before and after annealing*

Residual stresses in the x-axis direction σ_x, MPa								
Sample mark		Ordinal number of the measuring point on the x-axis						
		1	2	3	4	5	6	7
A	Before annealing (A0)	8	-	-10	-31	-58	-12	44
	After annealing (A1)	-16	-	12	64	7	-84	-14
B	After annealing (B1)	119	-	130	118	-33	88	124
C	After annealing (C1)	63	-	89	92	182	144	108
Residual stresses in the z-axis direction σ_z, MPa								
Sample mark		Ordinal number of the measuring point on the x-axis						
		1	2	3	4	5	6	7
A	Before annealing (A0)	61		52	71	-72	-31	30
	After annealing (A1)	-185		-237	-308	-190	-225	-263
B	After annealing (B1)	-143		-84	-141	-174	-108	-190
C	After annealing (C1)	-138		-130	-153	-119	-141	-141
Shear residual stresses τ_{xz}, MPa								
Sample mark		Ordinal number of the measuring point on the x-axis						
		1	2	3	4	5	6	7
A	Before annealing (A0)	-14	-	-22	-17	-58	-15	-18
	After annealing (A1)	41	-	13	10	4	0	-1
B	After annealing (B1)	29	-	8	28	20	0	14
C	After annealing (C1)	-8	-	45	-7	14	4	24

In sample A1, annealed at 550 °C/2 h, there was a change in the stress sign σ_x, compared to the state before heat treatment. In the center of the weld, the compressive stresses changed their sign to tensile after annealing and remained similar in amount to the stresses before annealing. The residual stresses σ_z in the axial direction changed their sign from tensile to compressive and increased significantly after annealing. The shear stresses of sample A1 decreased after annealing. A similar phenomenon after annealing occurred on the other two samples, on sample B1 annealed at 575 °C/3 h and sample C1 annealed at 650 °C/4 h. This phenomenon of insufficient residual stress reduction was already indicated by the results of the hardness test on the weld cross-section, and the residual stress measurements confirmed this assumption.

These results of uneven hardness and increase of residual stress in the weld cross-section after annealing are the result of heat treatment in a furnace of small volume compared to the volume of the welded samples. The length of the furnace floor where the annealing was carried out was 300 mm, and the length of the welded sample was 290 mm. Heat treatment was carried out with temperature regulation, which is measured by a thermocouple placed on the ceiling of the furnace at a distance of 280 mm from the furnace door. There was no air circulation in the oven and heat transfer was achieved by free convection and radiation from the heaters located on the side walls of the oven. Such a construction of the furnace could not allow a uniform temperature distribution in the entire volume of the furnace, and the part of the sample inside the furnace heated and cooled more slowly than the part of the sample next to the door of the furnace. A subsequent measurement of the distribution of the temperature field in the furnace revealed a temperature difference between 80 °C and 100 °C between the measuring point near the thermocouple for regulating the temperature of the furnace and the floor near the furnace door. From the obtained results, it can be assumed that

the residual stresses in the weld partially relaxed at the annealing temperature, and then, due to the difference in the cooling rate along the length of the sample, new stresses of the opposite sign were created.

To determine the relationship between residual stresses and hardness at the measurement points marked in Figure 1, the main normal stresses were calculated σ_1 and σ_2 according to Mohr's stress circle equation [10]:

$$\sigma_{1,2} = \frac{\sigma_x + \sigma_z}{2} \pm \sqrt{\left(\frac{\sigma_x - \sigma_z}{2}\right)^2 + \tau_{xz}^2} \tag{2}$$

where σ_x and σ_z are the residual stresses in the direction of the x and z axes, respectively, τxz is the shear stress in the x-z plane. The two-axis equivalent residual stress is determined according to the von Mises equation [10]:

$$\sigma_{eq} = \sqrt{\sigma_1^2 + \sigma_2^2 - \sigma_1\sigma_2} \tag{3}$$

Figure 5 shows the hardness and equivalent residual stress in the measurement points of sample A0 before heat treatment and after annealing at 550 °C/2 h (sample A1). Figure 6 shows the hardness and equivalent residual stress after annealing of samples B1 and C1.

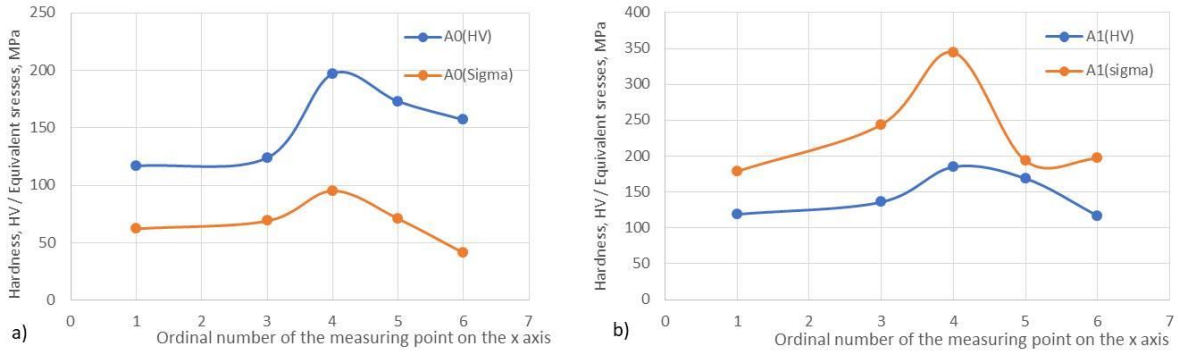

Figure 5. *Hardness and equivalent residual stress in the weld section on sample A: a) initial welded state, b) annealed at 550 °C/2 h*

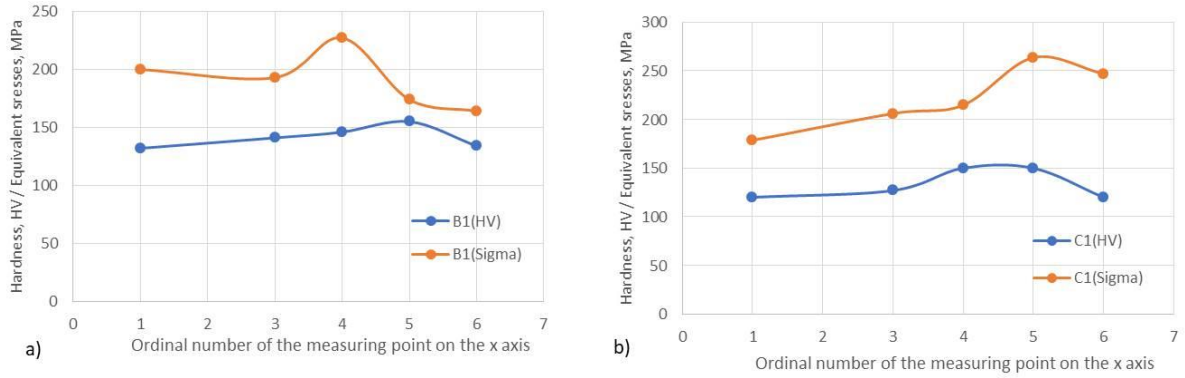

Figure 6. *Hardness and equivalent residual stress per weld section after annealing: a) sample B1 (575 °C/3 h), b) sample C1 (650 °C/4 h)*

From the diagrams in Figures 5 and 6, it is evident that the curve of changes in hardness follows the change in the equivalent residual stress. The increase in the value of the equivalent residual stresses in the centre of the weld coincides with the increase in hardness. Figure 7 shows a comparison of

hardness and equivalent residual stress at individual measurement points. It can be seen from the above figures that in the welded sample A0 a significantly lower level of equivalent residual stress was achieved compared to samples A1, B1 and C1 annealed in the furnace. By annealing in a small laboratory furnace for the same hardness values, the equivalent residual stresses increased 3 to 7 times compared to the initial state, which was an unfavourable outcome of the experiment. based on the regression analysis, propose a model for the approximate estimation of residual stress values based on hardness values.

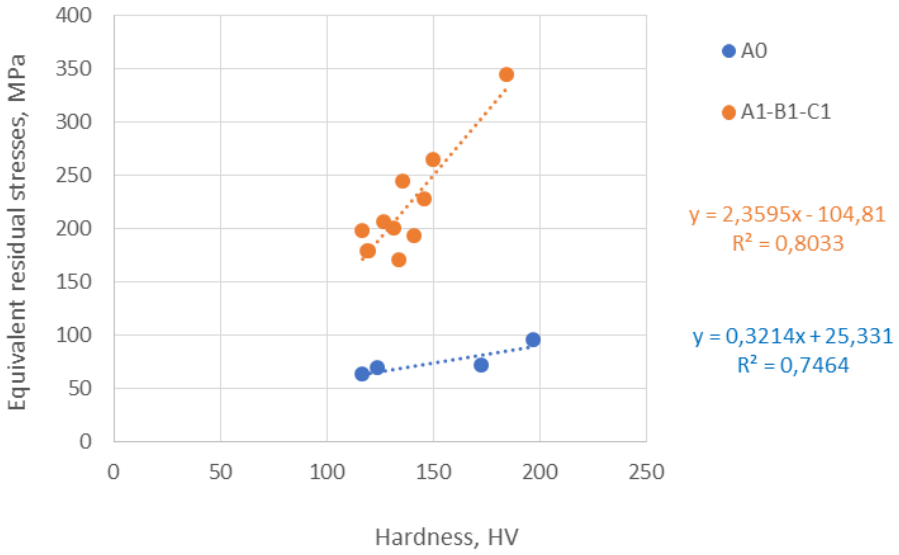

Figure 7. *Correlation of equivalent residual stresses and hardness per weld section on S235JR steel*

Based on the linear regression analysis of the dependence of the equivalent residual stress in the SAW weld on the hardness, the following regression equation was obtained:

$$\sigma_{eq} = 0.3214\ HV + 25.331 \qquad R^2 = 0.7464 \qquad (4)$$

It describes the relationship between stress and hardness in the weld after locally applied heating of the welded joint. During the welding process, there is a large mass of unheated S235JR steel around the weld with a minimal amount of residual stress. The hardness of the base material outside the heat-affected zone is 120 HV. According to equation (4), the equivalent residual stress in the material outside the weld is predicted to be 63.90 MPa, while the measured value on sample A0 at point 7, which was not used in the regression analysis, was 81 MPa.

Annealing of the welded samples in a small laboratory furnace was carried out in the uneven heating and cooling of the entire sample. From the already mentioned temperature difference between the inner wall and the door of the small laboratory furnace, it follows that during cooling, temperature gradients of 30 K/m to 40 K/m appeared on the sample, which caused the appearance of large residual stresses. The regression equation for predicting the equivalent residual stresses based on the hardness test in this case is:

$$\sigma_{eq} = 2.3595\ HV - 104.81 \qquad R^2 = 0.8033 \qquad (5)$$

The hardness of the base material away from the HAZ was 120 HV, and according to model (5) an equivalent residual stress of 178.33 MPa is predicted. The measured equivalent residual stress at point 7 on sample A1 was 261 MPa. Such an unfavourable case of cooling with high values of residual stresses can occur in massive structures annealed in a furnace with an inhomogeneous temperature field or heated in an open space using portable heaters.

The application of regression equations (4) and (5) should be investigated in future experiments and additional influencing factors on the relationship between hardness and equivalent residual stress should be determined. One of them is the temperature gradient that appears on the annealed structure, the other is the grain size in the weld and the heat-affected zone. The connection of these factors with the amount of residual stresses and hardness results from thermal-mechanical processes that appear in the decomposition of residual stresses. Decomposition of residual stresses is determined by the amount of possible plastic deformation of the material at elevated temperature, that is, by the possible movement of dislocations in the microstructure. The occurrence of a large temperature gradient in the volume of the annealed material causes a gradient in the distribution of plastic deformations, in the sense that in the part of the volume with a temperature higher than 500 °C, greater plastic deformation and greater decomposition of residual stresses is created, than in parts of the volume at a lower temperature. Also, the larger grains in the microstructure are more easily deformed plastically than the fine-grained microstructure. On the other hand, between parts of the volume with temperature differences, new thermal residual stresses occur proportional to the temperature gradient and the coefficient of thermal expansion of the material. During annealing in a small laboratory furnace, the process of creating thermal stresses prevailed over the process of stress decomposition, and the stresses in the weld increased further after annealing.

4. Conclusion

The following conclusions can be drawn from the conducted residual stress and hardness tests on welded samples of S235JR steel. Welding annealing to reduce residual stresses according to the ISO/NP 14745:2007 standard must be performed in a heat treatment furnace with a sufficiently large volume of the working chamber in which it will be possible to achieve temperatures from 500 °C to 650 °C in a minimum temperature gradient. The annealing furnace should be equipped with a thermoelement and automatic temperature regulation. Using regression analysis, it is possible to determine the relationship between hardness and equivalent residual stress per weld cross-section. The amount of residual stress after annealing is significantly affected by the annealing temperature and the appearance of a temperature gradient in the volume of the annealed object, while the annealing time and grain size in the weld microstructure have a smaller influence.

Acknowledgments

The authors wish to acknowledge theproject KK.0.1.1.07.0076 “ImproWE - Improvement of high efficiency welding technology” funded from the Ministry of Science and Education of Republic Croatian and The Central Agency for Financing and Contracting Programs and Projects of the European Union (SAFU) for their financial support.

References

[1] Kralj, S., Kožuh,Z., Andrić, Š. 2015. Priručnik Zavarivački i srodni postupci, HDTZ, Zagreb
[2] Allgood, L.E., 2011. Submerged Arc Welding, ASM Handbook, Vol 6A, Metals Park, USA
[3] Totten, G., Howes,M., Inoue, T., 2002. Handbook of Residual Stress and Deformation of Steel, ASM International, Metals Park, USA
[4] Lai, H.H. , Wu, W.2020. Practical examination of the welding residual stress in view of low-carbon steel welds, Journal of Materials Research and Technology, Vol. 9(3), 2717–2726
[5] Rossini, N.S. Dassisti, M., Benyounis, K.Y. , Olabi, A.G. 2012. Methods of measuring residual stresses in components, Materials & Design, Vol. 35, 572-588
[6] Frankel, J., Abbate, A., Scholz, W., 1993. The Effect of Residual Stresses on Hardness Measurements, Experimental Mechanics, Vol.33, 164–168
[7] Yuan, L., Yuan, W., Wang, G., 2020. Effects of Residual Stress on the Hardness of Elastoplastic Material Under Spherical Indentation, J. Appl. Mech. Vol. 87(5)
[8] Tanaka, K., 2019. The cosα method for X-ray residual stress measurement using two-dimensional detector, Mechanical Engineering Reviews, Vol.6, No.1, 1-15

[9] Zorić, K., 2022., Žarenje za smanjenje zaostalih naprezanja u zavarima čelika S235JR, diplomski rad, FSB, Sveučilište u Zagrebu
[10] Alfirević, I.1989., Nauka o čvrstoći I, Tehnička knjiga, Zagreb

Comparison of residual stresses and resistance to microabrasive wear of PACVD TiN and PVD TiN coatings on 100Cr6 steel

***Darko Landek*[1], *Jurica Jačan*[1], *Mislav Štefok*[1] *and Qi Yang*[2]**

1) University of Zagreb, Faculty of Mechanical Engineering and Naval Architecture, Ivana Lučića 5,

10002 Zagreb, Croatia

2) National Research Council (NRC) of Canada, Ottawa, Canada

Corresponding author: dlandek@fsb.hr

Original scientific article

Abstract: The paper compares the residual stresses on TiN coatings applied to a substrate of hardened and tempered 100Cr6 steel by physical vapor deposition (PVD) and plasma-assisted chemical vapor deposition (PACVD) from the vapor phase. In both procedures, a TiN coating with a thickness of 1-2 m was applied to equally prepared substrate samples. The samples were tested for the permeability of the coating according to the VDI 3822:2011standard, the thickness was determined by the calotest and the residual stresses were analysed by the X-ray diffraction (XRD) method. The coating applied by the PVD process showed better adhesion and three times lower residual stresses compared to the coating applied by the PACVD process. On both coatings, the residual stresses are lower compared to uncoated samples in the hardened and tempered state.

Keywords: *PVD; PACVD; TiN; 100Cr6 calotest; XRD analysis; residual stresses*

1. Introduction

By applying hard coatings, it is possible to significantly increase the wear resistance and durability of parts and tools. The choice of coating for a specific substrate depends on a number of influencing factors. In paper [1] it is proposed to consider 15 influential factors crucial for choosing a certain coating: operating temperatures, working environment conditions, hardness of the material protected by the coating, hardness of the material causing wear, combination of materials in the tribocouple, shape of the contact surface, contact (Hertz) stresses, relative motion of the members of the tribo pair, speed of movement, surface finish of the tribo pair, dimensions and shape of parts or tools in contact, thickness and adhesiveness of the coating, batch size and production costs. For frequently used hard tribological coatings, most of this data is available in the literature [2], [3],[4]. The remaining data should be collected in laboratory and exploitation tests. Based on consideration of factors influencing the choice of the coating, the requirements for the tribological coating are defined, which in most cases include the following 8 properties [5]: (a) good adhesion to the base material, (b) increased hardness to withstand abrasion, (c) sufficient toughness to prevent peeling, (d) good chemical stability, (e) activity in forming a tribological film of lubricant or oxide, (f) thermal stability, (g) sufficient shear strength to resist contact pressures, and (h) adaptability to the substrates. Steel 100Cr6 is used in construction and tool applications. In structural applications, it is used to make roller and sliding bearings and similar parts. In tool applications, it is used for woodworking tools, cutting tools, knives for paper and leather, smaller drills, reamers, dental drills, countersinks, processing tools, etc. 100Cr6 steel achieves its useful properties after hardening and tempering. The hardness of hardened and tempered steel 100Cr6 is in the value range of 675 - 800 HV, the modulus of elasticity is 210 ± 5 GPa, the coefficient of thermal expansion is (12.3-14.1)×10^{-6} K^{-1} [6]. Additional improvement in wear resistance is achieved by coating in the vapor phase with the PVD (Physical Vapor Deposition) and PACVD (Plasma Assisted Chemical Vapor Deposition) procedures. The

mentioned coating procedures on the surface of the material create a thin coating without diffusion into the base material and without significant changes in the microstructure of the base material.
The coating of titanium nitride (TiN) belongs to the group of non-oxide ceramics, which also includes coatings TiC, TiCN, TiAlN, SiC. All the mentioned coatings are known for their good properties of high hardness, increased wear resistance, corrosion resistance and good electrical conductivity. The TiN coating can be applied by CVD, PACVD and PVD processes [2], but each of them results in a different microstructure and combinations of certain values of the coating properties. The hardness of TiN is in the value range of 1800-2200 HV, the modulus of elasticity is 550 ± 50 GPa, the coefficient of thermal expansion is 9.35×10^{-6} K^{-1} , working temperature up to 500 °C, the coating thickness is 1-5 μm [2],[3],[7],[8]. Applying the TiN coating to metal substrates in a layer thicker than 10 μm results in poorer adhesiveness, the appearance of high residual stresses and microcracks in the coating.
Residual stresses in the coating are created during coating and cooling of the coating in the furnace. The overall state of stress in the coating is the result of the superposition of macro stresses (stresses of the first kind) that are distributed over the entire workpiece and microstresses that appear at the level of the crystal grain (stresses of the second kind) or inside the grain (stresses of the third kind). According to the cause of their occurrence, residual stresses are thermal and internal (microstructural). Thermal stresses arise during the cooling of the coating due to the difference in the coefficient of thermal expansion of the coating and the substrate and mainly act as macrostresses. Internal stresses are the result of voids, dislocations, inclusions and other forms of coating microstructural imperfection. These stresses are mainly second and third type stresses. Internal stresses increase significantly with increasing coating thickness [8].
The mechanical and tribological properties of the coatings are tested according to ISO 15787:2018 (Technical product documentation – Heat treated ferrous parts – Presentation and indications), ISO 6507-1:2018 (Metallic materials – Vickers hardness test), ISO 6508-1:1999 (Metallic materials - Rockwell hardness test), VDI 3198:1991 (coating adhesion test), DIN 50320:1979, DIN 50321-1:2019 (wear resistance), ASTM G-65-94:2001 (abrasion resistance), ASTM D-2783:2003 (adhesion resistance), etc. The thickness of the coating is tested by destructive methods: calotest, light or electron microscopy, chemical analysis on a metallographically prepared section of the coating, and non-destructive methods, using ultrasound, eddy currents, etc. [2],[8],[9].
Calotest is performed with a ball attached to the shaft or with a freely rotating ball placed on the shaft. Standard diameters of hardened and tempered 100Cr6 steel balls are 10 mm, 15 mm, 20 mm, 25 mm and 30 mm. The coating is worn by rotating a hardened steel ball coated with abrasive grains with a medium diameter of up to 5 μm. At the point of wear, a spherical crater with a circular crown on the outer edge is formed. The bottom of the crater is in the base material, and the ratio of the outer and inner diameter of the circular rim determines the thickness of the coating. The thickness of the coating that is tested by calotest is 0.1 - 50 μm [10]. In addition to determining the thickness of the coating, the calotester can also be used to determine the resistance of the coating to microabrasion. In the microabrasion test, the wear of the coating is carried out in one or more places by rotating a ball coated with an abrasive suspension with different wear times or different mass of the ball. In the initial wear, the wear mark is created only in the coating, and later there is simultaneous wear of the coating and the substrate.
This paper compares the influence of the PVD and PACVD coating processes on the generation of residual stresses and resistance to microabrasion of the TiN coating with the same chemical composition and previous heat treatment of the substrate.

2. Materials and methods

The TiN coating was applied to hardened and tempered steel 100Cr6. The chemical composition of steel 100Cr6 is listed in Table 1. The composition of the steel is in accordance with the guaranteed composition according to EN ISO 683-17:2014. For coating experiments, 6 discs with a diameter of 55 mm and a thickness of 10 mm were made by machining. The discs were hardened and tempered according to the process diagram shown in Figure 1. Preheating was carried out at 450°C / 1h in a

protective argon atmosphere. Austenitization was performed at 840℃ / 1h. Quenching was carried out in tempering oil INA Kalenol 22. Tempering was carried out in an electric furnace without a protective atmosphere at a temperature of 550℃ /2h, and after that the samples were cooled in air. After the heat treatment, the discs were ground and polished while cooling. Prior to coating deposition, the flat coupons and test rings were ultrasonically cleaned in isopropanol for 5 minutes and then dried with compressed air.

Table 1. *: Chemical composition of EN DIN 100Cr6 steel tested at the device LECO SPECTRUMAT 750 GDOES*

Chemical element	C (%)	Mn (%)	P (%)	S (%)	Si (%)	Ni (%)	Cr (%)
Steel sample 100Cr6	1.01	0.35	0.030	0.025	0.30	0.30	1.55

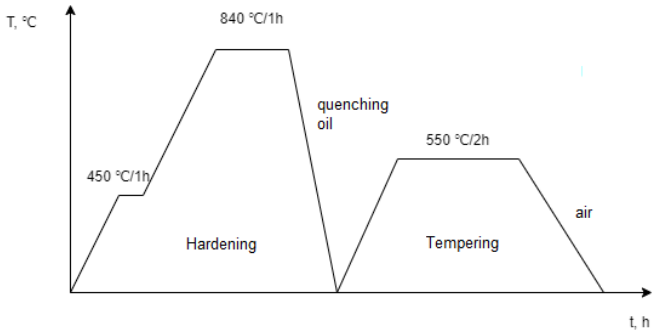

Figure 1. *The process of hardening and tempering of a 100Cr6 steel sample*

For PVD TiN coating the Metaplas Ionon MZR-304 cathodic arc coater was used as shown in Figure 2a. The coater is installed at the National Research Council of Canada (NRC). In the coater chamber, four titanium cathodes were mounted on two wall flanges opposite to each other, with two cathodes installed on each flange. In addition, an electrical heater and an arc-enhanced glow discharge (AEGD). Titanium cathode with a fixed front shutter used for substrate cleaning was mounted opposite to each other between the flanges. During coating deposition, the sample disc held by fixtures was placed on a dual-axial rotation table, which was rotated continuously at 2 rpm along the main rotation axis. The deposition process was executed in three processing stages: (1) pumping, (2) AEGD ion cleaning and (3) coating deposition as shown in Figure 2b. The deposition duration was set to 2000 seconds to achieve coating thickness in the range of 2.5 to 3 μm. The parameters of the PVD process and PACVD process were listed at table 2 and described in details in [11].

The Rübig PC 70/90 S system showed in Figure 2c was installed at the Faculty of Mechanical Engineering and Naval Arhitecture (FMENA) of the University of Zagreb. The vacuum furnace is equipped with a bipolar DC voltage-controlled micro pulse plasma generator. The metallic component of the coatings (i.e., Ti) was produced from a $TiCl_4$ precursor, while the non-metallic components of the coatings (i.e., N, C) came from dissociated high-purity nitrogen and methane gases. The parameters of the PACVD process were listed in Table 2. The position of the discs during PACVD coating is shown in Figure 2d.

The roughness test of uncoated and coated discs was performed on a Perthen Mahr device with a probe of radius r = 5 μm. The test parameters were: test length LT = 1.750 mm, evaluation length, LM = 1.250 mm and width of the measuring area VB = 12.50 μm, and the Gauss filter was used for filtering data (λc= 0.8 mm).

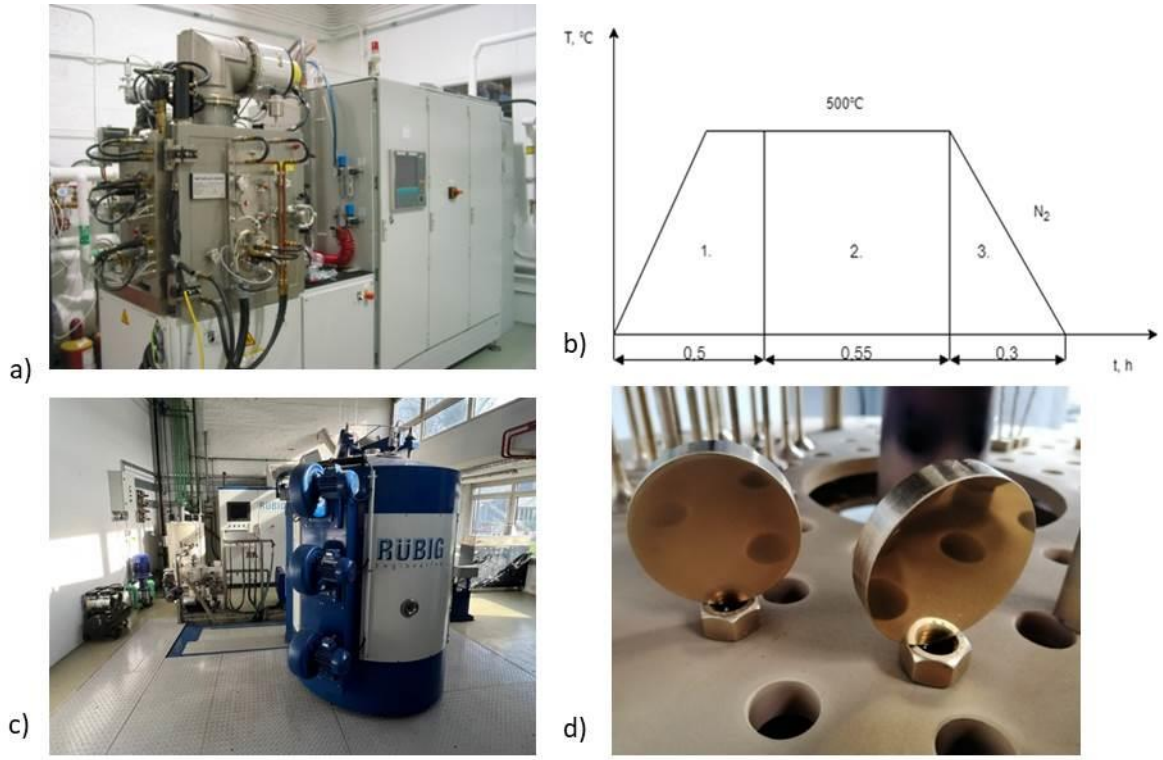

Figure 2. *Devices and procedures for TiN coating deposition: a) Metaplas Ionon MZR-304 cathodic arc coater, b) PVD temperature-time diagram, c) Rübig vacuum furnace PC 70/90, d) position of disc during PACVD process*

Table 2. *Parameters of PVD and PACVD coating steel discs*

Sample label	Surface modification process	Coating process parameters
D0	Hardenig and tempering	
D1	PVD TiN coating in the Metaplas Ionon MZR-304 coater	1. Cleaning the surface by ions sputtering: $8 \cdot 10^{-3}$ mbar/0.5 h; 80 A, -280 V 2. Coating TiN: 90 A, -100V; 0.55 h; 3. Cooling: 100% N2
D2	PACVD TiN coating in the Rübig PC 70/90 S system	1. Cleaning the surface by ions sputtering: 520 °C /2 h (2 mbar; 2000 W; 90 % H_2; 5 % N_2; 10 % Ar) 2. Coating by TiN: 520 °C / 6 h (2 mbar; 4000 W; 250 l/h H_2; 10 l/h N_2; 10 l/h Ar; 7.5 l/h $TiCl_4$) 4. Cooling: 3 h, 2 mbar, 100% N_2

The adhesivity of coatings was evaluated with the VDI 3198:1991 indentation test. In this test, a diamond indenter with a load of 1470 N is imprinted into the coating. Plastic deformation, microcracks or delamination of the coating appear around the place of embossing. Acceptable degrees of adhesion of the coating are imprint sites without delamination and circular cracks. The details of the test were described in [12].

The coating thickness and microabrasion resistance of the TiN coating was tested on the TRIBOtechnic calotester device shown in Figure 3. In the case when the conditions are met that the outer and inner diameter of the crater is smaller than the radius of the ball, the thickness of the coating (e) is determined by the expression:

$$e = \frac{D^2 - d^2}{8R} \quad (1)$$

where D (mm) is the outer diameter of the crater, d (mm) is the inner diameter, R (mm) is the radius of the ball.

The wear of the coating was carried out by a freely rotating ball made of hardened steel 100Cr6 with a diameter of 20 mm and a mass of m = 32.6 ± 0.05 g. The disk over which the ball rotates was placed at an angle of 75 ° in relation to the horizontal plane. Every 10 s, one drop of suspension with diamond grains with a mean diameter of 1 μm was added to the ball. The ball rotation speed was 300 rpm, and the wear time was t = (10 s, 20 s, 30 s, 40 s, 50 s and 60 s). The diameter of the calotte after microabrasion wear was measured on a Toolcraft light microscope at a magnification of 200:1 with image analysis using the Micro Capture Plus computer program.

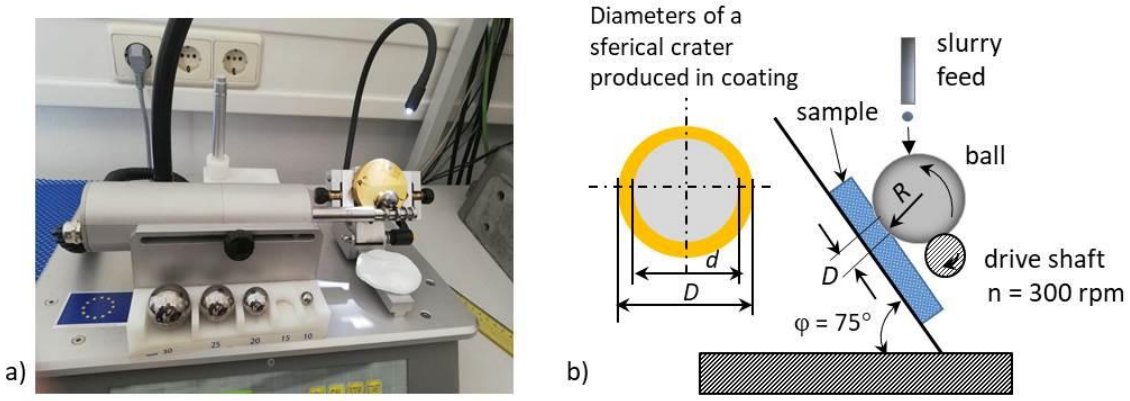

Figure 3. *Micro-abrasion wear by the freely rotating ball method: (a) a detail of testing on the TRIBOtechnic Calotester" device, (b) the relationship between the geometric dimensions of the ball and the crater on the surface of the sample*

With the assumption that calotest wear creates a spherical crater, whose outer diameter (*D*) is significantly smaller than the diameter of the steel ball, the loss of the coating material (*V*) and the depth of the crater (*h*) can be approximately determined by the expressions [13]:

$$V \approx \frac{\pi \cdot D^4}{64 \cdot R}, \quad \text{for } D << R \tag{2}$$

$$h \approx \sqrt{\frac{V}{\pi \cdot R}}, \text{ for } h << R \tag{3}$$

where *d* is the diameter of the crater (mm), *R* is the radius of the ball (mm). According to the Archard wear equation, the volume of material removed from the coating crater (V_c) is proportional to the wear path (*S*) and the normal force (*N*) that presses the ball onto the sample [14]:

$$V_c = \kappa_c \cdot (S \cdot N) \tag{4}$$

where κ_c is the wear coefficient of the coating. When additional wear of the substrate occurs, expression (4) takes on a more complex form [14]:

$$\left(\frac{V_c}{\kappa_c} + \frac{V_s}{\kappa_s}\right) = (S \cdot N) \tag{5}$$

where V_s is the volume of removed substrate material, κ_s is the wear coefficient of the substrate. In this work, the resistance to micro-abrasion wear of the TiN coating on the same substrate is compared, so new parameters are introduced into the wear model: the coefficient of micro-abrasion wear of the "coating-substrate" system κ_{cs} and the total crater volume V_{cs}:

$$\frac{V_{cs}}{\kappa_{cs}} = (S \cdot N) \tag{6}$$

$$\kappa_{cs} = \frac{V_{cs}}{S \cdot N} \tag{7}$$

where the total crater volume V_{cs} is determined by equation (2). The wear path (S) is determined by the expression:

$$S = 2 \cdot R \cdot \pi \cdot \frac{n}{60} \cdot t \tag{8}$$

where n is the rotation speed of the ball (rpm), t is the wear time (s). The normal force (N) with which the freely rotating ball presses the wear point on the coating is determined according to the expression:

$$N = m \cdot g \cdot \cos\varphi \tag{9}$$

where m is the mass of the ball (kg), g = 9.81 ms^{-2}, φ is the angle of inclination of the slope with the pattern in relation to the horizontal plane. With the parameters used in the experiment N = 0.083 N, S(60s) = 37.68 m.

Residual stresses were tested with a Sentenso Pulstec µ-X360s portable X-ray diffractometer, which was mounted on the robot arm shown in Figure 4. Residual stresses were measured at the centre of a disc, in the two perpendicular directions. The principle of measurement with this diffractometer is described in reference [15]. In conducted tests the disc samples were irradiated using a beam current of 1.5 mA and voltage of 30 kV. The X-ray beam was directed to be incident on each sample at an angle of 35.0 degrees. The distance from the specimen and detector to capture the Debye-Scherrer (D-S) ring image was set to D_r = 54 mm. The X-ray Cr K_α wavelength (λ) used for X-ray diffraction was 2.29Å.

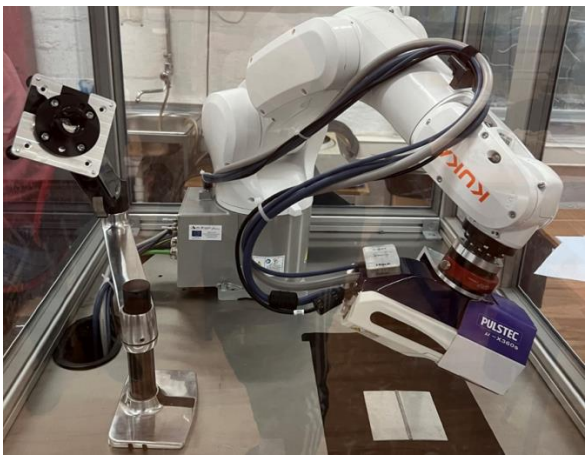

Figure 4. *Measurement of residual stresses with a portable XRD device Sentenso µ-X360s*

3. Results and discussion

3.1. Surface roughness

The results shown in Table 3 were obtained by testing the roughness. The results are presented by stating the mean value of the parameter and its standard deviation. The results show that the PVD coating process practically does not change the surface roughness compared to the initial state. After the PACVD process, the surface roughness increases as a result of ion sputtering prior to coating and the formation of the coating by plasma deposition of TiN droplets.

Table 3. *Surface roughness parameters of test samples made of steel 100Cr6*

Roughness parameters	Uncoated 100Cr6 steel	PVD TiN coating	PACVD TiN coating
$R_{max,}$ [μm]	0.470 ± 0.059	0.474 ± 0.126	1.256 ± 0.257
R_z, [μm]	0.400 ± 0.039	0.369 ± 0.036	1.,110 ± 0.158
R_a, [μm]	0.050 ± 0.003	0.045 ± 0.002	0.110 ± 0.009

3.2. Adhesiveness and coating thickness

Damage to the coating after indenting a diamond cone on the Rockwell C hardness tester is shown in Figure 5. The place of indenter indentation was recorded on an Olympus GX51 light microscope with a CCD camera. The appearance of the damage shows delamination around the print on the PACVD TiN coating, which represents the poor adhesiveness of the coating (HF = 6). In contrast, several microcracks and good plastic deformation of the coating are observed around the print on the PVD TiN coating, which is an indicator of good adhesiveness (HF = 3).

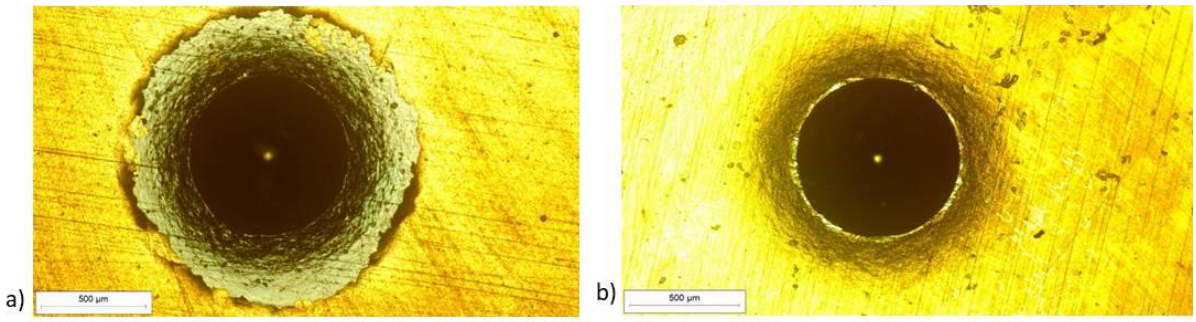

Figure 5. *Damage to the coating after the adhesion test using the VDI 3198 method: a) PACVD TiN coating, b) PVD TiN coating*

The thickness of the coating was determined by calotest and expression (1) after three consecutive wears at different places on the surface of the disc. For the PVD TiN coating, the mean thickness is *e* = 1.56 ± 0.15 μm, while for the PACVD TiN coating, the thickness is e = 2.07± 0.20 μm. The greater thickness of the TiN coating after the PACVD process is a consequence of the difference in the physical deposition processes and the longer coating application time compared to the PVD process.

3.3. Resistance to microabrasion

Figure 6 shows a series of prints on samples D1 (PACVD TiN) and D2 (PVD TiN) after microabrasion testing on a TRIBOtechnic calotester. The first print in the lower right corner of Figure 7 was created after 10 s of wear, and the last print in the sequence at the top left was created after 60 s of wear. In between are the wear marks after t = (20 s, 30 s, 40 s and 50 s). By comparing the appearance of the prints in Figure 6, it can be seen that in the case of prints on the PACVD coating in Figure 6a, the coating broke through after only 10 seconds of wear. The PVD TiN coating was penetrated only after 60 seconds of wear. Using a stereomicroscope and a CCD camera and a computer program for image

analysis *Image J*, the outer diameter of the crater was determined in two vertical directions. From these two diameter values, the mean diameter of the crater (*D*) was determined, and based on it and the wear path (*S*) from expression (8), the wear coefficient of the "coating-substrate" system was determined. The change in the wear coefficient depending on the product of the wear path and the normal load of the sample (*SN*) is shown in Figure 7.

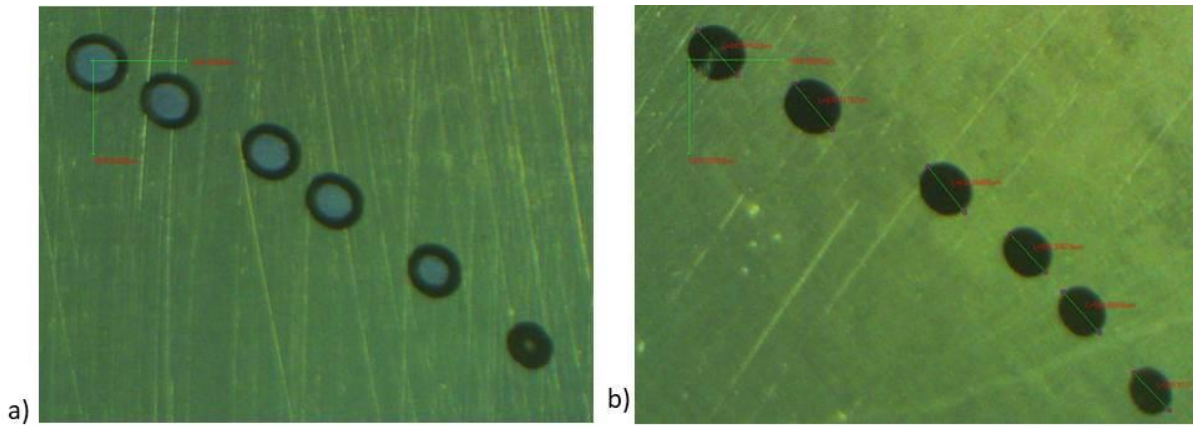

Figure 6. *A series of impressions after microabrasive wear of the coating: a) PACVD TiN, b) PVD TiN magnification 8:1*

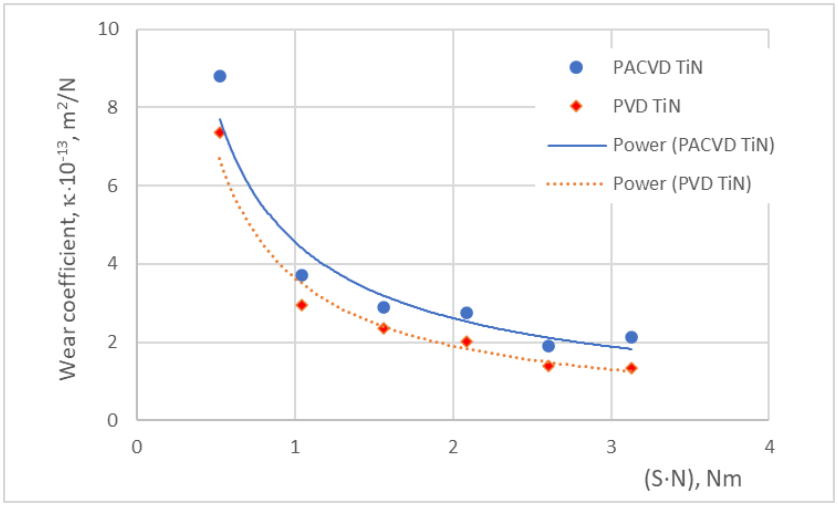

Figure 7. *Change in wear coefficient κ_{cs} depending on SN product for TiN coatings applied by PVD and PACVD processes*

3.4. Residual stresses

Residual stresses were measured by the XRD method in two vertical directions (x, y) and compared in Figure 8. On all tested disks, equal compressive residual stresses appear in both directions. The highest compressive residual stresses are found on the hardened and tempered disc (D0), σ_y = -189 MPa, which is a consequence of the presence of insufficiently tempered martensite in the microstructure of hardened steel 100Cr6. Residual stresses in the PVD TiN coating (sample D1) were reduced by 3 times compared to sample D0, while stresses in the PACVD tiN coating were reduced by 1.6 times compared to the hardened and tempered sample. The presence of increased residual stresses in the PACVD TiN coating coincides with its weaker adhesiveness and higher coefficient of micro-abrasive wear. the residual stresses in both coatings show less difference between the values in the x-axis compared to the y-axis. These differences can be explained by the position of the sample in the vacuum coating chamber, Figure 2d. Higher residual stresses in the coatings are located on the vertical axis of the disk. Their formation is a consequence of the difference in temperature between the upper and lower parts of the disk during cooling. The lower part of the disk rests on the cathode of the

coating device and cools more slowly than the upper part of the disk. During the cooling of the PACVD TiN sample from a coating temperature of 520 °C at a pressure of 2 mbar, larger temperature differences occurred along the height of the disk compared to the cooling of the PVD sample from a temperature of 500 °C in a high vacuum of $8 \cdot 10^{-3}$ mbar.

By comparing the change in the coefficient of microabrasion wear for the same worn path, less wear of the PVD TiN coating is observed by about 24% compared to the PACVD TiN coating. Both coatings after 50 s of wear (*SN* > 2.50 Nm) reach a stable wear regime in which the crater volume increase is dominantly caused by wear of the substrate. Greater wear resistance of the PVD TiN coating is in agreement with its better adhesion to the substrate

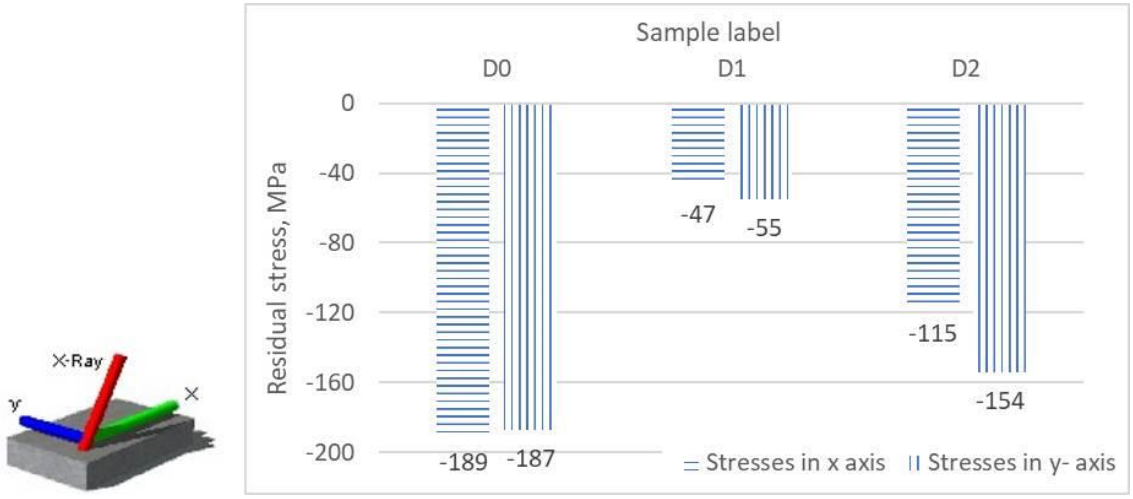

Figure 8. *Residual stresses on the surface of 100Cr6 steel discs with and without TiN coating*

4. Conclusion

The mechanical and tribological properties of the sample were improved by applying a TiN coating using the PVD and PACVD processes on hardened and tempered steel 100Cr6. By comparing the properties of the same coating applied by different methods, it is concluded that the PVD process resulted in a TiN coating with a smaller increase in surface roughness compared to the initial state, better adhesiveness on the substrate, a lower coefficient of microabrasion wear and lower residual compressive stresses compared to the PACVD process. In addition to comparing the properties of the TiN coating, the paper presents a microabrasive wear test procedure suitable for comparing the properties of thin coatings and describes a simple mathematical model derived from Archard's wear equation. By applying the derived model and using it to determine the wear coefficient, it is possible to compare the wear resistance of different types and thicknesses of coatings. The results of the research also point to the need to optimize the parameters of the PACVD process in order to increase the quality of the TiN coating with better adhesion of the coating to the substrate and lower residual stresses.

Acknowledgments

The authors wish to acknowledge the projects KK.01.1.1.07.0031 “Forecasted maintenance of industrial rotary equipment fundamental to machine learning and IoT technology in interaction with information systems” funded from the Ministry of Science and Education of Republic Croatian and The Central Agency for Financing and Contracting Programs and Projects of the European Union (SAFU) for their financial support.

References

[1] Syan, C.S., Matthews,A., Swift,K.G. 1986, Coating and Treatment Selection, Surface Engineering, 2:4, 249-256
[2] Burakowski, T., Wierzchon, T. 1999. Surface Engineering of Metals: Principles, Equipment, Technologies; CRC Press: Boca Raton, USA
[3] Neale, M.J. (Ed.), 2001. The Tribology Handbook; Butterworth-Heinemann Ltd.: Oxford, UK,
[4] M. Roy, M. Surface Engineering for Enhanced Performance against Wear, Springer-Verlag Wien 2013
[5] Jakovljević, S., Landek, D. 2023. Tribological Coatings—Properties, Mechanisms, and Applications in Surface Engineering, Coatings, Vol. 13
[6] Bhadeshia, H.K.D.H.2012. Steels for bearings, Progress in Materials Science 57, 268–435
[7] Stone, D. S. Yoder, K. B., Sproul, W. D. 1991. Hardness and elastic modulus of TiN based on continuous indentation technique and new correlation, Journal of Vacuum Science and Technology. A 9, 2543–2547
[8] Panjan, P., Čekada, M. 2005. Zaščita orodij s trdimi PVD-prevlakami, Inštitut J. Štefan, Ljubljana
[9] Filetin, T., Grilec, K., 2004. Postupci modificiranja i prevlačenja površina, Hrvatsko društvo za materijale i tribologiju, Zagreb
[10] Rutherford, K.L., HutchinsI, M., 1996. A Micro-Abrasive Wear Test, with Particular Application to Coated Systems, Surface and Coatings Technology, Vol 79, pp 231–239
[11] Landek, D., Zhao, L., Yang, Q., Dadouche, A. 2021. Increasing wear resistance of steel rings for sliding bearings by surface engineering procedures, Proceedings of the 21st International Conference on Materials, Tribology and Recycling MATRIB 2021, Vela Luka, Croatia June 30th - July 2nd, 314-325.
[14] Landek, D., Baršić, G. 2021. Wear of spiral drills coated by hard PACVD coatings, Proceedings of the 10th International Conference Mechanical Technologies and Structural Materials MTSM2021, 23-24. 09., Split, 87-90
[13] Fernandes, F.A.P.; Heck, S.C.; Pereira, R.G.; Lombardi-Neto, A.; Totten, G.E.; Castelettim L.C. 2010. Wear of plasma nitrided and nitrocarburized AISI 316L austenitic stainless steel. Journal of Achievements in Materials and Manufacturing Engineering, 40, 175-179
[14] Allsopp, D.N., Hutchings, I.M. 2001. Micro-scale abrasion and scratch response of PVD coatings at elevated temperatures. Wear, 251, 1308–1314
[15] Tanaka, K., 2019. The cos□ method for X-ray residual stress measurement using two-dimensional detector, Mechanical Engineering Reviews, Vol.6, No.1, 1-15

Influence of the sheet metal quality over the characteristics for the main girder at bridge crane applications

***Lachezar N. Lazov*[1], *Petko N. Nedyalkov*[2] *and Dragomir Ts. Vrazhilski*[1]**

1) Technical University of Sofia, 8 Kliment Ohridski Blvd., Sofia, Bulgaria

2) "St. Ivan Rilski" University of Mining and Geology, 1 prof. Boyan Kamenov str., Sofia, Bulgaria

Corresponding author: petko.nedyalkov@mgu.bg

Original scientific article

Abstract: The presented paper deals with simulation research of the probability density function of geometrical characteristics for main girder of one bridge crane. The bridge crane is represented through idealized calculation model of main girder witch is sheet material thickness relevant. The quality characteristics for the main girder is developed with material sheet thickness probability density function, cumulative density function and its inverse function. The functional dependence between parameters are revealed with triangular probability density function. Relevance between sheet metal thickness and cumulative density function for sectional inertial moment and girder stiffness is done with Monte-Carlo simulations.

Keywords: *bridge crane; girder; sheet thickness; simulation; triangular distribution*

1. Introduction

The main component of the hoisting bridge cranes is their steel construction which ensures reliable exploration. Reliability and exploration assurance are in the straight subjection to the main girder characteristics represented with its stiffness and sectional inertial moment values. Constructional design of the main girder and steel construction is valuated at the crane weight and price cost. At the engineering parameters it is valuated at required dynamical deformation, stiffness to frequency dependence, statically and fatigue strength. In the cases for small and middle class hoisting applications the main girder is formed by the steel profiles from standard or unified constructional catalogues. In the most usual case at heavy hoisting applications main girder is composed by the steel sheet weldment in a spatial box forming with respect to the mass and the price optimization.

The weldment construction is direct reflected to the mechanical characteristics of the main girder but also there is a dependence between mechanical parameters from the sheet metal quality and the main girder stiffness and sectional inertia moment. The quality property of the sheet metal have two main factors – the material compositional characteristics and the thickness value.

Previous researches [1], [2] shown that the typical sheet thickness values compared to nominal shown as histogram at Figure 1. The thickness value reflects over the strength amount for the weldment construction but also can be subjected as a fatigue and notch coefficient [3], [4], [5] factor with dual impact over the geometrical characteristics and material properties. Other researchers investigate [6], [7], [8] connection and dependence between carrying capacity, geometrical properties of main girder section ant its influence over proof of competence, reliability and durability.

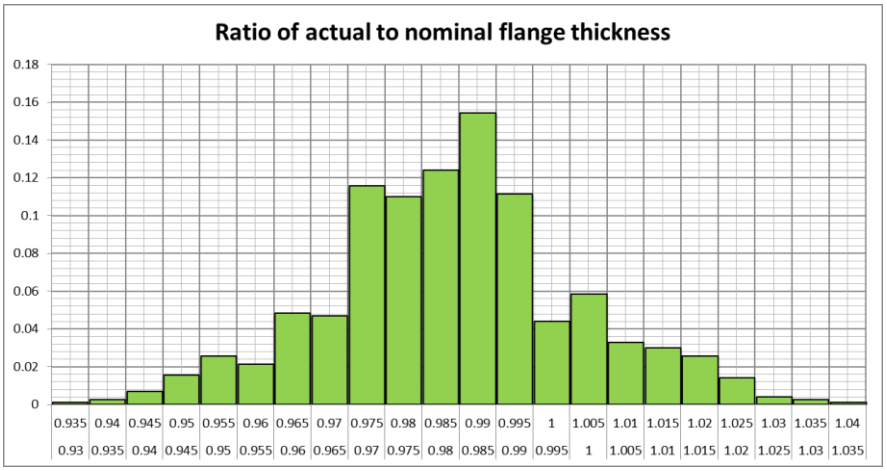

Figure 1. *Experimental density [1] for the sheet metal thickness*

2. Theoretical background

In a simulation study of the sectional inertia moment and stiffness characteristics the typical probability density function for variable values have to be represented with substitution theoretical density function. The substitution density function has to fulfill the requirements of any broadly-used non-parametrical criteria, non-parametrical Pearson's density type test or Kolmogorov-Smirnov's test. According to those criteria one can choose the triangular probability density function /Triangular(*a,m,b*)/ with parameters: - '*a*' is lower limit; - '*m*' is mode; - '*b*' is upper limit. Comparison between the experimental density from Figure 1 and triangular density function is presented at Figure 2, where: - '*Oi*' is the observed empirical density sample graph representation; - '*Ei*' is expected density from triangular pdf graph representation.

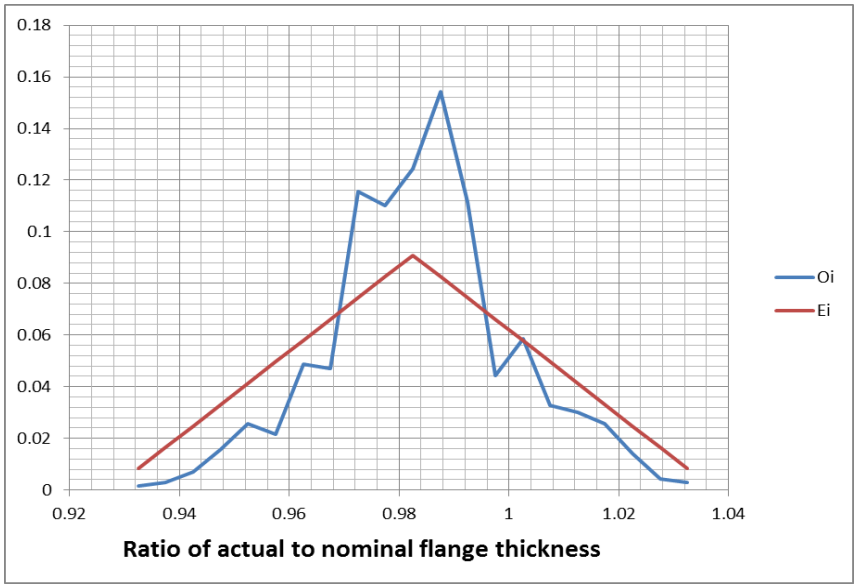

Figure 2. *Comparison between observed 'Oi' density and expected 'Ei' theoretical density functions*

The triangular density function is split at two continuity intervals according to the following formulas:

$$f_1(x) = \frac{2 \cdot (x-a)}{(a-m)\cdot(a-b)}, \qquad x \in [a,m] \tag{1}$$

$$f_2(x) = \frac{2 \cdot (x-b)}{(b-m)\cdot(a-b)}, \qquad x \in [m,b] \tag{2}$$

where the '*x*' is the variable; 'f_1' is the density at first continuity interval; and 'f_2' is the density at second continuity interval for triangular probability density function. The artificial history generation [9] for the input factor can be processed by different methods. One can choose the inverse function method which need cumulative distribution function (CDF), and for chosen triangular density function its CDF is presented by the following formulas and graph (Figure 3).

$$F_1(x) = \frac{(x-a)^2}{(a-m)\cdot(a-b)}, \qquad x \in [a, m] \tag{3}$$

$$F_2(x) = \frac{(x-b)^2}{(b-m)\cdot(a-b)} + 1\,, \qquad x \in [m, b] \tag{4}$$

where the '*x*' is the variable; 'F_1' is the cumulative distribution at the first continuity interval; and 'F_2' is the cumulative distribution at the second continuity interval for triangular probability density function.

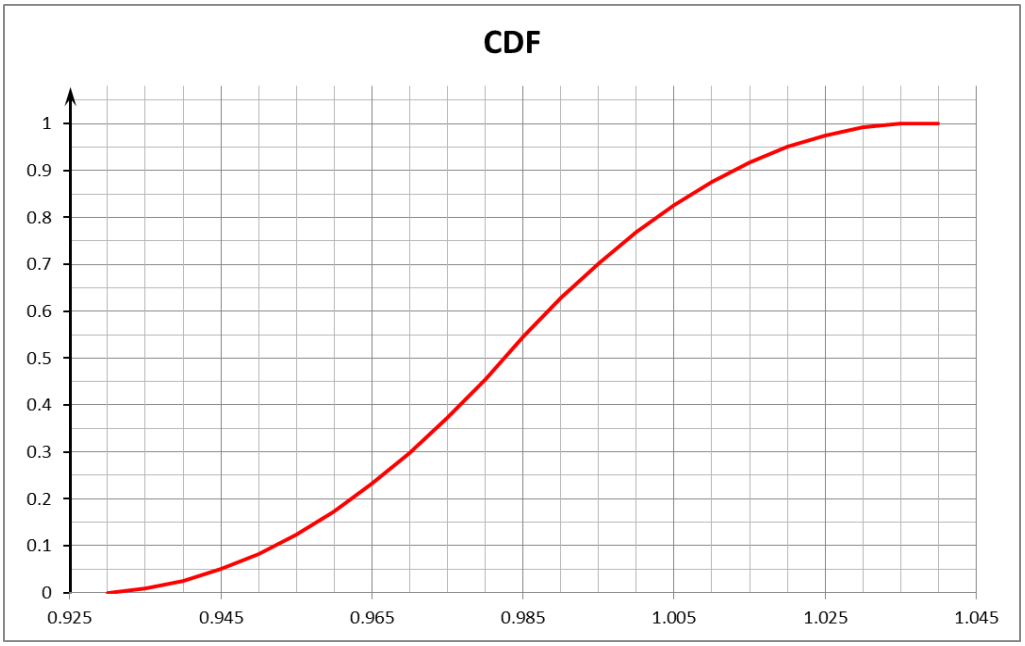

Figure 3. *Theoretical CDF for sheet thickness from triangular density*

The core of the Monte Carlo simulation calculation is a random number generation with suitable prepositional distribution. Usual case at the random number generator is by using random numbers from the uniform distribution whereafter had to be placed in the inverse function to calculate the variable random value at the chosen functional interval. The inverse cumulative distribution function is square root function for triangular probability density, represented by the following formulas:

$$x_1(F_1) = a + \sqrt{F_1 \cdot (a-m)\cdot(a-b)}, \qquad F_1 \in \left[0, \frac{m-a}{b-a}\right] \tag{5}$$

$$x_2(F_2) = b - \sqrt{(F_2 - 1)\cdot(b-m)\cdot(a-b)}, \qquad F_2 \in \left[\frac{m-a}{b-a}, 1\right] \tag{6}$$

where the 'x_1' and 'x_2' are the random variables; 'F_1' and 'F_2' are the values for random variables from the uniform distribution '*U[0, 1]*' sitting at the continuity interval for triangular probability density function. Those random values (represented with '*F*') generate the randomized values for sheet thickness, which randomized values are used in the Monte Carlo simulation.

3. Calculation and Simulation model

3.1. Section Inertia calculation

Sectional inertia moment for rectangular scheme, with typical form shown at Figure 4, is well known formula for box main girder, as presented below:¸

$$J = \frac{h^3 \cdot t_w}{6} + \frac{B \cdot {t_f}^3}{6} + 2 \cdot \left(\frac{h+t_f}{2}\right)^2 \cdot B \cdot t_f \ , \ m^4 \tag{7}$$

where the - ‘*h*’ is girder height; - ‘*B*’ is girder width; - ‘t_w’ is web thickness; - ‘t_f’ is flange thickness.

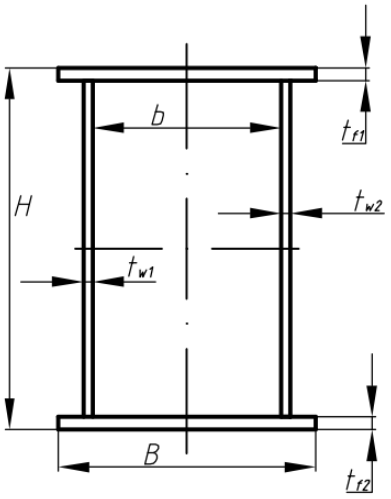

Figure 4. *Scheme of main girder dimensions*

Model for idealized bridge crane [10], [11] with parameters: - load capacity *Q* = 8 t; - bridge length *L* = 28,5 m; and with main girder section dimensions: - girder height *H* = 936 mm; - girder width *B* = 328 mm; - nominal flange thickness t_{fn} = 8 mm; - nominal wall thickness t_{wn} = 6 mm. Theoretical nominal value for sectional inertial moment, calculated according equation (7) is as follows:

$$J_n = \frac{h^3 \cdot t_w}{6} + \frac{B \cdot {t_f}^3}{6} + 2 \cdot \left(\frac{h + t_f}{2}\right)^2 \cdot B \cdot t_f \ = 19.087 \cdot 10^{-4} \ m^4 \tag{8}$$

3.2. Section Inertia for simulation model

The simulation model for sectional inertial moment have to use the formula without simplifications as follows:

$$\begin{aligned} J(t_{f1}, t_{f2}, t_{w1}, t_{w2}) = {} & \frac{h^3 \cdot (t_{w1} + t_{w2})}{12} + \frac{B \cdot (t_{f1} + t_{f2})^3}{12} + \cdots \\ & + \left(\frac{h + t_{f1}}{2}\right)^2 \cdot B \cdot t_{f1} + \left(\frac{h + t_{f2}}{2}\right)^2 \cdot B \cdot t_{f2} \ , \ m^4 \end{aligned} \tag{9}$$

where according to Figure 4: - t_{f1}, mm is upper flange thickness; - t_{f2}, mm is bottom flange thickness; - t_{w1}, mm is left web thickness; - t_{w2}, mm is the right web thickness.

The values for wall and flange thickness have to be taken as a random quantity with probability densities obtained from inverse transformation models from equations (5) and (6). Simulated thickness values are taken from computer software generated pseudo randomized real numbers from following intervals:

- ✓ flange thickness – $t_{fi}(F) = Triangular(0.93 \cdot t_{fn}, 0.975 \cdot t_{fn}, 1.04 \cdot t_{fn})$;
- ✓ wall thickness - $t_{wi}(F) = Triangular(0.93 \cdot t_{wn}, 0.975 \cdot t_{wn}, 1.04 \cdot t_{wn})$;

3.3. Results from simulation model

The result from simulation model represent particular realization for section inertial moment value. The control of the influence of the sheet metal quality over the main girder characteristics and specifically over the studied section inertial moment it is developed the diagram shown at Figure 5. That particular diagram is representation of estimated cumulative distribution function for relative frequencies of ten interval bins resulted from Monte Carlo simulation model.

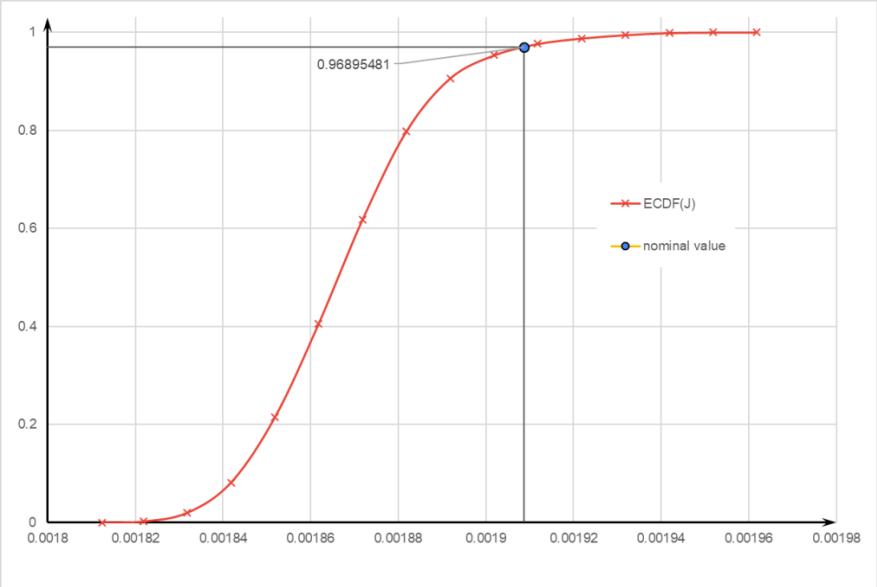

Figure 5. *Estimated cumulative distribution for section inertia moment value*

The diagram of estimated cumulative distribution function is pointing the nominal value towards the realizations of sectional inertial moment values from simulation model. The comparison between them shows that in 96.89 % of cases achieved moment value is smaller than the nominal.

3.4. Assessment for simulation results

The simulation model has to be assessed in some statistical criteria for stability of results values and statistical comparison. One can easy use the following two statistical indicators:

- ✓ Size effect /SE/ estimator:

$$efSd = \frac{\mu - \mu_0}{sd} \tag{10}$$

where: - $\mu = \mu(z) = mean(z_i)$ is the sample mean for the estimated variable; - $sd = sd(z) = stdev(z_i)$ is the sample standard deviation for the estimated variable; - $\mu_0 = z_n$ is the nominal value for the estimated variable;

- ✓ standard error of the sample mean:

$$sdSqn = \frac{sd}{\sqrt{n_s}} \tag{11}$$

where: - $sd = sd(z) = stdev(z_i)$ is the sample standard deviation for estimated variable; - $n_s = length(z_i)$ is the number of sample length in the estimated sample.

Usually [9], [12] the simulations using Monte Carlo method are recommended to be done with 'as much as could be calculated' number of calculations. The Figure 6 presented the algorithm one can

use to achieve a software programmable procedure in calculation the simulated values and some estimators and assessors.

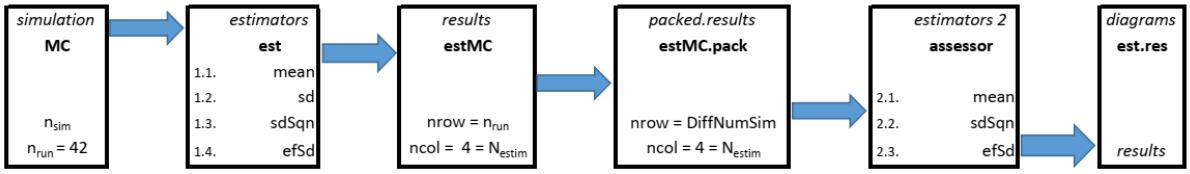

Figure 6. *Block scheme for estimation algorithm for Monte Carlo simulation.*

The secondary estimators algorithm was used to calculate an optimized 'n_{sim}' – number of simulations with randomized variables in particular spreadsheet which forms the resulting Monte Carlo simulated results. In purpose to estimate the stability of that particular result there were done a multiple runs 'n_{run}' at same conditions and same number of simulations. The results are stored at arrays and used in the calculation of second estimators.

The secondary estimator shown on Figure 7, size effect (SE) over the mean from different runs 'n_{run}' shows a table decreasing curve when rising the number of simulation. That curve is informative but there it is lacking with explicit inflex points. It is possible to use the change of drop angle between $20 \cdot 10^3$ and $200 \cdot 10^3$ number of simulations but not in definitive criteria because the changes in the slope can be influenced in particular complicatedness calculations.

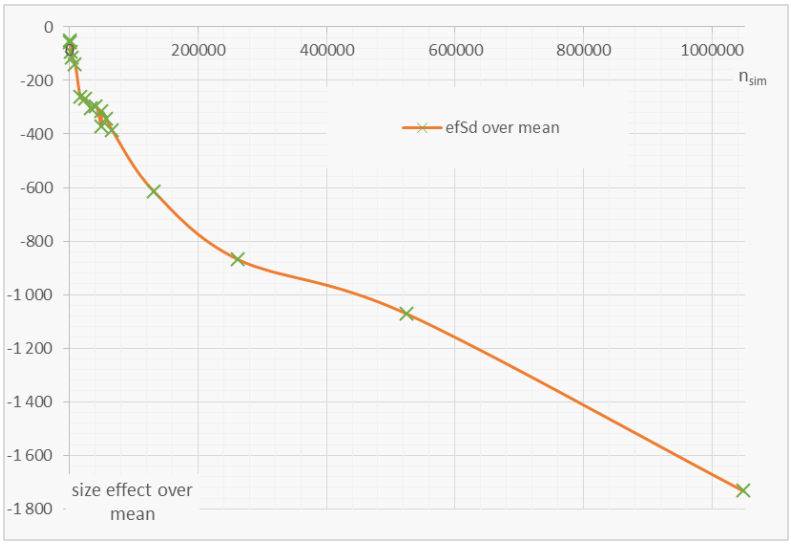

Figure 7. *Assessment diagram for the size effect over the mean.*

The secondary estimators shown on Figure 8, standard error of sample mean and mean over the size effect show different behavior. There is a definitive inflex of the slope (or drop down angle) and it is possible to be defined a minimum threshold level, for example $2.63 \cdot 10^{-10}$ for 'mean over SE' at near $10 \cdot 10^3$ simulations, and $1.68 \cdot 10^{-7}$ for '*sdSqn*' over SE at near $17 \cdot 10^3$ simulations. At Figure 9 is presented the interval of particular interest for number of simulations for Monte Carlo method between $1 \cdot 10^3$ and $100 \cdot 10^3$ simulations.

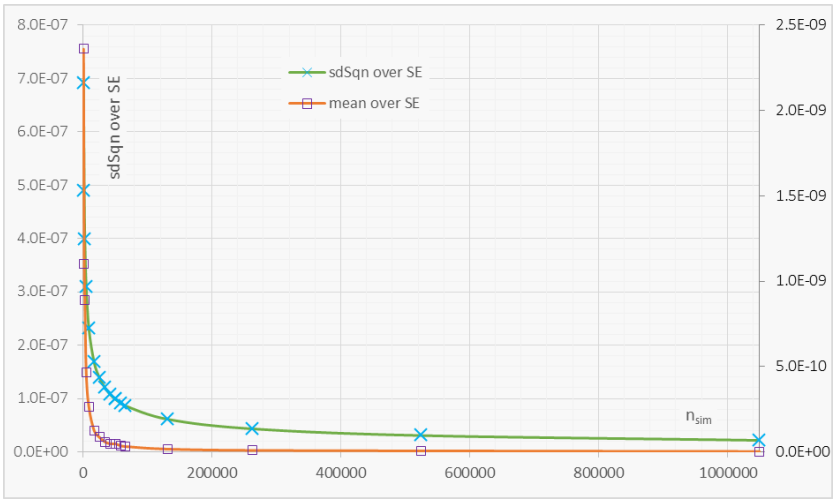

Figure 8. *Assessment diagram for the standard error of sample mean over the size effect and mean over the size effect.*

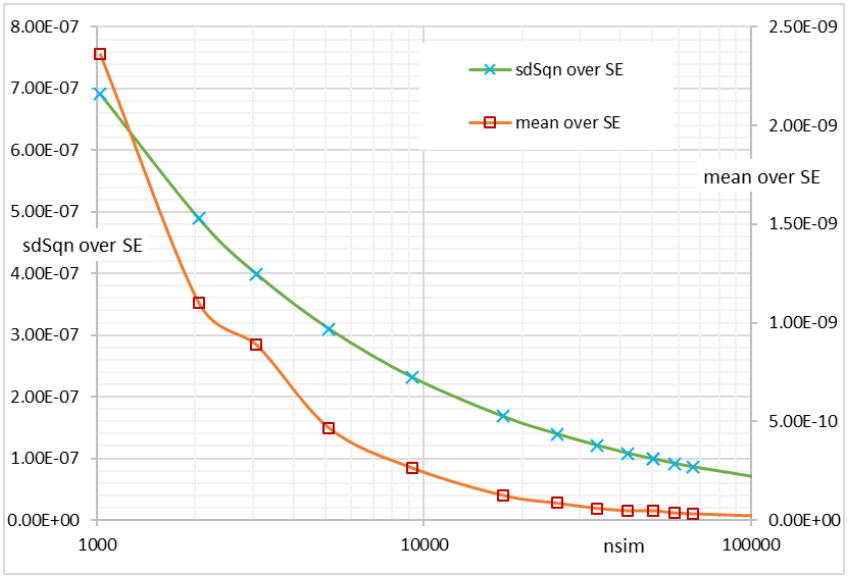

Figure 9. *Assessment diagram for the standard error of sample mean over the size effect and mean over the size effect with logarithmic horizontal axis.*

The total number of nearly twenty different samples with forty two (42) runs in a row and starting with thousand to more than one million ($1.0496 \cdot 10^6$) simulations were lead and results in global scale (Figures 7 and 8) shown that the stability of assessors was achieved over the one hundred thousands ($100 \cdot 10^3$) simulations where the curve of the assessor is asymptotiate to horizontal.

4. Conclusions

Deterministic approaches are at the heart of engineering education and engineering design. On the other hand, in operation, reliability, maintenance and testing, deviations are accounted for and realized, which are the basis for the development of probabilistic methods. The considered models and algorithms allow to reveal the relationship between deterministic and probabilistic approaches in a trivial engineering problem - calculation of geometrical characteristics of a main girder for a bridge crane. The presented comparative results show that ~97% physical performance of the structure cannot reach the design or nominal values.

The conducted multi length numerically-simulated experiment shows that number of simulations must exceed twenty thousands ($20 \cdot 10^3$) in order to ensure stability of numerical results at proposed model. The concluding remarks are summarized as follows:

✓ the presented model and algorithm is allowing to determine the influence of sheet metal quality over the main girder sectional inertia momentum and stiffness for bridge crane;

✓ the presented model is allowing to determine the limits for cumulative distribution function for sectional inertia moment value $J \in [J_{min}, J_{max}]$;

✓ it is possible to settle the type and parameters for the distribution of the sectional inertia moment;

✓ it is possible to conduct experimental ultrasonic thickness measurement and import data for the assessment of the section inertial moment characteristics about physical steel construction;

✓ algorithm is developed with criterial assessment values and steps for admission and estimation of minimal simulations in row for Monte Carlo method.

References

[1] Kirke Br., Al-Jamel I.H., 2011. Steel Structures Design Manual To AS 4100 1-st edition, Berkeley, USA.

[2] Byfield, M.P. and Nethercot, D.A., 1997. Material and geometric properties of structural steel for use in design - random variation in measured properties of nominally identical steel specimens, The Structural Engineer, Vol. 75, No. 21, 363-367

[3] Bright G. W. et. al., 2011. Variability in the mechanical properties and processing conditions of a High Strength Low Alloy steel, ISSN:1877-7058, doi:10.1016/j.proeng.2011.04.020, Procedia Engineering 10 (2011) 106–111.

[4] Motra, H.B., Hildebrand J. and Dimmig-Osburg A., 2014. Assessment of strain measurement techniques to characterize mechanical properties of structural steel, ISSN:2215-0986, http://dx.doi.org/10.1016/j.jestch.2014.07.006, Engineering Science and Technology, an International Journal 17 (2014) 260-269.

[5] MIhalikova M. and Janek J., 2007. Influence of the loading and strain rates on the strength properties and formability of higher-strength sheet, ISSN: 0543-5846(1334-2576), Metalurgija 46 (2007) 2, 107-110, Croatia

[6] Slavchev Ya., 2008. A Research on the Stressed State of Overhead Bridge Cranes Structure During the Steady-State Traverse of the Trolley, ISBN:978-954-580-248-5, Challenges in Higher Education and Research in the 21-st Century, vol. 6, part II, 393-396, Sozopol, Bulgaria

[7] Slavchev Ya., 2010. Research on Carrying Metal Structure of Overhead Bridge Cranes, ISBN: 978-3-8433-5644-2, Lambert Academic Publishing

[8] Radlov K., Mitrev R. and Rinkova, Ev. 2012. Statistical analysis methodics for hoisting crane failures. ISSN:1313-7530, Bulgarian Journal for Engineering Design, issue 12(2012), Sofia, Bulgaria

[9] Rubinstein R. Y. and Kroese D. P., 2017. Simulation and the monte carlo method, 3-rd Edition, ISBN: 978-111-8632-208, John Wiley & Sons, New Jersey, USA

[10] Lazov L., 2015. About the Influence of Camber Over Selection of the Main Girder Cross Sections of Bridge Cranes, ISSN:1314-9628, CAx Technologies, issue 3, 110-114, Sofia, Bulgaria

[11] Kotzev N., Lazov L., Dimitrov L., 2015. About numerical methods for strength calculations of steel crane structures, ISSN:1313-955X, BulTrans-2015, 46-50, Sozopol, Bulgaria

[12] Oberle W., 2015. Monte Carlo Simulations: Number of Iterations and Accuracy, ARL-TN-0684, July 2015

Cognitive manufacturing

Vidosav D. Majstorović[1]

1) University of Belgrade, Faculty of Mechanical Engineering, Belgrade, Serbia

Corresponding author: vidosav.majstorovic@gmail.com

Keynote lecture - Original scientific article

Abstract: Digital manufacturing technologies are already widely present in manufacturing and industry, and have become the foundation for the implementation of the Industry 4.0 model in practice. The transformation signified by the Industry 4.0 model has embraced a wide range of communication technologies, mechanisms for connecting machines and parts within a factory, and the capabilities of analyzing big data with the use of artificial intelligence tools. These technologies offer powerful instruments for creating more flexible and profitable data-driven manufacturing processes using the internet.

As more factories and equipment within them are being equipped with IoT, the volume of data will only continue to increase. Conventional computing is faced with demands to scale memory, processing speed, and decision-making accuracy after processing this data. For these reasons, a cognitive model must be applied for the processing, analysis, and optimization of information. To truly pave the way forward toward Industry 4.0 and beyond, manufacturing must evolve into cognitive manufacturing.

Cognitive manufacturing fully leverages data across systems, equipment, and processes to gain practical insight into the entire value chain from design, through production, to support in operation. Built upon the foundations of IoT and utilizing big data analytics in conjunction with cognitive technologies, cognitive production realizes crucial improvements in productivity, quality, efficiency and reliability throughout the manufacturing environment.

This paper provides a detailed analysis of the current context of cognitive manufacturing, as well as presents our some results in the development of a cognitive manufacturing metrology model.

Keywords: *Industy 4.0/5.0; Manufacturing; BDA; AI/ML; Congnitive*

1. Introductory remarks

The manufacturing industry is constantly faced with demands for high flexibility and adaptability in order to meet rapidly changing market requirements. Therefore, it is necessary to have adaptable planning processes (engineering and business) based on gathering real-time data about production and processes to generate feedback for the control of technological processes. This is where cognitive systems (CAPP, CAM intelligent systems, etc.) come into play, offering capabilities for automated reasoning and adaptation to unforeseen changes during the processing, enabling the realization of the concept of cognitive manufacturing at the workshop level [1].

Cognitive manufacturing is a new paradigm of technological systems, table 1 [2][(1-8)]. This paradigm has been in development and its concept has been defined for more than three decades.

Its establishment and application in manufacturing are based on the tools and techniques of artificial intelligence, which has been particularly highlighted in the Industry 4.0 model.

Cognitive manufacturing has several definitions, and one of the most common is [3]: ''*Cognitive manufacturing employs cognitive computing, industrial IoT, and advanced analytics to optimize production processes in ways that were not previously possible. It helps organizations improve fundamental business metrics such as productivity, delivery reliability, quality, business safety, and profits while simultaneously reducing downtime and operating costs''.*

Cognitive technologies delve deeply into the production process and business environment to glean information that holds tangible value for the manufacturer.

Cognitive computing utilizes models to simulate human thought processes in complex situations, particularly when the answers can be ambiguous or uncertain. It overlaps with AI and incorporates many of its foundational technologies to power cognitive applications, such as expert systems, neural networks, virtual reality (VR), and robotics [3].

Table 1. *Congnitive manufacturing – basic framework (adapted from [2])*

Congnitive manufacturing (Smart manufacturing / Industry 4.0 (4.1) / 5.0)	*Other manufacturing paradigms (with some elements of Congnitive manufacturing)*	*Enabling technology*
1. Digitalization of each part of factory by interoperability and increase productivity. 2. Conected devices (IoT), real time control (ERP/MES), distibuted intelligence (AI/ML). 3. Collaborative supply chain management, fast responsivness to market changes and suppling chain desruptive (SCM). 4. Integrated and optimal decision making for energy and resource efficiency. 5. Advanced sensors and big data analytics (BDA), thought product lifecycle to achive fast innovation lifecycle. 6. Sustainable, human-centric and resilence manufacturing (I 5.0). 7. Procesess of planing, designing and decision making support of advanced tools and techniques of AI/ML (Congnitvie manufacturing in I 4.0 / 5.0).	Lean manufacturing: set of tools for identification and steady elimination of all kinds waste in manufacturing.[1]	Work flow optimization, real time monitoring and visulation.
	Flexible manufacturing: integrated machine tools and material handling equipment by computer control of produce product.[2]	Modulazired design, interoperability, service orientied architecture.
	Sustainable manufacturing: creating product with min negative environmental impacts while consvering energy and natural resources.[3]	Advanced materials, sustainable processes metrics and measuerment, monitoring and control.
	Digital manufacturing: using digital technology through product lifecycle to improve product, process and enterprise performance and reduce the time and cost of manufacturing.[4]	3D modelling by engineering appraoch and product lifecycle management.
	Cloud manufacturing: form of decentralized and networking manufacturing based on cloud computing and service oriented architecture (SOA).[5]	Cloud computing, IoT, virtulization, service-oriented techologies and advanced data analitics.
	Intelligent manufacturing: implementing AI tools and techniques that can automaticlly adapt to changing process parameters with min human intervention.[6]	AI, advanced sensing, optimization and knowledge management.
	Holonic manufacturing: using agents to a dynamic and decentralized manufacturing process.[7]	Multi-agent systems, decentralized control and model based reasoning and planning.
	Agile manufacturing: using effective processes and tools to enable manufacturing systems to respond quickly to customer needs and market changes while still controlong costs and quality.[8]	Collaborative engineering, SCM, PDM.

[1] Strategies-International. Toyota Production System and Lean Manufacturing, http://www.strategosinc.com/toyota_production.htm.
[2] Flexible and reconfigurable manufacturing systems paradigms, Int J Flex Manuf Syst (2006) 17:261–276 DOI 10.1007/s10696-006-9028-7
[3] Glossary of Sustainable Manufacturing Terms, EPA, http://archive.epa.gov/sustainablemanufacturing/web/html/glossary.html.
[4] DOE-FOA-0001263 Manufacturing innovation institute for smart manufacturing: advanced sensors, controls, platforms, and modeling for manufacturing.
[5] Cloud-Based Manufacturing: Old Wine in New Bottles? , Proceedings of the 47th CIRP Conference on Manufacturing Systems
[6] http://www.astri.org/technologies/initiatives/intelligent-manufaturing/
[7] Gunasekaran, Agile Manufacturing: The 21st Century Competitive Strategy, Elsevier, 2010.
[8] LNS Research, 2013. 28 Manufacturing Metrics that Actually Matter, http://blog.lnsresearch.com/blog/bid/188295/28-Manufacturing-Metrics-that-Actually-Matter-The-Ones-We-Rely-On.

This paper consists of several sections. At the outset, it provides a fundamental definition of cognitive manufacturing as one of the paradigmatic technological systems that is gaining increasing significance. The second section features a detailed analysis of the development of cognitive manufacturing models across three periods, which have defined the framework for the development and implementation of this concept in real-life production. In the third section, we present a few examples of our research in

this area, which relate to manufacturing metrology, followed by a conclusion outlining the basic findings and future research directions in the field.

2. Congnitive manufacturing – the development of the concept

Cognitive manufacturing, as a new paradigm of technological systems, has a history dating back to the mid-1980s. Therefore, at the present time, we can categorize its evolution into three distinct periods, Table 2.

Table 2. *The evolution of cognitive manufacturing*

Period	*Characteristics*	*Elements of application*
Before 2010. year (level 1).	Support by AI tools and techniques (knowledge base, forward/backward search, reasoning, ES, ANN).	CAPP / CAI (Manufacturing / inspection on CMM planning).
Between 2010. and 2020. year (level 2).	As part of the model Industry 4.0 (AI/ML).	BDA, Intelligent design and planning.
After 2020. year (level 3).	As part of the model Industry 5.0 (ML deep).	BDA, Colaborative design and planning.

In the following analysis, a detailed examination of all levels of development will be provided, focusing on their application in manufacturing.

2.1. Cognitive manufacturing - the model prior to 2010

The initial exploration of this field commenced in the mid-1980s with the development of the Computer-Aided Process Planning (CAPP) model for CNC machine tools, particularly for prismatic parts. Simultaneously, research endeavors were initiated for inspection planning on CNC Coordinate Measuring Machines (CMM), again for prismatic parts. In both cases, the focus was on the implementation of expert systems (ES).

In [4] was given a data model and system structure for an automatic and integrated process planning for machining, inspection, and feedback based on the newly developed ISO standard STEP/STEP-NC. Developed model provides the cognitive capability for automatic on-line monitoring, automated reasoning, and adjustment to unforeseen changes during machining processes, table 3.

Table 3. *An overview of some of the most important features of cognitive manufacturing up to 2010. years*

Main issue	Source	Main messages
Integrated process planning for machining and inspection.	[4]	Automatic on-line monitoring and automated reasoning.
Using self-optimizing systems Cognitive Tolerance Matching (CTM).	[5]	Higher precision of delimited solution finders - Cognitive Failure Cluster (CFC).
Model of cognitive manufacturing.	[6]	Using Industrial Internet and Cognitive Control.
Cognitive production planning and control system.	[7]	RFID technology is used to create these smart products, on the shop floor (knowledege base).
Integrates cognitive capabilities into machines to produce customized parts.	[8]	Automatic parts selection, generative CNC machining planning, and automated fixture design.
The model effectively automates the decision-making process for employee evaluation in smart industries.	[9]	Game based model for automated decision making.
The brain-style information processing to apply the cognitive intelligence to the elements of a Cognitive Factory.	[10]	Neuroscience into engineering tasks that are suitable to build modern manufacturing systems, based on human-machinecollaboration.

The acoustic quality of rear axle drives is determined by the contact pattern of their gear sets, but the complexity of the production process means that many factors influence the result, making it difficult to develop a holistic analytical model to control the production process effectively. In [5] combines self-optimizing systems with clustering optimization for high precision and reduced training time of ANN.

Brain and biologically-inspired algorithms can provide flexible and robust self-X capabilities for manufacturing systems, enabling new levels of adaptability and re-configurability. In [6] proposes a cognitive manufacturing system architecture that utilizes benefits from Industrial Internet and Cognitive Control.

Paper [7] proposes a cognitive production planning and control system that uses smart products with knowledge about the production process and its state to achieve efficient production in an increasingly unpredictable environment. The system represents the executable production of each resource as capability profiles, allowing for better allocation of production steps. The proposed system can adapt to unforeseen events and autonomously update planning data based on real production values, leading to a reduction in resource idleness and waiting time for missing materials.

The model in [8] autonomous design-to-fabrication system integrates cognitive capabilities such as reasoning from knowledge models and autonomous planning into machines to fabricate customized parts. It includes automatic parts selection using an ontology, generative CNC machining planning using shape grammars, and automated fixture design based on a flexible fixture device hardware.

The paper [9] proposes an automated model for employee performance evaluation in smart industries using IoT sensors and GPS location data. The model classifies activities as positive, negative, or neutral and uses game theory to draw cognitive decisions. The concept of the Cognitive Factory aims to equip machines and processes with cognitive capabilities to assess and increase their scope of operation autonomously. However, practical implementation of this concept is limited by technical challenges. This paper [10] proposes a method inspired by the working mechanisms of the human brain that harnesses the reasoning capabilities of cognitive architecture.

The conducted analysis shows that the first generation of cognitive manufacturing models is characterized by the implementation of various simulation and modeling approaches to simulate the cognitive process of product design and process planning engineers.

2.2. Cognitive Manufacturing - the model from 2010 to 2020

Industry 4.0 represents a novel model of technological system automation that relies on the interconnectivity of Cyber-Physical Systems (CPS) through the Internet of Things (IoT), accompanied by Big Data Analytics (BDA) optimization through the implementation of Artificial Intelligence (AI) and Machine Learning (ML) techniques, operating in real-time. Therefore, cognitive manufacturing embodies the ideal framework for development within the Industry 4.0 concept, which will be further exemplified in subsequent analyses.

Currently, smart manufacturing systems are becoming more equipped with cognitive capabilities through advanced computing, data analytics, and the Internet of Things. However, the development of Self-X levels, such as self-configuration, self-optimization, and self-adjustment, is still in an early stage. To advance these capabilities, this paper introduces an industrial knowledge graph-based multi-agent reinforcement learning method [11], Table 4. This model is formulated based on empirical knowledge and patterns in the manufacturing process, which is then embedded using a proposed graph neural network algorithm for self-configurable solution searching and task decomposition. Additionally, a decentralized system is presented for self-optimizing the manufacturing process using ML techniques. Predictive maintenance (PdM) has the potential to reduce unexpected machine downtime and related cost, but existing approaches often have difficulty in identifying and estimating faults due to a lack of effective knowledge management and correlation analysis. Graph-based approaches (GbA) with cognitive intelligence are proposed as a solution, as they are superior in semantic causal inference, heterogeneous association, and visualized explanation [12]. To address this gap, this paper provides a comprehensive survey of GbA in PdM, organized by the stages of anomaly detection, diagnosis, prognosis, and maintenance decision-making.

Table 4. *An overview of some of the most important features of cognitive manufacturing from 2010. to 2020. years*

Main issue	Source	Main messages
Industrial knowledge graph (IKG)-based multi-agent reinforcement learning (MARL) approach torealizing the so-called Self-X cognitive manufacturing network.	[11]	Self-X cognitive manufacturing network for achieving cognitive mass personalization (multi-robot reaching task).
Four mainstream GbA in PdM domain: Graph neural network (GNN), Knowledge graph (KG), Bayesian network (BN), and Graph theoretic model (GTM).	[12]	Modeliranje i pretraživanje baze znanja održavanja mašinskih sistema pomoću različitih graph modela teorije.
The cognitive system experiences what is commonly referred to as cognitive load.	[13]	Cognitive load refers to the mental load that performing a specific task imposes on the human's cognitive system.
Cognitive manufacturing integrate the virtual – physical system era of technology with the tools and techniques like IOT, computing, smart manufacturing.	[14]	Intelligent plant environment which can achieves high quality reliable, flexible, efficient eco-friendly manufacturing.
A factory based on MES, PLC & SCADA model for maintenance management and scheduling.	[15]	Industrial Internet of Things (IIoT) platform.
Cognitive Manufacturing and Cognitive Enterprise, create an Enterprise Information Infrastructure.	[16]	Focused on information-based problem solving.
Architecture for cognitive manufacturing system: cognition, function and persistence layer.	[17]	Open Architecture manufacturing system.
Service-oriented SMS architecture, as support of cognitive manufacturing model.	[18]	The ISA 95 standard is frame which defines a 5-level model for the cognitive manufacturing enterprise.
The Industry 4.0 paradigm can benefit from the formalisation of the three-layer architecture (Cyber layer, Control layer and Physical object), in which the relationships between humans, technologies, and data flows are represented.	[19]	Social Human in the Loop Cyber-Physical Production Systems scenarios.
Decision interaction ontology (DIO) as information model for a Knowledge-Based Platform for Decision Support in the Design of Engineering Systems.	[20]	Example: Capturing the Decision Interaction Knowledgein the Design of a Gearbox by DIO.
Cognitive manufacturing and edge computing can help the iRobot- Factory to achieve the intelligent automation of the production process, enabling it to improve the efficiency, quality, and sustainability of the manufacturing industry.	[21]	The iRobot-Factory uses cognitive manufacturing to enable active operation and maintenance.
Quality improvement, data compression, ontologies for physical asset management, predictive maintenance, and remote monitoring, proposing innovative solutions for ZDM and predictive maintenance utilizing cognitive analytics and AI.	[2]	Model of cognitive manufacturing based on quality and maintenance model.
Smart manufacturing: Product development lifecycle standards, Production system lifecycle standards and Business cycle for supply chain management standards.	[3]	Standards support the participation of a wide range of organizations from small manufacturers to large multi-national corporations.

Cognitive manufacturing, which uses cognitive computing, the industrial IoT and advanced analytics, can improve major business metrics while reducing costs and downtime. However, the cognitive load, previously neglected in manufacturing, can impact Industry 4.0. In paper [13] investigates how human-computer interaction technologies can reduce cognitive load and examines applications of cognitive manufacturing that use these technologies. A conceptual framework is developed that links cognitive manufacturing to a reduction of the cognitive load.

The automation of manufacturing processes and manufacturing systems can achieve mass production levels of lead time and quality. This approach helps industries address production challenges, with the ability to produce versatile products in short timeframes with higher quality. Intelligent manufacturing, also known as cognitive manufacturing, plays a crucial role in achieving these objectives. It enables automation and productivity while improving collaboration between different functions like supply chain, engineering, sales, and operations. Intelligent manufacturing is vital for improving fundamental objectives like production output, reliability, versatility, quality, safety, and yield, while reducing downtime and costs. This paper [14] examines the impact of intelligent manufacturing techniques on industries.

From IBM’s point of view, we are really entering, at the Industry 4.0, or the cognitive manufacturing era, and it is fully differentiated from any that came before it. The digital transformation of production processes creates new opportunities to achieve levels of productivity and specialization not previously possible [15]. Transforming and improving manufacturing through production quality insights and production optimization is realized through the concept of an Industrial Internet of Things (IIoT) platform.

Paper [16] discusses the paradigms of Industry 4.0, Internet of Things, and Cyber-Physical Systems that are shaping the future design and functioning of enterprises. The paper introduces the concepts of Cognitive Manufacturing and Cognitive Enterprise, which use these paradigms to create an Enterprise Information Infrastructure that is focused on information-based problem solving. Also is proposes a Control approach for a Cognitive manufacturing enterprise that is inspired by the perception-reasoning-learning processes of the human brain.

In [17] explores the shift from mass production to mass customization in manufacturing and the need for new approaches to maintain automation. It suggests a cognitive approach utilizing brain and biologically-inspired algorithms for self-X capabilities that can adapt industrial systems to unforeseen conditions, enabling greater flexibility and re-configurability. Authors proposes a cognitive manufacturing system architecture that incorporates Industrial Internet and Cognitive Control.

Smart Manufacturing integrates advanced manufacturing methods, operational technologies, and information and communication technologies to drive the creation of manufacturing systems with greater capabilities in cost control and performance. Unlike the hierarchical layers of the past, Smart Manufacturing Systems are organized as networks of specialized manufacturing components that enable high levels of performance for manufacturers in agility, productivity, and quality. In [18], the impact of individual ICT technologies on the emerging manufacturing ecosystem as cognitive manufacturing is studied, proposing a service-oriented SMS architecture that leverages the benefits of ICT and the safety and security requirements from the OT domain.

In [19] discusses the development of smart factories through the use of Industry 4.0 technologies, where humans and machines interact. The paper emphasizes the importance of understanding and modeling the role of humans for efficient manufacturing systems, particularly in Social Human-in-the-Loop Cyber-Physical Production Systems. An architecture is proposed to represent social interactions in smart factories, depicting different human roles and exploring data-driven decision-making processes.

Design processes for complex engineered systems are complicated due to the interdependencies between subsystems, resulting in interactions among sets of design decisions. Representing and capturing knowledge related to decision interactions is crucial for decision-based design processes. To address these challenges, the paper [20] identifies nine basic interaction patterns among decisions and proposes an ontology to define the knowledge associated with these interaction patterns. The ontology captures both vertical and horizontal interactions between decisions, allowing for the design of flexible, reusable, and executable decision workflows. The usefulness of the ontology is illustrated through various design examples, including a reduction gearbox design and composite structure design.

Edge computing is introduced in intelligent factories to expand computing resources, network bandwidth, and storage capacity at the IoT edge and solve psychological problems of users through

the interaction of the Affective Interaction Intelligence Robot (iRobot). Paper [21] describes an iRobot-Factory that adopts a highly interconnected and deeply integrated production line, and discusses its overall structure, composition, characteristics, and advantages of cognitive manufacturing and edge computing. The implementation of iRobot volume production using the iRobot-Factory is explained, along with experimental results showing significant improvement in chip assembly, production efficiency, and reduction in system instructions.

Closed-Loop Lifecycle Management (CL2M) is an essential component of the circular economy and enables manufacturers to connect in-service issues to process conditions and product information at different stages of the lifecycle. Zero Defect Manufacturing (ZDM) can be implemented through two approaches: product-oriented and process-oriented ZDM. The Industrial Internet of Things, cloud and edge technologies, industrial AI, ontologies, and knowledge graphs enable data-driven cognitive manufacturing, facilitating smart maintenance and manufacturing development with increasing cognitive and predictive characteristics [2].

Manufacturers are facing increasing demands for customization, smaller lot sizes, and sudden supply chain disruptions, requiring the use of technologies that can quickly adapt to changes while optimizing resource usage and quality. A Smart Manufacturing System or Cognitive Manufacturing that prioritizes the flow and reuse of data will be crucial in meeting these demands. However, data exchange among disparate systems requires information standards. This report reviews the existing standards landscape for smart manufacturing systems across three dimensions: product, production system, and business [3]. This review will help manufacturing practitioners understand useful standards for integrating smart manufacturing technologies.

In conclusion of this chapter, we can emphasize that smart manufacturing, as an essential component of the Industry 4.0 model, provides the fundamental framework for the development of cognitive manufacturing, which relies on the implementation of Industry 4.0 elements.

2.3. Cognitive manufacturing - a post-2020 model

Industry 5.0 is an innovative approach to manufacturing that emphasizes the importance of human-machine collaboration, personalized production and customization, social responsibility, and sustainability. The integration of human intelligence with advanced technologies can lead to a more efficient, productive, and responsible manufacturing process, potentially creating new job opportunities while ensuring ethical and sustainable practices.

Industry 5.0 builds upon the foundations of Industry 4.0 and shares many of its features and technologies. Both Industry 4.0 and Industry 5.0 enable the use of automation, the Internet of Things (IoT), big data, and artificial intelligence to drive innovation and increase efficiency in manufacturing processes.

However, while Industry 4.0 focuses on the integration of machines and data in the manufacturing process, Industry 5.0 recognizes the importance of human intelligence to enhance the capabilities of machines. Industry 5.0 seeks to find a balance between the use of automation and the need for human input, highlighting the benefits of human-machine collaboration.

While Industry 4.0 focuses on increasing efficiency and productivity, Industry 5.0 addresses the limitations of Industry 4.0 by integrating human intuition and creativity, promoting ethical and responsible manufacturing practices, and embracing the customization of products to meet the needs of individual customers.

In [22] highlights the potential of Industry 5.0 to create a more sustainable, human-centered approach to industrial production. It reviews the key characteristics and connotation of Industry 5.0 and proposes a tri-dimension system architecture for implementation, including cognitive manufacturing. The paper also discusses key enablers, potential applications, and challenges for realizing Industry 5.0. However, the authors note that research in this area is still in its infancy, and further work is needed to fully realize the potential of Industry 5.0, table 5.

Table 5. *An overview of some of the most important features of cognitive manufacturing after 2020. years*

Main issue	Source	Main messages
The socially intelligent factory of Industry 5.0 seeks to promote a culture of collaboration, where workers and machines communicate and learn from each other, building a shared understanding of the manufacturing processes.	[22]	Industry 5.0 can also be considered an intelligent (cognitive) factory, as it integrates advanced technologies such as artificial intelligence, machine learning, and natural language processing to enable machines to make data-driven decisions and continuously learn and adapt to their environment.
The European industry has many opportunities to become more efficient and competitive in different stages of the value chain. This can be done by adopting technologies like IoT, AI/ML and blockchain to optimize logistics and reduce waste in the supply chain.	[23]	EU white paper for Industry 5.0.
The CEPC has installed a cognitive engine using a dynamic ontology to predict the best next move in a manufacturing operation.	[24]	The CEPC supplements human decision-making for process control purposes.
The OAR model-based cognitive framework is used to meet the dynamic cognitive needs of the production system.	[25]	Digital twins, industrial big data, and artificial intelligence, a multi-dimensional cognitive framework based on the OAR model is given.
Experts identified 16 functions of Industry 5.0 that deliver sustainable development values through interpretive structural modeling. These functions should be developed in a specific order to maximize their synergies and contribution to the intended sustainability values.	[26]	The study's roadmap offers insights into Industry 5.0's potential contributions to sustainable development and highlights enablers like Government 5.0 and Corporate Governance 5.0.
It is widely agreed that in all future production environments, humans should maintain a central position.	[27]	In Industry 5.0 use cases, expanding upon the "human in the loop" concept could be useful as a design tool.
Industry 5.0 integrates physical and virtual spaces and uses advanced IT technologies, the Internet of Things, robots, AI, and augmented reality for the benefit and convenience of citizens, not just for economic gain.	[28]	Industry 5.0 represents a new paradigm shift that places human needs and environmental sustainability at the forefront of production processes, while also embracing the importance of resilience in a rapidly changing global landscape.
Industry 5.0 represents a new phase in the evolution of the manufacturing industry, in which digital technologies are used to create more connected, intelligent, and sustainable production systems that benefit society as a whole.	[29]	Industry 5.0: from digital manufacturing to digital society.
Industry 5.0 has the potential to transform healthcare by creating more personalized, efficient, and intelligent systems that benefit patients and healthcare providers alike. From AI-powered diagnosis and treatment to remote monitoring and drug development, the possibilities for intelligent healthcare are vast and exciting.	[30]	Healthcare 5.0.
Operator 5.0 aims to integrate advanced technologies into the role of human operators in manufacturing and industrial processes. Robotics and Automation, AR and VR, and AI and Machine Learning will be crucial technologies to empower operators to work effectively and take on new tasks.	[31]	For Operator 5.0 several key technologies will be crucial: Robotics and Automation, Augmented Reality (AR) and Virtual Reality (VR), and Artificial Intelligence and Machine Learning, which will enable the creation of intelligent systems capable of learning from data and adapting to changing conditions.
Industry 5.0 utilizes a range of modern cutting-edge technologies such as AI, IoT, big data, cloud computing, blockchain, digital twins, edge computing, collaborative robots, and 6G to remove mundane, filthy, and repetitive activities from human workers.	[32]	Most successful businesses will be those that can combine the dual powers of technology and human ingenuity.

Observing and analyzing collaboration, developing the concept of operations with stakeholders, and including ethical considerations. The complementary approaches of actor-network theory, concept of operations, and ethically aware design are identified as potential solutions.	[33]	Joint cognitive systems have the potential to become highly adaptive and resilient, able to learn and evolve along with their human users.

Industry 5.0, which focuses on a socio-centred, sustainable, and competitive industry, was discussed during virtual workshops with European research and technology organizations [23]. Enablement in this area includes human-centric solutions, bio-inspired materials, real-time digital models, and artificial intelligence. Achieving Industry 5.0 calls for a systemic approach to address environmental challenges and a human-centric approach to social needs. Implementation challenges include interdisciplinary integration, agility of government policies, economics, scalability across domains and ecosystems.

The paper [24] discusses the Cognitive Engine Process Controller (CEPC), which is a framework aimed at improving human decision-making in manufacturing systems. The CEPC utilizes dynamic web ontology language ontologies, a conflict checker, and a learner to help the human operator select the next steps in the manufacturing workflow. It has the capability to monitor the completion of each step, manage the effects of a failed step, and suggest alternative suitable steps. The CEPC has been compared with an existing cognitive engine framework for workflow planning, and simulations have shown its potential to improve manufacturing workflows with multiple custom parts.

The shift towards multi-variety and small-batch production modes has led to more user requirements, changes, and uncertainties. To address these challenges, there is a need for information support for the dynamic adjustment and optimization of the production system. Cognitive manufacturing, which combines technologies such as the Internet of Things, industrial big data, and artificial intelligence, can help to address the dynamic changes and uncertainties of production systems. The Object-Attribute-Relation (OAR) model can guide the construction of the production process cognitive mechanism, and this paper proposes a multi-dimensional cognitive framework based on the OAR model for the dynamic cognitive needs of the production system [25]. The framework includes a computable digital twin model that provides important cognitive capabilities to support the dynamic cognition and optimization decision-making of the production system. The proposed framework is illustrated by the developed computational digital twin platform, and it lays a technical foundation for adaptive production and cognitive manufacturing.

Industry 5.0 has the potential to move beyond profit-centric productivity of Industry 4.0 and promote sustainable development goals such as human-centricity, socio-environmental sustainability, and resilience. This study developed a strategy roadmap to understand the mechanism by which Industry 5.0 delivers its intended sustainable development functions. The Industry 5.0 reference model describes the technical and functional properties of this phenomenon [26].

As automation and robotics become increasingly prevalent in industrial contexts, the role of humans in operating and supervising these systems is evolving. This paper [27] explores the concept of "human in the loop" and its relevance to human-automation interaction in the production sector, as a part Industry 5.0 model. The degree of automation and human involvement is categorized, and examples of current research projects are provided to reflect on the importance of this concept in innovating automated production processes.

Industry 5.0 is based on the concept of "Industry 4.0," which was developed in Germany in 2011 as a part of the country's high-tech strategy for future growth. Industry 4.0 was focused on maintaining stable employment levels in production while meeting economic and ecological requirements for "green production." It aimed to create a carbon-neutral and energy-efficient industry. In contrast, Industry 5.0 emphasizes the significance of innovation and research to support sustainable industry in serving humanity while staying within ecological limits [28].

The text discusses the current fourth industrial revolution, Industry 4.0, which merges physical and virtual worlds. However, a new paradigm of Industry 5.0 is emerging that integrates artificial

intelligence into everyday life, enhancing human capabilities and putting humans at the center of the universe. The paper [29] explores modern technologies, including IoT and emergent intelligence, and the authors believe that their convergence will transform Industry 4.0 into Industry 5.0.
Industry 5.0 aims to combine human creativity and expertise with intelligent and efficient machines to achieve resource-efficient manufacturing solutions and customized products. Paper [30] provides a survey-based tutorial on the potential applications and supporting technologies for Industry 5.0. The authors introduce new concepts and definitions of Industry 5.0 and discuss potential applications, such as intelligent healthcare and cloud manufacturing. They also describe supporting technologies, including edge computing, digital twins, and blockchain.
The concept of Operator 5.0 is centered on the integration of advanced technologies into the role of human operators in manufacturing and industrial processes. The objective is to empower these operators to work effectively with the latest technologies and to enable them to take on new tasks as machines and robots become increasingly sophisticated [31].
Industry 5.0 takes the human-machine connection to the next level by using modern technologies such as AI, IoT, blockchain, and more to empower humans and automate mundane tasks [32]. It's driven by customization and personalization demands from customers. The key to success is in understanding the role and potential of Industry 5.0, its technologies, and the opportunities and issues it poses to businesses. The finest businesses are those that combine the power of technology and human ingenuity.
The factory floor is seeing an increase in the use of smart machines like AI assistants and collaborative robots, which will require future workers to work in teams with both machines and humans. Industry 5.0 envisions a sustainable, resilient, and human-centered future factory that requires smart and resilient capabilities from both manufacturing systems and human operators. To design these resilient human-machine teams and collaborations, the paper proposes using the joint cognitive systems approach and complementing it with human-centric approaches [33].
The analysis reveals that the primary features of Industry 5.0 are sustainable, resilient, and human-centered manufacturing, within which the cognitive manufacturing model is developed and applied. Furthermore, this cognitive manufacturing model has a broader concept compared to Industry 4.0.

3. Cognitive manufacturing - some results of our research

Our research in the development of the cognitive manufacturing model coincides with the development of this concept in the field of manufacturing engineering. Specifically, we began developing knowledge-based expert systems for inspection planning on CMMs in the mid-eighties. To develop the knowledge base, we employed the theory of automata, IF-THEN rules, and engineering ontology [34-37]. Subsequently, in the first decade of this century, our research focused on developing an intelligent system for inspection planning on CMMs for prismatic parts, utilizing ANN modeling as well as ACO optimization models [38-40]. With the emergence of the Industry 4.0 model, our research has been concentrated on developing a digital twin model for intelligent inspection on CMMs [41,42]. Lastly, the final segment pertained to the development and application of BDA and AI/ML models, which incorporate elements of Industry 5.0 [43,44].

3.1. An expert system for inspection planning [34-37]

The conceptual inspection plan provides the basis for programming the CMM. Relying solely on the experience, intuition and knowledge of the inspection planner engineer to generate a conceptual inspection plan for the CMM is an approach that is avoided, particularly given the limited possibilities of intuition, especially when the CMM operates within a digital environment and deals with a large number of different parts. The starting point for a new conceptual plan is to use an expert system (ES) to generate the conceptual inspection plan. Thanks to the development of artificial intelligence tools and techniques, the foundations have been laid for the development and application of a new generation of ES. The basis of each ES model in this area is a knowledge base (its organization, scope and content of facts and heuristic knowledge). It must contain appropriate knowledge and information

regarding the measured object (MO) and its tolerances, geometric (GF) and metrological (MF) characteristics, inspection sequences (IS), the configuration of the measuring sensor (PC), the CMM (MM) and auxiliary equipment (FT), as shown in Figure 1.

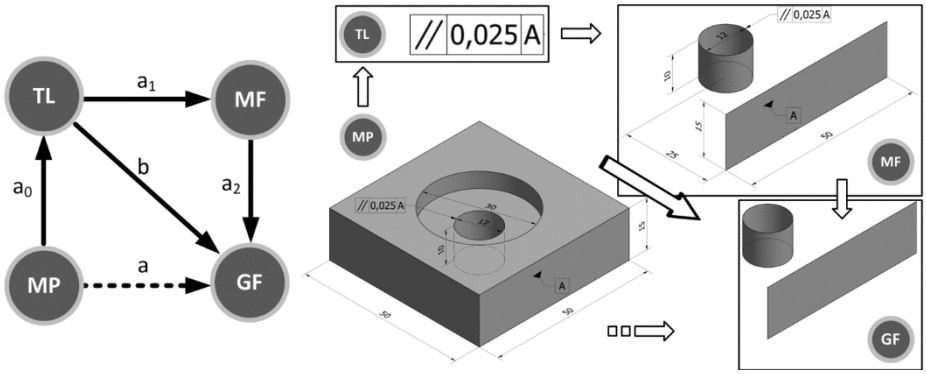

Figure 1. *The graph of knowledge base and their decomposition*

Non-terminating symbols, as entities of knowledge, are linked to terminating symbols, namely: **a0** = (tolerances, characteristics), **a1** = (metrological characteristic, characteristic, tolerances), **a2** = (geometric characteristic, characteristics), **b** = (tolerance, geometric characteristic, characteristics), and **a** = (measured object, geometric characteristics, characteristics). They are represented as ontological structures with hierarchical relations that define all the knowledge elements for this field. For example, the relations between MP - GF can be: a0 - a1 - a2 (reasoning line for generating the measuring sensor path), a0-b (reasoning line for generating the coordinate points on the geometric characteristic), and a (reasoning line for geometric characteristics on the measured object). Our approach integrates metrological-geometric information from the CAD digital model, where geometric information represents the parameters of geometric characteristics extracted from the IGES file after modeling the prismatic measuring part.

Following the previously outlined knowledge base model, the part tolerances have been reduced to geometric characteristics that include all metrological characteristics involved in creating the part tolerances. The tolerance forms that comprise the measured object are: dimension tolerances (TL), form tolerances (TF), orientation tolerances (TO) and position tolerances (TLC). The dimension tolerance consists of four length tolerances (TL1-6^1, TL1-6^2, TL1-6^2 and TL1-7) and five diameter tolerances (TL2-1^1, TL2-1^2 TL2-1^3, TL2-1^4 and TL2-1^5). The form tolerance is denoted by TF2-1, while the orientation tolerances are marked with TO2-1^1, TO2-1^2, TO2-1^3 TO2-1^4, TO2-1^1, and TO2-1^2. The position tolerance is identified with the TLC1-4 symbol, as shown in Figure 2.

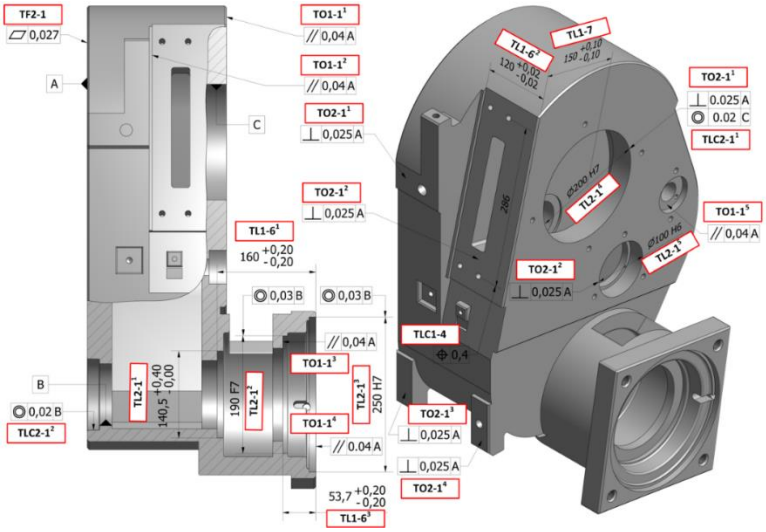

Figure 2. *The real metrological part (MP)*

The inspection planning of prismatic parts on a CMM depends on the number, position, and orientation of measuring probes installed in the measuring sensor in three mutually orthogonal directions. This assumption serves as a basis for developing methods for determining the inspection sequence of metrological characteristics when measuring prismatic parts on CMM, as shown in Figure 3.

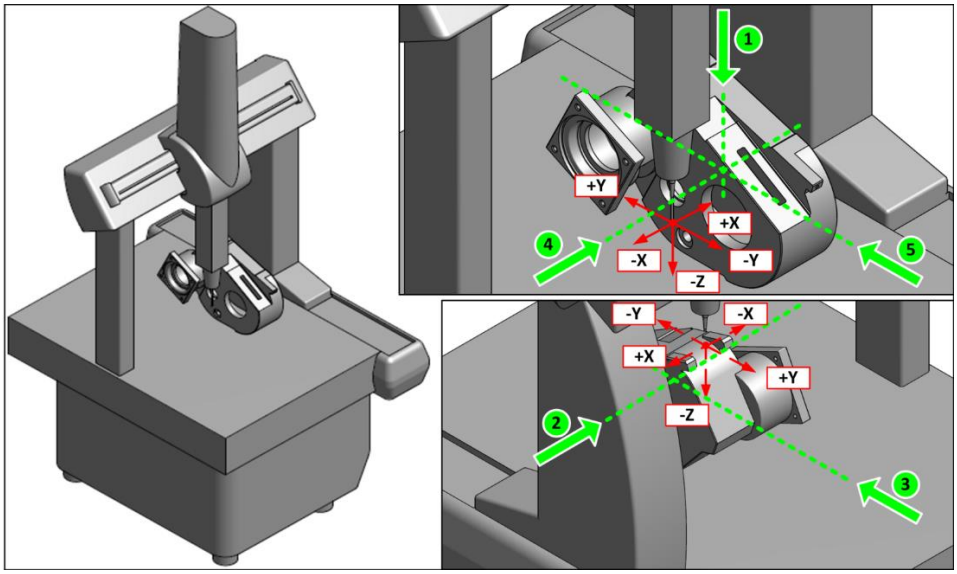

Figure 3. *The direction of probe accessibility for real MP*

At the level of a single geometric feature DPA, the vector n and np parameter are determined. For the inspection of a single primitive, the DPA can be 1, 2, 3, 4, or 5. A special case occurs when the vector n does not coincide with any of the DPA 1, 2, 3, 4 or 5. In this case, the movement of the measuring probe is divided into two DPA movements. The first is the closest (determined by the criterion of the smallest angle) of DPA 1, 2, 3, 4 and 5 for the movement immediately in front of the geometric primitive, and the second one is for n primitive. In this way, the ES provides an inspection sequence for each MF.

3.2. Intelligent inspection planning [38-40]

The framework of our CP3M model is presented in Fig. 4. It consists of the following sub-modules: (a) Module for recognition of geometrical features (GF) from CAD/GD&T model of the measurement part, (b) Intelligent inspection process planning (IIPP) module, that used AI methods and tools (ANN, ACO) for inspection plan generated, (c) Coordinate measuring machine (CMM) – generation of control data list for CMM that is transferred to CMM using cloud technology, and (d) Module for analysis of results and generation of the reports. Cloud services within the company provide the necessary information for integration of knowledge and data from various phases in product design and manufacturing into inspection planning, and make available information about inspection results to all interested parties in product lifecycle.

The role of IIPP module is to generate inspection sequence (IS) for probe configurations (PC) that CMM supports. It has geometrical features and tolerances (TL) at input. During inspection sequence generation, it is necessary to extract metrological features (MFs) from geometrical features.

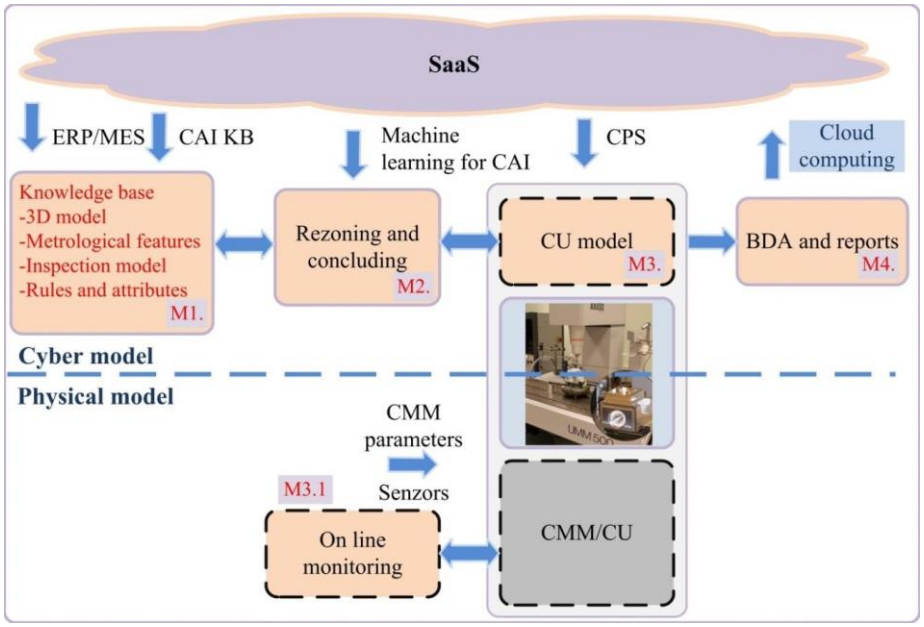

Figure 4*. Cyber physical model of manufacturing metrology (CP3M)*

Our approach implies the open interface for developing CP3M, as a feature-based model for probe path planning for sculptured surfaces using an example of turbine blades. In this model the geometricalinformation for feature description is taken from CAD modelof the part in IGES format. Figure 5 presents the complete inspection plan model. The plan consists of input CAD data, recognition of metrological and geometrical primitives, definition of inspection sequences, distribution of measuringpoints, collision avoidance principle, and measurement and analysis of the results.

The extraction of geometrical feature parameters from IGES file is based on the recognition of its structure. An IGES file is composed of the following five sections: start section, global section, directory entry section, parameter data section, and terminate section. All geometric entities are given in the directory entry section and parameter data section. The extraction of parameters is carried out using IGES type numbers that correspond to specific geometric entities (geometrical features). Metrological features are recognized using the tolerance of turbine blades (profile of surface) and the geometrical features parameters. They (MF) define the link between tolerance and geometrical features.

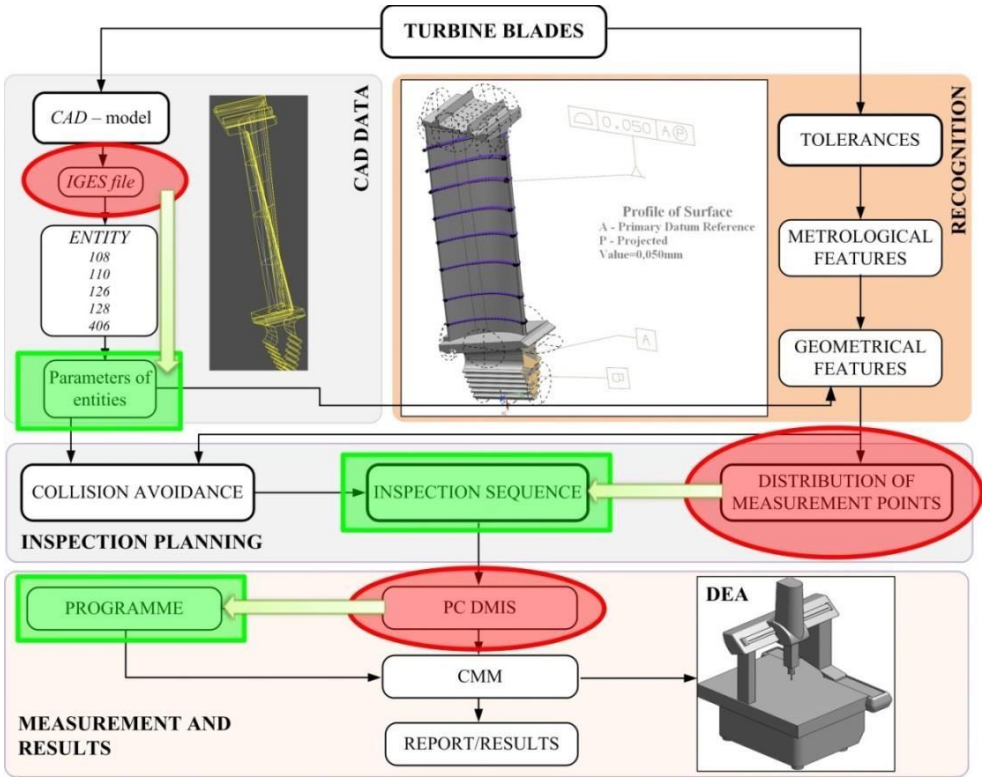

Figure 5. *Inspection planning of turbine blades CP3M model*

3.3. Digital twin for CMM [41,42]

The inspection planning system as a support of manufacturing metrology 4.0 (IP2SM 4.0) covers all elements of planning execution of parts inspection on CMM, using the models and connections between them according to Figure 6:

- EO model for extraction of geometric features from IGES and STL file and define GD&T of metrological feature of the PWs and integration by ontology knowledge base;
- ACO model for design of MP optimization as a first main part of IP2SM 4.0;
- GA model for optimal part setup and probes optimization, as a second main part of IP2SM 4.0;
- Mathematical model integrates distribution of the measurement points, accessibility and collision avoidance analysis;
- Simulation in MatLab (shown as a measurement path on MP), PTC Creo and STEP-NC Machine and generation of an appropriate output file.

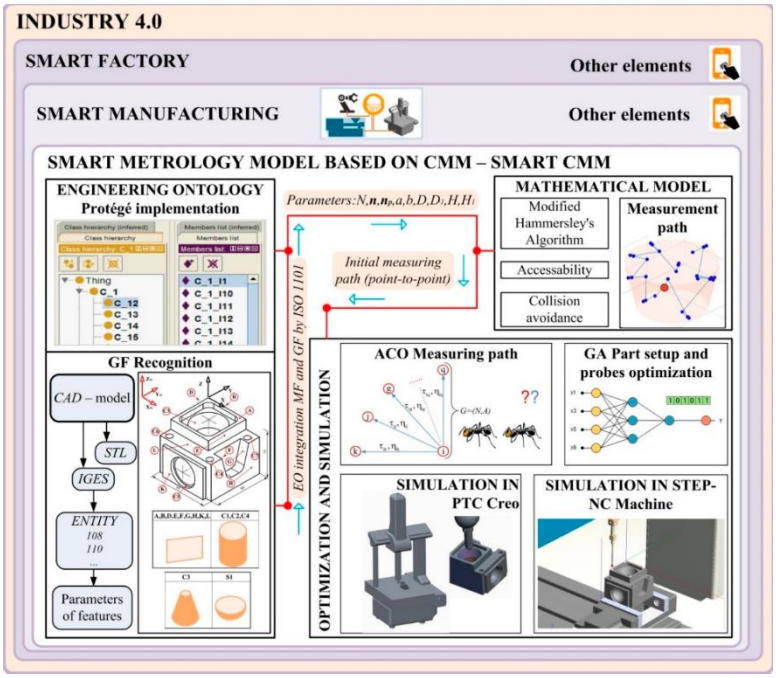

Figure 6. *New concept of Cyber physical model of manufacturing metrology (CP3M) - IP2SM 4.0*

Overall output IP2SM 4.0 is an optimal MP for real CMM and elimination of human errors through intelligent planning probe configuration and PW setup, which directly influences increased production efficiency, competitiveness, and productivity of enterprises.

As physical twin it our research was used CMMs DEA-IOTA-2203. As the data formatsits use DMIS file. A measuring path was programmed, a virtual inspection systems based on a virtual CMM IOTA-2203 as virtual twin. Matching the coordinate system of PW and coordinate system on working table enables the setting of the PW on the configured virtual twin based on CMM during the measuring simulation. Also, during the path simulation on virtual CMM, Figure 7a, besides PW and probe that moves through measuring path, it is possible to create and load fixture that is of importance in verification of measuring path and detection of the possible collisions.

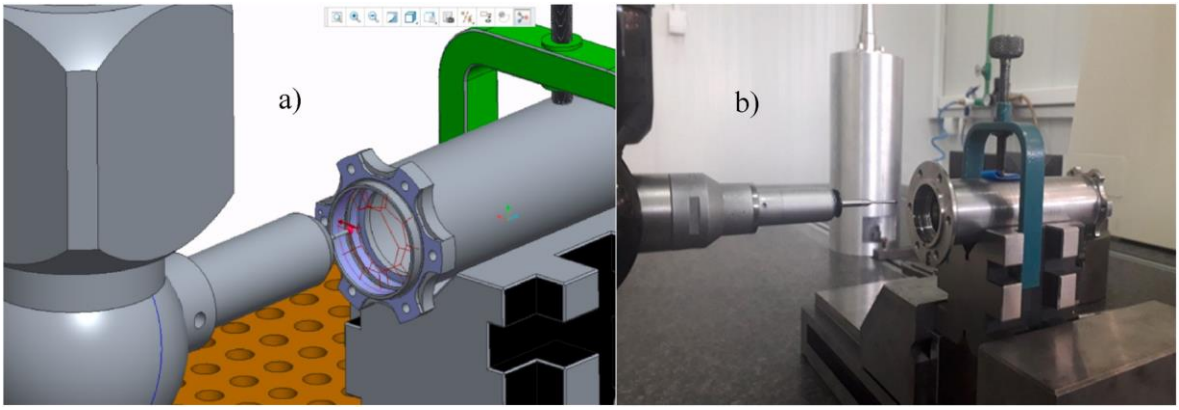

Figure 7*. DIT based on CMMs: a) PTC Creo measuring path simulation view; b) Display of the assembly of models and clamping accessories on the real CMM DEA-IOTA 2203*

In order to realize DT, it is necessary to harmonize the output-input. The PC-DMIS software allows the import of a.ncl (dmis) file, previously generated and tested in the PTC Creo software using the standard import → dmis command block. Previously, a.ncl (dmis) file was generated in PTC Creo to verify the inspection plan procedure on the virtual CMM. The machine in the functional sense completely coincides with the real measuring machine DEA-IOTA 2203, and on which the plan of inspection of the PW was performed. The final representation of the developed DIT is shown in Figure 7.

Communication between physical (Figure 7b) and digital twin (Figure 7a) andis done with unidirectional data flow via a CDL and.ncl (dmis) file.

3.4. BDA and AI/ML for CMM [43,44]

Presents a method in [43] for ensuring product quality in multistage manufacturing processes (MMP) through robust control of quality errors, even under worst-case scenarios involving uncertainty in knowledge of noise characteristics. The solution to this problem is sought approximately using a Tabu-search based meta heuristic optimization. The new algorithm is compared against the purely Bayesian stochastic control method introduced in using models of the flow of quality errors in an automotive cylinder head machining line, and stack up of overlay errors in a semiconductor lithography process. Simulation results from studies of automotive cylinder head machining and lithography overlay processes demonstrate that the proposed robust control method performs better than traditional stochastic control approaches as uncertainty in process noise characteristics increases. The paper also highlights that controlling MMP quality without accounting for inaccuracies in the noise model may lead to even worse quality than if no control is used at all. In this approach was used BDA analysis AI/ML tools and techniques.

In this paper [44], was introduce a new data curation methodology that enables data mining and analytics in the Cyber-Physical Manufacturing Metrology Model (CP3M). The approach involves organizing metrology data into tree-based database structures through the use of distance-based unsupervised clustering of raw metrology data. This structure accelerates searches of data, providing advantages for data mining. The methodology is evaluated in case studies of hyper-spectral metrology, coordinate measurement machine inspection, and imaging-based metrology, demonstrating significant improvements in search speeds without loss in precision or recall. The benefits of this methodology grow with the size of the data. Overall, the proposed methodology offers a new way to curate data for improved efficiency and accuracy in data mining and analytics, using tools and techniques from BDA method.

4. Conclusion and future research

Cognitive manufacturing (including and cognitive manufacturing metrology) is an emerging field that leverages artificial intelligence (AI) and other cutting-edge technologies to optimize manufacturing processes, improve product quality, and enhance the overall customer experience. As we look to the future, we can expect cognitive manufacturing to play an even greater role in the industry.

One key development will be the continued integration of AI and machine learning algorithms into manufacturing systems. These tools will enable manufacturers to analyze large amounts of data from sensors, machines, and other sources in real-time, in order to detect patterns, identify problems, and make faster and more informed decisions. This will help manufacturers optimize their production processes, reduce waste, and improve overall efficiency.

Another trend we can expect to see is the increased adoption of collaborative robots (cobots) and other robotic automation technologies. These systems will be designed to work alongside human operators, enabling them to complete repetitive, physically demanding tasks, while freeing up human workers to focus on more skilled and creative tasks. This will help to increase productivity, reduce costs, and improve worker safety.

In addition, we can expect to see advances in 3D printing and other additive manufacturing technologies, which will enable manufacturers to produce more complex and intricate designs, while reducing waste and shortening lead times. This will enable manufacturers to quickly respond to changing customer needs, reduce inventory costs, and bring new products to market faster than ever before.

Overall, the future of cognitive manufacturing is exciting and filled with possibilities. By leveraging AI, machine learning, robotics, and other advanced technologies, manufacturers can achieve greater efficiency, quality, and customer satisfaction, while driving innovation and staying ahead of the competition.

References

[1] Xiaochen Zheng, Jinzhi Lu & Dimitris Kiritsis (2022) The emergence of cognitive digital twin: vision, challenges and opportunities, International Journal of Production Research, 60:24, 7610-7632, DOI: 10.1080/00207543.2021.2014591.
[2] Lu, Yan & Morris, Kc & Frechette, Simon. (2016). Current Standards Landscape for Smart Manufacturing Systems. Nat. Inst. Stand. Technol. http://dx.doi.org/10.6028/NIST. IR.8107.
[3] Kiritsis, D., Hodkiewicz, M., Lazaro, O., Lee, J., Ni, J., eds. (2021). Data-Driven Cognitive Manufacturing - Applications in Predictive Maintenance and Zero Defect Manufacturing. Lausanne: Frontiers Media SA. https://doi.10.3389/978-2-88966-583-9.
[4] Yaoyao Fiona Zhao, Xun Xu, Enabling cognitive manufacturing through automated on-machine measurement planning and feedback, Advanced Engineering Informatics 24 (2010) 269–284, doi:10.1016/j.aei.2010.05.009.
[5] M.C. Laassa, C. Niggemann, R. Schmitt, Cognitive failure cluster as an approach to enhance the precision of a self-optimizing process model, Procedia CIRP 12 (2013) 486 – 491, doi: 10.1016/j.procir.2013.09.083.
[6] Iarovyi, Sergii, Jose Luis Martinez Lastra, Rodolfo E. Haber and Raúl M. del Toro. "From artificial cognitive systems and open architectures to cognitive manufacturing systems." 2015 IEEE 13th International Conference on Industrial Informatics (INDIN) (2015): 1225-1232. DOI:10.1109/INDIN.2015.7281910.
[7] Michael F. Zaeh, et al, A holistic approach for the cognitive control of production systems, Advanced Engineering Informatics 24 (2010) 300–307, doi:10.1016/j.aei.2010.05.014.
[8] Kristina Shea, et al, Design-to-fabrication automation for the cognitive machine shop, Advanced Engineering Informatics 24 (2010) 251–268, doi:10.1016/j.aei.2010.05.017.
[9] Navroop Kaur, Sandeep K. Sood, Cognitive decision making in smart industry, Computers in Industry 74 (2015) 151–161, http://dx.doi.org/10.1016/j.compind.2015.06.006.
[10] Indar Sugiarto, Cristian Axenie, Jörg Conradt, From Adaptive Reasoning to Cognitive Factory: Bringing Cognitive Intelligence to Manufacturing Technology, JIRAE, Vol. 1, No. 1, September 2016, 1-10.
[11] Pai Zheng, et al, Towards Self-X cognitive manufacturing network: An industrial knowledge graph-based multi-agent reinforcement learning approach, Journal of Manufacturing Systems 61 (2021) 16–26, https://doi.org/10.1016/j.jmsy.2021.08.002.
[12] Liqiao Xian, et al, Toward cognitive predictive maintenance: A survey of graph-based approaches, Journal of Manufacturing Systems 64 (2022) 107–120, https://doi.org/10.1016/j.jmsy.2022.06.002.
[13] Adriana Ventura Carvalho, et al, Cognitive Manufacturing in Industry 4.0 toward Cognitive Load Reduction: A Conceptual Framework, Appl. Syst. Innov. 2020, 3, 55; doi:10.3390/asi3040055.
[14] Mohammed Shoeab Sheikh, Rahul Kumar, Cognitive Manufacturing in Perspective of Future Manufacturing Industries, International Journal for Research in Applied Science & Engineering Technology (IJRASET), Volume 8 Issue X Oct 2020, https://doi.org/10.22214/ijraset.2020.32041.
[15] Serge Bonnaud, Christophe Didier and Arndt Kohler, Industry 4.0 and Cognitive Manufacturing, IBM Corporation New Orchard Road Armonk, NY 10504, 2019.
[16] Ioan Dumitrache, et al, Neuro-inspired Framework for cognitive manufacturing control, IFAC Papers On Line 52-13 (2019) 910–915, doi.org/0.1016/j.ifacol.2019.11.311.
[17] Dejan Podgoršek, Industry 4.0 and Cognitive Manufacturing, Solutions catalogue - 2nd edition, September 2017, IBM Corporation New Orchard Road Armonk, NY 10504.
[18] Yaoyao Fiona Zhao, Xun Xu, Enabling cognitive manufacturing through automated on-machine measurement planning and feedback, Advanced Engineering Informatics 24 (2010) 269–284, doi:10.1016/j.aei.2010.05.009.
[19] Chiara Cimini, et al, A human-in-the-loop manufacturing control architecture for the next generation of production systems, Journal of Manufacturing Systems 54 (2020) 258–271, https://doi.org/10.1016/j.jmsy.2020.01.002.

[20] Zhenjun Ming, et al, An Ontology for Representing Knowledge of Decision Interactions in Decision-Based Design, Computers in Industry 114 (2020) 103145, https://doi.org/10.1016/j.compind.2019.103145.
[21] Long Hu, et al, iRobot-Factory: An intelligent robot factory based on cognitive manufacturing and edge computing, Future Generation Computer Systems 90 (2019) 569–577, https://doi.org/10.1016/j.future.2018.08.006.
[22] Jiewu L., et al, Industry 5.0: Prospect and retrospect, Journal of Manufacturing Systems 65 (2022) 279–295, https://doi.org/10.1016/j.jmsy.2022.09.017.
[23] Müller, J., Enabling Technologies for Industry 5.0 (https://www.4bt.us/wp-content/uploads/2021/04/INDUSTRY-5.0.pdf). 2020.
[24] Pooi-Mun Wong, Chee-Kong Chui, Cognitive engine for augmented human decision-making in manufacturing process control, Journal of Manufacturing Systems 65 (2022) 115–129, https://doi.org/10.1016/j.jmsy.2022.09.007.
[25] Tengyuan Jiang, et al, A multi-dimensional cognitive framework for cognitive manufacturing based on OAR model, Journal of Manufacturing Systems 65 (2022) 469–485, https://doi.org/10.1016/j.jmsy.2022.09.019.
[26] Morteza Ghobakhloo, et al, Identifying industry 5.0 contributions to sustainable development: A strategy roadmap for delivering sustainability values, Sustainable Production and Consumption 33 (2022) 716–737, https://doi.org/10.1016/j.spc.2022.08.003.
[27] Peter Fröhlichn, et al, The Human in the Loop in Automated Production Processes: Terminology, Aspects and Current Challenges in HCI Research, https://matthiasbaldauf.com/automationxp23/papers/AutomationXP23_paper14.pdf.
[28] Maija Breque, Lars De Nul, Athanasios Petridis, Industry 5.0 Towards a sustainable, human-centric and resilient European industry, European Commission Directorate-General for Research and Innovation Directorate F — Prosperity Unit F.5 — Industry 5.0, doi: 10.2777/308407.
[29] Skobelev P.O., Borovik S.Yun, On the way from industry 4.0 to industry 5.0: from digital manufacturing to digital society, International scientific journal "Industry 4.0", year II, issue 6, p.p. 307-311 (2017).
[30] Praveen Kumar, et al, Industry 5.0: A Survey on Enabling Technologies and Potential Applications, Article in Journal of Industrial Information Integration, July 2021, DOI: 10.1016/j.jii.2021.100257.
[31] Mourtzis, D., Angelopoulos, J., Panopoulos, P., Operator 5.0: a survey on enabling technologies and a framework for digital manufacturing based on extended reality, Journal of Machine Engineering, 2022, Vol. 22, https://doi.org/10.36897/jme/147160.
[32] Mamoona Humayun, Industrial Revolution 5.0 and the Role of Cutting Edge Technologies, International Journal of Advanced Computer Science and Applications, Vol. 12, No. 12, 2021.
[33] Eija Kaasinen, et al, Smooth and Resilient Human–Machine Teamwork as an Industry 5.0 Design Challenge, Sustainability 2022, 14, 2773. https://doi.org/10.3390/su14052773.
[34] Stojadinovic, S., Majstorovic, V., Developing Engineering Ontology for Domain Coordinate Metrology, FME Transactions (2014) 42, 249-255, https://doi.10.5937/fmet1403249S.
[35] Vidosav D. Majstorovic, Slavenko M. Stojadinovic, Tatjana V. Sibalija, Development of a knowledge base for the planning of prismatic parts inspection on CMM, Acta IMEKO, vol. 4, no. 2, article 3, June 2015, identifier: IMEKO-ACTA-04 (2015)-02-0.
[36] Majstorović, V., Inspection Planning on CMM Based Expert System, Proceedings of 21st CIRP International Seminar on Manufacturing Systems, pp. 48 – 56, 1989. Saarbrucken, Germany.
[37] V. Majstorović, P. Bojanić, V. Milačić, Expert System for Inspection Planning on CMM, The First World Congress on Intelligent Manufacturing Process & Systems, Proceedings, pp. 120-126, San Juan, 1995.
[38] Stojadinovic, S.M.; Majstorovic, V.D.; Ga˛ska, A.; Sładek, J.; Durakbasa, N.M. Development of a Coordinate Measuring Machine - Based Inspection Planning System for Industry 4.0. Appl. Sci. **2021**, 11, 8411. https://doi.org/10.3390/app11188411.

[39] V D Majstorovic and S Stojadinovic 2020 IOP Conf. Ser.: Mater. Sci. Eng. **968** 012001. doi:10.1088/1757-899X/968/1/012001.
[40] Vidosav Majstorovic, Slavenko Stojadinovic, Srdjan Zivkovic, Dragan Djurdjanovic, Zivana Jakovljevic, Nemanja Gligorijevic, Cyber-Physical Manufacturing Metrology Model (CPM3) for Sculptured Surfaces – Turbine Blade Application, Procedia CIRP, Volume 63, 2017, Pages 658-663, https://doi.org/10.1016/j.procir.2017.03.093.
[41] Stojadinovic, S., Majstorovic, V, et al, Contribution to the development of a digital twin based on CMM to support the inspection process, Measurement: Sensors 22 (2022) 100372, https://doi.org/10.1016/j.measen.2022.100372.
[42] Stojadinovic, Slavenko & Vidosav, Majstorovic & Durakbasa, Numan. (2021). An approach to development of the digital inspection twin based on CMM. Measurement: Sensors. 18. 100300. doi.10.1016/j.measen.2021.100300.
[43] Dragan Djurdjanovic, D., et al, Multistage manufacturing process control robust to inaccurate knowledge about process noise, CIRP Annals - Manufacturing Technology 66 (2017) 437–440, http://dx.doi.org/10.1016/j.cirp.2017.04.012/.
[44] Sabbagh, R., et al, Organization of big metrology data within the Cyber-Physical Manufacturing Metrology Model (CPM^3), CIRP Journal of Manufacturing Science and Technology 36 (2022) 90–99, https://doi.org/10.1016/j.cirpj.2021.10.009.

Fracture resistance under static, dynamic and cyclic loading of welded joints of AA2219 alloy obtained by TIG

***Sviatoslav Motrunich*[1], *Alexey Milenin*[1], *Vitaliy Knysh*[1], *Ilya Klochkov*[1], *Massimo Rogante*[2] *and Anatoliy Zavdoveev*[1]**

1) E.O. Paton Electric Welding Institute of the NAS of Ukraine, 03150 Kyiv, Ukraine

2) Rogante Engineering Office, Contrada San Michele n. 61, I-62012 Civitanova Marche, Italy

Corresponding author: avzavdoveev@gmail.com

Original scientific article

Abstract: Aluminium alloys, specifically Al-Cu alloys, are widely used in supersonic aircraft and aerospace products due to their high strength and corrosion resistance. Yet, employing welding techniques offer advantages in reducing metal content and improving characteristics, however welding of high-strength aluminium alloys is challenging task due to potential negative effects on strength and fatigue resistance. The development of proper welding techniques gives sound joints, with 67% of the base metal's tensile strength and a weld metal impact strength up to 11.1 J/cm^2. This study analyse mechanical properties, fatigue behaviour and fatigue crack growth resistance of obtained TIG welds. Thou fatigue crack growth testing shows that the rate in the linear section of the diagram in the weld metal is 2 times higher than rate in the base metal. S-N curves for both base metal and welded joints were established, showing fatigue limit of welded joints at $2 \cdot 10^6$ is approximately 75% compared to the base metal.

Keywords: *TIG; aluminium alloy; microstructure; mechanical properties; fracture toughness; fatigue crack growth; fatigue life*

1. Introduction

Aluminium alloys, of Al-Cu alloying systems, characterized by high specific strength, resistance to corrosion cracking under stress, high cyclic crack resistance and durability are widely used in supersonic aircraft and aerospace products [1–4]. It is known that the use of welded joints in structures can significantly reduce the metal content of products and improve their technical and economic characteristics [5–7]. However, obtaining high-quality welded joints of high-strength heat-strengthened aluminium alloys is complicated due to the formation of a cast structure in the weld metal and the strengthening of the metal in the heat affected zone, which, as a result, can negatively affect the strength characteristics and fatigue behaviour of the welded structure [3, 8–13].

Depending on the purpose and operation conditions of welded structures, requirements for their strength characteristics are formulated, therefore structure design begin with picking of suitable material for manufacturing and efficient welding technique. So basically, it is necessary to conduct a set of appropriate tests, which will allow to establish the main factors that defines resistance to fracture of welds under static, dynamic and cyclic loading.

Considering the strength properties of AA2219 and its good weldability, this alloy has high promising possibilities in the manufacturing of modern welded structures and aerospace products. Therefore, the establishment of fracture resistance at static, dynamic and cyclic loading of AA2219 welds can be considered a priority direction of experimental research.

2. Experimental procedure

In the present work, rolled plates with a thickness of 10 mm were used for study. The chemical composition of AA2219 is given in Table 1.

Table 1. *Chemical composition of the AA2219*

Cu, %	Mn, %	Fe, %	Ti, %	Zn, %	Si	Al
5,8…6,8	0,4…0,2	< 0,30	0,1…0,02	< 0,25	< 0,20	bal.

The mechanical properties of the AA2219 were determined in accordance with ISO 6892-1:2019 Metallic materials — Tensile testing — Part 1: Method of test at room temperature” on prismatic samples. Control of parameters during tensile testing was carried out using the standard software TestWorks 4 of the MTS 318.25 system. The loading speed was displacement controlled. For a more accurate determination of the yield strength, the displacement speed on the linear section of the "stress-strain" diagram and in the zone of elastic-plastic deformation was 2 mm/min. At this stage, an extensometer MTS 632.27F-20 with a 25 mm gauge was used. Following, loading was 10 mm/min till fracture of specimen. The average values of the obtained mechanical properties of the studied AA2219 are shown in Table 2.

Table 2. *Mechanical properties.*

Ultimate tensile stress, MPa	Yield stress, MPa	Elongation, %	E, GPa	KCV, J/cm^2
458	370	9	75	15,4

The impact strength of the weld metal was determined in accordance with ISO 9016:2022 “Destructive tests on welds in metallic materials — Impact tests — Test specimen location, notch orientation and examination” of a batch of 5 samples with V-notches both parent metal and weld metal.

The fatigue crack growth resistance of the base metal and TIG weld metal were determined in accordance with ISO 12108:2018 “Metallic materials — Fatigue testing — Fatigue crack growth method”. Centre cracked tension specimens (160x64x8 mm) were used both for base metal and TIG-weld joints testing. Fatigue crack growth diagrams were obtained in the speed range of 10^{-5}…10^{-2} m/cycle. Fatigue crack growth testing of the specimens were carried out on the MTS universal servo-hydraulic complex with a maximum force of 250 kN using displacement gauge MTS 632.02F-20.

Samples for fatigue testing of the base metal and welded joints were prepared in accordance with standard ISO 1099:2017 "Metallic materials — Fatigue testing — Axial force-controlled method." The samples were tested under an axial tensile loading with sinusoidal form of the stress cycle at stress ratio R_s=0.1 until fracture or up to $2\cdot10^6$ cycles. The upper level of test frequency was limited up to 25 Hz, which excluded self-heating of the sample above 50°C. S-N curves were established at high cycle fatigue region of 10^4...$2\cdot10^6$ cycles. Fatigue tests of the welded joints specimens were carried out on the nanoBISS universal servo-hydraulic complex with a maximum force of 25 kN.

Under the same conditions, a series of 7...8 samples of the same type were tested. The experimental data of the fatigue tests were processed by the methods of linear regression analysis generally accepted for this kind of research. According to the results of the fatigue tests, for each series of samples, on the basis of the established fatigue strength values, the corresponding S-N curves - regression lines in the coordinates $2\sigma_a$ - lgN were established. To accurately determine the place of destruction of the samples, they were chemically treated. After degreasing with an organic solvent and etching in a 10% solution of caustic sodium at a temperature of 50°C for 2 minutes, the samples were illuminated in a 30% solution of nitric acid for 5 minutes, washed and dried.

3. Results and discussion

Structural features and strengthening of welded joints of AA2219 alloy obtained by TIG. The template from welded plate with a butt joints measuring 500x256x8 mm made of AA2219, obtained by TIG is presented on Figure 1.

Figure 1. *Weld shape of AA2219 produced by TIG*

Structural studies showed that in the base metal, the average grain size is 30 μm and with a pronounced direction of metal rolling Figure 2. Microstructural studies of the weld metal shoves that a defect-free cast structure of the metal with an average grain size of about 20 microns and a pronounce grains boundary is formed in the centre of the TIG welding (Figure 3). Recrystallization with partial dissolution of the eutectic took place in the metal of the heat-affected zone. The number of eutectic inclusions decreased, and the size of these inclusions decreased to 20 μm. The average grain size is 50 μm, while the subgrain structure remained unchanged (Figure 3).

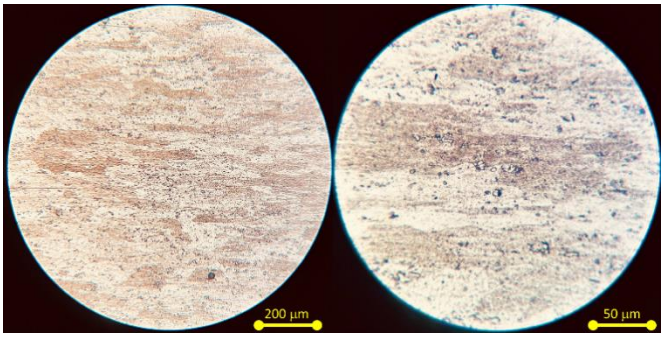

Figure 2. *Optical microstructure of the base metal.*

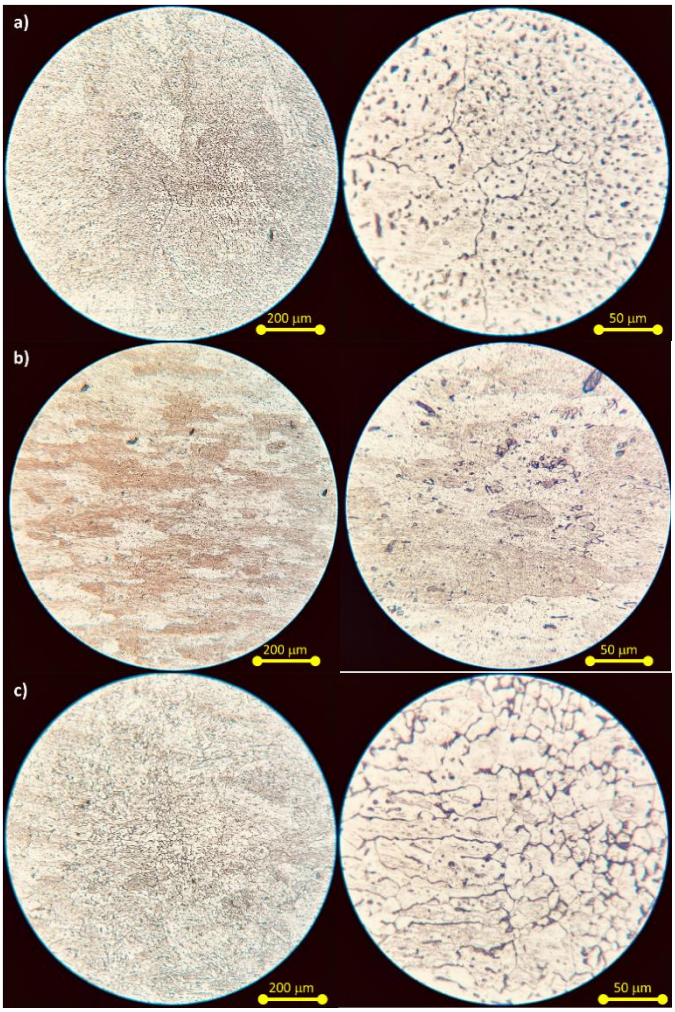

Figure 3. *Microstructure of weld metal (a), heat affected zone (b) and fusion line (c)*

Vickers microhardness in accordance with ISO 9015 of the welded joint was measured. The hardness distribution shows that the difference in weld joints is up to 28% to the values of parent metal HV 94 (Figure 4).

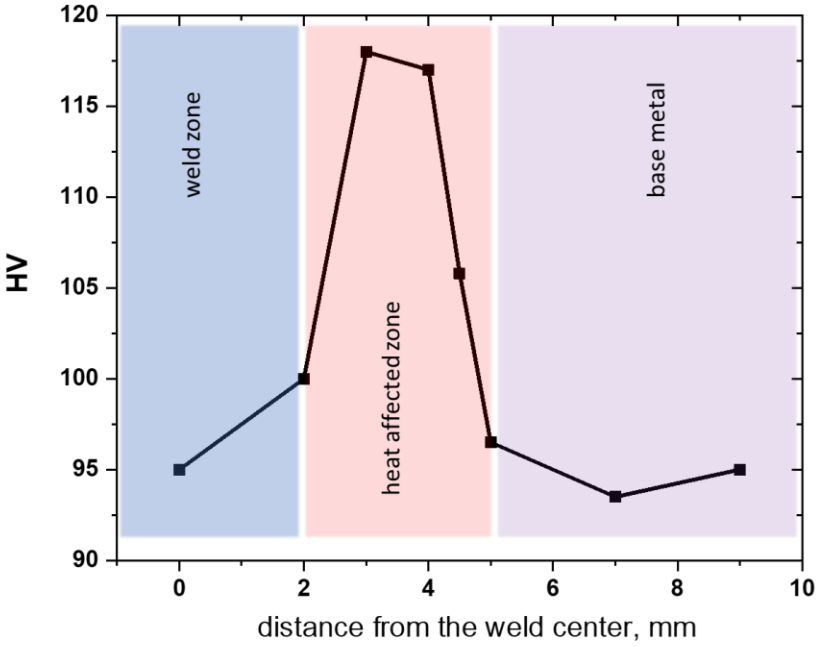

Figure 4. *Microhardness distribution of the welded joint produced by TIG*

Obtained values of mechanical properties of the base metal and welded joints are given in Table 3. Tensile testing shows that the welded samples fractures in the fusion zone of the weld metal with the base metal. The ultimate tensile strength of these samples are 284...308 MPa, which is 62...67% of the corresponding values of the base metal. At the same time, the value of relative elongation of samples of welded joints at 50 mm gauge length is 3...4%, thus for the base metal is 9...10%. The impact strength of the weld metal of TIG joints is KCV_{TIG} = 9.4...11.1 J/cm2, which is 62...72 % of the corresponding values of the base metal (KCV_{BM} = 15.2...15.6 J/ cm2).

Table 3. *Mechanical properties of the base metal and welded joints of AA2219*

	Base metal	TIG
UTS, MPa	454…462	284…308
δ, %	9…10	3…4
KCV, J/cm^2	15,2…15,6	9,4…11,1

Figure 5 shows obtained fatigue crack growth diagram of the AA2219 base metal and TIG weld metal. The range of speed change of fatigue crack growth up to fracture in the base metal was 10^{-5}...$2{\cdot}10^{-3}$ m/cycle, and in the TIG weld metal 10^{-5}...$9{\cdot}10^{-3}$ m/cycle. So, for the same span of the stress intensity factor, the crack growth rate in the linear section of the diagram in the weld metal is 2 times higher than rate in the base metal. The critical values of the stress intensity factor span before specimen fracture for the base metal is ΔK_{fc}^{BM} = 21 MPa·m$^{0.5}$ and for weld metal ΔK_{fc}^{TIG} = 19.8 MPa·m$^{0.5}$.
The *m* and *C* parameters of the Paris equation (da/dN=C ΔK^m) for the linear section of the diagram for AA2219 base metal and TIG-weld metal were established and are given in Table 3.

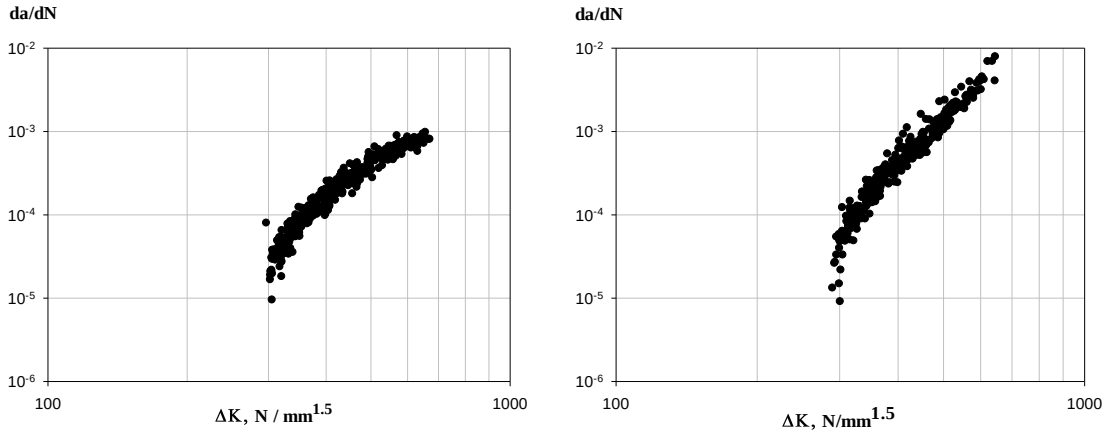

Figure 5. *Fatigue crack growth diagrams of a base metal (a), and weld metal (b) of a welded joint of AA2219 obtained by TIG sample of AA2219*

Table 3. *Parameters m and C of the Paris equation for the AA2219 base metal and TIG weld metal*

Parameters	Base metal	TIG weld
m	3,54	5,59
C	$1{,}71 \cdot 10^{-13}$	$2{,}18 \cdot 10^{-18}$

Obtained S-N curves of AA2219 base metal and TIG welded joints are shown in Figure 6. Fatigue limit at $2 \cdot 10^6$ cycles for TIG joints (130 MPa) is only 24% lower than values of base metal (170 MPa). The obtained values of the free slope *m* of the S-N curve equation (N=B/(Δσ)^m), are the following: m = 13.24 for the base metal; m = 12.97 for a welded joint. Welded joints fracture in the weld metal, were structural transformation occurs and minimum weld metal hardness observed.

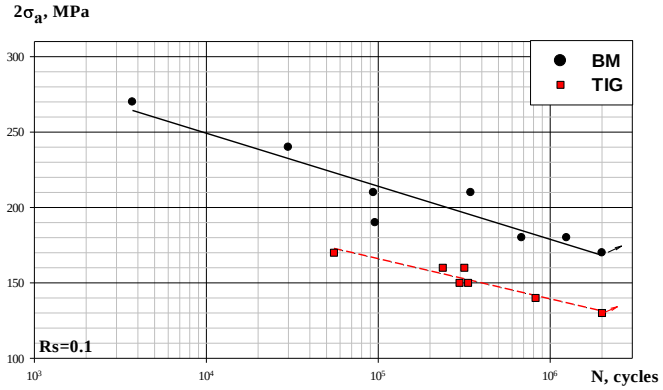

Figure 6. *S-N curves of the AA2219 base metal and TIG welded joints at stress ratio 0.1*

4. Conclusions

On the basis of experimental studies of strength, shows that the sound TIG welding joints of high-strength aluminium alloy 2219, gives ultimate tensile strength up to 308 MPa and the impact strength of the weld metal at the level of 11.1 J/cm^2, which is 67% of the values of the base metal.

Fatigue crack growth diagram of base metal and TIG weld metal are established. The obtained parameters of the Paris equation for the linear section of the diagram, are: m = 3.54 and $C = 1.71 \cdot 10^{-13}$ – for the base metal and m = 5.59 and $C = 2.18 \cdot 10^{-18}$ – for the weld metal. The critical value of the stress intensity factor span is: $\Delta K_{fc}^{BM} = 21.10$ MPa·m$^{0.5}$ – for the base metal and $\Delta K_{fc}^{TIG} = 19.8$ MPa·m$^{0.5}$ – for the weld metal.

Experimentally established S-N curves for the base metal and welded joints of AA2219 at a stress ratio R_s = 0.1. It is shown that the fatigue limit at 10^5 and $2 \cdot 10^6$ cycles for welded joints obtained from TIG is 165 and 130 MPa, respectively, which is about 75% of the corresponding values of the base metal. The obtained values of the free slope parameter *m* of the fatigue curve equation N=B/(Δσ)^m, are: m = 13.24 for the base metal; m = 12.97 for a welded joint.

References

[1] K.G. Prashanth, S. Scudino, H.J. Klauss, K.B. Surreddi, L. Löber, Z. Wang, A.K. Chaubey, U. Kühn, J. Eckert, Microstructure and mechanical properties of Al–12Si produced by selective laser melting: Effect of heat treatment, Mater. Sci. Eng. A. 590 (2014) 153–160. https://doi.org/https://doi.org/10.1016/j.msea.2013.10.023.

[2] T. Bajor, A. Kulakowska, H. Dyja, Analysis of the rolling process of alloy 6005 in a three-high skew rolling mill, Materials (Basel). 13 (2020). https://doi.org/10.3390/ma13051114.

[3] A.O. Lukinenko, S.I. Motrunich, D. Bajić, V.A. Kuleshov, A.G. Pokliatskyi, T.M. Labur, Noise level assessment and mechanical properties of welded joints of aluminium alloys of the Al-Cu-Li system in FSW and TIG welding, FME Trans. 49 (2021) 220–224.

[4] A. Zavdoveev, V. Tkachenko, V. Burkhovetskiy, E. Pashinska, V. Varyukhin, Structural modification of the aluminum alloy AA1135 by cold rolling with shear, Nanomater. Energy. (2014). https://doi.org/10.1680/nme.14.00014.

[5] Y. Bi, Z. Luo, J. Guo, Y. Yang, J. Su, Y. Zhang, Joint formation mechanism and performance of resistance butt spot welding for AA 5754 aluminum alloy sheet, Mater. Lett. 319 (2022) 132279. https://doi.org/https://doi.org/10.1016/j.matlet.2022.132279.

[6] L.L. Wang, H.L. Wei, J.X. Xue, T. DebRoy, A pathway to microstructural refinement through double pulsed gas metal arc welding, Scr. Mater. 134 (2017) 61–65. https://doi.org/https://doi.org/10.1016/j.scriptamat.2017.02.034.

[7] L. Wang, J. Xue, Perspective on Double Pulsed Gas Metal Arc Welding, Appl. Sci. 7 (2017) 894. https://doi.org/10.3390/app7090894.

[8] A.G. Poklaytsky, I.N. Klochkov, S.I. Motrunich, Structure and properties of AMg2M alloy joints made by argon nonconsumable –arc welding and friction stir welding, in: Appl. Mech. Mater., 2014: pp. 166–169. https://doi.org/10.4028/www.scientific.net/AMM.682.166.

[9] S. Motrunich, I. Klochkov, A. Poklaytsky, High cycle fatigue behaviour of thin sheet joints of aluminium-lithium alloys under constant and variable amplitude loading, Weld. World. 64 (2020) 1971–1979.

[10] A. Milenin, E. Velikoivanenko, G. Rozynka, N. Pivtorak, Residual Strength and Reliability of Corroded Pipelines—Monte-Carlo Approach for Consideration of Spatially Nonuniform Material Properties, Structural Integrity, Vol. 8, (2019): pp. 321 - 326. https://doi.org/10.1007/978-3-030-21894-2_59

[11] S.V. Akhonin, A.S. Milenin, A.N. Pikulin, Simulation of evaporation processes of alloying elements during electron beam surface melting of ingots-slabs from titanium-base alloys, Problemy Spetsial'noj Electrometallugii, 2005, (3), pp. 29–32

[12] A. Bernatskyi, M. Sokolovskyi, T. Nabok, O. Siora, N. Shamsutdinova, V. Lukashenko, Development of a Model Device of a Control System Device for Control of the Power Source for Hybrid Laser-Arc Welding of Aluminium Alloys, in: 2022 IEEE 4th Int. Conf. Mod. Electr. Energy Syst., 2022: pp. 1–6. https://doi.org/10.1109/MEES58014.2022.10005674.

[13] I. V Krivtsun, V.Y. Khaskin, A.S. Zatserkovny, A. V Bernatsky, Application of diode and CO2 lasers in laser-plasma welding of thin sheet aluminum alloys, BID-ISIM Weld. & Material Test. (2009) 392–1453.

3D printer selection using AHP method

***Ivan Nišević*[1], *Hana Vukotić*[1], *Zoran Jurković*[1], *Mladen Perinić*[1] *and Marko Fabić*[2]**

1) University of Rijeka, Faculty of Engineering, Vukovarska 58, 51000 Rijeka, Croatia

2) University of Rijeka, Study of Polytechnics, Sveučilišna avenija 4, 51000 Rijeka, Croatia

Corresponding author: zoran.jurkovic@riteh.hr

Original scientific article

Abstract: This paper aimed to determine optimal additive manufacturing technology using the *Analytic Hierarchy Process* or AHP method with a condition set that the chosen one must have an industrial and an at-home version of the machine. In the selection process numerous criteria was set and evaluated to make a decision. Complying with the condition set at the beginning of the paper and set criteria, chosen technology was FDM/FFF (*Fused Deposition Modeling/Fused Filament Fabrication*). A new aim was to determine the optimal 3D printer to perform FDM/FFF. This paper concluded that the AHP was viable method to select optimal AM technology and 3D printer while also providing key criteria to successfully navigate selection process of additive manufacturing technology and 3D printer for future use. It also pointed out to a subjectivity of the AHP method which could lead to a different result.

Keywords: *Multi-criteria decision making; AHP method; AM technologies; FDM/FFF; 3D printer*

1. Introduction

The evolution of humankind can be observed through the evolution of manufacturing. The more knowledge humans gained, the more complex the manufacturing process has become. Today's world has reached a phase where conventional manufacturing has gained an equal opponent - additive manufacturing. Additive manufacturing or AM is a process of building a physical model from a CAD model using different techniques of adding layer upon layer of material [1]. Over the last three decades, differing in the ways of binding the layers together, numerous technologies of additive manufacturing were developed. The main idea of all technologies stayed the same and it is shown in Figure 1. The 1980s were the years when the concept of additive manufacturing was introduced to the world. In 1981, Hideo Kodama from Nagoya Municipal Industrial Research Institute, Japan published information about the first printed solid model. However, merit for the first 3D printer goes to Charles Hull who designed it while working in the company named 3D Systems Corp.

***Figure 1**. Concept of AM technologies [5]*

Accessibility and relatively low costs of equipment used for AM have made it increasingly popular for do-it-yourself projects. Additive manufacturing has reached a phase where the user can decide which technique of binding layers suits his needs the best – Binder Jetting, Direct Energy Deposition, Material Extrusion, Material Jetting, Powder Bed Fusion, Sheet Lamination, or VAT Polymerization - as categorized by ISO/ASTM 52900 [2]. But the main question is, considering the vast number of technologies, how to choose the appropriate one scientifically and objectively? To choose between

them, one has to set certain criteria which by itself then implies that there are two or more alternatives to choose from. By developing methods of multi-criteria decision-making (MCDM), the process of decision-making has been made significantly easier and more accurate. Over the course of years, a few methods have been developed – MAUT (MultiAttribute Utility Theory) which enables the decision maker to evaluate several quantitive and qualitative attributes and handle the trade-off among them [3], PROMETHEE (Preference Ranking Organisation Method for Enrichment of Evaluation) which provides means to determine the priority of criteria to find best alternative, PROMETHEE II. which requires beforehand knowledge of the weight of criteria [4], ELECTRE method family (Élimination Et Choix Traduisant la Realité) and AHP method (Analytic Hierarchy Process). The AHP method of MCDM is today very frequently used due to its effectiveness and practicality. The aim of this paper was to demonstrate that relatively easy method of multi-criteria decision making such as the AHP method can be used in the selection process of additive manufacturing technology and the selection of a 3D printer with both industrial and at-home version. After setting a goal, criteria and subcriteria of analysis that will be instrumental for decision-making, the AHP method returned the optimal choice of an alternative. The whole analysis was done in Expert Choice software and the results provided by the software are shown in the article. Information upon which analysis was based around, were results of extensive research and advice provided by the company *Camteh d.o.o.* Given the large number of obtained graphs during the analysis only one of each type will be shown in the paper.

2. Literature survey

2.1. Overview of additive manufacturing

Table 1 shows a list of additive manufacturing technologies, between which the choice was made, with a short description of each one. Over the last few decades, all of the listed technologies have been improved and for every one of them there is more than one 3D printer to choose from. It makes decision-making very complex. That is why the AHP method was applied to try and reduce the subjectivity one could face when deciding between all of the alternatives.

Table 1. *Observed AM technologies overview*

AM technology	Description
SLA (Stereolithography)	Uses ultraviolet laser to cure photopolymer transforming it from liquid to solid [5]
SLS (Selective Laser Sintering)	Sinters particles of polymer powder into solid structure using high-power laser [5]
3D printing	Lays down successive thin layers of a material to form three-dimensional object [5]
PolyJet (Polymer Jetting)	Uses liquid photopolymers to print layer upon layer on build tray [6]
FDM/FFF (Fused Deposition Modeling/Fused Filament Fabrication)	A polymer filament is deposited layer by layer via heated nozzle [5]
LOM (Laminated Object Manufacturing)	Laminates together sheet materials combining heat and pressure after which cutting is done by laser or a knife to the desired shape [5]
DLP (Digital Light Processing)	Cures entire layer of photopolymer at once under light source [5]
LENS (Laser Engineering Net Shaping)	Uses high-power laser to melt a dimensionally small area onto which powdered material is placed to form a new layer [7]
DMD (Direct Metal Deposition)	Transforms powdered metal to solid object using a powder feed nozzle to propulse powdered metal into the laser beam fusing it layer after layer [8]
EBM (Electron Beam Melting)	Powdered material is metled by a electron beam [9]
SLM (Selective Laser Melting)	Fuses metal powder layer by layer via high-power laser [5]

2.2. Overview of AHP method

AHP method always follows five main steps for its implementation [10]:

1. Defining main goals
2. Defining criteria, subcriteria and alternatives of choice
3. Comparison of criteria for each alternative
4. Calculation of priority and consistency
5. Evaluation of alternatives

The hierarchical structure of the AHP method is shown in Figure 2.

To make the comparison one has to use the Saaty scale shown in Table 2. The scale establishes a correlation between two elements. Commonly, odd numbers of scale are preferentially used to define preferences between two elements. Even numbers represent in-between values of the scale. The higher the value on the Saaty scale, the more important one element is than the other one.

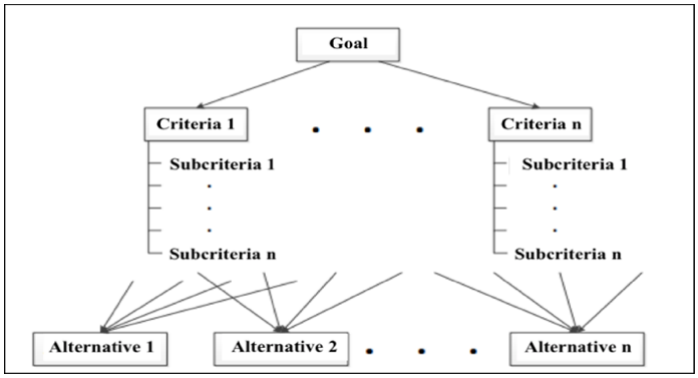

Figure 2. *The hierarchical structure of the AHP method [11]*

Table 2. *The Saaty scale [12]*

1	3	5	7	9
Equal importance	Moderate importance	Strong importance	Very strong importance	Extreme importance

After establishing a relationship between every element of the hierarchical structure using the Saaty scale, the construction of a pairwise comparison matrix is done. Values written in the matrix are values provided in the Saaty scale. If the element 1 has a higher preference then the element 2, value 5 is written in a position a_{12} of the matrix and value 1/5 in a position a_{21} [13].

$$\boldsymbol{A} = \begin{bmatrix} a_{11} & a_{12} & a_{13} \\ a_{21} & a_{22} & a_{23} \\ a_{31} & a_{32} & a_{33} \end{bmatrix} \tag{1}$$

The next step is to multiply the matrix with itself and get a 1. iteration matrix from which. By summing values of every row a vector of priority is formed. Once vectors of priority of criteria and vectors of priority of alternatives are formed, they are multiplied to form a new vector of priority of goal. The AHP method is frequently used because of its possibility of identifying inconsistencies done by the user in the decision-making process. The logic behind it is simple: if A is in relation to B and B is in relation with C then A is in relation with C. To evaluate consistency, the consistency index has to be calculated using the formula:

$$CI = \frac{\lambda_{MAX} - n}{n-1} \tag{2}$$

The ratio of the consistency index and random index *RI* forms the consistency ratio, *CR* [14]. In our analysis that value was set at 0.10 meaning if the result is less or equal to it, analysis done by AHP method is good.

3. Application of the method

3.1. Defining goal and criteria

The AHP method was used to choose an additive manufacturing technology. The first step was to determine the realistic and attainable main goal of this process and that was a suitable choice of AM technology. In-detail research was done to determine which additive manufacturing technology was currently available on the market and the results of the research are shown in Table 1. Following the steps of the AHP method, the next step was to define criteria and subcriteria based on which final choice will be made. Because of the large number of available technologies and the uniqueness that comes with every one of them, setting criteria and subcriteria had to be done in a general way in order to be applied on as many of them as possible. If criteria and subcriteria can not be applied to the alternative more than once during analysis, either criteria or alternative has to be changed. When defining a criteria there was a limitation – criteria had to be objectively relevant. It meant that criteria had to be set in a way that enables objective comparison of alternatives. That is because the value assignment based on the Saaty scale for criteria and subcriteria was done fairly subjectively based on beforehand knowledge and experience. Chosen criteria and subcriteria are shown in Figure 3.

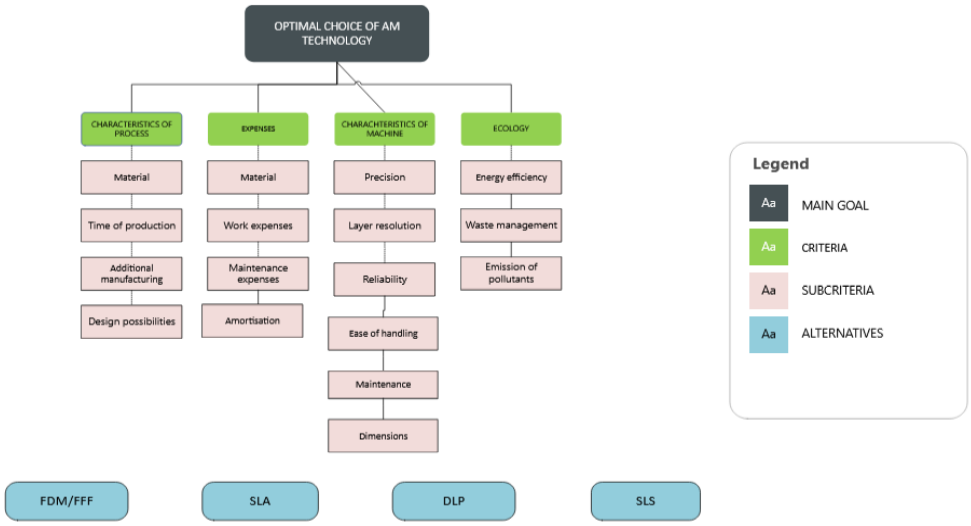

Figure 3. *Structure of criteria and subcriteria for the analysis*

Characteristics of the process were the most important criteria in the analysis. The real world, no matter if it's industrial or home life, revolves around money which put the criterion of expenses high on the scale of importance. Given that additive manufacturing does not exist without machines, criterion characteristics of the machine was necessary. Chosen AM technology at the end of the analysis needed to have a machine that will be suitable for the use. Ecology was put as a criterion because of the growing global importance of ecology in every aspect of industrial life including AM technologies. Chosen technology and the 3D printer had to be eco-friendly for the user and environment.

3.2. Evaluating criteria and subcriteria

A pairwise comparison of every criterion based on their relative importance and evaluated by the Saaty scale is shown in Figure 4. A value given to each alternative was based on experience or beforehand knowledge. Aim was to be as objective and realistic as possible when assigning the value

from the Saaty scale in order to have the final result of the analysis as accurate as possible. Because the naming of criteria in all figures is in Croatian, translation is necessary and therefore is shown in Table 3.

Table 3. *Translation of criteria*

Croatian	English
Karakteristike procesa	Characteristics of process
Troškovi	Expenses
Ekologija	Ecology
Karakteristike stroja	Characteristics of machine

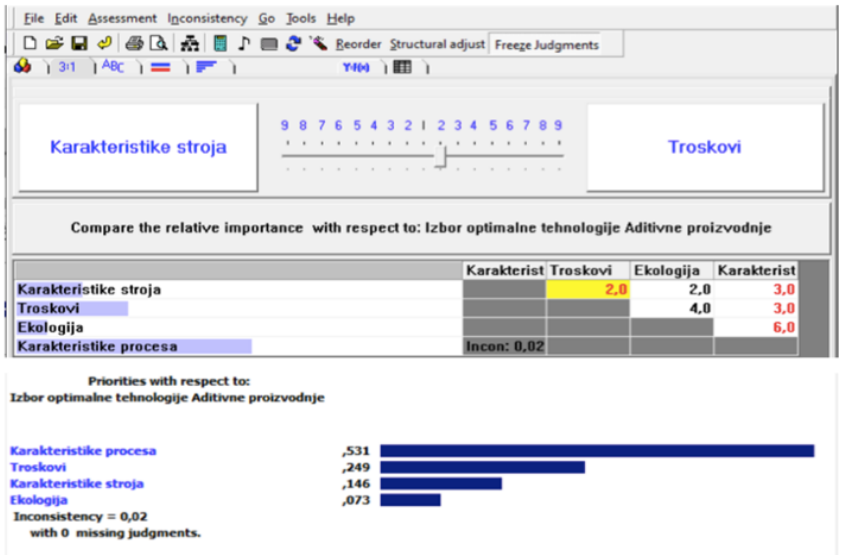

Figure 4. *Comparison of criteria*

If values are painted red, the criterion in the column is more important than the criterion in the row. If values are painted black, the criterion in a row is more important than the criterion in the column. It is visible that expenses had moderate importance over the characteristics of the machine. Inconsistency was evaluated at 0.02 which was less than the set limit of 0.10. This meant that this type of formulation of criteria was valid. Characteristics of the process were confirmed as the most important criteria considering the beforehand set goal. A pairwise comparison of subcriteria was done in the same way as it was done for the criteria. The next step of the analysis was to compare every alternative concerning all criteria and subcriteria as shown in Figure 5. Before further analysis, the limitation had to be set to lower the number of alternatives. The limitation imposed was that the alternative had to have an industrial and at-home version. With that in regard and the main goal set at the beginning, alternatives left were FDM/FFF, SLA, DLP and SLS. Based on the information in Figure 5, FDM/FFF had moderate importance over SLS. Same steps were taken for every criteria and subcriteria until all alternatives were compared.

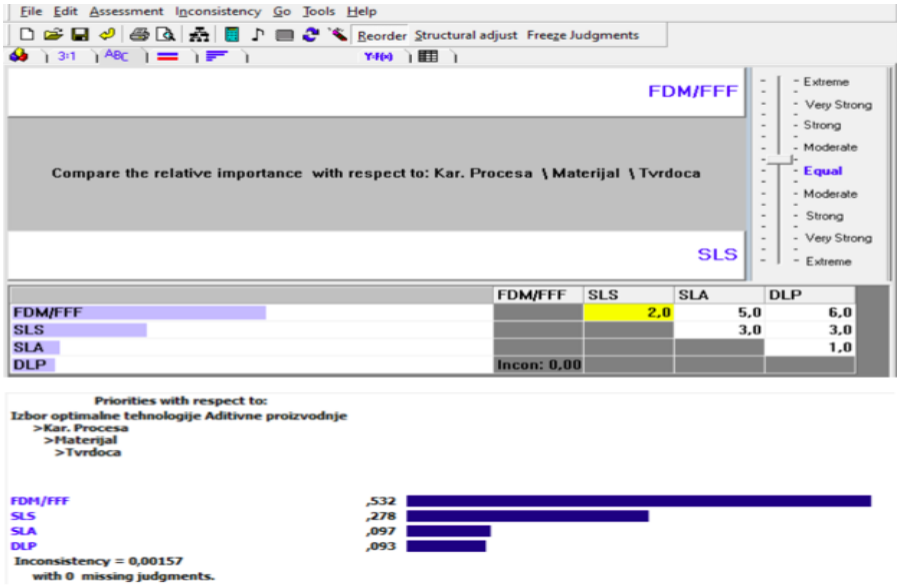

Figure 5. *Comparison of alternatives*

3.3. Results of analysis

Based on the comparison done, the final table of criteria weight and alternatives distribution was formed as shown in Figure 6. Translated subcriteria are shown in Figure 3.

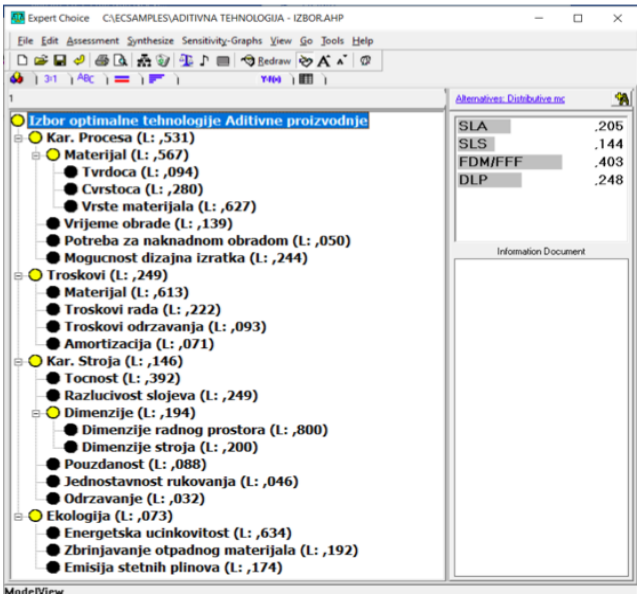

Figure 6. *The final table of criteria and subcriteria weight*

The criteria weight of characteristics of the process was 0.531 making it the most important criterion whose most important subcriterion was material with a weight of 0.567. The lowest impact on decision-making had ecology with a weight of 0.073 whose most important subcriterion was energy efficiency with a weight of 0.634. Expenses carried a weight of 0.249 while characteristics of the machine carried 0.146. The sum of the values of all of the criteria weights was 1. As for the alternatives, based on the analysis, FDM/FFF came out as the most appropriate choice with a weight of 0.403. The second best choice was DLP while SLS was the least appropriate choice based on the set criteria and subcriteria.

3.4. Sensitivity analysis

To make sure the chosen alternative was consistent in different conditions sensitivity analysis was done in Expert Choice. The first formed graph in the sensitivity analysis was the *Performance graph.* It showed how criteria and subcriteria affected alternatives with respect to set goals or criteria. The Performance graph for analysis is shown in Figure 7. Obtained graphs gave results with respect to set criteria (characteristics of the process-top left; expenses-top right, characteristics of the machine-bottom left, ecology-bottom right and main goal-bottom). It is visible from Figure 7 that FDM/FFF got the best overall result for 3 out of 4 criteria while for the criteria of ecology FDM/FFF was the best according to every subcriteria.

Graphic pairwise comparison between alternatives was done also with *Head-to-head* graphs in Expert Choice. A comparison could be done with respect to the main goal, criteria or subcriteria. Figure 8 shows a comparison of alternatives with respect to the main goal. It is visible that FDM/FFF was a better choice out of all of the alternatives with respect to the main goal. Compared to every alternative FDM/FFF had better results, as visible by the larger green horizontal columns. With provided information, FDM/FFF was chosen as the optimal choice of additive manufacturing technology. Decision was fully dependent on the set criteria and subcriteria. To further evaluate our analysis *Dynamic graph* was constructed which could have also been done in respect to the main goal, criteria and subcriteria. The graph in Figure 9 shows the weight of each criterion in the final assessment of alternatives with the visible color distinction between each. Characteristics of the process took up 53.1% of the weight of every alternative with the rest of the criteria distributed according to their value. With this graph, an analysis done by the AHP method for the selection of optimal AM technology was concluded. Chosen additive manufacturing technology was FDM/FFF.

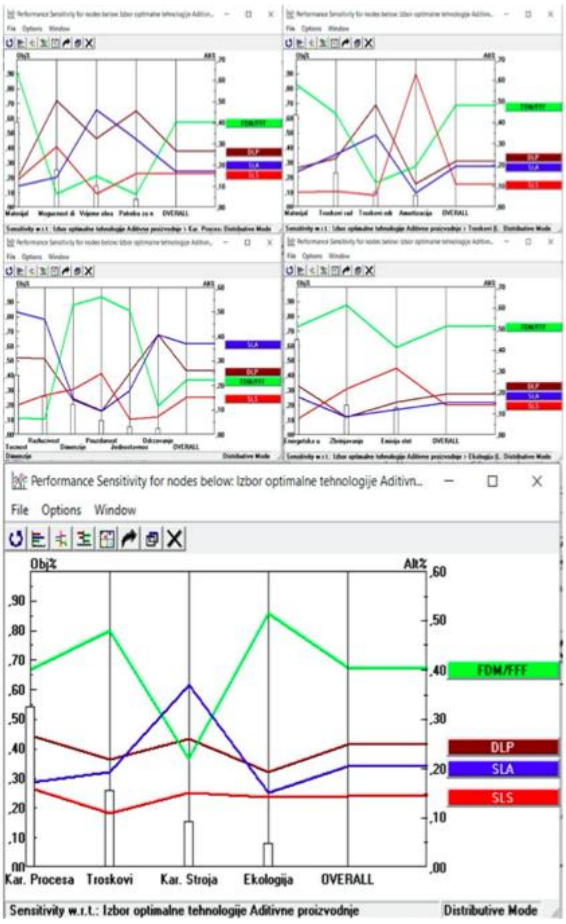

Figure 7. *Performance graph-1.analysis*

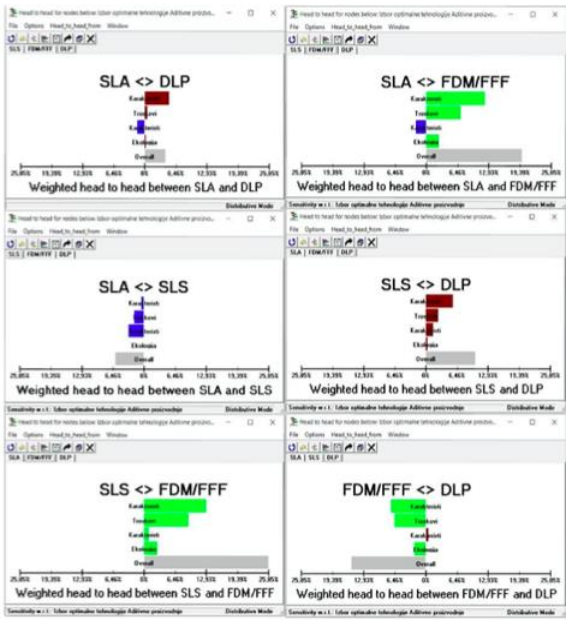

Figure 8. *Head-to-head graph-1. analysis*

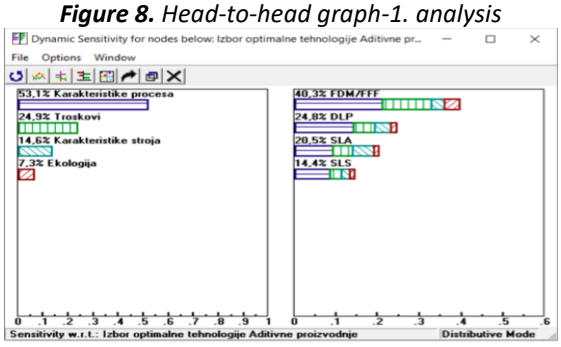

Figure 9. *Dynamic graph-1.analysis*

4. The AHP method for a 3D printer selection

4.1. Forming the AHP hierarchical structure

Based on the result of the analysis done with the AHP method for the selection of optimal additive manufacturing technology, a second analysis using the AHP method had to be done to choose the optimal 3D printer. Because of the vast number of possible choices of alternatives on the market at the moment, choosing was done at random. Chosen alternatives were: Flashforge Adventurer 3, Prusa Mini, Biqu B1, Creality Ender 3 V2 and Anycubic Mega X. Structure for the second analysis is shown in Figure 10. It states the main goal of this analysis was to select the optimal FDM/FFF 3D printer. The main difference between the first and the second analysis was in the distribution of criteria and subcriteria. While for the selection of additive manufacturing technology there were four criteria and a large number of subcriteria, for the selection of 3D printer all listed criteria were main criteria with no subcriteria. The translation of the set criteria is shown in Table 4.

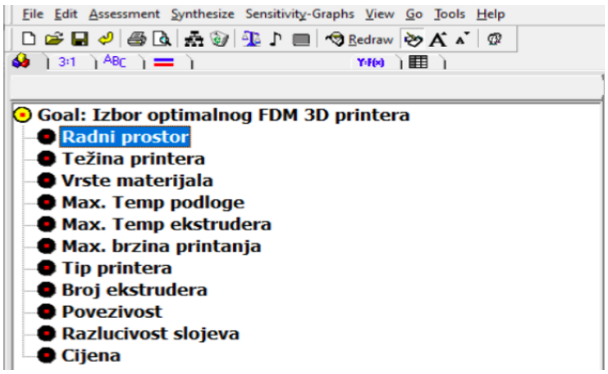

Figure 10. *Criteria for the second analysis*

Table 4. *Translation of criteria*

Croatian	English	Croatian	English
Radni prostor	Work space	Broj ekstrudera	Number of extruders
Težina printera	Weight of the printer	Povezivost	Connectivity
Vrsta materijala	Type of material	Razlučivost slojeva	Layer resolution
Max.temperatura podloge	Max.temperature of bed	Cijena	Price
Max.temperatura ekstrudera	Max.temperature of extruder	Tip printera	Type of printer
Max.brzina printanja	Max. print speed		

4.2. Evaluating criteria

Analysis was once again done in Expert Choice software and it followed the same steps taken in the first analysis done by the AHP method. A pairwise comparison between criteria by the Saaty scale and the results of it are shown in Figure 11. The weight of each criterion and their rank is visible in Figure 12. When choosing optimal 3D printer the most important criterion was type of material with criteria weight of 0.165. The weight of the printer was the least important criterion with criteria weight of 0.012. The next step was to compare all alternatives according to each criterion in order to form the final table of results. One of the comparisons between Prusa Mini and Flashforge Adventurer 3, with respect to the criterion of workspace, is shown in Figure 12. Figure clearly stated that Prusa Mini had moderate importance over Flashforge Adventurer 3.

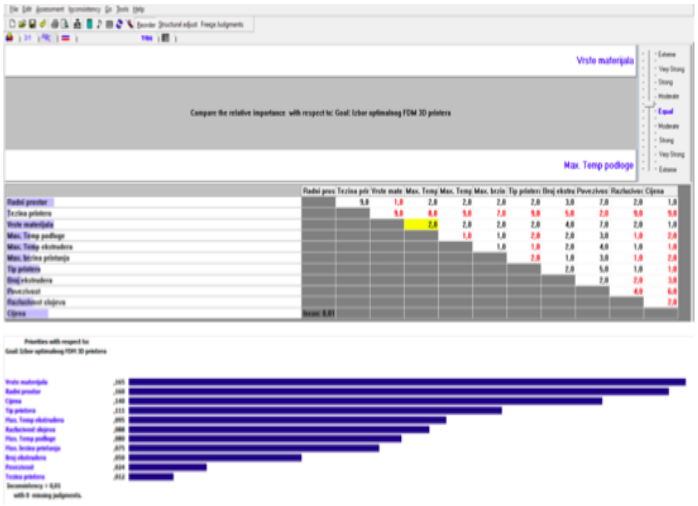

Figure 11. *Comparison between criteria*

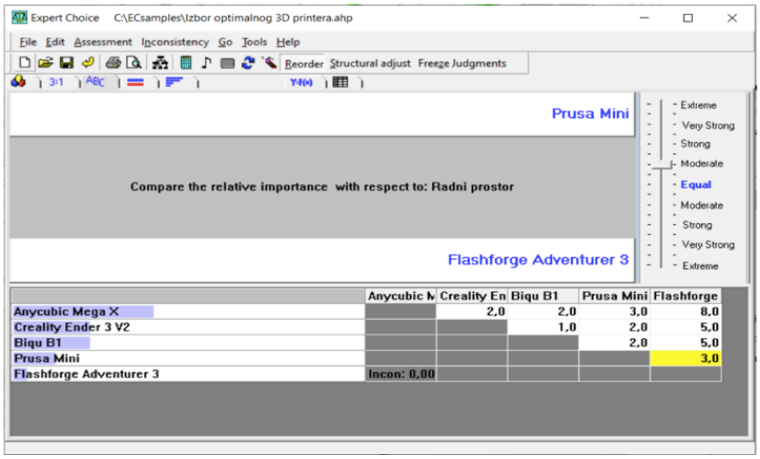

Figure 12. *Comparison of alternatives*

4.3. Results of analysis

Based on the done comparison, a final table showing the criteria weight and distribution of alternatives was formed - as shown in Figure 13. The results of the analysis were that the most important criterion, when choosing the optimal FDM/FFF 3D printer, was type of material. As for the actual 3D printer, based on the set criteria, Prusa Mini came out to be the optimal choice with a criteria weight of 0.245.

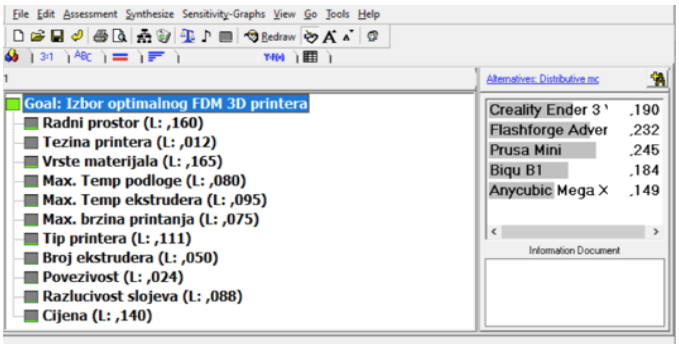

Figure 13. *The final table of criteria and subcriteria weight*

4.4. Sensitivity analysis

The same three types of graphs were constructed to perform sensitivity analysis - Performance graph, Head-to-head graph and Dynamic graph - in order to choose the optimal 3D printer. The Performance graph is shown in Figure 14 and it shows that Prusa Mini had the best overall result, making it the optimal choice. Part of the Head-to-head graph, shown in Figure 15, was done with respect to criteria because of a direct link between the main goal and all criteria set. Results were not as straightforward as they were when choosing additive manufacturing technology. Looking overall, Prusa Mini had more advantages over compared alternatives.

Almost always that advantage was present at the most important criteria - type of material. Both graphs showed very close results for Prusa Mini and Flashforge Adventurer 3. Further comparison to other alternatives provided clarity. Prusa Mini gave better results than Flashforge Adventurer 3. Although Flashforge Adventurer 3 had better results in head-to-head comparison over Prusa Mini in criterion of type of material, Prusa Mini had better overall results. The final graph, with which the second analysis was concluded, was the Dynamic graph shown in Figure 16. Although with a minimal advantage compared to other alternatives (as shown on right side of the Figure 16), the Dynamic graph confirmed that Prusa Mini was the optimal choice of 3D printer for FDM/FFF technology.

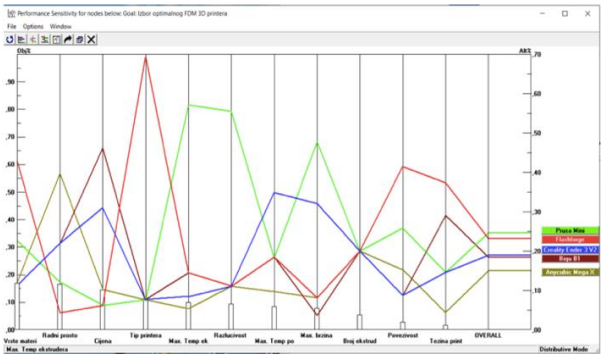

Figure 14. *Performance graph-2. analysis*

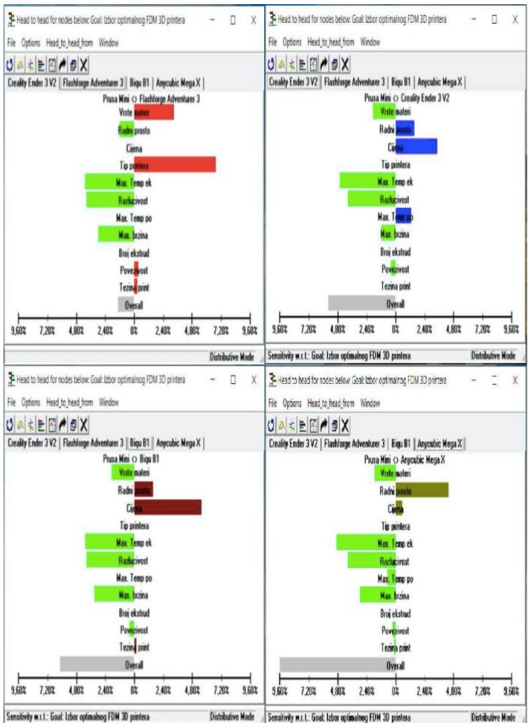

Figure 15. *Head-to-head graph-2. analysis*

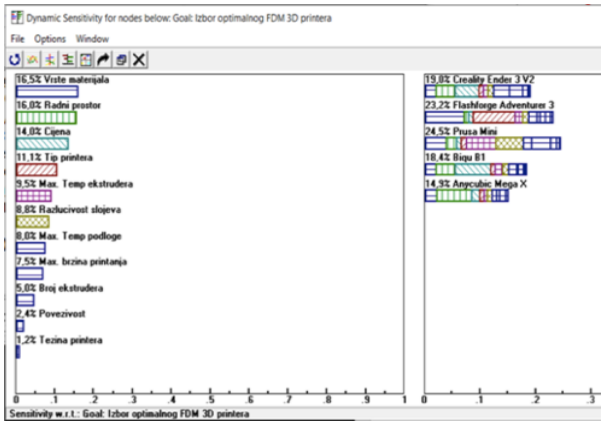

Figure 16. *Dynamic graph-2.analysis*

4.5. An alternative choice of a 3D printer

The results of the AHP method are very much relative to the set criteria and their evaluation done by the user of the method. That is why an experiment was done to observe how a change of criteria affects the choice of alternative. The type of printer was set as the most important criterion with a criteria weight of 0.202. The results of the analysis are shown in Figure 17. As seen in the Figure 17, Flashforge Adventurer 3 came out as the best choice when setting the type of printer as the most important criterion. It clearly shows that a small difference in setting the criteria can result in completely different results.

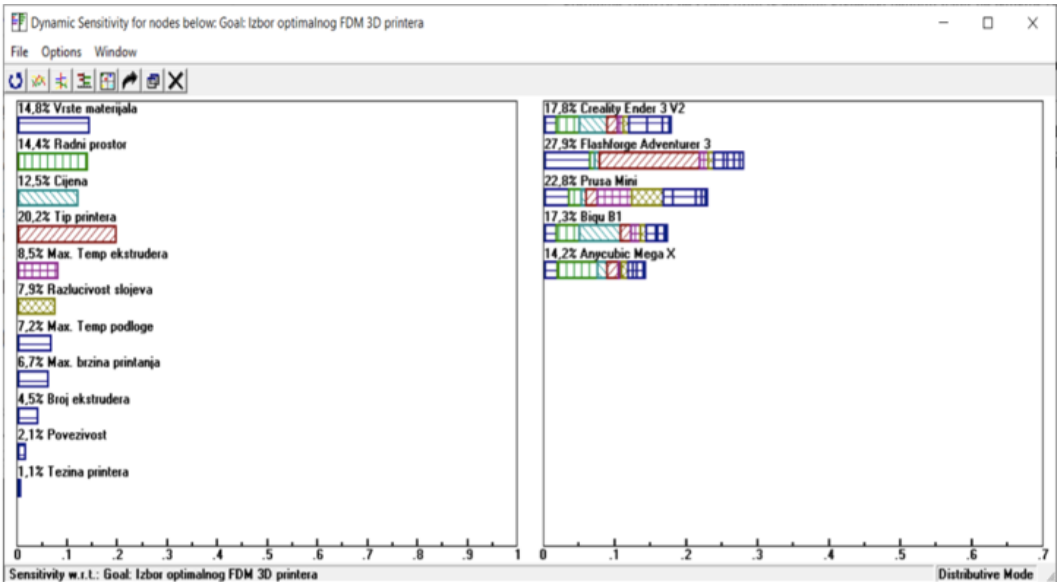

Figure 17. *An alternative choice of a 3D printer [15]*

5. Conclusion

The presented analysis of the application of the AHP method in selection of 3D printer has proved itself to be very useful and easy to comprehend. This paper provided step-by-step application of the AHP method in two separate but connected purposes - the selection of the optimal additive manufacturing technology and the selection of the 3D printer. Each analysis was successful and provided its own result – the optimal additive manufacturing technology, if characteristics of process is considered the most important criterion, was FDM/FFF while the optimal FDM/FFF 3D printer was Prusa Mini, provided that type of material is the most important criterion. Prusa Mini also met the requirements that stated the 3D printer had to have an industrial and an at-home version. Results obtained by the two analysis were relative to the set criteria and subcriteria. Any difference in the set criteria or subcriteria could have led to a different result, as shown in Chapter 4.5. Change of the most important criterion, from type of material to type of printer, in order to choose optimal FDM/FFF 3D printer led the analysis to different result – optimal FDM/FFF 3D printer was Flashforge Adventurer 3. This paper clearly pointed out the limitation of the application of AHP method – the results of the analysis are directly relative to the set criteria and subcriteria. Subjectivity the AHP method allows while setting and evaluating the criteria could present a problem where an objective decision is needed. That is why, even though the application of the AHP method has been greatly improved in the industry, attention must be paid to weighting the criteria and subcriteria in order to avoid inconsistencies. The method has proved itself to be very efficient to make a correct and fast decision once criteria and subcriteria are set but, if set and evaluated incorrectly, the method will lead to incorrect and inconsistent result. Due to its consistency in followed steps, the paper showed efficiency of the AHP method where more than two criteria are needed to make a decision. Considering the fast growth of additive manufacturing over the last few decades and a large number of different technologies and 3D printers, one should know beforehand what the main goal is and where priorities lay because the decision made could have profund implications in future work of a company or an individual. That is why all appropriate methods and tools should be used when making an decision in order for it to be valid.

Acknowledgements

This research was financially supported by the University of Rijeka, Croatia (contract number uniri-tehnic-18-100 and uniri-tehnic-18-223).

References

[1] Gibson, I., Rosen, D., Stucker, B., 2010. Additive Manufacturing Technologies 3D printing, Rapid Prototyping, Direct Digital Manufacturing, Springer, New York
[2] Autonomous Manufacturing, UK, 2023. The complete starting guide to additive manufacturing technologies. https://amfg.ai/2023/02/16/the-complete-starting-guide-to-additive-manufacturing-technologies/ (accessed May 5th 2023).
[3] Gass, S., 2005. Model world: The great debate-MAUT versus AHP. Interfaces. 35, 308-312.
[4] Goswami, S.S., 2020. Outranking methods: Promethee I and Promethee II. Foundation of Management. 12, 93-110.
[5] Gebhardt, A., 2011. Understanding additive manufacturing, Hanser Publishers, Munich
[6] 3DINSIDER, New Zealand, 2020. What is PolyJet 3D printing technology? https://3dinsider.com/polyjet-3d-printing/ (accessed May 8th 2023).
[7] Izadi, M., Farzaneh, A., Mohammed, M., Gibson, I., Rolfe, B., 2020. A review of laser-engineered net shaping (LENS) build and process parameters of metallic parts. Rapid Prototyping Journal. 26(6), 1061-1065.
[8] Sculpteo, France, Direct Metal Deposition Fabrication Process for Metal 3D Prints. https://www.sculpteo.com/en/glossary/dmd-definition/ (accessed May 8th 2023).
[9] Sharma, C.P., 2010. Biointegration of Medical Implant Materials, Woodhead Publishing, UK
[10] Saaty, T. L., 2009. Mathematical Principles of Decision Making, RWS Publications, USA
[11] Holjevac, N., Kuzle, I., Zidar, M., Razvoj modela analitičkog hijerarhijskog procesa i njegovo korištenje pri donošenju odluke o prelasku na 20 kV pogonski napon, HO CIRED 2014, Trogir, Seget Donji
[12] Primjena AHP metode i Expert Choice softwera u procesu donošenja odluke, Croatia, 2016. https://www.google.com/menadzersko-odlucivanje (accessed May 10th 2023).
[13] Damjanović, D., 2013. Primena AHP metode na selekciju i evaluaciju dobavljača, Sveučilište Singidunum, Beograd
[14] Kušmišević, M., 2016. Potpora odlučivanju kod razrade projekta “Car Sharing”, Sveučilište u Zagrebu, FSB, Zagreb
[15] Nišević, I., 2021. Primjena AHP metode pri odabiru 3D printera, diplomski rad, Sveučilište u Rijeci, Tehnički fakultet, Rijeka

Contactless collection of impurities on ultrasensitive nanofiber membrane

***Petr Novotný*[1], *Jiří Rulc*[1,4], *Radek Divín*[1,4,5], *Aleksei Pashchenko*[1,4,5,6], *Ján Varga*[2], *Massimo Rogante*[3], *Leontýna Varvařovská*[2], *Romana Siroka*[2], *Tatana Jarosikova*[2]*and Evžen Amler*[1,4,5]**

1) University Centre for Energy Efficient Buildings, Czech Technical University in Prague, Trinecka 1024, 27343 Bustehrad, Czech Republic.

2) FBMI ČVUT, nám. Sítná, Kladno, Czech Republic

3) Rogante Engineering Office, Contrada San Michele n. 61, 62012 Civitanova Marche, Italy

4) Student Science, s.r.o., Třinecká 1024, Buštěhrad, Czech Republic

5) Second Faculty of Medicine, Charles University, V Úvalu 84, 150 06 Prague, Czech Republic

6) University of Sassari, Piazza Università, 21, Sassari, Italy

Corresponding author: Amler@seznam.cz

Original scientific article

Abstract: In this work our novel contactless collection method is presented, based on nanobiosensor, which enables collection of impurities from surface, including textile material.
This paper clearly shows that our system, based on nanofiber membrane filter, is highly effective in contactless collection of microscopic and submicroscopic particles with an efficiency exceeding 99%.

Keywords: *NDT; nanofiber membrane; molecules*

1. Introduction

Ultrasensitive sensors belong among dynamically developing analytical devices since they can be efficiently used for the detection of substances at very low concentrations. Application of nanotechnology in sensor development opens a new perspective for ultrasensitive detection. Nanosensors are suitable for quick gas or liquid analyses and the construction of portable detection systems. The detectors could profit from nanofiber-based sensors, due to their unique structure-functional properties.
Nanofiber membranes are characterized by an exceptionally high surface-to-volume ratio, with an extremely high number of pores. These characteristics favour nanofiber membranes for broad medical applications and to produce medical devices as shown lately, e.g., for wound dressing, drug delivery, and biological sensing ([1], [2], [3], [4] and [5]). The high density of tiny pores, moreover, with the possibility to tune their diameters, favours nanofibers also for their exploiting as liquid filters for the smallest particles ([6], [7] and [8]). Unimportantly whether for water monitoring ([9], [10], [11] and [12]) or cleaning, detection of pathogens, or the creation of protective aids (such as masks and respirators), nanofibers are inexpensive, easy to use and highly effective alternatively to the long-lasting and expensive laboratory tests ([2] and [13]). In addition, a specific modification of the surface of nanofibers rockets them up to a superior industrial and medical applications since they can filter a large volume of liquid, not only with high efficiency but also with high selectivity. Nanofibers can be functionalized both on their surface and in their core.
The surface modification can be highly selective, which opens the door for advanced specific bionanosensors. As a result, when a relatively large amount of gas or fluid is filtered through a specific

filter, even a tiny impurity amount can be detected without the use of any complicated concentration processes.
The application of nanofiber filters in contactless impurity collection system is a main goal of this work, including the functional application for collection of viral particles. We also aimed to proof its extremely sensitivity and even specificity.

2. Materials and Methods

2.1 Contactless collector of particles

We have developed a contactless collection system (see Figures 1 and 2), composed of the following main parts:

- pressurize system which is able to develop low negative pressure
- hood for application of the low pressure and collection of particles from the material
- tubes for low pressure application and collection of particles
- holder of the filtration membrane
- nanofiber membrane.

Figure 1. *Apparatus for a contactless particle collection*

Figure 2. *Head of the collector*

The nanofiber membrane has ben placed among two plastic rings (Figure 3).

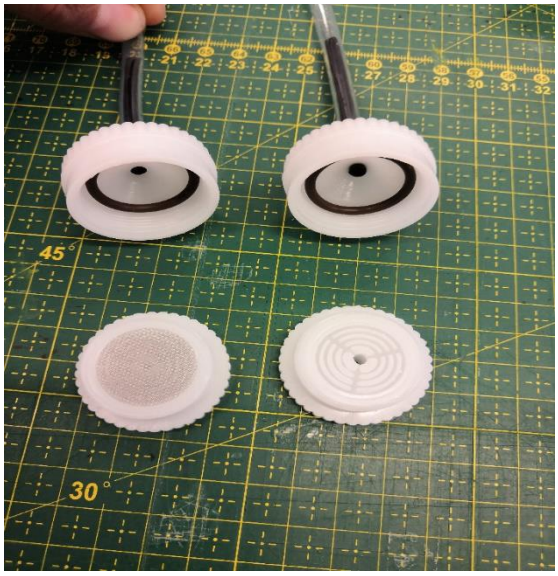

Figure 3. *Holder of the nanofiber membrane*

2.2 Preparation of the nanomembrane filters

The polyacrylonitrile (PAN) nanofibers of different area densities were obtained from Nanoprogress s.r.o. (Pardubice, Czech Republic) and they were visualized by scanning electron microscopy (SEM) Vega3 SB TESCAN a.s. (Brno, Czech Republic). Before the sample visualization, samples were sputtered (by using a Sputter Coater Q150R, Quorum Technologies Ltd, Lewes, UK) by a conductive 10 ± 2 nm layer of golden nanoparticles to prevent samples' charging during the SEM visualization. Images were analysed by the ImageJ software (NIH, Bethesda, USA) from five different areas of each sample.
Surface zeta potential was measured on PAN nanofiber samples by a Zetasizer nano ZS (Malvern Panalytical Ltd, Malvern, UK) at five different distances, using the incorporated Malvern software and a linear regression to calculate the final surface zeta potential.

2.3 Cultivation of Escherichia coli

The Gram-negative bacteria Escherichia coli was used as a model organism for the detection. The reference bacterial strains were provided from the bacterial collection of the University of Chemistry and Technology, Prague. The cultivation of bacterial colonies was performed on an agar medium. Chemicals used to prepare the agar medium (NaCl, peptone, agar and yeast extract) were obtained from Sigma Aldrich (St. Louis, USA).

3. Results

3.1 Collection of microscopic particles

The main goal of the experiment was to prove that the nanofiber filter in our experimental set-up is able to collect microscopic and submicroscopic particles. Thus, to collect the particles we have used our above mentioned home-made apparatus in suckling mode, i.e. we have yielded a single tube producing negative pressure only. All the air, therefore, has been sucked for 60 sec. and filtered through the nanofiber membrane attached inside the filter holder. We have tested the nanofiber membrane ability both for microscopic and submicroscopic particles.
First, wheat flour has been chosen to test the nanofiber ability to collect the wheat flour that has been poured in the heavy textile material. Suckling has been subsequently carried out for 60 sec. and the visualization has been performed by SEM.

3.1.1. Collection of wheat flour

In Figure 4 (SEM image) particles are shown of wheat flour on PVA nanofiber filter after 60 sec. filtration.

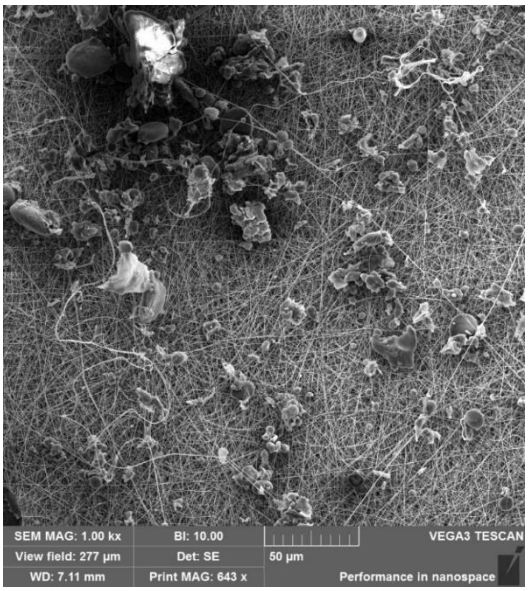

Figure 4. *Particles of wheat flour on PVA nanofiber filter after 60 sec filtration. Magnification 10.000x*

3.1.2. Collection of air dust

The PVA nanofiber filter has been used, successively, to collect air dust as an example of smaller particles (see Figures 5 and 6).

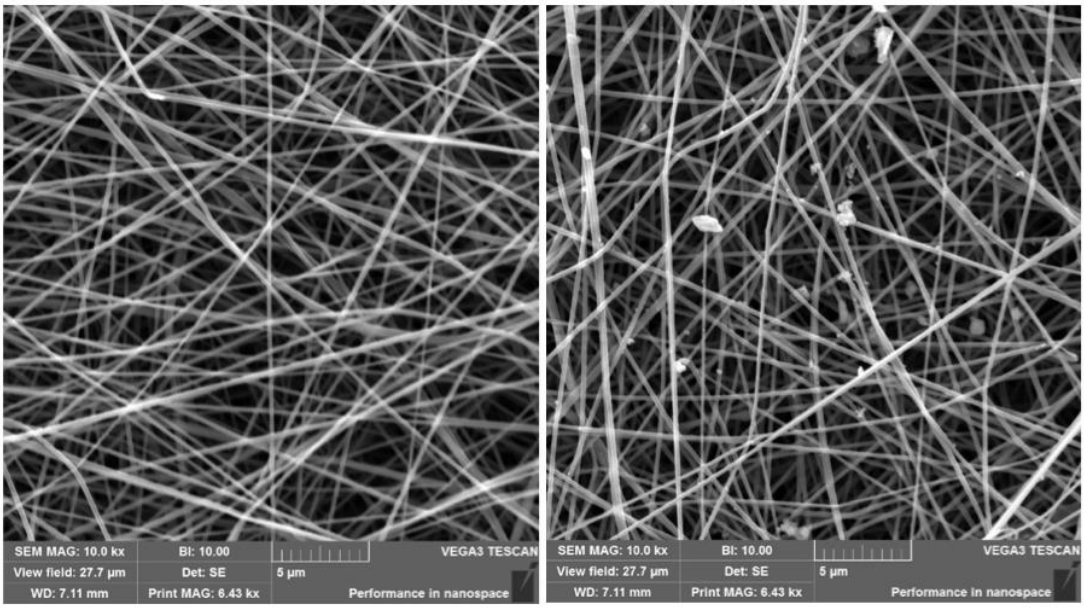

Figure 5. *PVA nanofiber filter: clean filter (left); filter after 60 sec. of filtration of laboratory air. Magnification 10.000x*

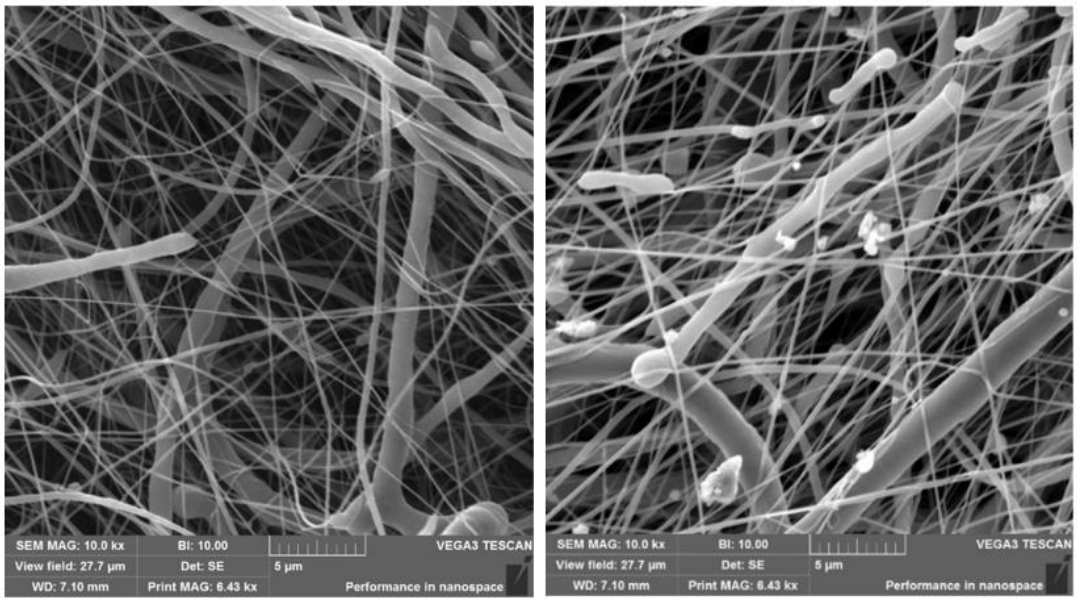

Figure 6. *PCL nanofiber filter: clean filter (left); filter after 60 sec. of filtration of laboratory air. Magnification 10.000x*

3.1.3. Collection of bacteria Escherichia coli

We have tested the system, successively, to collect bacteria Escherichia coli. In all cases, there was absorption and capture of bacteria, which was verified by placing the filter on a solid nutrient medium, with subsequent cultivation in an incubator (24 hours, 37 °C, 5% CO_2, Humidity 90%). The bacterial strain Escherichia Coli (gram-negative rod) was selected for testing. Colony growth on filter plates was high, beyond countable range. Figure 7 shows the detected bacteria.

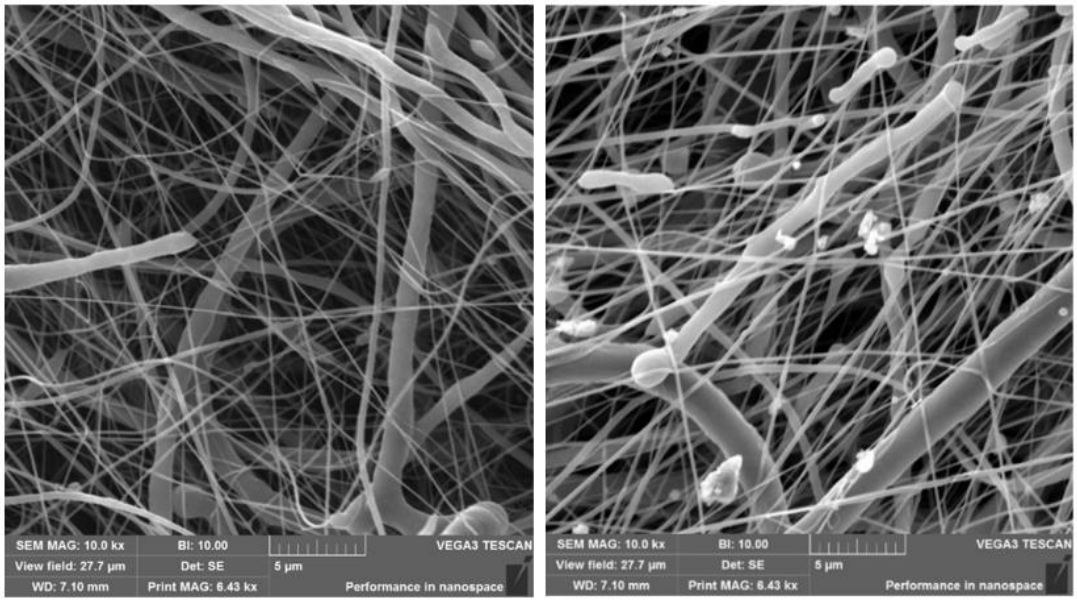

Figure 7. *Bacterial presence on the nanofiber membrane*

3.2 Trapping of submicroscopic particles

To test the trapping of submicroscopic particles, cat panleukopenia viruses have been selected. In this experimental setup, just a filtration of the viral solution throughout the nanofiber membrane has been performed. A sterile glass table (2×2 cm) has been covered with the nanofiber membrane and 105 viral particles (in 10µl suspension) have been applied. The membrane has been removed after 5 min. and the viral particles penetrated throughout the nanofiber membrane have been washed out into 10 µl sterile PBS. The virus presence in the solution has been determined by qPCR. Two types of membrane have been employed, i.e. without and with 10% povidone iodine. As Table 1 clearly shows, the concentration of penetrated viral particles has been lower than 1%. In addition, povidone iodine inactivated another ~90% of all viral particles penetrated throughout the nanofiber membrane.

Table 1. *Example of the table spread over the width of the document*

Sample	Number of viral particles	Coefficient of impermeability
Control	4,27E5	
PVA nanomembrane	2,95E3	144
PVA nanomembrane with povidone iodine ions	4,95E2	862

4. Discussion and Conclusion

We have demonstrated the effectiveness of our home-made apparatus for particle collection.
The nanofiber membrane can be used for trapping of differently sized particles. We have proved that the nanofiber filter, which is used at this apparatus, is able to collect microscopic as well as submicroscopic particles. We have been able to monitor particles from hundreds microns down to several dozen nanometres. This limit, however, is probably due only to the limit of the applied visualization technique. Since the collection of differently sized particles must be dependent on pore size of the nanofiber membranes, different nanofiber layers with diverse surface densities need to be used. This is easily achievable, however, since the pore size decreases with the surface density.
In conclusion, this system has an ambition for unspecific as well as specific detection of extremely low and particularly small particles, even individual molecules.
Collection of living organism on nanofiber, like bacteria, is not harmful. We have shown that these trapped bacteria can proliferate after removal from the nanofiber filter. This system, consequently, could be used also to detect and identify a very small number of bacteria.

Acknowledgements

The research was supported by the Charles University Grant Agency (project no. 312123).

References

[1] Kenry, Lim, Ch.T., 2017. Nanofiber technology: current status and emerging developments. Prog. Polym. Sci. 70, 1–17.
[2] Haider, A., Haider, S., Kang, I-K., 2018. A comprehensive review summarizing the effect of electrospinning parameters and potential applications of nanofibers in biomedical and biotechnology. Arab. J. Chem. 11, 1165–1188.
[3] Pashchenko, A., Stuchlíková, S., Varvařovská, L., Firment, P., Staňková, L., Nečasová, A., Amler, E., 2022. Smart nanofibres for specific and ultrasensitive nanobiosensors and drug delivery systems. Acta Vet. 91/2, 163–170.
[4] Coradduzza, D., Bellu, E., Congiargiu, A., Pashchenko, A., Amler, E., Nečas, A., Carru, C., Medici, S., Maioli, M., 2022. Role of Nano-miRNAs in Diagnostics and Therapeutics. Int. J. Mol. Sci. 23/12, 6836.

[5] Bocková, M., Pashchenko, A., Stuchlíková, S., Kalábová, H., Divín, R., Novotný, P., Kestlerová, A., Jelen, K., Kubový, P., Firment, P., Fedačko, J., Jarošíková, T., Rulc, J., Rosina, J., Nečas, A., Amler, E., Hoch, J., 2022. Low Concentrated Fractionalized Nanofibers as Suitable Fillers for Optimization of Structural-Functional Parameters of Dead Space Gel Implants after Rectal Extirpation. Gels 8/3), 158.
[6] Qin, X-H., Wang, S-Y., 2006. Filtration properties of electrospinning nanofibers. J. Appl. Polym. Sci. 102/2, 1285–1290.
[7] Sahto, M.O., 2021. Electrospun Nanofibers for Highly Efficient Air Filter Applications. https://www.inovenso.com/wp-content/uploads/2021/04/Inovenso_Electrospun-nanofibers-for-highly-efficient-air-filter-applications.pdf (accessed 31 August 2022).
[8] Zhou, Y., Liu, Y., Zhang, M., Feng, Z., Yu, D-G., Wang, K.. 2022. Electrospun Nanofiber Membranes for Air Filtration: A Review. Nanomaterials (Basel) 12/7, 1077.
[9] Markosian, Ch., Mirzoyan, N., 2019. Wastewater-based epidemiology as a novel assessment approach for population-level metal exposure. Sci. Tot. Environ 689, 1125–1132.
[10] Mao, K., Zhang, K., Du, W., Ali, W., Feng, X., Zhang, H., 2020. The potential of wastewater-based epidemiology as surveillance and early warning of infectious disease outbreaks. Curr. Opin. Environ. Sci. Health 17, 1–7.
[11] Mao, K., Zhan, H., Pan, Y., Yang, Z., 2021. Biosensors for wastewater-based epidemiology for monitoring public health. Water Res. 191, 116787.
[12] Khodayari, P., Jalilian, N., Ebrahimzadeh, H., Amini, S., 2021. Trace-level monitoring of anti-cancer drug residues in wastewater and biological samples by thin-film solid-phase micro-extraction using electrospun polyfam/Co-MOF-74 composite nanofibers prior to liquid chromatography analysis. J. Chromatogr. A 1655, 462484.
[13] Bellu, E., Diaz, N., Kralovič, M., Divin, R., Sarais, G., Fadda, A., Satta, R., Montesu, M.A., Medici, S., Brunetti, A., Pinheiro Barcessat, A.R., Jarošíková, T., Rulc, J., Amler, E., Margarita, V., Rappelli, P., Maioli, M. 2022. Myrtle-Functionalized Nanofibers Modulate Vaginal Cell Population Behavior While Counteracting Microbial Proliferation. Plants 11/12, 1577.

Comparative studies of stress-corrosion cracking of long-term exploited and storage pipes of X70 steel of main gas pipeline

***Lyudmila Nyrkova*[1], *Svetlana Osadchuk*[1], *Yulia Kharchenko*[1], *Larysa Goncharenko*[1], *Anatoly Klymenko*[1], *Valery Kostin*[1] *and Anatoy Rybakov*[1]**

1) E.O. Paton Electric Welding Institute of the National Academy of Sciences of Ukraine, 11, Kazymyr Malevych St., Kyiv, Ukraine

Corresponding author: lnyrkova@gmail.com

Original scientific article

Abstract: Comparative studies of stress-corrosion cracking (SCC) of the metal long-exploited pipe and the storage pipe of X70 steel after the same duration of operation and storage respectively were carried out. With the application of a complex of methods (voltammetry, slow strain rate tests, fractography, electrolytic hydrogenation) it was established that under the potential of cathode polarization from -0.75 V to -1.05 V in the NS4 solution, for the metal of the exploited pipe, the tendency to SCC, estimated by the K_S coefficient, increases from 1.02 to 1.53, for the storage pipe at the potentials -0.75 V $\rightarrow$ -0.95 V $\rightarrow$ -1.05 V K_S changes non-monotonously as -1.02 $\rightarrow$ 1.55 $\rightarrow$ 1.32. With increasing of cathodic polarization potential, the concentration of hydrogen penetrating into the exploited steel increases from 0 to 0.0241 mol/m^3. This correlates with an increasing tendency to brittle cracking under such conditions. The tendency to increasing the susceptibility to SCC of the exploited pipe may indicate on steel embrittlement under long term operation at external cathodic polarization.

Keywords: *pipe steel X70; long term operation; stress-corrosion cracking; electrolytic hydrogenation; voltammetry; slow strain test method; optical microscopy; SEM*

1. Introduction

Underground gas pipelines were built in the 70-80s of the twentieth century, and today their service period is from 40 to 50 years. During operation in conditions of comprehensive anti-corrosion protection (protective polymer coatings and electrochemical protection) they are subjected to the influence of mechanical and corrosive factors, particularly the corrosion of the external environment (from the impact of the soil in case of damage to the protective coating). The presence of hydrogen in environments, for example, formed under cathode polarization, can lead to deterioration of the mechanical properties of steels during plastic deformation. Particularly noticeable is this type of damage in ferrite steel ([1], [2]). Under cathodic polarization, there is cathodic disbandment of protective coatings, and under high polarization potential, hydrogen through the defect penetrates into the wall of the pipe ([2], [3]), contributing to hydrogen degradation of steel ([3], [4]). Hydrogen induced cracking took place under tension conditions ([2], [5], [6]). The relationship between hydrogen exposure and material characteristics such as microstructure, chemical composition, and mechanical properties is complex [7], so studies focused on hydrogen scattering steels often lead to contradictory conclusions.

It is proposed to distinguish between degradation of pipeline surfaces (damage under the influence of mechanical, corrosive and other factors) and degradation "in the volume" of the metal (deterioration of the properties, if not of the entire volume of metal, but the part of metal commensurate with the characteristic dimensions of the pipe - for example, wall thickness or a certain part of the pipe) [8].

In a series of works of the E.O. Paton Electric Welding Institute ([9], [10], [11] and [12]), the aging of metal of pipes made of controllable rolling steel after long-term operation and after storage from 2 to

21 years was evaluated. For the specimens of storage pipe did not reveal any differences in the exploitation characteristics (σ_{UTS}, σ_{YS}, δ_5, σ_{YS}/σ_{UTS}, impact toughness) of the base metal and welded joints comparatively to the regulatory documents of and correspondingly noticeable changes in the state of the metal as a result of natural ageing. But the sensitivity to the ageing of metal is confirmed, for example, for pipes of X70 steel, operated in complex conditions (at the section of the transition through the beams).

According to some indicators of mechanical properties, the metal of X70 steel after longterm operation, does not correspond the requirements of regulatory documents. However, due to the high values of the impact toughness and plasticity of the metal in as-received state, the state of exploited metal can be considered as satisfactory.

Other authors have shown that in X70 steel, microcracks are formed at the «inclusion-matrix» boundaries. Deep micro-layering in the central part of fracture surfaces of specimens for exploited steels was considered a sign of diffuse metal damage caused by texture and hydrogen absorbed by the metal [8]. The characteristics of stress-corrosion cracking of X52 and X60 steels in their initial states in a corrosive environment change slightly. Cracking occurs along the boundaries of the interface between the grains of ferrite and pearlite, with the formation of deep secondary intergranular cracks and the delamination of ferrite and cementite inside the grains of pearlite. Destruction by this mechanism was detected near the outer surface of the specimens and, according to the authors, indicates the key role of hydrogen during cracking. There is data [14] that hydrogen atoms are easily separated at the ferrite/pearlite interface without external loads. During rapid deformation, hydrogen penetrates pearlite and interacts with its internal vacancies, which leads to transgranular fracture, which begins with pearlite. At slow deformation, the ferrite/pearlite interface is more vulnerable to hydrogen degradation, which leads to intergranular cracks and an increased tendency to form secondary cracks.

Some authors point out that the long-term operation of gas pipelines leads to a slight decrease in the hardness, ultimate strength, and conditional yield strength and a noticeable increase in the relative elongation of low-alloyed manganese and silicon steels ([8] and [15]), as well as a shift in the corrosion potential of the used steel up to 20-30 mV to more negative values compared to the storage pipe. The work [16] confirmed the reduction of plasticity characteristics and the increase of strength characteristics due to operational degradation. It is emphasized that the higher the strength level of steel, the less its characteristics change. It is shown that the plasticity indicators of X70 steel practically do not change, and those of X60 steel decrease, which is due to the structural features of the steels.

Deterioration of the properties of the metal of the operated main gas pipeline revealed also by the authors ([17] and [18]) by decrease in impact toughness, relative narrowing, and an increase in hardness; the plasticity parameters of the metal changed in the opposite way. This is explained by the intensive development of defects at the micro- and sub-micro levels during longterm operation, which is confirmed by fractographic analysis.

Therefore, the results available in the literature contain data on the effect of long-term operation, mainly on the mechanical properties of steels. The purpose of the work is to investigate the susceptibility to stress-corrosion cracking under cathodic polarization of long-term operated pipe steel compared to emergency storage pipe that was not affected by operational factors.

2. Experimental Details

The research was carried out on specimens of pipe steel X70 of controllable rolling after 40 years of operation and emergency storage pipes after the same period of storage. Chemical composition of the metal was determined by spectral method using the Spektrovak-1000 device manufactured by the Biard company. The susceptibility to stress-corrosion cracking was studied in the model soil electrolyte NS4, g/l: 0.122 KCl + 0.483 $NaHCO_3$ + 0.181 $CaCl_2$ + 0.131 $MgSO_4$ [19].

Corrosion-mechanical studies were carried out by slow strain rate method (deformation rate was 10^{-6} s^{-1}) on the AIMA-5-1 breaking machine with periodic wetting with a solution for 50 min in the solution and 10 min in air. The scheme for cutting specimens for research is shown in Figure 1. The

cross-sectional area of the specimen in its initial state is 30 mm^2. All tests were carried out at cathodic polarization potentials of -0.75 V, -1.05 V, and -1.2 V (relative to the silver chloride reference electrode) using an PI-50-1 potentiostat and programator PR-8, thereby simulating cathodic protection applied to underground gas pipelines.

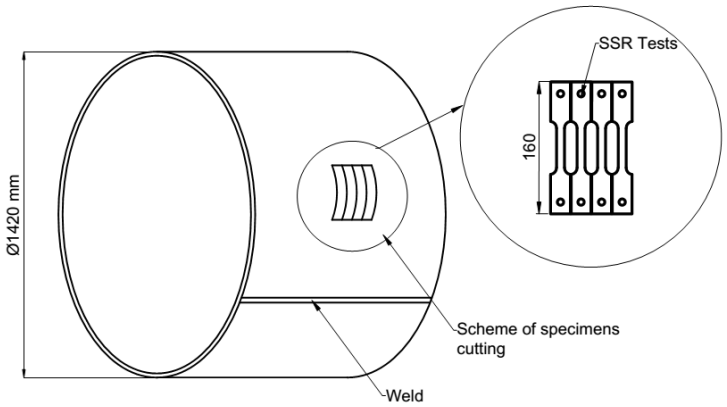

Figure 1. *Scheme of cutting specimens from a pipe fragment*

Grits for metallographic studies were made according to standard methods. The microstructure was detected by etching with a solution of 4% nitric acid in ethyl alcohol. Sections were studied using a NEOPHOT 21 microscope, and digital images of the microstructure were obtained using an Allied Vision digital camera and SEO ImageLabMet software. The grain size was determined according to DSTU 8972 [20]. The scanning electron microscopy was used to study the surface of the specimens after rupture. The research was carried out on a JSM 840 scanning electron microscope (JEOL, Japan). The surface was studied in the mode of secondary and backscattered electrons at an accelerating voltage of 20 kV and an electron beam current (10^{-7}-10^{-10}) A at different magnifications (from ×12 to ×500).

Polarization curves were measured on an MTech PGP-550F potentiostat with a potential scan rate of 0.5, 1 and 100 mV/sec.

3. Experimental results and discussion

3.1. Chemical composition

The results of determining the chemical composition are given in Table 1, which shows that the base metal of the operated pipe is low-carbon steel microalloyed with titanium (0.08-0.09%).

Table 1.*Chemical composition of the steels under investigation*

Specimen type	Weight part of elements, %								
	C	Mn	Si	S	P	V	Mo	Al	Nb
Exploited pipe	0.09	1.39	0.40	0.006	0.023	0.071	<0.01	0.021	0.029
Storage pipe	0.10	1.45	0.27	0.009	0.024	0.065	0.015	0.018	0.027
Requirements of TS 14-3-995 [21]	0.12	1.70	0.50	0.010	0.020	0.08	0.30	0.050	0.06

According to TU 14-3-995 [21] Pipes for the gas pipeline were made of low-carbon steel of controllable rolling, microalloyed with niobium and vanadium [21], and the amount of these elements was limited to 0.06 and 0.08%, respectively. In the base metal of the operated pipe and emergency storage pipe, the vanadium content did not exceed 0.071 and 0.65%, niobium - 0.29 and 0.27%, and the carbon content was within 0.09-0.10%. That is, the chemical composition of the steel fully met the requirements of regulatory documents.

3.2. Microstructure

The microstructure of the operated pipe metal is a mixture of ferrite and pearlite (Figure 2, a). The strips of the pearlite component are discontinuous, the amount of pearlite is about 10%, the pearlite components are located mainly on the grain boundaries. Small carbide formations were found along the body of the ferrite grain. The size of the ferrite grain is 10-20 μm according to [20] (Figure 3, a). The banding of the base metal of pipe B corresponds to 2 points, according to [20].

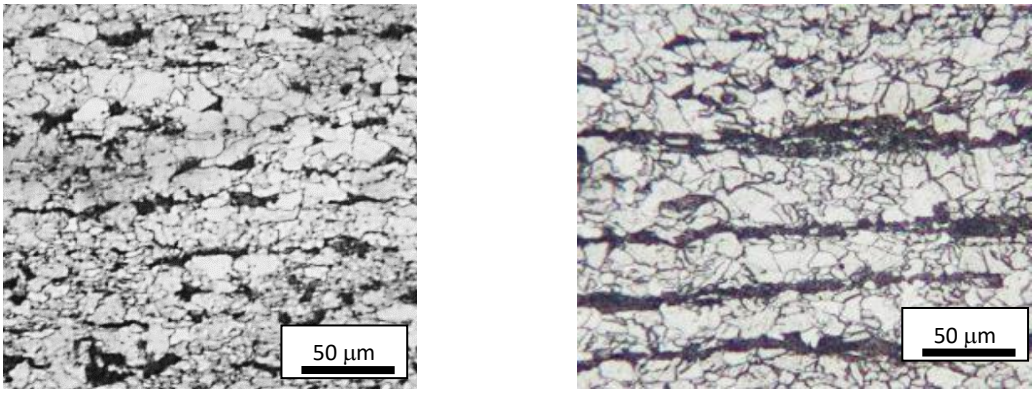

a *b*

Figure 2. *Microstructure of the base metal of the operated pipe (a) and the stock (b) pipe, ×320*

The microstructure of the base metal of the stock pipe is ferrite-pearlite, but more uniform, without local areas of finer grain, which are observed in the base metal of the operated pipe. The ferrite grain is larger and has a more balanced character, with no signs of deformation during rolling. The size of the ferrite grain is 14-20 μm. The structure of the base metal has a pronounced banding of the pearlite component, and according to [20] corresponds to 4 points. The volume of pearlite is about 20%.

3.3. Electrochemical properties

The change in the corrosion potential of the base metal of the X70 steel of the above-mentioned pipes is shown in Figure 3, a.

As can be seen from the Figure 3, during stabilization of a stationary value, the corrosion potentials of the operated pipe and the reserve pipe differed by approximately 14 mV, but after 1800 s, their values equalized and amounted to -0.737 V. From the polarization curves presented in Figure 3, b, it can be seen that the nature of the anodic and cathodic curves is similar. The limiting diffusion current of oxygen reduction on the specimens of both pipes is also very close, 1.69×10^{-4} A/m^2.

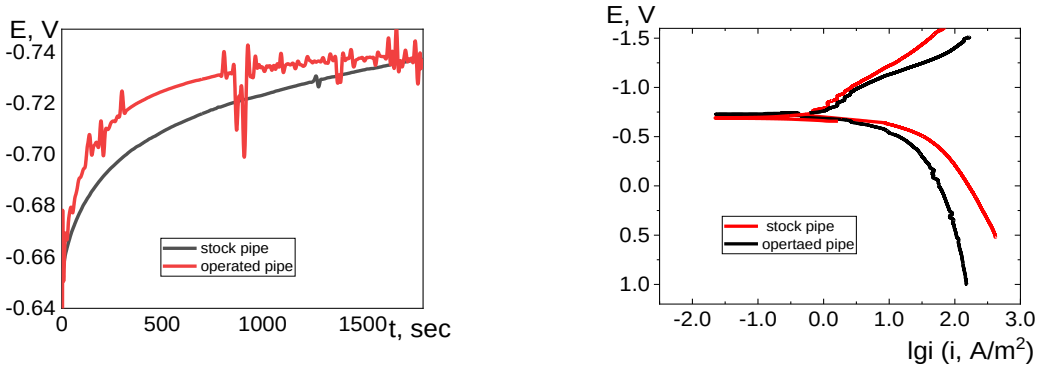

a *b*

Figure 3*. Corrosion potentials (a) and polarization curves (b) in the NS4 solution of the metal of operated pipe (1) and the emergency reserve pipe (2)*

***Table 2**. Electrochemical characteristics of pipe specimens of X70 steel*

Specimens type	E_{cor}, V	b_a, V	I_{O2}, A/m²	E_{H2}, V
Exploited pipe	-0.737	0.063	1.69	-1.04
Storage pipe	-0.737	0.139	2.09	-1.04

The hydrogen recovery potentials on the specimens of the operated pipe and the storage pipe are also the same and amount to -1.04 V (Table 2). The slopes of the anodic curves, determined in the area of 50 mV from the corrosion potential, are 0.063 V and 0.139 V, respectively. That is, in the NS4 model soil electrolyte, corrosion of the operated X70 steel pipe is described by the diffusion kinetics laws, and the anodic process is complicated for the reserve pipe. It can be assumed that the differences in electrochemical properties are due to differences in the chemical composition of the steels, in particular, a larger amount of manganese and molybdenum and a smaller amount of silicon, vanadium, and aluminum in the stock pipe metal.

3.4. Stress-corrosion cracking

To determine and compare the susceptibility to stress-corrosion cracking of the operated pipe and the storage pipe, a theoretical model [22] was used, according to which the state of the metal at the top of the crack during the development of stress-corrosion cracking can be simulated on a freshly cleaned surface of the metal in the solution, comparing the polarization curves , taken with low and high potential scanning speed. At the same time, the polarization curve with a high scanning rate of the potential reflects the electrochemical behavior at the top of the crack, and the polarization curve with a slow rate – the electrochemical state of the steel on a surface where there is no crack (for example, a flat surface or the edges of a crack). Usually, the potential at zero current on the polarization curve during a slow scan of the potential is positively than during a fast scanning, which indicates that there is a greater probability of an electrochemical reaction occurring at the top of the crack than on the part of the surface located at a distance from the top of the crack.

Potentiodynamic polarization curves in NS4 solution were obtained with fast (100 mV/s) and slow (0.5 mV/s) potential scanning speeds. It was determined that for the operated pipe, the null current potential $E^1_{i=o}$ at a low potential scanning rate equal to -0.87 V, and at a high scanning potential rate $E^2_{i=o}$ = -0.99 V. For the reserve pipe, the corresponding null current potentials are $E^1_{i=o}$ = -0.89 V and $E^2_{i=o}$ = -0.95 V. So, using the voltammetry method the areas of potentials in which the mechanism of stress-corrosion cracking of the investigated pipes changes were determined.

Next, we examined the failure diagrams of the specimens at cathodic polarization potentials selected in each of the above-mentioned areas of change in the stress-corrosion cracking mechanism - areas of anodic dissolution, mixed mechanism, and hydrogen embrittlement.

Susceptibility to stress-corrosion cracking was assessed by the dimensionless coefficient K_S [23, 24], which was calculated as the ratio of the relative narrowing of the specimens in air ψ_{air} to the relative narrowing in the solution ψ_{sol} according to the formula (1):

$$K_S = \frac{\psi_{air}}{\psi_{sol}} \tag{1}$$

The change in a complex of other indicators was also analyzed: relative elongation, relative narrowing, and the nature of the morphology of the fracture surface.

Breaking diagrams of specimens of the operated pipe and the reserve pipe in air and in the NS4 model soil electrolyte at different cathodic polarization potentials are shown in Figure 4, respectively, photographs of the morphology of the fracture surface of the specimens – in Figure 5.

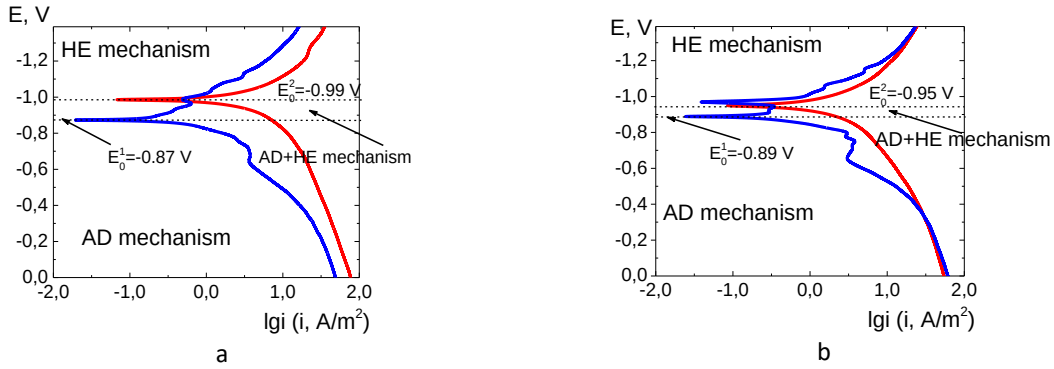

***Figure 4**. Polarization curves of the steel specimens measured at high (100 mV/s) and low (0.5 mV/s) potential scanning rates in NS4 solution: a – exploited pipe; b – storage pipe*

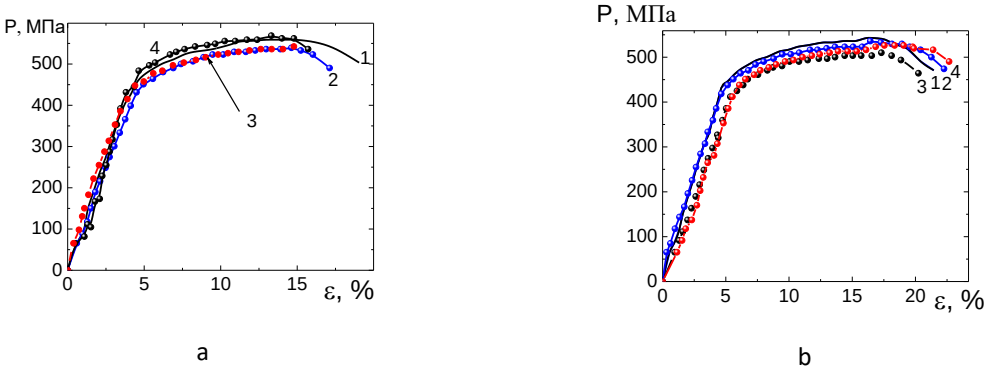

***Figure 5.** Breaking curves of specimens of the operated pipe (a) and reserve pipe (b) in NS4 solution: 1 – in air;*
2 – E_{pol} = - 0.75 V; 3 – E_{pol} = - 0.95 V; 4 – E_{pol} = - 1.05 V

After breaking in air, the specimen of the operated pipe is characterized by viscous destruction: shrinkage near the rupture place and the presence of areas that have undergone plastic deformation (Figure 5, a, curve 1). The relative elongation after rupture was 19.1%, the cross-sectional area was 8.79%, the relative narrowing was 70.71%. Holes of various sizes can be traced on the surface of the fracture, there are separate flat areas of brittle fracture, Figure 6, a.

Under the influence of a corrosive environment and cathodic polarization, the character of the fracture diagram changes: the maximum stress at rupture of the specimens and the relative elongation change compared to the same parameters in air (Figure 5, a, curves 2-4). On the destruction curves in the solution NS4 under cathodic polarization, a decrease in the length of the descending curve sections was noted, which indicates on a change in the nature of the destruction in a corrosive environment and polarization. Exfoliations was found on the fracture surfaces of all specimens, which may be due to the applied steel manufacturing technology (in particular, controlled rolling).

The breakdown at a polarization potential of -0.75 V (Figure 4, a, AD region) is viscous, the rupture line is quite smooth. The relative elongation decreased to 17.1%, the relative contraction increased to 13.09% (Table 2). The coefficient of susceptibility to corrosion cracking K_S = 1.25 (Figure 7). The nature of the destruction, as in air, is viscous, but according to a visual assessment, it was established that the share of brittle areas is no more than 10%, Figure 6.

At a potential of -0.95 V, which is in the area of the mixed mechanism SCC (Figure 4, a, region AD+HE), there is a tendency to decrease the proportion of viscous failure compared to air, as indicated by the appearance of step-like areas on the rupture line, a decrease in relative elongation to 15.71%, an increase in relative narrowing to 52.57%, and a corresponding increase in the K_S coefficient to 1.35 (Figure 7). On the surface of the fracture near one of the edges of the rupture, a long area with a flat nature of the fracture surface was found, which corresponds to (30-40)% of the area (Figure 6, c).

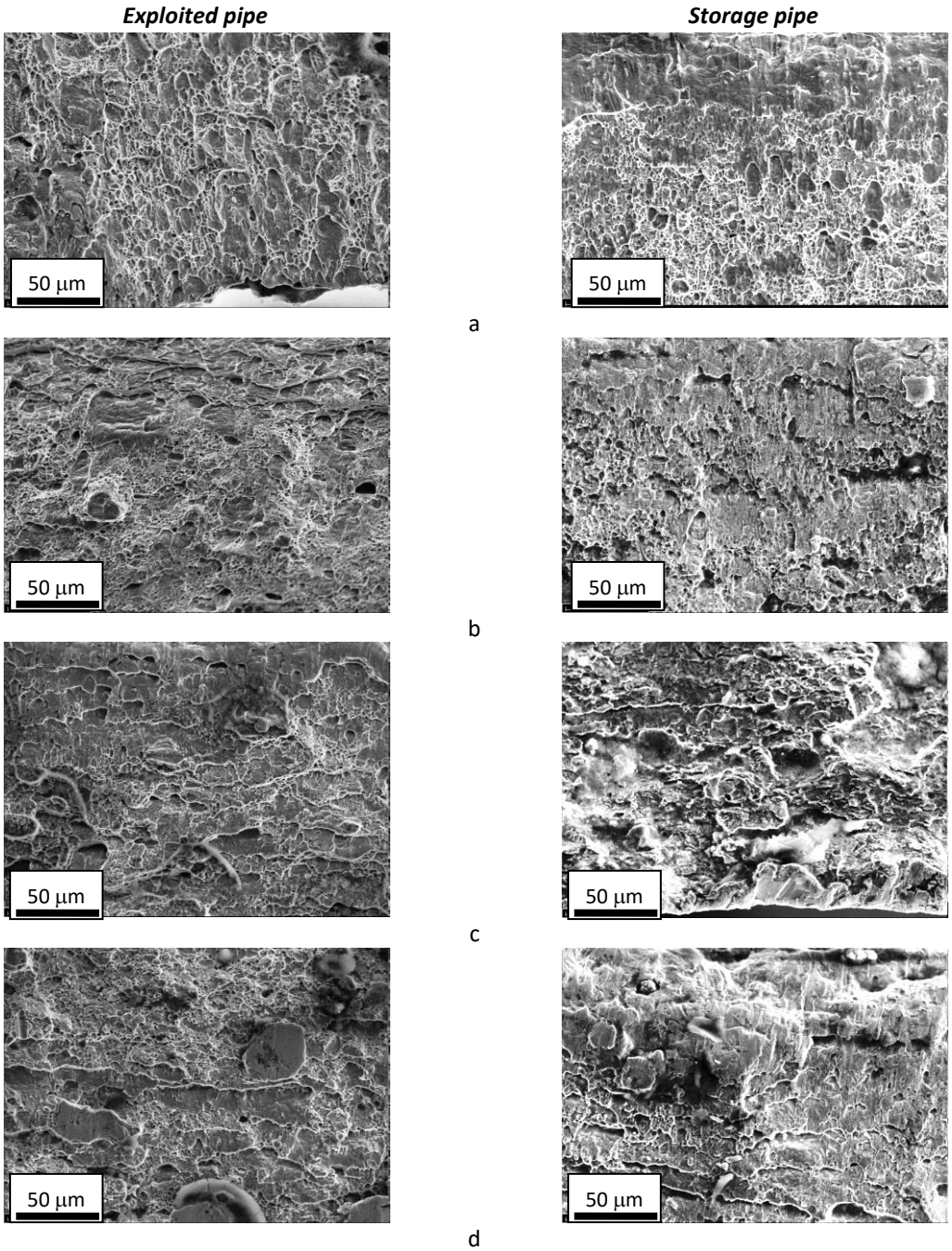

***Figure 6**. SEM views of the morphology of fracture surface after breaking the steel specimens, cutting from the exploited pipe and storage pipe at different potentials: a – in air, b – -0.750 V, c – -0.95 V and d – -1.05 V*

On specimens tested at a potential of -1.05 V (Figure 4, a, area HE), the external signs of destruction are similar to those characteristic of a specimen broken at a potential of -0.95 V: the relative elongation and relative narrowing decreased to 14.8% and 46.12%, respectively, the K_S increased to 1.53 (Figure 7). For this specimen, facets (elements of the fracture surface with clear boundaries lying in the same or close planes) of chipping were found on the fracture surface, the part of the brittle fracture surface is approximately 20-30% (Figure 6, d).

The rupture of the reserve pipe specimens in the air, as well as for the exploited pipe specimens, occurred viscously and was accompanied by plastic deformation near the rupture line (Figure 5, b). The relative elongation of the specimen was 21.5%, the relative narrowing was 57.12%. On the surface of the fracture there are holes of various sizes, on part of the surface there are flat areas of chips, the share of the brittle component is 40% (Figure 6). For this pipe, all the breaking curves under cathodic

polarization have a lower load; the relative elongation also differs from this indicator in air (Figure 5, b, curves 2-4).

At a polarization potential of -0.75 V from the area of anodic dissolution mechanism of SCC (Figure 4, b, AD area), plastic deformation is observed upon specimens' failure. The relative elongation and relative narrowing were 22.3% and 56.02%, respectively. The coefficient of susceptibility to stress-corrosion cracking K_S was equal to 1.02 (Figure 7). On the fracture surface, there was a large proportion of flat areas, which, according to visual assessment, is approximately 80% (Figure 6, b).

At a potential of -0.95 V, the upper limit of the potential from the region of the mixed mechanism of stress-corrosion cracking (Figure 4, b, area AD+HE), during destruction of the specimen to failure, retraction near the edge of the crack and steps on the crack line were observed. The relative elongation and narrowing decreased, respectively, to 20.2% and 43.28%, the K_S coefficient was 1.32 (Figure 7). The delaminations' part on the fracture surface also increased compared to air and a potential of -0.75 V, the flat areas of destruction are located between areas of dimlped fracture, their part does not exceed 40% of the surface area (Figure 6, c).

At a polarization potential of -1.05 V, at which stress-corrosion cracking occurs by the hydrogen embrittlement mechanism (Figure 4, b, area HE), the nature of the fracture remains viscous-brittle, with minimal plastic deformation and brittle rupture of part of the specimen. The relative elongation is 22.7%, the relative narrowing is 43.28%. The K_S coefficient was 1.32 (Figure 7). At this polarization potential, the share of areas of brittle failure is approximately 50% (Figure 6, b).

3.5. Electrolytic hydrogenation

In order to understand the action of stress-corrosion cracking mechanisms, the susceptibility to electrolytic hydrogenation of X70 steel was investigated and evaluated on specimens of the operated pipe in NS4 at cathodic polarization potentials from -0.75 to -1.05 V using the Defanathan-Stahursky method. The passivation potential on the anodic side of the steel specimen was set 0.2 V.

At a polarization potential of -0.75 V, hydrogen penetration was not observed. At a potential of -0.95 V, the increase in current under the background value was 2.51×10^{-6} A, which corresponded to a hydrogen concentration of 0.0191 mol/m³. At a potential of -1.05 V (Figure 7, curve 3), the hydrogenation current was 3.17×10^{-6} A, which corresponded to a hydrogen concentration of 0.0241 mol/m³. The delay time for the release of hydrogen at a polarisation potential of -0.95 V was 25 minutes, for -1.05 V – 6 minutes.

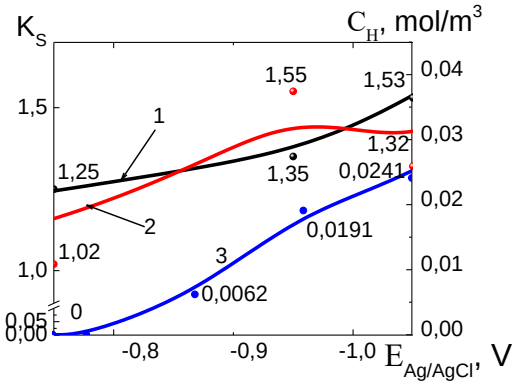

Figure 7. *Susceptibility to stress-corrosion cracking of the metal of the operated pipe (1), stock pipe (2) and the susceptibility of the metal of the operated pipe to electrolytic hydrogenation under cathodic polarization (3)*

According to the results of the carried out investigations, it was established that the concentration of hydrogen that penetrates through the steel increases with shifting of the potential to negatively values (Figure 7, curve 3).

Summarizing the obtained results, it can be emphasized that in the potentials' range from -0.75 to -1.05 V, and the concentration of hydrogen that penetrates into steel, increases by 1.3 times, and the

highest concentration of hydrogen that can penetrate into X70 steel is reached at a potential of -1.05 V (Figure 7).

It should be noted that long-term operation affected the susceptibility of X70 steel to stress corrosion cracking. In the range of potentials from -0.75 V to -1.05 V in the NS4 model soil electrolyte NS4, the coefficient of susceptibility to stress-corrosion cracking K_S for the operated pipe increases from 1.25 to 1.53 (Figure 7, curve 1), for the reserve pipe at potentials -0.75 V $\rightarrow$ -0.95 V $\rightarrow$ -1.05 V it changes non-monotonically such as – 1.02 $\rightarrow$ 1.55 $\rightarrow$ 1.32 (Figure 7, curve 2).

The tendency to increase susceptibility to stress-corrosion cracking when the potential is shifted from -0.75 V to -1.05 V for the operated pipe may indicate on the embrittlement of steel during long-term exposure to external cathodic polarization.

4. Conclusions

1. The studied pipes (operated for 40 years and the reserve pipe after storage for the same period) are made of low-carbon steel with alloying element additives, and the metal of the pipes meets the requirements of the technical conditions of TU 14-3-995 in terms of the content of the main elements.
2. The microstructure of the base metal of the investigated pipes is ferrite-pearlitic. The pipes' metal differ in ferrite grain size (10-20 μm and 14-20 μm), pearlite content (10 and 20%), and banding (2 and 4 points), respectively. But all these differences are within the limits allowed by regulatory documents.
3. In the range of cathodic polarization potentials from -0.75 V to -1.05 V (relative to silver chloride reference electrode) in the NS4 model soil electrolyte, the coefficient of susceptibility to stress-corrosion cracking K_S for the operated pipe metal, increases from 1.02 to 1.53, for the storage pipe at potentials -0.75 V $\rightarrow$ -0.95 V$\rightarrow$ -1.05 V K_S changes non-monotonically – 1.02 $\rightarrow$ 1.55 $\rightarrow$ 1.32. The tendency to increase of susceptibility to stress-corrosion cracking when the potential is shifted from -0.75 V to -1.05 V for the operated pipe may indicate on embrittlement of steel under longe-term exploitation at external cathodic polarization.
4. Based on the results of electrolytic hydrogenation of exploited steel in NS4 model soil electrolyte, it was established that with a shift in the cathodic polarization potential from -0.75 V to -1.05 V, the concentration of hydrogen penetrating into the steel increases from 0 to 0.0241 mol/m³. This correlates with an increased susceptibility to brittle failure under such conditions.

Acknowledgments

This work was performed with financial support of E.O. Paton Electric Welding Institute of National Academy of Sciences of Ukraine (State registration number 0118U100537).

References

[1] Laureys, A., Depraetere, R., Cauwels, M., Depover, T., Hertelé, S., & Verbeken, K., 2022. Use of existing steel pipeline infrastructure for gaseous hydrogen storage and transport: A review of factors affecting hydrogen induced degradation. Journal of Natural Gas Science and Engineering. 104534.

[2] Shirband, Z., Shishesaz, M. R., & Ashrafi, A., 2011. Hydrogen degradation of steels and its related parameters, a review. Phase Transit. 84, 924-943.

[3] Rybakov, A.A., Goncharenko, L.V., Filipchuk, T.N., Lokhman, I.V. and Burak, I.Z., 2014. Reasons of stress corrosion failure of erection girth joint of main gas pipeline. The Paton Welding Journal. 3, 49-52.

[4] Polyakov, S.G., Rybakov, A.A., 2009. The main mechanisms of stress corrosion cracking in natural gas trunk lines. *Strength Mater.* 41, 456–463.

[5] Ohaeri, E., Eduok, U., & Szpunar, J., 2018. Hydrogen related degradation in pipeline steel: A review. Int. J. Hydrog. Energy, 43, 14584-14617.

[6] Yu, H., Olsen, J. S., Alvaro, A., Olden, V., He, J., & Zhang, Z., 2016. A uniform hydrogen degradation law for high strength steels. Eng Fract Mech . 157, 56-71.

[7] Ohaeri, E. G., Qin, W., & Szpunar, J. (2021). A critical perspective on pipeline processing and failure risks in hydrogen service conditions. J. Alloys Compd. 857, 158240.
[8] Kryzhanivs’ kyi, E.I., Nykyforchyn, H.M. 2011. Specific features of hydrogen-induced corrosion degradation of steels of gas and oil pipelines and oil storage reservoirs. Mater. Sci. 47, 127-136.
[9] Paton, B. E., Semenov, S. E., Rybakov, A. A., Vasilenko, S. K., & Vasilyuk, V. M., 2000. Ageing and procedure of evaluation of the state of metal of the main pipelines in service. The Paton welding journal. 7, 2-20.
[10] Semenov, S. E., Rybakov, A. A., Kirian, V. I., Filipchuk, T. N., Goncharenko, L. V., Vasilyuk, V. M., & Vlasyuk, F. S., 2001. Experimental evaluation of the state of metal of long-serviced welded oil pipelines. The Paton welding journal. 5, 17-21.
[11] Semyonov, S. E., Rybakov, A. A., Goncharenko, L. V., Filipchuk, T. N., Drogomiretsky, M. N., & Pedko, B. I. (2003). Evaluation of condition of metal of welded pipes of long-operated gas pipelines. PATON WELDING JOURNAL. 2003(4), 2-6.
[12] Nyrkova L.I., Rybakov A. O., Goncharenko L.V., Osadchuk , Kharchenko Yu. O., 2023. Analysis of the causes of fracture of the main gas pipeline. ZASTITA MATERIJALA. 2, 177-186.
[13] Rahman, K. M. M., Qin, W., Szpunar, J. A., Kozinski, J., Song, M., & Zhu, N. (2021). New insight into the role of inclusions in hydrogen-induced degradation of fracture toughness: three-dimensional imaging and modeling. Philosophical Magazine, 101(8), 976-996.
[14] Peng, Z., Cao, C., Huang, F., Wang, L., Xue, Z., & Liu, J., 2023. Effect of slow strain rates on the hydrogen migration and different crack propagation modes in pipeline steel. Steel Res. Int.. 2300070.
[15] Zvirko, O.I., 2021, In-Service Degradation of Structural Steels. A Survey. Mater. Sci. 57, 319–330.
[16] Krechkovs’ka, H.V., Tsyrul’nyk, O.T. & Student, O.Z. In-Service Degradation of Mechanical Characteristics of Pipe Steels in Gas Mains, 2019. Strength Mater. 51, 406–417.
[17] Maruschak, P.O., Danyliuk, I.M., Bishchak, R.T. et al. Low temperature impact toughness of the main gas pipeline steel after long-term degradation. cent.eur.j.eng 4, 408–415 (2014). https://doi.org/10.2478/s13531-013-0178-6
[18] Maruschak, P. O., Danyliuk, I. M., Bishchak, R. T., & Vuherer, T., 2014. Low temperature impact toughness of the main gas pipeline steel after long-term degradation. Cent. Eur. J. Eng., 4, 408-415
[19] R. Antunes de Sena, I. Napoleão Bastos, G. Mendes Platt, 2012. Theoretical and Experimental Aspects of the Corrosivity of Simulated Soil Solutions, International Scholarly Research Notices. Article ID 103715, 6 pages.
[20] National standard of Ukraine 8972:2019. Steel and alloys. Methods for detection and determination of grain size
[21] Technical Specification 14-3-995-81. Expanded electric-welded longitudinally welded steel pipes with a diameter of 1420 mm from X70 grade steel
[22] Liu Z.Y., Li X.G., Cheng Y.F., 2012. Mechanistic aspect of near-neutral pH stress corrosion cracking of pipelines under cathodic polarization. Corros. Sci. 55, 54-60.
[23] Nyrkova L., 2020. Stress-corrosion cracking of pipe steel under complex influence of factors. Engineering Failure Analysis. 116, 104757.
[24] Nyrkova L. I., Osadchuk S. O., Rybakov A. O., Mel’nychuk S. L., 2020. Methodical approach and a criterion for the evaluation of the susceptibility of pipe steel to corrosion cracking. Mater. Sci. 55, 625–632.

Hybrid hydrogel as a delivery vehicle for bioactive ions to enhance bone regeneration

***Beatriz Oliveira*[1], *João Neves*[2], *Cândida Malça*[3,4], *Sofia Campos*[4], *Joel Sá*[4], *Marta Henriques*[5,6], *Ana Baptista*[1] *and Carla Moura*[3,7]**

1) CENIMAT|i3N, Department of Materials Science, School of Science and Technology, NOVA University Lisbon, Campus da Caparica, 2829-516 Caparica, Portugal

2) Polytechnic Institute of Leiria, School of Tourism and Maritime Technology, Campus 4, Rua do Conhecimento, n.º 4, 2520–614 Peniche, Portugal

3) Centre for Rapid and Sustainable Product Development (CDRSP), Polytechnic of Leiria, Portugal

4) Polytechnic Institute of Coimbra, Coimbra Institute of Engineering, Rua Pedro Nunes – Quinta da Nora, 3030-199 Coimbra, Portugal

5) Polytechnic Institute of Coimbra, Coimbra Agriculture School, Bencanta, 3045-601 Coimbra, Portugal

6) Research Centre for Natural Resources Environment and Society (CERNAS), Polytechnic Institute of Coimbra, Bencanta, 3045-601 Coimbra, Portugal

7) Polytechnic Institute of Coimbra, Applied Research Institute, Rua da Misericórdia, Lagar dos Cortiços – S. Martinho do Bispo, 3045-093 Coimbra, Portugal

Corresponding author: carla.moura@ipc.pt

Original scientific article

Abstract: Bone has a natural capacity to regenerate when slightly damaged. However, when injured at larger scale, it requires external intervention, such bone grafts, which introduces challenges, limiting their use in clinical applications. Therefore, polymeric scaffolds, namely hydrogels, appear as an interesting alternative to bone replacements. They are characterised by high water uptake and have excellent biomimetic properties. Magnesium (Mg) is a biodegradable mineral, mainly stored in bones, and possesses strong mechanical qualities closely resembling natural bone. Thus, the main objective of this work was the production of a hydrogel combining synthetic polymers to act as bone substitutes. For this purpose, polyethyleneglycol diacrylate (PEGDA) was used as the base hydrogel, in which Mg sulphate (bioactive ion) was incorporated. Mg addition led to an increase of about 19% of the compressive Young modulus, enhancing their mechanical strength and resistance to compression. Both groups, with and without Mg, presented very similar behaviours when submitted to a hydrated environment, not suffering considerable degradation during the month of the experiment.

Keywords: *Bone Regeneration; Hydrogel; Magnesium Sulphate; Tissue Engineering*

1. Introduction

A booming field that has played a significant role in providing advanced alternatives to organs and tissues transplantation and regeneration is Tissue Engineering (TE).

The human body comprises 206 bones, an important organ that provides support, stability, protection of other organs and facilitates movements. It has a natural capacity to regenerate when slightly damaged, but when injured at a larger scale, it requires external intervention, such as autografts and allografts. These approaches for bone replacements are commonly used but present some drawbacks,

such as size limitation, immune reactions, the supplies are limited, and there is risk of transmitting infectious diseases [1]. With this, their use in clinical applications is limited.

Thus, biomaterials, through TE and regenerative medicine approaches, are a good and innovative alternative to bone replacements. Hydrogels appear as a three-dimensional (3D) environment provider, great for cell growth, proliferation, adhesion, migration, and differentiation [2]. Besides, they have excellent biomimetic properties, similar to the native extracellular matrix (ECM) environment and are characterised by high water uptake. They are usually used as carriers of bioactive ions, molecules, cells, and drugs [2], [3].

Magnesium (Mg) is an abundant mineral in the human body, mainly stored in bone. With this, it appears as a promising biomaterial for bone regeneration. Besides being biodegradable, avoiding extra open surgery for implant removal, it possesses strong mechanical properties and qualities closely resembling natural bone [2]. Furthermore, the production of Mg^{2+} during Mg degradation stimulates bone formation, regulates cell behaviour [4] and improves osteoblasts attachment [5]. Despite these advantages, high and low levels of Mg can negatively affect bones. A lack of Mg can alter all stages of skeletal metabolism and retard bone growth, while Mg^{2+} in high quantities can inhibit ECM formation [6], [7]. Moderate levels benefit the process of healing, promoting angiogenesis. Several works in the literature support these benefits.

Yin et al. created an ionic crosslinked Mg^{2+}-alginate hydrogel [5]. Results demonstrated the improvement of the osteoblasts attachment with the addition of Mg and, surprisingly, with the increase of Mg^{2+} content, there was a similar decrease in Na^{+}, suggesting an exchange of ions within the gel. Moreover, the swelling ratio of the hydrogels decreased with the addition of Mg, suggesting alterations in the microstructure of the hydrogels, which positively influenced protein adsorption and cell addition [5].

Tang et al. concluded that Mg^{2+} ions generated during Mg degradation induced osteogenic differentiation of stem cells and bone regeneration. Also, the elastic modulus decreased upon nanoparticles increase as consequence of the higher porosity in the hydrogels. Moreover, no cytotoxicity levels were shown.

Even though it is beneficial, Mg, when used alone, presents some limitations for biomedical applications. Fast corrosion rate is one of them, rapidly decreasing the mechanical properties of the implants. This drawback can be avoided by combining Mg with other materials or by surface modifications [8].

Hybrid hydrogels were made to act as a delivery vehicle for bioactive ions to enhance bone formation, namely Mg ions. A combination of magnesium sulphate ($MgSO_4$) with polyethylene glycol diacrylate (PEGDA) was used. The degradation rate and mechanical properties to compression were evaluated to understand the behaviour of the hydrogels.

2. Materials and Methods

2.1 Hydrogels preparation

A synthetic polymer base, PEGDA 575 Mn (Sigma-Aldrich®), was used to prepare hydrogels with 2,5% (w/v) magnesium sulphate (99,5% $MgSO_4$, MERCK), as shown in Table 1. To prepare the hydrogels, 0,1% (w/v) IRGACURE 651 photoinitiator (BASF) was mixed with PEGDA and stirred for 10 minutes (340 rpm). Simultaneously, 5% (w/v) $MgSO_4$ was dissolved in distilled water (dH_2O) for 10 min at 340 rpm. Then, both mixtures 1:1 were put together and stirred for 25 minutes (340 rpm). PEGDA hydrogels were used as a control. Finally, they were deposited in cubic moulds and cured with 365 nm ultraviolet (UV) light for 8 minutes.

Table 1. *Hydrogels preparation with a synthetic base-polymer.*

Base-Polymer	***$MgSO_4$ content (w/v)***	***Nomenclature***
Synthetic base Polyethyleneglycol diacrylate, PEGDA	-	PEGDA
	2,5%	PEGDA:Mg

2.2 Degradation performance of hydrogels

Hydrolytic degradation tests were conducted to assess the hydrogels' behaviour (mass loss) in a hydrated environment (simulating the native environment) over time. The test lasted 5 weeks (N = 3). Weighting was performed on day 0 (initial mass). After 24h, a new weighing was performed. Then, they were evaluated twice a week.

2.3 Performance to compression of 3D hydrogels

A Texture Analyser equipment (TA.XT.plusC) was used to test the mechanical performance of the hydrogels to compression to better understand their behaviour when subjected to compressive stresses (N = 5). The extension rate of 1,2 mm/min and a cell load of 50 kg was used. The compressive Young Modulus was calculated as the slope in the linear region, coincident with the elastic zone of the material.

2.4 Statistical Analysis

The results were statistically analysed using GraphPad Prism© software. A confidence level of 95% was set as the level of statistical significance. At least triplicates (N=3) were always used. However, 5 samples (N=5) were used for compression to assure their reproducibility.

3. Results and Discussion

Hydrogels were successfully made combining a synthetic polymer (PEGDA) with the active ion Mg. The produced hydrogels present approximately 22 mm in width and length and 3 mm in height (Figure 1). The presence of Mg is easily observed in the hydrogels. It can be easily seen that the hydrogel with the presence of Mg (Figure 1b) appears with a white colour, confirming the existence of Mg, while the one without it is uncoloured (Figure 1a).

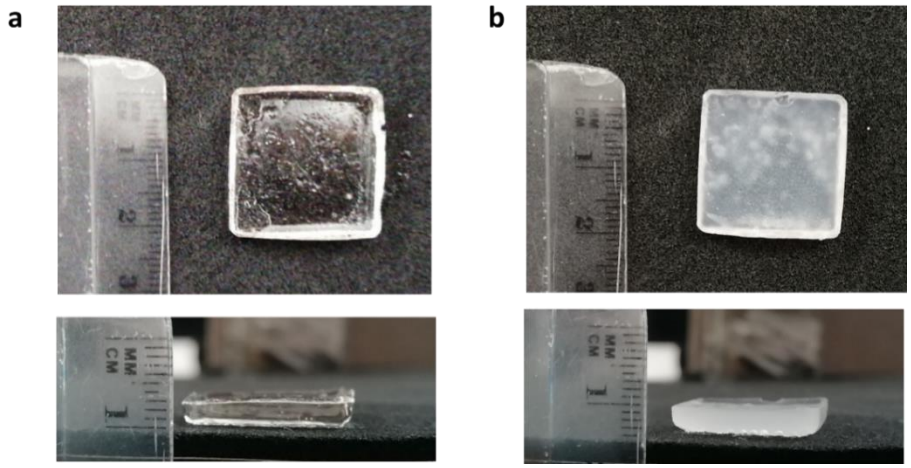

Figure 1. *Relative dimensions of produced PEGDA-based hydrogels (top and front views): (a) PEGDA; and (b) PEGDA:Mg. Scale is in centimetres.*

The degradation of the hydrogels under hydrated conditions was performed to assess their behaviour over time. Results are presented in Figure 2.

Results shows the noticeable increase of weight in the first days in PEGDA hydrogels, being more significant when compared with the increase of weight of PEGDA:Mg hydrogels. This is expectable since the PEGDA present an hydrophilic nature, and Mg is occupying part of the hydrogel limiting its capacity to absorb the medium. A plateau was reached, being the mass decrease very smooth but present. Both groups, with and without Mg, have very similar behaviours when submitted to a hydrated environment. They showed to be stable during the month of the experiment. The degradation characteristics are in accordance with the intended degradation for bone regeneration applications, being required a prolonged release of bioactive ions as a facilitator to promote bone regeneration [9], [10]. By gradually releasing bioactive ions over a prolonged period, the material ensures a continual delivery of the required elements for promoting bone formation, facilitating the healing process, and avoiding toxic levels.

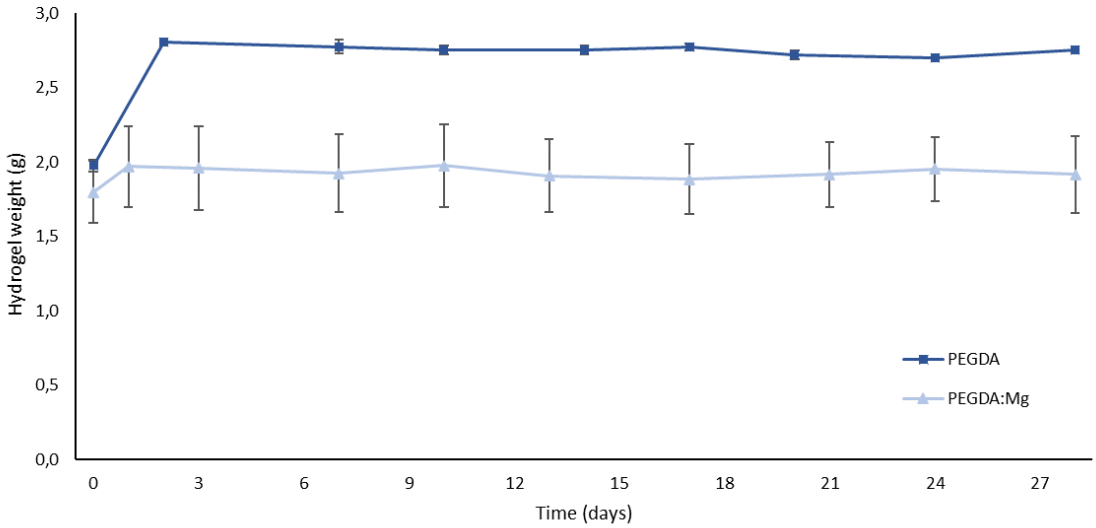

Figure 2. *Hydrolytic degradation results from the PEGDA and PEGDA:Mg hydrogels. Results are presented as the average weight with standard deviation (N = 3).*

Mechanical performance of the hydrogels was evaluated to comprehend the effect of the addition of Mg in the mechanical properties of the hydrogels, namely their behaviour in the presence of compression forces, the ones mainly suffered by the bones.

The results of the compression test are shown in Figure 3a. Mg addition led to an increase of about 19% of the compressive Young modulus of the hydrogels (1,854 ± 0,2033 MPa to 2,282 ± 0,1239 MPa), enhancing their mechanical strength and resistance to compression (Figure 2b) [11], [12]. None of the hydrogels reached their breaking point to the maximum force of the cell load. The ductility of the hydrogels also showed some improvement. A comparison between heights prior to and after the compression showed a greater capacity of elasticity in the samples with Mg incorporation (Figure 3c)).

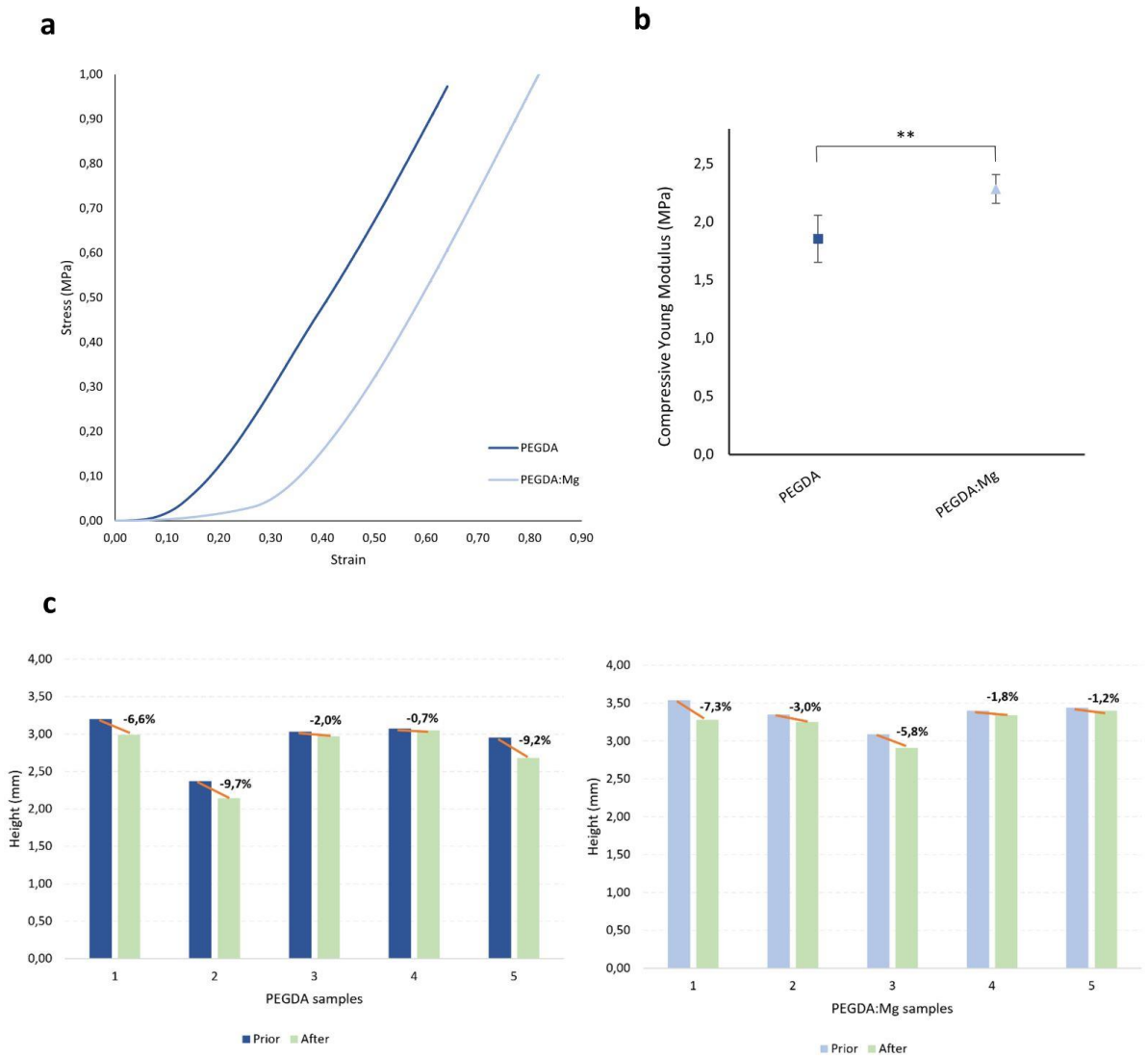

Figure 3. Mechanical performance of PEGDA and PEGDA:Mg hydrogels to compression (N = 5): (a) stress-strain curves; (b) compressive Young Modulus; and (c) difference in height prior and after compression. A t-test was performed, and the statistical differences are presented as: **P < 0.01.

4. Conclusions

In the present work, an effort was done to understand how the addition of magnesium in hydrogels would influence their mechanical properties, as well as their degradation behaviour under hydrolytic environment, being Mg a bioactive tool to be released over time to enhance bone regeneration.

With this study, PEGDA based hydrogels were successfully created, with the incorporation of biologically active ions of Mg. Their degradation in hydrolytic surroundings is executed in slow rate compared to other hydrogels, which is good for the slowly liberation of Mg ions for cells proliferation and enhancement and avoid toxic levels. Furthermore, considering the mechanical properties of the hydrogels, the addition of Mg improved the mechanical characteristics, increasing their resistance and elasticity to compression, presenting a higher compressive Young Modulus.

Future works will involve a comparison between synthetic- and natural-based hydrogels behaviour, with the incorporation of Mg. Moreover, cellular experiments would be interesting, to evaluate the behaviour of cells in terms of proliferation, growth, and bone formation.

Acknowledgments

This work was supported by the Fundação para a Ciência e a Tecnologia (FCT) and Centro2020 through the following Projects: UIDB/04044/2020, UIDP/04044/2020, PAMI - ROTEIRO/0328/2013 (Nº 022158), and LA/P/0037/2020.

C. S. Moura thanks the National funding by FCT- Foundation for Science and Technology, P.I., through the institutional scientific employment program-contract (CEECINST/00077/2021).

References

[1] S. Zhao *et al.*, "Fabrication and Biological Activity of 3D-Printed Polycaprolactone/Magnesium Porous Scaffolds for Critical Size Bone Defect Repair," *ACS Biomater Sci Eng*, vol. 6, no. 9, pp. 5120–5131, Sep. 2020, doi: 10.1021/acsbiomaterials.9b01911.

[2] Y. Tang *et al.*, "In situ gas foaming based on magnesium particle degradation: A novel approach to fabricate injectable macroporous hydrogels," *Biomaterials*, vol. 232, Feb. 2020, doi: 10.1016/j.biomaterials.2019.119727.

[3] Z. Yao *et al.*, "Magnesium-Encapsulated Injectable Hydrogel and 3D-Engineered Polycaprolactone Conduit Facilitate Peripheral Nerve Regeneration," *Advanced Science*, vol. 9, no. 21, Jul. 2022, doi: 10.1002/advs.202202102.

[4] K. Zhang *et al.*, "Nanocomposite hydrogels stabilized by self-assembled multivalent bisphosphonate-magnesium nanoparticles mediate sustained release of magnesium ion and promote in-situ bone regeneration," *Acta Biomater*, vol. 64, pp. 389–400, Dec. 2017, doi: 10.1016/j.actbio.2017.09.039.

[5] M. Yin, F. Xu, H. Ding, F. Tan, F. Song, and J. Wang, "Incorporation of magnesium ions into photo-crosslinked alginate hydrogel enhanced cell adhesion ability," *J Tissue Eng Regen Med*, vol. 9, no. 9, pp. 1088–1092, Sep. 2015, doi: 10.1002/term.2011.

[6] B. Chen *et al.*, "Enhancement of critical-sized bone defect regeneration by magnesium oxide-reinforced 3D scaffold with improved osteogenic and angiogenic properties," *J Mater Sci Technol*, vol. 135, pp. 186–198, Feb. 2023, doi: 10.1016/j.jmst.2022.06.036.

[7] H. S. Roh *et al.*, "Addition of MgO nanoparticles and plasma surface treatment of three-dimensional printed polycaprolactone/hydroxyapatite scaffolds for improving bone regeneration," *Materials Science and Engineering C*, vol. 74, pp. 525–535, May 2017, doi: 10.1016/j.msec.2016.12.054.

[8] P. Xiong *et al.*, "A pH-sensitive self-healing coating for biodegradable magnesium implants," *Acta Biomater*, vol. 98, pp. 160–173, Oct. 2019, doi: 10.1016/j.actbio.2019.04.045.

[9] M. S. Ghiasi, J. Chen, A. Vaziri, E. K. Rodriguez, and A. Nazarian, "Bone fracture healing in mechanobiological modeling: A review of principles and methods," *Bone Reports*, vol. 6. Elsevier Inc, pp. 87–100, Jun. 01, 2017. doi: 10.1016/j.bonr.2017.03.002.

[10] R. Rothe, S. Schulze, C. Neuber, S. Hauser, S. Rammelt, and J. Pietzsch, "Adjuvant drug-assisted bone healing: Part I-Modulation of inflammation," *Clin Hemorheol Microcirc*, vol. 73, no. 3, pp. 381–408, 2020, doi: 10.3233/CH-199102.

[11] E. F. Morgan, G. U. Unnikrisnan, and A. I. Hussein, "Annual Review of Biomedical Engineering Bone Mechanical Properties in Healthy and Diseased States," 2018, doi: 10.1146/annurev-bioeng-062117.

[12] L. C. Gerhardt and A. R. Boccaccini, "Bioactive glass and glass-ceramic scaffolds for bone tissue engineering," *Materials*, vol. 3, no. 7, pp. 3867–3910, 2010, doi: 10.3390/ma3073867.

Experimental determination of grinding parameters with a ball mill with trapezoidal lifters

***Miglena Paneva*[1], *Peter Panev*[1] *and Kristina Pavlova*[1]**

1) Institute of Information and Communication Technologies – Bulgarian Academy of Sciences, bl. 2, ac. G. Bonchev str, 1113 Sofia, Bulgaria

Corresponding author: m.paneva7@gmail.com

Original scientific article

Abstract: In the developed work, experiments were made with a laboratory ball mill containing a liner with eight symmetrically displaced trapezoidal lifters, one with a right angle and an angle of 22.5°. The number of the lifters with a trapezoidal shape, as well as their size were determined based on a study performed within a previous exepriment. All elements of the ball mill and the grinding bodies were printed on a 3D printer. The additive material used for grinding media is PLA whereas for grinding bodies PLA, CarbonFil™ and SteelFill were used. The parameters determined in the course of experiments were the critical speed (CS) of the mill, the angle of separation (shoulder angle) and the toe angle in the cataract mode of operation for each of the materials. Experiments were carried out with different mill filling percentages - 20% and 30%.

Keywords: *ball mill; trapezoidal lifter; 3D materials; critical speed; angle*

1. Introduction

Milling is the last stage of the comminution process in which particles (ore) are reduced to an optimum size range due to a combination of impact and abrasion. The impact mechanism occurs when the particle is smashed between a ball and the mill shell and/or between the balls. Particle breakage is due to compression resulting in fracture [1]. The size of theparticles are of a wide range resulting in the fragmentation of the initial particle for milling. Due to technological advances in 3D modeling and printing, experiments of a milling process are possible to be performed in a controlled experimental environment. With the help of a laboratory mill made of 3D materials the grinding processes will be analyzed. The significant factors affecting the productivity are the speed (% of critical), charge of the ball mill, mill shoulder, toe angle, coefficients of friction, rolling friction, and restitution [2]. Experiments with different sizes, shapes, materials of grinding bodies, and grinding environments, including testing of the yield point of different materials with acoustic emission methods, can be performed as they are important key parameters also for the output product [3], [4], [5] and [6]. The liner of the inside of the mill protects the grinding bodies and the drum from rapid wear [7].

The research is based on the interrelationship between the trapezoidal lifters and the grinding bodies with different charges. The present work focuses on the charge, type of liners with lifters, and flow behavior of the suspension, analyzing and interpreting the relationship between the mill load and the angle of separation and toe angle. The charging of the mill is done by hand, by counting the necessary number of spheres, and is compared and verified to a specialized gripper-dispenser for dosing laboratory mill with grinding bodies [8].

In the investigation of the parameters of the mill with 8 trapezoidal lifters with one right angle and an angle of 22.5°, the critical speed, the separation angle, and the toe angle of the mill at different percentages of filling will be experimentally determined. After determining the filling perentage and ball mill critical speed of rotation, the cataract regime will be calculated [9].

2. Apparatus and materials

The laboratory ball mill with which the experiments were carried out is with an outer diameter of the chamber of 0,269 m, an inner diameter of 0,228 m, and a length of the mill - 0,013 m (used for one row of spheres). It is equipped with 2 transparent plexiglass covers allowing for investigation of the interaction of the grinding ball, 1.1 kW motor with controllable speed and intelligent control. The used mill is constructed with options for easy change of a grinding media (lifters) and inserting/emptying different filling of grinding bodies (spheres with 9 mm from different materials). There are 8 trapezoidal lifters with one right angle and an angle of 22.5°, spaced circumferentially around the mill shell. The dimensions can be seen in Table 1.

Table 1. *Dimensions of an trapezoidal lifter*

Parameters, Init	**Values**
Width of the top, m	0.0176
Width of the bottom, m	0.0214
Height, m	0.0091
Angle,°	22.5
Volume, m^3	1,85. 10^{-6}

The PLA filament is used for the printing of the drum and the liners with lifters. This material is based on polylactide, which belongs to aliphatic polymers and shows complete biodegradability and a reliable 3D printing process. The basic properties are estimated as good mechanical properties - high stiffness and tensile strength. The grinding bodies are 3D printed from three types of materials - PLA, SteelFill, and CarbonFil™ according to the producer's recommendations and according to performed experiments with 100% infill [10] and [11].

The direction of rotation of the ball mill is clockwise. The speed of the ball mill will be determined with an electronical tachometer.

According to the volume of the trapezoidal lifters, the volume of the free inner space of a ball mill is V- 5,052.10^{-4} m^3.

The moments of critical speed, separation, and incidence are recorded with a high-speed camera NAC MEMRECAM HX-6. The videos are analyzed with Vicasso software. The camera allows shooting with different resolutions and frames per second (fps) up to 360 000 [12].

Experiments are performed without the presence of grinding material. The critical speed, separation angle and toe angle at 20% and 30% filling of the laboratory ball mill were determined experimentally. Each mill charge is determined experimentally, specifying the number and mass of spheres required, Table 2. The coefficients of sliding friction, rolling, and restitution for the pair PLA-PLA, PLA-SteelFill, and PLA-Carbon can be seen in [13], [14], [15] and [16].

Table 2. *Characteristics of a filling in a ball mill*

Material	**Number of spheres**	**Weight, g**	**Volume, cm^3**	**Density, g/cm^3**
PLA	1	0.4065	0,382	1,0641
CarbonFil™		0.4131		1,0814
SteelFill		1.0826		2,8340
PLA	137- 20% filling	55.6905	52,33	
CarbonFil™		58,6602		
SteelFill		148,3162		
PLA	195- 30% filling	79.2675	74,49	
CarbonFil™		86,751		
SteelFill		211,107		

3. Experimental Results and Discussion

The first experiment made with a laboratory ball mill is performed with 20 % filling of a sphere with three types of materials - PLA, SteelFill, and CarbonFil™. The critical speed of the mill is determined and it is reached when all the spheres fit evenly around the circumference. The measured rates are presented in Table 3, determined with the help of a tachometer and a high-speed camera. The voids between the spheres are taken into account as part of the percentage of filling of the mill [17].
The next examined mode of operation is the cataract mode, using the three abovementioned materials. This mode is determined by using the data from the video, recorded with the high-speed camera with a resolution of 1000 frames per second (fps). The principle of determination of the separation angle and toe angle is described in previous work [18]. The determination of the angles is performed with Vicasso 2009 software [19]. In Figure1 the detected speed of the ball mill is presented using the different materials.

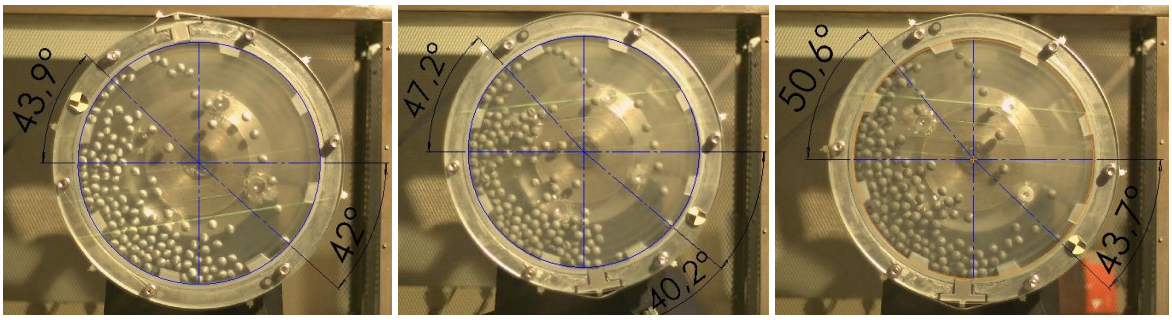

a) b) c)

Figure 1. *Shoulder angle and toe angle at 20% filling of the ball mill: a) PLA, b) SteelFill, c) CarbonFil™*

The same procedure of measurements of the parameters is performed at 30% filling of the ball mill. The determined critical speed and % of Vcr is measured with an electrical tachometer. The determined shoulder angle and toe angle are presented in Figure 2 for the three materials. The results of all experiments are presented in Table 3.

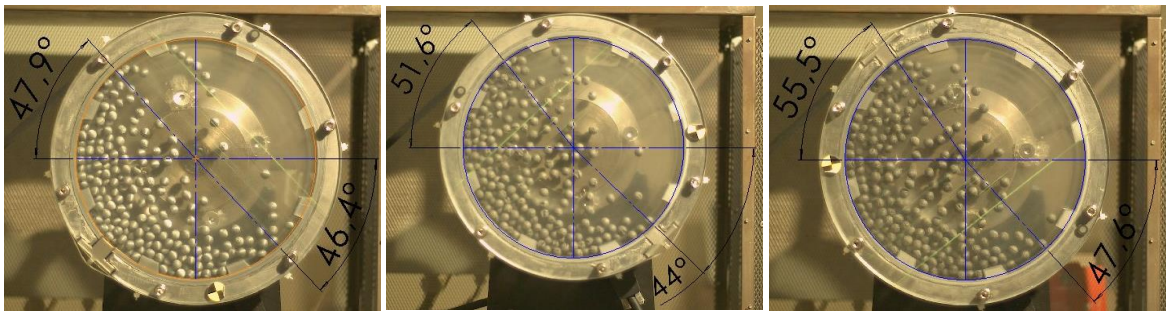

a) b) c)

Figure 2. *Shoulder angle at 30% filling: a) PLA, b) SteelFill, c) CarbonFil™*

The basis of measured values is calculated as a percentage of the critical speed at 20% and 30% filling of the mill at cataract mode of operation, as it is shown in Table 3.
At 20% filling of the ball mill, the lowest critical speed is at the interaction of the liner with lifters made of PLA material and grinding bodies made of CarbonFil™, which is 124.1 rpm. This PLA-Carbon couple has the biggest coefficient of rolling friction- 0,186, compared to the other cominations of materials. The shoulder angle is with a middle value of 47,2 whereas the toe angle is the smallest - 40,2. The mill speed varies between 41-44 % of Cs., with the largest separation angle and toe angle occurring with the SteelFill material, which has the greatest mass and density.
At 30% filling, the material with the lowest critical speed is again CarbonFil™, as well as SteelFill, but with CarbonFil™, the speed in cataract mode is the lowest, namely (% Vcr) - 38.5 %. The biggest shoulder angle and toe angle are achieved at the SteelFill material, which also has the greatest mass

and density. At 30% filling, the critical speed increases by 6 rpm, but the speed required to operate in cataract mode is 2 rpm lower compared to 20% filling.

Table 3. *Experimental Results*

% of Filling	Material	Critical speed, [rpm]	Shoulder angle,[˚]	Toe angle,[˚]	Ball mill speed, [rpm]	% of Critical speed
20% filling	PLA	134,7	43,9	42	55,2	41
	CarbonFil™	124,1	47,2	40,2	54,1	43,6
	SteelFill	133	50,6	43,7	58,5	44
30% filling	PLA	138,3	47,9	46,4	54,7	39,55
	CarbonFil™	135	51,6	44	52	38,5
	SteelFill	135,1	55,5	47,6	55,5	41,1

4. Conclusion

This study observes a cycle of work of a laboratory ball mill, composed of a drum, a liner with 8 trapezoidal lifters that are 3D printed with a PLA filament. The interaction between the grinding medium and grinding bodies is analyzed. The grinding bodies are 3D printed from three types of materials - PLA, SteelFill and CabronFil™ and the filling of the ball mill is performed at two amounts of charges – at 20 % and 30 %. The critical speeds, shoulder angles, and toe angles at the two levels of filling are experimentally determined using a high-speed camera and Vicasso 2009 software. The critical speed varies for the different percentages of filling, but in cataract mode, the ball mill operates with close values of around 41-44 % of Vcr. After the analysis, when the mill is filled with 20%, the material with the least energy consumption and good work efficiency is CabronFil™. In the case of 30 % filling of the ball mill in combination with the trapezoidal lifters again the carbon filament has the best parameters of energy efficiency and high productivity. When studying the movement and interaction between the grinding bodies, it is extremely important to consider side factors such as the weight of grinding bodies, coefficients of friction, restitution, shape, lifter size, etc.

5. Future steps

In future work, it is planned that the data from all the experiments with different shapes of lifters is compared to that of a mill without lifters. Simulations with software working on the discrete element method will be made with the same parameters, used in this publication aiming to compare the real experiment to the simulation modeling experiment [20].

Acknowledgments

This work was supported by project No КП-06-Н47/5 “Research and optimization of the interaction between grinding bodies and media with an innovative shape”, financed by the Bulgarian National Science Fund.

References

[1] Radial and axial mixing of particles in a dry batch ball mill. Available from: https://www.researchgate.net/publication/265272523_RADIAL_AND_AXIAL_MIXING_OF_PARTICLES_IN_A_DRY_BATCH_BALL_MILL [accessed Jul 11 2023].
[2] Paul W. Cleary, Charge behaviour and power consumption in ball mills: sensitivity to mill operating conditions, liner geometry and charge composition, Int. J. Miner. Process. 63 (2001), pp. 79–114
[3] Stoimenov N., Karastoyanov D., Klochkov L., Study of the Factors Increasing the Quality and Productivity of Drum, Rod and Ball mills, 2nd Int. Conf. on Environment, Chemical Engineering &

Materials, ECEM '18, Malta Sliema, June 22-24, 2018, AIP (American Institute of Physics) Publishing house, Vol. 2022, Issue 1, ISBN: 978-0-7354-1740-3, pp. 020024-1 - 020024-6.
[4] Dudzik K., The Possibility of Applying Acoustic Emission Method to Optimize Determination of Milling Parameters, WSEAS Transactions on Systems and Control, vol. 15, pp. 302-310, 2020.
[5] Stoimenov N., Paneva M. and Gyoshev St., Determination of Ball Mill Separation Angle of Different Materials, 26th International Conference on Circuits, Systems, Communications and Computers (CSCC 2022), Crete Island, Chania, Grece, July 19-22 2022, Published by IEEE, 2022, ISBN:978-1-6654-8186-1, 327-331.
[6] Gwiranai Danha, Identifying opportunities for increasing the milling efficiency of a Bushveld Igneous Complex (BIC), Upper Group (UG) 2 ore, May 2016, ReearchGate, DOI: 10.13140/RG.2.1.1771.6087
[7] Stoimenov N., Innovative Relative wear of lifters, XIV International Scientific Congress “Machines. Technologies. Materials. 2017”, 15-18 March 2017, Borovets, Bulgaria, volume 1, Section “Machines” pp. 25-28, ISSN: 2535-0021 (Print), 2535-003X (Online), Publisher: Scientific Technical Union of Mechanical Engineering Industry – 4.0
[8] Chivarov N., Stoev P., Yovkov S., Stoimenov N., Chivarov S., Specialized Gripper-Dispenser for Dosing Laboratory Mill With Grinding Bodies, IFAC-PapersOnLine, Publisher: IFAC Secretariat, ISSN:2405-8963, pp. 539-542, 20th IFAC Conference on Technology, Culture and International Stability, TECIS 2021, Volume 52, Issue 25, September 14-17 2021,
[9] Paneva M., Panev P. and Stoimenov N., Overview and Analysis of Lifter Types and Ball Mill Operating Parameters, 12th International Scientific Conference, “TechSys 2023” – ENGINEERING, TECHNOLOGIES AND SYSTEMS, Technical University of Sofia, Plovdiv Branch, 18-20 May 2023, AIP Conference Proceedings e-ISSN:1551-7616, (Scopus), Accepted for publication.
[10] 3D filaments, https://www.3djake.bg/filamjenti-za-3d-printjeri?gclid=Cj0KCQjwnrmlBhDHARIsADJ5b_mKH24g8IwVMypyQ6Lm8Y2VCVvM_Weyx-ZMF_IbTz9QcM2l3PnYKjMaAmF4EALw_wcB
[11] Paneva M., Panev P. and Kotseva G., SPHERES MODELLING AND EXTRUSION BY 3D ADDITIVE TECHNOLOGY, XXXI International Scientific and Technical Conference, ADP - 2022., 29.06 ÷ 02.07.2022, Sozopol, Bulgaria., Publishing house of TU-Sofia ISSN – 2682-9584, Publisher Department “Automation of Discrete Production Engineering“ Mechanical Engineering Faculty, Technical University – Sofia, pp. 253-258].
[12] NAC Memrecam HX-6 Data Sheet, https://rius.iict.bas.bg/smart_lab_bg.html#1 (last accessed May 2023)
[13] Stoimenov N., Gyoshev S., Paneva M. Panev P., Determination of the friction coefficient of 3D printed materials - Part I - Rolling friction, 10th International Conference on Mechanical Technologies and Structural Materials (MTSM 2021), Split, Croatia, September 23-24, 2021, Croatian Society for Mechanical Technologies, Croatia, ISSN: 1847-7917, pp. 149-152
[14] Gyoshev S., Stoimenov N., Paneva M., Determination of the friction coefficient of 3D printed materials - Part II - Sliding friction, 10th International Conference on Mechanical Technologies and Structural Materials (MTSM 2021), Split, Croatia, September 23-24, 2021, Croatian Society for Mechanical Technologies, Croatia, ISSN: 1847-7917, pp. 43-46
[15] Stoimenov, N., Gyoshev, S., Restitution Coefficient Determination of 3D Printed Materials, Proceedings of Seventh International Congress on Information and Communication Technology. Lecture Notes in Networks and Systems, vol. 465. Springer, Singapore, pp 663-669, 2022
[16] Stoimenov N., Paneva M., Kotseva G. and Sokolov Bl., Simulation Modelling of Coefficient of Restitution, XIX INTERNATIONAL SCIENTIFIC CONGRESS MACHINES, TECHNOLOGIES, MATERIALS, 09-12.03.2022, BOROVETS, BULGARIA, Proceedings VOLUME II, Scientific Technical Union of Mechanical Engineering Industry – 4.0, ISSN 2535-0021 (PRINT) ISSN 2535-003X (ONLINE), pp. 132-135.
[17] Ivanov, S. N., Dimitrov, G. S., & Nikolov, P. T., Experimental study of the volume of voids in a ball mill with different diameters of grinding bodies and different filling coefficients. Paper presented at

the Proceedings - 26th International Conference on Circuits, Systems, Communications and Computers, CSCC 2022, pp. 332-334. doi:10.1109/CSCC55931.2022.00064
[18] Paneva M., Panev P. and Stoimenov N., Experimental Determination of Grinding Parameters using a Ball Mill with Innovative Lifters, 2023 International Congress on Theoretical and Applied Mechanics, Fluid Mechanics, Heat and Mass Transfer (MECHANICA 2023), Lefkada Island, Greece. August 8-10, 2023, , Accepted for publication.
[19] Vicasso 2009 software - www.pixoft.co.uk (last accessed Julu 2023)
[20] Stoimenov N., Comparative Analysis of Theoretical and Experimental Determination of Ball Mill Critical Speed Simulation, 9th International Conference on Control, Decision and Information Technologies (CoDIT), E ISSN: 2576-3555, Publisher: IEEE, 2023

Application of artificial intelligence fuzzy logic technique in modelling of Industry 4.0 maturity level of production enterprises

***Ivan Peko*[1], *Marina Crnjac Žižić*[2], *Amanda Aljinović Meštrović*[2] *and Nikola Gjeldum*[2]**

1) Faculty of Science, University of Split, Ruđera Boškovića 33, 21000 Split, Croatia

2) Faculty of Electrical Engineering, Mechanical Engineering and Naval Architecture, University of Split, Ruđera Boškovića 32, 21000 Split, Croatia

Corresponding author: ipeko@pmfst.hr

Original scientific article

Abstract: Although Industry 4.0 is already widely known topic in industrial environment many enterprises still strive to acquire technologies and concepts of Industry 4.0 to be more competitive and successful on the global market. In order to find out the optimal path to reach Industry 4.0 advanced solutions enterprises have to validate their current state in the context of their maturity level. In this paper maturity level of production enterprises is defined by three main enterprises segments such as product development, technology and production management. Each of these segments was described by various solutions and their advancement degress that correspond with the enterprise progress towards Industry 4.0. By applying artificial intelligence (AI) fuzzy logic technique influence of advancement degrees of enterprise segments on overall enterprise maturity level towards Industry 4.0 was defined. Developed artificial intelligence model serves as good base for enterprises self-assessment and positioning in order to define their current state and identify appropriate actions to accelerate their transition to Industry 4.0. Defined AI model can be furtherly upgraded with new production enterprises segments. Such defined AI fuzzy logic system will significantly contribute to better management of analysed production enterprise segments as well as their orientation towards Industry 4.0 principles.

Keywords: *Industry 4.0; maturity level; artificial intelligence; fuzzy logic; modelling*

1. Introduction

The growing requirements and needs of the human population for industrial products throughout history have led to the development of production systems through several industrial revolutions. The first industrial revolution, called Industry 1.0, appeared in the eighteenth century with the introduction of steam engines in production [1]. The discrepancy between supply and demand for products was a feature of this phase. Respectively, demand was higher than the production system could produce. In order to satisfy growing demand and increase productivity, during the nineteenth century, steam was replaced by electrical energy, and mass production became a new production paradigm. This technological advancement is known as the 2nd industrial revolution or Industry 2.0. Further technological innovation resulted in switching from analog to digital systems and brought forth 3rd industrial revolution (Industry 3.0) [2]. Since then and now on, continuing investment in digital technologies has resulted in the introduction of the Internet of Things and Services in production systems. That enabled the development of smart environments within the production field, i.e. development of intelligent, self-regulated and interlinked manufacturing processes. This industrial revolution is known as Industry 4.0. Industry 4.0 is based on the concept of smart factories. Smart factories imply the usage of advanced information and communication technology that unites smart products, machines, storage systems and data in the form of cyber-physical production systems [1,3]. To achieve their integration, all subjects are equipped with sensors, software and microprocessors that enable data collection and data analysis. Smart products can be defined as

products that “know” their own history as well as their future actions such as their production time, delivery time, current status and other important information needed to achieve their targeted state [4]. They consist of physical components (electrical and mechanical parts), smart components (sensors, software…) and connectivity components (e.g. networks to product cloud) [5]. Industry 4.0 concept relies on vertical system integration, horizontal system integration and the integration of digital engineering through the whole chain involved in product development. This results in benefits for companies in terms of productivity, profitability, and production flexibility. Therefore, in order to be competitive in the global market, companies must adopt new production paradigm and adapt their production system. However, in order to take the right steps and direct their business towards I4.0 (Industry 4.0), production enterprises must objectively cognize their current state, that is, the level of maturity of those enterprises.

2. The definition of maturity levels

The maturity level in industry plays a crucial role, especially in the context of product development, technology and production management. Mature industries often have established processes, regulations and standards but as it is mentioned in introduction, when changes occur, companies have to adapt quickly. This is where the maturity level can determine how smoothly and rapidly the adaptation process can happen.

Many companies struggle with detection of industry maturity level. Some of them may lack the industry experience and knowledge needed to assess the maturity of important segments accurately. Sometimes they have limited access to industry data and benchmarks. It is challenging to measure maturity levels objectively. At the one side, rapid shifts and market disruptions make it difficult to pinpoint exact maturity level and at the other side, different researches or stakeholders in industry may have varying definitions and criteria for maturity, causing confusion.

The key enablers in practical context of new industrial paradigms are people, organization and technology [6]. This research is more focused on three important segments which arise from key enablers such as: product development (PD), technology (T) and production management (PM). The interconnection of these segments is important, when defining the maturity level.

The responses define the maturity level towards Industry 4.0, Table 1. Industries with maturity level 1 or 2 often have barriers such as lack of experience, problems with data collection and analysis, poor level of digitalization and weak monitoring. Industries with a higher maturity level 3 or 4, might be more resistant to changes but also have a wealth of experience and knowledge on how to establish and navigate cyber physical systems.

There are different ranks used in this research. It is observed how close an individual company is to the characteristics of specific industrial paradigm such as Industry 1.0, Industry 2.0, Industry 3.0 or Industry 4.0, Figure 1.

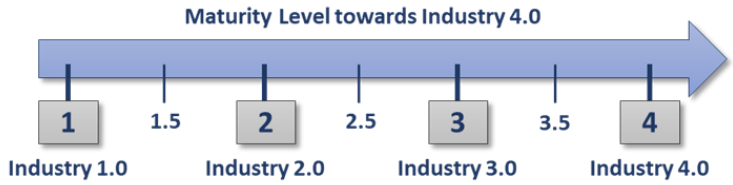

Figure 1. *Ranking of Maturity Level towards Industry 4.0 for main production enterprise segments*

These three analysed segments form a cube, which is useful for easier visualization of enterprise future state, Figure 2.

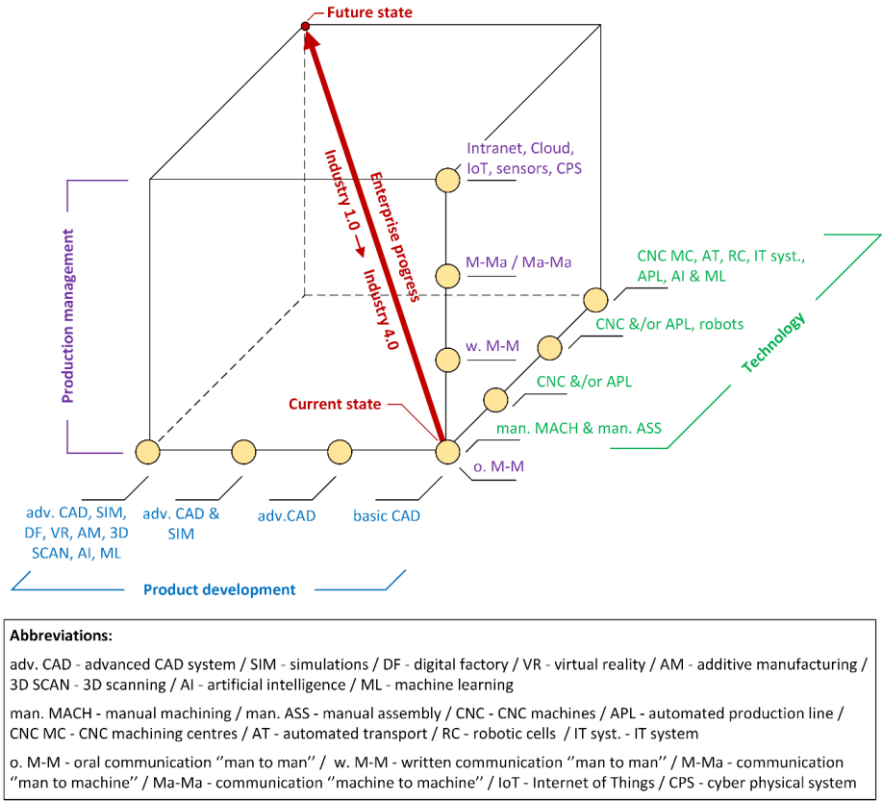

Figure 2. *Enterprise progress towards Industry 4.0 in all three analysed segments: product development, technology, production management*

How to define and detect the maturity level is a critical factor to move forward. It can influence how companies and other industrial stakeholders respond to and navigate the challenges and opportunities characteristic for each maturity level. Understanding this dynamic is essential for successful management and operation in rapidly changing technological landscapes.

Table 1. *Maturity levels towards Industry 4.0 for main production enterprise segments*

<table>
<tr><th colspan="3">Factors (Production Enterprise Segments)</th><th>Response</th></tr>
<tr><th>Product Development (PD)</th><th>Technology (T)</th><th>Production Management (PM)</th><th>Maturity Level towards Industry 4.0 (MLI4.0)</th></tr>
<tr><td>Product development manually or by using basic CAD system</td><td>Manual machining & assembly</td><td>Oral communication ''man to man''</td><td>1</td></tr>
<tr><td>Product development by using advanced CAD system</td><td>CNC machines and/or automated production line</td><td>Written communication ''man to man''</td><td>2</td></tr>
<tr><td rowspan="2">Application of advanced CAD system and simulations in product development</td><td rowspan="2">CNC machines and/or automated production line, robots</td><td>Communication ''man to machine''</td><td rowspan="2">3</td></tr>
<tr><td>Communication ''machine to machine''</td></tr>
<tr><td>Application of advanced CAD system, simulations, digital factory, Virtual Reality (VR), Additive Manufacturing (AM), 3D scanning, Artificial Intelligence (AI) & machine learning (ML) in product development</td><td>Modern CNC machining centres, automated transport, robotic cells, IT systems on automated production line, AI & ML</td><td>Communication by Intranet, Cloud, Internet of Things (IoT), sensors, Cyber Physical System (CPS), networks</td><td>4</td></tr>
</table>

3. AI fuzzy logic modelling

Fuzzy logic is one of the artificial intelligence (AI) methods that is proved quite useful to describe and model processes and systems where application of conventional mathematical modelling and optimization techniques is not possible due to imprecise, vague and incomplete data. Fuzzy logic modelling technique represents good basis for creating artificial intelligence reasoning system that will be able to predict and simulate future situations regarding various inputs and furtherly improve management and control of analysed process [7-9].

In this paper AI fuzzy logic technique was applied to define functional relations between inputs such as production enterprise segments: product development (PD), technology (T) and production management (PM) and maturity level towards Industry 4.0 (MLI4.0) as output. Developed AI fuzzy logic reasoning system will analyse effects of different advancement levels of production enterprise segments and derive appropriate conclusions regarding their optimal settings to achieve as high as possible production enterprise maturity level towards Industry 4.0.

In order to generate AI fuzzy logic model it is necessary to establish appropriate architecture of fuzzy logic system. Each fuzzy logic system consists of few modules: fuzzification module, fuzzy inference module and defuzzification module. Fuzzification module applies set of different membership functions to add to each real input value corresponding fuzzy linguistic variable. Fuzzy linguistic variables are defined by degree of membership between 0 and 1. Membership functions that can be applied are: Gaussian, triangular, trapezoidal etc. Fuzzy inference module consists of two knowledge bases: membership functions and fuzzy IF-THEN rules to establish relations between analysed inputs and outputs. Two most popular fuzzy inference systems are Mamdani and Sugeno. Mamdani is used more often due to its simplicity and intuitive approach. Defuzzification module converts aggregated fuzzy logic output data into a non-fuzzy real value. The most widely used defuzzification procedures are Center of Area, Weighted Average Formula and Mean of Maximum [10-13].

In this paper in order to develop AI fuzzy logic model that will forecast maturity level of production enterprises towards Industry 4.0 (output) depending on different advancement stages of production enterprise segments (inputs) Mamdani fuzzy inference system was applied. Architecture of AI fuzzy logic system is presented in Figure 3. Settings of Mamdani fuzzy inference system are: and method: min, or method: max, implication: min, aggregation: max, defuzzification method: centroid.

For each analysed enterprise segment as input four Gaussian membership functions were defined: LA (low advanced), MA (medium advanced), HA (high advanced), VHA (very high advanced), Figure 5 a), b) and c). This definition of membership functions is directly connected with enterprise segments advancements degrees presented in Table 1 and Figure 2. For example, for PD input: HA membership function corresponds to application of advanced CAD system and simulations in product development, for T input: VHA membership function corresponds to modern CNC machining centres, automated transport, robotic cells, IT systems as well as AI and ML on automated production line, for PM input: MA membership function corresponds to written communication ''man to man''. Output maturity level towards Industry 4.0 was also defined by four Gaussian membership functions: I1 (Industry 1.0), I2 (Industry 2.0), I3 (Industry 3.0), I4 (Industry 4.0). For each combination of three inputs corresponding value of MLI4.0 was calculated as mean value of ranks defined in Figure 1 and attached to given enterprise segment advancement degree. AI fuzzy logic system for modelling production enterprise maturity level towards Industry 4.0 as well as membership functions for inputs and output are presented in Figure 4 and Figure 5.

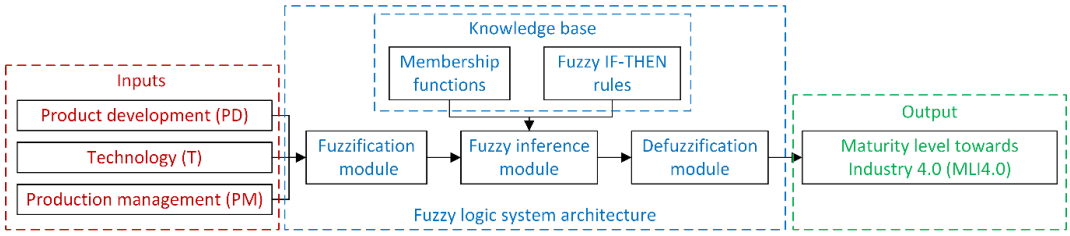

Figure 3. *AI fuzzy logic system architecture*

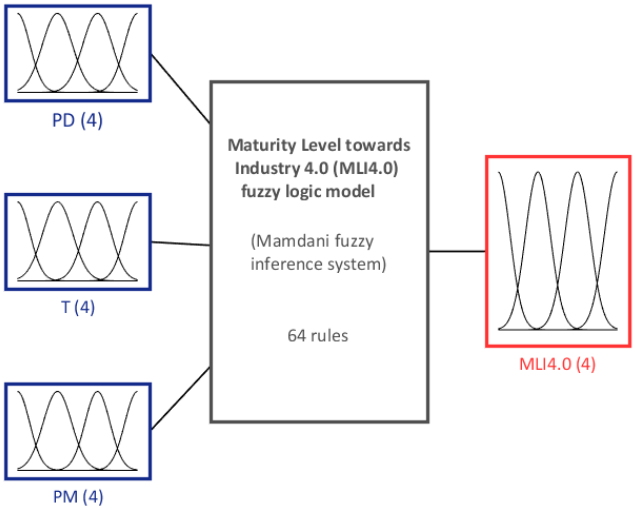

Figure 4. *AI fuzzy logic system for modelling Maturity Level towards Industry 4.0 (MLI4.0) of production enterprise*

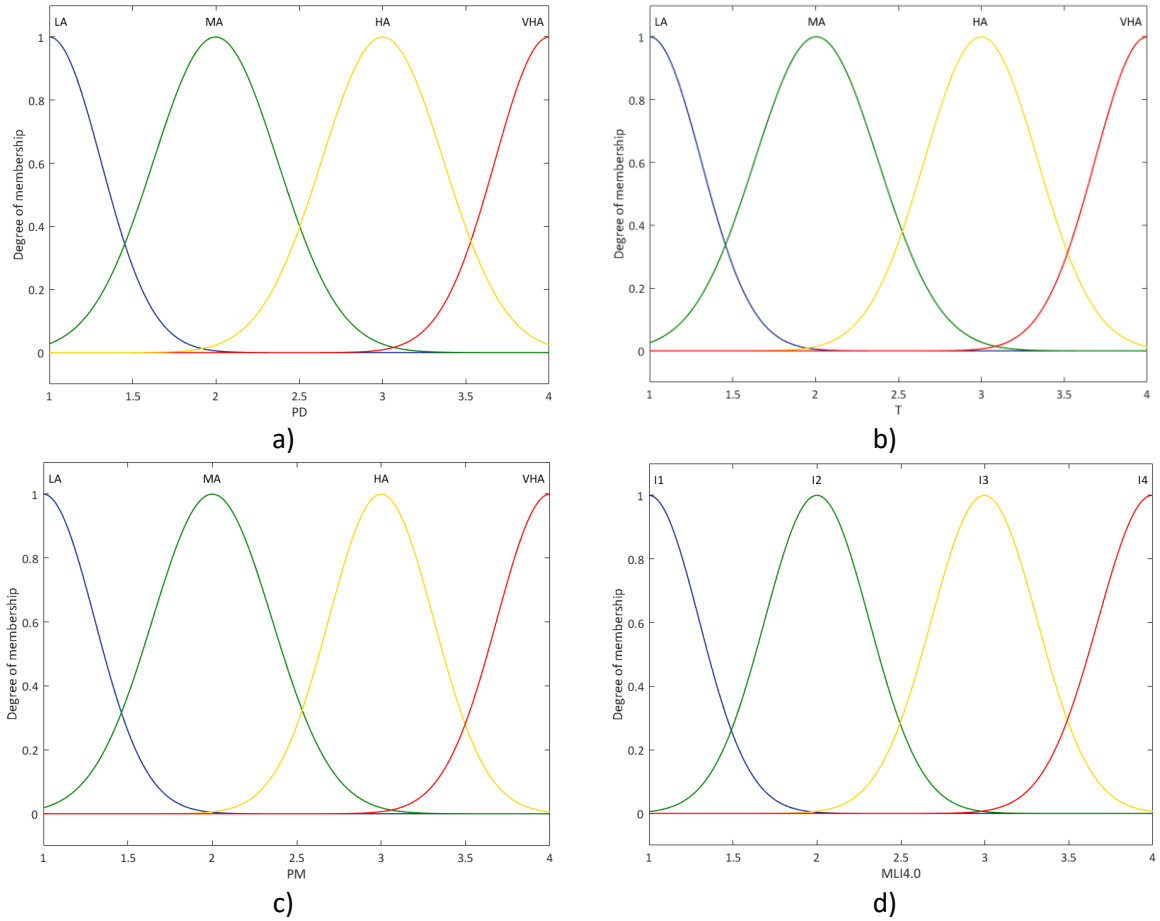

Figure 5. *Membership functions for: a) Product Development (PD), b) Technology (T), c) Production Management (PM), d) Maturity Level towards Industry 4.0 (MLI4.0)*

In order to establish functional relations between inputs and output and preform fuzzy reasoning set of 64 fuzzy IF-THEN rules was defined. These rules cover all possible combinations of inputs aiming to define for each of these combinations corresponding value of production enterprise maturity level towards Industry 4.0 (MLI4.0). Graphical presentation of defined fuzzy IF-THEN rules is shown in Figure 6.

Defuzzification process resulted with non-fuzzy values of aggregated fuzzy logic enterprise maturity level towards Industry 4.0 (MLI4.0) output. In order to validate prediction accuracy of developed fuzzy logic model of maturity level towards Industry 4.0 (MLI4.0) comparison between calculated and by AI fuzzy logic model predicted MLI4.0 values was performed. As validation measures mean absolute percentage error (MAPE) and coefficient of determination (R^2) were applied. Prediction accuracy validation results are presented in Figure 7. These results proved that AI fuzzy logic system was well defined and that developed model can be used for further analysis and discussion. Whole process of AI fuzzy logic system development was performed in MATLAB R2022a software.

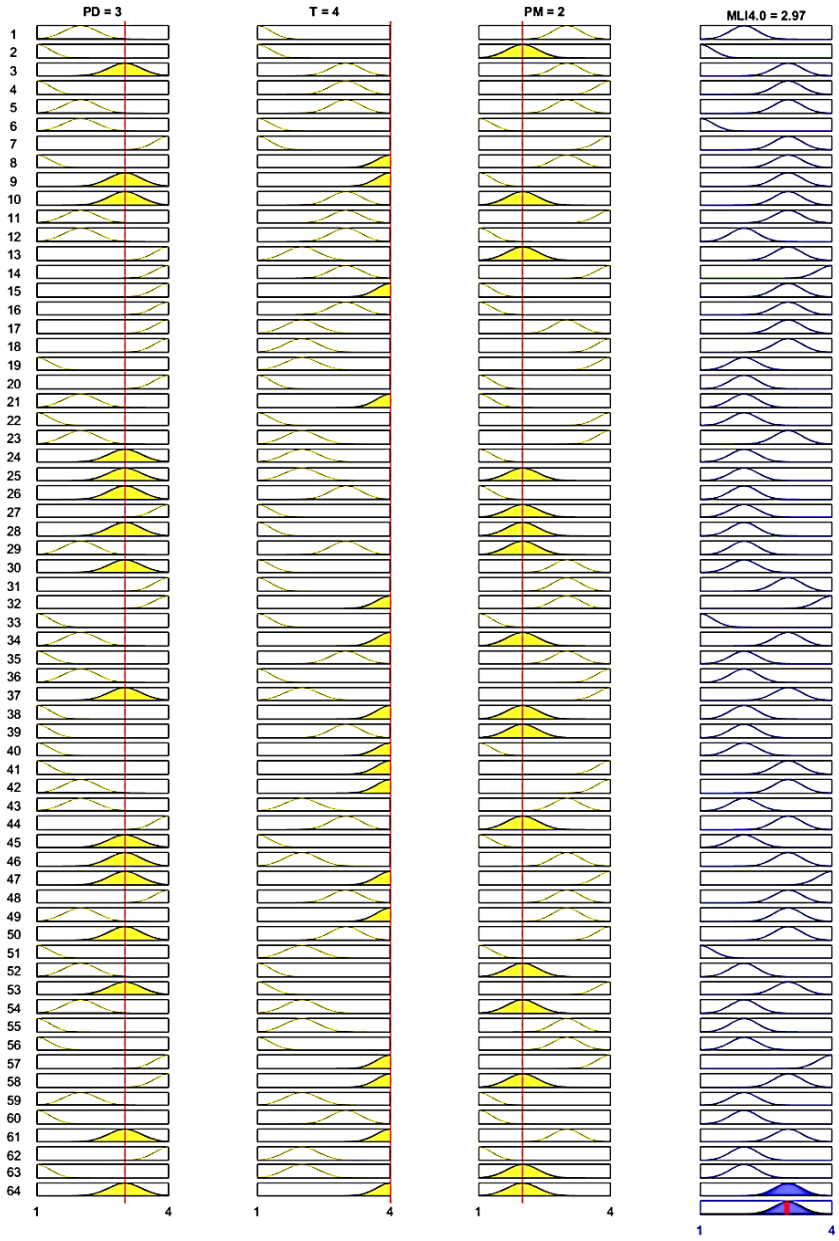

Figure 6. *Base of fuzzy IF-THEN rules between inputs: PD, T, PM and output: MLI4.0*

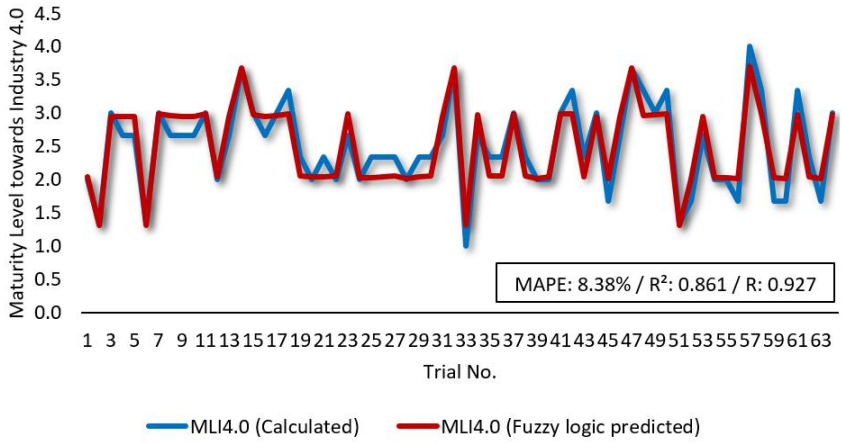

Figure 7. *Comparison between calculated and fuzzy logic predicted data of Maturity Level towards Industry 4.0 (MLI4.0) with presented validation measures*

4. Results and discussion

After prediction accuracy of developed AI fuzzy logic model was proved it can be furtherly used to analyse effects of enterprise segments advancement degrees on overall production enterprise maturity level towards Industry 4.0 (MLI4.0). Figure 8 presents surface and contour plots of two production enterprise segments interactions (PD-T, PD-PM, T-PM) effects while the third enterprise segment was kept constant.

From Figure 8 it is obvious and clear that higher advancement degree of each analysed production enterprise segment leads consequently to higher enterprise maturity level towards Industry 4.0 (MLI4.0). However these plots serve as good foundation for enterprise self-positioning regarding its implementation level of Industry 4.0 technologies and concepts. For example, if some enterprise estimates that its segments advancement degrees are for PD - medium advanced (2), for T - medium advanced (2) and for PM - high advanced (3) (Figure 8b) it can be derived that production enterprise maturity level towards Industry 4.0 (MLI4.0) is located into the area around value 2 that corresponds to Industry 2.0. Knowing its current state each production enterprise can bring appropriate measures and activities to improve segments with lower advancement degrees according to Figure 2 to accomplish higher overall maturity level towards Industry 4.0. Finally, this is exactly the main purpose of development AI fuzzy logic model of production enterprise maturity level towards Industry 4.0.

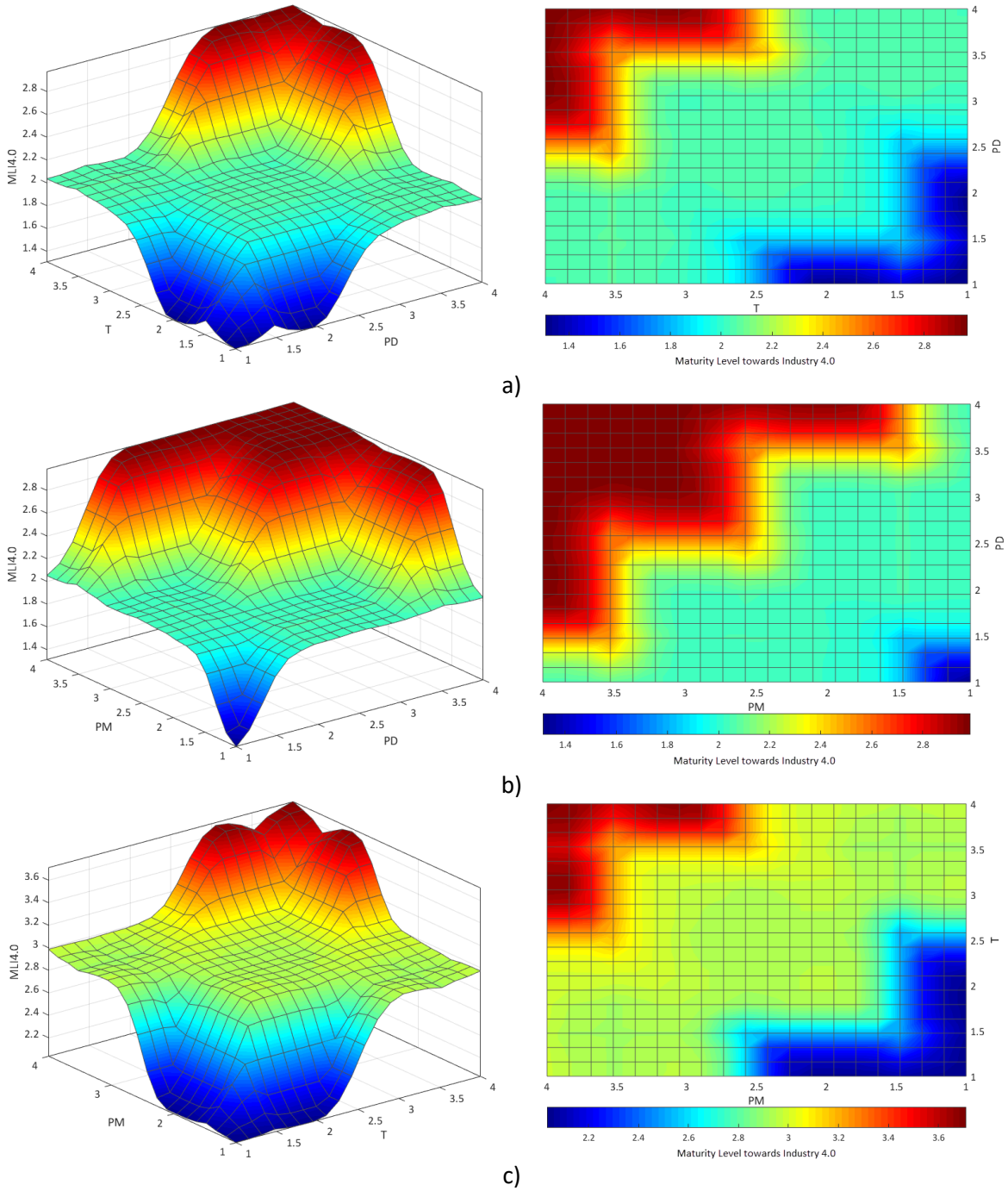

Figure 8. *Interactions effects of production enterprise segments on Maturity Level towards Industry 4.0 when: a) production management advancement degree is 1, b) technology advancement degree is 2, c) product development advancement degree is 4*

5. Conclusion

In this paper influence of advancement degrees of three main production enterprises segments such as product development, technology and production management on overall enterprise maturity level towards Industry 4.0 was analysed. In order to establish functional relations between inputs and output and develop system that will be able to predict and forecast enterprise future state artificial intelligence fuzzy logic technique was applied. Based on conducted investigations next findings can be derived:

- Artificial intelligence fuzzy logic techique represents good tool to establish mathematical model between analysed inputs and outputs especially in situations where input and output variables are linguistically defined as it is the case here and where application of conventional mathematical modelling procedures is not possible.
- Mamdani fuzzy inference system, as well as Gaussian membership functions and centroid defuzzification method proved as good settings to develop appropriate AI fuzzy logic system of maturity level towards Industry 4.0 (MLI4.0).
- Forecasting accuracy of developed AI system was validated by applying mean absolute percentage error (MAPE) as well as coefficient of determination (R^2). Their values of 8.38% and 0.861 refer to good match between calculated and forecasted values of maturity level towards Industry 4.0 (MLI4.0) and accordingly to good quality of developed AI fuzzy logic model.
- Based of developed AI fuzzy logic model 3D surface as well as contour plots were generated. These plots visualize enterprise segments interactions effects on MLI4.0 and serve for enterprise self positioning depending on different inputs advancements degrees.
- Developed AI fuzzy logic model of maturity level towards Industry 4.0 represents good base for further upgrading with additional enterprise segments data as well as for finding appropriate strategies in order to improve current company state and accelerate its transition towards Industry 4.0.

References

[1] Kagermann, H., Wahlster, W., Helbig, J., 2013. Recommendations for implementing the strategic initiative INDUSTRIE 4.0. National Academy of Science and Engineering: Final report of the Industrie 4.0 Working Group.

[2] Kozlovska, M., Klosova, D., Strukova, Z., 2021. Impact of Industry 4.0 Platform on the Formation of Construction 4.0 Concept: A Literature Review. Sustainability, 13.

[3] Lasi, H., Kemper, H.G., Fettke, P., Feld, T., Hoffmann, M., 2014. Industry 4.0. Bus. Inf. Syst. Eng. 6, 239-242.

[4] Crnjac, M., Veža, I., Banduka, N., 2017. From Concept to the Introduction of Industry 4.0. Int. J. Ind. Eng. Manag. 8, 21-30.

[5] Yin, Y., Stecke, K.E., Li. D., 2018. The evolution of production systems from Industry 2.0 through Industry 4.0. Int. J. Prod. Res. 56, 848-861.

[6] Crnjac Zizic M., Mladineo, M., Gjeldum, N., & Celent, L. (2022). From industry 4.0 towards industry 5.0: A review and analysis of paradigm shift for the people, organization and technology. Energies, 15(14), 5221.

[7] Peko, I., Nedić, B., Dunđer, M., Samardžić, I., 2020. Modelling of Dross Height in Plasma Jet Cutting Process of Aluminium Alloy 5083 Using Fuzzy Logic Technique. Tehnički vjesnik. 27(6), 1767-1773.

[8] Madić, M., Ćojbašić, Ž., Radovanović, M., 2016. Comparison of fuzzy logic, regression and ANN laser kerf width models. UPB Scientific Bulletin, Series D: Mechanical Engineering. 78(1), 197-212.

[9] Madić, M., Radovanović, M., Ćojbašić, Ž., Nedić, B., Gostimirović, M., 2015. Fuzzy Logic Approach for the Prediction of Dross Formation in CO2 Laser Cutting of Mild Steel. Journal of Engineering Science and Technology Review. 8(3), 143-150.

[10] Kovač, P., Rodić, D., Pucovsky, V., Savković, B., Gostimirović, M., 2013. Application of fuzzy logic and regression analysis for modelling surface roughness in face milling. Journal of Intelligent Manufacturing. 24, 755-762.

[11] Bašić, A., Peko, I., Krolo, J., Bagavac, P., 2021. Fuzzy logic modeling of ultimate tensile strength and cost in fused deposition modeling process of additive manufacturing, MTSM 2021, Split, Croatia
[12] Peko, I., Marić, D., Šolić, T., Matić, T., Samardžić, M., Samardžić, I., 2022. Fuzzy Logic Modelling of Dross Height in Plasma Jet Cutting of Shipbuilding Aluminium Alloy 5083, TEAM 2022, Slavonski Brod, Croatia
[13] Lan, T.S., Chuang, K.C., Chen, Y.M., 2018. Optimization of Machining Parameters Using Fuzzy Taguchi Method for Reducing Tool Wear. Applied Sciences. 8(7), 1011.

Feasibility study for the advanced characterization of musical string wires

***Massimo Rogante*[1,2], *György Lakatos*[2,3,4], *Daniele E. Lucchetta*[5] *and Ilija Nastovski*[2,6]**

1) Rogante Engineering Office, Contrada San Michele n. 61, 62012 Civitanova Marche, Italy - https://www.roganteengineering.it

2) Academy Liszt Music Art, Via Palmaroli 13/19, Grottammare, Italy - https://www.premioliszt.it

3) Liszt Ferenc Academy of Music, Nagymező utca n. 1, 1065 Budapest, Hungary

4) Snétberger Music Center, Hóvirág utca n. 28, 8227 Felsőörs, Hungary

5) Optoacoustic Lab., Dipartimento SIMAU, Università Politecnica delle Marche, Via Brecce Bianche, 60131 Ancona, Italy

6) Zdruzenie na gragjani muzicari Gradski Kameren Orkestar Veles, Lazo Trpkovski st. 44, 1400 Veles, North Macedonia

Corresponding author: main@roganteengineering.it

Original scientific article

Abstract: In chordophone musical instruments, each note played is the result of the vibration of a string or a series of two or more strings at a defined frequency, determined by the length, diameter, tension and density of the metal wire involved, as it is specific elastic element.
The durability and performance of musical strings depend on numerous factors, including the quality of the constitutive materials, the production process and specific treatments. With the aim of enhancing the characteristics of these strings and avoiding problems such as corrosive phenomena or breakage events of the musical strings during the concert, the industry of the sector dedicates considerable attention to the analysis of possible technological methods capable of giving the same threads high qualitative and functional properties.
This article, after a brief introduction on musical instrument strings and their inherent problems, concerns their possible advanced nano(micro)-characterization by neutron diffraction and small-angle neutron scattering. These techniques allow, in particular, to determine the residual strain and stresses and the crystallographic texture, and to identify and study important nano(micro)-defects such as matrix heterogeneity, porosity, gas bubbles and precipitates, among the main factors responsible for the wire's performances: thereby proving to be indispensable to completely study the structure and the effect of the constitutive materials' characteristics on the parameters of the acoustic properties.

Keywords: *nano(micro)-characterization; neutron techniques; structure; wires; strings*

1. Introduction

Wires and strings, fundamental acoustic elements of musical instruments, are mainly made of stainless steel wires and they are among the metal products that require precise observation regarding the choice of the most suitable constitutive materials and manufacturing methods.
The strings can be normal (consisting of a single steel-like material, as shown in Figure 1) or made up of a steel core with an outer winding made of other copper-like materials (as shown in Figure 2), so that they can vibrate more slowly.
Violins and guitars, as well as Arabian 'uds, Chinese pipas, Indian veenas, Indonesian rebalts, Mongolian domras, Russian balalaikas and West African koras, descend from lutes, an instruments' family involving strings that run parallel through a flat soundboard.

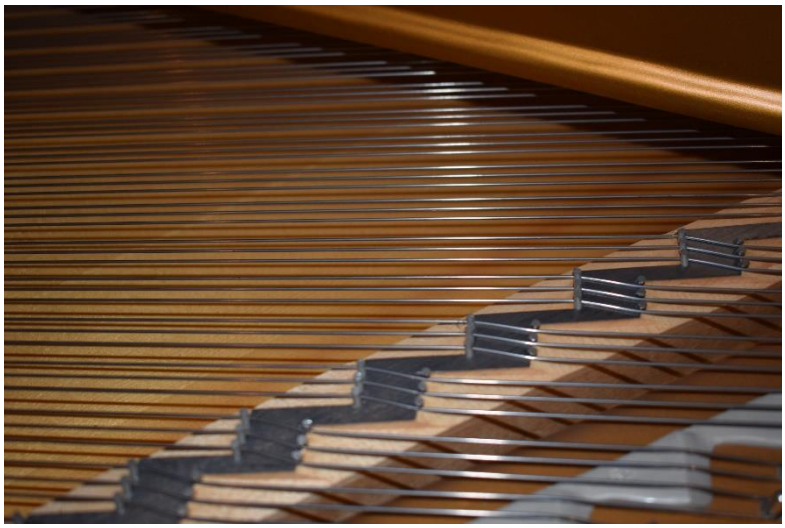

Figure 1. *Piano strings for higher pitches (groups of three steel strings tuned in unison)*

Figure 2. *Single piano strings, with copper outer winding for the lowest sounds*

The development of these musical instruments across the several past centuries included the doubling of the standard strings, attaining a fuller and richer sound: the vibrations of the strings, actually, travel through the bridge to the soundboard, pressing it in. The more strings, the larger the pressure and the more movement throughout the soundboard as it continually presses down and releases [1].
When a musical string vibrates, it carries many discrete frequencies, the so called "harmonics", which vibrate with frequencies that are perfect integer multiples of the fundamental, the lowest frequency being carried by the string.
The sound timbre of a string given by its frequency spectrum, and its acoustic properties, depend on shape and size of the cross section, length, density, tension of the string installed in the musical instrument, type of material used, distribution of internal defects (including those at of micro- and nano-scale), purity of the metal compared to non-metallic inclusions, treatments undergone by the material (including cryogenic ones) and the distribution of internal residual stresses (RS).
A main purpose in designing a piano is to enhance the string tension in order to get a more powerful sound, but it is limited by the tensile strength of the musical wire: therefore, for given string material, length and tension, the string diameter is enlarged, with consequent increase of the string bending stiffness and risk to adversely affect the tone quality [2]. Furthermore, trade-offs, mainly driven by the desired level of inharmonicity in the resulting piano tones, are involved in choosing tension, radius and length of the string [3].

The strings of a modern piano, subjected to standard specifications such as ASTM A228, are made of hardened and tempered steel wire drawn from selected raw material, i.e. a high-carbon steel alloy with high tensile strength and high elastic limit (characteristics, e.g., reported in [4]). After a successive surface treatment by soft polishing, a very tin protective coating can be also applied.
The wire drawing process is schematically shown in Figure 3.

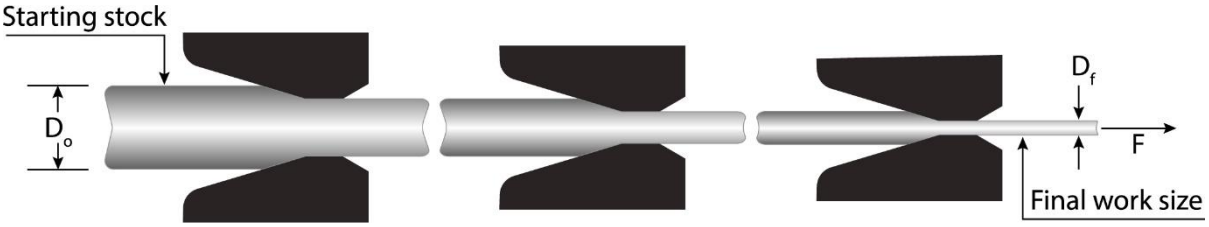

Figure 3. *Scheme of a wire drawing process*

In this cold working process, the wire is pulled through a series of drawing dies having a smaller and smaller bore diameter: the cross section area of the rod is more and more reduced, hence the drawn wire length increases.
The effect of shear deformation incorporated into the conventional drawing process has been shown, as experimental technology, involving a reduction of the structural anisotropy. An extensive increase in the fraction of small grains (less than 3 μm in size) and a decrease in the fraction of large grains resulted, registering a large amount of small grains with high-angle boundaries, as stronger grain refinement [5]. The formation of this kind of grains is explained by progress in competing processes of large grain fragmentation and continuous dynamic recrystallization. The result is the change of the grain boundaries type from smooth to serrated ones and the formation of unclosed high-angle grain boundaries. It has been demonstrated, besides, that a certain part of small grains provides grain boundary sliding. The comparative analysis of the hardness tests has demonstrated increasing hardness with deformation accumulation, but after the classical drawing the hardness grows linearly and stepwise after the experimental shear drawing. The physical reasons of such behaviour are explained by microstructural features.
The objective indices normally used for the level of acoustic properties of a musical string wire are the sounding length, the amount of nonharmonicity of the overtones [6] and the degree of nonharmonicity irregularity of the damping vibrations. For a general evaluation of the sound quality of a string, an index is used which takes into account the contribution of each of the acoustic characteristics above indicated for the formation of the acoustic properties [7].
The speed at which a pulse travels along a string depends on the tension and mass per unit length of the string. A tighter and lighter string results in a higher pulse velocity. The fundamental frequency, which is closely related to the perceived pitch, depends on the distance the pulse has to cover. Different notes are strung with the same thickness of wire, but cut at different lengths and tuned at different tensions to produce the desired pitches: the vibrations are then transmitted to the soundboard of the instrument. Longer strings take more time for a complete round trip, resulting in a lower pitch. Therefore, the pitch of a string is influenced by its length, tension, and mass per unit length accordingly to the following formula:

$$f = \frac{1}{Ld}\sqrt{\frac{T}{\pi\rho}} \tag{1}$$

where L is the string length, d its diameter, T the tension and ρ the density. Instruments can be designed with shorter strings by increasing their mass per unit length, as seen in the bass section, where copper layers are added to the strings (see Figure 2).
Piano strings, like all others, have preferred modes of vibration called resonances. When a string vibrates at one of its resonances, it produces a simple sine wave. In normal playing, all resonances are excited, creating a complex tone with multiple simultaneous sine waves or partials. The tone's pitch is

closely related to the frequency spacing between these partials, particularly the fundamental frequency. The relationship between the partials' amplitudes and their changes over time contributes to the perception of tone quality. Surprisingly, the traveling pulse on a piano string is mathematically related to all the string's modes (resonances). The pulse can be represented as an infinite sum of these string modes with appropriate amplitudes. Our eyes perceive the pulse motion, but our ears prefer to analyse the string motion in terms of its partials or Fourier components, named after the mathematician who first described this equivalence. Fourier also observed that if the string's motion is periodic, with events repeating at regular intervals, the frequencies of the corresponding partials will be harmonic (e.g. 1:2:3:4...). This creates a sound with a clear pitch and steady tone quality. In real pianos, the resonance frequencies of the strings are slightly larger than harmonic ratios, a property called inharmonicity, caused by the bending stiffness of the steel wire. This slight deviation from harmonicity gives the notes a more dynamic and "alive" quality as they decay. When a piano string is struck by a hammer, both the amplitude and shape of the initial pulse on the string change with the blow's strength. This is due to the nonlinear stiffness of the felt hammer, which means that harder blows not only increase the amplitude but also create sharper corners in the pulse waveform. According to Fourier, sharper wiggles in the waveform correspond to more prominent high-frequency partials in the spectrum. As a result, the piano tone has a different, more brilliant quality at loud (forte) compared to soft (piano) dynamics. The determination of the acoustic properties of a string by measuring its frequency spectrum using conventional opto-acoustic methods and their connections with the physical parameters derived by other experimental techniques such as neutron scattering, is of fundamental importance in order to establish the correct connection between robustness and sound quality. Even a study on the physical properties and movement of the felt hammer done with high speed camera can give an important contribution to the understanding and optimization of the sound production.

A carbon steel musical string wire can be produced, e.g., by patent heat treatment (HT) of a wire rod, with an austenitizing temperature of 930-940°C and an isothermal setting in a salt bath at about 460-480 °C with subsequent cold drawing and total reduction of 94%. Patenting - definite isothermal annealing where the transformation of metastable austenite is effected at the nose of the time-temperature-transformation (TTT) diagram of the material under HT - is normally carried out to develop a favourable nano(micro)-structure or the subsequent cold drawing of musical wires, imparting them high strength. The patented rod, indeed, is cold drawn to fine wire, to be used in musical instruments as joined nano(micro)-structural and strain-hardening results in a very high strength of the wire [8]. Medium and higher carbon steels are patented prior to cold drawing, while lower carbon and alloy steels are annealed to make them suitable for drawing. Annealing is also used as a final treatment for wires [9].

The influence of the carbon content on the acoustic properties of the wire and the determination of the correlation relationship between some physical and mechanical characteristics of the steel and the sound quality of the string given by its frequency spectrum have been the subject of various studies. An increase in the carbon content of the steel leads to a growth of the RS level, the most significant increase in tensile strength occurring in the outer layers of the wire. Related studies have shown that an increase in the carbon content from 0.51 to 0.92% leads to a growth of tensile stresses from 300 to 700 N/mm^2, and a post-deformation tempering at 300 °C for 20 min. causes a significant relaxation of RS, although a similar distribution of these RS remains stored with a significant jump in the cross section of the wire [10].

One of the most important characteristics of strings for musical instruments, therefore, is the RS state, the determination of which is essential to adequately improve the knowledge of the effect of intense plastic deformation on the metal. Despite the relevant amount of data available concerning the constitutive materials of strings for musical instruments, such as those relating to plasticity and strength, further investigations at an advanced level are essential.

Experimental studies have shown that successive steps of stainless steel wire drawing exhibited the kinetics of deformation-induced martensite creation from metastable austenitic feedstock, with a

defect density increase and formation of micro-strains. The early decrease of the Young's modulus determined by tensile tests was accompanied by a severe reduction in domain size and in grain diameter [11]. The course of the wire drawing process, thus, is correlated to the evolution of the nano(micro)-structural features.

Other occurrences concerning metal wires are oxidation and corrosion. Various metals used to make wires have significant affinity for substances such as oxygen, humidity and carbon dioxide. The possible consequent corrosive phenomena are of different types, with deep or progressive attacks, depending on the material and its characteristics of resistance to corrosion. The latter, in fact, depends on numerous factors, including analytical and structural conformation, environmental conditions, manufacturing processes and combinations with other materials.

In addition to the countless studies conducted, several patents have been filed in recent decades, with the main objective of improving the performance of musical instrument strings. A method was designed, for example, to make a wound musical instrument string with improved tone quality and life, involving the winding of a cover wire onto a core wire followed by a thermal conditioning step [12]. A treatment of the strings with a polymer vapour was designed, e.g., to be applied to the core of the strings and/or to strands wrapped around the core, to avoid problems common with spray type polymer coatings, extruded or laminate coatings or wipe-on liquid coatings, including heat damage, imprecise dimensional control, possible flaking, peeling or easy removal of the coating or adverse changes or damping of the musical qualities of the strings [13].

The methodological approach followed in the present study for the advanced characterization of musical string wires starts from the examination of the various existing problems concerning the these strings.

2. Problems regarding musical strings

2.1 Piano

Two standard forms exist for the piano, upright piano and concert piano or grand piano. Both types have their own subtypes or sizes, e.g. the vertical piano is found in the length from 110 to 150 cm and the concert piano from 140 to 290 cm. Depending on size and type of the instrument, there are the following variations in the strings arrangement:

- Viennese type of piano, years 1700-1950, in which parallel strings are used, which easily corrode under the influence of low humidity and can be easily damaged by using more finger pressure. This instrument is effortlessly out of tune: it does not tune at 440 Hz, a more stable tune is available on 435 Hz.
- English mechanics or new modern type of piano, from the year 1830 until today, in which folded arrangement and strengthening of the strings alloy, a metal frame in the instrument's body and setting of new parameters of length are used. This type of instrument, from the very beginning of its creation, has provided great opportunities in terms of tuning: it remained stable for a long time, providing mechanically much greater opportunities of better and refined performance and it gave great chances to perform pedalization using the so-called "half-pedals".

An unwanted occurrence in acoustic pianos is the breaking of a wire from any sector of the instrument, possibly due to wire's quality, storage in inappropriate conditions and excessive exposure to moisture. Such fracture is generally classified based on the how the wire breaks and as such is classified as brittle or ductile fracture. In the latter, the main characteristic is the visible plastic deformation prior to and during crack propagation.

Modern piano strings, anyhow, if calculated correctly, have limited breaking events. The latter, possibly, occurs especially after a few years of use and in the last two sectors of the acute part of the grand piano, where there are no aggrafs where the string is fixed, so the string is blocked only by the V-shaped bar of the cast iron made frame. Over time, the cast iron surface is slightly incised by the string which then begins to vibrate within such incision, thus creating an acoustic level anomaly, until the string breaks at that point. The goal is to deploy strategies to avoid such fractures: a solution can be to change the strings after suitably grinding the surface of the frame.

In concert type pianos having lengths of 220-290 cm, it is less common to break a wire from higher pressure on the hammer, nevertheless it can break due to the influence of oxidation and corrosion, which are other problems occurring not only with acoustic pianos, but also with stringed instruments. A particular corrosive phenomenon is represented by photo-oxidation, which markedly affects the quality of the sound. The strings, especially if exposed to light, darken and partially lose their original tonal characteristics. It would be interesting to refine the selection of the string material with one less sensitive to this photo-oxidation.

Piano manufacturing factories such as Steinway and Sons, Bösendorfer, Bechstein, Fazioli, Feurich and Ritmuler, in their production lines, manufacture pianos containing high-tech strings that provide greater durability. The Feurich Co, for instance, uses special "Stephen Paulello" strings in the middle sector and the soprano, for which the factory itself gives a declaration of high resistance to impacts and corrosion [14]. The Steinway and Sons Co. offers a durable grade of its strings by using special Swedish steel.

All these factories, although they offer new technological achievements in terms of the instruments' durability, still have the same unsolved problem with durability of the strings, which after a certain number of tunings or tensioning lose their elasticity: and the accuracy of vibrations during tuning, thus, is lost and with time they can be cracked.

The duration of a string, usually, is about 5 years for an upright piano and about 10 years for a concert piano. After this period, it is necessary to replace the strings with new ones in order to extend the usefulness of the instrument.

2.2 Stringed instruments

The duration of the strings for stringed instruments, compared to those of the piano, is very short: for the violin, for example, it can even be less than two months. Of course, it depends on how many times the instrument has been played. Moreover, the player has to know the string’s behaviour: it is very important when he or she gives a concert.

Weather (cold, warm, humidity) adds also its impact on these strings, as well air travel, which can add some string interference, as air and pressure conditions change with altitude. In conditions of significant altitude, in fact, there is less oxygen, which is important both for the strings (synthetic, metal, etc.) and for the wood constitutive of the musical instruments: this is why manufacturers develop new special cases for these instruments.

Strings for stringed instruments are susceptible to oxidation and corrosion (primarily affecting uncoated wound strings), which occur over time mainly due to moisture and salts from the player's fingers, resulting in a reduction in the string's brilliance. Possible remedies to protect the strings from corrosion or to slow down oxidation are the application of metal plating, polymer coatings or special lubricating oils.

Nowadays the sound of the strings is slightly different from the past. It may depend on the new materials adopted. The sound of good strings is warmer but a little bit with lower intensity. By considering the steel of the string’s material, it is harder and may be a bigger sound. The sound of synthetic strings (as a alternative to natural gut) is also different, maybe these strings are more powerful.

During the concert it can happen that a string breaks, as the string deforms with use. As a matter of fact, the main issue is related to the material. It is possibly due also to the climate change or to the fact that a new product does not achieve a quality level that can be satisfactory to both manufacturer and players.

3. Advanced characterization

Various methods exist, nowadays, normally adopted to carry out analysis and modelling of musical strings wires, e.g.: microscopic analysis to find microstructural characteristics; metallographic examination to analyse internal cracks, grain size, decarburized layer and microstructural defects such as martensite and net carbide; X-ray diffraction to detect surface residual macro-stresses.

Concerning corrosion events, the mechanical properties of the considered steel wires can be experimentally studied by corrosion test analyses at different corrosion degrees.
An adequate nano(micro)-characterization of wires for musical instrument strings, anyhow, is essential for an appropriate knowledge of the manufacturing process and for its possible improvement, with the aim of enhancing quality and duration of these strings as well as the characteristics of the sounds produced. This applies, in particular, to piano strings - for which a duration of decades is required -, which are subjected to high tension (overall, up to 15-20 tons) and repeated stresses. Neutron beam techniques are increasingly adopted in the study of industrial materials and components, following the availability of enhanced measurement and data processing procedures, e.g. those specifically developed by the Rogante Engineering Office, a landmark for Industrial Applications of Neutron Techniques [15]. These non-destructive and non-invasive diagnostic tools can be useful to investigate string wires of musical instruments, providing significant data on key parameters related to quality and performances. Neutrons can reveal important properties and allow the control of the main parameters at the nano(micro)-scale level, the knowledge of which is essential to correctly evaluate the origin of structural failures, with the possibility of improving quality of both products and production processes. Models built on the investigation by neutron techniques of real samples, combined with the finite element method (FEM), for instance, can be developed with the objectives of predicting the nano(micro)-structural evolution of the material following drawing and thermo-mechanical processes and to better understand the phenomena associated with use [16].
Neutron diffraction (ND) [17] has already proved in various experiments to give a substantial support in investigating steel wires, mainly allowing the determination of inner and subsurface RS, which are defined as those internal, existing in an isolated system in mechanical equilibrium, not subjected to any external force or moment. They arise as a consequence of the production processes or successive treatments and can reach very high levels ([15] and [18]). Experimental studies have shown that an uniform RS distribution has a favourable influence on the acoustic parameters and the quality of the sound, since the frequency of vibrations of a string depends linearly on the effective tensile stress [19]. ND, furthermore, can help studying the weaving evolution during the transformations that occur after drawing: the combination of numerical and experimental results is useful to optimize product quality, especially in relation to performance and reliability [20].
ND measurements on musical wires samples can be carried out, for instance, determining elastic strains and RS also under tensile loading (as a function of the applied tensile stress), adopting slits of 10 by 10 mm for the incident and diffraction beams. (110) diffraction profiles can be measured at different holding stresses. To study the strengthening mechanism of heavily drawn steel wires showing ultra-high strength, in situ ND investigations on ferrite and pearlite steels during tensile loading were performed, determining tensile strengths. The variation in (110) spacing with tensile stress was found elastic and a stress versus (110) lattice plane strain was found linear for the ferrite steel and nonlinear at higher stresses for the pearlite steel [21].
Phase micro-stresses can also be determined and the obtained data can be combined with complementary X-ray diffraction measurements. RS were measured by ND, e.g., in both the cementite and ferrite phases of cold-drawn pearlitic wires. The micro-stress phase was obtained in the axial direction and measurements on etched wires showed a micro-stress phase almost constant with the distance to the wire axis. Combination of the achieved data with X-ray diffraction measurements on the ferrite allowed determining the response of each phase to the macro-stress or to an applied stress [22]. Other ND experiments were performed investigating cold drawn steel wires. A significant change of the lattice parameter with the drawing level (not inherited from RS) was found and that variation resulted very sensitive to the cooling rate after processing [23]. A selection of high strength pearlitic steel wires drawn to different reductions was investigated by ND and X-ray diffraction to study the inner macro and micro RS evolution during cold drawing. To compare RS evolution in the ferrite phase, the lattice strain evolution was studied along the axial and transverse directions. Ex situ ND revealed a strong orientation dependence of the lattice spacing evolution; in situ ND revealed strong differences in yielding and stress partitioning among particular {hkl} reflections [24].

In a possible ND analysis of musical string wires samples, they can be positioned to measure both axial and radial component of the strain. Due to the samples' size, having diameters starting from ~0.6 mm, the measurement would be carried out in the centre of the wires. The peak positions and their widths can be determined by fitting Gaussian curve to the measured (310) peak of each sample. From the 2θ peak positions, the strains can be calculated by using equation 2:

$$\varepsilon_{hkl} = \frac{d_{hkl} - d_{0,hkl}}{d_{0,hkl}} = \frac{\Delta d_{hkl}}{d_{0,hkl}} = cot\theta_{hkl}\Delta\theta_{hkl} \quad (2)$$

obtained by differentiating *d* in equation 3 (Bragg's law) with respect to θ:

$$2dsin\theta = \lambda \quad (3)$$

RS can be evaluated from the measured strains by using equation 4.

$$\sigma_x = \frac{E_x}{(1-2\nu)(1+\nu)}\left[(1-\nu)E_x + \nu\left(E_y + E_z\right)\right] \quad (4)$$

To determine RS from the measured strains, it can be supposed that in the wire centre the hoop strain is equal to radial strain. Radial and axial RS, consequently, can be calculated by adopting e.g. the procedures described in [17] or [25].

Properties and structural particularities of the material under certain conditions (for instance, mechanical load) strongly depend on chemical composition and manufacturing technology. The physical basis of the fracture process, e.g., is closely related to nano-defects: mechanical properties of the considered wires such as creep resistance can be influenced by the variation in size and concentration of carbides, and in general by the nano(micro)-structure formed in the metal. The heterogeneity of a material, indeed, induces a greater density of mechanical defects and a lower chemical stability, reducing the life of parts such as the said wires, which are subjected to high loads. A non-uniformity of the metallic material of the wires can lead to the development of nano(micro)-cracks, so as to reduce the residual life in a crucial way.

Despite a significant amount of available data - such as those related to resistance and plasticity - concerning the steels constitutive of wires, further advanced investigations are necessary to achieve a deeper information. Knowledge of defects at the nano(micro)-scale directly responsible for performance, such as inhomogeneities, precipitates and voids that may be present in the considered wires, can play a fundamental role in setting up suitable procedures of material selection and in meeting design requirements. The search for such factors, therefore, can provide a fundamental support for the diagnosis of the materials constitutive of the wires and to improve their quality and duration. The final products, indeed, can present a nano(micro)-structural configuration still susceptible to development. Comparative analyses of shape and size of the precipitates after different treatments can be useful to evaluate the involved processes and to trace the areas of greatest alteration.

An analysis of these wires and their constitutive materials by means of small angle neutron scattering (SANS) [26], as main objectives, has:

- the determination of the morphology of grains, cracks and pores at the nano(micro)-level, assuming that the wire drawing process mostly modify the voids
- the detection of eventual presence of anisotropy, which can be attributed to the elongation of the pores
- the detection of eventual dynamic healing of nanosized defects during the drawing process
- the detection of nanovoids nucleation during the deformation process

- the study of correlation between nano(micro)-phase inclusions (i.e., porosity and precipitates or carbides) with their physical and mechanical characteristics
- the study of the impact of these characteristics on the wire drawing process
- to acquire information about other nano-structural effects of the wire drawing process.

The SANS curves contain information about the morphology of the scattering objects, i.e. nanometre sized regions where the neutron scattering length density differs from that in their surroundings. Of these defects it is possible to determine shape, size, size-distribution, concentration, interface area, volume fraction, orientation and surface characteristics. A "Guinier type" scattering is attributed mainly to pores, cracks and defects or crystallites and precipitates at the nano(micro)-scale level.
The acquired information is averaged over the total volume of the sample placed into the neutron beam. The average sizes of these defects as well as their aspect ratios can be determined by applying appropriate model analyses.
A SANS analysis of material samples with variations in the mechanical load can provide information on the development of these defects, also investigating the thinnest porosity. The sample can be studied, e.g., before and after treatment, to verify its nano(micro)-structural evolution: this comparison, in particular, provides data on the distribution of dimensions and the concentration of new defects due to the processes undergone.
In a SANS measurement the neutrons, scattered in angles smaller than 10 degrees, are detected by a position sensitive detector. The Q scattering vector:

$$Q = (4\pi/\lambda)sin(\theta/2) \tag{5}$$

is defined by the scattering angle θ and the incoming neutron wavelength λ. After the instrumental calibration, the detected neutron intensity *I* is plotted vs. *Q*. Figure 4 shows, for reference purposes and not specifically related to musical string wires, a typical output of SANS measurements.

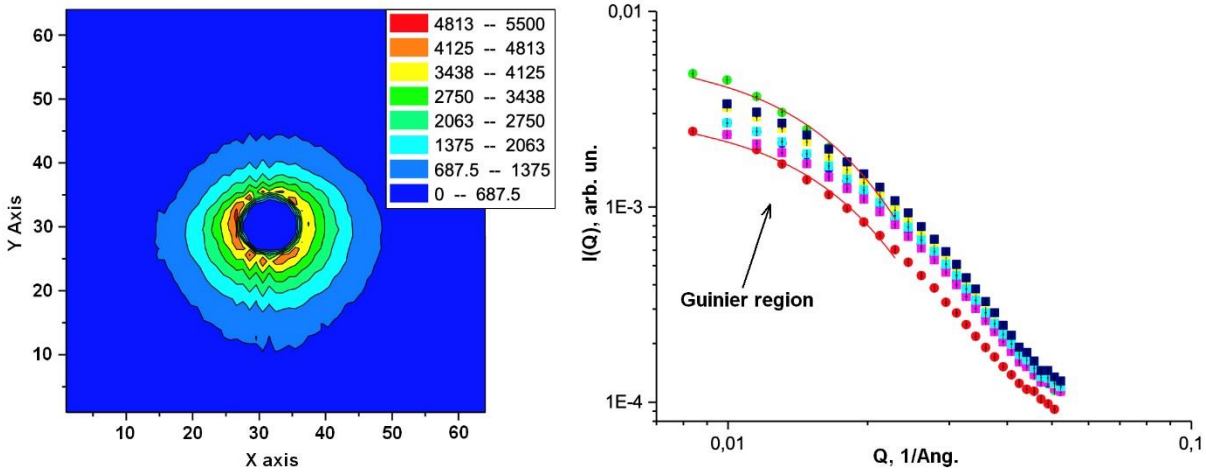

Figure 4. *Typical SANS diffraction pattern and curves*

In the left part, a diffraction pattern is shown directly obtained from a 64 × 64 pixels (1cm × 1cm pixel size) two-dimensional position sensitive detector of neutrons of a SANS diffractometer. The reported values indicate the total number of scattered neutrons detected in correspondence of 1 pixel. Such pattern is obtained for each investigated point. The isotropic form obtained in this case indicates that there is no texture in the precipitates. From the same figure, the data averaged through the circles at a given value of *Q* are successively analysed.
In the right part, SANS curves are shown, with the Guinier approximation (solid lines) of SANS data.
Considering the present feasibility study, the samples to be analysed by SANS can be chosen from the different steps of the drawing.

The Rogante Engineering Office has been carrying out various analyses of wires made of different materials, e.g. steel ([20] and [27]) and W, aimed at deepening their defectoscopy. Advanced characterizations were performed, in particular, using SANS to acquire useful information at the nano(micro)-scale level on the mentioned parameters responsible for performance. The results have confirmed the advisability of a neutron beam advanced analysis of strings wires for musical instruments, aimed at their refinement and ultimately at improving quality of the sounds produced.

4. Conclusions

Current features and problematics related to strings wires for musical instruments advise for their characterization using the most advanced techniques, with the aim to improve quality and enhance performances and lifetime.
Neutron beam techniques can supply an impressive contribution, complementing the other analytical methods conventionally used, especially in investigating the development of key nano(micro)-parameters related to structure with the progress of the manufacture process.

Acknowledgments

M° Enrico Ricci is acknowledged for useful discussions.

References

[1] Lawrence, L., 2023. Bridging lyres and lutes. Aramcoworld 3, 34–37.
[2] Fletcher, N.H., Rossing, T.D., 1998. The Physics of Musical Instruments, Springer, New York
[3] Giordano, N., 2011. Evolution of Music Wire and its Impact on the Development of the Piano, 161st Meeting Acoustical Society of America, Seattle, Washington
[4] Fushun Special Steel Co., Ltd., China, 2022. ASTM A228 Music Wire. https://www.fushunspecialsteel.com/astm-a228-music-wire/ (accessed 08 August 2023).
[5] Zavdoveev, A., Baudin, T., Rogante, M., Pashinska, E., Skoryk, M., 2020. Shear impact during steel wire drawing on grain boundaries and mechanical properties. Letters on Materials 10/4s, 558–565.
[6] Barbieri, P., 1998. The Inharmonicity of Musical String Instruments (1543-1993) with an unpublished memoir by J.B. Mercadier (1784). Studi Musicali XXVII, 383–419.
[7] Parvenkov, V.G., Mal'gina, L.A., Baraz V.R., et al., 1988. Determination of the sound quality of piano wire. Zavod. Lab. 55/9, 62–64.
[8] Banerjee, M.K., 2017. Fundamentals of Heat Treating Metals and Alloys. Reference Module in Materials Science and Materials Engineering, Comprehensive Materials Finishing 2, 1–49.
[9] Nerurkar, H.M., Lakhani, I., 1977. Heat treatments in the wire industry. TISCO 24/4, 133–141.
[10] Baraz, V.R., Rundkvist, N.A., Belov, A.V., 1992. Piano wire and strings with high acoustic properties. Met. Sci. Heat Treat. 34, 283–287.
[11] Haas, R., Degischer, H.P., Pongratz, P., Pyzalla, A.R., 2009. Microstructure and properties of violin strings made of metastable austenitic steel. Int. J. Mat. Res. 100/ 11, 1557–1565.
[12] Stone, W.N., Falcone, A.S., 1977. Method of making a wound musical instrument string, Patent US 4063674A. https://patentimages.storage.googleapis.com/80/51/55/4a38e705731c0f/US4063674.pdf (accessed 08 August 2023).
[13] Schlesinger, T., 2004. Musical instrument strings with polymer treated surface, Patent US20040255751A1. https://patentimages.storage.googleapis.com/b8/a1/9f/57215a8999fec0/US20040255751A1.pdf (accessed 08 August 2023).
[14] Stephen Paulello Music Wire, 2012. https://www.stephenpaulello.com/sites/default/files/paulello/intros-de-pages/stephenpaulellomusicwire.pdf (accessed 08 August 2023).
[15] Rogante M., 2008. Applicazioni Industriali delle Tecniche Neutroniche, AITN2008, Civitanova Marche, Italy

[16] Mimaki, T. 1975. On Corrosion Fatigue Damage of 0.82%C Piano Wire. J. Soc. Mat. Sci. Japan 24/261, 540–544.
[17] Determinazione delle tensioni residue mediante diffrazione neutronica, 2008. http://www.roganteengineering.it/pagine_servizi/servizi1.pdf (accessed 08 August 2023).
[18] Rogante, M., Rosta, L., 2005. Nanoscale characterisation by SANS and residual stresses determination by neutron diffraction related to materials and components of technological interest. Proc. SPIE 5824, 294–305.
[19] Baraz, V.R., Rundkvist, N.A., Belov, A.V., 1992. Piano wire and strings with high acoustic properties. Met. Sci. Heat Treat. 34, 283–287.
[20] Rogante, M., Mikula, P., Strunz, P., Zavdoveev, A., 2017. Residual stress determination by neutron diffraction in low-carbon steel wires with accumulated shear deformation, MTMS2017, Split
[21] Tomota, Y., Suzuki, T., Kanie, A., Shiota, Y., Uno, M., Moriai, A., Minakawa, N., Morii, Y., 2005. In situ neutron diffraction of heavily drawn steel wires with ultra-high strength under tensile loading. Acta Materialia 53, 463–467.
[22] Van Acker, K., Root, J., Van Houtte, P., Aernoudt, E., 1996. Neutron diffraction measurement of the residual stress in the cementite and ferrite phases of cold-drawn steel wires. Acta Materialia 44/10, 4039–4049.
[23] Phelippeau, A., Pommier, S., Zakharchenko, I., Levy-Tubiana, R., Tsakalakos, T., Clavel, M., Croft, M., Zhong, Z., Prioul C., 2006. Cold drawn steel wires–processing, residual stresses and ductility Part II: Synchrotron and neutron diffraction. Fatigue Fract. Engng. Mater. Struct. 29, 255–265.
[24] Kriška, M., Tacq, J., Van Acker, K., Seefeldt, M., Van Petegem, S., 2012. Neutron and X-ray diffraction study of residual and internal stress evolution in pearlitic steel during cold drawing. J. Phys.: Conf. Ser. 340, 012101.
[25] Hutchings, M.T., Withers, P.J., Holden, T.M., Lorentzen, T., 2005. Introduction to the characterization of residual stress by neutron diffraction, Boca Raton, Florida, U.S.A.
[26] Caratterizzazione di materiali e componenti a livello di micro- e nano-scala mediante diffusione neutronica a piccoli angoli, 2008. http://www.roganteengineering.it/pagine_servizi/servizi2.pdf (accessed 08 August 2023).
[27] Zavdoveev, A., Baudin, T., Pashinska, E., Kim, H.S., Brisset, F., Heaton, M., Poznyakov, V., Rogante, M., Tkachenko, V., Klochkov, I., Skoryk, M., 2020. Continuous severe plastic deformation of low-carbon steel: physical-mechanical properties and multi-scale structure analysis. Steel Research international 92/3, 2000645.

Photobiomodulation: applications in vivo and in structural biomaterials through the activation of cellular chromophores by specific light frequencies

Claudio Santelli[1]

1) Santelli Medical Office, Viale Europa n. 81, 63831 Rapagnano (FM), Italy

Corresponding author: claudiosantelli8@gmail.com

Original scientific article

Abstract: This article focuses on PhotoBioModulation (PBM) that uses electromagnetic light signals to stimulate, with specific frequencies, both differentiation in stem cells and increased mitochondrial energy and antioxidant effects in damaged mature cells. The photoreceptors of light signals are chromophores, atomic groupings located within protein structures present in mitochondria and other biostructures capable of absorbing the electromagnetic radiation of light.
PBM is applied in ophthalmology, neurology, anti-aging medicine, regenerative medicine. It is also used in bioengineering for the production of tissue in vitro for autotransplantation. Human Adipose tissue-Derived Stem Cells (hADSC) from the same patient are grown on structural biomaterials with specific growth factors according to the desired cell lineage and can be stimulated by irradiation via PBM with specific wavelengths.

Keywords: *photobiomodulation; chromophores; structural biomaterials; scaffold; bioengineering*

1. Introduction

The possibility of modulating biological dynamics and stimulating tissue healing through the use of light can probably be traced back to 1967, when Endre Mester replicated an experiment conducted by McGuff in Boston. After more than twenty years, the method was developed with the PhotoBioModulation (PBM) technique that directs light in precise wavelengths to allow a selective regulation of stem cell proliferation and differentiation. Initially known as Low-Level Laser Therapy (LLLT), since 2015 the term PBM has been used more appropriate than the previous definition [1].
With these applications it is possible to modulate biological processes, stimulating or inhibiting them, depending on the selected wavelength and the programmed energy dose [2].
PBM is performed with a medical device equipped with Light-Emitting Diodes (LED) [3].
Therapeutic applications are already in use in the medical field such as PBM using electromagnetic signals (light) with Near-InfraRed (NIR) frequencies, to:

- potentiate and modulate the differentiation of totipotent stem cells into specific cells of single tissues and organs [4]
- perform antioxidant therapies on mature cryo-damaged cells that, when irradiated with NIR light at 950 nm, are able to avoid apoptosis and to increase mitochondrial energy production, resulting in augmented activity of Mitochondrial Membrane Potential (MMP), Adenosine TriPhosphate (ATP) and Cytochrome C Oxidase (CCO) [5] (Figure 1).

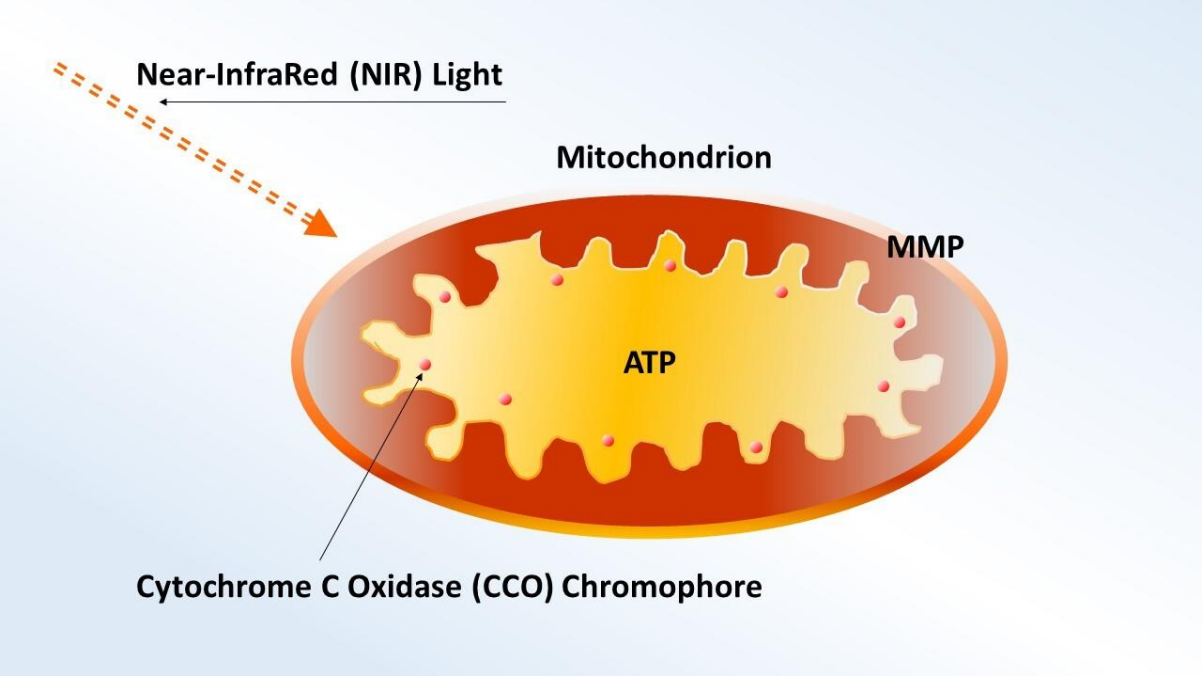

Figure 1. *Mitochondrion with Cytochrome C Oxidase (CCO) chromophore*

PBM, by stimulating the production of ATP in mitochondria, has useful therapeutic effects in the healing of chronic wounds through increased tissue regeneration and repair, reduction of inflammation, pain and oxidative stress [6].

In acute inflammation, PBM modulates cell inflow, release of chemical mediators and macrophage polarization [7]. PBM improved musculoskeletal pain, muscle performance, muscle recovery after exercise, neuropathic pain, lymphedema and oral mucositis [3].

The photoreceptors of light signals are chromophores, atomic groupings (Figure 2) located within protein structures present in mitochondria and other biostructures, capable of absorbing electromagnetic radiation (light). The chromophore CCO, present within the mitochondria, has been identified as one of the most active in the role of tissue repair [1].

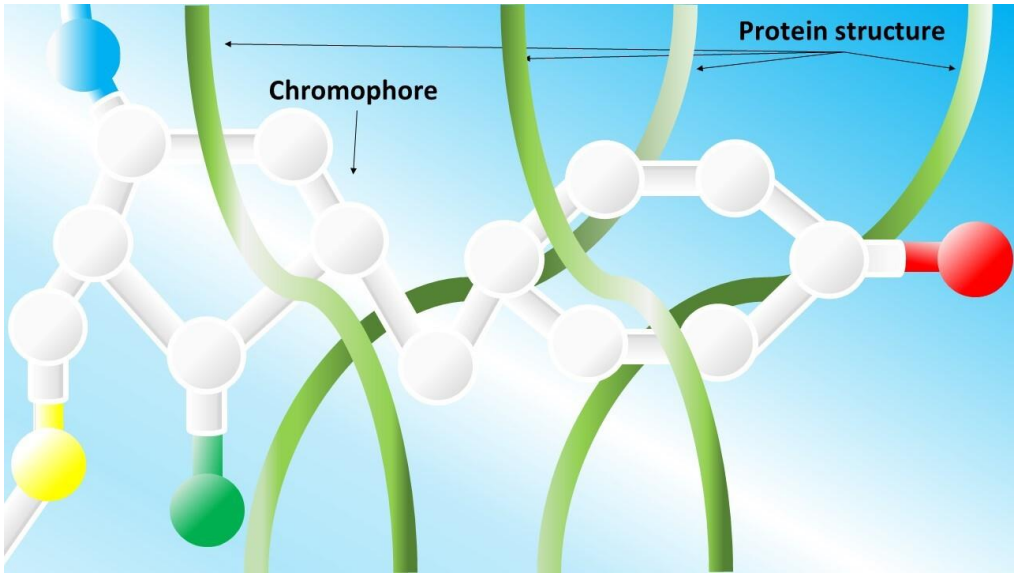

Figure 2. *Chromophore within a protein structure (particular)*

PBM is not a heat therapy. Photoactive protein structures naturally transform light energy into a physical function such as in plant photosynthesis or vision in which most animals acquire light

information through rhodopsin-like proteins known as opsin pigments [8]. When the chromophore is activated by light, it undergoes slight structural changes perceived and amplified by the protein that surrounds it that will activate a macromolecular response and a consequent biological activity [9]. This photochemical reaction activates enzymes that determine a cellular and systemic response even on tissues that have not absorbed photons [3].
The most studied chromophore for these wavelengths is the CCO, which represents the IV unit of the mitochondrial respiratory chain [2].
In addition to the main role played by the CCO chromophore, there are other cellular photoreceptors sensitive to specific wavelengths of light even outside the mitochondria. This was demonstrated by in vitro studies conducted on red blood cells, cells without mitochondria, of pig blood where samples irradiated by PBM with Red (R) light and in the Near InfraRed (NIR) were more resistant to haemolysis and osmotic stress and had better to ability deformation and aggregation than the control sample. The number of potential photoacceptors, therefore, is expanding [10].
Flavins, flavoproteins and cytochromes are thought to be involved in the generation of Reactive Oxygen Species (ROS) and Nitric Oxide (NO) with pleiotropic effects in cell biology. We can represent the interior of cells populated by a network of molecules that behave as bioelectronic circuits and chromophore photosensors [1] (Figure 3).

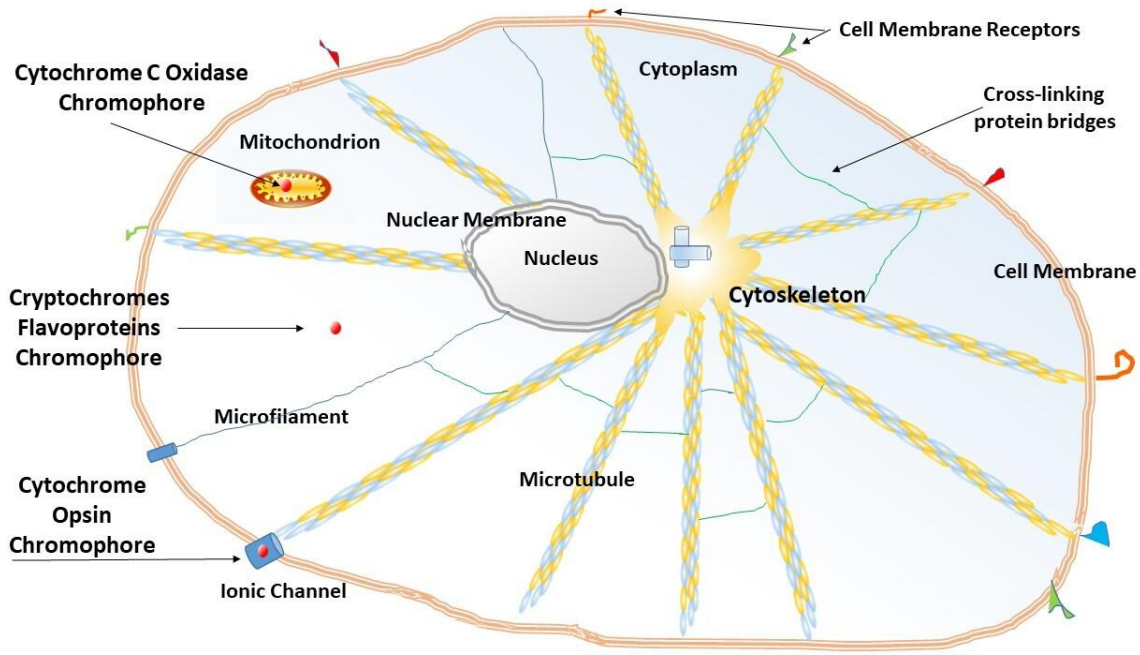

Figure 3. *Cell with cytoskeleton and chromophores*

Through MultiSpectral Imaging (MSI), which provides measurement of reflected electromagnetic radiation (light) from an object over multiple wavelengths in narrow bands, cellular signal patterns can be monitored. The first wavelengths used were those of R, 600-700 nm and NIR, 780-1100 nm. However, there is an increasing evidence that even the shortest wavelengths of green or blue light have biological effects on cells with marked differences as compared to R and NIR light [2]. Opsins are believed to be chromophores sensitive primarily to blue and green photons, since melanopsin has been irradiated with blue light to treat jet-lag, insomnia, depression and affective disorders. The use of light with defined wavelengths allows to selectively manage the type of effect on stem cells, depending on the tissues and the desired results [1] (Figure 4).

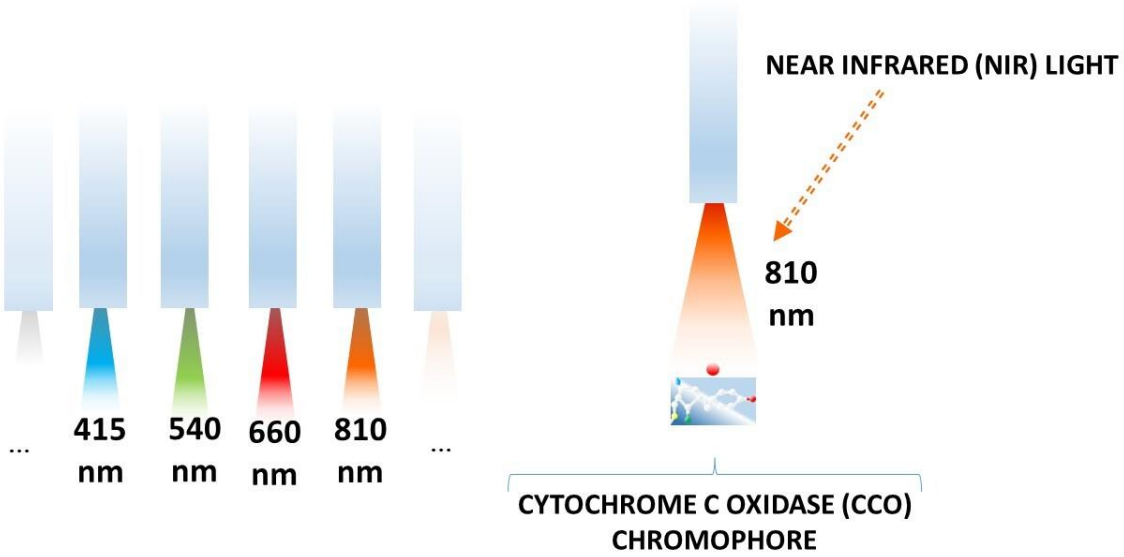

Figure 4. *PBM applies different wavelengths of light based on the desired tissues and effects*

Red and near-infrared light reduces inflammation and pain and stimulates healing through the activation of CCO chromophores within mitochondria and cytochromes opsins that regulate calcium ion channels (Figure 5). It results in increased ATP and NO, and in the modulation of calcium levels with improved cell proliferation and survival and new protein synthesis [11].

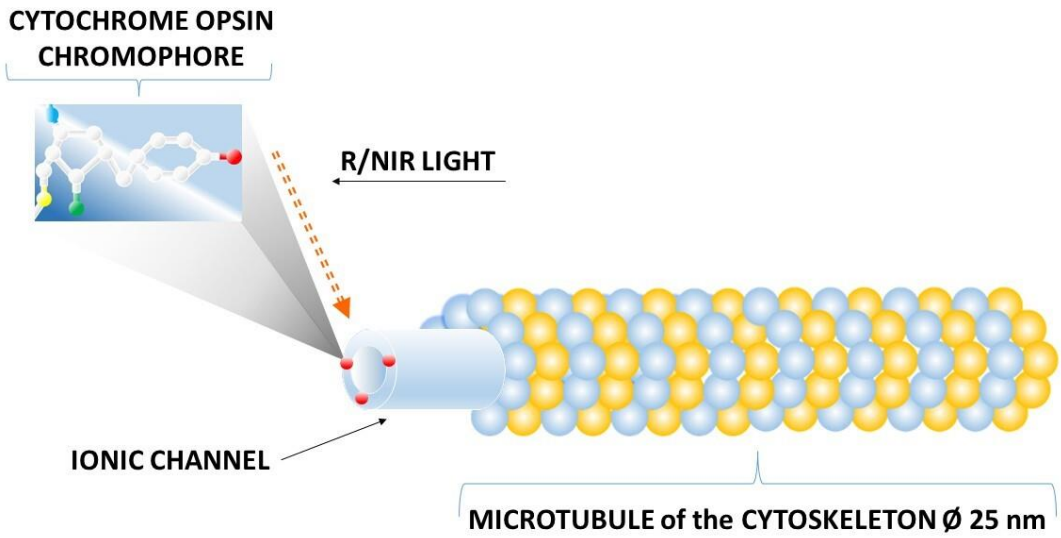

Figure 5. *Opsin cytochromes in an ion channel*

2. Applications and results

In ophthalmology, PBM is used by Dr. Roberto Pinelli in acute and chronic eye diseases such as dry Age-related Macular Degeneration (AMD). In custom treatments, light with wavelengths between 590 nm and 850 nm is radiated for about 4 minutes per eye. The results obtained on the improvement of the vision quality, less eye strain, greater color contrast, better definition and visual acuity are also confirmed by the scanning by Optical Coherence Tomography (OCT) that shows a reduction in drusen. These clinical outcomes remain stable at follow-up after 3 and 6 months, demonstrating that this non-invasive and adverse effect-free treatment can, at certain wavelengths, stimulate the retinal stem cell regeneration [3].

Dr. Pinelli has developed a protocol for the clinical application of PBM with dietary supplementation of antioxidants such as lutein, resveratrol, vaccinium myrtillus, etc. [12].

It is a particular mode of light radiation combined with specific phytochemicals that, in synergy with photons, promote ocular functionality: the Lugano Protocol [13].

Another important field of application of PBM concerns neurobiology [1]. PBM has beneficial neuroprotective, metabolic and hemodynamic effects on the brain demonstrated in both animal and human studies by improving the circulatory system and mitochondrial activity. In older people, PBM has also been shown to have favourable effects on brain's electrical activity by improving mood, learning, attention and memory. These data are very important as PBM can be used, among non-pharmacological interventions, as prevention or companion therapy in age-related cognitive impairment in a population that, worldwide, sees an increase in longevity and the number of elderly people with the consequent decline in cognitive functions and an increase in diseases such as Alzheimer and Parkinson [14].

Even in healthy older adults without neurological problems, PBM improves the frontal cognitive function. Cognitive tests (Eriksen flankers and category fluidity tests) were performed by applying, in the frontal region, PBM devices emitting light at 633 nm and 870 nm. After a single 7.5 minute application in two groups of older adults (one experimental and one control), only patients who received real PBM had a safe and economical improvement in executive frontal brain function compared both to before the test and to the control group that received a fictitious PBM [15].

In bioengineering, tissues are produced to be used for autotransplantation, through the stem cells of the same patient that are grown on structural biomaterials combined with specific growth factors.

The scaffolds used for the cell culture have a morphology, at the nano-scale, similar to the ExtraCellular Matrix (ECM) with two fundamental characteristics: bioconductivity and bioinductivity. These scaffolds can be made from different materials such as biopolymers, bioceramics, composites or metals. In the design phase, their porous architecture, their level of biocompatibility, cell adhesion and proliferation as well as the degree of mineralization are defined [16] (Figure 6).

According to their differentiation potential, stem cells are classified into totipotent, pluripotent, multipotent and unipotent. Recently, human Adipose tissue-Derived Stem Cells (hADSC) are the most widely used for cell cultures in vitro. Adipose tissue has proved to be a preferable source over the others for the availability and ease of removal from the abdomen or hip and for the three methods of collection, through the Coleman technique, liposuction or excision, which are minimally invasive [16].

PBM, combined with chemical factors such as, for example, the basic Fibroblast Growth Factor (bFGF), also finds applications in the field of tissue regenerative medicine and bioengineering thanks to the demonstrated ability to accelerate the differentiation, in various lineages, of stem cells for tissue culture in vitro starting from the patient's cells to subsequently perform an autotransplant [17] (Figure 7).

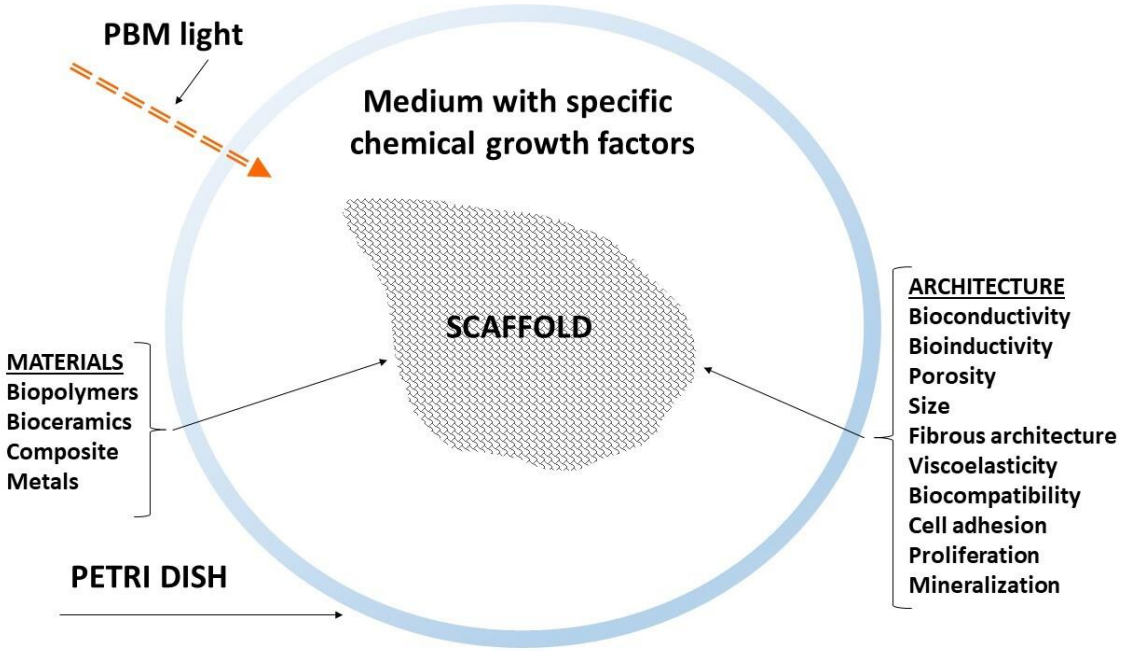

Figure 6. *Structural features of the scaffold*

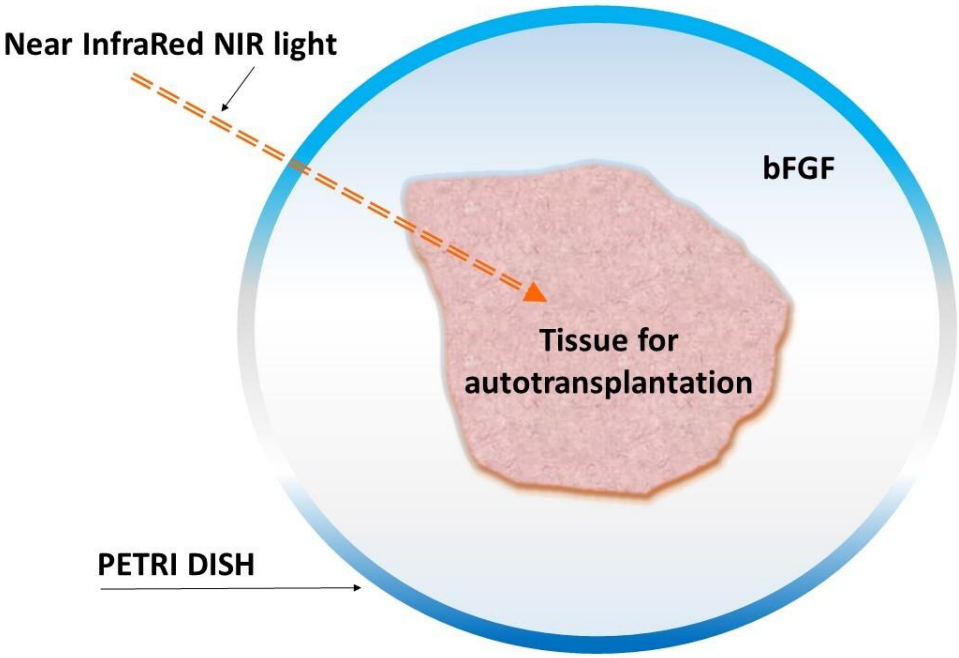

Figure 7. *Biocompatible tissue for autotransplantation grown in Petri dish with patient stem cells and basic Fibroblast Growth Factor (bFGF) stimulated by Near InfraRed (NIR) light*

The hADSC can proliferate if they are grown in a culture medium or they can differentiate if they are grown in an appropriate soil where some factors specific to the desired tissue are added. Chemical growth factors are needed to induce stem cell differentiation into a specific cell phenotype. Stem cells, in fact, can differentiate into various cell lines driven by the type of culture medium and stimulated by the specific wavelength of PBM [17].

If osteoblasts are desired, e.g., factors such as glycerophosphate, bone morphogenetic protein-2, ascorbic acid, 25-dihydroxyvitamin D3, valproic acid are added to the osteogenic culture medium [2].

In this specific case, the most effective PBM, also compared to R light and NIR, to stimulate the differentiation of hADSC stem cells into osteoblasts, will be that with blue wavelengths, 415 nm, and green, 540 nm administered at a dose of 3 J/cm² five times, every 2 days, in cells grown in an osteogenic medium for 3 weeks [2], [18] (Figure 8).

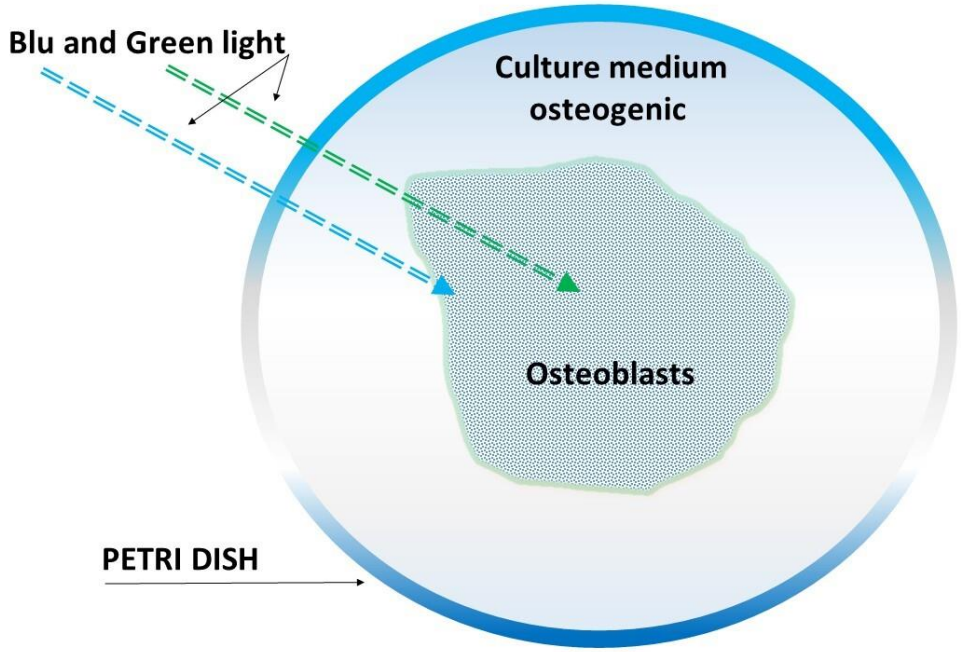

Figure 8. *hADSC stem cells in Petri dish, with osteogenic culture medium, stimulated by blue light, 415 nm and green, 540 nm to obtain osteoblasts.*

PBM in synergy with growth factors stimulates the differentiation of hADSC based on the chosen wavelength and the fluence factor which, generally, to have favourable effects is delivered within 10 J/cm² with output powers below 100 mW to avoid the thermal effect, calculating a defined number of exposures and intervals between each exposure.

These results, obtained on bone biomaterial structures grown in vitro, can represent a useful reference to refine the clinical protocols applied in vivo. In periodontal bone recessions, maxillary bone atrophy to promote pre-implant bone regeneration and osteoporosis therapy many studies have shown positive photobiostimulatory effects on bone regeneration. PBM accelerates the synthesis of new bone matrix by increasing vascularization and osteocytes in irradiated bone by stimulating the release of specific growth factors for the formation of epithelial cells, collagen and fibroblasts [19].

The new biomaterials for regenerative medicine also use the decellularized ExtraCellular Matrix (dECM) to engineer over 15 types of tissues and organs. The most used models are electrospun scaffolds, bioprinted scaffolds and injectable hydrogels [20].

The dECM promotes the adhesion, proliferation, differentiation and migration of stem cells. In periodontal tissue engineering it is a promising structural biomaterial for the repair of damaged tissue as it maintains the complete characteristics of the ECM components as they are present in the native tissue [21].

The incidence of osteoporosis, which is increasing globally, leads to bone fragility and an increased risk of fractures. Regenerative medicine is a developing field and it is considered a possible solution by medical science to restore function and heal diseased or senescent tissues. Stem cells represent the main target of regenerative medicine, since their capacity for self-renewal and for the possibility of differentiating into various cell types, stimulated by PBM which, through the activation of endogenous chromophores, determines both photochemical and photophysical reactions [16].

An effect on the influence of PBM in vitro is also related to cellular senescence and telomere length. Some human dermal fibroblasts, in an in vitro culture, were irradiated by light-emitting diodes with a wavelength of 590 nm at a dose of 30 J/cm² accumulated in 1.200 seconds and applied in a 4-day cycle within a total period of 40 days. The proportion of senescent cells treated with PBM was approximately 20% lower than those in the control group and maintained a longer relative telomere length than those not treated. This study demonstrates that PBM may have antisenescent effects by delaying telomere shortening and suggesting potential reactivation of the telomerase enzyme [22].
The antisenescent effects exerted by PBM on stem cells can be a stimulus both for the search for new applications capable of rejuvenating tissues in vivo, and for finding innovative methods able to program the development, in vitro, of stem cells without unwanted senescence [1].
In ophthalmology, PBM in synergy with phytochemicals and nutraceuticals has been shown to have additional beneficial effects deriving from the removal of toxic residues and the stimulation of mitochondrial turnover [23], [24].
In the future, there will be an increasing tendency to develop non-invasive therapies that can increase our self-healing potential. The discovery, in cells, of an increasing number of sensors and transducers of physical energies, will allow using the diffusive properties of luminous electromagnetic waves. Reprogramming of stem cells, where possible, will take place on site to restore the health of damaged tissues [1].

3. Conclusions

PBM stimulated stem cells to differentiate, while on mature cells it had antioxidant effects preventing apoptosis and increased mitochondrial energy production.
Favourable results have been achieved in the healing of chronic wounds with pain reduction. Red blood cells, after irradiation with PBM, resulted more resistant to haemolysis and oxidative stress and they enhanced their deformability.
Neuroprotective effects have been obtained both in healthy elderly and in those suffering from senile pathologies by improving mood, learning, attention and memory. In ophthalmology it offers a valid therapy for dry AMD and it is useful to prevent and repair retinal pigment epithelium.
PBM is a non-invasive technique that can find more and more applications in regenerative, precision and antiaging medicine, based on the reprogramming of stem cells residing in tissues, to improve the life quality in elderly people who are increasingly numerous all over the world.
The results obtained on red blood cells, devoid of mitochondria, are a stimulus to discover other potential endogenous chromophores present outside the mitochondria.
PBM in combination with growth factors stimulated stem cells grown in vitro to differentiate into a specific biocompatible tissue for autotransplantation.
Research is also oriented to study the therapeutic synergies between photobiomodulation and nutraceuticals with the aim of formulating less and less invasive therapeutic protocols.

Acknowledgments

Dr. Ing. Massimo Rogante is acknowledged for useful discussions.

References

[1] Facchin, F., Canaider, S., Tassinari, R., Zannini, C., Bianconi, E., Taglioli, V., Olivi, E., Cavallini, C., Tausel, M., Ventura, C., 2019. Physical energies to the rescue of damaged tissues. World J Stem Cells. 11(6): 297-321. https://www.ncbi.nlm.nih.gov/pmc/articles/PMC6600852/ (accessed 09 June 2023).
[2] Wang, Y., Huang, Y.Y., Wang, Y., Lyu, P., Hamblin, M.R., 2017. Red (660 nm) or near-infrared (810 nm) photobiomodulation stimulates, while blue (415 nm), green (540 nm) light inhibits proliferation in human adipose-derived stem cells. Sci Rep., 7 :7781. https://pubmed.ncbi.nlm.nih.gov/28798481/ (accessed 01 June 2023).

[3] Pinelli, R., 2020. Photobiomodulation shows the power of light. Ophthalmology Times. https://www.ophthalmologytimes.com/view/photobiomodulation-shows-the-power-of-light (accessed 20 June 2023).
[4] Zomorrodi, R., Loheswaran, G., Pushparaj, A., Lim, L., 2019. Pulsed Near Infrared Transcranial and Intranasal Photobiomodulation Significantly Modulates Neural Oscillations: a pilot exploratory study. Scientific Reports 9, 6309 United Kingdom. https://www.nature.com/articles/s41598-019-42693-x (accessed 24 May 2023).
[5] Choi, W., Baik, K.Y., Jeong, S., et al., 2021. Photobiomodulation as an antioxidant substitute in post-thawing trauma of human stem cells from the apical papilla. Sci Rep 11, 17329. https://www.nature.com/articles/s41598-021-96841-3 (accessed 24 May 2023).
[6] Leyane, T.S., Jere, S.W., Houreld, N.N., 2021. Cellular Signalling and Photobiomodulation in Chronic Wound Repair. International Journal of Molecular Sciences. 22(20):11223. https://www.mdpi.com/1422-0067/22/20/11223 (accessed 27 May 2023).
[7] de Brito Sousa, K., Rodrigues M.F.S.D., de Souza Santos, D., Mesquita-Ferrari, R.A., Nunes, F.D., de Fátima Teixeira da Silva, D., Bussadori, S.K., Fernandes, K.P.S., 2020. Differential expression of inflammatory and anti-inflammatory mediators by M1 and M2 macrophages after photobiomodulation with red or infrared lasers. Laser Med Sci. 35, 337–343. https://link.springer.com/article/10.1007/s10103-019-02817-1 (accessed 04 June 2023).
[8] Terakita, A., Nagata, T., 2014. Functional properties of opsins and their contribution to light-sensing physiology. Zoolog Sci. 31(10):653-9. https://pubmed.ncbi.nlm.nih.gov/25284384/ (accessed 19 May 2023).
[9] Tau, O., Henley, A., Boichenko, A.N., et al., 2022. Liquid-microjet photoelectron spectroscopy of the green fluorescent protein chromophore. Nat Commun 13, 507. https://www.nature.com/articles/s41467-022-28155-5 (accessed 27 May 2023).
[10] Walski, T., Grzeszczuk-Kuć, K., Gałecka, K. et al., 2022. Near-infrared photobiomodulation of blood reversibly inhibits platelet reactivity and reduces hemolysis. Sci Rep 12, 4042. https://www.nature.com/articles/s41598-022-08053-y (accessed 30 May 2023).
[11] Hamblin, M.R., 2017. Mechanisms and applications of the anti-inflammatory effects of photobiomodulation. AIMS Biophys. 4(3):337-361. https://pubmed.ncbi.nlm.nih.gov/28748217/ (accessed 27 May 2023).
[12] Pinelli, R., Bertelli, M., Scaffidi, E., 2020. The first clinical case of dry age-related macular degeneration treated with photobiomodulation and nutraceuticals: a protocol proposal. CellR4, 8: e2833. https://www.cellr4.org/article/2833 (accessed 09 June 2023).
[13] Pinelli, R., Bertelli, M., Scaffidi, E., Bumah, V.V., Biagioni, F., Busceti, C.L., Puglisi-Allegra, S., Fornai, F., 2021. The neurobiology of nutraceuticals combined with light exposure, a case report in the course of retinal degeneration. Arch Ital Biol. 159(3-4):134-150. https://pubmed.ncbi.nlm.nih.gov/35077571/ (accessed 19 May 2023).
[14] Cardoso, F.D.S., Gonzalez-Lima, F., Gomes da Silva, S., 2021. Photobiomodulation for the aging brain. Ageing Res Rev. https://pubmed.ncbi.nlm.nih.gov/34325071/ (accessed 27 May 2023).
[15] Chan, A.S., Lee, T.L., Yeung, M.K., Hamblin, M.R., 2019. Photobiomodulation improves the frontal cognitive function of older adults. Int J Geriatr Psychiatry. 34(2):369-377. https://pubmed.ncbi.nlm.nih.gov/30474306/ (accessed 30 May 2023).
[16] Da Silva, D., Crous, A., Abrahamse, H., 2021. Photobiomodulation: An Effective Approach to Enhance Proliferation and Differentiation of Adipose-Derived Stem Cells into Osteoblasts. Stem Cells :88431 https://www.hindawi.com/journals/sci/2021/8843179/ (accessed 25 July 2023).
[17] Muneekaew, S., Wang, M.J. & Chen, Sy., 2022. Control of stem cell differentiation by using extrinsic photobiomodulation in conjunction with cell adhesion pattern. Sci Rep 12, 1812. https://www.nature.com/articles/s41598-022-05888-3 (accessed 18 June 2023).
[18] Wang, Y., Huang, Y.Y., Wang. Y., Lyu, P., Hamblin, M.R., 2016. Photobiomodulation (blue and green light) encourages osteoblastic-differentiation of human adipose-derived stem cells: role of

intracellular calcium and light-gated ion channels. Sci Rep., 6:33719. https://pubmed.ncbi.nlm.nih.gov/27650508/ (accessed 10 June 2023).
[19] Escudero, J.S.B., Perez, M.G.B., de Oliveira Rosso, M.P., Buchaim, D.V., Pomini, K.T., Campos, L.M.G., Audi, M., Buchaim, R.L., 2019. Photobiomodulation therapy (PBMT) in bone repair: A systematic review. Injury. 50(11):1853-1867. https://pubmed.ncbi.nlm.nih.gov/31585673/ (accessed 15 June 2023).
[20] Brown, M., Li, J., Moraes, C., Tabrizian, M., Li-Jessen, N.Y.K., 2022. Decellularized extracellular matrix: New promising and challenging biomaterials for regenerative medicine. Biomaterials. 289:121786. https://pubmed.ncbi.nlm.nih.gov/36116171/ (accessed 01 July 2023).
[21] Liang, C., Liao, L., Tian, W., 2023. Advances Focusing on the Application of Decellularized Extracellular Matrix in Periodontal Regeneration. Biomolecules. 14;13(4):673. https://pubmed.ncbi.nlm.nih.gov/37189420/ (accessed 01 July 2023).
[22] Arabadjiev, B., Pankov, R., Vassileva, I., Petrov, L.S., Buchvarov, I., 2020. Photobiomodulation with 590 nm Wavelength Delays the Telomere Shortening and Replicative Senescence of Human Dermal Fibroblasts In Vitro. Photobiomodul Photomed Laser Surg., 38(11):656-660. https://pubmed.ncbi.nlm.nih.gov/33090930/ (accessed 20 June 2023).
[23] Pinelli, R., Biagioni, F., Scaffidi, E., Vakunseth Bumah, V., Busceti, C.L., Puglisi-Allegra, S., Lazzeri, G., Fornai, F., 2022. The potential effects of nutrients and light on autophagy-mediated visual function and clearance of retinal aggregates. Arch Ital Biol., 160(3-4):115-135. https://pubmed.ncbi.nlm.nih.gov/36881917/ (accessed 11 June 2023).
[24] Pinelli, R., Ferrucci, M., Berti, C., Biagioni, F., Scaffidi, E., Bumah, V.V., Busceti, C.L., Lenzi, P., Lazzeri, G., Fornai, F., 2023. The Essential Role of Light-Induced Autophagy in the Inner Choroid/Outer Retinal Neurovascular Unit in Baseline Conditions and Degeneration. Int J Mol Sci., 24(10):8979. https://pubmed.ncbi.nlm.nih.gov/37240326/ (accessed 11 June 2023).

Experimental determination of grinding parameters with a ball mill with rectangular lifters

***Nikolay Stoimenov*[1], *Miglena Paneva*[1] *and Peter Panev*[1]**

1) Institute of Information and Communication Technologies – Bulgarian Academy of Sciences, bl. 2, ac. G. Bonchev str, 1113 Sofia, Bulgaria

Corresponding author: nikistoimenow@gmail.com

Original scientific article

Abstract: The investigation of this paper aims to determine experimentally the grinding parameters of a laboratory ball mill with rectangular lifters. The type, shape, dimensions and numbers of lifters were determined in previous work. The design, namely a liner with lifters, is developed for the purposes of easier recharge/change. A liner with eight trapezoidal lifters, that are symmetrically displaced is chosen. The parts of a laboratory ball mill – the drum and the liners with lifters are 3D printed from PLA additive material. The grinding bodies, which are spheres with 9 mm diameter are also produced from 3D material. In order to analyze the interaction of the lifter type with different types of materials, the grinding bodies will be made of 3 different materials - PLA, CarbonFil™ and SteelFill. The critical speed (CS) of the mill, the angle of separation (shoulder angle) and the toe angle in cataract mode of operation are determined experimentally. Experiments are carried out with two different amounts of mill charges - 20% and 30% filling.

Keywords: *laboratory ball mill; rectangular lifter, 3D additive materials; critical speed; angle*

1. Introduction

The study of the interaction between the grinding bodies and the media is important because it affects the production rate of the mill and accelerates the wear of the media, thus being relevant to reducing the costs of the grinding process. In order to investigate the milling processes, it is necessary to work in laboratory conditions. Due to technological advances in 3D modeling and printing this is possible to be done in a controlled environment. The use of a laboratory mill, which grinding medium and bodies are made of 3D materials, allows to analyze the excavation and grinding processes. Through investigating various factors that affect the grinding, it is established that the listed factors have a decisive influence on the high productivity. They include speed (% of critical), fill level (% fraction of the mixer volume occupied by the charge), the shape of the lifters, size and density of particles being processed. [1], [2], [3], [4] and [5]. It is approved that the change in the percentage of filling of a ball mill lead to changes in the charge distribution inside the mill and the power draw [6]. Changes in the charging of a ball mill have the opposite effect on the charge shape and power consumption which weaken the interlocking of particles. The shape and profiles of the liners used for shield plates and lifters have a significant influence on the productivity and effective grinding of the output product. The liner of the inside of the mill protects the drum from rapid wear [7]. Other important factors are the coefficients of friction, rolling friction, and restitution which affect the mode of operation and the resulting shoulder angle and toe angle. The measurements taken are described in [8], [9], [10] and [11]. Danha [12] illustrates the view of the cataract mode of operation in which the grinding has optimal results. It is this mode that will be sought and in which the grinding parameters will be determined.

The investigation aims to determine the parameters of grinding - critical speed, separation angle, and toe angle of a laboratory ball mill in the presence of rectangular lifters whose parts are made of PLA material and grinding bodies made of PLA, CarbonFil™, and SteelFill at different percentage of charge.

2. Apparatus and materials

The laboratory ball mill used throughout this investigation has an outer diameter of the chamber of 0,269 m, an inner diameter of 0,228 m, a length of the mill of 0,013 m (used for one row of balls), 2 transparent plexiglass covers allowing to investigate the interaction of the grinding ball, 1.1 kW motor with controllable speed and intelligent control. The used mill is constructed with options for easy change of different grinding media (lifters), and inserting or emptying grinding bodies from different materials and sizes. There are 8 innovative lifters spaced circumferentially around the mill shell. The dimensions of the mill are presented in Table 1. The direction of rotation of the ball mill is clockwise. The speed of the ball mill will be determined with an electronical tachometer.

Table 1. *Dimensions of a rectangular lifter*

Parameters, Init	Values
Width, m	0.0214
Height, m	0.0129
Volume, m^3	$3.73.\ 10^{-6}$

According to the volume of the rectangular lifters, the volume of the free inner space of a ball mill is V- $4{,}9016.10^{-4}$ m^3.

In order to determine the moment of critical speed and separation and incidence angle a high-speed camera NAC MEMRECAM HX-6 [13] is used. The camera allows for shooting at different resolutions and frames per second (fps). For this study the frames are set to 1000 fps, allowing to catch every frame. The processing of the videos from the high-speed cameras was carried out by Vicasso 2009 software [14].

A 3D Printer Tevo Tornado is used for the printing of the drum, the liner with lifters, and the grinding bodies, which are sphere-shaped. The used material for the parts of the ball mill is PLA additive filament. The 3D printed spheres are with a diameter of 9 mm and 100 % infill which are printed according to the producer's recommendations and according to performed experiments [15] with infill of 100%. The weight, volume, and density of spheres are measured in [16] and [17] and each mill charge is determined experimentally. The investigation of the grinding bodies was made with two different percentages of charge of the ball mill - 20 % and 30 %. For 20% filling of a ball mill, the number of spheres is 125, and for 30% filling - 175 pieces. Experiments are performed without the presence of grinding material.

3. Experimental Results and Discussion

Firstly, the critical speed of the mill at 20% filling with spheres made of the three types of materials- PLA, SteelFill, and CarbonFil™ is determined. The critical speed is reached when all the spheres fit evenly around the circumference.

The achieved velocity is measured with a tachometer and the moment is determined with the help of the high-speed camera. The data are presented in Table 2.

The next searched mode of operation is the cataract mode. It is determined by using the data from the video, recorded with the high-speed camera. The measurement of the shoulder angle is performed in 3 points. The starting point is the moment of separation (shoulder angle) of the grinding bodies, the second point is the center of the mill and the third point is the end of the mill horizontally from the center. The toe angles are performed also in 3 points. The starting point is the moment of incident of the grinding bodies with the chamber, the second point is the center of the mill, and the third point is the end of the mill horizontally from the center. The measurements of the angles were performed with Vicasso 2009 software. In Figure 1 views from the detected shoulder angle and toe angle of the ball mill using different grinding materials are shown.

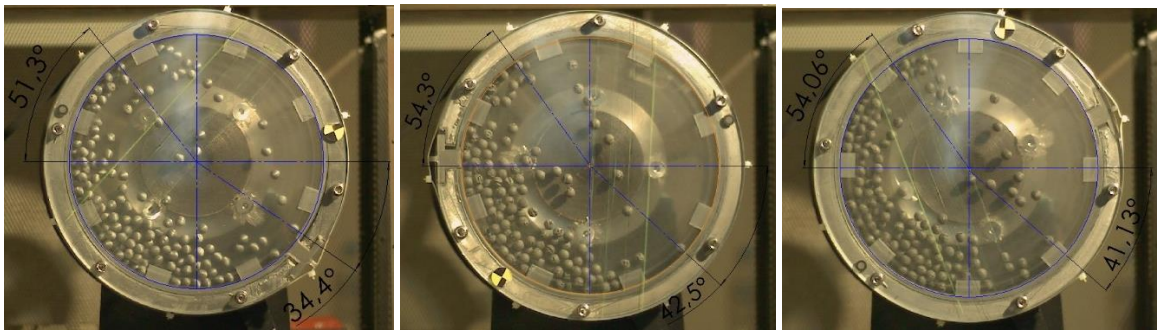

a) b) c)

Figure 1. *Shoulder and toe angle at 20% filling of the ball mill: a) PLA, b) SteelFill, c) CarbonFil™*

At 30 % charge of the ball mill, the same procedure of measurements of the grinding parameters is used. The determined critical speed, shoulder angle, and toe angle are measured with a tachometer and Vicasso software. The snapshots are presented in Figure 2. The results of all experiments are presented in Table 2.

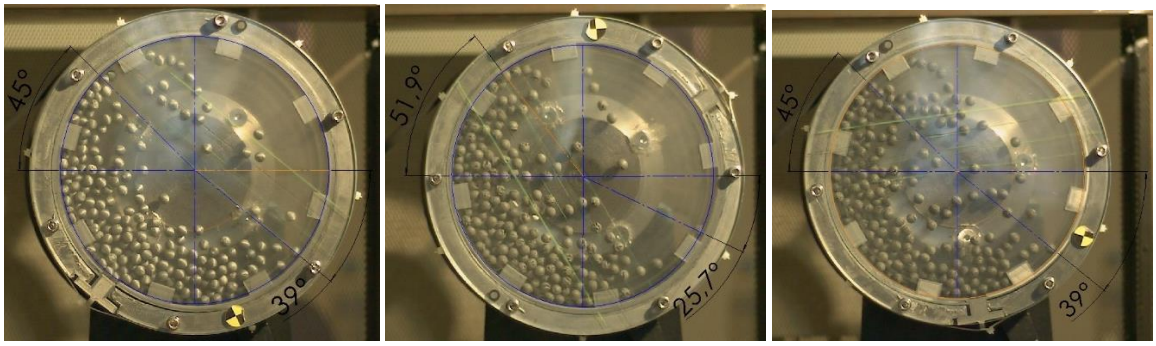

a) b) c)

Figure 2. *Shoulder and toe angle at 30% filling: a) PLA, b) SteelFill, c) CarbonFil™*

Table 2. *Experimental Results*

% of Filling	Material	Critical speed, [rpm]	Shoulder angle,[°]	Toe angle,[°]	Ball mill speed, [rpm]	% of Critical speed
20% filling	PLA	137,2	51,3	34,4	58,6	42,7
	CarbonFil™	130,4	54,3	42,5	54,8	42,02
	SteelFill	130	54,06	41,13	51,5	39,6
30% filling	PLA	138,2	45	39	57,2	41,4
	CarbonFil™	127,6	51,9	25,7	54,7	42,9
	SteelFill	123,7	45	39	56,3	45,5

After determining the critical speed and the speed of the mill at the optimal cataract mode of operation, the % V_{Cr} was calculated. At 20% and 30% filling % V_{Cr} is in the range between 39,6 % and 45,5 % which are with close borders. From the conducted experiments it is seen that the values of critical speed at the two charges of filling, the PLA filament is with the biggest values and SteelFill with lower ones. The PLA is with the lightest weight and in interaction with the rectangular lifters it needs a higher power, compared to the other materials. SteelFill is the heaviest material and in this case, it needs the least power. At 20 % filling the material with the biggest shoulder angle and smallest energy consumption is SteelFill. At 30 % filling the material with the biggest shoulder angle and smallest toe angle is CarbonFil™ which means the highest performance is achieved. Those grinding bodies have also the smallest speed in the cataract regime and good energy consumption.

4. Conclusion

In the present work, the parameters of work of a laboratory ball mill with 8 rectangular lifters, produced from PLA material interacting with grinding bodies produced from three different materials - PLA, SteelFill, and CabronFil™ are determined at two different charge amounts - 20% and 30% filling of the ball mill. The critical speeds, shoulder angles, and toe angles at the two levels of filling are experimentally determined. Due to the use of the high-speed camera, the exact moments for determining the parameters were recorded. The data are reported with Vicasso 2009 software. The ball mill rotates in a clockwise direction, the critical speed at which the particles start to centrifuge differs for each material and for the different % of filling of the ball mill. The results show that the required speed of the ball mill with grinding media with rectangular lifters to reach the cataract mode of operation is in the range between 39,6 % and 45,5 % for the three types of materials - on average 42,4 % of CS. From the observed materials, the best energy efficiency and grinding efficiency at 20% filling of the mill is obtained with the SteelFill filament, and at 30% - with the CarbonFil™ filament. When studying the movement and interaction between grinding bodies, it is extremely important to consider side factors such as the weight of grinding bodies, coefficients of friction, restitution, shape, lifter size, etc.

5. Future steps

In future work, it is planned that the data of the conducted experiments with the three types of lifters made with innovative, trapezoidal, and rectangular shapes to be compared to that of a laboratory ball mill without lifters. The purpose is to verify in the working process which shape of the lifter and which material of the grinding bodies obtain the best performance and energy efficiency results. Simulations with software working on the discrete element method will be made with the same parameters, used in this publication aiming to compare the real experiment to the simulation modelling experiment.

Acknowledgments

This work was supported by project No КП-06-Н47/5 “Research and optimization of the interaction between grinding bodies and media with an innovative shape”, financed by the Bulgarian National Science Fund.

References

[1] Stoimenov N., Karastoyanov D., Klochkov L., Study of the Factors Increasing the Quality and Productivity of Drum, Rod and Ball mills, 2nd Int. Conf. on Environment, Chemical Engineering & Materials, ECEM '18, Malta Sliema, June 22-24, 2018, AIP (American Institute of Physics) Publishing house, Vol. 2022, Issue 1, ISBN: 978-0-7354-1740-3, pp. 020024-1 - 020024-6.

[2] RADIAL AND AXIAL MIXING OF PARTICLES IN A DRY BATCH BALL MILL. Available from: https://www.researchgate.net/publication/265272523_RADIAL_AND_AXIAL_MIXING_OF_PARTICLES_IN_A_DRY_BATCH_BALL_MILL [accessed Jul 11 2023].

[3] M. Jahani Chegeni* and S. Kolahi, An Investigation on Effect of Shell Liner Type on Performance of Industrial SAG Mills Using DEM, Journal of Mining and Environment (JME), Vol. 11, No. 2, 2020, 387-404, DOI: 10.22044/jme.2020.9048.1794.

[4] Nikolay Stoimenov, Miglena Paneva and Stanislav Gyoshev, Determination of Ball Mill Separation Angle of Different Materials, 26th International Conference on Circuits, Systems, Communications and Computers (CSCC 2022), Crete Island, Chania, Grece, July 19-22 2022, Published by IEEE, 2022, ISBN:978-1-6654-8186-1, 327-331.

[5] Miglena Paneva, Peter Panev and Nikolay Stoimenov, Overview and Analysis of Lifter Types and Ball Mill Operating Parameters, 12th International Scientific Conference, “TechSys 2023” – ENGINEERING, TECHNOLOGIES AND SYSTEMS, Technical University of Sofia, Plovdiv Branch, 18-20 May 2023, AIP Conference Proceedings e-ISSN:1551-7616, (Scopus), Accepted for publication.

[6] Paul W. Cleary, Charge behaviour and power consumption in ball mills: sensitivity to mill operating conditions, liner geometry and charge composition, Int. J. Miner. Process. 63 (2001), pp. 79–114.

[7] Stoimenov N., Innovative Relative wear of lifters, XIV International Scientific Congress “Machines. Technologies. Materials. 2017”, 15-18 March 2017, Borovets, Bulgaria, volume 1, Section “Machines” pp. 25-28, ISSN: 2535-0021 (Print), 2535-003X (Online), Publisher: Scientific Technical Union of Mechanical Engineering Industry – 4.0.
[8] Stoimenov N., Gyoshev S., Paneva M. and Panev P., Determination of the friction coefficient of 3D printed materials - Part I - Rolling friction, 10th International Conference on Mechanical Technologies and Structural Materials (MTSM 2021), Split, Croatia, September 23-24, 2021, Croatian Society for Mechanical Technologies, Croatia, ISSN: 1847-7917, pp. 149-152.
[9] Gyoshev S., Stoimenov N., Paneva M., Determination of the friction coefficient of 3D printed materials - Part II - Sliding friction, 10th International Conference on Mechanical Technologies and Structural Materials (MTSM 2021), Split, Croatia, September 23-24, 2021, Croatian Society for Mechanical Technologies, Croatia, ISSN: 1847-7917, pp. 43-46.
[10] Stoimenov, N., Gyoshev, S., 2022, Restitution Coefficient Determination of 3D Printed Materials, Proceedings of Seventh International Congress on Information and Communication Technology. Lecture Notes in Networks and Systems, vol. 465. Springer, Singapore, pp. 663-669.
[11] Stoimenov N., Paneva M., Kotseva G. and Sokolov Bl., Simulation Modelling of Coefficient of Restitution, XIX INTERNATIONAL SCIENTIFIC CONGRESS MACHINES, TECHNOLOGIES, MATERIALS, 09-12.03.2022, BOROVETS, BULGARIA, Proceedings VOLUME II, Scientific Technical Union of Mechanical Engineering Industry – 4.0, ISSN 2535-0021 (PRINT) ISSN 2535-003X (ONLINE), pp. 132-135.
[12] Gwiranai Danha, Identifying opportunities for increasing the milling efficiency of a Bushveld Igneous Complex (BIC) Upper Group (UG)2 ore, May 2016, ReearchGate, DOI: 10.13140/RG.2.1.1771.6087.
[13] NAC Memrecam HX-6 Data Sheet, https://rius.iict.bas.bg/smart_lab_bg.html#1 (last accessed May 2023).
[14] Vicasso 2009 software - www.pixoft.co.uk (last accessed July 2023).
[15] Paneva M., Panev P. and Kotseva G., SPHERES MODELLING AND EXTRUSION BY 3D ADDITIVE TECHNOLOGY, XXXI International Scientific and Technical Conference, ADP - 2022., 29.06 ÷ 02.07.2022, Sozopol, Bulgaria., Publishing house of TU-Sofia ISSN – 2682-9584, Publisher Department “Automation of Discrete Production Engineering“ Mechanical Engineering Faculty, Technical University – Sofia, pp. 253-258
[16] Stoimenov N., Paneva M. and Gyoshev St., Determination of Ball Mill Separation Angle of Different Materials, 26th International Conference on Circuits, Systems, Communications and Computers (CSCC 2022), Crete Island, Chania, Grece, July 19-22 2022, Published by IEEE, 2022, ISBN:978-1-6654-8186-1, 327-331.
[17] Paneva M., Stoimenov N., Panev P., Comparison of determined theoretically and experimentally critical speed of a ball mill. 11th International Conference on Mechanical Technologies and Structural Materials (MTSM 2022), Croatian Society for Mechanical Technologies, 2022, ISSN:1847-7917, pp. 131-135.

Digitalization in the CAD/CAM process chain of customized products

Josip Florian Strutz[1,2]

1) Ceratizit Besigheim, Zeppelinstraße 3, 74354 Besigheim, Germany

2) University of Slavonski Brod, Mechanical Engineering Faculty in Slavonski Brod, Trg I. Brlić-Mažuranić 2, 35000 Slavonski Brod, Croatia

Corresponding author: josip.strutz@gmail.com

Professional paper

Abstract: The digitalisation of the CAD/CAM process chain has revolutionised the manufacture of customised products. This publication examines the impact of digitalisation on the design and manufacturing stages, focusing on the integration of standardisation in CAD/CAM with algorithms, detailed job shop scheduling, tool management and logistics, centralised data flow (ERP integration), paperless production and quality assurance. The traditional process chain involved extensive manual work, resulting in longer lead times and higher costs. However, with the advent of digitalization, CAD/CAM technologies have streamlined the entire process, enabling faster and more efficient production of customised products. Overall, the digitalization of the CAD/CAM process chain has significantly improved the efficiency and accuracy of the production of customised products. This paper highlights the benefits of digitalization, such as reduced lead times, greater planning reliability, enhanced design capabilities and improved manufacturing precision, which contribute to increased customer satisfaction and business competitiveness in the era of customisation.

Keywords: *CAD/CAM; customised products; digitalization; process chain*

1. Introduction and Motivation

Producing components in small quantities with high quality requirements to meet specific customer requirements poses significant challenges for companies ([1], [2], [3] and [4]). Manufacturers need to pass on the full cost of downtime and overheads to their customers. Often, the high costs are misunderstood by customers who are used to mass production and find it difficult to estimate the high costs [5]. To be able to offer competitive prices to customers as a large company with typically high administrative costs, it is important to establish an optimal process chain. To administrate and maintain a drawing in such companies can cost up to 3400 € [6].

These process chains require the flexibility to dynamically process orders at the right time while minimising set-up times. The result is capacity-tested and cost-optimised manufacturing (MFG) from a quantity of one.

2. Process Architecture

In the world of complex products, typically made up of individual components, the challenges start with gathering customer requirements. Well-defined procedures and forms create a solid database on which to build. During the quotation process in sales support, it is necessary to systematically process the collected customer requirements and include them in the price calculation without exception. Product configurators, running on laptops or tablets, guide the salesperson through the process and ensure a comprehensive data base through an intelligent modular structure. Ideally, the configurator can be operated online by the customer, reducing sales costs and directly generating the 3D CAD file. However, this is not usually feasible for complex products or a company's entire product range.

The completed data fields are directly accessible in the company's Enterprise Resource Planning (ERP) system, providing a data-based cost structure. Personal dependencies in pricing are minimised as only individual transactions are considered by sales support. This approach has proven effective for complex products, as it requires coordination of individual aspects prior to quotation.
In the design phase, the generated requirements profile is seamlessly integrated as it is linked to the manufacturing order. It forms the basis of the product lifecycle and is stored in the Product Lifecycle Management (PLM) system accordingly. Any changes to the requirements result in a new version of the previous profile. Versioning links the CAD model to the requirements that have been created, enabling target/actual comparisons to be made.
As mentioned earlier, CAD data is managed in a PLM system. Ideally, the CAD/CAM and PLM systems should be from the same vendor to avoid media disruption. In addition, it is essential that the entire engineering process can be carried out exclusively within a single system. Undoubtedly, the ERP system serves as the foundation of any well-established company, encompassing all operations from finance to quality assurance. However, in engineering there is always a media break, but relevant information such as bills of materials (BOMs) must be controlled and transferred. The exemplary BOM of an assembly is redundant and must be automatically updated in the ERP with each CAD change, providing controlled redundancy.
When designing custom products, it is also important to implement design guidelines, as they bring many benefits. Uniform aesthetics for customer drawings may not directly result in measurable success, but standardised processes also produce machine-readable files. These readable files are ensured by attributes with defined algorithms programmed in the application programming interface (API) of the CAD software [7], model-based definition (MBD) and product manufacturing information (PMI). In addition, design guidelines provide a means of eliminating unnecessary detail and focusing on the essential aspects of a design. They are a way of capturing and applying knowledge on a daily basis, which is particularly important in one-off or low-volume production. Figure 16 shows an example of the indexable insert pocket which is designed with the help of the API program (left). On the right the figure shows the manufacturing strategy for the CAM-Programmer, which is loaded simultaneously in the background within the design process. In the process, both the tool paths including the production strategy, the necessary tools and the following in-situ measurement are loaded and imported to the part.

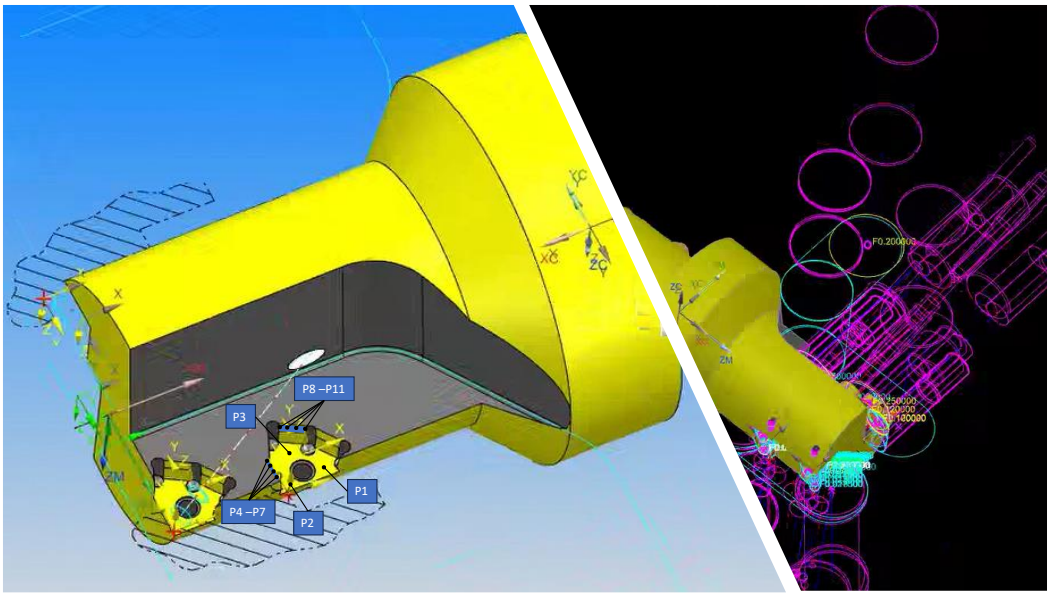

Figure 16. *Example of the automatic generation of the indexable insert pockets (left) with the adaptive control measure points and showing the corresponding MFG strategy (right) by using the CAD/CAM API interface*

CAM programming also uses the 3D design as a basis, incorporating the features defined in the design guidelines for further machining. Individual programmes can be used, or they can be based on the features used or the MBD [8]. Modern CAD-/CAM software of course offer the opportunity to use templates and feature based design or manufacturing, but these methods can’t compete with a unique programmed solution in the API. The results of the API programs are defined and proven manufacturing strategies that are repeated for all custom products. In a series of tests comparing various geometries using feature-based design, templates and the programmed API application, an average time saving of 66% was achieved in CAM programming.

The finished CAM programmes are stored in the PLM system on completion and made available to the machine. Distributed numerical control (DNC) provides controlled file storage on the machine, ensuring that the correct programme is always available. When a file is being edited by design or CAM programming, locking triggers immediate deletion on all machines, effectively eliminating production errors, although not completely as programmes in progress cannot be locked. A further improvement is full integration with the machine control, which informs the operator and stops the machining process. This integration is particularly recommended for customised solutions, as customer requirements can change dynamically and the production of the entire job scope incurs higher costs.

Standardisation in the previous steps not only results in significant time savings, but also reduces tool variance [9]. The complexity of products increases exponentially due to different customer requirements, as does the number of tools required for machining. This is due not only to geometry but also to the materials used. The use of aluminium, tool steels, heat-treated steels or pre-treated steels requires a variety of tools. While aluminium can be efficiently machined with ultra-hard cutting materials (PCD, CBN, etc.), these cutting materials have their limitations when it comes to steel. The same applies to the machining of tool or heat treated steels compared to pre-treated steels. While the machining of untreated steels does not require complex manufacturing strategies, hard machining is much more challenging. Manufacturing strategies (depth of cut, feed movements, etc.) require special know-how and, above all, special tools.

In order to minimise tool variance further, even for non-standard geometries, intelligent algorithms are needed to support the CAM programmer. The basis for this intelligence is provided by previously programmed workpieces [10]. These workpieces contain all the necessary information, even though they are rarely used. By automatically comparing the finished design with the geometric features of previous jobs, tool recommendations are displayed.

To display these suggestions, the existing CAD models are pre-matched to the required customer application via a knowledge database. To do this, every CAD file in the PLM system is broken down into its individual components [11]. The PMIs and the geometry data in the CAD model ensure that the classification of the features is guaranteed. This ensures that the design and CAM programming do not have to start from scratch, but only have to make adjustments. These adjustments are usually limited to changes in the manufacturing strategy, which is recorded in appropriate rule sets. When new rules are implemented or tools are replaced, all data affected by the changes is locked in the PLM system. Reasons to change rules or tools can be caused by newer developments and improvements.

Tool storage is a core task in a comprehensive view of the digitalization of machine tool processes. Inventory management in the ERP system offers many advantages, as components can be automatically reordered. In addition, individual identification numbers (IDs) in an item management system ensure that the entire lifecycle of a tool is covered, as well as automatic commissioning [12]. Ideally, both the cutting components and the tool holders have unique IDs.

For cutting components, Data Matrix Codes (DMC) are suitable because they can be very small and readable on a 3 mm diameter shaft. For toolholders, RFID chips have proven to be more reliable than DMCs in terms of machine readability. Once the cutting component and holder are assembled, a link is created between the two in the tool management software to form a complete tool [13]. The RFID on the holder acts as a unique ID. When the RFID is scanned after linkage, the instances used for that complete tool, the complete tool number and the stored correction measurements from the tool presetter are displayed. By scanning the tool as it is inserted into the machine and fully integrating it

into the machine control system, mix-ups and typing errors are eliminated. The entire cycle is shown in Figure 17. With this shown workflow the time savings are enormous in the tool presetting and a return on invest lower than three years is achieved. Furthermore, the downtime of the machines could be significantly reduced, because of missing tools.

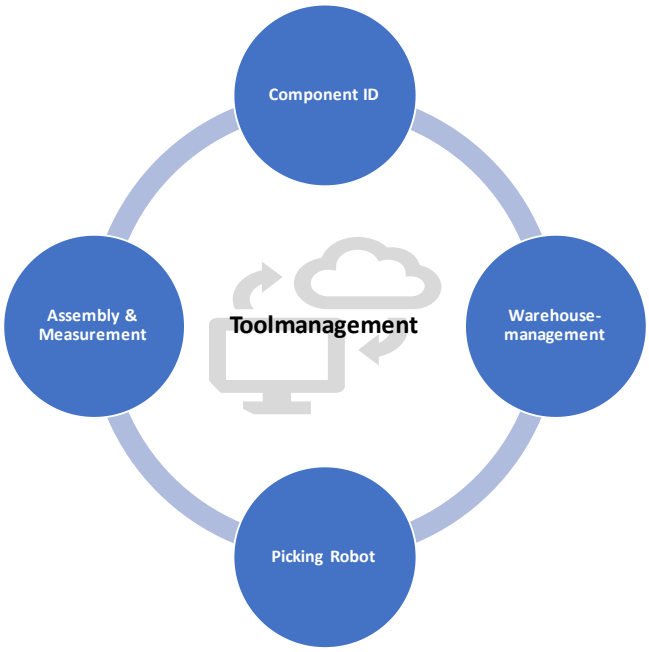

Figure 17. *Idealized organization in tool management*

When manufacturing products, it is important to continue to use the fully integrated process chain. To this end, only 3D models enriched with PMI and MBD are used, completely eliminating paper-based drawings. Accompanying order documents will be replaced by energy-efficient electronic labels with a display. In addition, the planned complete moulds, including fixtures, are used for set-up-optimised planning of production orders on the machines.
The DNC connection of the machines described above is a necessary step. However, the final stage of the production process is the measurement.
Chips and coolant can reflect when an optical measurement system is used during milling. Therefore, a more robust system is needed to withstand these influences ([14] and [15]).
For standardised geometries, the inspection is carried out in situ using a tactile 3D touch probe to compare nominal and actual data. If a deviation is detected, a correction is made immediately, enabling adaptive process control. Such a project was carried out on a DMG CTX Beta turn-mill centre using a BLUM LC50 3D touch probe to measure insert seats (Figure 16, left, Point P1 to P11). The difficulty with this measurement is the complex geometric relationship of the measuring points P4 to P11, as they are measured using a virtual sphere. The sphere is in contact with the inclined contact surfaces (blue), so manual corrections by the machine operator can quickly be too large or too small. Between those four points on the surface a regression line is calculated. The difference between two points is calculated and stored in the machine control via the additional application "Vectorprobing" with the following formula:

$$Inspection\ point\ difference\ two\ axis_i = \sqrt{(X_i - X_{min})^2 + (Y_i - Y_{min})^2} \quad (1)$$

The accuracy of the measurement was determined by repeating the measurement of one insert seat, randomly measuring four insert seats and manufacturing them, and then deliberately manufacturing

insert seats that were too small (-0.05 mm radius correction) to determine the acceptance of the correction values. All those test scenarios are made three times to exclude a random error. In total, an accuracy of 3.6 µm was achieved in the worst case - the process has been validated for use and is in production.

To ensure the quality of the manufactured parts, a 3D scanners is used as measuring devices to compare the manufactured product with the CAD data. MBD is essential in this process as it automatically compares the nominal and actual contours. In the final step, the measurement results are uploaded to the CAQ system and stored together with the serialised customer products. These data sets are redundantly available in the ERP system to provide the supply chain with access to this data for further use. Figure 18 visualizes the entire process chain from the beginning in the sales department to the finished quality assurance.

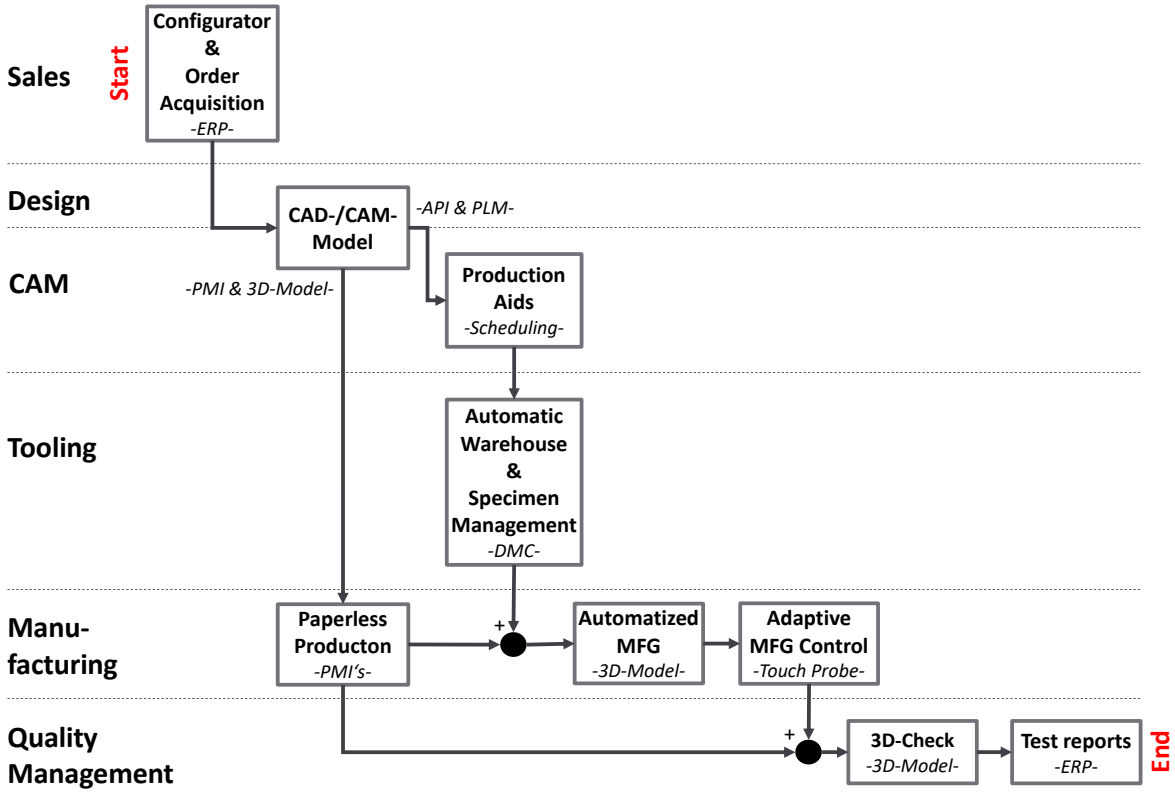

Figure 18. *From sales to quality check in a digitalized process chain centralized in the ERP-System*

3. Conclusion and Outlook

The process chain shown here demonstrates a seamless process from sales through to quality control of the finished, customised product. By implementing well-designed digitisation solutions, errors are eliminated as early as the requirements profile stage, paving the way for full system integration. The seamless integration of the ERP and engineering software suite enables a controlled transition between systems. In engineering, starting with the design department, it is essential to work according to well-defined, cross-location guidelines. Design, with strict implementation of guidelines, MBD and PMI, forms the basis for all subsequent processes, including automated measurement control using 3D scanners.

The limitations of the process outlined here are the pre-established standardisation in design, programming and manufacturing. In the case described, customised components are produced, but these are often made up of recurring geometric elements. In special machine manufacturing, this approach is very limited and applicable to only a few geometric elements. Depending on the complexity of the contour, in-situ inspection of the manufactured geometry can involve a significant development effort, which requires careful consideration during implementation.

Overall, achieving end-to-end digitalization in a company does not mean limiting it to a specific area, but always considering the entire process. Value-creating activities can be consistently and efficiently improved through digitisation, especially because standardised and transparent processes are established.

References

[1] Ogunsakin, R., Marin, C.A., Mehandjiev, N., 2021. Towards engineering manufacturing systems for mass personalization: a stigmergic approach. International Journal of Computer Integrated Manufacturing, vol. 34, no. 4, 341–369.
[2] Mourtzis, D., Doukas, M., 2014. Design and Planning of Manufacturing Networks for Mass Customisation and Personalization: Challenges and Outlook. Procedia CIRP, vol. 19, 1–13.
[3] Hu, S.J., 2013. Evolving Paradigms of Manufacturing: From Mass Production to Mass Customization and Personalization. Procedia CIRP, vol. 7, 3–8.
[4] Fang, F.Z., Li, Z., Arokiam, A., Gorman, T., 2016. Closed Loop PMI Driven Dimensional Quality Lifecycle Management Approach for Smart Manufacturing System. Procedia CIRP, vol. 56, 614–619.
[5] Wang, Y., Ma, H.-S., Yang, J.-H., Wang, K.-S., 2017. Industry 4.0: a way from mass customization to mass personalization production. Adv. Manuf., vol. 5, no. 4, 311–320.
[6] Ehrlenspiel, K., Kiewert, A., Lindemann, U., 1998. Grundlagen der Kostenrechnung für die Produktentwicklung. In: Kostengünstig Entwickeln und Konstruieren. VDI-Buch. Springer, Berlin, Heidelberg.
[7] Lobov, A., Tran, T.A., 2020. Object-oriented approach to product design using extended NX Open API. Procedia Manufacturing, vol. 51, 1014–1020.
[8] Wang, Z., Zhang, S.-W., Wang, N., Xu, J.-Y., Cheng, D.-J., 2023. A feature-based assembly information modeling method for complex products’ 3D assembly design. Proceedings of the Institution of Mechanical Engineers, Part B: Journal of Engineering Manufacture, vol. 237, no. 9. 1311–1325.
[9] Wellmann, F., 2019. Datengetriebene, kontextadaptive Produktivitätssteigerung von NC-Zerspanprozessen. Apprimus Wissenschaftsverlag.
[10] Schuh, G., Guetzlaff, A., Schmidhuber, M., Krug, M., 2021. Creating Transparency on Product Variety Through Data-driven Similarity Analysis, 2021 IEEE International Conference on Industrial Engineering and Engineering Management (IEEM), Singapore.
[11] Hedicke-Claus, Y., Langner, J., Stonis, M., Behrens, B.A., 2019. Klassifizierung von Schmiedeteilen mittels KNN. WT Werkstattstechnik, vol. 109, no. 11-12, 822–827.
[12] Ried, F., Härdtlein, C., Ziegler, S., Miller, A., Fottner, J., 2020. Intelligente Steuerung einer automatisierten Werkzeuglogistik mittels mobiler Robotik. Zeitschrift für wirtschaftlichen Fabrikbetrieb, vol. 115, no. 10, 707–710.
[13] Chen, J.-Y., Yi-Ling, L., Lee, B.-Y., 2023. Development of the Adaptive System for Tool Management. Tehnicki vjesnik - Technical Gazette, vol. 30, no. 2, 648–654.
[14] Bulgaru, M., Bocăneț, V., Muntean, M., 2003. Research regarding tactile scanning versus optical scanning. MATEC Web Conf., vol. 299, 4013.
[15] Lehmann, P., 2003. Optical versus tactile geometry measurement: alternatives or counterparts. Proc. SPIE, vol. 5144, 183–196.

Ship bearings testing system - shaft repair welding process technology

***Slaven Šitić*[1] *and Josip Palinić*[1]**

1) University of Split, University Department of Professional Studies, Kopilica 5, 21000 Split, Croatia

Corresponding author: sl.sitic@oss.unist.hr, jp48789@oss.unist.hr

Professional article

Abstract: Shafts have important uses in many diferent branches such as aerospace, agriculture, automotive, consumer products, transportation, oil and gas, mining, and industrial manufacturing fields. These tools generate and channel force in a wide range of mechanical equipment, from cars and planes to machines and appliances. The focus of this work is on this type of shaft.This paper describes one process of repairing a shaft that, due to the impossibility of obtaining new one it in a short period of time, was made of two different steel materials. The shaft is made of quenched and tempered medium carbon steel and the flange is made of low carbon structural steel. Medium carbon content in steel can cause, if inadequate care in the welding process, the appearance of a crack in the welded joint. Proper preparation of the welded joint, appropriate technologies and heat treatment before, during and after the welding process will result in quality weld and enable the normal functioning of the shaft for testing ship bearings.

Keywords: *heat treatment; welding technology; carbon steel*

1. Introduction

Shafts are most often made in such a way that they can ensure normal operation in the intended conditions and lifetime. Ship shafts have the task of transmitting forces and moments and are most often located between the driving machine and the propulsion device that enables the movement of the assembly. The subject of this work is the repair of a shaft that serves the purpose of testing bearings and their properties as an intermediate piece. The standard shaft was not supplied due to time constraints, but was made from existing and available materials by welding and machining. The welding technology was not prescribed, and during welding, a crack appeared between the flange and the shaft. It is common for shafts to be produced by forging as a single piece and by subsequent machining of the appropriate dimensions or by friction welding of the shaft and flange. As a rule, this flange is blind with a neck, and the process of welding and heat treatment after the welding process makes it possible to achieve the optimal properties necessary for the exploitation of the shaft.

2. Welding procedure specification and heat treatment

2.1 Preparation for welding and joint positioning

A crack was observed on the shaft and flange around the entire circumference, in the area of the heat-affected zone next to the weld itself. It is also visible on the axis of Figure 1 that the zone affected by heat is very narrow, only a few millimeters, which indicates that the preheating process was not carried out. In order to carry out a high-quality repair, it is necessary to remove the weld as well as the part on the shaft that has penetrated so that the eventual irregularity and remnants of microcracks can be removed by the grinding process. Preparation for welding has been completed

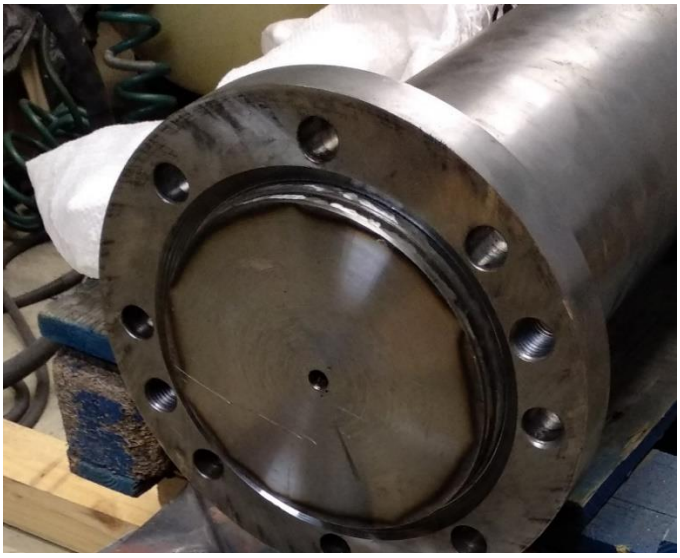

Figure 1. *The picture shows the heat affected zone and the sliding flange with the weld and cracks removed*

2.2 The influence of chemical composition and CE on the welding process

As previously emphasized, due to the short period of time for the acquisition of the appropriate shaft material, an available shaft was procured, and the connection to the drive element will be achieved by means of a flange. The flange is the so-called sliding flange that passes over the shaft. The material of the shaft is CK 45, i.e. according to EN 1.0503 Ø 240 , and the flange material is St 37-2, i.e. EN 10025. Both are carbon steels, one low carbon (flange) and medium carbon (shaft). The carbon content of the shaft is less than 0.45% carbon and CE approximately 0.45, this can create an apparent problem in the welding process. According to some authors [1], for thicknesses above 25 mm and CE greater than 0.45, it is mandatory to preheat particularly thick material. In the process of constructing such a complex system, an oversight may occur and this information, that is, the preheating process, may be ignored. It is very important to consider the dimensions of the joint and the corresponding chemical composition of the material given in Table 1.

Table 1. *Chemical composition of the based and filer material*

Material		*C*	*Mn*	*P*	*S*	*Si*	*N*
CK 45 (1.0503)	*Shaft*	*O,42 -0,45*	*0,5-0,8*	*0.035*	*0,03*	*0,4*	
St 37-2,	*Flange*	*0,17 -0,20*		*0,05*	*0,05*		*0,009*
VAC 60	*Filler material*	*0,08*	*1,5*	*0,025*	*0,025*	*0,9*	

In Carbon Equivalent (CE) calculations, it can be concluded that for steel with a lower percentage of carbon, as is the case with the shaft material, lower preheating temperatures are required. From Table 2 [2] it is evident that preheating should be done already at CE above 0.41. According to some authors, preheating between 150 and 250 °C [3] is suggested due to the limit result of CE, and the possibility is also left that preheating is "not necessary" in the limit case. According to Upton's diagram[4], for a percentage of carbon higher than 0.4%, the martensite start is slightly below 300 °C, which indicates the need for a higher preheating temperature compared to the proposed one.

According to the TTT diagram in Figure 2 [5], steel CK 45 has a very high martensite start temperature, already at 340 °C. Given that the speed of heat removal in the heat-affected zone is close to the cooling speeds at which a martensite structure can form in that area, it is clear that preheating temperatures must be higher than the martensite start temperature and prevent the formation of a martensite structure.

Table 2. *Common Carbon Equivalent, weldability and preheating*

Common CE Value Classifications		
Carbon Equivalent (CE)	*Weldability*	*Preheating*
Up to 0.35	*Excellent*	*Not necessary*
0.36-0.40	*Very Good*	*Not necessary*
0.41-0.45	*Good*	*Necessary*
0.46-0.50	*Fair*	*Necessary*
Over 0.50	*Poor*	*Necessary*

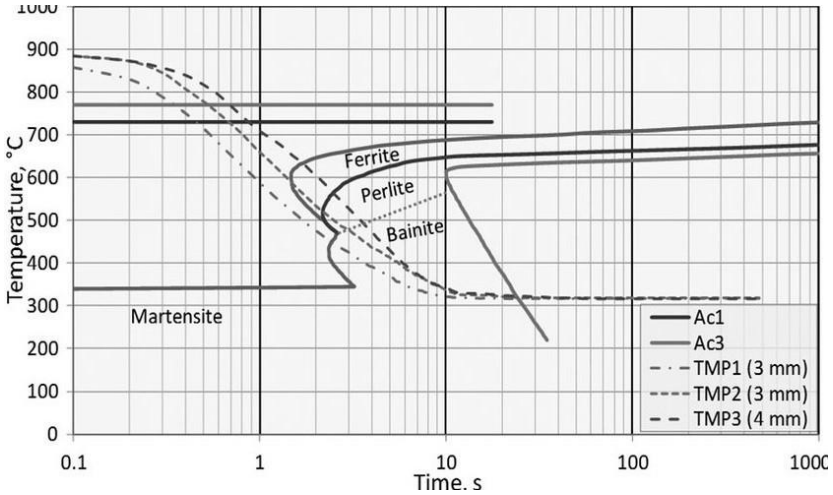

Figure 2*. TTT diagram CK 45 [5]*

This indicates the problem of welding CK 45 steel. Manufacturers [6] classify this steel in the group of materials that are intended to be welded by the friction process [7] with controlled heat input and appropriate heat treatment after the welding process, as well as that the welding process is problematic. The approach to welding must be strictly defined as preheating, temperature control during the welding process and final heat treatment by softening. Due to its heat input, the welding process must be defined through welding technology. It is also important to note that after the preheating process, the welding process begins. After each pass, the temperature is controlled and care is taken to ensure that the preheating temperature does not fall below 350°C.

2.3 Welding technology and heat treatment diagram

It is necessary to follow the instructions for welding. Welded joint (shaft and flange) will be positioned and preheated to temperatures of 350 °C as can be seen in the diagram heat treatment Figure 3. Heat treatment refers to preheating, temperature control during welding and reheating, and heat treatment of softening after the welding process is completed. This is done in order to avoid the possibility of martensitic structure and thus the appearance of cracks.

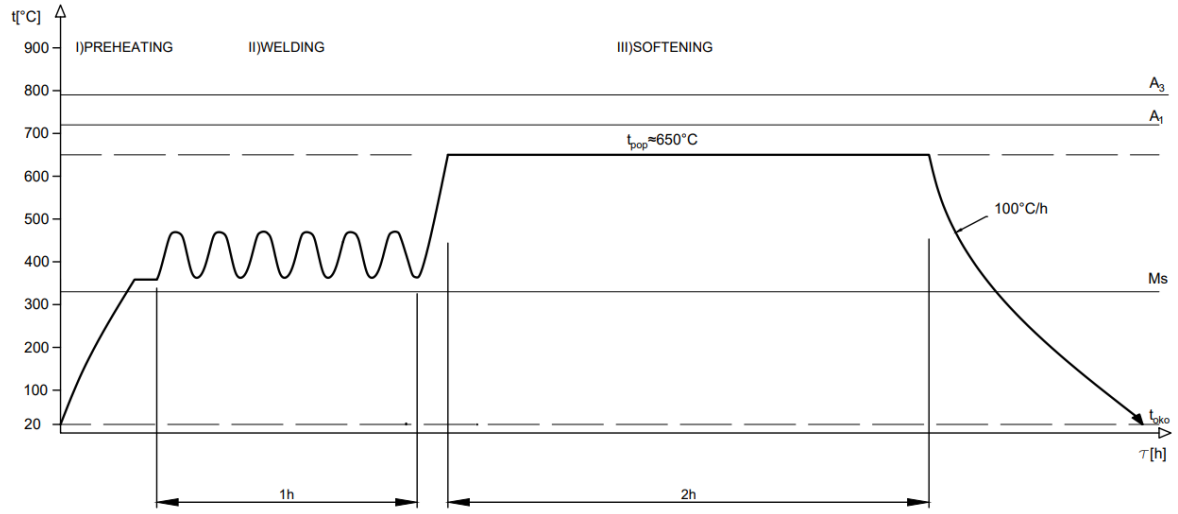

***Figure 3**. Time temperature dijagram of Preheating,welding and heat treatment of softening*

The MIG process with a mixture of argon and 2% oxygen gases will be used for welding. The additional material is VAC 60 wire with a diameter of Ø 1.2 and the weld is an angle joint as in Figure 4. The welding sequence is defined in such a way as to reduce the angular deformation and bring it within the limits provided for machining. Intermediate layers and passages will enable optimal heat input and the required weld geometry.

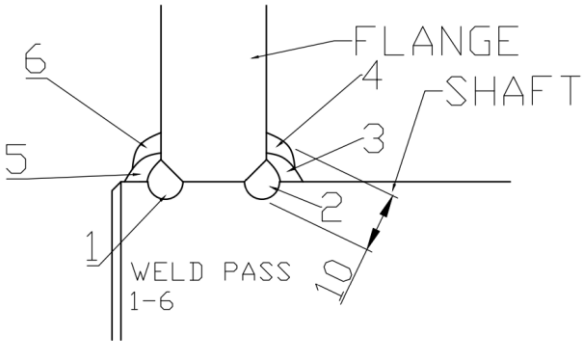

***Figure 4.** Weld joint (flange and shaft) shown with numbered sequence of passes*

During the transport and delivery of the shaft, it was agreed that the bearings should not be removed. The bearings placed in this way will enable the rotation of the shaft and facilitate the welding process. In Figure 5.a, the bearings that will be used for turning and enabling welding in a horizontal position are shown.

Figure 5. a *shaft with bearings* ***b.*** *furnace bilt around flange and shaft*

All passages will be made continuously with a current of 150A and a voltage of 16V. The speed of the wire will be 4 meters per minute and the height of the arc 2 mm. The arch will be of transitional type. After each pass, the temperature will be controlled and reheating will be performed if necessary. Welding technology will reduce deformations. The welded flange is wider so that the finish will eliminate deformation by the cutting process. The welds will be visually controlled after each pass. If irregularities are observed, the welding process will be interrupted. After laying the last pass and visual control, the welded joint continues to be heated up to the yield temperature of 650 °C. At this temperature, the piece will be kept for two hours and slowly cooled in an improvised oven as in Figure 5.b. The welded joint after heat treatment and visual inspection must have a suitable overhang. During the machining process by cutting on a lathe, it is necessary to control the machining parameters in order to confirm that the welded joint is free of hard and brittle martensitic structure and the corresponding overhang.

After machining, the shaft is mounted on a bearing testing device. Once the system passes the control measurements satisfactorily, it is put into trial operation as shown in Figure 6.

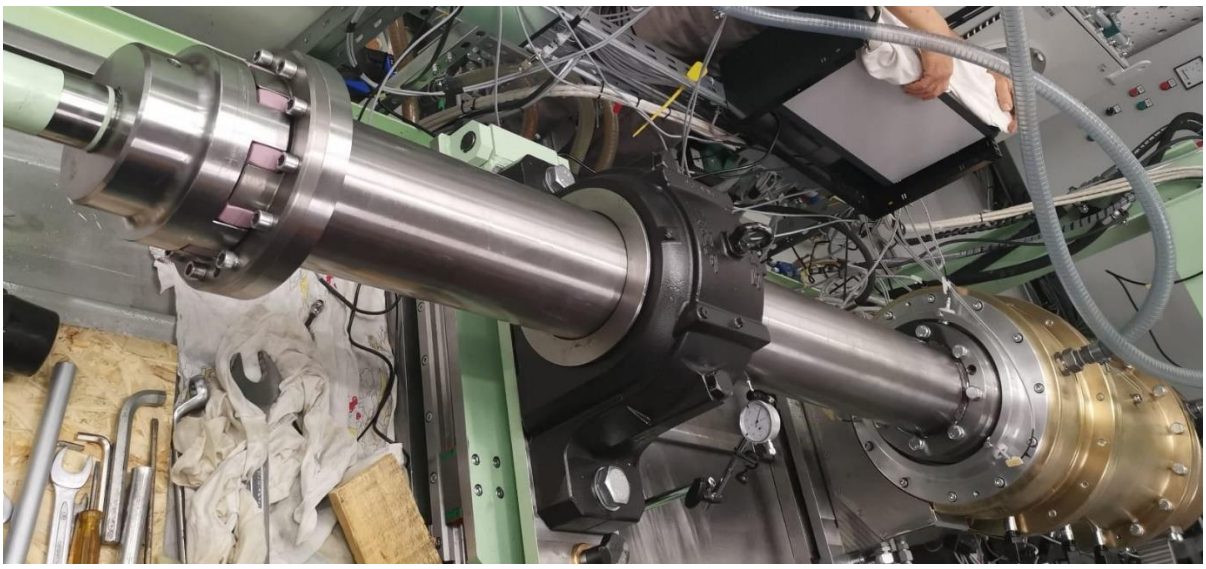

Figure 6. *Testing and controling period*

3. Conclusion

Only with the correct welding technology that corresponds to the given material is it possible to achieve a fit-for-purpose joint. We often do not find suitable materials or the necessary dimensions on the market, so various constructive solutions are used to overcome the problems that may appear on the production process. There is always the question of economic profitability and technical possibilities, but also the limit of production time. This paper presents one such solution. Different materials welded by the appropriate welding process with proper heat treatment and adherence to welding instructions can result in a quality welded joint.

References

[1] Boris Anzulović, Zavarivanje, FESB 1990
[2] https://www.round-bars.com/products/ck45-carbon-steel-din-1-1191-sew550/ Halden special steel (accessed 27 July 2023)
[3] https://www. Carbon Equivalency in Welded Steel Components with LIBS - Analyzing Metals.html Thermo Fisher scientific (accessed 25 July 2023)
[4]Stupnišek, M., Cajner, F.: “Osnove toplinske obradbe metala“, Zagreb, 2001.
[5] https://www.weltstahl.com/1-0503-werkstoff-c45-stahl-datenblatt/ Welt stahl sorten (accessed 29 July 2023)
[6] Čelici za poboljšavanje Slovenske Železarne, Železarna Ravne, Ravne na koroškem 1111/84
[7] Characterization of Friction Stir and TIG Welded CK45 Carbon Steel Mohammadreza Rafati,[1] Amir Mostafapour,[1,*] Hossein Laieghi,[1] Mahesh Chandra Somani,[2] and Jukka Kömi[2] Bolv Xiao, Academic Editor

Numerical analysis of the fracture zone during bending in layers of different types of wood

***Amra Talić-Čikmiš*[1], *Nedim Hurem*[2] *and Nermina Zaimović-Uzunović*[1]**

1) Faculty of Mechanical Engineering, Fakultetska 1, 72000 Zenica, Bosnia and Herzegovina

2) HARA d.o.o., Gračanica bb, 71 300 Visoko, Bosnia and Herzegovina

Corresponding author: amra.talic.cikmis@unze.ba

Original scientific article

Abstract: Different experimental configurations, in which there are also different definitions of initial conditions, were numerically simulated using the finite element method. A three-dimensional nonlinear numerical model was developed to simulate the behavior of unreinforced beams of different types of wood. Numerically modeled flexural strength test was performed in accordance with ISO 13061-4. The maximum breaking force and the obtained results are defined by the previously defined mathematical model. The numerical model can readily accommodate different geometries and material properties, and is therefore a useful tool to optimize the design of the beams.

Keywords: *wood; numerical simulation; flexural strength test; mathematical model; FEM*

1. Introduction

The aim of the research is to examine the significance of the influenced parameters of solid wood board, specifically its density *(ρ)* and thickness *(d)* on its bending strength in parallel with the stretching of wood fibers and the analysis of experimental data from the aspect of possible higher bending strength, while not compromising the quality of the plate material and reducing the total cost of production. Based on the experimental results, i.e. the maximum bending force at four points, in accordance with the standard BAS EN 789, modelling of the influencing parameters to the maximum fracture force (F_{max}) has to be done [1,2].

2. Design of experiment

Experimental research related to this work is based on measuring the maximum bending stress forced up to the moment of fracture of a solid board, made in five different thicknesses and five types of wood: spruce, poplar, beech, ash and oak, previously processed into clean workpieces and thereafter cut into sample dimensions according to BAS EN 789[3].

The experiment used pure specimens of 20 mm thick spruce, 18 mm and 22 mm thick poplar, 16 mm, 20 mm and 24 mm thick beech, 18 mm and 22 mm thick oak and 20 mm thick ash, of different dimensions in length and width. Determination of wood density (bulk density) was done according to the standard BAS EN 13061-2: 2016, where small samples of dimensions 30 x 30 x d mm were taken.

The experiment used pure specimens of 20 mm thick spruce, 18 mm and 22 mm thick poplar, 16 mm, 20 mm and 24 mm thick beech, 18 mm and 22 mm thick oak and 20 mm thick ash, of different dimensions in length and width.

Determination of wood density (bulk density) was done according to the standard BAS EN 13061-2: 2016, where small samples of dimensions 30 x 30 x d mm were taken.

Final expression of the model for determining the fracture force of a board, in which the stretching of wood fibers are parallel, is as follows[4]:

$$F_{\max} = -21{,}97 + 0{,}029\rho + 0{,}53b \quad (1)$$

After obtaining the model equation, it is useful to check the homogeneity of the dispersions of the experiment at the point of replication using the Cochran criterion and the adequacy of the model by determining the multiple regression coefficient. Checking the homogeneity of dispersions according to the Cochran criterion showed that the Cochran coefficient of the model *Kh = 0.533,* which is less than the tabular value for the presented central plan of the experiment which is *Kt = 0.544*, so it can be concluded that the dispersion of experimental results is homogeneous. The value of the regression coefficient of the model was calculated and is R = 0.9288, which means that the linear model of the plate fracture force describes the accuracy of the experimental results with 92.88%, which is a very good accuracy of the model.

3. Numerical modeling

3.1. 3D slab model

The main goal of numerical modeling of appropriate wood treatment procedures is to compare the results of numerical analysis and the results obtained by experimental testing[6]. Numerical analysis was performed using the finite element method (FEM) with the commercial software Abaqus. This program enables three-dimensional nonlinear analysis of elements made of orthotropic materials, as well as analysis of solutions to constant problems.

All elements of the system are modeled with "solid" finite elements (C3D8) – spatial 3D finite elements with 8 nodes (Figure 1). These elements in each node have 6 degrees of freedom, three displacements and three rotations. The deflection at the center of the girder and the support reaction are recorded for each step to draw a load-deflection diagram, which best describes the behavior of the girder.

In the transverse plane of symmetry, the boundary conditions are set so that displacement in the longitudinal direction and rotation around the horizontal and vertical axes are limited ($u_x \neq 0$, $u_y \neq 0$, $u_z = 0$, $\phi_x = 0$, $\phi_y = 0$, $\phi_z \neq 0$). Similarly, in the longitudinal plane of symmetry, movement in the direction of the transverse horizontal axis and rotation around the longitudinal axis and the transverse vertical axis are limited ($u_x = 0$, $u_y \neq 0$, $u_z \neq 0$, $\phi_x \neq 0$, $\phi_y = 0$, $\phi_z = 0$). The support at the end of the support is modeled as a roller support preventing the movement of the support in the vertical direction. Movement of the support in the longitudinal direction is allowed, as it is allowed during the experimental test.

According to the results of the experimental test, the fracture criteria are based on the state of maximum stress, that is, when the tensile stress in the longitudinal direction, in a certain step of the movement, reaches the limit value force F_{max}.

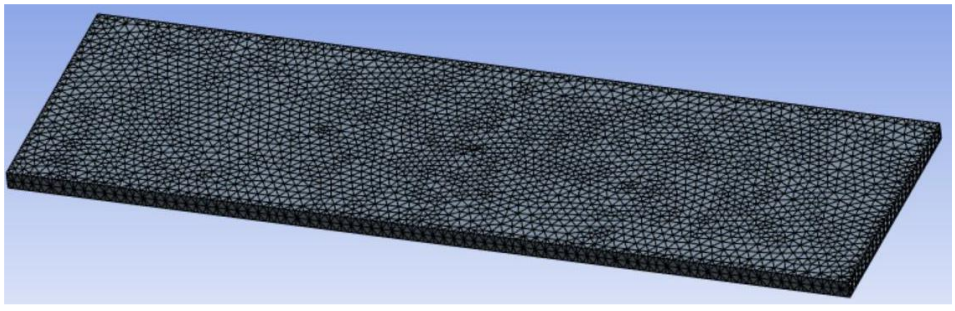

Figure 1. *Divided into finite elements - 3D slab model*

Defining an appropriate model for the material is essential to achieve an accurate prediction of the mechanical characteristics of the support. In unstrengthened beams, failure usually occurs in the tension zone, before any plasticization occurs in the compression zone, so the linear-elastic model is quite appropriate. A linear-elastic ideal-plastic material model was used for the behavior of wood under pressure, while a linear-elastic (brittle) model was used for wood exposed to tension.

The theory of anisotropic plasticity is applied in the model to include the plastic behavior of the wood in the three upper lamellas in the pressure zone.

The theory includes bilinear behavior for wood in three orthogonal directions as well as in three shear planes. Hill's criterion [5] was used as a condition for the transition of the material into the plastic region. This criterion is a generalized version of the Mises condition of plastic flow, which takes into account the anisotropy in the strength of the material. Hill's potential function can be expressed over the component voltages as:

$$f(\sigma)=\sqrt{F(\sigma_{22}-\sigma_{33})^2+G(\sigma_{33}-\sigma_{11})^2+H(\sigma_{11}-\sigma_{22})^2+2L\sigma_{23}^2+2M\sigma_{31}^2+2N\sigma_{12}^2} \quad (2)$$

where F, G, H, L, M and N are constants calculated on the basis of material strength characteristics for different directions.

The material characteristics used in the numerical models were determined on the basis of experimental testing of the material [6] and on the basis of well-established relations and published data in the literature. It is assumed that the characteristics of the material are independent of the speed of load application. The presence of bumps and other imperfections in the wood is not taken into account. The effects of the environment, such as humidity and temperature, on the behavior of the wood were also not considered.

Wood is considered as an orthotropic material, therefore it has independent mechanical characteristics in three mutually perpendicular directions (ie the longitudinal direction, parallel to the wood fibers, and two directions perpendicular to the longitudinal direction). Twelve elastic constants (nine of them are independent) are needed to characterize the elastic behavior of wood. These constants are three elastic moduli (Ei), three slip moduli (Gij) and six Poisson's ratios (vij). The modulus of elasticity (E1) in the direction of wood fibers was determined experimentally. Other modules: E2, E3, G12, G13, G23 were calculated according to the following relations given by Bodig and Jayne [7].

The material constants used in the numerical analysis are given in Table 1. Wood has a different modulus of elasticity in tension, compression and bending in the direction and perpendicular to the direction of the fibers. However, the differences are small, and for practical reasons it was adopted that the elastic moduli of wood have the same values regardless of the type of stress.

Table 1. *Overview of the characteristics of the materials*

Wood	
Modulus of elasticity E [MPa]	
E_1	11080
E_2	886
E_3	554
Poisson’s coefficients [-]	
ν_1	0.37
ν_2	0.42
ν_3	0.47
Modulus of sliding [MPa]	
G_{12}	791
G_{13}	744
G_{23}	79

The adopted stresses at the yield point necessary for defining the plastic behavior of wood are presented in Table 2. The values were determined experimentally and based on data available in the literature. For calculation purposes, it was assumed that the strengths in the transverse directions (radial and tangential) are the same. Otherwise, the strength in the radial direction is slightly higher, due to the increased resistance due to the presence of numerous core rays.

Table 2. *Yield strength adopted in numerical analysis*

Yield stress (MPa)						
$\bar{\sigma}_{11}$	$\bar{\sigma}_{22}$	$\bar{\sigma}_{33}$	$\bar{\sigma}_{12}$	$\bar{\sigma}_{13}$	$\bar{\sigma}_{23}$	$\bar{\sigma}^{0}$
36.3	5.0	5.0	6.1	6.1	3.0	36.3

3.2. Results of numerical analysis

Numerical analysis, on previously described models formed by finite elements, was performed for an support made of five type of wood. The models were loaded incrementally until the limit load was reached. Fracture zone during bending in layers are shown in Figure 2. The values of the bending deflection determined by numerical calculation with average values are shown in Figure 3.

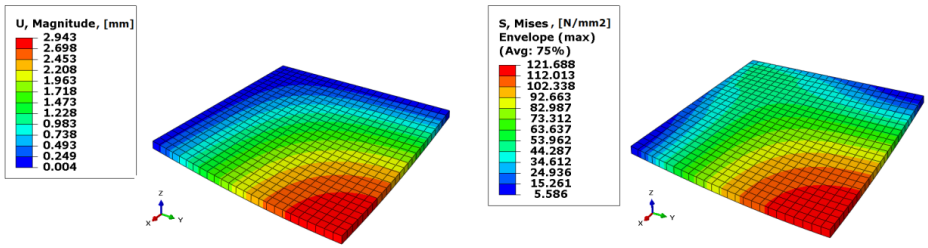

a) b)

Figure 2. *Fracture zone during bending in layers a) deflection [mm]; b) stress according to von Mises*

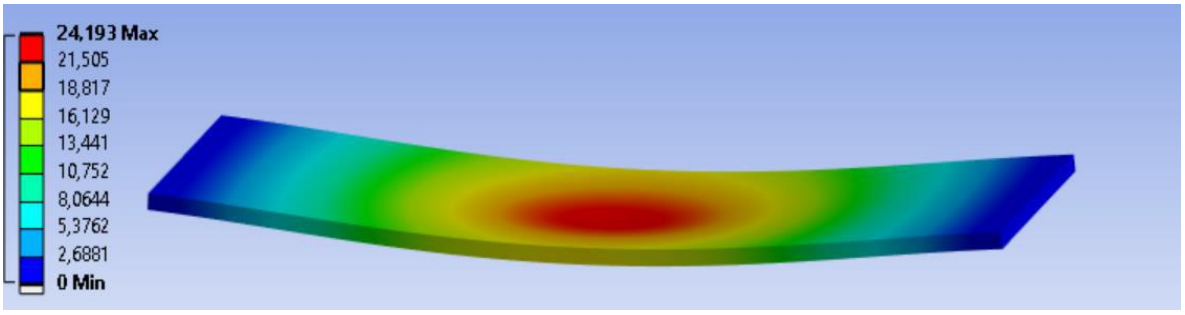

a)

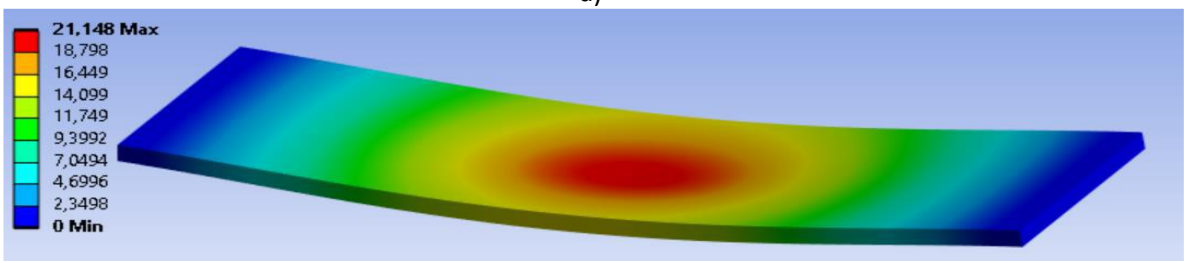

b)

Figure 3. *Values of vertical displacement (mm) in the MKE model,*

a) beech 18 mm, b) oak 22 mm

Figure 3 shows the stress distribution in the wood at the ultimate load. The longitudinal section in the axis of symmetry allows easy monitoring of the voltage change along the support, as well as in cross sections. Based on the default displays of normal voltages, the area of maximum voltages is clearly visible. The results (Figure 3 and Figure 4) are shown for beech with a thickness of 18 mm and oak with a thickness of 22 mm. Other obtained results obtained by numerical simulation of different types of wood and thickness are given in Table 3.

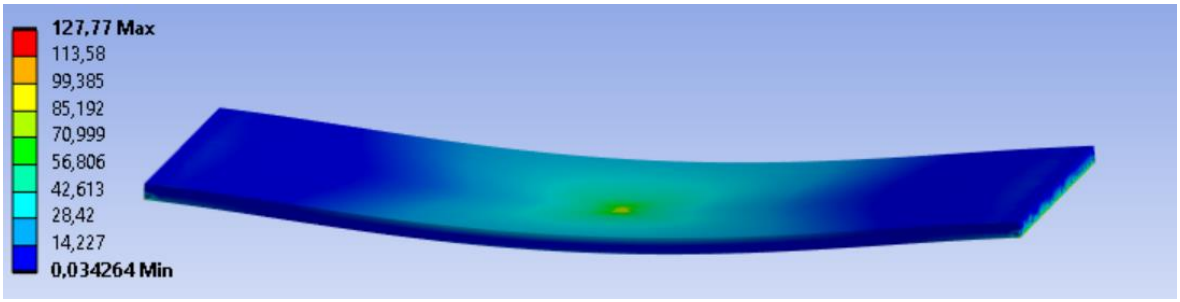

a)

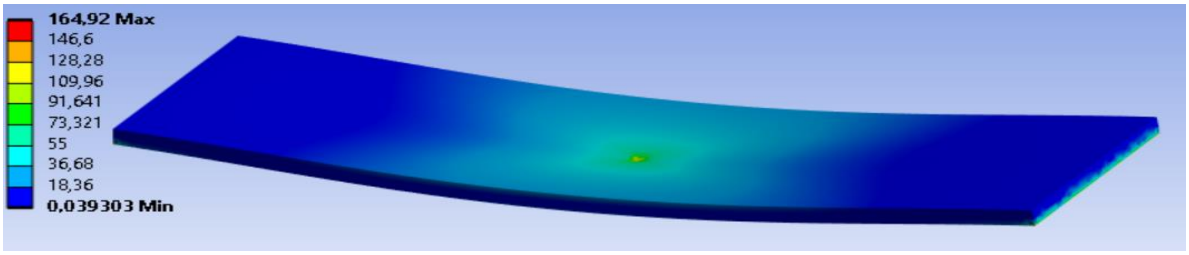

b)

Figure 4. *Stress distribution in layers on the section of the MKE model, a) beech 18 mm, b) oak 22 mm*

Table 3. *Display of input parameters and SW simulation results*

Number	Type of wood	Thickness [mm]	Density [kg/m^3]	Breaking force of the plate [kN]	Max. deflection [mm]	Max stresses [MPa]
1	beech	18	560	3.81	24.84	127.77
2	beech	20	560	4.87	22.82	163.54
3	beech	24	560	6.99	19.55	168.47
4	poplar	18	450	0.62	4.2	20.787
5	spruce	20	450	1.68	7.47	56.417
6	ash	20	450	1.68	7.87	56.417
7	oak	22	560	5.93	21.15	164.92

The diagrams in Figure 5 show the dependence of the output value of the model, the fracture force on the input quantities, wood density and plate thickness. On the abscissa of the input quantities, the minimum value is shown with "-1" and the maximum value of the input quantity with "+1". It can be seen from the diagram that the value of the fracture force depends more significantly on the density of the wood, i.e. that the values of the fracture force grow faster as the density increases [6].

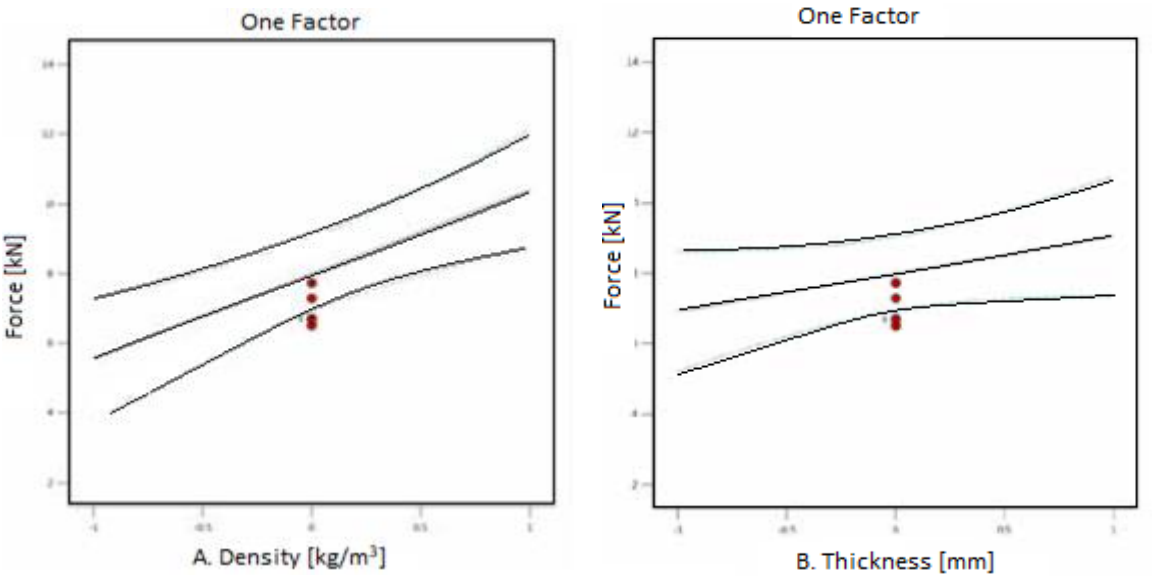

Figure 5. *Dependence of the fracture force on the input parameters, a) density, b) thickness*

The dependence of the fracture force on the interaction of the input quantities can be graphically represented by a contour two - dimensional diagram, Figure 6a, as well as by a three-dimensional representation, Figure 6b.

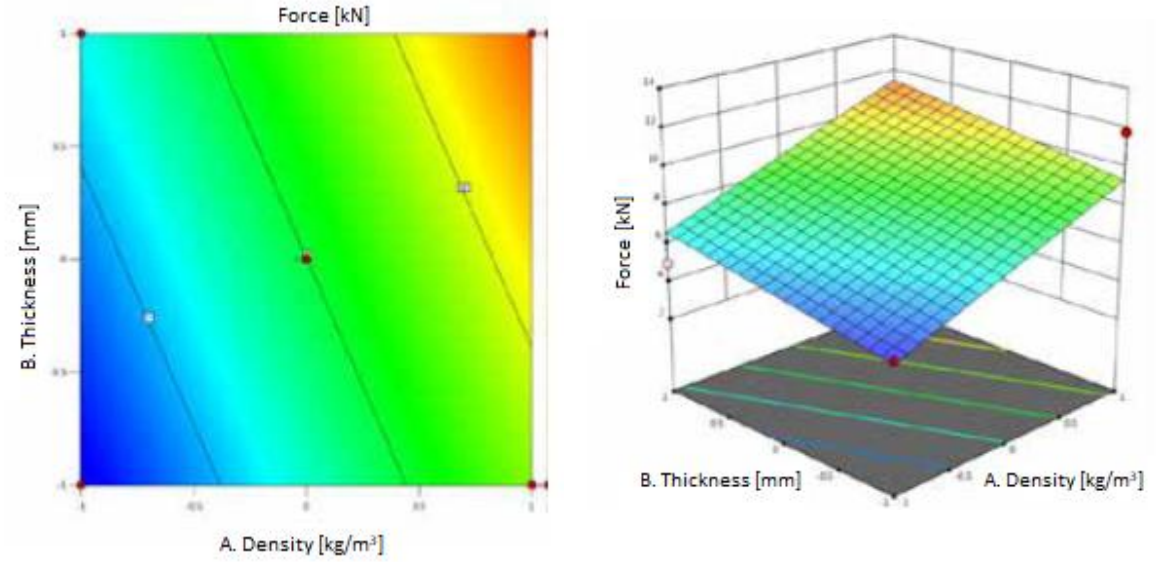

Figure 6. *Graphical contour representation, a) two-dimensional, b) three-dimensional*

It is possible to graphically show the distribution of experimental and model values of the fracture force of Figure 7. This diagram helps detecting experimental states in which the output values do not match well with the experimental quantities.

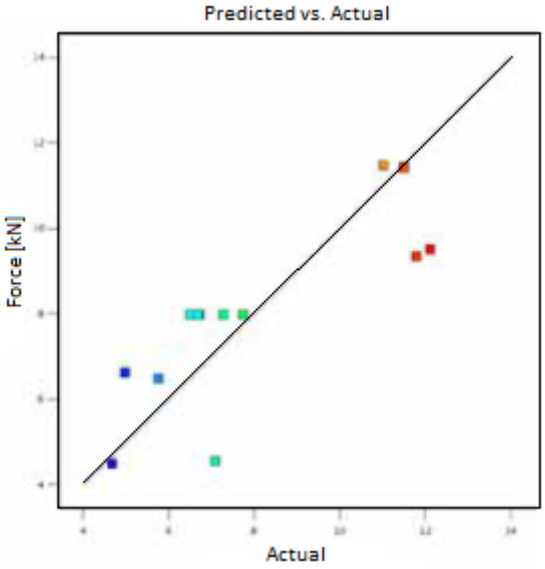

Figure 7. *Distribution of experimental and model values of fracture force*

According to the theory, the data points should be evenly distributed in relation to the line, which should be at an angle of 45°. In the example, the output magnitudes of the fracture force parameter in a plate with parallel fiber stretching on the horizontal axis are experimental and, on the vertical, the model values and the distribution of model values in relation to the experimental ones is good.
While in the experimentally tested samples the fracture was predominantly due to reaching the limit shear stress, in the numerical model the fracture is a consequence of exceeding the limit tensile stress during bending [6]. The breaking force obtained experimentally was used for the simulation. The obtained numerical result is slightly lower than the experimental one, with good agreement [8].

4. Conclusion

After obtaining the results of experiment and the breaking force model, it can be concluded that the obtained model is good enough and adequate for the presented initial conditions, which define the density of wood or the thickness of solid wood panel. The dispersion of the results at the point of repeating the experiment is homogeneous and the adequacy of the model calculated using the multiple regression coefficient is over 90% and it can be concluded that the model is very good. The value of the breaking force of a solid wood board depends on both the density of the wood and the thickness of the board. As both values increase, so does the magnitude of the fracture force, but the growth increases as the material density increases, which means this parameter is more influential in the model.
The model obtained and used in the numerical simulation of beam bending can be easily adapted to different geometries and material properties, and is therefore an useful tool for beam design optimization. Based on the analysis of the model and its results, it can be concluded that the finite element method is a useful tool for predicting the behavior of the fracture zone during bending in layers of different types of wood.
The given modeling concept can be further used to carry out an extensive parametric study in order to optimally dimension the beam, but also in the case of an optimal choice of reinforcement system, but also to make a qualitative analysis of the behavior of the beam during bending for different types of wood.

References

[1] Montgomery, D.C. 2015. Design and Analysis ofExperiment, Arizone State University, John Wiley and Sons, USA

[2] Jurković, M. 1999. Matematičko modeliranje inženjerskih procesa i sistema, Univerzitet u Bihaću, Mašinski fakultet, Bihać
[3] BAS EN 789 standard, 2005. Konstrukcije od drveta – Postupci ispitivanja – Određivanje mehaničkih svojstava ploča od drveta
[4] Hurem, N., Hodžić, D.,Hodžić, A., 2020. Application of Comparative Experiment in Analysis of Wood Strength, Conf. ICAS 2020, Hunedoara Romania
[5] CNR Advisory Committee on Technical Recommendations for Construction, 2005. Guidelines for the design and construction of externally bonded FRP systems for strengthening existing structures. Timber structures, CNR-DT 201/2005
[6] Hurem, N., Hodžić, D., 2020. Planiranje eksperimenta i matematički model čvrstoče na savijanje ploče od masivnog drveta, časopis Mašinstvo, Vol. 17, No. 3-4, pp. 93-102
[7] Bodig, J., Jayne, B. A., 1989. Mechanics of wood and wood composites, Van Nostrand Reinhold Company, New York, USA
[8] Hurem, N., Talić-Čikmiš, A., Imamović, A, 2022. Exsperimental analisis of distribution of bending stresses in layers of wood with numerical verification, 11^{8h} MTSM 2022, Split

Relevant aspects in in industrial engineering for quality management of medical devices according to current EU legislation

***Gerardo Tricarico*[1] *and Valter Travagli*[2]**

1) Dipartimento di Odontostomatologia, Presidio Ospedaliero Sant'Andrea, Corso Mario Abbiate, 21, 13100 Vercelli, Italy

2) Dipartimento di Biotecnologie, Chimica e Farmacia, Università degli Studi di Siena, Viale Aldo Moro, 2, 53100 Siena, Italy

Corresponding author: gerardo.tricarico@aslvc.piemonte.it; trigerard@gmail.com

Professional paper

Abstract: The topical changes presented by the Regulation (EU) 2017/745 of the European Parliament and of the Council, compel new approaches on European Market introduction and quality management of the new medical devices (MDs) and of the follow up of the old ones. Consequently, the requirements falling upon the manufacturers to certify products according to updated safety and efficacy parameters are much more complicated and difficult compared to what was previously in force. Agreeing with the current regulations, the Notified Bodies allowing the sale of the MDs following the CE Marking ensure a periodic inspection to verify the safety and effectiveness of both the equipment and the proposed treatment. Accordingly, the industrial engineering gets a paramount importance to keep the certification of the medical device conforming to proper Quality Management System. The purpose of this contribution is to highlight, by means of specific patterns, some topics that should be observed by medical personnel using medical devices for either diagnostic or therapeutic purposes.

Keywords: *Medical devices; Safety; EU Regulation; MDR 2017/745; MDD 93/42; Regulation (EU) 2023/607*

1. Introduction

The lack of precise statement on electromedical devices carried out by the manufacturers for marketing reasons generates doubts and bad decisions by operators especially after the introduction of the new EU rules [1]. The aim of this paper is to contribute to a debate which puts the various players (physicians, health cares, sellers, manufactures) in a right position to evaluate and choose the best choice for every patient in terms of of medical devices (MDs). In fact, the current Regulation (EU) MDR 2017/745 of the European Parliament and of the Council of 5 April 2017 on MDs obliges electromedical machine manufacturers to certify machines according to updated safety and efficacy parameters [1] with respect to the Council Directive 93/42/EEC (MDD 93/42) that was previously in force [2]. The regulatory bodies have identified the Notified Bodies that, according to the regulations in force, authorize the sale following the issue of a CE mark. A periodic inspection (annual or biannual) will then be carried out to verify the safety and effectiveness of the equipment and the proposed diagnosis or treatment following the re-evaluation of the products and following the post-marketing surveillance. In the event that the annual or biannual audit does not pass the safety and efficacy specifications. In this case, the reference is to the rules laid down by the Post Marketing Surveillance and Clinical Evidence Requirements. Amongst other things, these standards oblige the end user to keep a register of all abnormal or unsafe events encountered in the use of MDs and to communicate them to the manufacturer so that the latter can open a ticket to analyse the technical problem, and also to keep a register of all the follow-ups of the therapeutic treatments carried out to assess the

therapeutic efficacy [3]. In the absence of all this the certificate can be suspended or withdrawn. These event can contribute to stop the sale of some MDs, reducing the effectiveness of therapeutic treatments due to the non-availability on the market of MDs to which the CE Mark has been withdrawn.

2. New EU Regulation and its potential issues

The legislative aim of making MDs safer and more effective and, therefore, better for patients is certainly laudable. However, in clinical practice, the new rules that have been adopted generate a considerable number of problems, including higher costs, the expenditure of years to get the system up and running, and the likely disappearance of many devices from the market with potential problems for patients. In detail, the new definitions of technical limits of MDs that have been on the market even for dozens of years without ever having generated major criticalities, obliges the manufacturer of the same to carry out a new industrialisation of the same, which is not always feasible and in most cases not feasible. Moreover, the technical reassessment may not be adequate with the new definitions, making a new certification necessary. In this respect, the costs that the manufacturer would have to bear for this phase could be unsustainable for small and medium-sized companies in the sector. Similarly, quality control according to the new rules requires company departments whose costs are only sustainable for large companies.

Moreover, in the case of MDs that have multiple uses based not only on different therapeutic and diagnostic procedures, but also on different individual patient characteristics would oblige the manufacturer to certify the MDs countless times.

Finally, maintaining the data of patients treated for the purpose of post-marketing monitoring of MDs would oblige hospitals, outpatient clinics, medical centres and individual doctors to maintain a huge amount of data, which is difficult to sustain at present.

The Guidelines have been carefully drafted through a process of intensive consultation of the various interested parties (competent Authorities, Commission services, industries, other interested stakeholders) during which intermediate drafts where circulated and comments were taken up in the document. Therefore, this document reflects positions taken by representatives of interest parties in the MDs sector. At the moment, the indicated Guidelines relating to questions of application of EU-Directives on MDs are legally not binding. On the other hand, there is no trace of the point of view of patient's organizations and of medical and scientific societies is present, despite they are the main participants of these rules.

Based on the considerable reports of the previously reported problems, and taking into account the fact that MDs have a fundamental role in saving lives by providing innovative healthcare solutions for the diagnosis, prevention, monitoring, treatment or alleviation of disease, Regulation (EU) 2023/607 amending MDR 2017/745 was implemented with regard to the EU further postponed the entry into force of MDR 2017 to December 2027 and December 2028 for high and low risk MDs, respectively [4].

3. Discussion

Taking advantage of this additional latency period that refers to the postpone of the application of the MDR 2017/745 in force of the previously cited EU regulation 2023/607, we believe it is important to discuss and analyse the various aspects in every setting where this regulatory framework can be considered. In fact, much of the criticism is due to the lack of analysis of the problems and the practical effects on patients, hospitals, healthcare professionals, and finally also on manufacturers, as the new rules are being prepared. At this point, it is very important to define the way in which the improving of this new regulation has to be developed. About this topic it is necessary a deep collaboration between doctors, scientific societies, patient's organizations and producers.

In this regard, we consider it of interest report a practical example based on the practical example of the therapeutic use of oxygen-ozone gas mixtures [5]. In this respect, the physician must have suitable instrumentation capable of:

i. defining concentrations and dosages for any kind of treatments as for instance, systemic or infiltrative treatments.
ii. Customising treatment procedures on the basis of the patient's redox balance characteristics.

Thus, the application of the MDs Regulations complicates enormously the certification procedures and the availability of the generator devices in the certification and in the re-evaluation phase. In fact, a comprehensive approach to patient eligibility, along with compliance with standard operational procedures, is essential to normalize the safety of the practice of ozone therapy. Moreover, both the concepts of low dose and proper dose represent the achievement of the objectives of safety and efficacy of treatments, respecting the biological relationships between substrates and molecules contained in the systems used [6], [7]. The need for the clinician to ensure the greatest possible accuracy of dosage correlates with the hormetic response of the patient during treatment, results in time customisation in relation to patient feedback as a confirmation of the effectiveness of the therapeutic approach. Finally, a well-documented treatment report is important for promoting continuous evaluation of healthcare services, and leading to safer and better practice. The same reports have to be maintained as data for producer for the post marketing evaluation of the devices (PMS,MEDDEV2.7.1. rev4), and in case this will not be accomplished by the producers for different reasons, the certification of the device will be retired and the device will be not more suitable for that kind of treatment. That point has to be clear to the buyers for the assistance, for the warranties, and for the regular manutention of the devices.
However, even if ozone generator had obtained the compulsory certification (CE Mark), its user manual should be properly explained to the purchaser. In fact, the latter will decide whether those specifications are sufficient for therapy. Therefore, for the end user, the fundamental document is the user manual, which thus becomes the guide with which to operate that device.
As schematized in Figure 1, all electromedical devices should be certified in a way that the healthcare user is placed in the best possible position to make an informed choice of appropriate use with respect to sensitive parameters. For example, in the case of ozone generators the therapist is put in the best possible position to make an informed choice of appropriate administration with regard to sensitive parameters such as actual concentration to be used, time to reach it, compliance with tolerance with regard to average values, and so on.

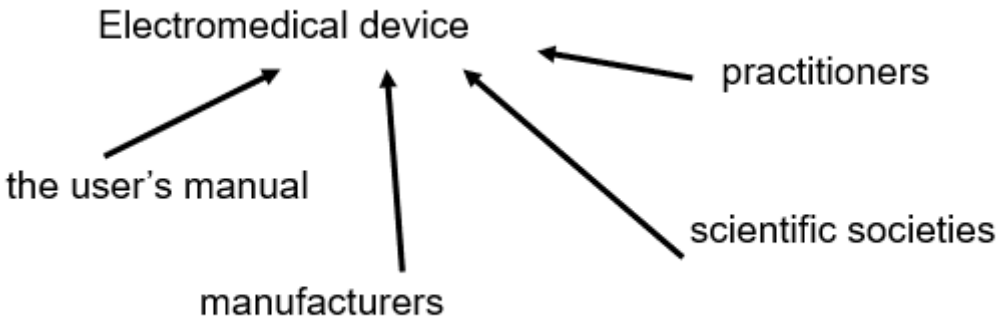

Figure 1. *Interrelationships to ensure the best level of Quality for MDs*

In conclusion, the purpose of this contribution is to improve the discussion based on the efficacy and safety appraisals about some topics that should be observed by medical personnel using a medical device for diagnostic and therapeutic purposes. For example, our suggestion is that a manufacturer of a medical device should, before proceeding with the design of a medical device, on the one hand have knowledge of the broad panorama of the different peculiarities of clinical, diagnostic and therapeutic frameworks found in human nature, and on the other hand discuss with experts the rules and

procedures for certification and maintenance of the CE Mark in the light of the new rules introduced with MDR (EU) 2017/745.

References

[1] Regulation (EU) 2017/745 of the European Parliament and of the Council of 5 April 2017 on medical devices, amending Directive 2001/83/EC, Regulation (EC) No 178/2002 and Regulation (EC) No 1223/2009 and repealing Council Directives 90/385/EEC and 93/42/EEC (Official Journal of the European Union, L 117, 5.5.2017, pp. 1-175)
[2] Council Directive 93/42/EEC of 14 June 1993 concerning medical devices (OJ L 169, 12.7.1993, p. 1)
[3] Garzotto, F., Comoretto, R. I., Dorigo, L., Gregori, D., Zotti, A., Meneghesso, G., Gerosa, G., & Bonin, M., 2022. Preparing healthcare, academic institutions, and notified bodies for their involvement in the innovation of medical devices under the new European regulation. Expert Rev. Med. Devices, 19(8), 613–621.
[4] Regulation (EU) 2023/607 of the European Parliament and of the Council of 15 March 2023 amending Regulations (EU) 2017/745 and (EU) 2017/746 as regards the transitional provisions for certain medical devices and in vitro diagnostic medical devices (OJ L 80, 20.3.2023, pp. 24-29)
[5] Re, L., Baéza-Noci, J., Gadelha Serra, ME., Mollica, P., Bonetti, M., & Travagli, V., 2020. Safety, pitfalls, and misunderstandings about the use of ozone therapy as a regenerative medicine tool. A narrative review. J. Biol. Regul. Homeost. 34 (4, Suppl. 1), 1-13.
[6] Viebahn-Haensler, R., & León Fernández, OS., 2021. Ozone in Medicine. The low-dose ozone concept and its basic biochemical mechanisms of action in chronic inflammatory diseases. Int. J. Mol. Sci. 22, 7890. doi: 10.3390/ijms22157890.
[7] Tricarico, G, & Travagli, V., 2021. The relationship between ozone and human blood in the course of a well-controlled, mild, and transitory oxidative eustress. Antioxidants (Basel). 10, 1946. doi: 10.3390/antiox10121946.

The influence of the mixing speed and the concentration of the supportive electrolyte NaCl on the removal efficiency of Crystal Violet dye

Ladislav Vrsalović[1], Senka Gudić[1], B. Kordić[1], N. Vukojević Medvidović[1], S. Svilović[1], Aleš Nagode[2], Borut Kosec[2] and Nikša Čatipović[3]

1) University of Split, Faculty of Chemistry and Technology, Ruđera Boškovića 35, 21000 Split, Croatia

2) University of Ljubljana, Faculty of Natural Sciences and Engineering, Aškarčeva cesta 12, 1000 Ljubljana, Slovenia

3) University of Split, Faculty of Electrical Engineering, Mechanical Engineering and Naval Arhitecture, Ruđera Boškovića 32, 21000 Split, Croatia

Corresponding author: ladislav@ktf-split.hr

Original scientific article

Abstract: There are more than 100,000 types of commercially available dyes, with over 7 x 10^5 tonnes produced annually. Azo dyes account for over 80% of the dyes produced annually worldwide and are used extensively in the textile, dyeing, paper making, printing, leather, cosmetics and pharmaceutical industries. Azo dyes can have a negative impact on water quality and accumulate in the aquatic systems, leading to significant health problems for aquatic organisms and a variety of environmental problems. In this work, electrocoagulation method (EC) was used to remove crystal violet (CV) dye from aqueous medium using AA2007 aluminium alloy electrodes. The base solution was 4 mg/L CV (pH = 3.2) with the addition of 1, 2 and 3 g/L NaCl and with the mixing speed of the magnetic stirrer of 100, 300 and 500 rpm. During the EC process, which lasted 50 minutes, changes in pH, temperature, electrical conductivity, and CV dye concentration were measured. During the EC process, the temperature of the solution as well as the pH increased, while the electrical conductivity remained almost constant.

The dye removal increased with the duration of the process and the highest removal rate (99.11%) was achieved with 1/L g NaCl and a magnetic stirrer mixing speed of 100 rpm. During the EC process, anodic and cathodic material is consumed, which can be explained by the electrochemical dissolution of the aluminium anode accompanied with the chemical dissolution of the anode and cathode.

The appearance of the electrode surfaces (taken with an optical microscope) shows that the anodes dissolve uniformly and locally during the EC process, while the cathodes are mostly subject to uniform corrosion.

Keywords: *wastewater, electrocoagulation; Crystal Violet dye; aluminium electrodes; optical microscopy*

1. Introduction

Although dyes have been known to mankind since ancient times, in the past most dyes were natural and obtained from plant sources: roots, berries, bark, leaves, wood, fungi and lichens, before the discovery of synthetic dyes in 1856 [1]. With the development of the chemical industry, especially organic chemistry, the natural dyes were largely replaced by the synthetic dyes as they were more economical, easier to synthesize, and generally had better properties than the natural dyes. Nowadays, synthetic dyes are used in many fields, e.g., textile and paper industry [2,3], food production, cosmetics, plastics, rubber, printing and dyeing industry, and leather processing [4-7]. Most dyes are complex organic molecules that must be resistant to many external influences, such as

detergents. According to current data, there are more than 100,000 chemical dyes [8]. The production and disposal of synthetic dyes can lead to pollution of water and soil, which in turn has a negative impact on the environment and wildlife. Exposure to high doses of these substances can be toxic and have serious effects on severe diseases such as various types of allergies, skin irritation and respiratory diseases, and even cancer. In addition, most dyes are not biodegradable and can remain in the environment for a long time, resulting in long-term negative environmental effects [9-13].

Various chemical, physical, and biological processes such as activated carbon adsorption, ozonation, chlorine oxidation, advanced oxidation, and combined anaerobic-aerobic treatment can be used to treat dye wastewater [14-16]. The use of chemical processes may be ineffective and can lead to secondary pollution [17]. The physical processes do not always achieve the discharge limits and are associated with high costs [18]. The disadvantage of biological processes is their long start-up time and the need for several post-treatments to completely remove organic pollutants [19].

Electrocoagulation (EC) has received considerable attention in recent years due to its positive features, such as versatility, energy efficiency, automation, and cost-effectiveness. In its simplest form, a EC reactor consists of an electrolytic cell with an anode and a cathode. The conducting metal plates are commonly referred to as "sacrificial electrodes" and may be made of the same or different materials as the anode and/or cathode [20]. The two most commonly used metals for sacrificial electrodes are Al and Fe. Dissolution of sacrificial metal anodes leads to the formation of metal cations (usually Fe^{2+} or Al^{3+}), which result in spontaneous hydrolysis reactions and the formation of amorphous metal oxides/hydroxides/oxyhydroxides that exhibit excellent adsorption properties for soluble substances. Electrolysis of water at the cathode produces hydroxide ions that combine with the metal cations formed at the anode to form a hydroxide precipitate at a suitable pH, which removes the pollutants by the sweep-floc mechanism [21]. The formation of H_2 by water electrolysis at the cathode can promote the flotation of some of the coagulated contaminants to the surface. [21] The process involves coagulation of the insoluble (oxy)hydroxides with the contaminants in the water and easier removal of the contaminants by sedimentation and flotation [22,23].

The important factors affecting dye removal by EC include nature of dye, electrode material, applied current, solution pH, conductivity and mixing speed [24,25]. Mixing speed is one of the essential parameter in EC procedures as it enhances the mass transfer processes by increasing the mobility of the ions in the solution, and increases the release of metal ions and hydroxyl groups. But very high mixing speed may induce breaking the flocs formed during EC [24,25]. Addition of supporting electrolyte increase the conductivity of the medium and reduce the risk of the passivation of the working electrodes [26].

In this paper, part of the preliminary results of the studies on the removal of the dye Crystal Violet are presented. The influence of the conductivity of the solution (different concentrations of NaCl, 1 g/L, 2 g/L and 3 g/L) and the different mixing speeds of the magnetic stirrer (100, 300 and 500 rpm) on the removal efficiency of Crystal Violet (CV) are shown.

2. Experimental procedure

Pyrex glass electrochemical batch reactor of capacity 600 mL was placed on a magnetic stirrer IKA RCT5 which allowed the fine adjustment and maintenance of a constant mixing speed of the magnetic stirrer at the desired value. The reactor was equipped with the two electrodes made of aluminium alloy AA 2007 with the chemical composition shown in Table 1. The distance between the electrodes was constant (*d*=3 cm). Electrodes were connected to a digital power source (Wanptek DPS605U; 60V, 5A, 300W) (Figure 1).

Table 1. *Chemical composition of the AA 2007 alloy*

Element	Al	Cu	Pb	Mg	Mn	Fe	Si	Bi	Zn	Ti
(wt.%)	92.5812	3.8375	1.0193	0.8814	0.6665	0.6237	0.2147	0.06768	0.0477	0.0268

Before each treatment, electrodes were mechanically grinded with the SiC emery papers of P280 to P800 using grinder/polisher Metkon Forcipol 1V, ultrasonically washed with 70 % ethanol and deionised water using A-Sonic Pro 30 ultrasonic cleaner (Figure 1). The electrodes were then dried and weighed on an analytical balance.

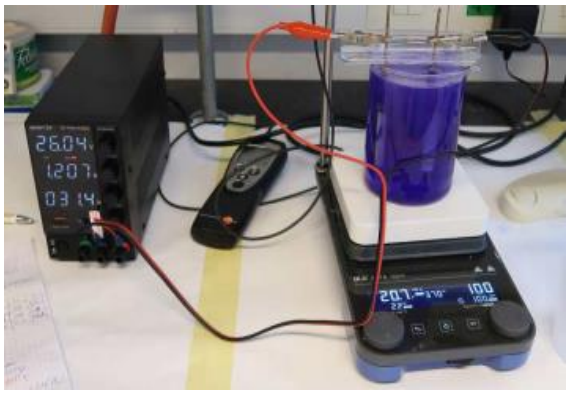

Figure 1. *Photography of the electrocoagualtion apparatus setup*

For experimental purposes, 5 L of the solution CV was prepared at a mass concentration of 4 mg/L. The solution was prepared by dissolving a precisely calculated and weighed (on an analytical balance) mass of CV in deionized water (in volumetric flask). As a suportive electrolyte NaCl was used which was added in the CV solution to obtained concentration of 1 g/L, 2 g/L or 3 g/L.
Changes in the pH of the solutions were measured with a Metler Toledo Seven Multi pH meter at time intervals of 5 minutes. Temperature changes were measured with a Testo 925 digital thermometer at time intervals of 5 minutes by immersing the temperature probe in the solution. The electrical conductivity of the solution CV was also determined every 5 minutes using a Schott Handylab LF 12 conductivity meter.
Concentration of CV was determined using a Perkin Elmer Lambda 25 UV/VIS spectrophotometer. Samples were analyzed at the beginning of the measurement (initial solution) and after 15, 20, 30, 40, and 50 minutes and the CV removal efficiencies were calculated (equation 1). The same volume of solution (10 mL) was pipetted from the reactor each time for analysis.

$$E\ (\%) = \frac{c_0 - c_t}{c_0} \times 100 \qquad (1)$$

where c_0 is CV initial concentration and the c_t is the concentration at the time t (sampling time).
The masses of the electrodes (anode and cathode) were determined by weighing on a Kern ALj 160-4NM analytical balance before and after each EC process, and the mass loss of the electrodes were obtained. The state of the surface of the aluminium electrodes (anode and cathode) after the EC processes was analysed using an optical microscope MXFMS-BD, Ningbo Sunny Instruments Co. with a magnification of 100×.

3. Results and discussion

Results of the investigations were shown on Figures 2-4.

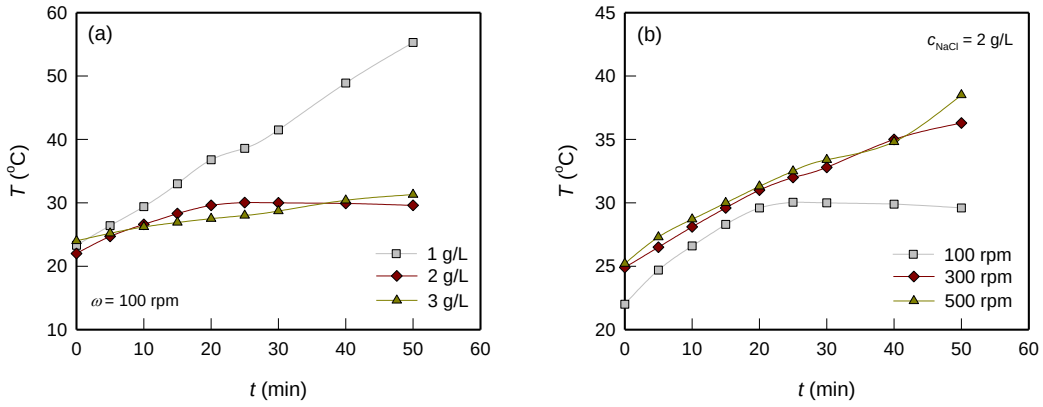

Figure 2. *Variation of temperature of the solution during EC process a) at different initial concentration of NaCl and b) at different mixing speed*

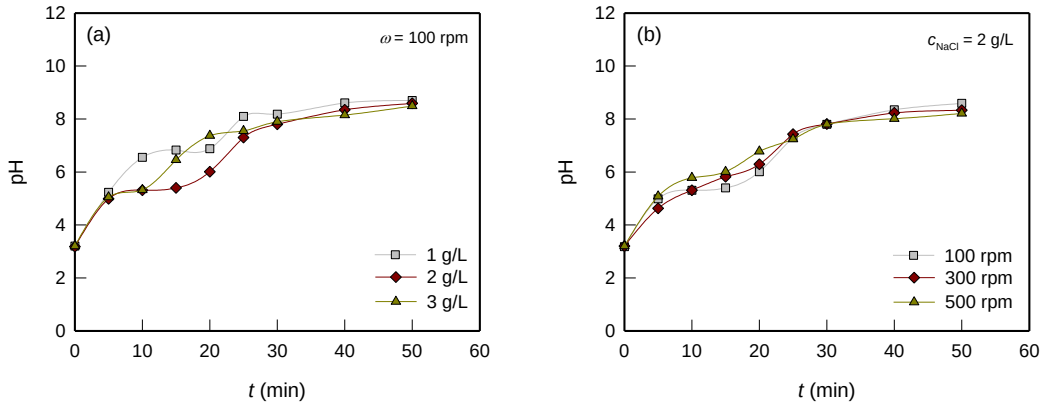

Figure 3. *Variation of pH of the solution during EC process a) at different initial concentration of NaCl and b) at different mixing speed*

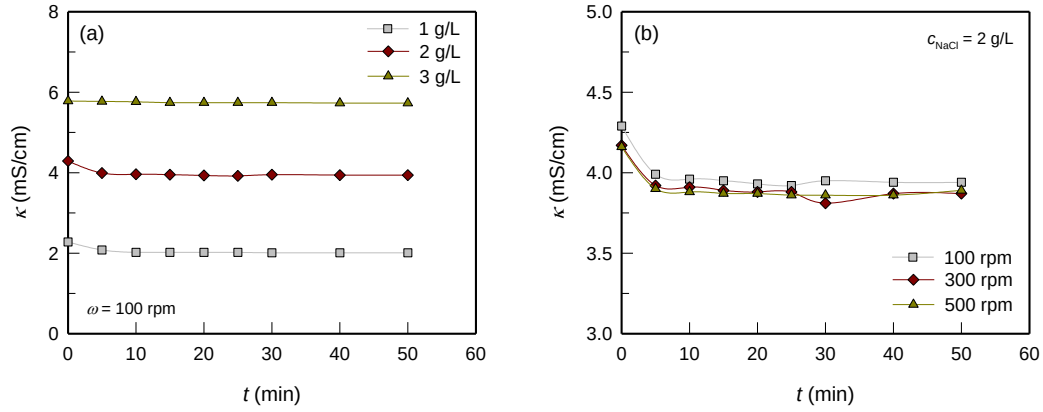

Figure 4. *Variation of conductivity of the solution during EC process a) at differnet initial concentration of NaCl and b) at different mixing speed*

It can be seen from Figures 2(a) and (b) that the temperature increases with time, which is observed in all measurements. The highest temperature increase was recorded for the solutions with the lowest NaCl concentration, which can be explained by the higher resistance of the solution to the current flow, as a result, part of the current is lost as heat [26]. In experiments with the NaCl concentrations

of 2 g/L and 3 g/L similar temperature values are observed, indicating that the optimal NaCl concentration in the solution could be 2 g/L according to this parameter.

Figure 3 shows the changes in pH during the EC process as a function of the initial concentration of the supporting electrolyte (a) and the different stirring speeds of the magnetic stirrer (b). The pH of the solution changes from the acidic values at the beginning of the experiment (pH = 3.2) to the alkaline values at the end of the experiment (pH ≈ 8.2). The significant pH changes take place in the first 30 minutes of the experiments, then changes slow down, and at the end of the experiment (after 50 minutes) they have approximately the same values. Similar observations were find in literature [26,27]. Chen et al.[28] observed a large pH increase when the influent pH was 3-6. At higher initial pH values (8-12), the increase becomes less significant. The increase of pH in acidic conditions can be attributed to the several factors and one of them is a chatodic reduction reaction [26,27]:

$$2H_2O + 2e^- \rightarrow 2OH^- + H_2 \quad (2)$$

Besides hydrogen evolution, the formation of $Al(OH)_3$ near the anode would influence on lowering the pH values due to the OH^- ion consummation [24]. It is also believed that the increase of pH is connected with the CO_2 release from hydrogen bubling which also leads to the CO_2 removal from the solution [24]. Removal of carbonate from solution leads to a corresponding pH increase, as it results in a shift in the equilibrium with carbonic acid according to the following mechanisms:

$$CO_2(aq) \leftrightarrow CO_2(g) \quad (3)$$
$$H_2CO_3(aq) \leftrightarrow CO_2(aq) + H_2O \quad (4)$$
$$HCO_2^- + H^+ \leftrightarrow H_2CO_3(aq) \quad (5)$$
$$CO_3^{2-} + H^+ \leftrightarrow HCO_3^- \quad (6)$$

If the organic species in the solution have a negative charge, they can also react directly with the positive Al^{3+} ions, which can also contribute to the increase in the pH of the solution. For that reason, the increase in the pH of the solution may also be related to the excess of OH^- ions that would otherwise combine with Al^{3+} ions.

The conductivity of the solution increases significantly with NaCl concentration, which is expected (Figure 4 (a)). The conductivity decreases with time in all studies, indicating that the number of ionic species in the solution slowly decreases with time (Figure 4 (b)). This is due to the formation of oxide and hydroxide species that consume Al^{3+} cations and OH^- anions.

Figure 5 (a) and (b) shows the CV removal eficciency with time as a function of NaCl electrolyte concentration and stirring speed (for the NaCl concentration of 2 g/L.

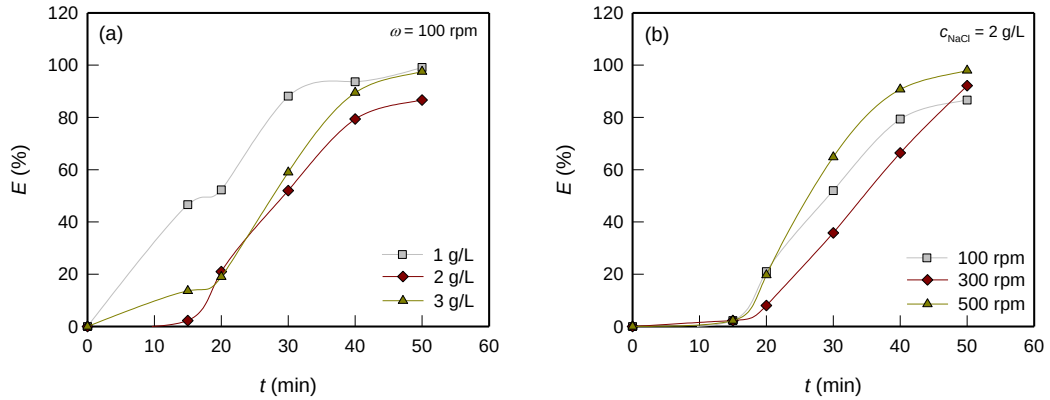

Figure 5. *Changes of the CV removal efficeince with time (a) for the different concentration of NaCl and (b) for the different mixing speed of magnetic stirrer*

It is obvious that the removal efficiency increases with time and after 50 minutes, depending on the conditions, and high removal efficiency (between 86-99%) was achieved. According to the results obtained, the highest removal efficiency for this EC process are achieved with 1 g/L NaCl and a mixing speed of 100 rpm.
Figure 6 shows the mass loss for the anode and cathode in the EC process for the measurement with stirrer mixing speed of 100 rpm at different NaCl concentration (a) and with the NaCl concentration of 2 g/L and different mixing speed (b).

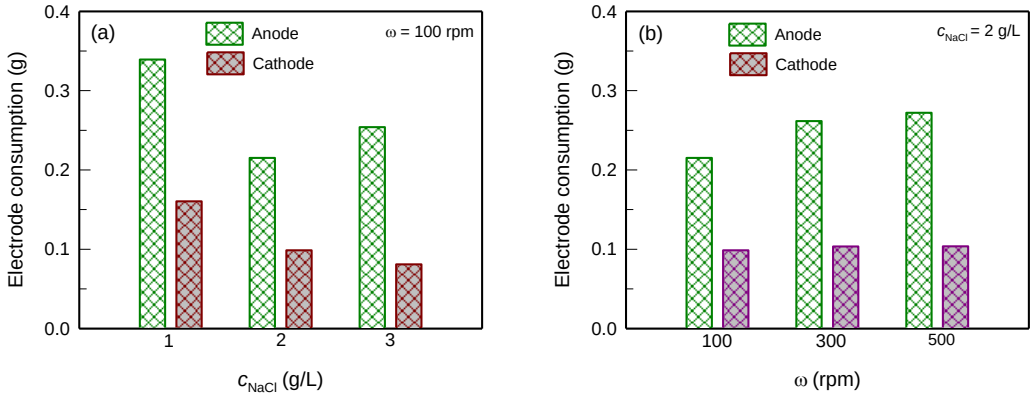

Figure 6. *Electrode consumption during EC experiments (a) at mixing speed of 100 rpm and different NaCl concentration and (b) at NaCl concentration of 2 g/L and different mixing speed*

Both anode and cathode are consumed during the electrocoagulation process. The reduction in the mass of the anode is the result mostly of its electrochemical anodic dissolution, while the reduction in the mass of the cathode is the result of the chemical dissolution of the electrode which is observed in other EC treatment of different types of wastewater with aluminium electrodes [26,29-31].
Figure 7 shows the surface condition of the electrodes after the electrocoagulation process performed at pH = 3.2 and 500 rpm in the presence of different concentrations of NaCl as supporting electrolyte.

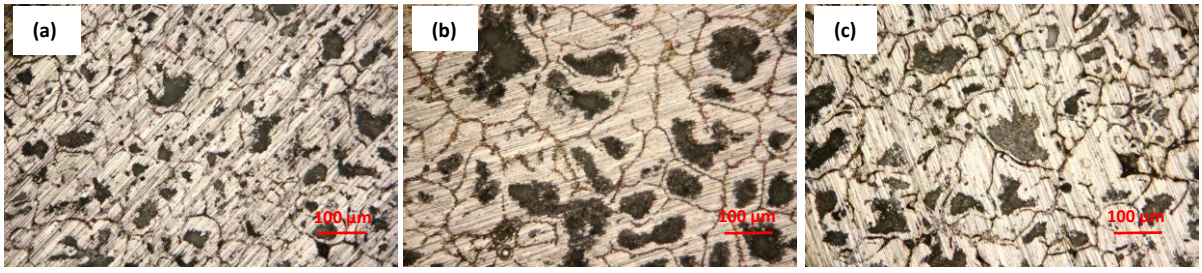

Figure 7. *Appearance of the anode surfaces after electrocoagulation process in the presence of the suportive electrolite in concentration (a) 1 g/L, (b) 2 g/L and (c) 3 g/L.*

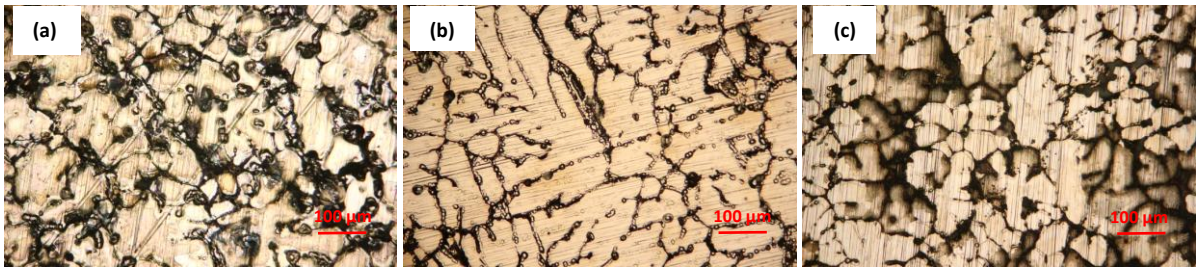

Figure 8. *Appearance of the cathode surfaces after electrocoagulation process in the presence of the suportive electrolite NaCl in concentration (a) 1 g/L, (b) 2 g/L and (c) 3 g/L*

From Figure 7, it can be seen that the anodic surfaces of the electrodes are rough and damaged due to anodic dissolution. The surface damage also indicates that the anode dissolution is similar, which Is

expected considering that the anode current density is the same and the differences are only due to the different mixing speed. Visible channels on the surface could indicate corrosion at the grain boundaries, while dark spots could indicate dissolution inside the grains. The surfaces of the cathodes look completely different compared to the anodes (Figure 8). The predominant cathodic process during EC is the hydrogen evolution reaction, which is quite intense, and this is the reason for visible damage on the cathode surfaces. The retention time of hydrogen bubbles on the surface is changing with the mixing speed, being shortest at the highest speed.
For more detailed analysis of electrode surface conditions and surface composition, SEM /EDS analysis should be used together with XRD analysis.

4. Conclusions

Electrocoagulation method (EC) was sucesfuly used to remove crystal violet (CV) dye from aqueous medium using AA2007 aluminium alloy electrodes.
The changes of mixing speed and concentration of NaCl as supportive electrolyte have influence on the colour removal as well as electrode dissolution rate, which is observed through changes of measuring variables during the EC process.
The dye removal increased with the duration of the process and the highest removal efficiency (99.11%) was achieved with 1 g/L NaCl and a magnetic stirrer mixing speed of 100 rpm. Even anode consumption during EC was expected due to electrochemical dissolution and corrosion, cathode consumption was also observed, confirming typical characteristic behavior of Al electrodes.

Acknowledgments

This resarch was supported by the Institutional scientific research project of the Faculty of Chemistry and Technology University of Split: “*Investigation of electrochemical behavior and corrosion stability of metals and alloys”*.

References

[1] Ziarani, G.M., Moradi, R., Lashgari, N., Kruger, H.G., 2018. Introduction and Importance of Synthetic Organic Dyes. Metal-Free Synthetic Organic Dyes, 1–7.
[2] Sokolowska-Gajda, J., Freeman, H.S., Reife, A. 1996. Synthetic dyes based on environmental considerations. Part 2: iron complexes formazan dyes. Dyes Pigm. 30, 1–20.
[3] Ivanov, K., Gruber, E., Schempp, W., Kirov, D., 1996. Possibilities of using zeolite as filler and carrier for dyestuffs in paper. Papier 50, 456–460.
[4] Bensalah, N., Quiroz Alfaro, M.A., Martínez-Huitle, C., 2009. Electrochemical treatment of synthetic wastewaters containing Alphazurine A dye. Chem. Eng. J. 149, 348–352.
[5] Wróbel, D., Boguta, A., Ion, R.M., 2001. Mixtures of synthetic organic dyes in a photoelectrochemical cell. J. Photoch. Photobio. A. 138, 7–22.
[6] Oguzie, K., Oguzie, E. Nwanonenyi, S., Edoziem, J. Vrsalović, L., 2021. Electrochemical decolorization of disperse blue-1 dye in aqueous solution, Environ. Eng. Manag. J. 20, 1467-1476.
[7] Nkwoada, A., Onyedika, G. Oguzie, E. Ogwuegbu, M., 2023. Photoadsorption and reaction mechanism of periwinkle shell ash in the removal of hazardous dye, Water Pract. Technol. 18, 574-591.
[8] Sen, T.K., Afroze, S., Ang, H.M., 2011. Equilibrium, kinetics and mechanism of removal of methylene blue from aqueous solution by adsorption onto pine cone biomass of *Pinus radiata*. Water Air Soil Pollut. 218, 499–515.
[9] Devlin, J., David, T.J. 1992. Tartrazine in atopic eczema, Arch. Dis. Child., 67, 709-711.
[10] Synthetic Dyes: Properties, Types, Classification and Application, Dyeing, 2023.,https://textileengineering.net/synthetic-dyes-properties-types-application/ (accessed 1 July 2023)
[11] Affat, S.S., 2021., Classifications, Advantages, Disadvantages, Toxicity Effects of Natural and Synthetic Dyes: A review, UTJSci. 8, 130-135.

[12] Lellis, B., Fávaro-Polonio, Z.C., Alencar Pamphile, J., Cesar Polonio, J., 2019. Effects of textile dyes on health and the environment and bioremediation potential of living organisms, Biotechnol. Res. Innov., 3, 275-290.
[13] Khan, S., Malik, A. 2018., Toxicity evaluation of textile effluents and role of native soil bacterium in biodegradation of a textile dye, Environ. Sci. Pollut. Res., 25, 4446-4458.
[14] Martínez-Huitle, C.A., Brillas, E. 2009. Decontamination of wastewaters containing synthetic organic dyes by electrochemical methods: a general review, Appl. Catal. B 87, 105–145.
[15] Chang, S.H., Chuang, S.H., Li, H.C., Liang, H.H., Huang, L.C., 2009. Comparative study on the degradation of I.C. Remazol Brilliant Blue R and I.C. Acid Black 1 by Fenton oxidation and Fe0/air process and toxicity evaluation, J. Hazard. Mater. 166, 1279–1288.
[16] Brosillon, S., Djelal, H., Merienne, N., Amrane, A., 2008. Innovative integrated process for the treatment of azo dyes: coupling of photocatalysis and biological treatment, Desalination 222, 331–339.
[17] Chequer, F.D., de Oliveira, G.A.R., Ferraz, E.R.A., Carvalho, J., Zanoni, M.B., de Oliveir, D.P. 2013. Textile dyes: Dyeing process and environmental impact. Eco-Friendly Text. Dye. Finish., 6, 151–176.
[18] Al-Mamun, M.R.; Islam, M.S.; Hossain, M.R.; Kader, S.; Islam, M.S.; Khan, M.Z.H. 2021. A novel and highly efficient Ag and GO co-synthesized ZnO nano photocatalyst for methylene blue dye degradation under UV irradiation. Environ. Nanotechnol. Monit. Manag., 16, 100495.
[19] Huang, D., Hu, C., Zeng, G., Cheng, M., Xu, P., Gong, X., Wang, R., Xue,W. 2017. Combination of Fenton processes and biotreatment for wastewater treatment and soil remediation. Sci. Total. Environ., 574, 1599–1610.
[20] Mollah, M.Y., Morkovsky, P., Gomes, J.A., Kesmez, M., Parga, J., Cocke, D.L., 2004.Fundamentals, present and future perspectives of electrocoagulation. J. Hazard.Mater. 114, 199–210.
[21] Vukojević Medvidović, N., Vrsalović, L., Svilović, S., Bobanović, A., 2022. Electrocoagulation vs. integrate electrocoagulation-natural zeolite for treatment of biowaste compost leachate—whether the optimum is truly optimal, Minerals 12, 442.
[22] Mollah, M.Y., Gomes, J.A., Das, K.K., Cocke, D.L., 2010. Electrochemical treatmentof Orange II dye solution–use of aluminum sacrificial electrodes and floc char-acterization. J. Hazard. Mater. 174, 851–858.
[23] Tegladza, I.D., Xu, Q., Xu, K., Lv G., Lu J., 2021. Electrocoagulation processes: A general review about role ofelectro-generated flocs in pollutant removal, Process Saf. Environ. Prot. 146, 169–189.
[24] Chen, G., 2004. Electrochemical technologies in wastewater treatment, Sep. Purif. Technol. 38 11-41.
[25] Boinpally, S., Kolla, A., Kainthola, J., Koidali, R., Vemuri A., 2023. A state-of-the-art review of the electrocoagulation technology for wastewater treatment, J. Water Cycle 4, 26–36.
[26] Mansouri, K., Ibrik, K., Bansalah, N., Abdel-Wahab, A. 2011. Anodic dissolution of pure aluminium during electrocoagulation process: influence of supporting electrolyte, initial pH and current density, I&EC Research 50, 13362-13372.
[27] Ingelsson, M., Yasti, N., Roberts. E.P.L., 2020. Electrode passivation, faradaic efficiency, and performance enhancement strategies in electrocoagulation – a review, Water Research 187, 116433.
[28] Chen, X., Chen, G., Yue, P.L. 2000. Separation of pollutants from restaurant wastewater by electrocoagulation. Sep Purif. Technol. 19,65-76.
[29] Singh, T.S.A., Ramesh, S.T., 2014. An experimental study of CI Reactive Blue 25 removal from aqueous solution by electrocoagulation using aluminium sacrificial electrode: kinetics and influence of parameters on electrocoagulation performance, Desalin. Water Treat. 52, 2634-2642.,
[30] Vrsalović, L., Vukojević Medvidović, N., Svilović, S., Šarić, J., 2023. Application of different metals as electrode material in compost leachate treatment, Kem. Ind. 72, 297–304.
[31] Svilović, S., Vukojević Medvidović, N., Vrsalović, L., Kulić, A., 2022. Combining natural zeolite and electrocoagulation with different electrode materials – electrode surface analysis and Taguchi optimization, Appl. Surf. Sci. Adv. 12, 100330.

X-ray analysis of the microstructure of the wire arc additively manufactured high entropy alloy

***Anatoliy Zavdoveev*[1], *Andrej Klapatyuk*[1], *Olga Karasevska*[2], *Thierry Baudin*[3], *Massimo Rogante*[4], *Valeriy Pozniakov*[1]*and Alexandr Gaivoronskii*[1]**

1) E. O. Paton Electric Welding Institute of NAS of Ukraine, K.Malevicha 11, 03150 Kiev

2) G. V. Kurdyumov Institute of Metal Physics of the NAS of Ukraine; Kyiv, Ukraine

3) Université Paris-Saclay, CNRS, Institut de chimie moléculaire et des matériaux d'Orsay, 91405, Orsay, France

4) Rogante Engineering Office, Contrada San Michele n.61, 62012 Civitanova Marche, Italy

Corresponding author: avzavdoveev@gmail.com

Original scientific article

Abstract: Cantor alloy CrMnFeCoNi as the first described high-entropy alloy (HEA) that has great potential in terms of mechanical and structural properties. This alloy exhibits high strength and impact toughness and retains its characteristics even in cryogenic conditions. Cantor's alloy has a simple single-phase face-centred cubic (fcc) structure. Despite the extensive study of the properties of this alloy, a limited number of works are devoted to its production by modern methods of wire arc additive manufacturing (WAAM). Therefore, in this work, an analysis of the phase and structural state, as well as the study of some properties, was carried out.

Keywords: *high entropy alloy; X-Ray analysis; microstructure; wire arc additive manufacturing*

1. Introduction

Cantor's alloy CrMnFeCoNi is considered the first described high-entropy alloy (HEA) and, nevertheless, remains one of the most promising in terms of its mechanical and structural properties [1]. This alloy is able to demonstrate excellent strength and impact toughness, which only improves with increasing temperature. Its properties, even in cryogenic conditions, remain unusually high, not obeying the typical compromise between strength and impact toughness, which is observed in most metals at low temperatures [2],[3],[4].

The traditional point of view in physical metallurgy is that multicomponent alloys should have a complex phase structure consisting of several different phases and intermetallic compounds [5]. However, Cantor's alloy, as a representative of HEAs, violates this conventional concept, as it has a simple single-phase face-centred cubic (fcc) structure. This makes it a particularly interesting object of research, as such alloys appear to be an inexhaustible source of new opportunities and prospects in the field of materials science and engineering.

Despite extensive research into the mechanical and structural properties of Cantor's alloy [6][7][8][9], a rather limited number of works are devoted to its production by modern methods. Therefore, it is of great importance to further study the process of WAAM production of this alloy, in particular, the application of modern methods of researching microstructural features.

2. Experimental

A wall with a width of 20 mm and a height of 40 mm was grown by the method of wire arc additive manufacturing with layer-by-layer deposition of the Fe+CrMnCoNi alloy (Table 1, determined by energy dispersive X-Ray analyzer using a Tscan Mira 3 LMU facility).

Table 1. *Chemical composition of the WAAMed Cantor type alloy, at.%*

Fe	Cr	Mn	Co	Ni
49.20	13.85	11.93	12.17	12.85

Layer-by-layer deposition of 12 layers was carried out with the temperature between successive layers of 250-300° C (Figure 1)[10],[11] . The previous layer was heated up to ~1500° C during the sputtering of the next one, according to the welding thermal cycle. Thus, the thermal effect of the pre-heated layers was imposed on each subsequent layer like a tempering. Samples for the study of layer-by-layer surfacing were cut from the bottom, middle, and top parts of the surfacing, each measuring 2x6x10mm. The cross section for research was chosen in the scanning direction (SD) – transverse direction (TD).

Figure 1. *General view of WAAMed billet.*

To compare the phase and structural states of 3 deposited layers, a reference sample with a single-phase fcc crystallographic structure was made by heating the middle part of the deposition to 1000°C and holding for 1 hour with cooling in the oven. The equilibrium state of the reference sample was controlled by the X-ray method based on the angular position of the diffraction peaks on the "θ–2θ" X-ray pattern obtained on the DRON-3M installation in Cuk$_\alpha$ radiation in automatic mode. According to the "θ–2θ" diffraction pattern on 4 different states of the Fe+CrMnCoNi alloy, the phase composition was determined by the intensity and position of the diffraction peaks and the presence of a textural state in them was assessed, and the macro- and micro-deformation, the dimensions of the OCR were determined according to the Williamson-Hall method [12].
EBSD analysis was conducted using a Zeiss SUPRA 55 VP scanning-electron microscope (FEG-SEM) operating at 20 kV. The EBSD data acquisition and analysis was undertaken using EDAX-TSL Orientation Imaging Microscopy with OIM^{TM} software.

3. Results and discussion

X-ray diffraction patterns of the Fe+ Ni, Cr, Mn alloy are presented in Figure 2. All samples have an fcc crystal lattice with different values of intensity and broadening of diffraction peaks. The normalized values of the intensity of {hkl} diffraction peaks (I{hkl}) relative to the {200} diffraction peaks (I{200}), i.e. I{hkl}/I{200}, for all samples are presented in Table 2 and Figure 3.

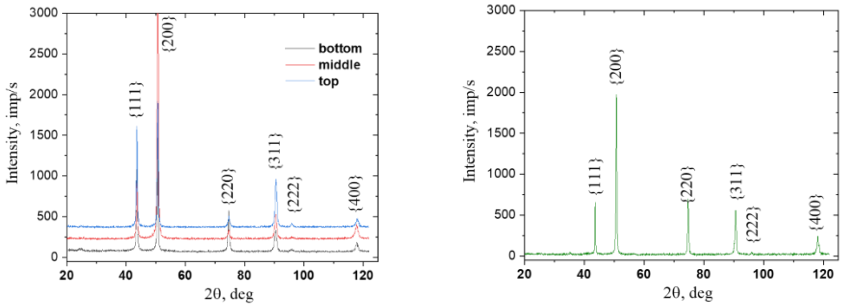

a) *b)*

***Figure 2**. "θ–2θ" diffraction pattern of the alloy; and – deposited layers where 1 - bottom one. 2- middle, 3- top parts of these layers; b - initial state.*

***Table 2**. Normalized values of the intensity of diffraction peaks in the standard and welded sections*

{hkl}	$I_{\{hkl\}}/I_{\{200\}}$			
	standard	bottom	middle	top
{111}	0,32205	0,678	0,171	0,768
{200}	1	1	1	1
{220}	0,33221	0,327	0,018	0,069
{311}	0,23463	0,16	0,069	0,345
{400}	0,032	0,044	0,03	0,035

In the plane of reflection for the obtained X-ray reflections compared to $I_{\{hkl\}}$ of the etalon, the following largest changes are observed in the layers: a) in the lower layer, the $I_{\{111\}}$ reflection increases by ~ 2 times, and the $I_{\{311\}}$ reflection decreases by ~ 1.5 times; b) in the middle part $I_{\{111\}}$ of the diffraction peak decreases by ~ 2 times; c) in the upper layer, the $I_{\{111\}}$ diffraction peak increases ~2.5 times, and the $I_{\{200\}}$ diffraction peak decreases almost ~5 times. Thus, the largest changes in the crystallographic structure of the layers undergo the largest changes in the lower and upper layers.

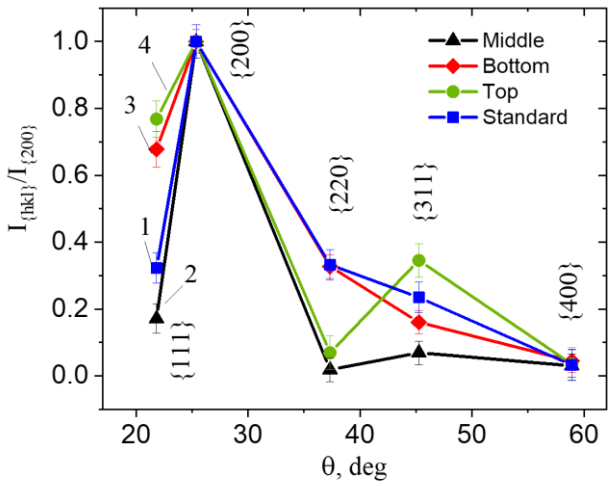

***Figure 3.** Normalized values of the intensity of diffraction peaks in the standard (1) and deposited (2-4) alloy samples. 2- bottom, 3- middle, 4- top part of deposited layers*

In the deposited HEA, the formation of textured states is observed in the upper and lower layers under the influence of crystallization features during welding. The investigation of the crystallographic

orientation of the layers by the "EBSD" method (backscattered electron diffraction) is presented in Figure 4.

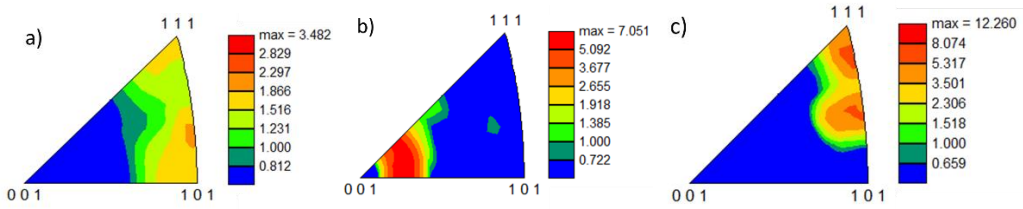

Figure 4. *Inverse pole figures for SD-TD section. a) – bottom, b) – middle, c) – top.*

The analysis of the location of the zones of maximum intensity in the stereographic triangle 001-101-111 on the electron backscatter diffraction maps (Fig. 4) indicates changes in the predominant orientation of the reflection plane of samples from different layers of the sprayed alloy. In the lower part of the deposited layer (Fig. 4b), a textured state (maximum EBSD intensity “3”) is observed with a two-component texture component {221} and {111}, which forms a sharp texture {111} and {221} with a maximum EBSD intensity "12". Such textural transformations correspond to the change in I{hkl} diffraction peaks on the "θ–2θ" diffraction pattern and occur as a result of the crystallization characteristics of the welding bath.

An assessment of residual deformation and macrostress was carried out on X-ray images of the surfacing layers and in the shift diffraction peak reference (Fig. 5). In the standard, as it was determined during the formation of the equilibrium state, the residual macrodeformation is practically absent according to the calculations of the displacement of the positions of all diffraction peaks (Figure 5, curve 1).

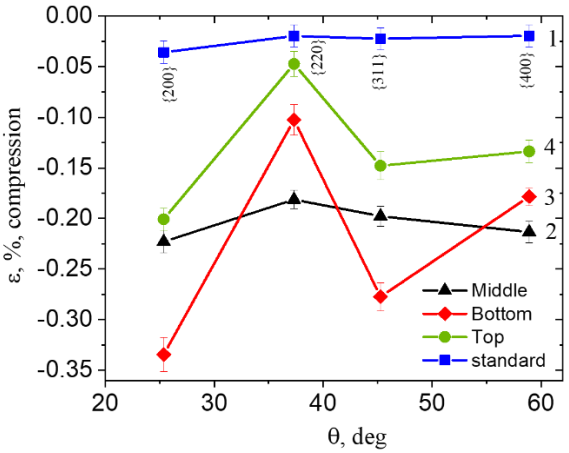

Figure 5. *Residual macrodeformation (ε, %) in the standard (1) and 2- bottom, 3- middle, 4- top parts of the deposited layers.*

In the bottom and top layers of the deposition, the residual compression macrodeformation differs significantly in different crystallographic directions in the lattice (Figure 5, curve 2 and curve 4, respectively). In the lower layer, the absolute values of compression deformation reach greater values and fluctuations in directions than in the upper layer. The middle part of the surfacing has a homogeneous residual deformation of the lattice (Figure 5, curve 3) with a compression value of ~0.22%, practically averaged between the lower and upper layers. The inhomogeneity of the macrodeformation in the lower and upper parts of the deposition is related to the reorientation of grains during the formation of textural predominant orientations, while in the middle part of the deposition, textural changes relative to the standard are the smallest.

The broadening of X-ray diffraction peaks is related to microstrains and the size of coherent scattering regions (CSR). The Williamson-Hall method makes it possible to separate the contributions of the CSR size and microvoltages to the expansion of diffraction peaks. The size of the CSR is determined (estimated) by the Selyakov Scherrer formula $D_{CSR} = \lambda/(\beta \times Cos\theta)$, and microdeformation by the formula $\varepsilon_{micro} = \beta_\varepsilon/4tg\Theta -$ that is, the slope of the curves on the Williamson-Hall graph. In Figure 6, curve 1, the change in the values of $\beta cos\theta$ from the angle of reflection $(4sin\theta)$ is practically parallel to the abscissa axis, so micro-deformation in the standard is practically absent, as well as macro-deformation (Figure 5, curve 1).

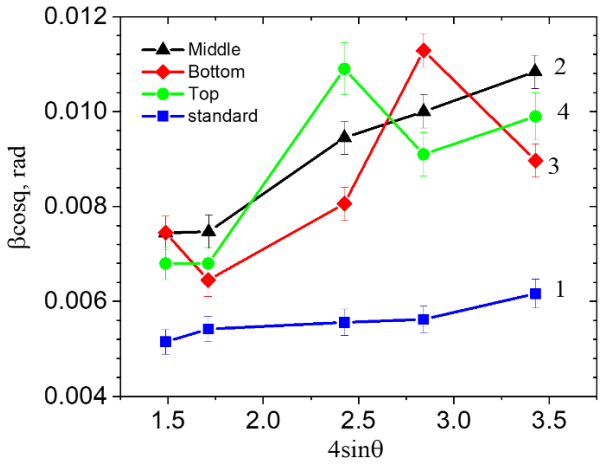

Figure 6. *Dependence of the expansion of X-ray diffraction peaks (β) on the angle of reflection on the Williamson-Hall graph [12] in samples: 1- standard, 2- bottom, 3- middle, 4- top parts of the deposited layer.*

The size of the CSR equal to ~ 300 Å and its sections have a shape close to spherical. In the middle part of the deposition (Figure 6, curve 3), the CSR R also have a shape close to spherical with a size of ~ 310 Å, however, the grains have a microdeformation εmicro ~ 0.22%. In the lower and in the upper parts of the deposited layer, the shape of the OCR changes from spherical to elongated with dimensions of ~ 310x670 Å and ~ 275x1000 Å, respectively. Inhomogeneous microdeformation of grains in different crystallographic directions is also a characteristic of the lower and upper parts of the deposited layer. The variation of microdeformation in the lower part is ~0.5% - ~0.27 %, and in the upper part of the deposited layer - ~0.47% to ~0.31%. The microdeformation and the nature of the shape of the CSR are determined by the formation of textural states in different deposition layers. The residual microstresses can be estimated by Hooke's formula for elastic deformation using the obtained values of elastic microstrain and measured Young's moduli.

4. Conclusion

The study of Cantor's alloy, in particular its production by modern methods, is a topical topic that requires a comprehensive analysis of the features of structure formation. On the basis of the conducted research, it was found that all areas of the alloy have an fcc crystal lattice with different values of the intensity and broadening of diffraction peaks. The analysis of the zone’s location of maximum intensity in the stereographic triangle on the electron backscatter diffraction maps indicates changes in the texture from the lower to the upper part of the alloy. Changes in the crystallographic structure of the layers are most significant in the lower and upper layers. On the basis of X-ray structural analysis, the presence of residual deformations and macrostresses in the surfacing layers, as well as their change in different parts of the surfacing workpiece, was established. The size and shape of the crystallite regions (CR), as well as the microdeformation, vary depending on the location in the surfacing layers.

References

[1] B. Cantor, I.T.H. Chang, P. Knight, A.J.B. Vincent, Microstructural development in equiatomic multicomponent alloys, Mater. Sci. Eng. A. 375–377 (2004) 213–218. https://doi.org/https://doi.org/10.1016/j.msea.2003.10.257.

[2] D. Lin, L. Xu, H. Jing, Y. Han, L. Zhao, F. Minami, Effects of annealing on the structure and mechanical properties of FeCoCrNi high-entropy alloy fabricated via selective laser melting, Addit. Manuf. 32 (2020) 101058. https://doi.org/https://doi.org/10.1016/j.addma.2020.101058.

[3] L. Ladani, M. Sadeghilaridjani, Review of Powder Bed Fusion Additive Manufacturing for Metals, Met. . 11 (2021). https://doi.org/10.3390/met11091391.

[4] Y. Brif, M. Thomas, I. Todd, The use of high-entropy alloys in additive manufacturing, Scr. Mater. 99 (2015). https://doi.org/10.1016/j.scriptamat.2014.11.037.

[5] F. Otto, Y. Yang, H. Bei, E.P. George, Relative effects of enthalpy and entropy on the phase stability of equiatomic high-entropy alloys, Acta Mater. 61 (2013) 2628–2638.

[6] K. Kuwabara, H. Shiratori, T. Fujieda, K. Yamanaka, Y. Koizumi, A. Chiba, Mechanical and corrosion properties of AlCoCrFeNi high-entropy alloy fabricated with selective electron beam melting, Addit. Manuf. 23 (2018) 264–271. https://doi.org/https://doi.org/10.1016/j.addma.2018.06.006.

[7] A. Gali, E.P. George, Tensile properties of high- and medium-entropy alloys, Intermetallics. 39 (2013) 74–78. https://doi.org/https://doi.org/10.1016/j.intermet.2013.03.018.

[8] M. Naeem, H. He, S. Harjo, T. Kawasaki, F. Zhang, B. Wang, S. Lan, Z. Wu, Y. Wu, Z. Lu, C.T. Liu, X.-L. Wang, Extremely high dislocation density and deformation pathway of CrMnFeCoNi high entropy alloy at ultralow temperature, Scr. Mater. 188 (2020) 21–25. https://doi.org/https://doi.org/10.1016/j.scriptamat.2020.07.004.

[9] Z. Wu, H. Bei, G.M. Pharr, E.P. George, Temperature dependence of the mechanical properties of equiatomic solid solution alloys with face-centered cubic crystal structures, Acta Mater. 81 (2014) 428–441. https://doi.org/https://doi.org/10.1016/j.actamat.2014.08.026.

[10] A. Zavdoveev, A. Klapatyuk, T. Baudin, E. MacDonald, D. Mohan, J. Oliveira, A. Gajvoronskiy, V. Poznyakov, H.S. Kim, F. Brisset, M. Khokhlov, M. Heaton, M. Rogante, M. Skoryk, D. Vedel, R. Kozin, I. Klochkov, S. Motrunich, Non-equimolar Cantor high entropy alloy fabrication using metal powder cored wire arc additive manufacturing, Addit. Manuf. Lett. (2023) 100124. https://doi.org/https://doi.org/10.1016/j.addlet.2023.100124.

[11] A. V Zavdoveev, O.A. Gaivoronsky, V.D. Poznyakov, A. V Klapatyuk, D. V Vedel, T. Baudin, O.A. Los, R.A. Kozin, M.A. Skoryk, Powder Welding Wire of Cantor’s High-Entropy Alloying System for Surfacing, Met. Noveishie Tekhnol. 44 (n.d.) 1025–1035.

[12] G.K. Williamson, W.H. Hall, X-ray line broadening from filed aluminium and wolfram, Acta Metall. 1 (1953) 22–31. https://doi.org/https://doi.org/10.1016/0001-6160(53)90006-6.

Potentiodynamic measurements of selective laser melting additively manufactured Ti6Al4V alloy

***Matija Zorc*[1], *Borut Kosec*[1], *Aleš Nagode*[1], *Maja Pogačar*[1] *and Milan Bizjak*[1]**

1) University of Ljubljana, Faculty of Natural Sciences and Engineering, Aškerčeva 12, 1000 Ljubljana, Slovenia

Corresponding author: matija.zorc@ntf.uni-lj.si

Professional article

Abstract: In this research, we tested the corrosion resistance of additively manufactured Ti6Al4V samples using potentiodynamic measurements in Hank's solution. Two sets of manufacturing parameters were used and two cylindrical specimens produced using each set. The laser power was kept at 200 W in both cases, while the scanning speed was set at 400 mm/s and 1000 mm/s, respectively. It was found that both samples exhibited surface passivation. The passive layer was not broken down under the experimental conditions (Hank's solution (pH = 7.8), room temperature and a potential sweep of 1 mV/s). It was found that the corrosion resistance was practically the same in all four samples. From the results, we conclude that the additive manufacturing parameters do not fundamentally affect the corrosion resistance.

Keywords: *potentiodynamic measurements; additive manufacturing; selective laser melting; Ti6Al4V alloy; corrosion resistance*

1. Introduction

Ti6Al4V or Ti64 is the best known (α+β) titanium alloy and is widely used in aerospace and medical applications due to its relatively low density, high strength, high fracture toughness, good corrosion resistance and biocompatibility. The alloy was developed in the USA in the early 1950s. Ti6Al4V alloys contain a maximum of 15 wt.% β-phase. More than 50 % of all titanium alloys used today fall into this group. Table 1 shows the chemical composition of the Ti6Al4V alloy [1], [2], [3].

Table 5. *Chemical composition of Ti6Al4V alloy in wt.%*

V	Al	Fe	C	N	O	H	Ti
3.5–4.5	5.5–6.5	≤ 0.25	≤ 0.08	≤ 0.05	≤ 0.13	≤ 0.015	rest

Casting, forming and machining of titanium alloys is very challenging. This leads to higher manufacturing costs and thus higher prices for the end products. As an alternative, additive manufacturing (AM) is now considered one of the most promising technologies for metallic materials, as it can produce complex geometries with high density and accuracy in a short time.

Potentiodynamic polarisation is one of the most commonly used DC electrochemical methods in corrosion measurements. A wide range of potentials is applied to the test electrode. This causes oxidation or reduction reaction at the metal surface, which generates a corresponding current. Potentiodynamic measurements are a destructive method. The gradual increase of the potential towards the positive values reduces the thermodynamic stability of the material, which is reflected in an increase of the corrosion current. Thus a diagram is obtained, showing the material properties in a used medium (Figure 1). The shape of the anodic part of the curve can be used to predict corrosion resistance and passivation. From the cathodic part and the upper anodic part of the curve, the corrosion rate and polarisation resistance can be calculated. Anodic potentiodynamic polarisation is suitable for determining the corrosion resistance of metals that undergo passivation. In other cases, the Tafel method is more suitable [4], [5], [6].

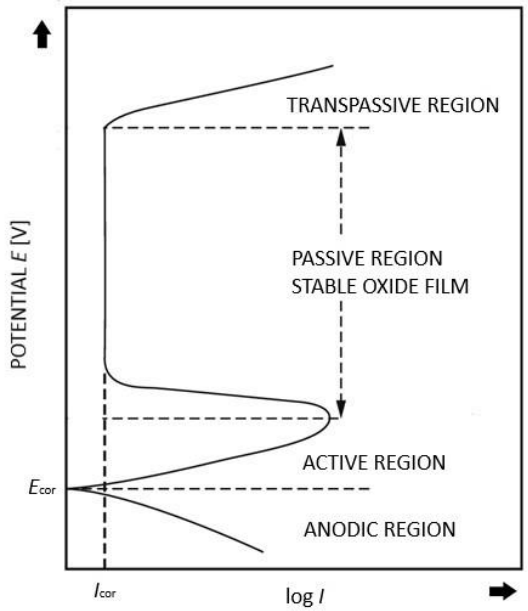

Figure 19. *An example of potentiodynamic polarisation curve [7]*

The Tafel method (Figure 2) is used to determine the corrosion rate of metals, in which there is a constant corrosion rate. The range around the corrosion potential values of ± 250 mV is called the Tafel range. Here the measurements can be made to determine the corrosion parameters that can later be used to calculate the corrosion rate [5], [8], [9].

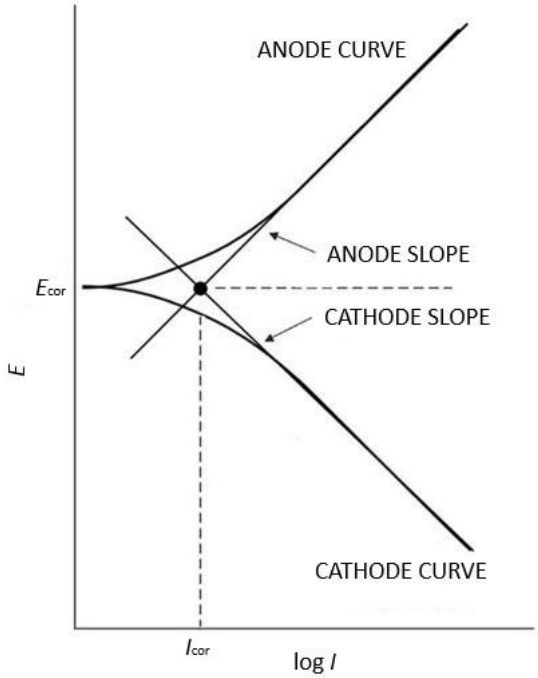

Figure 20. *Potentiodynamic measurement with Tafel tangent lines* [10]

2. Methods and materials

Before the samples were prepared, the powder was analysed to confirm its suitability for the experiments. Fluidity of the powder was measured according to the ASTM B213 standard, apparent density according to the ASTM B212 standard, the angle of repose according to the ASTM C1444 standard and the tap density according to the ASTM B527 standard. The Ti6Al4V samples were

modelled in Solidworks and printed using the Aconity3D MINI printer (Figure 3) at the Institute for Materials and Technology in Ljubljana. They were produced at two different scanning speeds, while the other parameters were kept at fixed values. The laser power was set to 200 W, the layer thickness to 30 µm, the hatch spacing to 30 µm and laser beam diameter to 60 µm. The parameters are listed in Table 2. The microstructures of the samples were checked with the light microscope ZEISS Imager Z2m before the potentiodynamic measurements. The samples were metallographically prepared by grinding with SiC papers and polishing with a diamond paste.

Figure 21. *Aconity3D MINI*

Table 6. *Parameters used during experimental work*

Sample	Laser power *P* [W]	Scanning speed *v* [mm/s]	Layer thickness *t* [µm]	Hatch spacing *H* [µm]	Laser beam diameter *d* [µm]
MP200/400	200	400	30	30	60
MP200/1000	200	1000	30	30	60

The samples for the potentiodynamic measurements were 5 mm high cylinders with a diameter of 15 mm. The surface of the samples was ground and polished before the experiments. Due to the large variations in current density, the measurements are presented as potential as a function of the logarithm of the current density *E*(V)-log *I*. Experiments were performed in Hank's solution (8 g/L NaCl, 0.40 g/L KCl, 0.35 g/L $NaHCO_3$, 0.25 g/L $NaH_2PO_4 \times 2H_2O$, 0.06 g/L $Na_2HPO_4 \times 2H_2O$, 0.19 g/L $CaCl_2 \times 2H_2O$, 0.41 g/L $MgCl_2 \times 6H_2O$, 0.06 g/L $MgSO_4 \times 7H_2O$, 1 g/L glucose) at pH = 7.8 and room temperature. The corrosion cell was connected to the BioLogic SP-300 potentiostat. EC-Lab V11.27 software was used to record the results. The results were recorded up to a potential of 2.5 V in the first case and up to 1 V in the other cases. A three-electrode system was used, the working electrode being the sample, the reference electrode a saturated calomel electrode and the counter electrode a platinum mesh. The corrosion cell is shown in Figure 4.

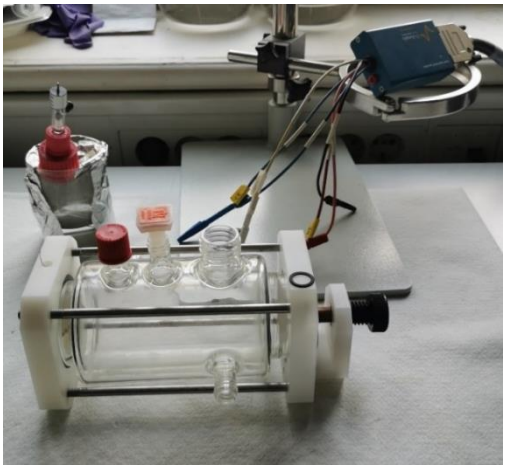

Figure 22. *The corrosion cell with electrodes*

3. Results and discussion

The microstructure of both samples consists of martensite α', which has grown from the grain boundaries of elongated columnar β grains. These are oriented in the building direction. With higher scanning speed, the columnar β grains become thinner (Figure 5).

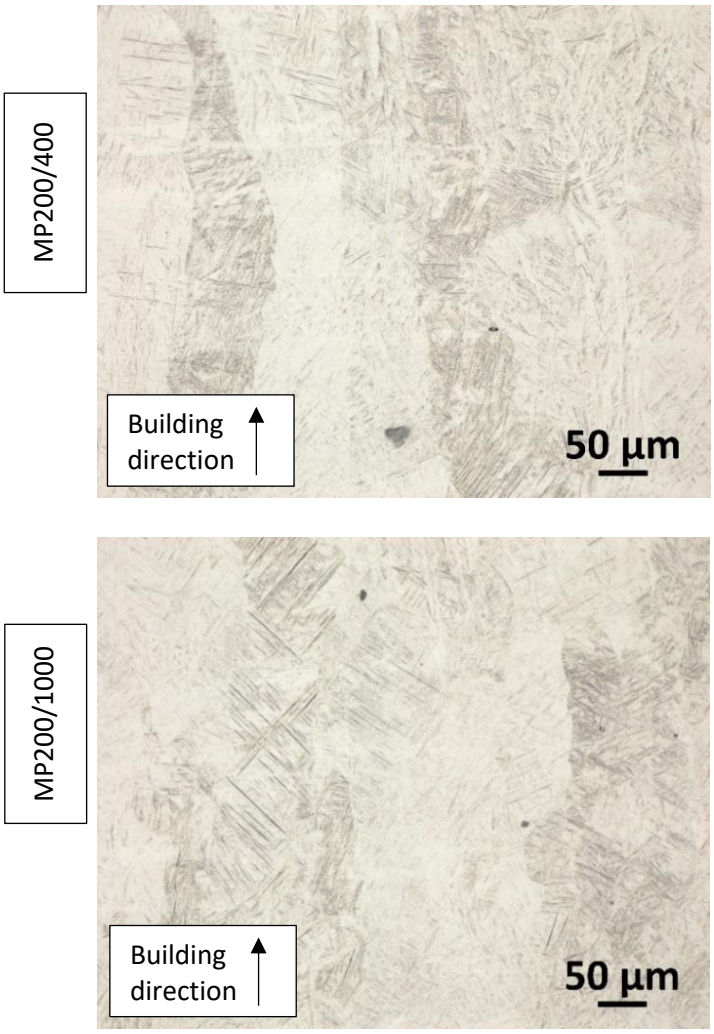

Figure 23. *Microstructures in samples produced with chosen parameters - optical microscope*

Figure 6 and Table 3 show the results of the potentiodynamic measurements for MP200/400 and MP200/1000 samples. The first set of measurements was performed up to a potential of 2.5 V. Since the passive layer was not breached, the following experiments were performed up to a potential of 1 V or 0.8 V. Two measurements were made on each sample. Sample MP200/1000 has a slightly lower corrosion potential than MP200/400, with average values of –0.340 and –0.322, respectively. All samples indicate at the passivation. The most corrosion resistant sample is MP200/1000, as it has a lower corrosion current and consequently a lower corrosion rate.
If the samples were tested over a longer period of time, the passive layer would probably be broken at a certain voltage. If cyclic potentiodynamic polarisation were used, more information would be obtained about the mechanism of passivation, the breaking of the passive layer through the formation and enlargement of corrosion pits, and re-passivation.

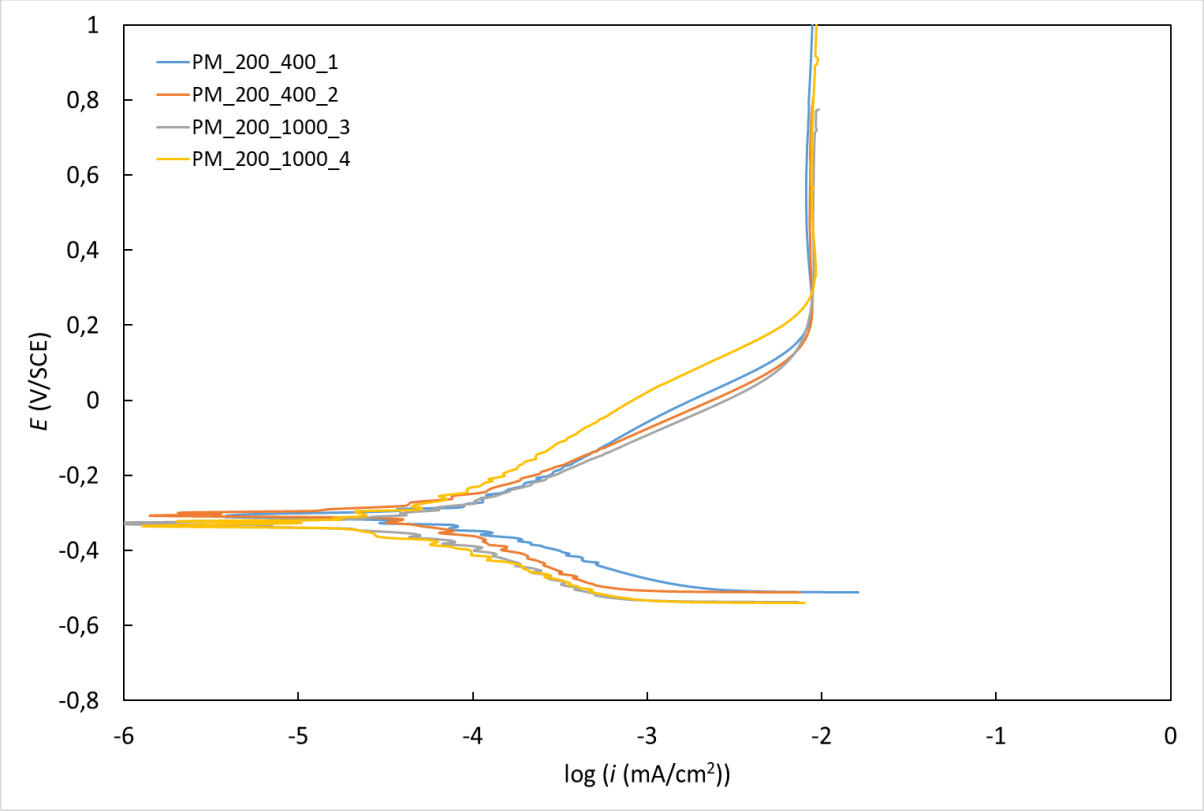

Figure 24. *Potentiodynamic measurements of MP200/400 and MP200/1000 samples in Hank's solution at room temperature*

Table 7. *The results of the potentiodynamic measurements of MP200/400 and MP200/1000 samples*

Sample	E_{cor} [V]	I_{cor} [µA]	*CR* (µm/year)
MP200/400 1	–0.332	0.069	0.606
MP200/400 2	–0.312	0.050	0.439
Average	–0.322	0.059	0.523
MP200/1000 1	–0.337	0.052	0.457
MP200/1000 2	–0.339	0.032	0.281
Average	–0.340	0.042	0.369

4. Conslusions

Samples from Ti6Al4V alloy powder were produced using the SLM method. The laser power was kept at 200 W, while the scanning speeds were 400 mm/s (MP200/400) and 1000 mm/s (MP200/1000). Based on the metallographic analysis and potentiodynamic measurements performed, it can be concluded:

- The microstructure of the Ti6Al4V samples consists of α' needles, which grow from the grain boundaries of prior columnar β grains. The width of the β grains depends on the scanning speed.
- The MP200/1000 sample has a slightly lower corrosion potential than MP200/400.
- The corrosion current is lowest for sample MP200/1000 2 at 0.032 µA and highest for sample MP200/400 1 at 0.069 µA.
- The average corrosion rate of the MP200/400 samples is 0.523 µm/year, while that of the MP200/1000 samples is 0.369 µm/year.
- The corrosion properties do not differ fundamentally between the samples.
- All samples underwent passivation. The passive layer was not broken through during the experiments.

References

[1] Gialanella, S., Malandruccolo, A., 2020. Aerospace alloys, Springer, Bolzano/Bozen, Italy.
[2] Herzog, D., Seyda, V., Wycisk, E., Emmelmann, C., 2016. Additive manufacturing of metals. Acta Materialia. 117, 371-392.
[3] Lui, S., C Shin, Y., 2019. Additive manufacturing of Ti6Al4V alloy : A review. Materials and Design. 164.
[4] Telegdi, J., Shaban, A., Vastag, G., 2018. Encyclopedia of Interfacial Chemistry, Elsevier, Amsterdam, Netherlands.
[5] Vehovar, L., 1991. Korozija kovin in korozijsko preskušanje, Samozaložba, Ljubljana, Slovenia.
[6] Pogačar, M., 2022. Izdelava in karakterizacija zlitine Ti6Al4V s postopkom selektivnega laserskega taljenja, Master’s thesis, Univerza v Ljubljani, NTF, Ljubljana, Slovenia.
[7] Duran, A., Castro, Y., Conde, A., De Damborenea, J.J., 2018. Handbook of sol-gel science and technology. Springer international publishing, Madrid, Spain.
[8] Stephen Tait, W., 2003. Using electrochemical measurements to estimate coating and polymer film durability. Journal of Coatings Technology. 75, 45-50.
[9] Stephen Tait, W., 1994. An introduction to electrochemical corrosion testing for practicing engineers and scientists, PairODocs Publications, University of Glasgow, Glasgow, UK.
[10] Palanisamy, G., 2019. Corrosion Inhibitors, IntechOpen, London, UK.

Analysis of abrasion and erosion resistance of hot-work tool steel and martensitic stainless steel with ticn coating applied by the PACVD process

***Matija Živoder*[1], *Suzana Jakovljević*[1], *Danko Ćorić*[1] *and Viktor Smrkulj*[1]**

(1) University of Zagreb, Faculty of Mechanical Engineering and Naval Architecture, Ivana Lučića 5, 10000 Zagreb, Croatia

Corresponding author: Matija.Zivoder@fsb.hr

Professional article

Abstract: Machine parts, and most commonly tools, are thermally coated with thin and very hard layers with the aim of increasing wear resistance, thus extending their service life. In this paper, two groups of steels were used to test the resistance to abrasive and erosive wear; hot-work tool steel - X37CrMoV5-1 and martensitic stainless steel - X22CrMoV12-1. At both groups of steel were applied PACVD single-layer non-oxide ceramic coating (TiCN) of different thicknesses (2 µm and 3 µm). The hot-work steel samples were previously additionally plasma nitrided. The testing was conducted using an abrasion and a erosion wear resistance testing apparatus, with dry quartz sand used as the abrasive. During both tests, the loss of sample mass were observed. It was shown that the thickness of the applied coating affects the wear resistance.

Keywords: *abrasion; erosion; TiCN; PACVD; steel*

1. Introduction

In some cases, it may not be possible or cost-effective to make constructional changes or change material in order to solve a wear problem. In those situations, different layers for wear protection may be a rational solution. However, choosing the most suitable method for applying layers or modifying the surface can be challenging due to the wide variety of different processes and methods available. In addition, the specific wear situation must also be taken into account. [1]. The most common form of material wear is an abrasion wear mechanism, which contributing 63% of the total wear-related costs, where a harder abrasive penetrates into a softer material surface. [2]. This study investigates the influence of a single-layer TiCN coating on the abrasion and the erosion wear of hot-work tool steel X37CrMoV5-1 and stainless steel X22CrMoV12-1. The hard gradient multi-layer and single-layer titanium-based coatings are known for increasing the wear resistance of hot-work tool steel and stainless steel. [3], [4]. Plasma assisted chemical vapour deposition (PACVD) is a widely used method for producing coatings on metallic materials at deposition temperatures between 450 and 600 °C. Using PACVD, it is possible to produce the coatings in deposition vacuum chamber by combining the pretreatment of the substrate surface in terms of sputter cleaning and plasma nitriding before actual deposition of the coating. This technique results in the creation of a support zone for the coating and better adhesion between coating and substrate, such as hot – work tool steel, martensitic stainless steel and high-speed steel [5]. Compared to the physical vapour deposition (PVD) process, PACVD provides better homogeneity of the coating on pieces with more complex geometries. Also, tools coated with hard layers, such as TiN, TiCN, TiC, have already been successfully applied in industrial use. [6] In this article the single-layer non-oxide ceramic TiCN coating was applied on to stainless steel samples - X22CrMoV12-1, using the PACVD process. The TiCN coating was also applied on to samples of hot-work tool steel - X37CrMoV5-1, but they were previously plasma nitrated. After the application of the coating, the samples were tested in terms of abrasion and erosion wear conditions. The change in the mass of samples was measured. Also, the surface of the samples was examined using a optical microscope and the wear tracks were analyzed in order to determine the durability of the coating.

2. Materials and methods

The samples used for testing were hot - work tool steels - X37CrMoV5-1 and martensitic stainless steels - X22CrMoV12-1. The chemical composition (wt.%) of those two substrates is shown in Table 1.

Table 1. *Chemical composition of substrate materials [6]*

Sample	%C	%P	%S	%Si	%Mn	%Cr	%Ni	%Mo	%V	%Fe
X22CrMoV12-1	0.25	0.017	0.008	0.4	0.65	12.08	0.64	0.95	0.63	rest
X37CrMoV5-1	0.37	0,015	0,013	0.1	0.4	5.2	/	1.2	0.4	rest

Before PACVD process of coating deposition, all test samples were wet fine grinded with the various sandpaper gradations (the P320, P1000, P2000, and P4000 grit sandpaper) on a Buehler Phoenix Alpha machine. After grinding, the samples were mechanically polished on a Struers DAP-V machine. They were first polished with 9 µm diamond paste and after that with liquid silica with a particle granulation of 0,03 µm. To enhance adhesion X37CrMoV5-1 steel samples were plasma nitrided (PN) in an industrial Rübig PC 70/90 furnace as a pretreatment process of PACVD process. X22CrMoV12-1 stainless steel samples were not nitrided before plasma-assisted chemical vapor deposition. Both steel samples (hot - work tool steels and martensitic stainless steels) were coated with the gradient multilayer TiCN coating in the same Rübig PC 70/90 furnace. Two different thickness were deposited, 2 µm and 3 µm. Parameters of plasma nitriding are given in Table 2. Parameters of PACVD deposition of TiCN coating on the samples are given in Table 3 (for thickness of 2 µm) and in Table 4 (for thickness of 3 µm).

Table 2. *Process parameters of plasma nitriding*

Process parameters	**Cleaning - dusting**	**Nitriding**
Temperature	420 - 500°C	500 °C
Time	2 h	6 h
Flow rate H_2	200 l/h	190 l/h
Flow rate N_2	20 l/h	10 l/h
Flow rate Ar	10 l/h	10 l/h
Composition of gases	4% Ar, 9% N_2, 87% H_2	5% Ar, 5% N_2, 90% H_2
Plasma power	1000 W	1000 W
Voltage	540 V	560 V
Pressure	2 mbar	2 mbar

Table 3. *Parameters of PACVD process TiCN coating 2 µm*

Step	**1**	**2**	**3**	**4**	**5**	**6**
Step description	**Heating**	**Cleaning**	**TiN**	**Transition TiN→TiCN**	**TiCN**	**Cooling/ rinsing**
Duration [h]	1.5	2	1.5	0.5	3	1
Pressure [mbar]	2	2	2	2	2	2
Temperature [°C]	420	420→500	500	500	500	500→20
H_2 [l/h]	140	140	140	140	140	100
Ar [l/h]	0	10	10	10	10	-
CH_4 [l/h]	-	-	-	0→4.5	4.5	-
$TiCl_4$ [l/h]	-	-	3	3	3	-
N_2 [l/h]	-	23	15	15→13	13	-
Pulsating N_2	-	-	12s/12s	12s/12s	12s/12s	-
Voltage [V]	-	520→540	490	490	490	-
Plasma power [W]	-	900→1800	1650	1400	1400	-

Table 4. *Parameters of PACVD process TiCN coating 3 µm*

Step	**1**	**2**	**3**	**4**	**5**	**6**
Step description	**Heating**	**Cleaning**	**TiN**	**Transition TiN→TiCN**	**TiCN**	**Cooling/ rinsing**
Duration [h]	1.5	2	1.5	0.5	5.5	1
Pressure [mbar]	2	2	2	2	2	2
Temperature [°C]	420	420→500	500	500	500	500→20
H_2 [l/h]	140	140	140	140	140	100
Ar [l/h]	0	10	10	10	10	-
CH_4 [l/h]	-	-	-	0→4.5	4.5	-
$TiCl_4$ [l/h]	-	-	3	3	3	-
N_2 [l/h]	-	23	15	15→13	13	-
Pulsating N_2	-	-	12s/12s	12s/12s	12s/12s	-
Voltage [V]	-	520→540	490	490	490	-
Plasma power [W]	-	900→1800	1650	1400	1400	-

The list of a test samples with labels, material and coating thickness is shown in Table 5.

Table 5. *List of samples*

Label	Sample
B00	X37CrMoV5-1 + PN+TiCN 2 µm
B01	X37CrMoV5-1 + PN+TiCN 3 µm
MS00	X22CrMoV12-1 + TiCN 2 µm
MS01	X22CrMoV12-1 + TiCN 3 µm

Abrasion wear resistance were tested using the “Dry sand - Rubber wheel” method according to the ASTM G 65 standard with normal load of 45 N. Quartz sand particles Otawa AFS 50/70 were abrasive. Samples were produced in dimensions 12x25x75 mm, Figure 1, in both group (TiCN coating/ steel substrate). The mass of the samples was weighed before and after abrasion test with a defined number of revolutions (20, 50 and 70 revolutions). After each test cycle, the samples were cleaned in an ultrasonic bath and were weighed on a METTLER TOLEDO device. Parameters of " Dry sand - Rubber wheel" are given in Table 6.

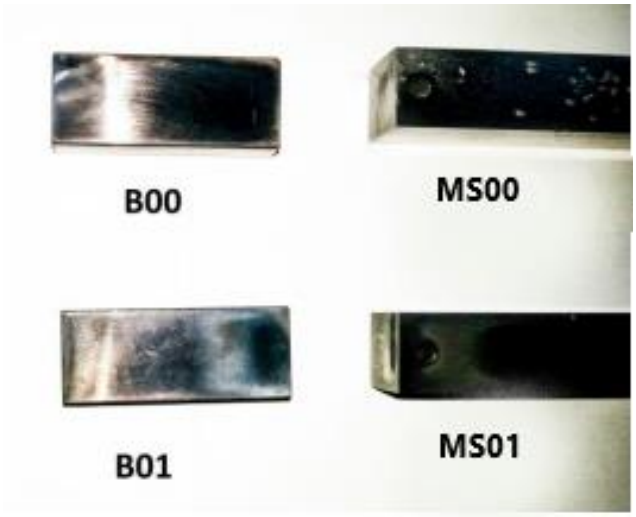

Figure 1. *Samples for abrasion wear test*

Table 6. *Parameters of "dry sand rubber wheel"*

Wheel rotation speed	200 ± 10 rpm
Load	45 N
Abrasive flow rate	250 - 400 g/min
Abrasive	quartz sand, granulation 0.063 - 0.315 mm

The erosion wear resistance test was performed in dry conditions at an angle of 90° between the sample and the erosion erodent. Erodent were quartz sand particles Otawa AFS 50/70. The test was carried out at intervals of 15 min and 30 min. Samples were produced in dimensions 17 × 17 × 17 mm, in both group (TiCN coating/ steel substrate), Figure 2. The mass of the samples was weighed in the same way as in the abrasive wear test, at the beginning and after each defined time interval of the test. The test parameters are presented in Table 7.

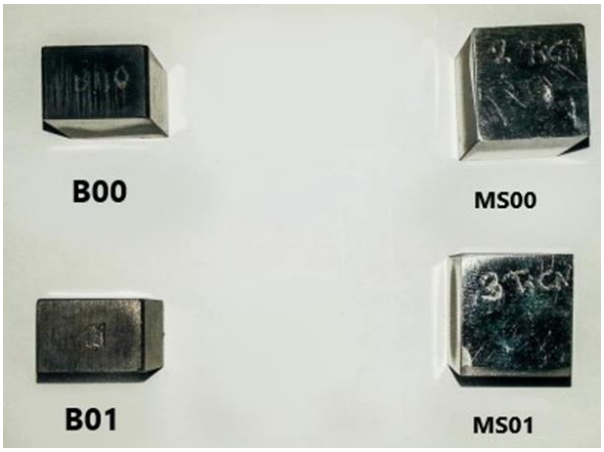

Figure 2. *Samples for erosion wear resistance testing*

Table 7. *Parameters of erosion testing*

Rotation speed	1440 rpm
Erodent impact angle	90°
Test duration	15 and 30 min
Erodent flow rate	3.0 g/s
Sample speed	24.265 m/s
Erodent	quartz sand, granulation 0.063 – 0.315 mm

Wear tracks were examined using a optical microscope ''Leica MZ6'' and analysis were always carried out on the same wear trace.

3. Results

In Table 8 is shown the measured mass of the samples after the abrasion test as a function of the number of revolutions, while Table 9 shows the change in the mass of the samples after the abrasion test. In Table 10 is shown the mass of the samples after the erosion test in dry conditions, while Table 11 shows the change in the mass of samples after the erosion test. A graphic representation of mass loss of samples is also given in Figures 3 and 4.

Table 8. *Results of measuring the mass of samples after the abrasion test*

Sample	Initial mass *m* [g]	*m* [g] (after 20 rev)	*m* [g] (after 50 rev)	*m* [g] (after 70 rev)
B00	74.7269	74.7265	74.7253	74.7249
B01	76.0569	76.0550	76.0540	76.0533
MS00	165.8789	165.8780	165.8770	165.8762
MS01	164.9572	164.9548	164.9535	164.9533

Table 9. *Change in the mass of samples after the abrasion test*

Sample	Δ*m* [mg] (after 20 rev)	Δ*m* [mg] (after 50 rev)	Δ*m* [mg] (after 70 rev)
B00	0.4	1.6	2.0
B01	1.9	2.9	3.6
MS00	0.9	1.9	2.7
MS01	2.4	3.7	3.9

Table 10. *Results of measuring the mass of samples after the erosion test*

Sample	Initial mass *m* [g]	*m* [g] (after 15 min)	*m* [g] (after 30 min)
B00	21.6905	21.6876	21.6868
B01	21.8497	21.8469	21.8462
MS00	39.2458	39.2438	39.2415
MS01	40.7825	40.7790	40.7772

Table 11. *Change in the mass of samples after the erosion test*

Sample	Δ*m* [mg] (after 15 min)	Δ*m* [mg] (after 30 min)
B00	2.9	3.7
B01	2.8	3.5
MS00	2.0	4.3
MS01	3.5	5.3

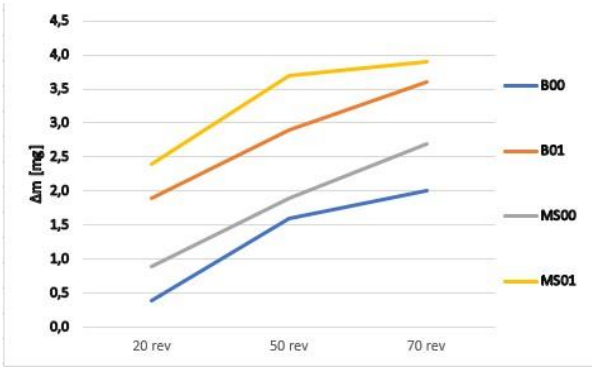

Figure 3. *Graphic representation of the change in the mass of samples after abrasive wear test*

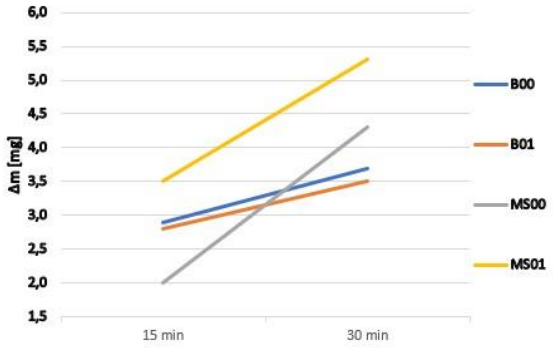

Figure 4. *Graphic representation of the change in the mass of samples after erosive wear test*

Along with the change in the mass of the samples, wear tracks on the samples were also analyzed after the test. Places marked as wear tracks represent places where the coating has not been penetrated, while places marked as substrate indicate places where the coating has been completely

worn out. Figure 5 shows the damage of the samples during the abrasion test and Figure 6 shows the damage on to the samples during the erosion test.

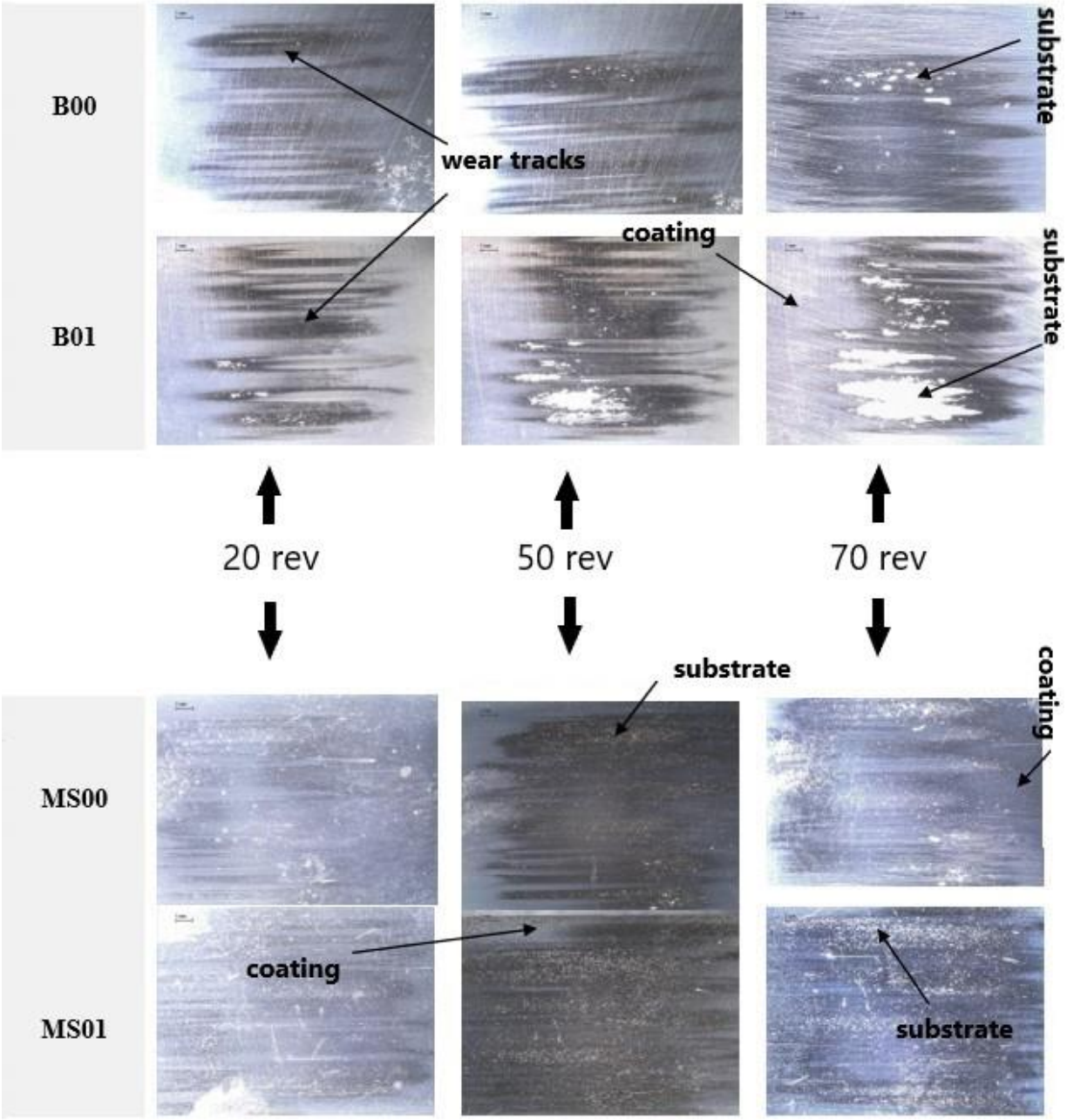

Figure 5. *Abrasion wear tracks*

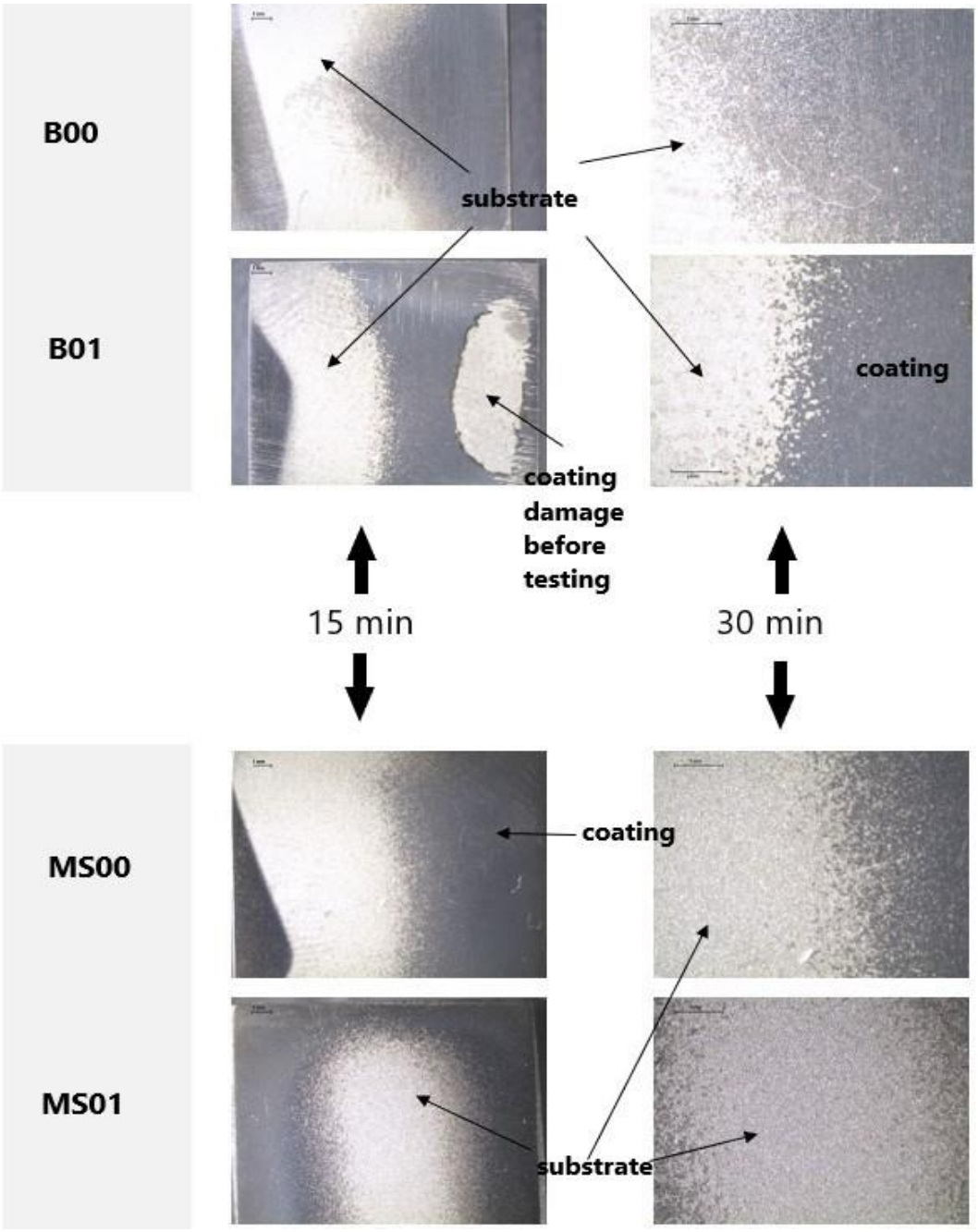

Figure 6. *Erosion wear tracks*

On both types of steel, it was shown that a coating with a thickness of 2 µm has better abrasion and erosion resistant compared to a coating with a thickness of 3 µm. The previous plasma nitriding of hot – work tool steel has also proven to be advantageous because, overall, there is less mass loss during erosive wear and abrasive wear, for the same thickness of the TiCN coating. The wear track analysis follow these conclusions and shows that during the abrasive wear of sample B00, the coating was not penetrated after 20 revolutions. Supstrate of sample B00 was visible after 50 revolutions while at all other samples, the supstrate was visible after 20 revolutions. The erosion wear track analysis show that the coating was worn out in all samples after interval of 15 minutes of erosion testing. After erosion interval testing of 30 minutes the wear tracks were larger, which is directly related to greater mass loss. The lowest total mass loss of samples is for samples B00 and B01. Sample MS00 has the lowest mass loss after an interval of 15 min. After it, more intense wear occurs, so the total mass loss after an interval of 30 minutes is greater than for samples B00 and B01. The highest mass loss, in both erosion intervals, has sample MS01.

In the abrasion wear test, samples coated with a thinner coating (B00 and MS00) show less mass loss, which means that they have better abrasion wear resistant. In the erosion wear test, samples that were previously plasma nitrited (B00 and B01) show less wear compared to the others.
It is assumed that the coatings have imperfections in the form of microclusters and microcracks. Such imperfections during wear are “bad spots” that lead to faster wear of the coating. Such wear situations are more pronounced with larger thicknesses of thin hard coatings. To confirm this assumption, it is necessary to make an SEM analysis of the coating surface.

4. Conclusion

In this article, two different thicknesses of PACVD TiCN coating on hot – work tool steel and martensitic steel were examined. After the abrasion and erosion tests, it can be concluded that:

- TiCN coatings on tool steel have better abrasion wear resistance with both coating thicknesses, (2 µm and 3 µm,)
- both TiCN coating thicknesses (2 µm and 3 µm) on the hot – work tool steel have the highest overall erosion wear resistance, which indicate to the positive influence of prior nitriding before the coating process.

References

[1] Filetin, T., Grilec K., 2004. Postupci modificiranja i prevlačenja površina – Priručnik za primjenu, Sveučilište u Zagrebu, FSB, Zagreb.
[2] Ren, X., Peng, Z., Hu, Y., Wang, C., Fu, Z., Yue, W., Qi, L., Miao, H., 2013. Abrasive wear behavior of TiCN cermets under water-based slurries with different abrasives. Tribology International. 66, 35 – 43.
[3] Chen, W.-C., Liu, X.-D., 2000. Study on the various coated twist drills for stainless steels drilling. Journal of Materials Processing Technology. 99, 226 – 330.
[4] Kovačić, S., Cajner, F., Landek, D., 2016. Influence of steel substrate on the properties of PACVD gradient multilayer TiCN coating, 3rd Mediterranean Conference on Heat Treatment and Surface Engineering 2016., Portorož, Slovenija.
[5] Landek, D., Jakovljević, S., Alar, V., Kovačić, S., 2019. Effect of steel substrate on the corrosion properties of a gradient multilayer TiN/TiCN coating deposited by the PACVD process. Materials and Corrosion. 70, 307 – 318.
[6] Shafiei, S.M.M., Divandari, M., Boutorabi, S.M.A., Naghizadeh, R., 2014. Materials Research. 17, 1651 – 1657.

Determination and Comparison of Stress Depending on the Diameter of the Extrusion Disc and the Type of Various Food Based Filling

***Mirna Tadić*[1], *Goran Bosanac*[1], *Mario Božić*[2], *Damir Ježek*[1] *and Mladen Brnčić*[1]**

(1) Faculty of Food Technology and Biotechnology, University of Zagreb, Pierottijeva 6, Zagreb, Croatia

(2) Procesteh d.o.o., Ulica Kreše Golika 3, Zagreb, Croatia

Corresponding author: mbrncic@pbf.hr

Abstract

Abstract: The assessment of textural/mechanical properties, in conjunction with other product attributes, provides information to food companies which enables them to make informed decisions about their products and the machines the use. Textural (mechanical) properties of six different foodstuff fillings (chocolate, vanilla, apple, apricot, cherry and strudel) were studied in this work by using the Texture Analyser, using the device’s official Exponent software ("Comparison of spreadability/firmness of two margarine types by the ability to extrude through a 3 mm hole"). Depending on the texture of the sample, only the diameter of the extrusion disc was changed. From the extrusion forces (defined as firmness in food engineering terminology) and the diameters of the extrusion discs, the average, maximum and minimum stresses were calculated. In addition, from the graphs, the work required for the extrusion of the sample was read, and then the required extrusion power was calculated. The relation between the extrusion force, the diameter of the extrusion disc and the stress in the extrusion disc should be noticed: for example, the maximum forces are by far the highest in apple filling because of the non-homogeneous material, but given the (larger) 10 mm extrusion disc diameter, the stresses are not that high. On the other hand, vanilla filling has several times lesser force because of the homogeneous material, but due to the (three times smaller) 3 mm extrusion disc diameter, the stresses in the extrusion disc are higher than in apple filling. Stresses in the extrusion disc are important due to the wear of the extrusion disc material, and even more so due to the condition of the sample at the exit of the extrusion disc. If the stress in the extrusion disc is too high, then the sample does not flow smoothly at the exit of the extrusion disc. Instead, small cracks appear on the surface of the sample or sample cracks completely and leaks intermittently. Stresses in the extrusion disc can be reduced by increasing the diameter of the extrusion disc or by reducing the extrusion force, which means by reducing the extrusion speed. Work and power are important from a technological point of view for the purpose of choosing an appropriate extrusion machine.

Keywords: *texture analysis; extrusion; stress; power; fillings*

Acknowledgments

This work was supported by the project "Increasing the development of new products and services arising from research and development activities - phase II\": Development of innovative products to increase food quality \"- KK.01.2.1.02.0282.

Split

Tourist Board of Split

TURISTIČKA ZAJEDNICA


EVN
Zemni plin. Komfor. Budućnost.
Priključite se
ugodnijoj budućnosti.
evn.hr